Biological and Medical Physics, Biomedical Engineering

Muhammad Maqbool *Editor*

An Introduction to Medical Physics

Springer

Biological and Medical Physics, Biomedical Engineering

More information about this series at http://www.springer.com/series/3740

BIOLOGICAL AND MEDICAL PHYSICS, BIOMEDICAL ENGINEERING

The fields of biological and medical physics and biomedical engineering are broad, multidisciplinary and dynamic. They lie at the crossroads of frontier research in physics, biology, chemistry, and medicine. The Biological and Medical Physics, Biomedical Engineering Series is intended to be comprehensive, covering a broad range of topics important to the study of the physical, chemical and biological sciences. Its goal is to provide scientists and engineers with textbooks, monographs, and reference works to address the growing need for information.

Books in the series emphasize established and emergent areas of science includingmolecular,membrane, and mathematical biophysics; photosynthetic energy harvesting and conversion; information processing; physical principles of genetics; sensory communications; automata networks, neural networks, and cellular automata. Equally important will be coverage of applied aspects of biological and medical physics and biomedical engineering such as molecular electronic components and devices, biosensors, medicine, imaging, physical principles of renewable energy production, advanced prostheses, and environmental control and engineering.

Muhammad Maqbool
Editor

An Introduction to Medical Physics

Springer

Editor
Muhammad Maqbool
Department of Clinical and Diagnostic Sciences
Health Physics Program
The University of Alabama at Birmingham
Birmingham, AL, USA

ISSN 1618-7210 ISSN 2197-5647 (electronic)
ISBN 978-3-319-61538-7 ISBN 978-3-319-61540-0 (eBook)
DOI 10.1007/978-3-319-61540-0

Library of Congress Control Number: 2017954503

Printed on acid-free paper

This Springer imprint is published by Springer Nature
The registered company is Springer International Publishing AG
The registered company address is: Gewerbestrasse 11, 6330 Cham, Switzerland

This book is dedicated to my late brother Muhammad Zahir. He is not just my brother but was my great friend too. We have spent our childhood together full of fun and enjoyment. He died during an open heart surgery on July 4, 2015. That was the most shocking day of my life. I still miss him a lot and I pray to Allah (God) to bless his soul and give him the highest place in paradise along with my parents.

Preface

In the name of Allah, the Most Beneficent, the Most Merciful.

I am very thankful to Allah Almighty for giving me the skills, the ability, and the courage to complete this task.

Medical physics is one of the fast-growing fields around the world in general and in the USA in particular. Diagnosing and treating cancer using radiation has widely been used successfully. Considerable research and investigations have also been done in medical physics to provide the best possible treatment to patients. Due to the high demand of this field, many undergraduate-level programs in medical physics have also been developed, and more are developing along with graduate programs in many universities. Most of the textbooks used in those programs are graduate level. Very little undergraduate-level material is present in this field. The purpose of this book is to explain the concepts of medical physics and highlight the use of physics in medicine and biology on a junior/senior undergraduate level. This book is written on a level where it can be used for undergraduate students, but at the same time graduate students and professional clinical physicists can also take help from this book. Discussing each concept in a simple way and providing solved example in fundamental chapters is one of the unique aspects of this book.

Well-known authors and experts of their fields have contributed to this book from the USA and abroad. I am very thankful to all authors who contributed their valuable ideas to flourish the beauty and depth of the subject discussed in this book.

I am very thankful to Chris Laughlin and the Springer publishers who helped and cooperated to achieve this astonishing goal.

Birmingham, AL, USA — Muhammad Maqbool, PhD

Contents

1 Introduction 1
Muhammad Maqbool

2 Basic Concepts in Radiation Dosimetry 9
Wazir Muhammad, Amjad Hussain, and Muhammad Maqbool

3 Interaction of Gamma Rays and X-Rays with Matter 43
Muhammad Maqbool

4 Treatment Planning in Radiation Therapy 63
Amjad Hussain and Wazir Muhammad

5 Image-Guided Radiation Therapy 131
X. Sharon Qi

6 Introduction to Radiological Images 175
Sikander M. Mirza

7 Mammography 199
Bing Ma

8 Computed Tomography 221
Muhammad Maqbool

9 Magnetic Resonance Imaging (MRI) 263
Steffen Sammet

10 CT and MRI in Radiotherapy 281
Minsong Cao

11 Nuclear Medicine Physics 301
Jianqiao Luo and Muhammad Maqbool

12 Ultrasound 329
James R. Costello, Hina Arif, Bobby Kalb, and Diego R. Martin

13 Radiation Shielding and Protection, Part I: Measurement, Dosimetry, Shielding, and Protection 371
Christopher J. Watchman

14 Radiation Shielding and Protection, Part II 403
Jianqiao Luo

Erratum to: An Introduction to Medical Physics E1

The original version of this book was revised. An erratum to this book can be found at https://doi.org/10.1007/978-3-319-61540-0_15

Contributors

Hina Arif, MD Department of Medical Imaging, University of Arizona, Tucson, AZ, USA

Minsong Cao, PhD Department of Radiation Oncology, University of California at Los Angeles, Los Angeles, CA, USA

James R. Costello, MD, PhD Department of Medical Imaging, University of Arizona, Tucson, AZ, USA

Radiology Associates of Macon, PC, Macon, GA, USA

Amjad Hussain, PhD, MCCPM Radiation Oncology, Western Manitoba Cancer Centre, Brandon, MB, Canada

Bobby Kalb, MD Department of Medical Imaging, University of Arizona, Tucson, AZ, USA

Jianqiao Luo, PhD Department of Radiology, Virginia Commonwealth University, Richmond, VA, USA

Bing Ma, PhD Department of Health Physics and Diagnostic Sciences, University of Nevada, Los Vegas, NV, USA

Muhammad Maqbool, PhD Department of Clinical and Diagnostic Sciences, Health Physics Program, The University of Alabama at Birmingham, Birmingham, AL, USA

Diego R. Martin, MD, PhD, FRCPC Department of Medical Imaging, University of Arizona, Tucson, AZ, USA

Sikander M. Mirza, PhD Department of Physics & Applied Mathematics, Pakistan Institute of Engineering & Applied Sciences, Nilore, Islamabad, Pakistan

Wazir Muhammad, PhD Department of Therapeutic Radiology, Yale University School of Medicine, New Haven, CT, USA

Steffen Sammet, MD, PhD, DABR, DABMRS, FAMP University of Chicago Medical Center, Department of Radiology, Chicago, IL, USA

X. Sharon Qi, PhD Department of Radiation Oncology, University of California at Los Angeles, Los Angeles, CA, USA

Christopher J. Watchman, PhD, DABR Department of Radiation Oncology, University of Arizona, Tucson, AZ, USA

Chapter 1
Introduction

Muhammad Maqbool

Contents

1.1 Background 1
References 8

1.1 Background

The branch of physics that concerns the applications of physics to medicine is called medical physics. The discovery of x-rays by Wilhelm Conrad Roentgen in 1895 brought a revolution in the fields of science and medicine and has opened a path to a new interdisciplinary branch medical physics. In fact, the first x-ray photograph was made by Roentgen himself in late 1895, within about a month of his discovery. Physicians on both sides of the Atlantic were routinely using x-rays in diagnostic radiography within a year (Ahmad 1999 and Grupen 2010). This set a record for the rapid adoption of a new technology in practical applications. Today medical physics has become a very broad area, and it is considered as a separate field of studies. Medical physics is an applied physics that uses the principles of physics in more practical problems of diagnosing and treating abnormal tissues. Radiations are generally used for both diagnoses and treatment purposes. The birth and spread of abnormal tissues or a tumor have been a major problem human beings face. Cancer is considered as the second major cause of death in the world after heart attack. The major work of a medical physicist is to diagnose and treat a tumor or cancer. It can be classified in a number of subfields or specialties. The branch of medical physics that deals with the treatment of abnormal tissues or a tumor is called therapeutic medical physics. Though treating cancer is very important but if it is not diagnosed in its early stages, then the spread of tumor makes it impossible to treat. Therefore, along with its treatment, it is equally important to diagnose a tumor in its early stages. The subspecialty of medical

M. Maqbool, PhD (✉)
Department of Clinical and Diagnostic Sciences, Health Physics Program, The University of Alabama at Birmingham, Birmingham, AL 35294, USA
e-mail: mmaqbool@uab.edu

M. Maqbool (ed.), *An Introduction to Medical Physics*, Biological and Medical Physics, Biomedical Engineering, DOI 10.1007/978-3-319-61540-0_1

physics that handles the diagnoses of a tumor or abnormal tissues is called diagnostic imaging physics. It is also possible that a tumor be diagnosed and treated using radiopharmaceuticals instead of treating or diagnosing externally. This area of medical physics is referred as nuclear medicine. No matter it is the diagnoses of abnormal tissues or the treatment of a tumor but saving and providing minimum possible damage to the normal tissues is the top priority of a medical physicist. This branch of medical physics concerns with the saving and protection of normal tissues from the hazardous effects of radiation and is called radiation protection or medical health physics. In all branches of medical physics it is, mainly, the radiation used to diagnose or treat an abnormal tissue or cells (Ahmad 1999 and Grupen 2010).

1.1.1 Classification of Radiation

Radiations are generally classified into two categories: ionizing radiation and non-ionizing radiation. Ionizing radiations are those radiations that can ionize an atom by ejecting one or more orbital electrons from the atom leaving behind a positively charged ion. The energy of ionizing radiation is big enough to overcome the binding energy of the electron in an atom and knock it out. Alpha (α) rays, beta (β) rays, gamma (γ) rays, and protons are examples of ionizing radiation (Ahmad 1999; Grupen 2010; Hendee et al. 2005). A nucleus or an element that emits these radiations is called parent nucleus or parent element, and the newly produced nucleus as a result of the emission of radiation is called daughter nucleus. Non-ionizing radiations do not have the ability to knock out an electron from atom to ionize it. Ultrasound waves and microwaves are examples of non-ionizing radiation.

Ionizing radiations are further divided into two types: directly ionizing radiations and indirectly ionizing radiations.

Directly ionizing radiations are that kind of ionizing radiations that impart their energy to matter directly, through many small electrostatic interactions along the track of the radiation. For example, α-particle, a directly ionizing radiation, ionizes matter directly upon interaction.

Indirectly ionizing radiations are that kind of radiations which first transfer their energy to charged particles in the matter through which they pass. Those charged particles then deliver the energy to the matter. Electromagnetic radiation (x-rays and γ-rays) and neutrons (uncharged particle) transfer their energy to electrons and protons inside matter first followed by the transfer of that energy to matter by those electrons and protons (Grupen 2010; Hunt 1983; Liu et al. 2006; Martin 2013; Prise et al. 1994).

1.1.2 Types of Ionizing Radiation

There are different types of ionizing radiation. Everyone has got its distinct characteristic properties and can be used in various applications. These radiations are emitted by unstable nuclei called radioactive nuclei or radioactive material, and the process is called radioactivity.

1.1.2.1 X-Rays

These are electromagnetic radiations emitted as a result of electrons jumping from higher-energy level into lower-energy level in an atom. X-rays emitted as a result of the electronic transitions inside an atom are called characteristic x-rays. On the other hand, slowing down of a fast-moving electron in an electrostatic field also results in the emission of electromagnetic radiation or x-rays called continuous x-rays or bremsstrahlung radiation. X-rays possess energy, frequency, wavelength, and linear momentum. The energy of an x-ray photon is related to its frequency, wavelength, and momentum by the following equations:

$$E = hf \tag{1.1}$$

$$E = hc/\lambda \tag{1.2}$$

$$E = pc \tag{1.3}$$

where "h" is the Planck's constant and its value in the International System or SI system is 6.626×10^{-34} J.s, "c" is the speed of light in vacuum or free space and its value in SI system is approximately 3×10^8 m/s, "f"' is the frequency, "λ" is the wavelength, and "p" is the linear momentum of an x-ray photon, respectively. X-rays are highly energetic radiation and could damage normal tissues if exposed. Therefore, in spite of their frequent and wide use in medicine, shielding of normal tissue is mandatory.

In practical applications in medicine, the energy of x-ray is usually given in terms of the generating voltage. The energy ranges of x-rays, in terms of the generating voltage, are given below (Ahmad 1999; Grupen 2010; Stagg et al. 2001):

- 0.1–20 kV Low-energy or soft x-rays
- 20–120 kV Diagnostic-range x-rays
- 120–300 kV Orthovoltage x-rays
- 300 kV–1 MV Intermediate-energy x-rays
- 1 MV and above Megavoltage x-rays

X-rays are frequently used in both therapeutic and diagnostic medical physics.

1.1.2.2 γ-Rays

Gamma rays are electromagnetic radiation emitted either from the nucleus of an atom or produced in annihilation process between matter and antimatter (e.g., electron and positron). When a γ-ray emits from the nucleus of an atom, it does not change the mass number or the charge number of the atom. The nature of γ-rays is exactly the same as x-rays. Both are electromagnetic radiation. In the old days, some people were relating the difference between a γ-ray and an x-ray to their energies and thought γ-rays are more energetic than x-rays. However, this concept is not true. The difference between the two kinds of radiations is based on their origin. X-rays originate as a result from electronic transitions inside an atom. On the other hand γ-rays originate from the nucleus of an atom. It is possible that in some cases, the energy of an x-ray photon may be higher than a γ-ray photon. For example, the energy of a megavoltage x-ray photon is higher than the energy of the highest-energy (1.33 MeV) γ-ray photon emitted from Co^{60}. In calculating energy, frequency, wavelength, or momentum of both kinds of radiation (x-rays and γ-rays), the same equations are used. Radioactive materials emitting γ-rays are widely used in nuclear medicine (Martin 2013; Prise et al. 1994; Stagg et al.2001).

Example 1 The frequency of a γ-ray photon is 2 × 1018 Hertz (Hz). Find the energy, wavelength, and linear momentum of this photon.

Solution Frequency of the γ-ray photon = f = 2×10^{18} Hz.
(a) Energy = E =? (b) Wavelength = λ =? (c) Momentum = p =?

(a) Using Eq. (1.1), $E = hf = 6.626 \times 10^{-34} \times 2 \times 10^{18}$
$= 1.3252 \times 10^{-15}\text{Joule(J)}$.
To write the answer in electron volts,
1 electronvolt (eV) = 1.6×10^{-19}J,
$1\text{J} = 1/\left(1.6 \times 10^{-19}\right)\text{eV}$.
Therefore,
$1.3252 \times 10^{-15}\text{J} = \left(1.3252 \times 10^{-15}\right)/\left(1.6 \times 10^{-19}\right)$
$= 8.282 \times 10^{3}\text{eV}$
$= 8.282\ \text{keV}$

Thus, $\boldsymbol{E = 1.32 \times 10^{-15}\ \text{J}}$ or **8.28 keV**

(b) From Eqs. (1.1) and (1.2) $E = hf = hc/\lambda$
$\lambda = c/f$
=> $= 3 \times 10^{8}/2 \times 10^{18}$
$= 1.5 \times 10^{-10}\text{m}$
Since 10^{-10} m = 1 Å
Therefore, λ = 1.5 Å
Thus, $\boldsymbol{\lambda = 1.5 \times 10^{-10}\ \text{m}}$ or **1.5 Å**

(c) Using Eq. (1.3) $E = pc$

$p = E/c$

Or $p = 1.3252 \times 10^{-15}/3 \times 10^{8}$

$\boldsymbol{p = 4.42 \times 10^{-24}\text{N.s}}$

Example 2 6 MV voltage is provided to accelerate electron beam in a linear accelerator. As a result x-rays are produced. Find the energy and wavelength of the x-ray photon.

Solution Voltage provided to produce x-rays = V = 6 MV = 6×10^{6} volts
Magnitude of the charge of an electron = e = 1.6×10^{-19} C
Energy lost by electrons is used to produce x-rays.
Energy of an x-ray photon = Voltage × magnitude of the charge of an electron

$$\begin{aligned} E &= e.V \\ &= 1.6 \times 10^{-19} \times 6 \times 10^{6} \\ &= 9.6 \times 10^{-13}\text{J} \end{aligned}$$

Since 1 eV = 1.6×10^{-19} J
Therefore,

$$\begin{aligned} E &= 9.6 \times 10^{-13}/1.6 \times 10^{-19} \\ &= 6 \times 10^{6}\text{eV} \\ \boldsymbol{E} &\boldsymbol{= 6\ \text{MeV}} \end{aligned}$$

Thus, the energy of a 6 MV x-ray photon is 6 MeV.

Conclusion 1 V voltage when converted to energy gives 1 eV energy.
In order to find wavelength of the x-ray we use Eq. (1.2)

$$\begin{aligned} E &= hc/\lambda \\ \lambda &= hc/E \\ &= 6.626 \times 10^{-34} \times 3 \times 10^{8}/9.6 \times 10^{-13} \\ \boldsymbol{\lambda} &\boldsymbol{= 2.07 \times 10^{-13}\text{m}} \end{aligned}$$

Since 1 nm = 10^{-9} m; therefore $\lambda = 0.000207$ nm. Also 1 Å = 10^{-10} m, thus $\lambda = 0.00207$ Å.

Alternative Method An alternative short method can be used to find wavelength in nanometers if energy of photon is given in the unit of eV and vice versa. This method relates energy and wavelength using the following relationship:

$$\lambda\,(\text{in nm}) = 1240/E\,(\text{in eV})$$

The energy of the x-ray photon we determined in eV is $E = 6 \times 10^6$ eV.

Therefore, $\lambda = 1240/6 \times 10^6$

$$\boldsymbol{\lambda = 0.000207\ \text{nm}}$$

Similarly, a photon of $\lambda = 450$ nm has an energy of $E = 1240/450 = 2.75$ eV.

This rule is true for photons of all energies and wavelengths. Moreover, this rule applies to photons or electromagnetic radiations only.

1.1.2.3 β-Rays

Beta rays are ionizing radiations that originate in the nucleus of an atom. A β-ray is exactly like an electron with the only difference being the separate origins of the two. As mentioned, a β-ray originates from the nucleus of an atom, while an electron resides in an orbit around a nucleus. Beta rays are subdivided into two types: β^- and β^+. β^- has the same charge and mass as possessed by an electron, given as $m_0 = 9.109 \times 10^{-31}$ kg and $e = -1.6 \times 10^{-19}$ C. β^+ is like a positron and has the same mass as possessed by an electron but opposite charge. The charge number (Z) and mass number (A) of a β^- are -1 and 0, respectively. β^+ has $Z = +1$ and $A = 0$. When a β^- is emitted by a nucleus, the charge number of that atom increases by 1 unit, and the mass number remains unaffected according to the following reaction (Ahmad 1999; Grupen 2010; Martin 2013; Stagg et al. 2001).

$$_{Z}X^{A} \rightarrow {}_{Z+1}Y^{A} + \beta^- + \overline{\upsilon} \qquad \text{(i)}$$

On the other hand, when a β^+ emits from a nucleus, the charge number of the atom decreases by one unit, and the mass number is unaffected. The following reaction describes this information.

$$_{Z}X^{A} \rightarrow {}_{Z-1}Y^{A} + \beta^+ + \nu \qquad \text{(ii)}$$

where additional particles called neutrino (ν) and anti-neutrino ($\bar{u}$) are also emitted along with beta rays in order to conserve spin in the above reactions. However, we do not want to discuss that aspect because that is out of the scope of this chapter.

Example 3 Radioactive aluminum ($_{13}Al^{28}$) emits β^- and radioactive nitrogen ($_7N^{13}$) emits β^+. Show the reactions in both cases and identify the nuclei formed after the emission of these radiations.

Solution Since the emission of β^- raise the charge number by one unit, but the mass number remains unaffected therefore,

$$_{13}Al^{28} \rightarrow 14Si^{28} + \beta^{-} \quad \text{(iii)}$$

Thus, the newly formed nucleus or atom is silicon.

In case of β^{+} emission, the charge number lowers by one unit, and mass number remains the same, therefore,

$$_{7}N^{13} \rightarrow 6C^{13} + \beta^{+} \quad \text{(iv)}$$

Thus, $_{6}C^{13}$ is the newly formed atom.

1.1.2.4 α-Rays

Alpha rays are ionizing radiations that originate inside the nucleus of a radioactive element. An α-ray has a mass number $A = 4$ and charge number $Z = 2$. The same mass number and charge number are also possessed by a helium nucleus; therefore, an α-ray is also called a helium nucleus. Therefore, α-ray can also be expressed as $_{2}He^{4}$. Since an α-ray possesses higher charge and mass as compared to a β-ray, therefore its ionizing ability is also greater than the ionizing ability of a β-ray (Hendee et al. 2005; Liu et al. 2006, Prise et al. 1994; Stagg et al. 2001). When emitted from a nucleus, the charge number and mass number of the atom reduce by 2 and 4, respectively, according to the following reaction:

$$_{Z}X^{A} \rightarrow Z - 2Y^{A-4} +_{2}He^{4}(\alpha) \quad (1.(v))$$

Example 4 A radioactive element disintegrates into $_{86}Rn^{222}$ by emitting an α-ray. Find Z and A of the parent nucleus.

Solution Considering the general reaction for the α-ray emission.

$$_{Z}X^{A} \rightarrow_{Z-2} Y^{A-4} +_{2}He^{4}$$

Since the daughter element is $_{86}Rn^{222}$. Therefore, by comparison

$$Z - 2 = 86 \quad \text{and} \quad A - 4 = 222 \quad \text{which}$$
$$mathrmgives \quad Z = 88 \quad \text{and} \quad A = 226$$

Thus the parent nucleus had $Z = 88$ and $A = 226$. These Z and A are possessed by radium; therefore, the exact parent nucleus is $_{88}Ra^{226}$.

Problems

1. Find the energy and frequency of a photon with wavelength of 530×10^{-9} m.
2. The momentum of a photon is 3.8×10^{-26} N.S. Find the wavelength, frequency, and energy of this photon.
3. Write complete reactions for the following:
   (a) An α-ray emitted from $_{86}Rn^{222}$
   (b) A β^- emitted from $_{6}C^{14}$
   (c) A β^+ emitted from $_{11}Na^{2}$
   (d) An α-ray and a γ-ray emitted simultaneously from $_{92}U^{235}$

References

Ahmad N (1999) Radiation physics-1. Allama Iqbal Open University Publisher, Islamabad

Grupen C (2010) Introduction to radiation protection. Springer-Verlag Publisher, Berlin/Heidelberg

Hendee WR, Ibbott GS, Hendee EG (2005) Radiation therapy physics, 3rd edn. New Jersey, USA

Hunt WA (1983) Comparative effects of exposure to high-energy electrons and gamma radiation on active avoidance behaviour. Int J Radiat Biol Relat Stud Phys Chem Med 44(3):257–260

Liu G, Gong P, Zhao H, Wang Z, Gong S, Cai L (2006) Effect of low-level radiation on the death of male germ cells. Radiat Res 165(4):379–389

Martin JE (2013) Physics for radiation protection, 3rd edn. Wiley-VCH, Weinheim, Germany

Prise KM, Folkard M, Newman HC, Michael BD (1994) Effect of radiation quality on lesion complexity in cellular DNA. Int J Radiat Biol 66(5):537–542

Stagg RB, Hawel LH III, Pastorian K, Cain C, Adey WR, Byus CV (2001) Effect of immobilization and concurrent exposure to a pulse-modulated microwave field on core body temperature, plasma ACTH and corticosteroid, and brain ornithine decarboxylase, Fos and Jun mRNA. Radiat Res 155(4):584–592

Chapter 2
Basic Concepts in Radiation Dosimetry

Wazir Muhammad, Amjad Hussain, and Muhammad Maqbool

Contents

2.1 Introduction 9
2.2 Definitions of Dosimetric Quantities 10
2.3 Units of Dosimetric Quantities 17
2.4 Relationship between Dosimetric Quantities 20
2.5 Relative Biological Effectiveness 25
2.6 Radiation Weighting Factor, Equivalent Dose and Sievert 25
2.7 Linear Energy Transfer 27
2.8 Tissue Weighting Factor and Effective Dose 29
2.9 Classification of People Exposed to Radiation 29
2.10 Annual Limit on Intake (ALI) 30
2.11 Charged Particle Equilibrium 32
2.12 Stopping Power 33
2.13 Cavity Theory 35
2.14 Biological Effects of Radiation 37
References 41

2.1 Introduction

Directly and indirectly ionizing radiations deposit their energy in a medium while passing through it. Radiation dosimetry is a procedure that deals with the methods for quantitative determination of that deposited energy. To be more specific, quantitative determination of energy absorbed in a given medium by directly or

W. Muhammad, PhD (✉)
Department of Therapeutic Radiology, Yale University School of Medicine, New Haven 06520-8040, CT, USA
e-mail: wazir.muhammad@yale.edu

A. Hussain, PhD, MCCPM
Radiation Oncology, Western Manitoba Cancer Centre, Brandon R7A 2B4, MB, Canada

M. Maqbool, PhD
Department of Clinical & Diagnostic Sciences, Health Physics Program, The University of Alabama at Birmingham, 1716 9th Avenue South, Birmingham, Alabama 35294, United States

M. Maqbool (ed.), *An Introduction to Medical Physics*, Biological and Medical Physics, Biomedical Engineering, DOI 10.1007/978-3-319-61540-0_2

indirectly ionizing radiations is called radiation dosimetry. It plays a crucial role in radiation therapy, nuclear medicine and radiation protection. Due to its significance, accurate determination of the deposited energy (often termed a radiation absorbed dose) at the point of interest in the medium (i.e., human body or phantom) is needed. A number of quantities and units have been defined for describing the radiation beam, which ultimately leads to the determination of radiation absorbed dose to the medium by incident radiation. These quantities and units are explained in this chapter. Furthermore it covers the fundamental ideas and principles involved in radiation dosimetry.

2.2 Definitions of Dosimetric Quantities

2.2.1 Radiation and Energy Fluence

Generally, fluence is termed as the flux of radiation particles (e.g. photons, electrons, protons heavy ions, neutrons etc.) or energy integrated over a period of time. For radiation, it is defined as the total number of radiation particles that intersect a unit area in a specific time interval. It has units of number of the particles per m^2 (#/m^2 or simply, m^{-2}). Whereas, energy fluence which is measured in Joul/m^2 is defined as the energy delivered per unit area.

If dN is the number of the particles incident on a cross-sectional area dA (see, Fig. 2.1) then, the particle fluence (Φ), is given by [Nahum A (2007), Podgorsak (2005), Seuntjens et al. (2005)]:

$$\Phi = \frac{dN}{dA} \tag{2.1}$$

To make Φ independent of the incident angle of the radiation, it is assumed that the direction of each radiation particle is perpendicular to dA as shown in Fig. 2.1. The directional dependent Φ is often called planar particle fluence. It is defined as, the number of particles crossing a plane of unit area.

Now, if, dR is the radiant energy incident on a sphere of cross-sectional area dA, then mathematically, the energy fluence (Ψ) can be expressed as follows [Nahum A (2007), Podgorsak (2005), Seuntjens et al. (2005)]:

$$\psi = \frac{dR}{dA} \tag{2.2}$$

For a mono-energetic radiation beam, R is the product of N number of the particle and their energy E (i.e. $dR = dNE$). Equation (2.2) can now be written as follows [Seuntjens et al. (2005)]:

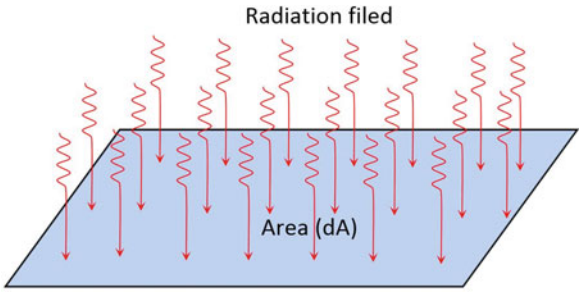

Fig. 2.1 Particle/energy incident on a unit area

$$\psi = \left(\frac{d(NE)}{dA}\right) = \left(\frac{dN}{dA}\right)E = \phi E \tag{2.3}$$

Equation (2.3) gives a relationship between Φ and Ψ for mono-energetic beams. However, in most cases, electromagnetic or particle radiation are not mono-energetic and the above mentioned concepts need to be modified accordingly. In these cases, the particle fluence and energy fluence is replaced by particle fluence spectrum $\Phi_E(E)$, and energy fluence spectrum $\Psi_E(E)$ differential in energy E, respectively and mathematically these are given as [Seuntjens et al. (2005)]:

$$\varphi_E(E) = \frac{d\varphi(E)}{dE} \tag{2.4}$$

$$\psi_E(E) = \frac{d\psi(E)}{dE} = \frac{d\varphi(E)}{dE}E \tag{2.5}$$

2.2.2 Radiation and Energy Fluence Rate

The particle and energy fluence rate are also useful quantities that describe mono-energetic photon and charged particle beams.

Mathematically, the particle fluence rate $\dot{\phi}$ is given as [Seuntjens et al. (2005)]:

$$\dot{\phi} = \frac{d\phi}{dt} \tag{2.6}$$

Here, $d\phi$ is the rate of change of the radiation particle fluence in time interval dt. It is measured in the units of $m^{-2}\ s^{-1}$.

Similarly, the energy fluence rate is given by [Podgorsak (2005), Seuntjens et al. (2005)]:

$$\dot{\psi} = \frac{d\psi}{dt} \tag{2.7}$$

Where, $d\psi$ is the rate of change of the energy fluence in time interval dt. $\dot{\psi}$ is measured in the units of $W.m^{-2}.s^{-1}$ or $J.m.s^{-1}$.

2.2.3 KERMA

The indirectly ionizing radiation such as photons and neutrons encounter different interactions while passing through a medium. In case of photons, these interactions include, Rayleigh (coherent) scattering, Compton (incoherent) scattering, pair (including triplet and higher order) production and the photoelectric effect [Podgorsak EB (2005), Stabin MG (2007), Seuntjens JP (2005)]. For neutron interactions, neutrons-nuclei is the main mode of transfer of its energy to the medium. However, both for photons and neutrons, some of kinetic energy of the incident radiation is transferred to the primary ionizing particles produced inside the medium. Photoelectrons, Compton electrons, or positron–electron pairs are the resultant charged particles produced in case of photon interactions and the scattered nuclei, α-particles and heavy ions in the case of fast neutrons. The above mentioned interactions for photons are governed by their individual microscopic cross-section, and the mass attenuation coefficients [Podgorsak EB (2005), Stabin MG (2007)]. As there is no energy transfer in case of Rayleigh scattering, therefore, this will not be discussed further. The initial kinetic energy transferred to the primary ionizing particles from indirectly ionizing radiation is known as KERMA, *K*. It is measured in joules per kilogram or Gy (these units will be explained in the later section of this chapter). KERMA is an acronym for *K*inetic *E*nergy *R*eleased per unit *MA*ss. From the above discussion, *K* can be defined as "the measure of energy transfer from indirectly ionizing radiation (i.e., photons and neutrons) to ionizing radiation (i.e., electrons, protons, α-particles and heavy ions) inside a medium". What happens to these charged particles later on, has nothing to do with the KERMA [Cember and Johnson (2009), Seuntjens et al. (2005)].

Figure 2.2 gives a clear picture of KERMA. Here, indirectly ionizing radiation incident on a medium of volume '*V*'. Some of these radiations will transfer their kinetic energy to secondary charged particles inside volume 'V' (i.e., $E_{K,1}$ and $E_{K,2}$) and some may interact outside and will transfer their energy to the secondary charged particles (i.e., $E_{K,3}$). The collisional energy transferred to volume '*V*' is; $E_{tr} = E_{K,1} + E_{K,2}$.

Now, for N particles, if, $d\bar{E}_{tr}$ is the mean energy transferred from indirectly ionizing radiation to charged particles per unit mass of volume '*V*', then mathematically *K* can be written as [Attix FH (2004), Nahum A 2007, Seuntjens et al. (2005), Stabin (2007)]:

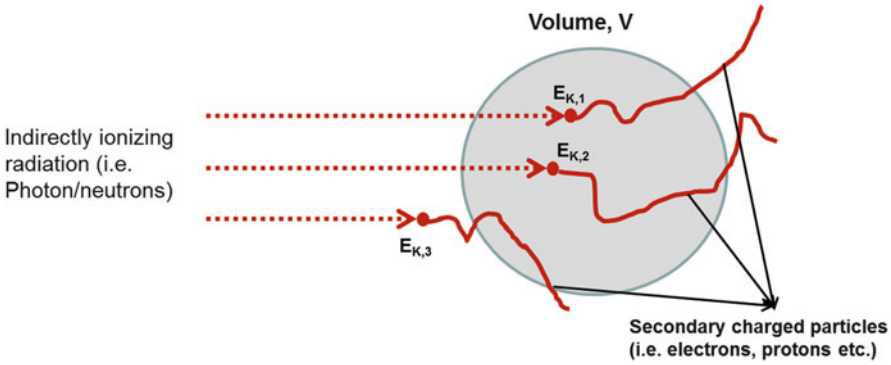

Fig. 2.2 Illustration of KERMA

$$K = \frac{d\bar{E}_{\mathrm{tr}}}{dm}. \tag{2.8}$$

The kinetic energy transferred to charged particles may be spent in two different ways:

(a) Local dissipation of the energy in ionization and excitation as a result of Coulomb-force interactions with atomic electrons in the medium. This is called collisional KERMA.
(b) Radiative loss of the energy due to Coulomb interaction of charged particles with the atomic nuclei. This is called radiative interaction. The bremsstrahlung x-rays produced are more penetrating and thus deposit their energy away from the point of interaction.

The KERMA can be expressed as [Attix FH (2004), Nahum A (2007)]:

$$K = K_{\mathrm{c}} + K_{\mathrm{r}} \tag{2.9}$$

where, K_{c} and K_{r} are the collisional and radiative KERMA respectively.

The average fraction of the energy transferred to the primary charges within the medium that is lost through radiative processes is represented by a factor called the radiative fraction, denoted by $\bar{g}$. K_{c} and K are related to each other as [Nahum A 2007]:

$$K_{\mathrm{c}} = K\left(1 - \bar{g}\right) \tag{2.10}$$

2.2.4 CEMA

CEMA is the acronym for *C*onverted *E*nergy per unit *MA*ss. The analogy of CEMA (*C*) is same as KERMA despite that it is defined for directly ionization radiation. It is a measure of the energy lost by directly ionizing radiation (i.e., electrons, protons, heavy ion beam etc.) except secondary charged particles to a medium, without the concern as to what happens after this transfer. In case of CEMA, the energy is transferred to the medium through various charged particle interactions. Mathematically '*C*' can be written as [Seuntjens et al. (2005)]:

$$C = \frac{d\bar{E}_{\mathrm{tr}}}{dm}. \tag{2.11}$$

Here, $d\bar{E}_{\mathrm{tr}}$ is the energy lost by primary charged particles, as a result of collisions per unit mass dm of the medium. It is also measured in joules per kilogram or Gray (Gy) [Seuntjens et al. (2005)].

2.2.5 Absorbed Dose

The energy transferred to the primary charged particles per unit mass from incident radiation beam (either directly or indirectly ionizing radiation) may not be necessarily absorbed in the volume of interest. Some of this energy, as discussed earlier is absorbed elsewhere after escaping the volume [Attix FH (2004)].

Now, if, R_{in} and R_{out} is the radiant energy entering and leaving a volume (V) respectively and $\sum Q$ is the sum of changes of all mass-energy conversions of nuclei and of all particles involved in the interaction within V (as illustrated in Fig. 2.3), the mean energy ($\bar{\varepsilon}$) imparted to the medium of volume 'V' can be written as (Nahum A 2007):

$$\bar{\varepsilon}_{\mathrm{tr}} = R_{\mathrm{in}} - R_{\mathrm{out}} + \sum Q \tag{2.12}$$

From the above equation, absorbed dose is a measure of the amount of energy imparted $d\bar{\varepsilon}$ by secondary ionizing radiation to a volume V containing a finite mass dm [Attix FH (2004), Nahum A (2007), Seuntjens et al. (2005)]:

$$D = \frac{d\bar{\varepsilon}}{dm} \tag{2.13}$$

More simply, it can be defined as the energy absorbed per unit mass of any material. It is a non-stochastic quantity and is applicable to both directly and indirectly ionizing radiations.

The energy imparted from indirectly ionizing radiation to the medium is a two steps process. Firstly, the energy is transferred to the secondary charged particles (mainly electrons)[Cember and Johnson (2009), Hendee WR et al (2005)]. This

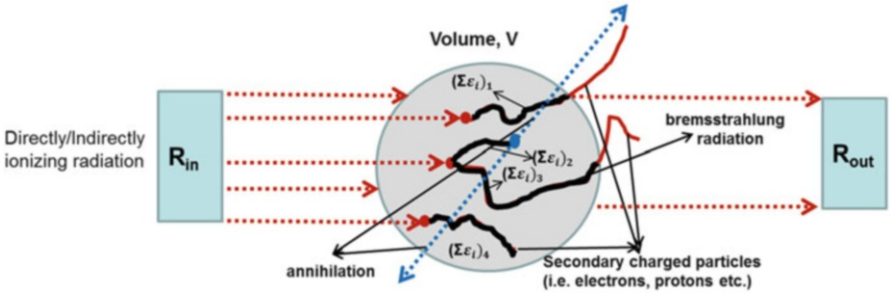

Fig. 2.3 Schematic diagram for energy imparted to volume '*V*'

process is described as KERMA. In the second step, some of the kinetic energy of the charged particles (i.e., KERMA) is transferred to the medium through various interactions (i.e., atomic excitations and ionizations etc.) within the medium (resulting in absorbed dose) and the remaining kinetic energy is lost in the form of radioactive losses (i.e., bremsstrahlung and annihilation in flight).

From the above discussion, it is concluded that both KERMA and dose have same physical dimensions (i.e. same units) but are different dosimetric quantities. The KERMA is a measure of all the energy transferred from the indirectly ionizing radiation (photon or neutron) to primary charged particles per unit mass, while absorbed dose is a measure of the energy absorbed per unit mass.

In an absorbing medium, KERMA decreases continuously with increasing depth. This is due to the continuous decrease in the flux of indirectly ionizing radiation. On the other hand, the absorbed dose is initially lower than KERMA level at the surface and below the surface (to some extent) in the medium. The increasing trend of absorbed dose continues until a maximum is reached. With increasing depth the ionization density increases due to the production of secondary charged particles. After reaching a maximum value, the dose starts decreasing with increasing depth. In fact, the maximum range of the primary charged particles determine the depth of maximum absorbed dose [Cember and Johnson (2009), Hendee WR et al (2005)]. A relation between KERMA and dose for photon/fast neutrons is shown in Fig. 2.4.

2.2.6 Exposure

The X- or γ radiation interaction with matter leads to the production of ion pairs. The simplest way to measure the quantitative effects of these radiations is to measure the number of ion pairs produced in air by using oppositely charged surfaces (typically charged metallic plates) [Podgorsak EB (2005), Stabin MG (2007)]. This approach is called exposure which was introduced early in the history of radioisotope research and in the design of early radiation monitoring devices.

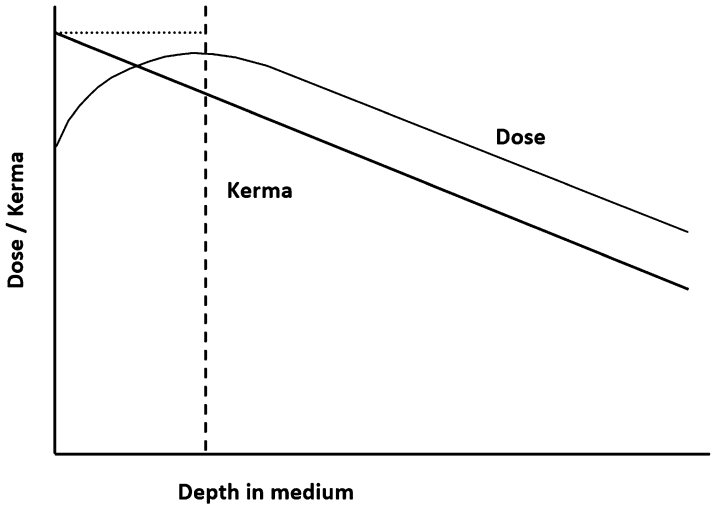

Fig. 2.4 KERMA and absorbed dose relationship for photon and neutrons radiations

Exposure is defined as the total charge dQ of either sign produced by X- or γ radiation in air of mass dm. The ions must not escape the air and must be collected. Mathematically it can be presented as follows [Attix FH (2004)]:

$$X = \frac{dQ}{dm} \tag{2.14}$$

According to the definition of exposure, it is measured in coulomb per kilogram (C/kg) in air which is the SI unit of exposure. However, there is no special name for the SI unit of exposure. For convenience here, its unit is being called an exposure unit (X-unit). Exposure is considered a convenient and useful quantity for describing X- or γ-rays, because of the following reasons:

(a) The energy fluence Φ_E is proportional to the exposure X. This is important in the determination of absorbed dose in other medium, if exposure is known for any given photon energy.

$$X \propto \left(\frac{\mu_{en}}{\rho}\right)_{E,air} \tag{2.15}$$

(b) The effective atomic number of air is approximately equal to that of soft biological tissue. Air filled ionization chambers are therefore used in most of the dosimetric measurements. This implies that quantitatively in soft tissue the quotient of collisional KERMA $\boldsymbol{K_c}$ and exposure X, is almost photon energy independent. In the energy range 4 keV to 10 MeV the following relation approximately holds:

$$\frac{(\mu_{en}/\rho)_{E,\text{tissue}}}{(\mu_{en}/\rho)_{E,\text{air}}} \approx 1.07 \pm 3\% \tag{2.16}$$

In early days (until late 1970s) exposure was the only quantity used for the calibration of ionization chambers. Currently majority of the chambers are calibrated in terms of absorbed dose to water. For photon energies greater than few mega electron volts, exposure measurement is impractical. Exposure is therefore limited to X- or γ-rays with energies lower than 3 MeV.

2.3 Units of Dosimetric Quantities

2.3.1 Gray

The physical dimension of KERMA, CEMA and absorbed dose is $[E/m]$ (i.e. E = energy & m = mass of any material) is the same [Nahum A (2007), Podgorsak EB (2005)]. Hence, these can be measured in J/kg or erg/g. However, special unit defined for these quantities in the SI system is called the gray (Gy) that corresponds to the absorption of one joule per kilogram (i.e. 1Gy = 1 J/kg). Gray is also used for KERMA and CEMA [Cember and Johnson (2009)].

It is universally applicable in the dosimetry of all types of ionizing radiation (i.e. irradiation due to external fields of electromagnetic radiation, neutrons, or charged particles as well as due to the internally deposited radionuclides).

Example 2.3 During the cancer treatment of a patient, 6 Joule energy is deposited in a 1.5 kilogram tissue exposed to radiation. Find the absorbed dose delivered in Gy to the tissue? How much energy is needed to deliver the same absorbed dose to a tissue whose mass is 0.6 kilogram?

Solution The amount of energy deposited in the tissue = dE = 6 J
Mass of the exposed tissue = dm = 1.5 kg
Absorbed dose = D =?
Using Eq. (2.6)

$$D = dE/dm = 6/1.5$$
$$\boldsymbol{D = 4\ \text{Gy}}$$

In the second part of the question we have to calculate the deposited energy from the calculated D. In this case D = 4 Gy, dm = 0.6 kg. Using and rearranging the same equation,

$$\text{Integrating,} \quad \begin{aligned} dE &= D.dm \\ E &= D.m \\ E &= 4 \times 0.6 \\ \boldsymbol{E} &= \mathbf{2.4\ J} \end{aligned}$$

2.3.2 RAD

The rad is an acronym for "radiation absorbed dose" and was introduced before the introduction of the SI units. One rad is defined as [Cember and Johnson (2009), Stabin (2007)]:

$$1\ \text{rad} = \frac{100\,\text{ergs}}{\text{g}} \tag{2.17}$$

Since, $1\ \text{J} = 10^7\text{ergs}$ & $1\ \text{kg} = 10^3\text{g}$, hence,

$$1\ \text{rad} = \left(\frac{100\ \text{ergs}}{\text{g}}\right) \times \frac{(1\text{J}/10^7\text{ergs})}{(1\text{kg}/10^3\text{g})} = 10^{2+3-7} \times \left(\frac{\text{J} \times \text{ergs} \times \text{g}}{\text{kg} \times \text{ergs} \times \text{g}}\right) = 0.01\frac{\text{J}}{\text{kg}}$$
$$= 0.01\ \text{Gy} = 1\ \text{cGy}$$

or,

$$1\ \text{Gy} = 100\ \text{rad} \tag{2.18}$$

2.3.3 Exposure Unit

As mentioned earlier SI unit of exposure is measured in X unit. By definition exposure X is [Cember and Johnson (2009)]:

$$1\text{X} = \left(1\frac{\text{C}}{\text{kg}}\right)_{\text{air}} \times \left(\frac{1\ \text{ion}}{1.6 \times 10^{-19}\text{C}}\right) \times \left(\frac{34\ \text{eV}}{\text{ion}}\right) \times \left(\frac{1.6 \times 10^{-19}\text{J}}{\text{eV}}\right) \times \left(1\frac{\text{Gy}}{\text{J/kg}}\right)$$
$$= 34\ \text{Gy}_{\text{air}} \tag{2.19}$$

2.3.4 Roentgen

The conventional unit for exposure is roentgen R, which is equal to 2.58×10^{-4} C/kg in the SI system.

1R can be expressed as [Cember and Johnson (2009)]:

$$1\ \mathrm{R} = \left(1\,\frac{\mathrm{sC}}{\mathrm{cm}^3}\right)_{\mathrm{air}} \times \left(\frac{1\ \mathrm{cm}^3\mathrm{air}}{1.29 \times 10^{-3}\ \mathrm{g/cm}^3\mathrm{air}}\right) \times \left(\frac{1\mathrm{ion}}{4.8 \times 10^{-10}\mathrm{sC}}\right) \times \left(\frac{34\ \mathrm{eV}}{\mathrm{ion}}\right) \times \left(\frac{1.6 \times 10^{-12}\mathrm{erg}}{\mathrm{eV}}\right) \times \left(\frac{1\ \mathrm{rad}}{100\ \mathrm{erg/g}}\right) = 0.877\ \mathrm{rad}_{\mathrm{air}} \tag{2.20}$$

where, sC is charge in statcoulomb ($1\mathrm{sC} = 3 \times 10^9$ C), and 1 erg $= 1 \times 10^{-7}$ Joul.

The relationship between the X and R may be calculated as follows:

$$\frac{34\left(\frac{\mathrm{J/kg}}{\mathrm{C/kg}}\right) \times \left(\frac{10^7\mathrm{erg}}{\mathrm{J}}\right) \times \left(\frac{1\mathrm{kg}}{1000\mathrm{g}}\right)}{\left(\frac{87.7\mathrm{erg/g}}{\mathrm{R}}\right)} = 3877\left(\frac{\mathrm{R}}{\mathrm{C/kg}}\right) \tag{2.21}$$

or

$$\begin{aligned} 1\mathrm{X} &= 3877\ \mathrm{R} \\ 1\mathrm{R} &= (1/3877)\mathrm{X} = 2.58 \times 10^{-4}\mathrm{X} \end{aligned} \tag{2.22}$$

Example 2.1 In an experiment, 2 kg of dry air is exposed to x-rays. As a result of ionization in dry air, 5.16×10^{-3} C charge is produced. Determine the Exposure in the units of Roentgen.

Solution Quantity of charge produced as a result of air ionization $= 5.16 \times 10^{-3}$ C.

Quantity of dry air exposed to x-rays $= 2$ kg

$$\begin{aligned} \text{Exposure} &= 5.16 \times 10^{-3}\mathrm{C}/2\ \mathrm{kg} \\ &= 2.58 \times 10^{-3}\mathrm{C/kg} \\ &= 25.8 \times 10^{-4}\mathrm{C/kg} \\ &= 10 \times 2.58 \times 10^{-4}\mathrm{C/kg} \\ &= \mathbf{10\ Roentgen} \\ \text{Thus,}\quad &\mathbf{Exposure = 10\ R} \end{aligned}$$

Example 2.2 Calculate the quantity of charge produced as a result of 4 R Exposure in dry air of mass 0.008 mg. If this charge is the result of electrons production then find the number of electrons produced.

Solution Exposure $= 4\ \mathrm{R} = 4 \times 2.58 \times 10^{-4}$ C/kg $= 1.032 \times 10^{-3}$ C/kg

Mass of the air ionized $= 0.008$ mg $= 8 \times 10^{-9}$ kg, ($1\ \mathrm{mg} = 10^{-6}$ kg).

$$\text{Charge produced} = q = \text{Exposure} \times \text{mass}$$
$$= 1.032 \times 10^{-3}(\text{C/kg}) \times 8 \times 10^{-9}\text{kg}$$
$$\textbf{Charge produced} = \boldsymbol{q} = \mathbf{8.256 \times 10^{-12} C}$$

Magnitude of the charge of a single electron $= e = 1.6 \times 10^{-19}$ C
Number of electrons produced $= n = ?$

$$n = q/e = 8.256 \times 10^{-12}\text{C}/1.6 \times 10^{-19}\text{C}$$
$$= 5.16 \times 10^{7}$$

Number of electrons produced $= \boldsymbol{n} = \mathbf{5.16 \times 10^{7}}$

2.4 Relationship between Dosimetric Quantities

In this section, correlations will be established between quantities that describe radiation fields (photons fluence and energy fluence etc.) and other dosimetric quantities (KERMA, radiation dose and exposure etc.).

2.4.1 Fluence—KERMA Relationship

Consider a thin layer of a medium of thickness dl and surface area dA (i.e. volume $V = dl \times dA$). Suppose N is the number of photons each having energy E, entering into this volume element perpendicularly as shown in Fig. 2.5.

The interaction coefficient for this medium will give the amount of energy transferred to the medium from incident photons[Ahmad N (1999), Martin JE (2013)]. The mass energy-transfer coefficient (μ_{tr}/ρ) is given as [Nahum A (2007)]:

$$\frac{\mu_{tr}}{\rho} = \frac{1}{\rho dl}\frac{dR_{tr}}{R} \tag{2.23}$$

The fraction of incident radiant energy $\frac{dR_{tr}}{R}$ can be written as $\frac{dE_{tr}}{N \times E}$, and by rearranging Eq. (2.23), we have [Nahum A (2007)]:

$$dE_{tr} = \mu_{tr} dlNE \tag{2.24}$$

Dividing both sides of Eq. (2.24) by the mass of the layer 'dm' and rearranging [Nahum A (2007)]:

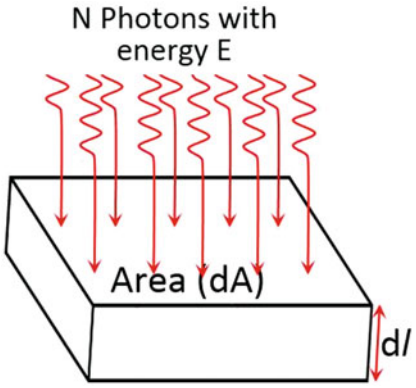

Fig. 2.5 Illustration of N radiation tracks of energy E crossing thin layer of a medium having dl, dA, dm and ρ as thickness, area, mass and density respectively

$$\frac{dE_{\mathrm{tr}}}{dm} = \mu_{\mathrm{tr}} E \left[\frac{Ndl}{dm}\right] \tag{2.25}$$

Now, by replacing dm with ρdV, the following relation can be developed [Nahum A (2007)]:

$$\frac{dE_{\mathrm{tr}}}{dm} = \frac{\mu_{\mathrm{tr}}}{\rho} E \left[\frac{Ndl}{dV}\right] \tag{2.26}$$

where, the left hand side of Eq. (2.26) is KERMA in a medium 'w' and the quantity in the square brackets is the fluence. The above equation will take the following form [Nahum A (2007)]:

$$K_{\mathrm{w}} = \left(\frac{\mu_{\mathrm{tr}}}{\rho}\right) E\phi \tag{2.27}$$

or in terms of energy fluence ψ [Nahum A (2007)]:

$$K_{\mathrm{w}} = \left(\frac{\mu_{\mathrm{tr}}}{\rho}\right)_{\mathrm{w}} \psi \tag{2.28}$$

It is to be noted that the perpendicular incidence of radiation mentioned in Fig. 2.5 was assumed for simplicity. However, Eqs. (2.25) and (2.26) are valid for arbitrary angles of radiation incidence as well.

The above calculations were done for mono-energetic radiation. In majority of practical cases, however, one deals with spectrum of energies. In such situations, Eq. (2.27) can be re-written as follows [Nahum A (2007)]:

$$K_{\mathrm{w}} = \int_{0}^{E_{\max}} E\phi_{\mathrm{E}} \left(\frac{\mu_{\mathrm{tr}}}{\rho}\right)_{\mathrm{w}} dE \tag{2.29}$$

where, the energy dependence of has been shown explicitly.

By definition, using Eq. (2.28), collisional KERMA K_{c} can be expressed in terms of mass energy absorption coefficient (μ_{en}/ρ). It is assumed that, part of the initial kinetic energy of charged particles that is converted into bremsstrahlung photons is excluded from the energy absorbed. The two coefficients $(\mu_{\mathrm{en}} \,\&\, \mu_{\mathrm{tr}})$ can be related by the following equation [Nahum A (2007)]:

$$\mu_{\mathrm{en}} = \mu_{\mathrm{tr}}(1 - g) \tag{2.30}$$

This is similar to what relates K_c and K in Eq. (2.9).

For mono-energetic beam,

$$(K_{\mathrm{c}})_{\mathrm{w}} = \left(\frac{\mu_{\mathrm{en}}}{\rho}\right)_{\mathrm{w}} E\phi \tag{2.31}$$

whereas for a spectrum of incident photon energies:

$$(K_{\mathrm{c}})_{\mathrm{w}} = \int_{0}^{E_{\max}} E\phi_{\mathrm{E}} \left(\frac{\mu_{\mathrm{en}}}{\rho}\right)_{\mathrm{w}} dE \tag{2.32}$$

2.4.2 KERMA—Absorbed Dose Relationship

Mathematical relationship between KERMA and absorbed dose for photons/neutrons can be derived from fluence-KERMA relationship. As discussed earlier, KERMA is the energy transfer to primary charged particles and the absorbed dose in a medium accounts for the mean value of energy absorbed in an elementary volume. Furthermore, the primary charged particles can leave the elementary volume after getting energy from incident radiation and taking a fraction of the initial transferred kinetic energy out of the volume. The situation is illustrated in Fig. 2.6, where E_{tr}^{n} is the net energy transferred to primary charged particles. Part of the initial kinetic energy that is converted into bremsstrahlung photons escape the volume of interest. Suppose ε is the imparted energy to the volume, E_{in}^{n} and E_{out}^{n} is the net kinetic energy enter and leaves the volume respectively. Then, Eq. (2.12) can be rewrite as [Nahum A (2007)]:

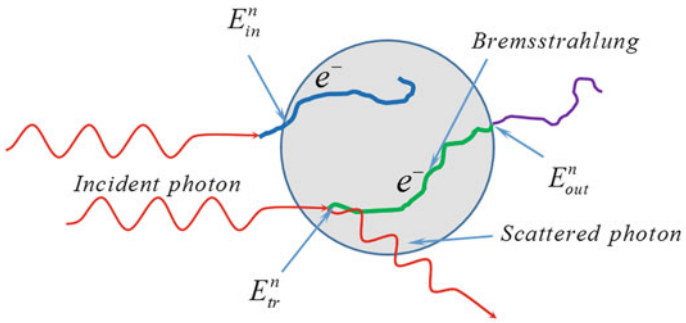

Fig. 2.6 Schematic Illustration for energy imparted (E^n_{tr}) by secondary electrons created by photons, and how the loss of charged particles is compensated

$$\varepsilon = E^n_{\mathrm{tr}} - E^n_{\mathrm{out}} + E^n_{\mathrm{in}} \tag{2.33}$$

Now, if the primary charged particle track that leaves the volume is compensated by an identical track (i.e., $E^n_{\mathrm{out}} = E^n_{\mathrm{in}}$, known as charged particle equilibrium) then Eq. (2.33) can be written as [Nahum A (2007)]:

$$\varepsilon = E^n_{\mathrm{tr}} \tag{2.34}$$

In this case, absorbed dose will be equal to collision KERMA (K_c)

If Eq. (2.34) is divided by the mass of the layer/volume element, the following relation can easily be obtained [Nahum A (2007)]:

$$(D)_{\mathrm{w}} \overset{\mathrm{CPE}}{=} (K_{\mathrm{c}})_{\mathrm{w}} \tag{2.35}$$

where CPE is the charged particle equilibrium (will be explained in a later section).

It should be noted that the absorbed dose is equal to the collision KERMA under the special condition of charged particle equilibrium.

For mono-energetic, indirectly ionizing radiation using Eq. (2.35) the following relation can be obtained from Eq. (2.31)[Nahum A (2007)]:

$$D \overset{\mathrm{CPE}}{=} \left(\frac{\mu_{\mathrm{en}}}{\rho}\right) E\varphi \tag{2.36}$$

Similarly, in case of spectrum of incident photon energies [Nahum A (2007)]:

$$D \overset{\mathrm{CPE}}{=} \int_0^{E_{\max}} E\phi_{\mathrm{E}} \left(\frac{\mu_{\mathrm{en(E)}}}{\rho}\right) dE \tag{2.37}$$

These are very important relationships, often used in radiation dosimetry.

2.4.3 Exposure–Dose Relationship

With the help of ionization chambers, dose is measured in the air cavity of the chamber. Air is however, not always the medium of interest for dose determination. Dose measured in air can be converted to dose in other medium. The energy absorption (dose) is approximately proportional to the electronic density of the medium in the energy region where Compton scattering is dominant. The tissue dose may not be necessarily equal to the air dose. For human tissue the electron density is 3.28×10^{23} electrons/gram, whereas for air it is 3.01×10^{23} electrons/gram. The absorbed dose in tissue, from an exposure of 1 C/kg air is therefore:

$$\begin{aligned} \mathrm{D_{tissue}}(\text{from } 1\mathrm{C/kg}) &= \mathrm{D_{air}} \times \frac{\text{tissue electron density}}{\text{air electron density}} \\ \mathrm{D_{tissue}}(\text{from } 1\mathrm{C/kg}) &= 34(\mathrm{Gy}) \times \frac{3.28 \times 10^{23}}{3.01 \times 10^{23}} = 37\,\mathrm{Gy} \end{aligned} \tag{2.38}$$

In Eq. (2.38), the ratio of electron densities can be approximated by the ratios of mass absorption coefficients, i.e.,

$$\mathrm{D_{tissue}}(\text{from } 1\,\mathrm{C/kg}) = 34 \times \left(\frac{\mu_{\mathrm{med}}/\rho}{\mu_{\mathrm{air}}/\rho}\right)\mathrm{Gy} \tag{2.39}$$

2.4.4 Roentgen Equivalent Man (rem)

Roentgen equivalent man or rem is one of the old units used in medical and radiation physics. REM has the same relationship with Sievert as RAD has with Gray.

$$\mathbf{1\,Sv = 100\,rem} \tag{2.11}$$

For example a dose of 1500 rem is equivalent to 15 Sv.

The smaller unit, usually used, is millirem, where 1 mrem $= 10^{-3}$ rem.

How much is a millirem? The following information gives an idea of a millirem dose.

- The annual background radiation for a typical American is 370 mrems.
- The average from watching color TV is two mrem each year.
- The nuclear industry contributes to less than 1 mrem/year to an individual's background radiation.

2.5 Relative Biological Effectiveness

The effects of various radiations on a body tissues compared to a reference effect gives the idea of effectiveness of different radiations in providing the same effect. This comparison of the effectiveness is generally known by a term called relative biological effectiveness RBE. The biological effects of radiation are not only directly proportional to the energy deposited per unit mass or per unit volume, but also on the way in which this energy is distributed along the path length of the radiation. Thus the relative biological effectiveness is defined as the ratio of the doses required by two radiations to cause the same level of effect. Thus, the RBE depends upon the dose and the biological end point. Mathematically it is defined as,

$$\text{RBE} = \frac{\text{Dose of reference } \textit{radiation} \text{ required to produce a particular effect}}{\text{Dose of radiation required to produce the same effect}} \tag{2.8}$$

The reference radiation is generally taken as 250 keV x-rays. The RBE for the reference radiation is considered as 1. Suppose that it takes 200 mGy of x-rays but only 20 mGy of neutrons to produce the same biological effect, the RBE would be $200/20 = 10$ using x-rays as the reference radiation.

Example 2.4 During an experiment on a certain tissue it is observed that 25% of the tissue cells are damaged by 12 Gy of 250 keV energy x-rays. The same damage is produced to the same tissue by 4 Gy of protons, 1 Gy of neutrons and 0.6 Gy of α-rays in separate trials. Calculate the RBE for protons, neutrons and α-rays used in that experiment.

Solution Using Eq. (2.8) for these radiations *we get,*

$$\text{RBE for protons} = 12/4 = 3$$
$$\text{RBE for neutrons} = 12/1 = 12$$
$$\text{RBE for } \alpha\text{-rays} = 12/0.6 = 20$$

The same biological effect can be provided to the tissues by 20 times smaller dose of α-rays as compared to the dose of x-rays providing the same effect.

2.6 Radiation Weighting Factor, Equivalent Dose and Sievert

The exact dose delivery to body tissues is important when radiations interact with a patient in diagnostics or treatment procedures. However, it must also be paid attention that different kinds of radiations have different effects on tissues even if the quantity of dose is the same. For example, α-rays are more dangerous to the tissues due to their high ionization ability as compared to γ-rays. Thus, in order to take into account the differences in the biological effects of different radiations,

Table 2.1 Radiation weighting factors of various kinds of radiations

Type of radiation	Energy range	Radiation weighting factor, W_R
X-rays and γ-rays	All energies	1
Electrons, positrons and muons	All energies	1
Neutrons	<10 keV	5
Neutrons	10 keV–100 keV	10
Neutrons	>100 keV–2 MeV	20
Neutrons	>2 MeV–20 MeV	10
Neutrons	>20 MeV	5
Protons (other than recoil protons)	>2 MeV	2–5
α-rays, fission fragments and heavy nuclei	All energies	20

ICRU 60 (1998)

International Committee for Radiological Units (ICRU) and International Commission on Radiological Protection (ICRP) introduced a new term called Q*uality Factor*. Quality factor, denoted by '*Q*', is a dimensionless factor or a number that represents the effectiveness of a particular radiation that interacts with human body. Later on its name quality factor was changed by a new term *Radiation Weighting factor* 'W_R'[Grupen C (2010), Khan FM (2005)].

As a result of introducing radiation weighting factor, ICRU defined a new quantity called Equivalent Dose. *Equivalent Dose* is obtained by multiplying radiation weighting factor to the absorbed dose. Equivalent Dose 'H' is mathematically given below.

$$\mathbf{H} = \mathbf{D}.\mathbf{W_R} \tag{2.8}$$

The radiation weighting factors of different radiations are given in Table 2.1.

Equivalent Dose is measured in the units of Sievert 'S_v'. Mathematically, Sievert is the same unit as Gray but conceptually Gy represents the delivery of dose to treat or diagnose an effect. On the other hand, Sievert relates the absorbed dose in human tissue to the effective biological damage of the radiation. Sievert is more concerned about the damaging effect of different radiations to normal tissues.

Example 2.3 A radiation worker received 2 Gy of absorbed dose during a leak in the radiation safety set up. Find the equivalent dose H, if the absorbed is received through (i) γ-rays of energy 5 MeV (ii) neutrons of energy 2.5 MeV (iii) α-particles of energy 1.2 MeV.

Solution Absorbed Dose $= D = 2$ Gy. Using Eq. (2.8), $\boldsymbol{H = D.W_R}$

(i)	5 MeV γ-rays :	$W_R = 1,$	$H = D.W_R = 2 \times 1 = 2$ Sv
(ii)	2.5 MeV neutrons :	$W_R = 10$	$H = D.W_R = 2 \times 10 = 20$ Sv
(iii)	1.2 MeV α-particles :	$W_R = 20$	$H = D.W_R = 2 \times 20 = 40$ Sv

Example 2.4 An equivalent dose of 25 Sv is recommended in a certain application of radiations. How much absorbed dose should be given to achieve the goal if it has to be supplied through (i) positrons
of energy 5 MeV (ii) neutrons of energy 6 keV (iii) protons of energy 2 MeV ($W_R = 2$) (iv) α-rays of energy 3 MeV.

Solution Equivalent dose $= H = 25$ Sv. Using Eq. (2.8) $\boldsymbol{H = D.W_R}$ or $\boldsymbol{D = H/W_R}$

(i)	5 MeV positrons :	$W_R = 1,$	$D = H/W_R = 25/1 = 25$ Gy.
(ii)	6 keV neutrons :	$W_R = 5,$	$D = H/W_R = 25/5 = 5$ Gy.
(iii)	2 MeV protons :	$W_R = 2,$	$D = H/W_R = 25/2 = 12.5$ Gy.
(iv)	3 MeV α-rays :	$W_R = 20,$	$D = H/W_R = 25/20 = 1.25$ Gy

2.7 Linear Energy Transfer

Linear Energy Transfer, represented by LET, is another concept taken into account when radiation dose is provided to patients or radiation exposure of workers occurs in radiation area. When passing through a medium, ionizing radiation may interact with it during its passage and, as a result, deposit energy along its path (called a *track*). The average energy deposited per unit length of track is called *linear energy transfer (LET)*. In simple words It describes the energy deposition ability of a charged radiation and is defined as the amount of energy deposited per unit length of a tissue or a material by radiation. The energy average is calculated by dividing the track into equal energy intervals and averaging the lengths of the tracks that contain that specific energy amount. LET is generally expressed in the unit of keV/μm. Mathematically, the LET is described below.

$$\mathbf{LET} = -\boldsymbol{dE/dX} \tag{2.9}$$

where the negative sign shows more loss in energy when bigger length is traversed by the radiation. The SI unit of LET, obtained from Eq. (2.9), is J/m. However, Joule is a big unit of energy. Similarly, for a small body section or a material, meter is also a big unit measuring length. Therefore, keV/μm is used as a common unit for LET.

Because the amount of ionization produced in an irradiated object corresponds to the amount of energy it absorbs and because both chemical and biologic effects in

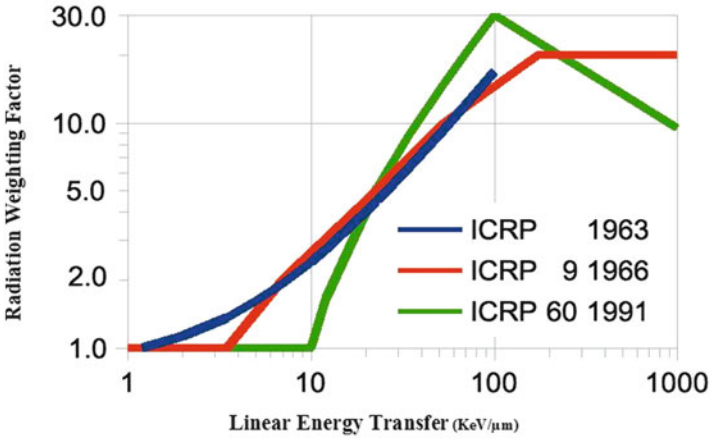

Fig. 2.7 Curves showing variation in radiation weighting factor with changing LET

Table 2.2 Linear energy transfer and radiation weighting factor

LET (keV/μm)	W_R
<3.5	1
3.5–7.0	1–2
7.0–23	2–5
23–53	5–10
53–175	10–20
X-rays and γ-rays of any energy	1
Electron and positron of any energy	1

tissue coincide with the degree of ionization experienced by the tissue, LET is an important factor in assessing potential tissue and organ damage from exposure to ionizing radiation. LET can also be related to the radiation weighting factor of various radiations used in a particular event. Higher is the LET of a particular kind of radiation in certain tissue or material, more energy is deposited by that radiation and hence the quality factor or radiation weighting factor of that radiation is high. LET generally depends upon the nature of radiation as well as the tissue or material exposed.

Figure 2.7 gives a graph between LET and radiation weighting factor given and modified by ICRP. Table 2.2 also gives a comparison and a way of changes in W_T with changes in LET. Though modification was brought by ICRP with time but the overall trend of the curve is still the same [Ahmad N (1999), Martin JE (2013)].

The figure shows that the radiation weighting factor increases to a maximum for LET around 100 keV/μm followed by a decrease with increasing LET. The reason being more energy deposition by a radiation causes more damage to the tissues and hence W_T increases with increasing LET. At LET around 100 keV/μm, the energy of radiation provides maximum damage to the tissues. With LET $>$ 100 a decrease occurs instead of further increase. At this stage the amount of energy deposited in

tissues is more than the body cells available to be damaged. Thus, the energy deposition rate is higher than the damage given to the tissues, causing a waste of huge energy as compared to the ratio in which tissues are damaged. Therefore, we can say that a portion of energy is wasted because the same effect can be given to the tissues with much less energy deposition.

2.8 Tissue Weighting Factor and Effective Dose

We are now familiar with the importance of the type of radiation when body tissues are exposed to radiations. Another important factor that must not be ignored when radiation is used to deliver dose to human body in diagnoses and treatment applications is the tissues response to radiation. Even if the same equivalent dose is provided to various parts of the body, the response of different tissues is different. Some tissues are more sensitive to radiation while some others are relatively less sensitive[Grupen C (2010), Khan FM (2005)]. Thus, even under the same equivalent dose, the damage provided to different tissues is different. In order to take into account for the response of various tissues into the interacting radiation a new factor called *Tissue Weighting Factor* 'W_T' is introduced by ICRU and a new quantity called *Effective Dose* 'E' is obtained when W_T is also taken into account during radiation exposure. The effective dose is obtained by multiplying equivalent dose with the tissue weighting factor of the tissue exposed to radiation. Mathematically,

$$\boldsymbol{E = H.W_T} \tag{2.9}$$

Since from Eq. (2.8),

$$\boldsymbol{H = D.W_R}$$

Thus Eq. (2.9) becomes,

$$\boldsymbol{E = D.W_R.W_T} \tag{2.10}$$

Equations (2.9) and (2.10) gives mathematical expressions for effective dose in terms of equivalent dose and absorbed dose, taking into account both radiation weighting factor and tissue weighting factor. Effective dose is always used as a measure of risk.

Tissue weighting factors for various tissues are given in Table 2.3.

2.9 Classification of People Exposed to Radiation

For the purpose of radiation safety and protection, ICRP has classified people exposed to radiation in three categories. Those three categories are listed below.

Table 2.3 Tissue weighting factors W_T of various tissues (ICRP.org)

Organ	Tissue weighting factor W_T, (ICRP 2007)
Breast	0.12
Colon	0.12
Bone Marrow (Red)	0.12
Lung	0.12
Stomach	0.12
Gonads	0.08
Bladder	0.05
Liver	0.05
Thyroid gland	0.05
Esophagus	0.05
Skin	0.01
Bone surface	0.01
Brain	0.01
Salivary glands	0.1
Remainder	0.05
Whole body	1.0

(a) *Radiation Workers.*
This category consists of those people who work directly in radiation area. For example a person working as a radiation safety officer or a person working in a nuclear reactor is classified as radiation worker.
(b) *General Public.*
This category includes common people in public. This category has different exposure limits than the radiation workers.
(c) *Medical Exposure.*
This category consists of patients exposed to radiation for diagnostic or therapeutic purposes.

The dose limits for people in different categories are different. A person from general public cannot receive the same maximum dose or exposure as a radiation worker gets and a patient cannot get the same maximum dose a person from the general public is allowed to obtain.

2.10 Annual Limit on Intake (ALI)

In order to restrict human body against excessive exposure to radiation, ICRP defines the term Annual Limit on Intake. ALI imposes a maximum limit on each individual organ as well as the whole body in each year. However, this maximum limit is different for different categories.

The maximum annual dose limit for all three categories is given below.

Radiation Workers For radiation workers ICRP recommends the following annual effective dose limit.

(i) 500 mSv (50 rem) to all tissues except the lens of an eye.
(ii) 150 mSv (15 rem) to the lens of an eye.
(iii) 50 mSv (5 rem) to the whole body per year, with not more than 100 mSv over five years.

It must be noted that the whole body limit and any individual organ limit must be satisfied at the same time. For example if the lungs of a person is exposed to 30 rem annually and at the same the whole body receives 8 rem then it is not allowed according to the rules.

Mathematically, the above mentioned limits can be summarized as follows.

$$\text{For a single organ} \quad \boldsymbol{W_T H \leq 500\ \text{mSv}} \tag{2.12}$$

$$\text{For the whole body} \quad \sum_{\text{T}} \boldsymbol{W_T H \leq 50\ \text{mSv per year}} \tag{2.13}$$

General Public The ICRP recommendation of the annual limit on intake for a member of general public is 5 mSv or 500 rem.

Medical Exposure No specific dose limit is recommended by the ICRP for medical exposure. The commission, however, did recommend that only necessary exposure should be made.

Example 2.5 Using the tissue weighting factors in Table 2.3, calculate the implied limits for each of the following organs, assuming that each organ is irradiated completely in isolation: the bone surface, the lungs and the bladder.

Solution

Use equation	$\boldsymbol{W_T H \leq 50\ \text{mSv}}$
	$\boldsymbol{H = 50/W_T \text{mSv}}$
For bone surface	$\boldsymbol{H = 50/0.01 = 5000\ \text{mSv}\ (500\ \text{rem})}$
For lungs	$\boldsymbol{H = 50/0.12 = 416.66\ \text{mSv}\ (41.66\ \text{rem})}$
For bladder	$\boldsymbol{H = 50/0.05 = 1000\ \text{mSv}\ (100\ \text{rem})}$

Since the maximum allowed dose to each individual tissue is 500 mSv per year therefore, the bone surface and the bladder can still not have the above calculated dose. Each of these tissue has a maximum of 500 mSv restrictions which must be followed to avoid radiation hazards and damages.

Example 2.6 A student, working in a radiation laboratory, is exposed to radiation and received the given equivalent doses to exposed organs in 1 year. Thyroid = 120 mSv, Stomach = 80 mSv, Bone Marrow = 160 mSv, Bladder = 100 mSv, and Lungs = 140 mSv.

Is he safe according to the ICRP regulations?

Solution Use the equation $\sum W_T H \leq 0.05\ \text{Sv}^{\ \text{T}}$.

Expanding the sum over all tissues

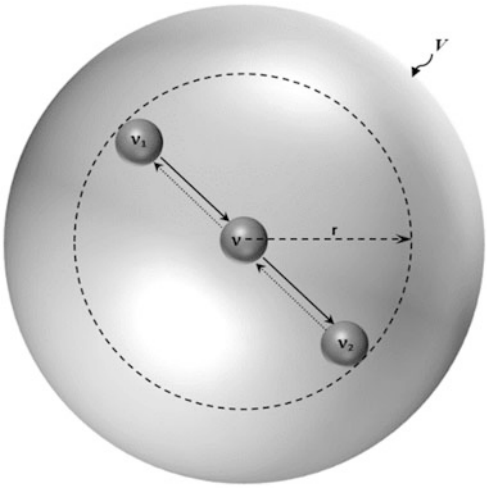

Fig. 2.8 Charged particle equilibrium in an elemental volume ν inside a hypothetical bigger volume V

$$(W_T H)_{\text{thyroid}} + (W_T H)_{\text{stomach}} + (W_T H)_{\text{bone marrow}} + (W_T H)_{\text{bladder}} + (W_T H)_{\text{lungs}} \leq 50\ \text{mSv}$$

$$(0.05 \times 120)_T + (0.12 \times 80)_S + (0.12 \times 160)_{BM} + (0.05 \times 100)_B + (0.12 \times 140)_L$$

$$= (0.05 \times 120)_T + (0.12 \times 80\text{mSv})_S + (0.12 \times 160)_{BM} + (0.05 \times 100)_B + (0.12 \times 140)_L$$

$$= 6.0 + 9.6 + 19.2 + 5 + 16.8$$

$$= 56.6\text{mSv}$$

Since 56.6 mSv $>$ 50 mSv thus, the dose exceeds the annual allowable dose limit. Therefore, the student is not safe according to the ICRP regulations.

2.11 Charged Particle Equilibrium

Charged particle equilibrium (CPE) for the volume of interest v exists if each of the outgoing charged particle is replaced by an identical charged particle of the same energy. CPE will generally exist in a homogeneous medium provided that the separation of the outer boundaries of the medium and the volume of interest is greater than the range of the charged particles. Generally, CPE will not exist around the interfaces of heterogeneous media. Absorbed dose measurement at a given point is however independent of CPE. Charged particle equilibrium can be achieved whether the radiation source is inside or outside of the medium. Consider a hypothetical sphere of extended volume V as shown in Fig. 2.8. A radioactive source is uniformly distributed in V, emitting radiations isotropically. Suppose a smaller volume ν inside the bigger V is the volume of interest. In the surrounding, two other elemental volumes (ν_1 and ν_2) are symmetrically defined. Charge particles (solid lines) moving from ν_1 to ν are identical to those traveling from ν to ν_2.

On the other side, lesser but identical particles (dotted lines) flow from ν_2 to ν and ν to ν_1. The same is applicable to all symmetrically defined elemental volumes inside the sphere of radius r ($r >$ range of the charged particles). Based on this analogy the net charge leaving and entering volume ν is zero, i.e., CPE exits in this volume.

2.12 Stopping Power

For indirectly ionizing radiations, linear and mass attenuation coefficients are used to determine beam attenuation in a medium of interest. For directly ionizing radiations, however, linear and mass stopping powers are the quantities of relevance. The linear stopping power is defined as the rate of energy loss (*dE)* per unit track length (*dx*) in the medium. The mass stopping power is obtained by normalizing the linear stopping power to the mass density (ρ) of the medium, as in Eq. (2.40).

$$ {}_{\rho}S_{\mathrm{c}} = \left(\frac{dE}{Ndx}\right)_{\mathrm{c}} \tag{2.40} $$

The subscript *c* and *N* indicates the collisional stopping power and no. of incident particle respectively. Like KERMA, the total stopping power for directly ionizing radiation can also be split into two components i.e. collisional stopping power (S_{c}), and the energy lost in the form of bremsstrahlung (i.e. radiative component; S_{r}). However, the later part may escape the elemental volume and for dosimetric purposes we are less interested in the radiative component of the stopping power as S_{c} has the main contribution in the locally deposited energy in the elemental volume. Mass stopping power is typically measured in MeV·cm^2/g.

2.12.1 Stopping Power and CEMA

Equation (2.40) can be rewrite as:

$$ dE = {}_{\rho}S^{\rho}\mathrm{c}Ndx \tag{2.41} $$

Now dividing both sides by the mass of the layer *dm*. by using $dm = \rho dV$ and rearrangements of Eq. (2.41) will lead us to the result:

$$ \frac{dE}{dm} = \frac{{}_{\rho}S^{\rho}\mathrm{c}}{\rho}\left(\frac{Ndx}{dV}\right) \tag{2.42} $$

If we recall our memory, the quantity in the brackets is the fluence ϕ, therefore:

$$\frac{dE}{dm} = \frac{{}_{\rho}S^{\rho}{}_{\mathrm{c}}}{\rho}\phi \tag{2.43}$$

As mentioned earlier, CEMA is used instead of KERMA for directly ionizing radiation.

The secondary charged particles produce due to interactions of directly ionizing radiation in the medium are often called delta-rays (δ-rays). The δ-rays equilibrium is the situation in which any charged particle kinetic energy leaving the volume of interest is replaced by an exactly equal amount entering the volume and being deposited in it or imparted to it.

Like KERMA, CEMA is also not necessarily equal to absorbed dose, as some of the secondary charged particles (i.e. δ-rays) may leave the volume of interest. The analogy of absorbed dose for directly ionizing radiation is the same as for indirectly ionizing radiation. The difference is in only the type of interaction with the medium and may be the generated secondary particles. Now, to calculate absorbed dose for directly ionizing radiation, it must be assumed that there is δ-ray equilibrium in order to be able to equate CEMA with absorbed dose. The dose for mono-energetic directly ionizing radiation is given as:

$$D \overset{\delta-\mathrm{eqm}}{=} \left(\frac{S_{\mathrm{c}}}{\rho}\right)\phi \tag{2.44}$$

Similarly, in the case of a spectrum of incident directly ionizing radiation:

$$D \overset{\delta-\mathrm{eqm}}{=} \int_{0}^{E_{\max}} \phi_{\mathrm{E}}\left(\frac{S_{\mathrm{c}}(E)}{\rho}\right)dE \tag{2.45}$$

2.12.2 Fluence and Dose Relationship for Electrons

The absorbed dose D in a medium 'w' can be related to the electron fluence (Φ) by Eq. (2.46), provided the following two conditions met:

(a) Radiative photons escape the volume of interest and
(b) Secondary electrons are locally absorbed or there exists a charged particle equilibrium (CPE) of secondary electrons.

$$D_{\mathrm{w}} = \Phi\left[\left(\frac{dE}{\rho dx}\right)_{\mathrm{c,w}}\right]_{\mathrm{E}} \tag{2.46}$$

As expected, absorbed dose is proportional to charge particle fluence and collisional mass stopping power in the medium.

2.13 Cavity Theory

Radiation detectors of various types are used for absorbed dose measurements in a medium. The composition of the dose sensitive part of dosimeter (cavity in case of ionization chamber) is different from the medium in which it is inserted. The signal from the detector can be related to the absorbed in the medium using certain calibration and correction factors. Cavity theory in reality is the determination of a dose conversion factor '*f*' for a given detector medium '*g*' to the surrounding medium '*w*' containing the cavity (Eq. (2.47))[Nahum A (2007)]

$$f = \frac{D_{\mathrm{w}}}{D_{\mathrm{g}}} \tag{2.47}$$

where D_{g} and D_{w} are doses measured in the cavity and the medium of interest respectively.

2.13.1 Bragg–Gray Cavity Theory

The Bragg–Gray cavity theory was developed for the first time to determine the '*f*' factor (Eq. (2.48)) in an arbitrary radiation quality *Q*.

A detector cavity that do not disturb the electron fluence, when it is inserted into the medium, is known as Bragg–Gray (B-G) cavity [Turner JE (2007)]. Consider Fig. 2.9 where a uniform medium '*w*' contains a small cavity filled with a different medium '*g*'. The cavity dimension is such that the fluence of the charged particles (Φ) remains unperturbed with its presence in the medium '*w*'.

For absorbed dose in cavity medium '*g*' (cavity) Eq. (2.46) can be written as [Attix FH (2004)],

$$D_{\mathrm{g}} = \Phi \left[\left(\frac{dE}{\rho dx} \right)_{\mathrm{c,g}} \right]_{\mathrm{E}} \tag{2.48}$$

It is reasonable to assume that for the Brag-Gray cavity the fluence Φ remains the same with and without the introduction of the detector cavity in the medium. From Eqs. (2.46) and (2.48) the ratio of absorbed doses in '*g*' and '*w*' is [Attix FH (2004)]:

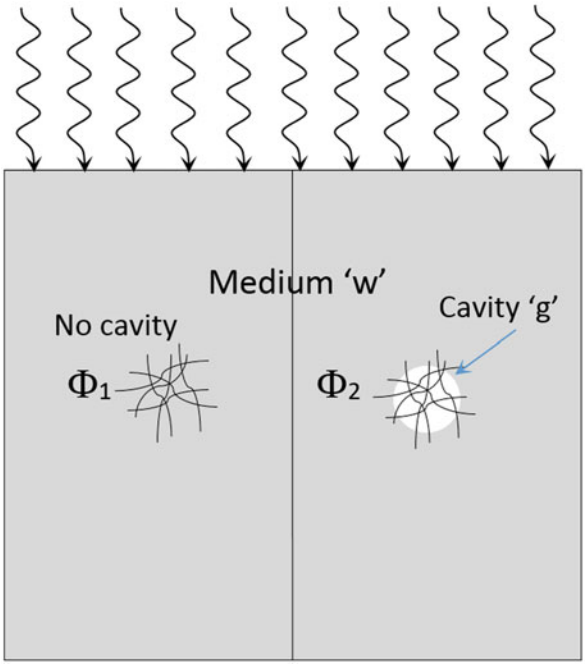

Fig. 2.9 Charge particles fluence is not affected by the insertion of detector cavity (B-G cavity) in the medium compared to the fluence exits on the left side with no cavity in place (i.e., $\Phi_1 = \Phi_2$)

$$\frac{D_w}{D_g} = \frac{\left(dE/\rho dx\right)_w}{\left(dE/\rho dx\right)_g} \tag{2.49}$$

The subscript '*c*' is not used in the above equation, since it is understood that local absorbed dose depends on collisional stopping power '$_{\rho}S_c$' only. The term on the right hand side of Eq. (2.49) is simply the ratio of mass collision stopping powers $_{\rho}S^{\rho}g^{w}$. Hence it transforms into the following form [Attix FH (2004)].

$$\frac{D_w}{D_g} = {}_{\rho}S^{\rho}g^{w} \tag{2.50}$$

The detector must fulfill a necessary condition if it is to be considered as Bragg–Gray cavity, that is "the introduction of the detector cavity in the medium must not perturb the charged particles fluence and energy distribution" [Nahum A (2007)].

A corollary that can be deduced from the first condition is:

The absorbed dose in the cavity is supposed to be deposited entirely by the charged particles crossing it.

Bragg–Gray cavity conditions are reasonably fulfilled for the majority of air-filled ionization chambers used in radiotherapy (megavoltage photon and electron beams) dosimetry [Turner JE (2007)].

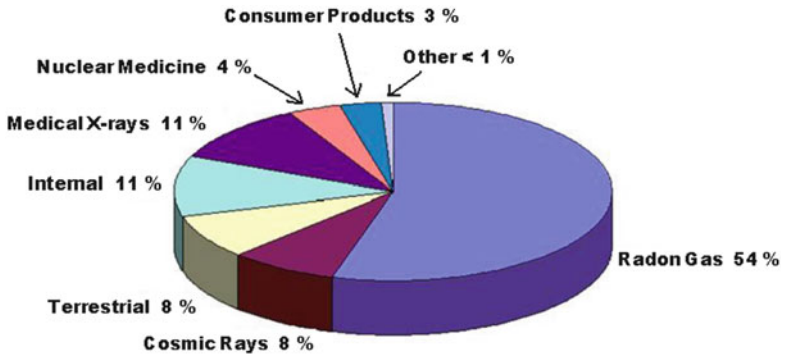

Fig. 2.10 Public exposure of radiation in the USA [Turner JE (2007)]

2.14 Biological Effects of Radiation

Radiations have been used widely in cancer treatment and other health issues. The successful outcomes and benefits of radiations have broadened the horizon of its use in a number of ways. Both directly and indirectly ionizing radiation have great impact on health care technology [Caon M, Bibbo G, Pattison J (1997)]. However, radiations can also be very dangerous to health if exposed in an unwanted and uncontrolled way. Human body can be affected in different ways when exposed to radiations. Despite of the NRC regulations to protect public from excessive expose to radiation still people expose to radiation coming out from various sources. Figure 2.10 shows public exposure to radiation in the USA. The figure shows that the highest contributor radon gas [Orabi M (2017)] and other natural sources of radiation are the major source or cause of radiation an average American is exposed to every year.

Human-made sources of radiation like medical x-rays, radiation during nuclear medicine diagnosis and treatment and other consumer products like watches, mobile phones and televisions are provide considerable amount of radiations to an average American each year. Though, the exposure from human made sources is less than the exposure from natural sources, but still big enough to produce damaging effects in the tissues.

Example 2.7 Assume that an average American person receives 40 rem of dose in 1 year. Find the dose he receives from radon gas, cosmic rays and consumer products?

Solution Total dose an average American receives per annum = 40 rem.

Figure 2.10 shows that 54% of this dose is received by exposure to radon gas. Therefore, the dose he receives from radon gas = $40 \times 54/100 = 21.6$ rem.

8% of the annual dose is given by cosmic rays. Therefore, the dose he receives from cosmic rays = $40 \times 8/100 = 3.2$ rem.

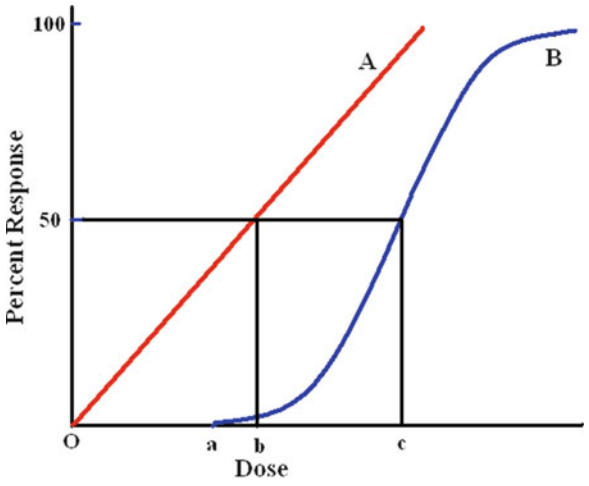

Fig. 2.11 Deterministic and stochastic effects, and tissues response to given dose

The dose he gets when exposed to radiation emitted by consumer products is 3%. Therefore, the dose he receives from consumer products = 40 × 3/100 = 1.2 rem.

All radiations have various effects on body tissues. Based on the quantity of dose and the body or exposed tissues response the biological effects of radiations can be classified into two major categories; Deterministic Effects and Stochastic Effects. Response of tissues to a given dose and the occurrence and chances of both kinds of effects are given in Fig. 2.11. Both effects are discussed below.

(A) *Stochastic Effects*. Stochastic effects are statistical effects for which there is no minimum dose required. Curve A in Fig. 2.11 shows a response curve representing stochastic effects. It is a probabilistic effect or a statistical phenomenon. It is possible that an effect can start in the body tissues when exposed to a very low dose. On the other hand a person may not get affected even exposed to a higher dose, though those chances are very low. The curve shows that the tissue response is linearly proportional to the quantity of radiation dose tissues are exposed to. That means, despite of its probabilistic nature, the chances of stochastic effects in the exposed tissues increase with increasing dose. Stochastic effects are also referred as late effects because these effects do not appear immediately after tissues are being exposed to radiation. Examples of such late effects or stochastic effects are cancer and hereditary effects in a part or whole body exposed to radiation. The legend scientist Marie Curie died of Aplastic Anemia, brought on by exposure to radiation. Overall, we can summarize the characteristics of stochastic effects in the following points.

- They have no threshold dose.
- They increase in likelihood as dose increases.
- Their severity is not dose related.
- There is no dose above which stochastic effects are certain to occur.

Table 2.4 Threshold doses for some deterministic effects in case of radiation exposure for many years

Dose in gray	Effect on tissues (when exposed for many years)
0.1 Gy	Detectible opacities
0.2 Gy	Sterility for woman
0.4 Gy	Visual impairment
0.4 Gy	Temporary sterility for man
0.4 Gy	Depression of haematopoiesis
1.0 Gy	Chronic radiation syndrome
2.0 Gy	Permanent sterility for man
3.0 Gy	Erythema

(B) *Deterministic effects*. Deterministic effects or non-stochastic effects are those kinds of effects that need a minimum dose or a threshold dose to start occurring. Depending upon the nature of the effect, the threshold dose could be little or more. Curve B in Fig. 2.11 shows a response curve representing deterministic effects. No effect can be observed if tissues or body is exposed to a dose smaller than the threshold dose. Example of such kind of effects is burning of the skin when exposed to radiation. During tanning process or sun bath, body is exposed to high energy ultraviolet radiations. If exposed to a high dose skin burning occurs which gets severe with more exposure. It is found that 200–300 rad (2–3 rem) to the skin can result in the reddening of the skin (erythema), similar to a mild sunburn that may result in hair loss due to damage to hair follicles. Similarly 125–200 rad (1.25–2 rem) to the ovaries can result in prolonged or permanent suppression of menstruation in about 50 percent (50%) of women, 600 rad (6 rem) to the ovaries or testicles can result in permanent sterilization and 50 rad to the thyroid gland can result in benign (non-cancerous) tumors [Cember and Johnson (2009)].

(C) The response of the tissues is low in the beginning when tissues are exposed to a dose higher than threshold dose however, increases very rapidly when exposed to high dose as shown in the figure. When the dose increases to a very high level affecting most of the tissues exposed the response decreases again. The reason being at such a high dose most of the tissues or cells are already affected and very few are left behind that will still affect. Some examples of deterministic effects are given in Table 2.4. Overall, we can summarize the characteristics of deterministic effects in the following points [Cember and Johnson (2009)].

- A threshold dose is required below which no effect is seen.
- They always occur once the threshold dose is reached.
- Worsening of the effect occurs as dose increases over the threshold.
- Different effects, tissues and people have different threshold doses for deterministic effects.
- These effects could be early or could appear late.

Table 2.5 Deterministic effects in the body with dose and time to onset

Exposure (rem)	Effect or outcome	Time to onset (without treatment)
5–10	Changes in blood counts	
50	Nausea	Hours
55	Fatigue	
70	Vomiting	
75	Hair loss	2–3 weeks
90	Diarrhea	
100	Hemorrhage	
400	Possible death	Within 2 months
1000	Destruction of intestinal lining	
	Internal bleeding	
	And death	1–2 weeks
2000	Damage to central nervous system	
	Loss of consciousness;	Minutes
	And death	Hours to days

Table 2.4 gives some of the effects on various tissues and organs when exposed to radiation for many years. In Table 2.5 the dose given to tissues or organs and its effect is shown along with the time in which the effect starts appearing.

Problems

1. A student, working on an experiment, exposed 12 kg of dry air to x-rays. As a result of ionization in the air, 3.612×10^{-3} C charge is produced. Determine the Exposure in the units of Roentgen.
2. A person received an average whole-body x-ray dose of 0.6 mGy and 0.8 mGy from 10-MeV neutrons. What is the whole-body equivalent dose in mSv?
3. A patient is recommended with 12 Gy absorbed dose to treat a tumor in his bladder. If this dose is delivered through (i) electrons (ii) neutrons of energy 5 MeV, and (iii) α-rays of energy 4 MeV, then find the effective dose received by the bladder of the patient in each case.
4. A female radiation worker receives the following equivalent doses to various organs when worked in a radiation area for 1 year. Bone Surface = 200 mSv, Breast = 150 mSv, Lungs = 40 mSv, and Liver =?

   Keeping the maximum allowed annual limit in mind, find the maximum dose received by lungs to keep her in the ALI limits? Do you think she is safe according to ICRP rules?
5. Calculate the allowable equivalent dose to the thyroid of a worker for a year in which he is exposed to non-uniform irradiation involving the whole body, the lungs and the thyroids. During the year he receives equivalent doses of 25 mSv to the whole body and 150 mSv to the lungs.

6. A person working in a grocery store in the US received an average dose of 80 rem in 1 year. Find the average contribution from radon gas and from medical x-rays.

References

Ahmad N (1999) Radiation physics-1. Allama Iqbal Open University Publisher, Islamabad
Attix FH (2004) Introduction to radiological physics and radiation dosimetry. Wiley-VCH Verlag GmbH & Co. KGaA, Weinheim
Caon M, Bibbo G, Pattison J (1997) A comparison of radiation dose measured in CT dosimetry phantoms with calculations using EGS4 and voxel-based computational models. Phys Med Biol 42:219–229
Cember H, Johnson TE (2009) Introduction to health physics. McGraw-Hill Medical, New York, pp 203–270
Grupen C (2010) Introduction to radiation protection. Springer-Verlag Publisher, Berlin Heidelberg
Hendee WR, Ibbott GS, Hendee EG (2005) Radiation therapy physics, 3rd edn. Wiley, New Jersey
ICRU Report 60 (1998), "Fundamental Quantities and Units for Ionizing Radiations"
ICRP International Commission on Radiological Protection (2007) Recommendations of the International Commission on Radiological Protection. ICRP Publication 103, Annals of the ICRP, 103,
Khan FM (2005) The physics of radiation therapy, 3rd edn. Lippincott Williams & Wilkins, USA
Martin JE (2013) Physics for radiation protection, 3rd edn. Wiley, USA
Nahum A (2007) Principles and basic concepts in radiation dosimetry. In: Mayles P, Nahum A, Rosenwald JC (eds) Handbook of radiotherapy physics: theory and practice. Taylor & Francis Group, LLC, pp 89–114
Orabi M (2017) Radon release and its simulated effect on radiation doses. Health Phys 112 (3):294–299
Podgorsak EB (2005) External photon beams: physical aspects. In: Podgorsak EB (ed) Radiation oncology physics: a handbook for teachers and students. International Atomic Energy Agency (IAEA), Vienna, pp 161–217
Seuntjens JP, Strydom W, Short KR (2005) Dosimetric principles, quantities and units. In: Podgorsak EB (ed) Radiation oncology physics: a handbook for teachers and students. International Atomic Energy Agency (IAEA), Vienna, pp 45–70
Stabin MG (2007a) Radiation protection and dosimetry: an introduction to health physics. Springer Science & Business Media, New York, pp 67–74
Stabin MG (2007b) Radiation protection and dosimetry: an introduction to health physics. Springer Science + Business Media, LLC, New York
Turner JE (2007) Atom radiation and radiation protection, 3rd edn. Wiley-VCH Verlag GmbH & Co. KGaA, Weinheim
Wall BF (2004) Radiation protection dosimetry for diagnostic radiology patients. Radiat Prot Dosim 109(4):409–419

Chapter 3
Interaction of Gamma Rays and X-Rays with Matter

Muhammad Maqbool

Contents

3.1 Introduction 43
3.2 Types of Interaction with Matter 46
3.3 Overall Interaction of Photons with Matter 55
References 61

3.1 Introduction

Gamma rays are electromagnetic radiation either emitted from a nucleus or an annihilation reaction between matter and antimatter (Attix 1986). X-rays are electromagnetic radiation emitted by charged particles (usually electrons) in changing atomic energy levels or in slowing down in a Coulomb force field. X-rays and gamma rays have identical properties, only differing in their origin. The two used to be distinguishable by energy of the particle, but now linear accelerators are able to produce high-energy X-rays that have the same or higher energy as gamma rays. The practical range of photon energies emitted by radioactive atoms extends from a few thousand eV up to over 7 MeV. On the other hand, linear accelerators are able to produce more energetic photons. The energy ranges of X-rays in terms of generating voltage are given in Table 3.1.

Understanding the interaction of X-ray and γ-ray with matter is very important because it is the same interaction that occurs when these radiations come across the human body and tissues.

X-ray interactions are important in diagnostic examinations for many reasons. For example, the selective interaction of X-ray photons with the structure of the human body produces the image; the interaction of photons with the receptor converts an X-ray or gamma image into one that can be viewed or recorded. This chapter considers the basic interactions between X-ray and gamma photons and

M. Maqbool, PhD (✉)
Department of Clinical & Diagnostic Sciences, Health Physics Program, The University of Alabama at Birmingham, Birmingham, AL 35294, USA
e-mail: mmaqbool@uab.edu

M. Maqbool (ed.), *An Introduction to Medical Physics*, Biological and Medical Physics, Biomedical Engineering, DOI 10.1007/978-3-319-61540-0_3

Table 3.1 Energy range and corresponding categories of X-rays

Energy	X-Rays
0.1–20 kV	Soft, low energy
20–120 kV	Diagnostic range
120–300 kV	Orthovoltage
300 kV–1 MV	Intermediate energy
1 MV+	Megavoltage

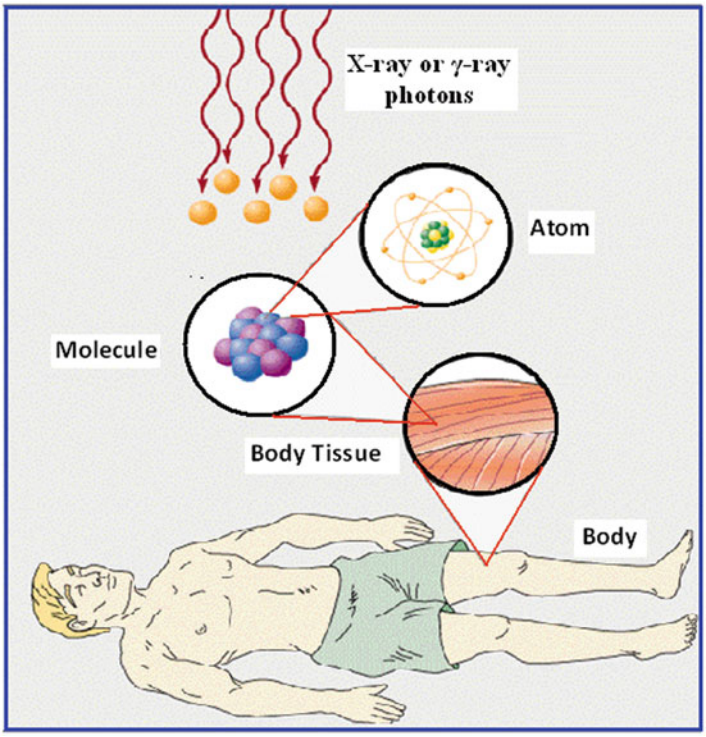

Fig. 3.1 Schematic diagram of photon interacting and transferring energy to the human body

matter including the human body and tissues. When a γ-ray or X-ray passes through a medium, an interaction occurs between the photons and matter resulting in energy transfer to the medium. The interaction can result in a large energy transfer or even complete absorption of the photon. However, a photon can be scattered rather than absorbed and retain most of the initial energy while only changing direction. An X-ray or γ-ray photon transfers its energy to the atoms and molecules of the body cells they interact with. As a result, the exposed cells are affected. Those cells take part in the construction of tissues which are also affected by the interaction. The tissues compose the whole body which is eventually affected by the interaction of such X-rays or γ-rays. A schematic arrangement of these steps is given in Fig. 3.1 (Hopkins et al. 2012).

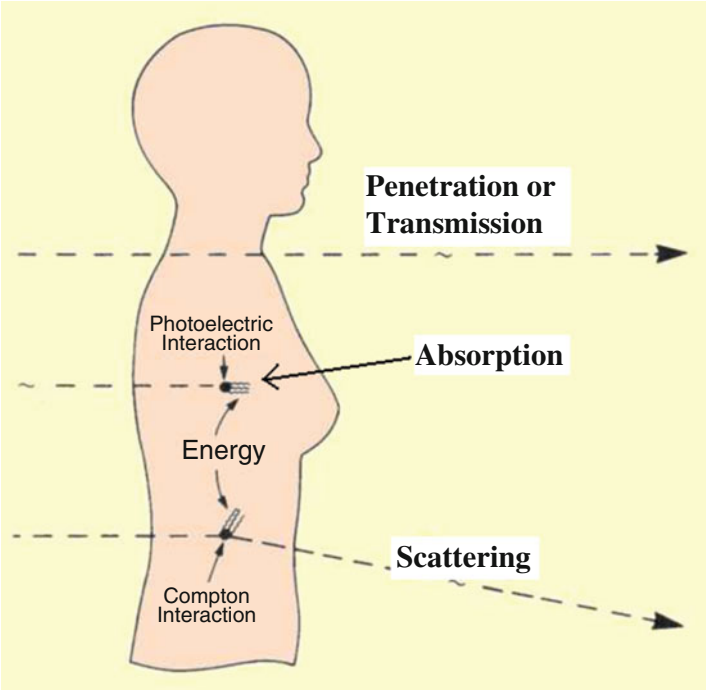

Fig. 3.2 Interaction of gamma rays or X-rays with the human body or matter

Overall when an X-ray beam or gamma radiation passes through an object, three possible fates await each photon, as shown in Fig. 3.2:

1. It can penetrate and transmit the section of matter without interacting.
2. It can interact with the matter and be completely absorbed by depositing its energy.
3. It can interact and be scattered or deflected from its original direction and deposit part of its energy.

These three outcomes are described in Fig. 3.2 which shows how photons entering the human body will either penetrate or transmit through, be absorbed, or produce scattered radiation. The last two processes are mainly responsible for the photon energy transferred to tissues. This energy is exploited to kill tumor cells during cancer treatment by radiation.

Since these different ways of photons interacting with matter result in many important outcomes and impacts on body tissues, therefore, it is mandatory to discuss some of those important ways or mechanisms.

3.2 Types of Interaction with Matter

There are five ways or mechanisms by which photons can interact with matter. Those are photoelectric absorption, Compton scattering, pair production, coherent scattering, and photodisintegration with the first three being the major and most important ways of interaction [23]. All these mechanisms of interaction result in the transfer of energy to the electrons of matter or tissues. The electrons then transfer this energy to matter in many small Coulomb-force interactions. The relative importance of Compton scattering, photoelectric absorption, and pair production depends on both the photon quantum energy and the atomic number of the absorbing medium.

These interactions play very important role in therapeutic as well as in diagnostic medical physics. In imaging physics, the nature of interaction has also a great effect on the quality of image as described below:

- *No interaction*. X-ray or γ-ray passes completely through the tissue and into the image recording device.
- *Complete absorption*. X-ray energy is completely absorbed by the tissue. No imaging information results.
- *Partial absorption with scatter*. Scattering involves a partial transfer of energy to the tissue, with the resulting scattered X-ray having less energy and a different trajectory. Scattered radiation tends to degrade image quality and is the primary source of radiation exposure to operator and staff.

3.2.1 Photoelectric Absorption

The photoelectric absorption or effect is the most important interaction of low-energy photons with matter. This effect is dominant in the 0–0.5 MeV photon energy range. Due to its dominancy in low-energy range, this phenomenon plays a major role in radiation dosimetry, diagnostic imaging, and low-energy therapeutic applications (Hopkins et al. 2012). It has been determined experimentally that when light shines on a metal surface, the surface emits electrons. For example, you can start a current in a circuit just by shining a light on a metal plate. This leads to the explanation of photoelectric effect which can be defined as the phenomenon in which a light photon interacts with a material and gives up all its energy to detach and move out an electron from the surface of the material. The interacting photon gives up its energy completely and is lost. This energy appears in two forms. A part of this energy is utilized to detach or eject an electron. This energy is called work function of the material. The remaining energy of the incident photon is taken away by the electron as its kinetic energy. The ejected electron is called photoelectron.

Every electron is bound to its atom or material by certain energy, and in order to remove that electron from its atom, some energy is required. This minimum amount of energy required to detach or eject an electron from its respective atom is called

work function Φ of that material. If we want to provide this minimum energy or work function through a photon, then this will correspond to certain minimum frequency of the photon. This minimum frequency is called threshold frequency. Thus, the minimum frequency of incident light photon that can eject an electron from a material is called threshold frequency represented by ν_0.

This phenomenon is dominant in energy levels from a few eV up to 0.5 MeV. Photoelectric effect occurs when a bound electron from the atom is ejected after interaction with a photon of energy $h\nu$. Since the incident photon transfers its energy in two portions, therefore, the following mathematical equation can be developed to express this transfer of energy.

$$\boldsymbol{h\nu = \Phi + T} \tag{3.1}$$

where h is the Planck's constant, $h\nu$ is the energy of incident photon, $\Phi = h\nu_0$ is the work function of the material, and T is the kinetic energy of the ejected photoelectron. If the maximum kinetic energy corresponds to a potential called stopping potential V_0 and e is the charge of an electron, then $T = eV_0$ and Eq. (3.1) becomes,

$$\boldsymbol{h\nu = \Phi + eV_0} \tag{3.2}$$

The photoelectric cross section τ or the probability of occurring photoelectric effects depends upon the incident photon energy as well as on the charge number Z of the interacting material. As the energy of a photon decreases, the probability of photoelectric absorption or the photoelectric cross-sectional "τ" increases rapidly. The energy dependence of the photoelectric effect cross section is between E^{-2} and E^{-4}. The Z and E dependence on the photoelectric cross section near 100 keV is approximate:

$$\boldsymbol{\tau \propto Z^n E^{-3} \text{ or } \tau \propto Z^n/(h\nu)^3} \tag{3.3}$$

where the exponent n varies between 3 and 4 over the X-ray or gamma ray energy region of interest.

The following points should be noted about photoelectric absorption:

- A photon, after interaction with an absorber atom, completely disappears.
- In its place, a photoelectron is ejected with its kinetic energy equal to the difference of the absorbed photon's energy and the work function of the absorbing atom.
- For γ-ray or X-ray with sufficient energy, the most probable origin of the photoelectron is the most tightly bound lower shell or the K-shell of the atom.
- The photoelectric interaction is most likely to occur if the energy of the incident photon is just greater than the binding energy of the electron with which it interacts.
- No photoelectric effect will occur if the frequency of the incident photon is smaller than the threshold frequency needed to eject photoelectron.
- No photoelectric absorption will occur if the energy of incident photon is smaller than the work function of the absorbing material.

Example 3.1 The threshold frequency for photoelectric absorption to occur in certain material is 8×10^{14} Hz. Find the work function of the material. Can a photon of wavelength 450 nm eject a photoelectron from this material?

Solution Threshold frequency $= \nu_0 = 8 \times 10^{14}$ Hz, Planck's constant $= h = 6.626 \times 10^{-34}$ J.s

$$\text{Work function} = \Phi = h\nu_0 = 6.626 \times 10^{-34} \times 8 \times 10^{14}$$
$$= 1.325 \times 10^{-19}\text{J}$$
$$\Phi = \mathbf{3.312\ eV}$$

Can a photon of wavelength 450 nm eject a photoelectron?

In order to find an answer, we have to find the threshold wavelength λ_0 first. The threshold wavelength is related to its threshold frequency by the relation $\lambda_0 = c/\nu_0$, where c is the speed of light in free space and is equal to 3×10^8 m/s. Thus,

$$\text{Threshold wavelength } \lambda_0 = 3 \times 10^8 / 8 \times 10^{14}$$
$$= 3.75 \times 10^{-7}\text{m}$$
$$\boldsymbol{\lambda_0 = 375\ nm}$$

Since the wavelength 450 nm is longer than the threshold wavelength, therefore, the frequency of the incident photon is smaller than the threshold frequency because frequency and wavelength of a photon are inversely proportional to each other. Thus, a photon with wavelength 450 nm cannot eject an electron from this material.

Example 3.2 An X-ray photon beam of photon energy 9 eV is allowed to fall on a metal surface. If the threshold frequency for the metal is 1.4×10^{15} Hz, then find the maximum kinetic energy gained by a photoelectron, the maximum speed of a photoelectron, and the stopping potential corresponding to the maximum kinetic energy.

Solution Energy of the incident photon $= E = h\nu = 9$ eV
Threshold frequency $= \nu_0 = 1.4 \times 10^{15}$ Hz

$$\text{Work function of the metal} = \Phi = h\nu_0 = 6.626 \times 10^{-34} \times 1.4 \times 10^{15}$$
$$\Phi = 9.276 \times 10^{-19}\text{J}$$
$$\Phi = 5.797\ \text{eV}$$

Now using Eq. (3.1)

$$h\nu = \Phi + T$$
$$T = h\nu - \Phi$$
$$T = 9 - 5.797$$
$$\boldsymbol{T = 3.2\ eV}$$

Thus, the maximum kinetic energy of a photoelectron is 3.2 eV or 5.12×10^{-19} J.

To find the maximum speed v of a photoelectron, use the kinetic energy relation $T = ½\ mv^2$

$$\text{or} \qquad v = (2T/m)^{1/2}$$

where m is the rest mass of an electron and is given by $m = 9.11 \times 10^{-31}$ kg.

Therefore, $v = (2 \times 5.12 \times 10^{-19}/9.11 \times 10^{-31})^{1/2}$

$$\boldsymbol{v = 1.06 \times 10^6 \text{m/s}}$$

To find the stopping potential V_0, we use the relation $T = eV_0$.

$$\text{or} \qquad V_0 = T/e$$

Putting the values $T = 5.12 \times 10^{-19}$ J and $e = 1.6 \times 10^{-19}$ C, we get

$$V_0 = 5.12 \times 10^{-19}/1.6 \times 10^{-19}$$

$$\boldsymbol{V_0 = 3.2 \text{ volt}}$$

Thus, the stopping potential corresponding to the maximum kinetic energy is 3.2 volts.

3.2.2 Compton Scattering

Compton's scattering is the most important interaction in both therapeutic and diagnostic medical physics. For low-Z materials such as air, water, and human tissues, Compton scattering dominantly occurs in approximately 100 keV–30 MeV photon energy range. In high-Z materials, its dominant energy range is 0.5 MeV–10 MeV (Attix 1986). Compton scattering gets special importance in therapeutic medical physics because many of the treatment planning by photon beam are carried out in this energy range. A tumor and normal tissues surrounding the tumor, scatter radiation in various directions, making Compton scattering an important phenomenon to concentrate on.

Compton effect occurs when photons interact with free or weakly bound electrons in the γ-ray incident beam. In this incoherent scattering, all atomic electrons act independently of one another [24]. In Compton scattering, a single photon strikes an electron, giving a part of its energy and momentum to the electron. This electron is stationary or almost stationary and is called target electron. As a result, the photon scatters with a reduced energy and longer wavelength. The difference in the energy of photon before and after scattering is taken away by the electron as its kinetic energy. This electron is called *recoil electron*. If a beam of photons is interacting with matter or body tissues, then a number of photons are scattered by the electrons of the atoms that compose the matter or tissues. As a

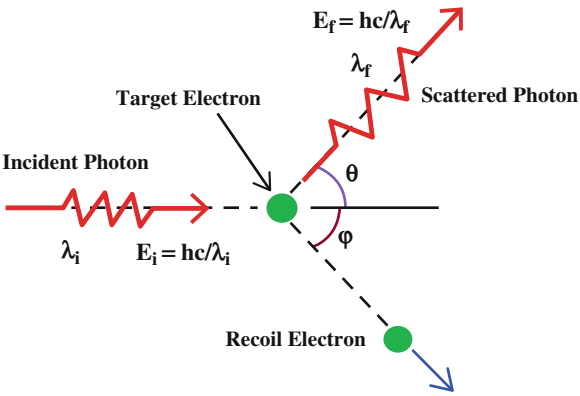

Fig. 3.3 Compton scattering of a photon by an electron

result, the beam attenuation occurs. Moreover, ionization of atoms also occurs as a result of such scattering.

The initial photon of energy E_i, momentum p_i, and wavelength λ_i has a much higher energy than the binding energy of the electron. When the photon collides with the electron, the electron receives energy from the photon and is emitted at an angle φ. The reduced-energy photon of wavelength λ_f is scattered at an angle θ as shown in Fig. 3.3.

The initial photon has energy hc/λ_i and collides with a stationary or almost stationary electron, as seen in Fig. 3.3. The electron has no initial kinetic energy or momentum. The scattered photon has lower energy of hc/λ_f. Applying the law of conservation of energy and the law of conservation of momentum along the direction of initial photon and perpendicular to that, we obtain the following relationship between the wavelengths of the photon before and after scattering [23].

$$\nabla\lambda = \lambda_f - \lambda_i = h(1 - \cos\theta)/mc \tag{3.4}$$

where m is the rest mass of the electron. The term $\Delta\lambda$ is called wavelength shift and is equal to the difference in the wavelength of photon after and before scattering, and h is the Planck's constant.

Maximum wavelength shift occurs at $\theta = 180°$ giving us,

$$\nabla\lambda = 2h/mc$$

This condition is called backscattering, and the photon loses maximum energy to the electron.

Minimum wavelength shift of $\Delta\lambda = 0$ occurs at $\theta = 0°$. No energy is lost in this kind of scattering and is called coherent scattering. Further discussion about coherent scattering will be included later.

The energies of photons before and after scattering are given by the following relationship.

$$E_f = E_i[1 + \alpha(1 - \cos\theta)]^{-1} \tag{3.5}$$

where $\boldsymbol{E_f = hc/\lambda_f}$ is the energy of photon after scattering, $\boldsymbol{E_i = hc/\lambda_i}$ is the energy of photon before scattering, and $\boldsymbol{\alpha = h\nu_i/mc^2 = h/mc\lambda_i}$. The factor $mc^2 = 0.511$ MeV is the rest mass energy of an electron. Like the maximum wavelength transfer, maximum energy transfer also occurs when $\theta = 180°$. When photon scatters at this angle, the final energy of photon reaches to a minimum value of

$$\boldsymbol{E_f = E_i[1 + 2\alpha]^{-1}} \tag{3.6}$$

The probability of occurring Compton scattering "σ" slowly varies with the charge number Z of the host material of the interacting electron. Mathematically,

$$\boldsymbol{\sigma \propto Z} \tag{3.7}$$

The following points should be noted about photoelectric absorption:

- Compton scattering takes place between the incident gamma ray photon and an electron in the absorbing material.
- It is most often the predominant interaction mechanism for gamma ray energies typical of radioisotope sources.
- It is the most dominant interaction mechanism in tissue.
- The energy transferred to the electron can vary from zero to a large fraction of the gamma ray energy.
- The Compton process is most important for energy absorption for soft tissues in the range from 100 keV to 10 MeV.
- The Compton scattering probability σ decreases as the photon energy increases and is directly proportional to the electronic density of the material.

Example 3.3 An X-ray photon of wavelength 0.05 nm is scattered through an angle of 60 ° by a stationary electron. Find the wavelength, frequency, and energy of the scattered photon.

Solution Data: $\lambda_i = 0.05$ nm $= 5 \times 10^{-11}$ m $\theta = 60°$, $m = 9.11 \times 10^{-31}$ kg, $c = 3 \times 10^8$ m/s, and $h = 6.626 \times 10^{-34}$J . s

To find the wavelength λ_f of the scattered photon, we use Eq. (3.4)

$$\lambda_f - \lambda_i = h(1 - \cos\theta)/mc$$
$$\lambda_f = \lambda_i + h(1 - \cos\theta)/mc$$
$$\lambda_f = 5 \times 10^{-11} + 6.626 \times 10^{-34}(1 - \cos 60)/\left(9.11 \times 10^{-31} \times 3 \times 10^8\right)$$
$$\lambda_f = (5 - 0.12) \times 10^{-11}\text{m}$$
$$\lambda_f = 4.88 \times 10^{-11}\text{m}$$

$\boldsymbol{\lambda_f = 0.0488\ nm}$

To find the frequency ν_f of the scattered photon, we use the following equation.

$$c = \nu_f.\lambda_f$$
$$3 \times 10^8 = \nu_f \times 4.88 \times 10^{-11}$$

This gives,

$$\boldsymbol{\nu_f = 6.14 \times 10^{18} Hz}$$

To calculate the energy of the scattered photon, we take help of the following equation.

$$\begin{aligned} E_f &= h\nu_f \\ E_f &= 6.626 \times 10^{-34} \times 6.14 \times 10^{18} \\ \text{or} \quad E_f &= 4.068 \times 10^{-15} \text{J} \\ E_f &= 4.068 \times 10^{-15} / 1.602 \times 10^{-19} \\ E_f &= \mathbf{2.54 \times 10^5\ eV} \end{aligned}$$

Example 3.4 Compare the maximum energy transferred by 5.11 keV photon and 5.11 MeV photon scattered by stationary free electrons. Find the speed of each electron.

Solution To find the maximum energy transferred by 5.11 keV photon, let's find the α-factor given by
$\alpha = h\nu_i/mc^2$

$$\alpha = E_i/mc^2$$

$\alpha = 5.11$ keV /0.511 MeV $= 0.01$
Next, we find the energy of photon after scattering, using Eq. (3.6).
$E_f = E_i[1 + 2\alpha]^{-1} = 5.11(\text{keV})[1 + 0.02]^{-1} = 5.11(\text{keV})[1.02]^{-1}$
$E_f = 5.01$ keV

Loss in the energy of photon after scattering $= E_f - E_i = (5.11–5.01)$ keV $= 0.01$ keV
Percent loss in the energy of photon $= [(E_f - E_i)/ E_i]100 = [0.01/5.11]100 = 2\%$
Thus, the energy transferred to electron = 2%
This energy lost by the photon is gained as kinetic energy by the electron. Thus,
Kinetic energy (KE) gained by electron $= ½\ mv^2$
Which gives the speed of this electron $= v = [2(KE)/m]^{1/2}$
Using $KE = 0.01$ keV, and $m = 9.11 \times 10^{-31}$ kg, $v = 1.87 \times 10^6$ m/s
Thus the recoil electron will move with a speed of 1.87×10^6 m/s
To find the maximum energy transferred by 5.11 MeV photon, we find the α-factor using $\alpha = h\nu_i/mc^2 = 5.11$ MeV/0.511 MeV $= 10$.
Energy of photon after scattering is given by

$$E_f = E_i[1 + 2\alpha]^{-1} = 5.11(\text{MeV})[1 + 2 \times 10]^{-1} = 5.11(\text{MeV})[21]^{-1}$$

$$E_f = 0.24\ \text{MeV}$$

Loss in the energy of photon after scattering $= E_f - E_i = (5.11–0.24)$ MeV $= 4.87$ MeV

Percent loss in the energy of photon $= [(E_f - E_i)/E_i]100 = [4.87/5.11]100 = 95\%$

Thus, the energy transferred to electron $= 95\%$

Conclusion: high-energy photons will lose more energy in Compton scattering phenomenon.

3.2.3 Pair Production

Pair production is dominant in interactions of higher-energy photons with matter.

In this phenomenon, a γ-ray or X-ray photon passing near the nucleus of an atom is subjected to strong field effects from the nucleus and splits into an electron-positron pair [24]. Broadly speaking, a negatively charged electron (e^-) and a positively charged positron (e^+) are created from a photon interacting with the electromagnetic field while energy and momentum are conserved. Positron is a positively charged electron and is created as result of the conservation of momentum when a photon passes near the nucleus of an atom. Since electron (e^-) and positron (e^+) possess particle nature and take part in the construction of matter, therefore, pair production is also called *materialization of energy*. The photon should have at least 1.022 MeV or more energy to take part in this process, which is the sum of the rest mass energies of an electron (0.511 MeV) and a positron (0,511 MeV). If the energy of the photon is more than the sum of the rest mass energies of both electron and positron, then the remaining energy is taken by the electron and positron as their kinetic energies. Mathematically

$$h\nu = \mathbf{1.022\ MeV} + KE_{e^-} + KE_{e^+} \tag{3.7}$$

where $h\nu$ is the energy of the photon interacting with the nucleus of the atom.

In order to conserve the momentum, electron and positron must move in the opposite directions after being created. Moreover, pair production dominates over photoelectric absorption and Compton scattering when the energy of photon is bigger than 10 MeV.

The probability of this effect increases with increasing atomic number due to the fact that pair production is caused by an interaction with the electromagnetic field of the nucleus [23].

The probability of occurring pair production "κ" varies with the charge number Z of the material as follows.

$$\kappa \propto Z^2 \tag{3.8}$$

Thus, high-Z materials like lead are more favorable for pair production to take place.

The electron and positron pair do not exist free for long time and recombine through a process called *annihilation of matter*. In the annihilation process, the electron and positron combine with each other, disappear, and give rise to two γ-ray photons each with an energy of 0.511 MeV. The two photons move in opposite directions to conserve momentum.

The interaction probability "μ" of a photon with matter by all three processes is simply the sum of each individual probability of occurrence (Ma et al. 2001). Mathematically,

$$\boldsymbol{\mu} = \boldsymbol{\tau} + \boldsymbol{\sigma} + \boldsymbol{\kappa} \tag{3.9}$$

where the interaction probability μ is also called linear attenuation coefficient of a material.

τ is the photoelectric effect interaction probability.

σ is the Compton scattering interaction probability.

κ is the pair production interaction probability.

μ is the overall interaction probability.

Along with the major modes of interaction as described above, a photon can also interact with matter through one of the following additional processes though the probability is very little as compared to the three major phenomena.

3.2.4 Coherent Scattering

Coherent scattering, often called Rayleigh scattering, involves the scattering of a photon with no energy transfer [22, 23]. Such kind of scattering is also called elastic scattering. The electron is oscillated by the electromagnetic wave from the photon. The electron, in turn, reradiates the energy at the same frequency as the incident wave. The scattered photon has the same wavelength as the incident photon [22]. The only effect is the scattering of the photon at a small angle. This scattering occurs in high atomic number materials and with low-energy photons. In a nutshell, a photon is scattered without losing or gaining any energy.

3.2.5 Photodisintegration

Photodisintegration occurs in high-energy γ-rays at energies over 10 MeV. The γ-ray interacts with the nucleus of an atom, therefore exciting it. The excited nucleus immediately decays into two or more daughter nuclei. A neutron or proton is emitted as a result of this interaction. This is seen in nuclear fission, or the breakdown of an atomic nucleus. The neutrons produced in this reaction can cause radiation protection problems if they are not accounted for.

3.3 Overall Interaction of Photons with Matter

When a photon beam passes through a material or a tissue it interacts at the same time with all possible mechanisms described earlier (Teli et al. 2000). For example, when a 2 MeV gamma ray photon interacts with a tissue, it dominantly interacts by Compton scattering. During this process, a photon loses part of its energy every time it interacts with a tissue cell. As a result, the energy of the photon continuously decreases and reduces to a range of energies where photoelectric absorption is dominant. At this stage, the photon is absorbed by the tissue by the process of photoelectric absorption (Meyerhof 1967; Parham et al. 2009; Teli et al. 2000).

The attenuation of an X-ray gamma ray photon beam is governed by the linear attenuation law given below

$$N = N_0 e^{-\mu x} \tag{3.10}$$

where μ represents the linear attenuation coefficient and x gives the thickness of the attenuator.

Equation (3.10) is valid only in narrow-beam geometry when a collimated beam of radiation is used.

3.3.1 Linear Attenuation Coefficient

When a photon passes through an attenuator material, the probability that an interaction will occur depends on its energy and the composition and thickness of the attenuator (Ma et al. 2001) [29]. The thicker the attenuator material, the more likely an interaction will occur. The dependence on photon energy and attenuator composition is more complicated.

Consider an incident beam of photons of intensity I. This beam is directed onto an attenuator of thickness Δx. Assume for now the attenuator consists of a single element of atomic number Z and that the beam is monoenergetic with energy E. A photon detector records the transmitted beam intensity. Only the photons passing through the attenuator without interaction are detected. For a thin attenuator, it is found that the fractional decrease in beam intensity is related to absorber thickness:

$$\Delta I / I \approx -\mu \cdot \Delta x \tag{3.11}$$

The intensity I of the beam can also be replaced by the number of photons N in the beam. The quantity μ is the linear attenuation coefficient of the attenuator material. The minus sign indicates the beam intensity decreases with increasing attenuator thickness. The linear attenuation coefficient represents the absorptivity of the attenuating material. The quantity μ is found to increase linearly with attenuator density ρ. This value can be used to calculate values such as the intensity

of the energy transmitted through an attenuating material, intensity of the incident beam, or the thickness of the material. It may also be used to identify the material if the previously mentioned values are already known.

3.3.2 Mass Attenuation Coefficient

Mass attenuation coefficient can be a useful coefficient because only the atomic composition of the attenuator is taken into account and not the individual density of the material (Meyerhof 1967; Teli et al. 2000). To obtain the mass attenuation coefficient, the linear attenuation coefficient, μ, is divided by the density, ρ. It has units of cm^2/g because μ/ρ has unit $cm^{-1}/(g/cm^3)$. The attenuator thickness can also be expressed in units of electrons/cm^2 and atoms/cm^2. The associated coefficients are the electronic attenuation coefficient, ${}_e\mu$, and the atomic attenuation coefficient ${}_a\mu$.

3.3.3 Half-Value Thickness (HVT)

The half-value thickness, or half-value layer, is the thickness of the material that reduces the intensity of the beam to half its original value. When the attenuator thickness is equivalent to the HVT, N/N_0 is equal to ½ (Parham et al. 2009). Thus, it can be shown that

$$\mathbf{HVT} = \ln \mathbf{2}/\boldsymbol{\mu} \tag{3.12}$$

This value is used clinically quite often in place of the linear attenuation coefficient.

The mean free path is related to the HVT according to

$$\boldsymbol{X}_{\mathbf{m}} = \mathbf{HVT}/\ln \mathbf{2} \tag{3.13}$$

3.3.4 Mean Free Path

The mean free path, or relaxation length, is the quantity

$$\boldsymbol{X}_{\mathbf{m}} = \mathbf{1}/\boldsymbol{\mu} \tag{3.14}$$

This is the average distance a single particle travels through a given attenuating medium before interacting. It is also the depth to which a fraction $1/e$ (~37%) of a large homogeneous population of particles in a beam can penetrate. For example, a distance of three free mean paths, $3/\mu$, reduces the primary beam intensity to 5%.

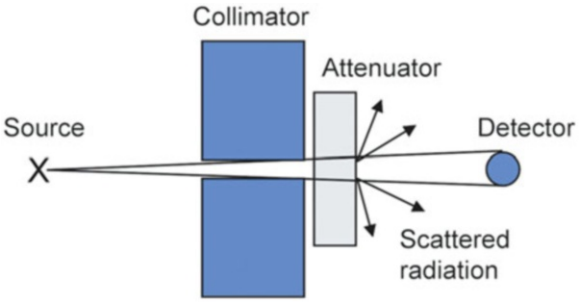

Fig. 3.4 A photon beam passes through a collimator before interacting with attenuator in a narrow-beam geometry

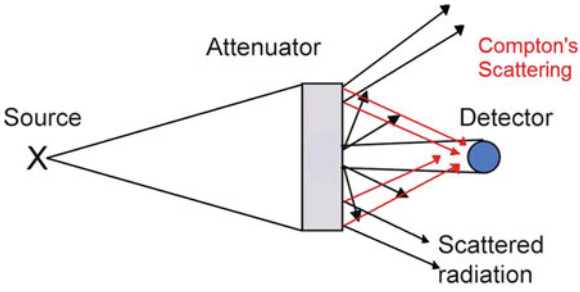

Fig. 3.5 Some of the photons are scattered back toward the detector, in a broad-beam geometry

3.3.5 Beam Geometry and Buildup Factor

When a beam of radiation is collimated by a collimator and passed through an attenuator, it follows the linear attenuation law. This arrangement is called narrow-beam geometry and is shown in Fig. 3.4. Narrow-beam geometry prevents or minimizes scattering of radiation.

In a broad-beam geometry, there is no collimator used, and the radiation beam is broad at the time it interacts with a tissue or material. As a result, scattered and secondary radiations are also allowed to reach the detector in addition to the primary beam. This arrangement is shown in Fig. 3.5. The figure is clearly showing that some of the radiations that could miss the detector or the target tissues can be scattered back toward it mostly through scattering of those photons by electrons inside the material or tissues. As a result, the additional number of photons is received at the target. In such arrangement, the dose or number of radiations received at the target is higher than the dose or radiations calculated by linear attenuation law. Thus, the linear attenuation law needs to be modified for broad-beam geometry to compensate for this additional dose or radiations received at the target point or tissue. In order to cover and compensate for this additional number of radiations delivered at the target tissues, a new factor called buildup factor "*B*" is introduced in the linear attenuation law (Parham et al. 2009; Turner 2007). The linear attenuation law gets a modified form given below.

$$N = B.N_0.e^{-\mu x} \tag{3.15}$$

where B is the buildup factor of the attenuator.

The buildup factor B is a dimensionless quantity used to account for secondary and scattered radiation in a broad-beam system. It can be applied with respect to any specified geometry, attenuator, or physical quantity in radiological physics. Buildup factor is one of the important properties of a material or tissue used for beam collimation, tissue compensation, or radiation shielding and protection. It directly affects the dose quantity, and hence, correct and precise dose delivery to a tumor is not possible without knowing the buildup factor of a material for tissue compensation purpose. It is also important to determine buildup factor of the normal tissues, radiations are passing through before reaching to a tumor, because scattering of radiation from those normal tissues also changes the dose quantity that needs to be given to a tumor (Attix 1986).

$$B = (\textbf{Total broad beam counts})/(\textbf{total narrow beam counts}) \tag{3.16}$$

For narrow-beam geometry $B = 1$ exactly, and for broad-beam geometry $B > 1$. In narrow-beam geometry, ideally there is no scattered or secondary radiation to detect, so there is no buildup factor contributing to the detection of radiation. However, the broad-beam geometry will usually produce some type of secondary scattered radiation depending on the geometry and components involved. The value of B is a function of radiation type and energy, attenuating medium and thickness, geometry, and measured quantity.

Buildup factor depends upon a number of factors listed below:

(a) Size of attenuator

Buildup factor of an attenuator or tissue increases linearly with the increasing size or volume of the tissue. The reason being buildup develops due to the scattering of photons. Therefore, Compton scattering plays a major role in buildup factor's development and variation. The probability of Compton scattering increases as the number of electrons or scattering sites increase inside a material or tissue, causing an increase in the buildup factor. The scattering sites are proportional to the volume of the attenuating material; the larger the volume V, the more scattering sites are available, and hence, there is a greater contribution to the buildup factor (Wang 1995). Mathematically,

$$B = 1 + CV \tag{3.17}$$

where C is a constant. In most of the attenuators used in experimental setup or tissues, the area of cross-section or width of attenuator is constant. In that case, an increase in volume occurs with increasing thickness X of the attenuator of tissue as the cross-sectional area A remains constant. Thus,

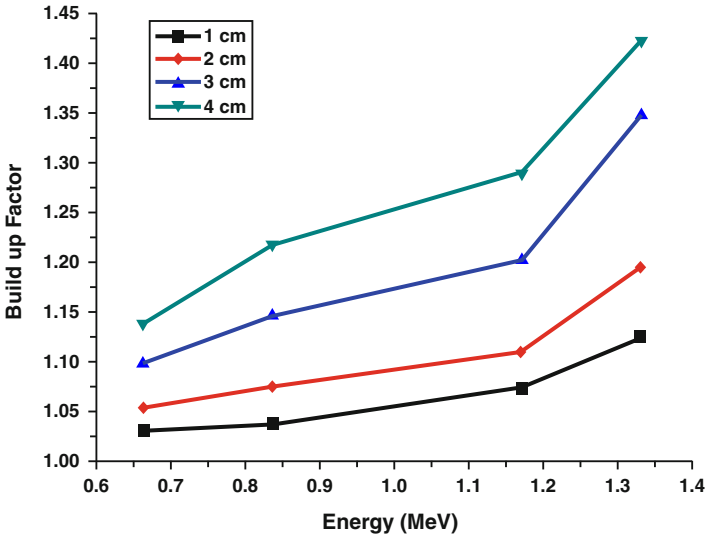

Fig. 3.6 Variation in buildup factor with photon energy for MCP-96 alloy

$$B = 1 + CAX \tag{3.18}$$

Replacing both constants C and A by a single constant D, we get, (Attix 1986),

$$B = 1 + DX \tag{3.19}$$

(b) Energy of photons

Variation in buildup factor with energy of the interacting photons depends upon the range of energy (Turner 2007). As discussed earlier, a photon can interact with a tissue or material in three possible ways: photoelectric absorption, Compton scattering, and pair production. Photoelectric effect is dominant for photon energy less than 0.5 MeV. Compton scattering is dominant over an energy range of 0.5 MeV–12 MeV, and pair production dominates for photon energy above 12 MeV. Since buildup factor is mainly contributed by the Compton scattering, therefore, it increases with energy in the beginning followed by a decrease when the energy of photon beam exceeds 12 MeV. Variation in the buildup factor of MCP-96 (an alloy of bismuth = 52.5%, lead = 32%, and tin = 15.5%) in 0.6–1.4 MeV photon energy range is given in Fig. 3.6.

(c) Geometry of the experiment

Buildup factor also depend upon the geometry of the experimental setup. Usually an attenuator or tissue comes in between the radiation source and detector. If an attenuator is placed close to the radiation source, it would be far from the target (Wang et al. 1995). Thus, scattered radiation from the attenuator will lose intensity due to inverse square law, before reaching the

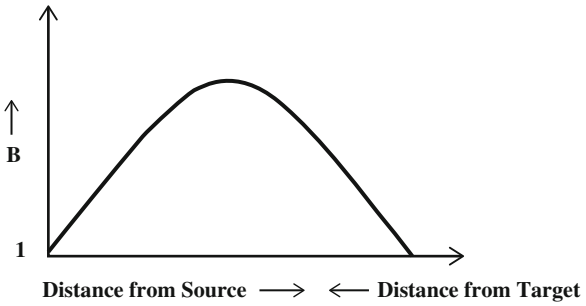

Fig. 3.7 Variation in buildup factor with distance from source and target

target. This effect will cause a reduction in buildup factor. On the other hand, if the attenuator is placed close to the target, it would be far from the radiation source. In that case, the primary radiations, which go for scattering from the attenuator, will lose intensity before reaching the attenuator. As a result, fewer scattered radiation will be produced and delivered at the target. This will eventually decrease the buildup factor. Therefore, an optimum position to get higher buildup is the middle of radiation source and target (Attix 1986). Figure 3.7 gives variation in buildup when attenuator is moved from radiation source toward target.

Problems

1. (a) Find the frequency and energy of a light photon of wavelength 250 nm. Express your answer in joule and in electron volt.
   (b) Two photons have their wavelengths 350 nm and 570 nm. Find the difference in their energies and frequencies.

2. (a) The threshold frequency of a photon for certain metal is 8×10^{14} Hz. Find the threshold wavelength (in nanometer) and work function (in eV) of that metal.
   (b) An electron moving with kinetic energy 9 eV passes through a material. It is slowed down, and its energy is reduced to 2 eV. As a result X-rays are emitted.
   Find the energy and wavelength of the emitted X-ray photon.

3. In a photoelectric effect, an X-ray photon of wavelength 0.1 nm is allowed to fall on sodium metal (work function = 2.28 eV). Find the following:
   (i) Kinetic energy of the ejected photoelectron
   (ii) Speed of the ejected photoelectron
   (iii) The voltage applied in the photoelectric circuit

4. (a) In a Compton scattering experiment, an X-ray photon of wavelength 0.01 nm is scattered by a stationary electron. The scattered photon makes an angle of

75° with its initial direction of motion. Find the wavelength, energy, and momentum of the scattered photon.
(b) Find the velocity of the scattered electron.

5. A beam of X-rays with wavelength 0.2400 nm is directed toward a sample. The X-rays scatter from the electrons within the sample, imparting momentum to the electrons, which are initially at rest. After scattering, the X-rays are detected at various angles relative to the direction of the incoming beam.
   (a) What is the longest wavelength measured by the detector, and at what scattering angle does this occur?
   (b) For this scattering angle, what is the kinetic energy of the recoiling electrons?
   (c) If the detector measures a wavelength for the scattered X-rays of 0.2412 nm, what is the X-ray scattering angle?
   (d) What is the direction of travel of the recoiling electrons in this case?

6. (a) The buildup factor of a 2-cm-thick attenuator is 1.6 for gamma ray photons each of energy 1.33 MeV. If the detector receives 20% of the initial 1×10^6 photons striking the attenuator in a broad-beam geometry, then find the linear attenuation coefficient of the attenuator.
   (b) How many photons will the detector receive if the initial number of gamma ray photons striking the detector is the same (1×10^6) but you replaced the broad-beam geometry by a narrow-beam geometry (buildup factor = 1)?

References

Attix FH (1986) An introduction to radiological physics and radiation dosimetry. Wiley
Hopkins DN, Maqbool M, Islam MS (2012) Linear attenuation coefficient and buildup factor of MCP-96 alloy for dose accuracy, beam collimation, and radiation protection. Radiol Phys Technol 5:229–236
Ma CM, Coffey CW, DeWerd LA, Liu C, Nath R, Seltzer SM, Seuntjens JP (2001) AAPM protocol for 40–300 kV x-ray beam dosimetry in radiotherapy and radiobiology. Med Phys 28 (6):868–893
Meyerhof WE (1967) Elements of nuclear physics. McGraw-Hill Book Company, New York
Parham C, Zhong Z, Connor DM, Chapman LD, Pisano ED (2009) Design and implementation of a compact low-dose diffraction enhanced medical imaging system. Acad Radiol 16 (8):911–917
Teli MT, Nathuram R, Mahajan CS (2000) Radiation measurements, vol 32, pp 329–333
Turner JE (2007) Atom, radiation and radiation protection, 3rd edn. Wiley, Weinheim
Wang D, Luo P, Yang H (1995) Nucl Inst Methods B 95:161

Chapter 4
Treatment Planning in Radiation Therapy

Amjad Hussain and Wazir Muhammad

Contents

4.1 Section A: Photon Beam Treatment Planning 63
4.2 Section B: Electron Beam Treatment Planning 115
References 127

4.1 Section A: Photon Beam Treatment Planning

4.1.1 Introduction

Radiation therapy is the clinical use of ionizing radiation as part of a comprehensive cancer treatment to eradicate malignant/cancerous cells. It works by damaging the DNA of cancerous cells, which is the primary cause of cell death. Normal cells are also damaged by ionizing radiation; however, they generally have a better recovery mechanism than the cancerous cells.

Radiotherapy is used to treat cancer with two main intentions: *Radical radiotherapy* is meant to cure the patient, while *palliative radiotherapy* is mainly used to relieve the symptoms caused by the cancer. There are two major types of radiation therapy strategies: external beam radiotherapy (EBRT) and brachytherapy. EBRT is the most frequently used form of radiotherapy, where the radiation source is at a certain distance outside the patient, during treatment. Brachytherapy treatment is performed by placing a radioactive source inside or next to the tumor.

More than 50% of cancer patients would benefit from radiation as part of their treatment (Porter et al. 1999). The benefits of cancer treatment using ionizing radiation are widely known in terms of increase in disease-free survival rates,

A. Hussain, PhD, MCCPM (✉)
Radiation Oncology, Western Manitoba Cancer Centre, Brandon R7A 2B3, MB, Canada
e-mail: amjadso_76@yhaoo.com

W. Muhammad, PhD
Department of Therapeutic Radiology, Yale University School of Medicine, New Haven, CT, USA

M. Maqbool (ed.), *An Introduction to Medical Physics*, Biological and Medical Physics, Biomedical Engineering, DOI 10.1007/978-3-319-61540-0_4

prolongation of life, and improvement in quality of life (Fodo et al. 2000; Ferreri et al. 2000; Vargas et al. 2005). Radiation therapy relies significantly on technological innovations and the collaborative technical reports developed by teams of professionals that heavily influence the outcome of cancer treatment worldwide.

4.1.1.1 Historical Evolution

X-rays were discovered by Wilhelm Roentgen in 1895. As a result of the investigations performed by Henri Becquerel and Marie Curie in 1896, a new treatment method using radioisotopes was implemented. The noninvasive and penetrating nature of ionizing radiation made it an alternative treatment to surgery. The first ever patient was successfully treated using ionizing radiation in 1899 (Kramme et al. 2011). Bremsstrahlung x-rays with peak energy of ~300 kVp were widely used for treatment purposes, up until 1950s. Cobalt-60 teletherapy machines were very popular during the 1950s for cancer treatment (Khan 2010) and were subsequently complemented by high-energy medical linear accelerators. Currently, linear accelerators are the most commonly used medical devices for treating cancer patients with megavoltage photon and electron beams, worldwide. Radiation therapy technology has evolved immensely over the last 50 years. Computers were introduced for complicated dose distribution calculations, in the early 1960s. In the 1970s, computed tomography (CT) scanners were developed for imaging purposes (Curry et al. 1990). These CT scanners played a key role in localization and delineation of radiotherapy targets and healthy organs, thus providing the basis for three-dimensional conformal radiation therapy (3D–CRT). Multileaf collimators (MLC) were available during 1970s; however, intensity-modulated radiation therapy (IMRT) was not developed until the 1990s (Bortfeld et al. 1990a; Keller-Reichenbecher et al. 1999).

4.1.2 Therapeutic Response

Optimally effective radiotherapy is not possible without some understanding of the biological effects of radiation. Radiation biology describes the complex biological response of tissue in relation to the given radiation dose. With increasing radiation dose above a certain threshold, tissue response may increase. Practically, such a dose response is expressed by a sigmoidal relationship, shown in Fig. 4.1, where tumor control probability (TCP) and normal tissue complication probability (NTCP) are plotted as a function of absorbed dose. In reality, a typical radiotherapy treatment is considered to be effective if the magnitude of TCP is 50% and NTCP is 5% (Podgorsak and IAEA 2005). For a given NTCP (usually 5%), the therapeutic response or therapeutic index is defined as the ratio of TCP to NTCP (Podgorsak and IAEA 2005; Hall and Giaccia 2006). Hence, the farther apart the NTCP and TCP curves are from each other, the higher is the therapeutic index. Different

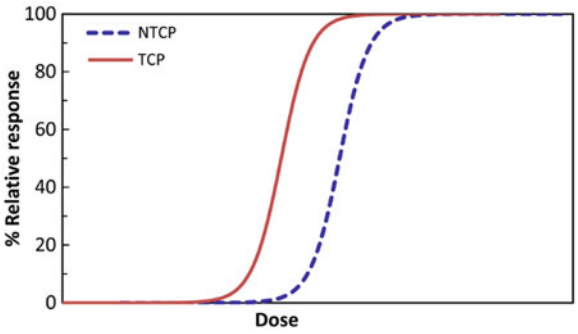

Fig. 4.1 Conventional representation of normal tissue and tumor response to radiation dose. Cell kill increases in a sigmoidal fashion above a threshold

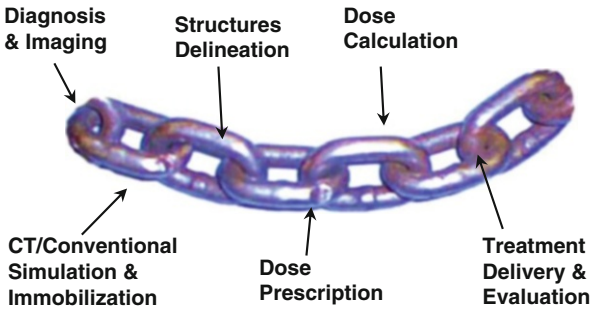

Fig. 4.2 Radiotherapy treatment planning chain

fractionation schemes and, in selected cases, chemotherapy drugs are used to increase the therapeutic index. Frequently, the tumor response to radiation is greater than that of the adjacent normal tissue. This makes radiotherapy an effective cancer treatment methodology in many cases.

4.1.3 Radiation Therapy Process

Radiotherapy treatment planning is the process of determining optimal treatment parameters for patient irradiation. The entire process encompasses the following essential activities:

- Diagnostic and imaging
- Patient positioning and immobilization
- Simulation imaging
- Treatment volume and dose-limiting structures delineation
- Radiation dose prescription and fractionation
- Optimal dose distribution calculation and evaluation
- Dose delivery and verification

Figure 4.2 summarizes these points as a treatment planning chain. Determination of the extent and nature of the tumor, using various diagnostic tools, prior to treatment planning is essential. Depending on the type, extent, and location of the

tumor and the patient condition, the tumor is either surgically removed or treated with radiation and/or chemotherapy agents. Frequently there is a remnant of the tumor, even after surgery, which needs to be irradiated to avoid recurrences. Such a group of patients is referred to radiation oncologists for further management. The treatment planning process starts from this point of referral onward.

4.1.4 Patient Data Acquisition

Figure 4.2 describes the entire radiation treatment planning procedure. The radiation oncologist assesses the patient and decides a suitable treatment protocol. The first step in the treatment planning process is to decide which volume of the patient needs to be irradiated and which volumes are to be spared. Such information is available to radiation oncologists from state-of-the-art imaging modalities such as CT, MRI, ultrasound, and PET. Generally, there are two types of imaging intentions: diagnosis and treatment planning. The former is a requirement for detailed, disease diagnosis and staging and is therefore acquired in high resolution and contrast. Treatment planning imaging, also called simulation imaging, may not need to be of high resolution and contrast. However, all planning images must be acquired in the geometrical configuration intended for treatment. In other words it is essential to be able to reproduce the simulation imaging coordinates during actual treatment on the radiotherapy machine. Simulation can be performed on a conventional simulator, CT or MR simulator, depending on the type of tumor and treatment intent and equipment availability. During conventional simulation, beam directions and apertures are determined, while the patient is on the couch for a short period of time. Whereas in CT simulation, the patient's anatomical information is acquired in three dimensions and is available for radiation beam arrangement design even in the absence of the patient. This concept, known as virtual simulation, is pivotal in achieving optimal and conformal dose distributions.

4.1.5 Patient Positioning and Immobilization

Patient positioning is one of the most crucial and frequently weakest links in the treatment process (Fig. 4.2). Accurate and reproducible patient positioning is necessary to make it possible to deliver the prescribed dose precisely to the target and spare healthy tissues over the many fractions that a course of radiotherapy entails. There is also, of course, the possibility that patient who is not immobilized moves during an individual treatment, while on the treatment table. One of the reasons for patient movement during treatment is uncomfortable positioning. Extended treatment duration is another common reason for these movements. Involuntary actions, such as breathing and coughing may also cause the tumor to move away from the intended treatment position. In order to facilitate positioning

reproducibility and to limit patient movement during treatment, various immobilization devices are employed. Body supports, straps, thermoplastic sheets, vacuum bags, and stereotactic frames are few examples of commonly used immobilization devices.

In addition, there are a number of systems and methods, used to locate patient position relative to the treatment unit geometry and/or the treatment beam, e.g., portal images/films, cone beam CT, radio-opaque markers, lasers, infrared tracking cameras, etc.

4.1.6 Pretreatment Simulation

Prior to external beam radiation therapy of the patient, it is essential to simulate the proposed treatment on the individual patient anatomy. This can be done with the patient present and positioned on a conventional simulator which mimics the geometry of the treatment machine. Or the simulation can be performed on a computer using three-dimensional images, from CT, for example, of the patient. This entire process is time consuming and therefore cannot be performed on a treatment unit.

4.1.6.1 Conventional Simulator

A conventional simulator (Fig. 4.3) is a machine with a diagnostic x-ray tube that mimics the functions and motions of a radiation therapy treatment unit. The main function of a simulator is to correctly position the treatment fields in order to accurately encompass the target and avoid surrounding normal tissues from receiving excessive irradiation. Internal body structures are dynamically visualized using the fluoroscopic capability of the simulator. Radiographic images are finally acquired for the appropriate body site. The radiation oncologist may draw outlines for shielding blocks based on these images. The radiographic images and patient and machine coordinates can be transferred to the treatment planning system via DICOM, instantly. During simulation the patient separation/thickness is also measured for dosimetric calculation.

There is a strong justification for using simulators prior to treatment. The need for simulators arises from four facts (Khan 2010): (a) commercially available diagnostic x-ray machines cannot be used because their geometric properties are different from those of treatment machines; (b) field localization on the patient needs to be done with high-quality images, which can not be acquired with high-energy therapy machines; (c) the entire simulation process is time consuming and hence impractical to be performed in a treatment room; and (d) unanticipated problems with a patient positioning or beam arrangements can be resolved in the simulation room, hence conserving time on the treatment machine.

Fig. 4.3 A photograph of a conventional radiographic simulator (Courtesy Medical Systems, Palo Alto, CA)

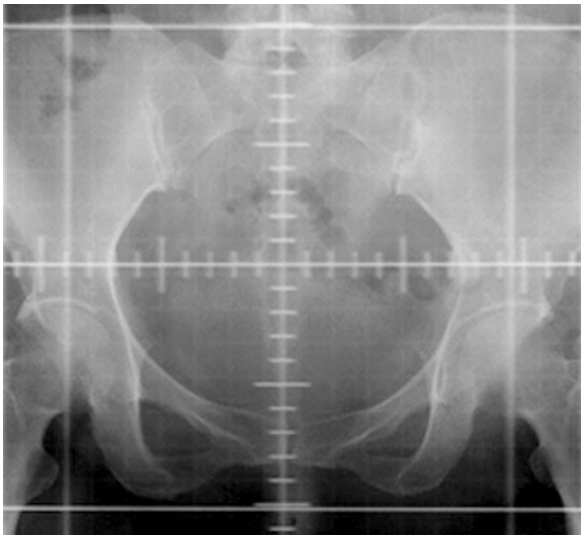

Fig. 4.4 A planar radiograph of the pelvis, taken on a conventional simulator

Patient body contouring, treatment depth measurement, and preparation of immobilization devices are also performed, while the patient is on the simulator table. Another important use of a simulator is pretreatment QA of patient-specific shielding blocks and boluses. In Fig. 4.4 a planar radiograph of a pelvis is shown. The square region marked by bold white lines encompasses the volume to be

treated. The intersection of the dashed lines denotes the central axis of radiation beam. If additional shielding needs to be implemented, for example, to protect a structure in the corner of the rectangular field, it is marked on such a radiograph.

4.1.6.2 Computed Tomography Simulator

CT simulators have become an essential part of patient simulation for the majority of radiation therapy practices all over the world. CT images provide good tissue contrast in three dimensions, as opposed to the two-dimensional projection of a conventional simulator, allowing for improved tumor localization and contouring. The CT data also provides relative electron density, which can be converted to physical density, of the various body tissues. Modern dose calculation algorithms use this information for dose determination in heterogeneous media, i.e., patient body. A therapy CT simulator as shown in Fig. 4.5 is similar to a conventional diagnostic CT with a few additional features. The tabletop is flat, to mimic the couch top on the treatment machine. The bore of the gantry is generally larger than that of a diagnostic unit to accommodate immobilization devices during special patient positions. The CT room is equipped with movable lasers for setup purposes including marking the patient.

A complete CT data set provides a 3D anatomical model of the patient. The CT images can be visualized in transverse, sagittal, and coronal planes (Fig. 4.6). The 3D planning process in the modern radiotherapy era is performed on planning computers in the absence of the patient. Most CT simulators are equipped with virtual simulation software. This software is used to determine field

Fig. 4.5 A photograph of computed tomography simulator (Courtesy: Philips Healthcare, Cleveland OH)

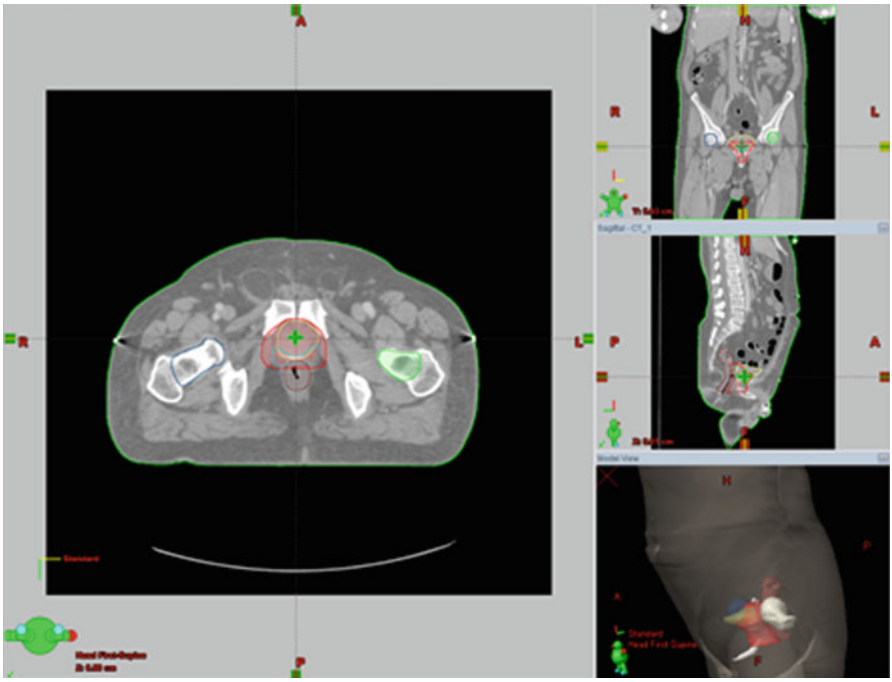

Fig. 4.6 Three-dimensional view of the patient anatomy, reconstructed from CT data in Eclipse™

arrangements for optimal tumor coverage and maximal avoidance of normal critical structures.

In contrast to acquiring conventional simulation projection radiographs, virtual simulation is based on digitally reconstructed radiographs (DRRs) for treatment field arrangement. These DDRs are produced from the patient CT data set using various reconstruction methods. The DRRs have become more important in newer treatment planning systems and have largely replaced the conventional radiographic/fluoroscopic imaging methods. The main advantage of DRRs is that any field arrangement can be simulated without calling the patient back which is not the case with conventional simulation. DRRs are also used for treatment verification purposes (to be discussed later). Figure 4.7 shows a DRR for an anteroposterior (AP) view of the pelvis.

4.1.6.3 Magnetic Resonance Imaging (MRI)

Treatment planning calculations are generally performed on CT images. However, for target delineation, additional modalities can be helpful in some cases. Magnetic resonance (MR) imaging is one such modality that provides better soft tissue contrast compared to CT, and this can be especially useful in brain and prostate

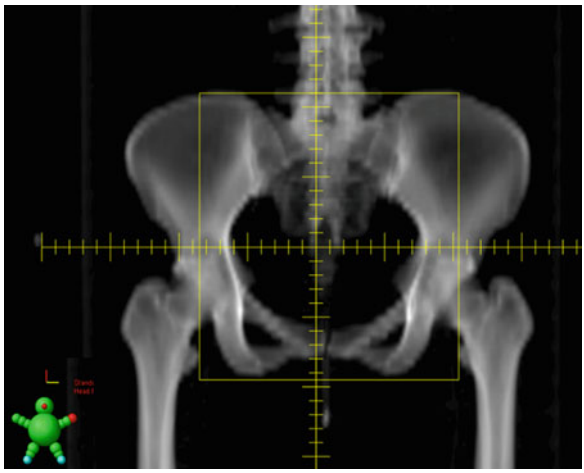

Fig. 4.7 An anteroposterior DRR of pelvis, showing field borders and the beam central axis

tumors. For contouring purposes, MR images are fused (overlapped) with the CT data set. Newer sophisticated algorithms may use MR images for dose computation.

4.1.6.4 Positron Emission Tomography (PET)

Positron emission tomography (PET) is also used as a complementary imaging tool for target delineation. PET provides useful information on the physiological function of organs based on their metabolic activity. PET-CT is a technique where both the CT and PET images are acquired simultaneously with the same patient setup. The additional information can help the oncologist to accurately and precisely contour certain target volumes.

4.1.7 Contouring

Contouring of various anatomical structures and the tumor volume is an essential part of the 3D treatment planning process. Contouring is performed, most of the time, on CT simulator images alone (Fig. 4.6). However, diagnostic CT, PET, and/or MRI scans can also be used for accurate contouring in selected patients.

ICRU Reports (No. 50 and No. 60) (International Commission on Radiation Units and Measurements (ICRU) 1993, 1999) provide recommendations on defining several target and critical structure volumes and for specifying absorbed dose, in order to provide standardization for the comparison of treatment outcomes. For 3D treatment planning, the following volumes, shown in Fig. 4.8, are defined.

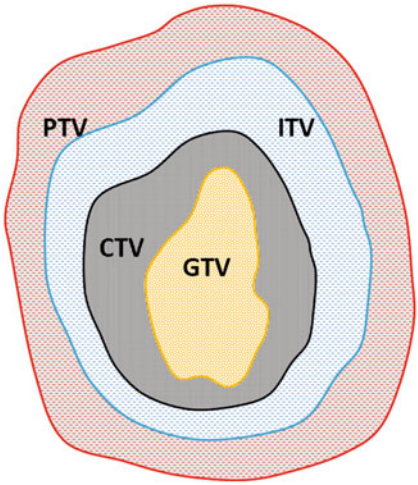

Fig. 4.8 Schematics of ICRU defined volumes of interest for radiotherapy

4.1.7.1 Gross Tumor Volume (GTV)

GTV is the gross palpable, visible, or demonstrable position and extent of malignant growth (International Commission on Radiation Units and Measurements (ICRU) 1993).

4.1.7.2 Clinical Target Volume (CTV)

The clinical target volume is a volume of tissue that contains a GTV and/or subclinical microscopic malignant disease. The CTV is therefore a conceptual anatomical-clinical volume. This entire volume has to be eradicated with radiotherapy for recurrence free cure of the disease.

4.1.7.3 Internal Target Volume (ITV)

The relative position of the CTV is not always fixed with reference to bony anatomy of the patient. Variation in size and position of CTV may be due to breathing or filling of the rectum or bladder. The ITV is thus formed by CTV plus extra margin for these variations.

4.1.7.4 Planning Target Volume (PTV)

The PTV is a geometrical definition, used in treatment planning and evaluation. PTV is the ultimate target volume that includes GTV and CTV with added margins,

to account for setup and motion uncertainties. The aim is to deliver the prescribed dose to the entire GTV/CTV with a clinically acceptable probability.

4.1.7.5 Organs at Risk (OAR)

The ultimate goal of radiotherapy is to deliver the prescribed dose to the target while minimizing the dose to the adjacent tissue, known as organs at risk (OAR). OARs need to be accurately delineated and spared during treatment, to avoid radiation-induced morbidity. The spinal cord, eye lens, parotids, lungs, optic chiasm, brain stem, kidneys, rectum, and bladder are common examples of OARs. Specific tolerance doses and expected morbidities are defined for these OARs (Emami et al. 1991).

4.1.8 Dose Prescription and Reporting

A general rule for prescribing and reporting doses to a reference point in the PTV is based on the recommendations of ICRU (International Commission on Radiation Units and Measurements (ICRU) 1993, 1999). The reference point is selected such that it is clearly defined and where the dose can be accurately determined, e.g., not in a steep dose gradient region. For dose prescription and reporting, it is recommended that minimum, maximum, and mean target doses be included.

4.1.9 Dosimetric Data for Clinical Photon Beams

It is obviously not possible to measure radiation dose distributions in patients directly. An alternative is to acquire dose distribution data from measurements in tissue-equivalent, flat phantoms and to use such data as the basis of calculations of dose distributions in complex patient geometries. Water is the best (soft) tissue-equivalent material, since its effective atomic number and electron density are almost identical to those muscles. However, solid water phantoms and acrylic phantoms can also be used for certain relative measurements. The dimensions of the phantom needs to be large enough to provide the full-scatter conditions necessary for dose measurements. Dosimetric measurements are typically performed for standard field sizes and with the beam axis normal to the phantom surface. The measured data is then used in a dose calculation engine for the estimation of the dose distribution in an actual patient.

In order to present the measured data in a convenient and useful format for manual and computerized dose calculations, a number of physical parameters and mathematical functions are used. Details are given below.

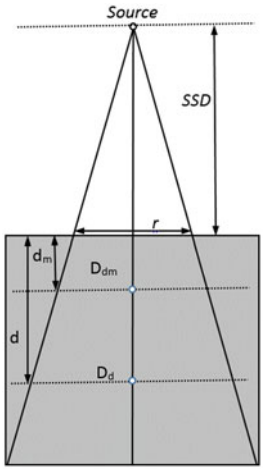

Fig. 4.9 Measurement setup for percent depth dose (PDD)

4.1.10 Depth-Dose Profiles

The absorbed dose in the patient (or a phantom) from an incident beam varies with depth. This variation depends not only on penetration depth but also on beam energy, distance from the radiation source, and field size and shape. Depth-dose variation along the beam central axis is an essential concept in dose calculation systems. Depending on the measurement setup, this variation can be described as percent depth dose (PDD), tissue-air ratio (TAR), tissue-phantom ratio (TPR), or tissue-maximum ratio (TMR).

4.1.10.1 Percent Depth Dose (PDD)

Percent depth dose (PDD) is the ratio of the absorbed dose at a given depth d to the absorbed dose at a fixed reference depth d_{ref} (usually the depth of maximum dose, d_{m}) along the central axis of the beam, expressed as a percentage (Fig. 4.9). Mathematically,

$$\text{PDD}(d, r, \text{SSD}) = \frac{D_{\text{d}}}{D_{d_{\text{m}}}} \times 100 \tag{4.1}$$

where r represents the edge of an equivalent field size at the surface of the phantom and SSD is the source-surface distance, which is kept fixed during measurements. Note: the field size is always defined at the surface when referring to PDD and SSD geometries.

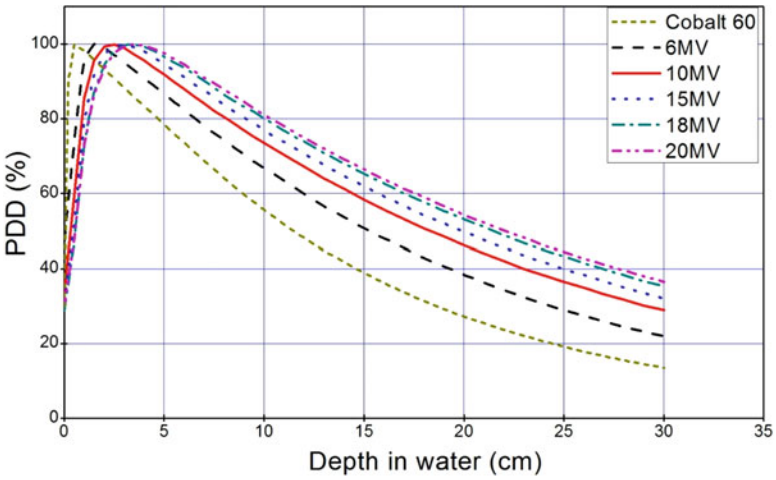

Fig. 4.10 Percent depth dose, measured along central axis for various photon beams with 10×10 cm^2 field size

Variation of PDD with Beam Quality

The percentage depth dose (beyond the dose buildup region) decreases almost exponentially for all therapeutic photon beams. At a given depth, higher-energy photons deliver a higher percentage depth dose because of their greater penetrating power. Therefore, at a given depth, beyond the depth of maximum dose, PDD increases with increasing beam quality (which is a way of describing the beam's energy spectrum), as shown in Fig. 4.10.

For x-rays generated at potentials up to about 400 kVp, the maximum dose is effectively at the surface. Since the dose is deposited by secondary electrons and because the range of the secondary electrons (along the beam direction) is $<$0.4 mm at these low energies, energy deposition (absorbed dose) occurs almost at the site of the photon interaction. For higher-energy photons, however, the dose maximum occurs at some depth below the surface. Because the range of the secondary electrons increases with photon energy, the depth of maximum dose, d_m, also increases with increasing photon energy. This is called dose buildup or the skin-sparing effect. For deep-seated tumors, dose buildup is an inherent benefit of megavoltage beams to spare healthy skin tissues. Table 4.1 summarizes characteristics of the surface doses and depths of maximum dose for various photon beams.

Field Size Dependence

Until the advent of highly conformal techniques, the radiation beam irradiating the patient was often in the form of a rectangle or square. This shape is defined by four independently adjustable collimator jaws. An example of a square field is

Table 4.1 Characteristics of the surface doses and depth of maximum dose (d_m) for various photon beams

Photon energy	Depth (d_m)	Field size	Surface dose
Orthovoltage	~ at surface	All apertures	~100%
Cobalt 60	~ 5 mm	10×10 cm^2	~30%
6 mv	~ 15 mm	10×10 cm^2	~15%
18 mv	~ 35 mm	10×10 cm^2	~10%

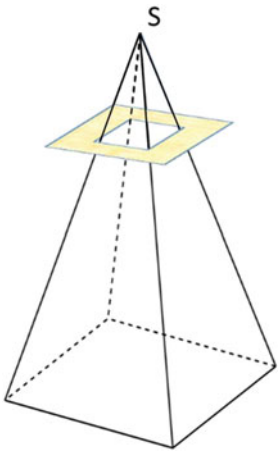

Fig. 4.11 A square field defined by four adjustable collimator jaws

shown in Fig. 4.11. For an infinitesimally small field size, the dose distribution in an irradiated medium is due to the primary, unscattered radiation. However, for non-zero field sizes, the scatter contribution to the dose in the phantom from scatter within the phantom and from the machine head increases with increasing the field size. Hence, the percentage depth dose, which includes both primary and scattered radiation, increases with field size. For larger field sizes, this dependence is less prominent, since very little extra scatter reaches the central axis within the phantom and contributes to the depth dose.

Depth dose also varies with the shape of the field. It is slightly higher for a circular field of a given area than for a square field with the same area. For elongated field of the same area, dose at a given point is even smaller. This is because scatter from the field edges of elongated fields and corners of square fields is less likely to reach the central axis and hence contribute to the dose there, compared to the scatter from circular fields.

The majority of the beam data, including depth-dose profiles, acquired for calculation purposes, are measured for square fields. However, during patient treatment, the radiation field is generally not. Much of the time rectangular fields are used. It is therefore necessary to be able to deduce rectangular field depth doses from square field measurements. Sterling et al. (Sterling et al. 1964) developed a simple rule of thumb for this calculation. The rule states that, rectangular and square field are equivalent if they have the same area to perimeter ratio (A/P).

Area of rectangle with sides "a" and "b" $= a \times b$
Perimeter of rectangle $= 2(a \times b)$
Area of square with sides "x" $= x^2$
Perimeter of square $= 4\,x$
Now, according to the A/P definition:

$$\left.\frac{x^2}{4x}\right|_{\text{square}} = \left.\frac{a \times b}{2(a+b)}\right|_{\text{rectangle}} \tag{4.2}$$

therefore,

$$x = \frac{2 \times a \times b}{(a+b)} \tag{4.3}$$

The field of side x which satisfies this relationship is known as the equivalent square of the $a \times b$ rectangular field.

SSD Dependence

The absolute dose at a given point in a medium decreases with increasing SSD from a point source, whereas the percentage depth dose increases. This is due to the inverse square law and can be understood from Fig. 4.12. Consider three points A, B, and C on the curve with the same intervals along the abscissa (distance). The dose rate drop from point A to point B is greater than that between points B and C. Stated another way, the ratio of dose rates at C to B is higher than that at point B to A, which means that the percent depth dose increases with increasing SSD. By

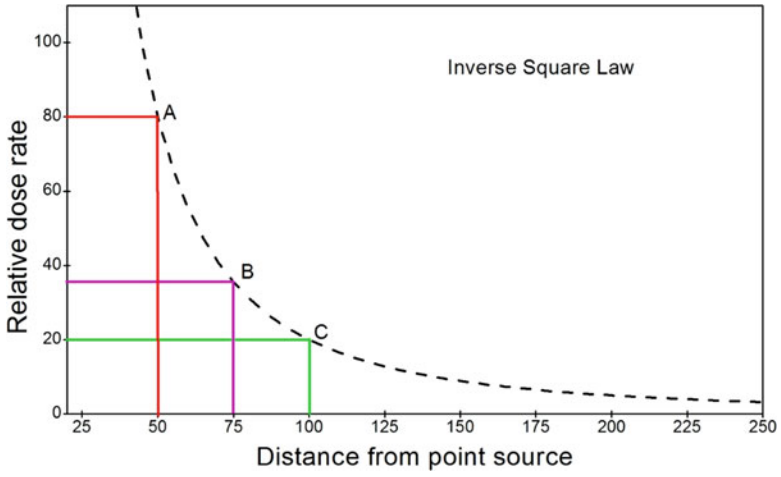

Fig. 4.12 The effect of Inverse Square Law on percent depth dose

multiplying by the Mayneord factor, a PPD measured at one SSD (SSD_1) can be closely approximated to a PDD at another SSD (SSD_2). The field size r is always defined at the phantom or patient surface:

$$\mathrm{PDD}(d, r, \mathrm{SSD}_2) = \mathrm{PDD}(d, r, \mathrm{SSD}_1) \times \frac{[(\mathrm{SSD}_1 + d)/(\mathrm{SSD}_2 + d)]^2}{[(\mathrm{SSD}_1 + d_\mathrm{m})/(\mathrm{SSD}_2 + d_\mathrm{m})]^2} \tag{4.4}$$

where

$$\frac{[(SSD_1 + d)/(SSD_2 + d)]^2}{[(SSD_1 + d_\mathrm{m})/(SSD_2 + d_\mathrm{m})]^2} = \text{Mayneord factor} \tag{4.5}$$

Example 4.1 Calculate the treatment time required to deliver 150 cGy to a point 7 cm below surface, using 8×8 cm^2 ^{60}Co beam at an SSD of 80 cm with a dose rate of 135.3 cGy/min at d_m. Percent depth dose for 8×8 cm^2 field size at 7 cm depth is 67.6%.

Solution The given dose at d_m may be determined using Eq. (4.1):

$$\frac{100 \times 150\,\mathrm{cGy}}{67.6} = 222\,\mathrm{cGy}$$

Since dose rate at d_m is 135.3 cGy/min, so:

$$\text{Treatment time} = \frac{222\,\mathrm{cGy}}{135.3\,\mathrm{cGy/min}} = 1.64\,\mathrm{min}$$

Example 4.2 The percent depth dose for a 10×10 cm^2 field size ^{60}Co beam at 80 cm SSD is 55.0% for a 10 cm depth. Calculate the corresponding PDD at an SSD of 100 cm.

Solution The Mayneord factor using Eq. (4.5) will be:

$$\text{Mayneord Factor} = \frac{[(80 + 10)/(100 + 10)]^2}{[(80 + 0.5)/(100 + 0.5)]^2} = 1.043$$

Hence:
$\mathrm{PDD}(10, 10 \times 10, 100) = 55.0\,\% \times 1.043 = 57.4\%$ (From Eq. (4.4))
An increase of ~2% in PDD is noted for every 10 cm increase in SSD for ^{60}Co.

Example 4.3 The PDD at 10 cm depth for 6 MV photons and 10×10 cm^2 field size at 100 cm SSD is 67.0%. At what SSD will the PDD be 70% for the same energy and field size?

Solution Using Eq. (4.4), the Mayneord factor is calculated to be 70/67 = 1.0448. The extended SSD_2 can be calculated from Eq. (4.5) as follows:

$$1.0448 = \frac{[(100 + 10)/(SSD_2 + 10)]^2}{[(100 + 1.5)/(SSD_2 + 1.5)]^2}$$

Taking the square root on both sides and solving for SSD_2 gives a value of ~140 cm.

Note that the increase in PDD is ~1.1% for every 10 cm increase in SSD for a 6 MV photon beam.

4.1.10.2 Tissue-Air Ratio (TAR)

In radiotherapy, mostly multiple fields, each coming from a different direction, are used for the treatment of tumors other than skin lesions. These fields are typically delivered by treatment units that are mounted isocentrically with a source to axis distance (SAD) of 80 cm or 100 cm. Hence, SSDs on the patient will change for the different fields which are incident on the patient from different angles. It is important that the patient remains stationary during the entire isocentric treatment as the treatment plan has been generated under this assumption. Planning an isocentric treatment requires a dosimetric quantity that is independent of SSD. *Tissue-air ratio* (TAR) and *tissue-phantom ratio* (TPR) are the quantities introduced for dosimetric calculations under isocentric or *SAD* treatment conditions.

*Tissue-air ratio (*TAR*)* is the ratio of the absorbed dose D_d at a given point in the phantom to the absorbed dose at the same point in air (D_a). As shown in Fig. 4.13,

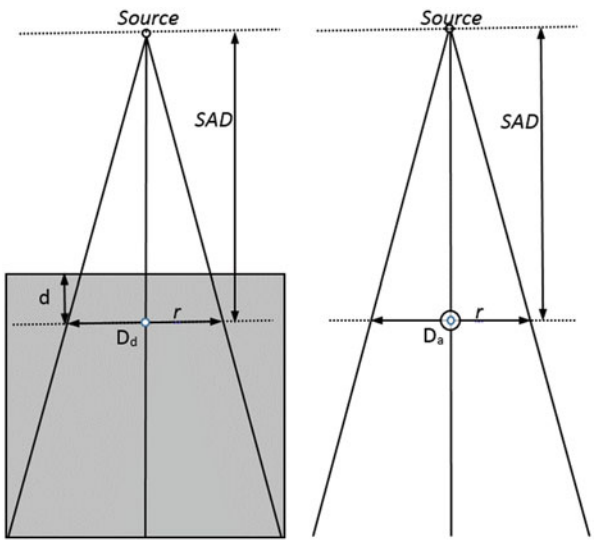

Fig. 4.13 Experimental setup for measuring tissue-air ratio (TAR)

the points of measurement should be at the same distance from the source, to avoid the inverse square effect. A buildup cap, with thickness large enough to provide electronic equilibrium, is used with the ionization chamber, in air. By definition:

$$\mathrm{TAR}(d, r) = \frac{D_\mathrm{d}}{D_\mathrm{a}} \tag{4.6}$$

where r represents the field size at the point of measurement. The point of measurement is usually at the isocenter of the machine.

Characteristics of Tissue-Air Ratio

The *tissue-air ratio* and percentage depth dose both vary with beam energy, field size and shape, and depth, almost in a similar fashion. However, the TAR does not vary with SSD. In the special case, when the measurement depth d in phantom is at the depth of maximum dose (d_m), the tissue-air ratio is called the backscatter factor *(*BSF*)* or peak scatter factor *(*PSF*)*.

Limitations of TAR

For high-energy photon beams, larger buildup caps are required to provide electronic equilibrium at the point of measurement. Such buildup caps are impractical for measurements with small fields. TAR is therefore rarely used in modern radiation therapy.

Example 4.4 A ^{60}Co teletherapy unit delivers a dose rate of 197 cGy/min in air at the isocenter (80 cm) for a reference 10×10 cm^2 field size. Calculate the dose rate and daily treatment time for a 5 cm deep tumor, to receive 180 cGy daily dose with a field size of 6×6 cm^2. The dose rate for a 6×6 cm^2 field is 0.966 relative to a 10×10 cm^2 field.

Solution The output factor relative to a 10×10^2 field in air for this machine for a 6×6 cm^2 beam is 0.966 and TAR is 0.875.

Dose rate for 6×6 cm^2 beam in air $= (197 \times 0.966)$ cGy/min
$= 189$ cGy/min

Tumor dose rate at 5 cm depth (Eq. (4.6), for dose rates) $= 189$ cGy/min $\times\ 0.875 = 165$ cGy/min

$$\text{Daily treatment time} = \frac{180 \text{ cGy}}{165 \text{ cGy/min}} = 1.09 \text{ min}$$

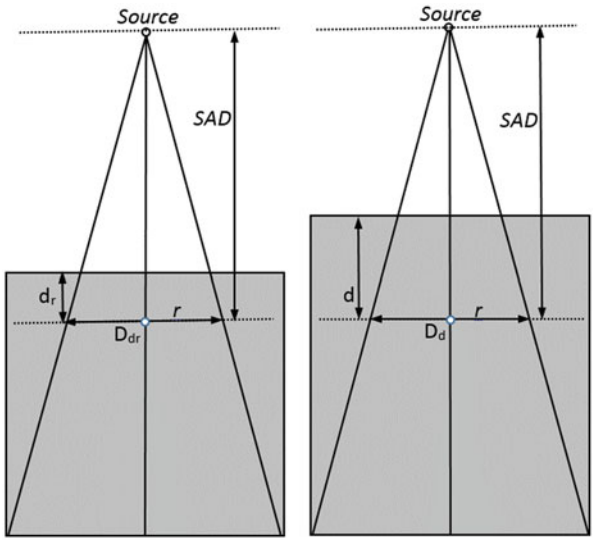

Fig. 4.14 Experimental setup for measuring tissue-phantom ratio

4.1.10.3 Tissue-Phantom Ratio (TPR) and Tissue-Maximum Ratio (TMR)

The *tissue-phantom ratio (*TPR*)* is defined as the ratio of the absorbed dose D_d at a given depth d in a phantom to the absorbed dose D_{dr} at the same point at a fixed reference depth d_r in the phantom, as shown in Fig. 4.14.

The point of measurement is usually at the isocenter of the machine. Mathematically:

$$TPR(d, r_d) = \frac{D_d}{D_{dr}} \tag{4.7}$$

The *tissue-maximum ratio (*TMR*)* is a special case of TPR where the reference depth d_r is considered to be at the depth of maximum dose, d_m. TMR may be defined as the absorbed dose at a given point in a phantom to the absorbed dose at the same point, but at the depth of maximum dose in the phantom.

Note that d_m also varies slightly with field size.

$$\text{TMR}(d, r_d) = \frac{D_d}{D_{d_m}} \tag{4.8}$$

TMR and TAR can be related using the following equation:

$$TMR(d, r_d) = \frac{TAR(d, r_d)}{TAR(d_m, r_d)} = \frac{TAR(d, r_d)}{BSF(r_d)} \tag{4.9}$$

Figures 4.9 and 4.13 may be used to derive the relationship between TMR and PDD:

$$\mathrm{TMR}(d, r_{\mathrm{d}}) = \frac{\mathrm{PDD}(d, r, \mathrm{SSD})}{100} \times \frac{\mathrm{BSF}(r_{d_{\mathrm{m}}})}{\mathrm{BSF}(r_{\mathrm{d}})} \times \left[\frac{\mathrm{SSD} + d}{\mathrm{SSD} + d_{\mathrm{m}}}\right]^2 \tag{4.10}$$

where

$$r_{d_{\mathrm{m}}} = r \cdot \left(\frac{\mathrm{SSD} + d_{\mathrm{m}}}{\mathrm{SSD}}\right) \quad \textit{and} \quad r_{\mathrm{d}} = r \cdot \left(\frac{\mathrm{SSD} + d}{\mathrm{SSD}}\right)$$

4.1.11 *Practical Applications of Dosimetric Data*

The absorbed dose at a given point in a medium or in air is the sum of the contributions from primary and scattered radiation. The radiation reaching the point that originates from the source and experiences no interaction in the machine head or phantom is known as the primary radiation. Radiation that interacts in the medium and is deflected from its original path to the point of interest is called scattered radiation. The scattered radiation can be classified as collimator scatter and phantom scatter, depending on where the interaction takes place. For accurate dose calculation, collimator and phantom scatter need to be calculated explicitly. The effect of partial blocking of the field on collimator scatter may not be important under many conditions; nevertheless, such blocking may reduce the phantom scatter significantly. In contrast to primary radiation, scattered radiation is directly related to the field size and shape (Fig. 4.15).

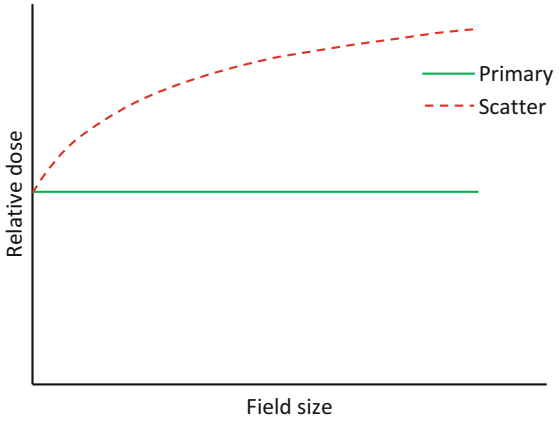

Fig. 4.15 Diagram (not to scale) showing primary and scattered components of radiation beam

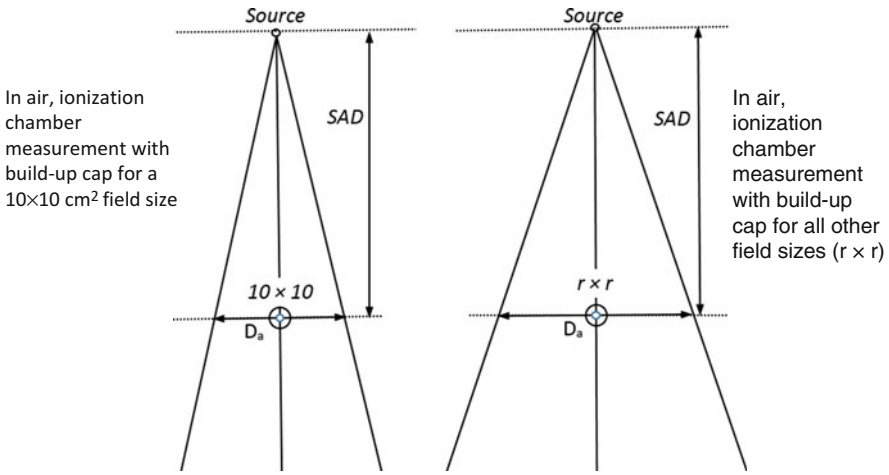

Fig. 4.16 Experimental setup for the measurement of collimator scatter factor (S_c)

4.1.12 Collimator Scatter Factor

The collimator scatter comes mainly from the flattening filter and collimator jaws. Interactions of photons with other components in the treatment head and air may also contribute to this scatter. The collimator scatter factor (S_c) is the ratio of the dose in air for a given field to that for a reference field, usually 10×10 cm^2. The setup for S_c measurement is shown in Fig. 4.16. It can be measured with an ionization chamber inside a buildup cap that provides electronic equilibrium for the given beam energy. S_c is most appropriately measured at the source to axis distance (SAD).

4.1.13 Phantom Scatter Factor

The scatter at a given depth in a phantom depends also on the volume of the phantom in the field. The phantom scatter factor (S_p) is the ratio of the dose or dose rate for a given field at a reference depth to the dose or dose rate at the same depth for the reference field size, with fixed collimator scatter. This definition excludes the effect of collimator scatter, which will change, and is limited purely to phantom scatter so S_p cannot be measured directly for higher photon energies. However, for ^{60}Co, it may be defined as the ratio of backscatter factor (BSF) for the given field to that for the reference field as in Eq. (4.13). (Khan 2010):

$$S_p(r) = \frac{\mathrm{BSF}(r)}{\mathrm{BSF}(r_0)} \tag{4.11}$$

For higher energies S_p has to be calculated from the total scatter factor $S_{c,p}(r)$ that includes both the collimator and phantom scatters, as presented in following equation:

$$S_{cp}(r) = S_c(r) \times S_p(r) \tag{4.12}$$

By excluding the collimator scatter component, $S_{c,p}(r)$ may be expressed as a quotient of the dose rate at a reference point in a phantom for a given field size r and the dose rate at the same point for the reference field size r_o. It is also known as the relative output factor or relative dose factor. Linear accelerators are calibrated such that 1 monitor unit is equal to 1 cGy dose at a stated reference depth for a stated reference field. The beam output $O(r)$ for a given field size can then be represented as follows:

$$O(r) = \frac{1cGy}{MU} \times S_{cp}(r) \qquad O(r) = S_{cp}(r)\frac{\text{cGy}}{\text{MU}} \tag{4.13}$$

4.1.14 Off-Axis Dose Profile

A one-dimensional dose distribution representation in an irradiated volume is referred to as a dose profile. Dose profiles are usually measured normal to the central axis. Measurement of these profiles is very important, especially for the description of beam flatness, symmetry, and penumbra. The data is usually normalized to the dose on the central axis (Fig. 4.17).

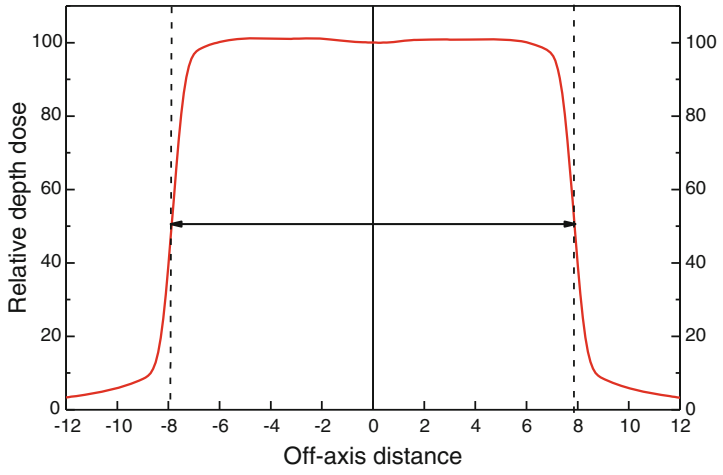

Fig. 4.17 Dose profile taken along a normal to the central axis

Measurement of off-axis factors or off-axis ratios is also essential for dose determination at off-axis points in a phantom. The projected field size can be determined from the profile, which is defined as the lateral distance between 50% dose points (represented by the arrow in Fig. 4.17).

4.1.15 Central Axis Dose Calculations

In radiation therapy, as per ICRU guidelines (International Commission on Radiation Units and Measurements (ICRU) 1993, 1999), the prescribed tumor dose must be delivered to a reference point, using either the constant SSD or the fixed SAD (isocentric) treatment setup.

4.1.15.1 Fixed SSD (Non-isocentric) Setup

In this method the patient is positioned such that the skin is at a fixed distance (nominal SSD) from the source. The field size is also defined at this distance on the patient skin. Linear accelerators are usually calibrated to deliver 1 cGy per monitor unit (MU) to a reference point in a water phantom for a 10×10 cm^2 field size. Source to calibration point distance (SCD) may vary depending on the calibration protocol used. The output of a Cobalt-60 machine is expressed in terms of cGy per minute at a reference point. For a prescribed dose *PD* (the dose to be delivered) to point p at depth d for fixed SSD setup, MUs may be calculated using the following equation:

$$\text{Monitor Units} = \frac{\text{Prescribed dose} \times 100}{\dot{D} \times \text{PDD}(d,r) \times S_c(r_c) \times S_p(r) \times \text{ISF}_{\text{SSD}} \times \text{TF}} \tag{4.14}$$

where $\dot{D}$ is the machine dose rate (1 cGy/MU for linear accelerator), r_c is the collimator defined field size $\left(r_c = r \cdot \frac{\text{SAD}}{SSD}\right)$, ISF_{SSD} is the inverse square factor $\left(\frac{\text{SCD}}{\text{SSD}+d_m}\right)^2$, and TF ($\leq 1$) is the combined transmission factor for in-beam modifying devices. The modifying devices could be the physical wedges, compensators, or acrylic trays used for supporting the shielding blocks on treatment machine. These devices will be discussed in details in later sections.

Example 4.5 Beam output from a 15 MV linear accelerator is 1 cGy/MU at d_m under reference conditions (10×10 cm^2 field size and 100 cm SSD). Determine the number of MU if an 18-cm-thick patient needs 250 cGy to be delivered at midpoint, with a single field (12×8.5 cm^2) and 100 cm SSD. What is the maximum dose received by the tissue in this case. No beam modifier is used.

Solution From Eq. (4.3), the side of the equivalent square field: $\frac{2\times12\times8.5}{(12+8.5)} \approx 10$ cm Equivalent square field: 10×10 cm^2

PDD = 79.2%
$ISF_{SSD} = 1.000$
Using Eq. (4.16):

$$MU = \frac{250 \times 100}{1.000 \times 79.2 \times 1.000 \times 1.000 \times 1.000} = 316$$

The maximum dose is at d_m and is:

$$D_{max} = \frac{250 \times 100}{79.2} = 316\,\text{cGy}$$

Example 4.6 The whole spine, at a depth of 4 cm, is to be treated to 3600 cGy in 18 fractions on a 6 MV linac ($d_m = 1.5$ cm) using fixed SSD setup. The patient is lying in the prone position. To accommodate the entire spine, a field size of 54 × 8 cm^2 at the patient's skin is required.

(i) Determine the minimum required treatment SSD for a linac with maximum field size of 40 × 40 cm^2 at isocenter.
(ii) What should the collimator settings be for the required SSD to achieve the required treatment field?
(iii) Calculate the required number of MUs per treatment fraction.

Solution

(i) The field size is directly proportional to the distance. To obtain a 54-cm-long field edge, the required extended SSD will be (54/40) × 100 cm = **135 cm**.
(ii) The collimator settings are 54 cm × [100/135] = **40 cm** and
8 cm × [100/135] = **6 cm**.
(iii) The PDD at an extended SSD of 135 cm, field size of 40 × 6 cm^2 (equivalent field, 10 × 10 cm^2 at iso-centre) and depth of 4 cm, can be calculated from the PDD at 100 cm SSD, using Eq. (4.5):

$$PDD = 91\% \times \frac{[(100+4)/(135+4)]^2}{[(100+1.5)/(135+1.5)]^2} = 92\%$$

The relative output factor for a field size of 10 × 10 cm^2 at the extended SSD of 135 cm can be derived from the standard data (Appendix-A2) by applying inverse square law. Change in the phantom scatter factor for larger field at extended SSD is, however ignored.

Output at standard SSD = 1.000 cGy/MU

Using the inverse square law, output at 135 cm $= 1.000 \times \left(\frac{100+1.5}{135+1.5}\right)^2 = 0.553$ cGy/MU

$$MU = \frac{200 \times 100}{92.3 \times 0.553} = 392$$

4.1.15.2 Fixed SAD (Isocentric) Setup

The main advantage of an isocentric technique is that the patient does not need to be repositioned between fields. The patient is usually positioned such that the isocenter of the machine lies in the tumor. The field size is always defined at the isocenter. TMR or TPR data may be used for dose calculation at the point of interest using Eq. (4.17):

$$\text{Monitor units} = \frac{\text{Prescribed dose}}{\dot{D} \times \text{TPR}(d, r) \times S_c(r_c) \times S_p(r) \times \text{ISF}_{\text{SAD}} \times \text{TF}} \tag{4.15}$$

where ISF_{SAD} is equal to $\left(\frac{\text{SCD}}{\text{SAD}}\right)^2$

Example 4.7 A total dose of 200 cGy is prescribed to a depth of 7 cm using a single 15 MV photon beam with SAD setup. The treatment field size is 8×8 cm^2 and the beam is calibrated at d_m (1.0 cGy/MU; 10×10 cm^2 field, 100 cm SSD). Calculate the required MU.

Solution Dose rate at $d_m = 1.000$ cGy/MU
TMR (8×8 cm^2, 7) = 0.943
Relative output factor = 0.983
Source to calibration distance (SCD) = 100 + 3(d_m) = 103 cm, hence:

$$\text{ISF}_{\text{SAD}} = \left(\frac{103}{100}\right)^2 = 1.061$$

From Eq. (4.17):

$$\text{MU} = \frac{200}{1.0 \times 0.943 \times 0.983 \times 1.000 \times 1.061} = 203$$

Example 4.8 A 6 MV linear accelerator is calibrated to deliver 1.2 cGy/MU for a 10×10 cm^2 field at depth of d_m for 100 cm SAD. The relative output factor for a 12×16 cm^2 field is 1.031. Calculate the monitor units to deliver 300 cGy at midpoint using equally weighted, parallel opposed fields in an SAD setup. The patient is 16 cm thick.

Solution From Eq. (4.3), equivalent square field = 13.7 × 13.7 cm^2
Dose rate at d_m for 10 cm × 10 cm field is 1 cGy/MU
ROF for 13.7 × 13.7 cm^2 field = 1.031 cGy/MU
TMR at 8 cm depth for 13.7 cm × 13.7 cm field is 0.855
$ISF_{SAD} = 1$, TF = 1
Use Eq. 4.17 to determine MUs per field:

$$MU = \frac{150}{1.200 \times 0.855 \times 1.031 \times 1.000 \times 1.000} = 142$$

Example 4.9 A brain tumor is treated isocentrically with an orthogonal 6 MV wedged pair, using 45° wedges. A daily tumor dose of 200 cGy is prescribed at isocenter (9 cm from anterior and 7 cm from lateral beam entry points). The beam output factor at d_m = 1.0 cGy/MU (SAD setup). With 1.2 and 1.0 weightings for the anterior and lateral fields, respectively, calculate the MU per fraction for both fields (7 × 7 cm^2 each).

Solution Anterior field weightage: 1.2
Prescribed dose = (1.2/2.2) × 200 cGy = 109 cGy
Treatment depth = 9 cm, wedge transmission factor = 0.720
TMR = 0.795 **Appendix-A1**
ROF = 0.963 **Appendix-A**2
Using Eq. (4.17):

$$MU = \frac{109}{1.000 \times 0.795 \times 0.963 \times 0.720} = 197$$

Lateral field weightage: 1.0
Prescribed dose = (1.0/2.2) × 200 cGy = 91 cGy
Treatment depth = 7 cm, wedge transmission factor = 0.720
TMR = 0.857 **Appendix-A1**
ROF = 0.963 **Appendix-A2**
Using Eq. (4.17):

$$MU = \frac{91}{1.000 \times 0.857 \times 0.963 \times 0.720} = 153$$

Example 4.10 A large tumor is to be treated with a single, 30 × 50 cm^2 field at an extended SSD of 125 cm, using 6 MV photon beam. A total tumor dose of 3000 cGy is prescribed in 10 daily fractions on the central axis at a depth of 6 cm. The machine is calibrated to deliver 1 cGy/MU at d_m with an SAD setup. S_c and S_p data for 6 MV beam is given in Table 4.2. Other values can be approximated by linear interpolation.

(a) Calculate the number of monitor units, using Appendix-A1 TMR data.
(b) Calculate the number of monitor units, using Appendix-A2 PDD data.

Table 4.2 Scatter factors (S_c and S_p) for 6 MV beam

Field size	30 × 30 cm^2	40 × 40 cm^2
S_c	1.041	1.051
S_p	1.060	1.072

Solution Prescribed daily dose at 10 cm depth = 300 cGy
At 125 cm SSD, the jaw setting = 24 × 40
Equivalent square (eq. sq.) fields using Eq. (4.3) are:

For collimator settings = 24 × 40 cm^2 eq. sq. = 30 × 30 cm^2
Field size at surface, A_o at 125 cm = 30 × 50 cm^2 eq. sq. = 37.5 × 37.5 cm^2
Field size at depth d (=6 cm), A_d at 131 cm = 31.5 × 52.5 cm^2 eq. sq. = 39.5 × 39.5 cm^2

(a) MU calculation at extended SSD – using TMRs
TMR(39.5 × 39.5, d = 6) = 0.930
S_c(30 × 30) = 1.041 (for actual collimator setting)
S_p(39.5 × 39.5) = 1.071 (for the field size defined at 131 cm in patient)
ISF = (100/131)^2 = 0.583
$D^{'}$ = 1.0 cGy/MU
Using Eq. (4.17):

$$\text{MU} = \frac{300}{1.0 \times 0.930 \times 1.041 \times 1.071 \times 0.582} = 497$$

(b) MU calculation at extended SSD – using PDDs
PDD(SSD = 100, 30 × 30, d = 6) = 85.0%
Using the Mayneord factor:

$$PDD(SSD = 125, 30 \times 30, d = 6) = \left[\frac{(106/131)}{(126.5/101.5)}\right]^2 \times 85.0\% = 86.4\%$$

S_c(30 × 30) = 1.041 (for fixed collimator jaws)
S_p(37.5 × 37.5) = 1.069 (for field size defined at 126.5 cm)
ISF = (100/126.5)^2 = 0.6249
$D^{'}$ = 1.0 cGy/MU
Use Eq. (4.16):

$$\text{MU} \frac{300 \times 100}{1.00 \times 86.4 \times 1.041 \times 1.069 \times 0.625} = 499$$

4.1.15.3 Clarkson's Dose Calculation Method

As discussed earlier, basic beam data is available for rectangular or square fields only. These data may not be directly applied for dose calculation in cases where

very irregular fields are used. Furthermore, central axis beam data are not sufficient for dose determination at off-axis points. Those fields in which metallic blocks are used to shield normal structures from irradiation are considered irregular fields. Inverted Y and mantle fields used for the treatment of Hodgkin's disease are two examples of irregular fields. Although every irregular field can be represented by an equivalent square or circular field, it is not always easy to determine the dimensions of the equivalent field.

A simple solution to this problem was presented by Clarkson (1941) and is referred to as the Clarkson segmental integration technique. The technique is based on separate calculations of primary and scattered radiation. The primary radiation is independent of the field size and shape, whereas scatter is not. To account for the scatter at a given point, the irregular field is divided into sectors of circular beams surrounding the point of interest. The scatter is calculated from each sector, using the concept of scatter-air ratio (SAR). SAR is defined as the quotient of the scattered dose at a given point in a phantom to the primary dose at the same point in air.

Let us consider a point P at depth d in an irregularly shaped field as shown in Fig. 4.18. To find the scattered dose at point P, the field is divided into sectors of fixed angular width (10° in this case). Each sector is characterized by a radius r and approximated as a part of a circular field of the same radius r. For a sector of 10° angle, the scatter contribution to point P from this sector will be 1/36 (10/360) of the total scatter contributed by a circular field of the same radius, centered at P. Similarly, the scatter contribution from all other sectors are calculated and summed for the entire irregular field and the average value of the scatter-air ratio ($\overline{\text{SAR}}$) is finally determined at point P.

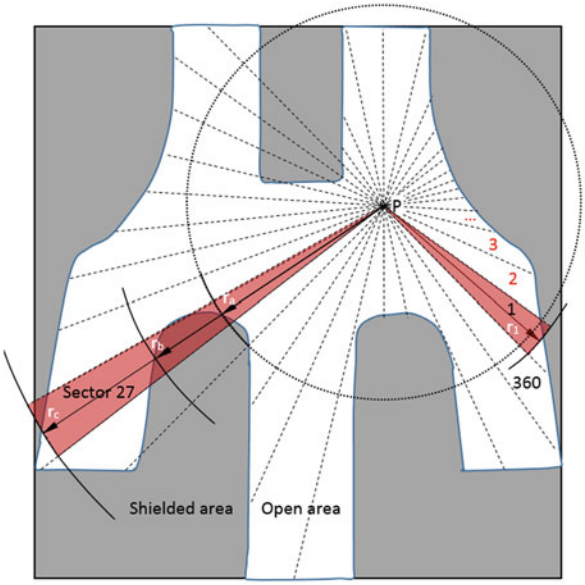

Fig. 4.18 An irregular mantle field, divided into 36 segments. The first sector with radius r_1 is fully open with no shielded region, whereas the 27th sector includes one blocked and two open portions

Consider the 27th sector that passes through both open and blocked areas. In this case the sector is divided into three portions with three radii ($r_a < r_b < r_c$). The net SAR for this entire sector is estimated by subtracting the scatter contribution of the blocked portion of the sector. For this sector, the net SAR is:

$$SAR = (SAR)_{r_c} - (SAR)_{r_b} + (SAR)_{r_a}.$$

Finally, the average tissue-air ratio ($\overline{TAR}$) is determined by Eq. (4.18) below:

$$\overline{\text{TAR}} = \text{TAR}(0) + \overline{\text{SAR}} \tag{4.16}$$

where TAR(0) is the *TAR* for the primary contribution only, i.e., that received from a notional 0 × 0 field size and is approximated by:

$$\text{TAR}(0) = e^{-\overline{\mu}d}$$

where $\overline{\mu}$ is the mean linear attenuation coefficient of the photon beam and d is the depth of point P beyond d_m.

The rest of the calculation is similar to those performed earlier.

4.1.15.4 Field Shaping

Asymmetric Fields

Unlike symmetric fields (Fig. 4.19a), asymmetric fields may be described as those in which the beam central axis (i.e., the axis of rotation of the collimator) is not coincident with the geometric center of the field. Such a geometry can be achieved by independently moving the collimator jaws with reference to the central axis of the beam (Fig. 4.19b). Both x and y jaws can be independently adjusted to produce doubly asymmetric fields. This helps the radiation oncologist to easily and appropriately shape the field to the tumor. It also helps in producing a half beam blocked shape in order to remove beam divergence at field matching (e.g., tangent breast and mono-isocentric techniques).

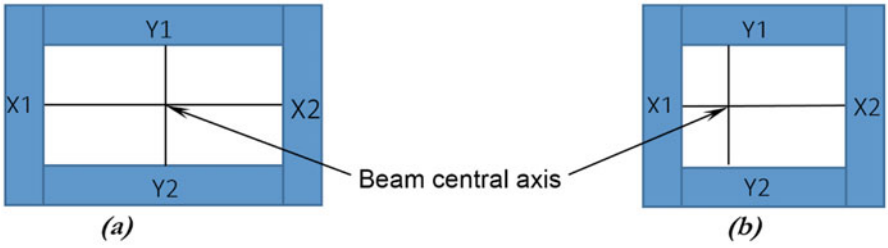

Fig. 4.19 Collimator jaw setting for (**a**) symmetric field and (**b**) asymmetric field.

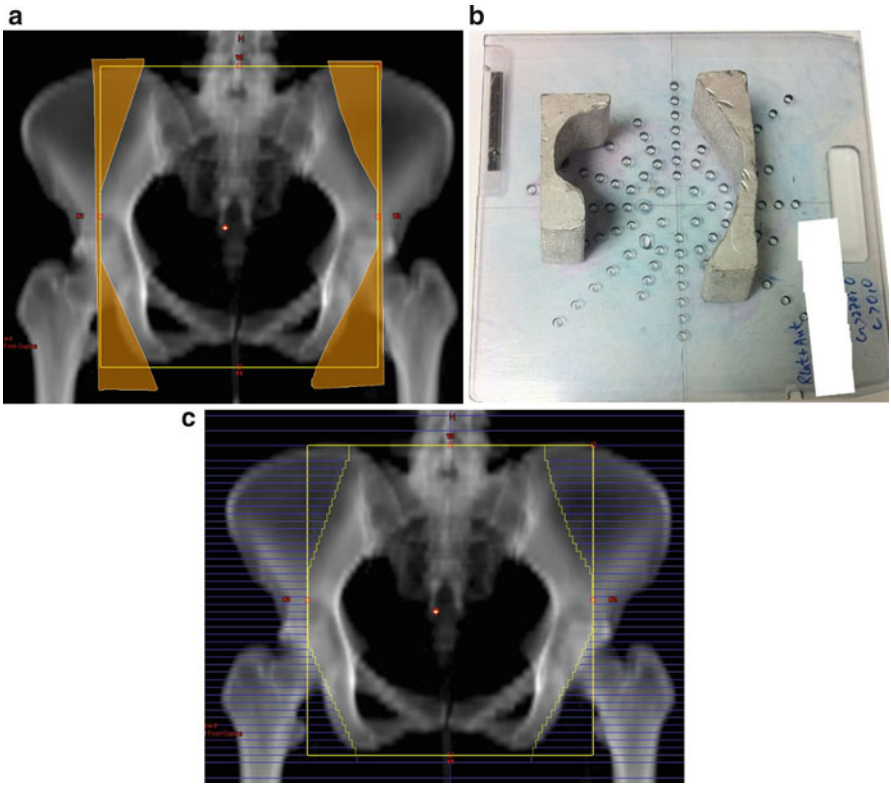

Fig. 4.20 (**a**) Beam eye view of shielded region drawn on DRR, (**b**) a custom Cerrobend block on acrylic tray, and (**c**) MLC adjusted to shielded area drawn in (**a**)

Irregular Fields

In Fig. 4.20a, the planning target volume (not shown) is to be irradiated to a uniform dose. In order for the field aperture to conform to the shape of the treated area, the rectangular field defined by the collimator jaws (x and y) needs to be modified. This may be achieved either with custom made blocks or a MLC.

Custom Shielding Blocks

One of the purposes of radiotherapy simulation is to assist the radiation oncologist with the design of field arrangements and beam shaping. As has been noted earlier, to achieve a higher therapeutic ratio, it is necessary to keep radiation doses to normal tissues as low as possible. This can be achieved, in part at least, through treatment field shaping. With a reasonably thick lead or metallic alloy blocks, megavoltage photon beams can be attenuated by a clinically meaningful amount. Ninety-five percent attenuation of the primary beam through a block is generally

considered clinically acceptable for the majority of the cases. This corresponds to a block thickness of 4.5–5.0 half-value layers. One of the low melting point alloys, known as Cerrobend (brand name), is commonly used for casting shielding blocks. It is a high-density alloy that melts at about 70 °C. The shielding blocks are mounted on an acrylic tray for loading into the treatment machine head (Fig. 4.20b). The mounting tray also attenuates the radiation beam, and this effect needs to be quantified and corrected for in dosimetry calculations. Placement of shielding blocks in the field also changes the phantom/patient scatter component of the radiation beam by changing the effective area of the beam.

Multileaf Collimator

An alternative to custom-made blocking is the multileaf collimator (MLC) (Sofia 1979) available on modern teletherapy machines. It consists of a set of motorized leaves, made of tungsten alloy, that can easily produce the required field shape (Fig. 4.20c). Depending on the type of MLC, the projected leaf width at the isocenter ranges from 10 mm down to 1.6 mm. The thickness of the leaves along the beam direction is sufficient to provide acceptably low beam transmission ($\leq$3%), whereas the inter-leaf leakage is ~3–4% (LoSasso et al. 1998; Boyer et al. 1992; Galvin et al. 1993).

Three-dimensional conformal radiotherapy (3DCRT) techniques require an increased number of fields per fraction as well as more complex field shaping. This makes the use of MLC for field shaping the most practical approach.

Using a MLC for blocking purposes offers many advantages. Fabrication and mounting of poured blocks is time consuming and labor intensive and involves the handling of a toxic material (alloys). The mounting and demounting of heavy blocks is both strenuous for therapists and poses a risk of injury to both therapists and patients. The use of MLCs overcomes these inherent disadvantages and considerably reduces patient setup time.

4.1.16 Treatment Planning

4.1.16.1 Isodose Distribution

For simplicity, dose distributions in two dimensions are represented by isodose lines. The dose at each point along an isodose line is the same. An isodose chart is a representation of *isodose curves*, drawn at regular increments, for a given beam in a plane parallel to the central axis. As shown in Fig. 4.21, each isodose line represents a percentage of the dose at some reference point. These charts are useful in treatment planning calculations with fixed SSD setup.

The regions near the field edges where the dose drops sharply represent the beam penumbra. Penumbra is some times expressed by the lateral distance between two isodose lines at a certain depth. The field size at any depth is defined by the lateral

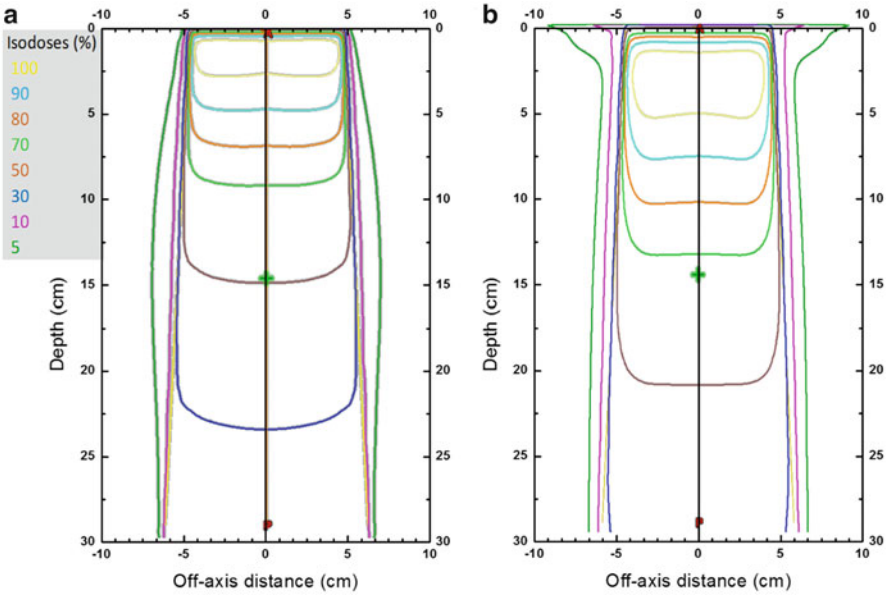

Fig. 4.21 Isodose charts for (**a**) 6 MV and (**b**) 18 MV beams, calculated at fixed 100 cm SSD and 10×10 cm^2 field size

distance between the 50% isodose lines. It may also be obtained from the corresponding off-axis beam profile (Fig. 4.17). A sharper penumbra is generally better for patient treatment as it affords more dose sparing of normal tissues adjacent to the target. The penumbra size depends on the beam energy and source size. Because of their smaller source sizes and less side scatter, penumbras from high-energy linacs are sharper than that for ^{60}Co beams and also sharper for higher-energy photon beams (Fig. 4.21b) than for low-energy photons.

4.1.16.2 Wedge Filters

Wedge filters are frequently used in treatment planning to modify the isodose distribution as shown in Fig. 4.22. There are three designs of wedge filters currently in use: physical, motorized, and dynamic. A physical wedge is made of a wedge-shaped metallic block, manually placed in the beam. A motorized wedge is a physical wedge, but one which is installed permanently in the machine head and remotely controlled. Unlike physical wedges, a dynamic wedge produces a tilted profile by gradually moving one of the collimator jaws during dose delivery.

The degree of isodose tilt depends on the slope of the physical wedge filter. For dynamic wedges, the tilt depends on speed of the jaw and machine dose rate. The modern intensity-modulated radiation therapy (IMRT) treatment techniques take advantage of the considerable flexibility of the multileaf collimator (MLC), with no need to use wedge filters at all.

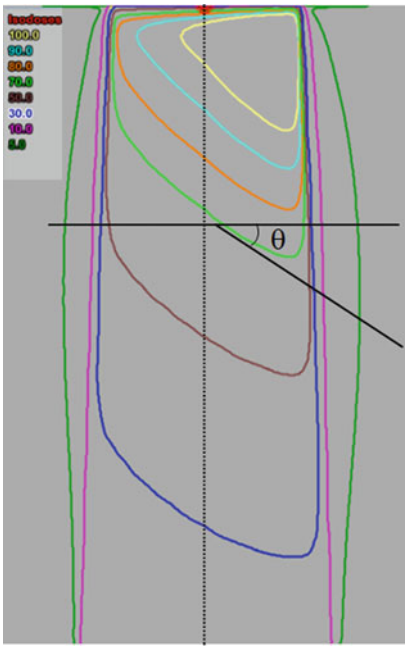

Fig. 4.22 Wedged isodose curves and wedge angle definition

The wedge angle *(θ)* for a given wedge is defined as "the angle made by the isodose curve and the normal to the central axis, at a given depth in a water phantom," as shown in Fig. 4.22. The wedge transmission factor or simply wedge factor (WF) is the ratio of doses at a reference depth in a water phantom at the beam central axis with and without the wedge in the beam.

4.1.16.3 Bolus

Bolus is a tissue equivalent material placed on top of the skin to increase the skin dose by reducing the skin-sparing effect within the patient of megavoltage x-ray beams. Tissue equivalence means an electron density similar or very close to tissue (or water). The thickness of the bolus is selected on the basis of beam energy. Bolus may also be used to even out patient surface irregularities.

4.1.16.4 Compensators

Compensators are used to account for the non-planar nature of the patient's surface contour or to modify the beam intensity to conform the dose to irregular target shapes (Khan et al. 1970; Sewchand et al. 1980). These are usually made of lead or Cerrobend. Custom-made compensators are placed at a distance of 10–15 cm above the patient in the beam (Fig. 4.23) to maintain the skin-sparing effect.

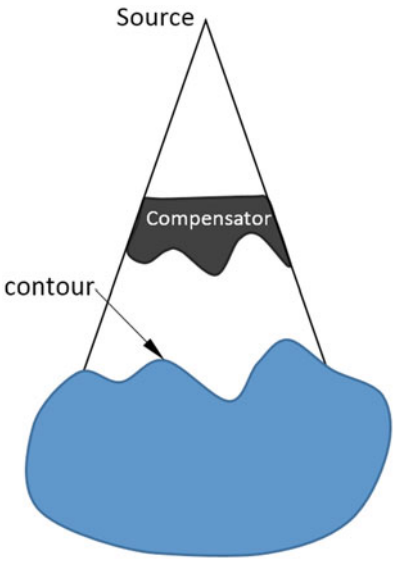

Fig. 4.23 Design and placement irregular surface compensator

4.1.17 Treatment Planning Techniques

4.1.17.1 Single Field Treatment

Single field treatment with high-energy photons are used only for shallow tumors. For a single-photon beam, the dose gradient across the PTV is large, especially for low energies due to exponential attenuation. Beyond d_m, the dose fall off for 18 MV, 6 MV, and ^{60}Co photon beams in water is approximately 2%, 3.5%, and 4.5% per cm, respectively (Halperin et al. 2008a). Care should be taken with such treatments, since dose homogeneity as recommended by ICRU 50 may not be achieved within the tumor, for a single field. By using higher-energy beams, the distribution will be more uniform, but the exit dose will increase as well. Sites commonly treated with single, photon fields are the supraclavicular region, internal mammary nodes, and the spinal cord.

4.1.17.2 Two-Field Treatment

Sometimes a combination of two beams may be used to obtain an acceptable dose distribution within the tumor as well as to reduce the dose to adjacent normal tissue. The simplest combination is a pair of opposing fields along the same axis. These parallel opposed beams are used for situations where a uniform dose is required throughout the irradiated volume but a high level of conformity is not required. The shape of the isodose distribution is that of an hourglass as can be seen in Fig. 4.24a.

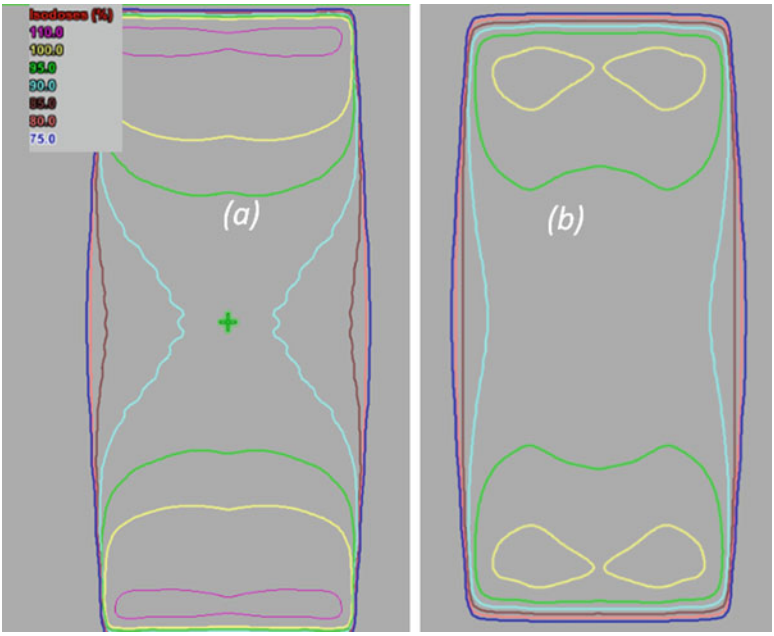

Fig. 4.24 Isodose distribution from parallel opposed beams, (**a**) hourglass effect in a water phantom with 6 MV beam, (**b**) 18 MV beam

However, with increasing patient separation, the dose distribution uniformity decreases. The dose uniformity can be improved by using higher-energy beams as clear from Figs. 4.24b and 4.25. If the tumor is not in the center of the body and is closer to one side, beam weighting can be adjusted to improve the dose uniformity.

Wedges can be used with parallel opposed beams when treating shallow tumors under sloping surfaces. Treatment of the breast, chest wall, and larynx is an example of such applications. In these situations, wedges are essentially used to compensate for missing tissue but obviously only in one plane. The thick edge of the wedge is always toward the thinner section of the treated volume (Fig. 4.26). In some situations, combinations of nonparallel wedged beams are used. One such example is treating brain lesions with an orthogonal, wedged (45°) pair of beams (Fig. 4.27).

4.1.17.3 Multiple Fields

In order to confine higher doses to the tumor only, the use of multiple fields/beams is essential. Three or more beams may provide better dose conformality to the tumor and with minimal doses to the organs at risk. The selection of appropriate beam angles and beam modifiers is crucial for producing acceptable treatment

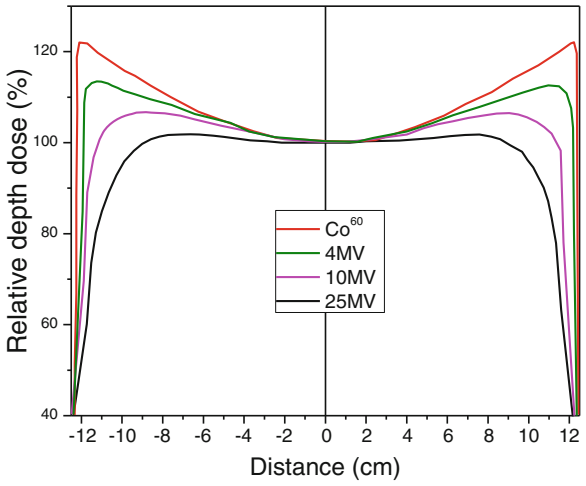

Fig. 4.25 Percent depth doses along the central axis from parallel opposed beams in a 25-cm-thick water phantom for different photon energies

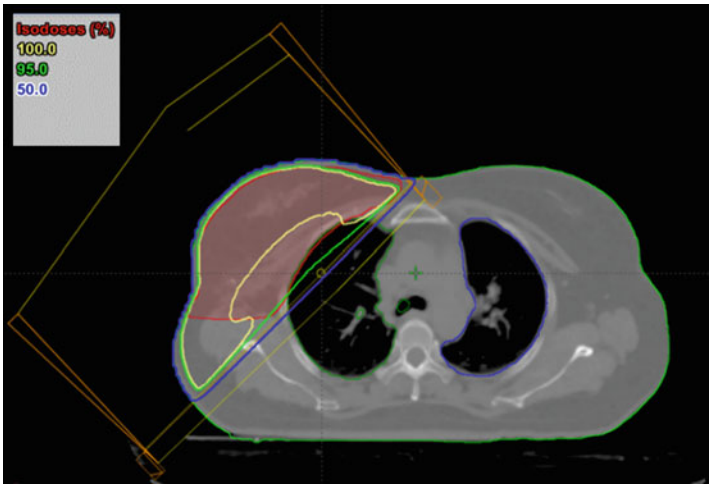

Fig. 4.26 Chest wall and breast irradiation planning with wedged parallel opposed beams

plans. An example of a three-field rectum treatment plan is shown in Fig. 4.28. In this case two lateral wedged fields and one open posterior field are used. This arrangement results in reduced dose to the bladder.

Four-field box technique is extensively used in treating pelvic tumors. An example of a phase-1 prostate plan with a four-field box is shown in Fig. 4.29a. A four-field Bedford plan for prostate phase-2 is shown in Fig. 4.29b.

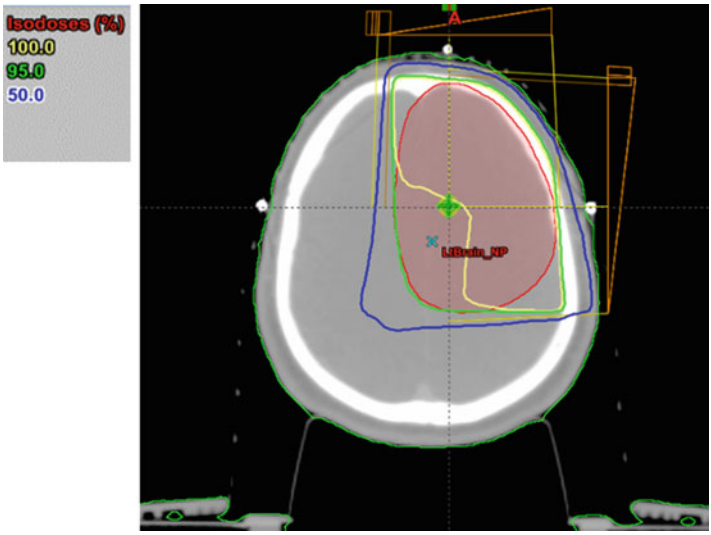

Fig. 4.27 Treating brain lesion with an orthogonal pair of wedged beams

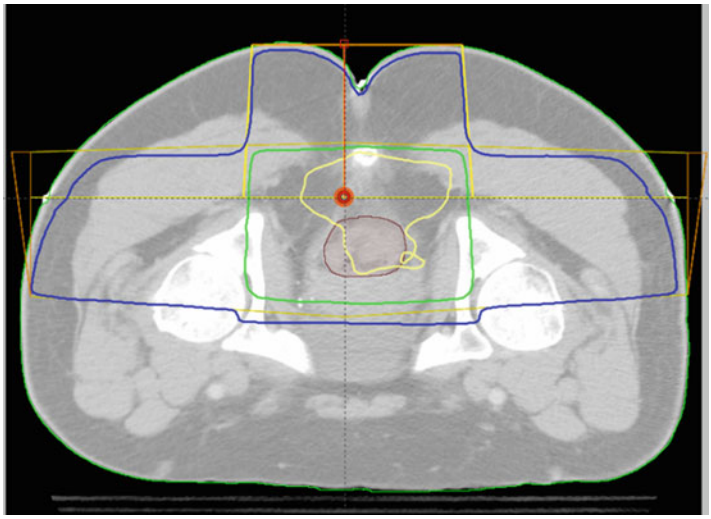

Fig. 4.28 Three-field setup for the treatment of the rectum in a prone position

4.1.18 Rotation (or Arc) Therapy

In the multiple field isocentric technique, the tumor is irradiated with a number of fields of different shape, directed from different fixed angles (e.g., the four-field technique for prostate cancer). A logical extension of this method is to use a single

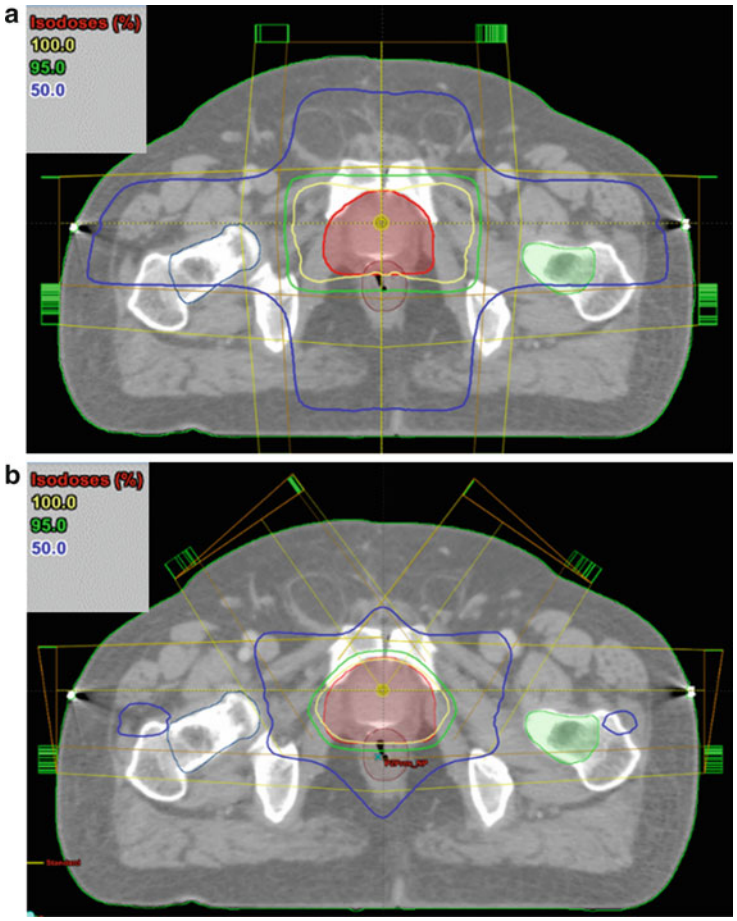

Fig. 4.29 Prostate plans, (**a**) phase-1 four-field box technique, (**b**) phase-2 four-field Bedford technique

radiation field and rotate it around the isocenter (which is placed inside the tumor) at a constant speed, for single or multiple partial or complete revolutions. This technique is referred to as *rotation therapy*. If the radiation source moves through an arc around the patient, this is known as *arc therapy*. It should be noted that this is possible only with the machines capable of isocentric treatments. The technique is well suited for small, deep-seated tumors in pelvic region.

Theoretically rotation therapy can be considered as treating the patient isocentrically with an infinite number of fixed fields, directed at the PTV. In practice, 18 fields, equally weighted and equally spaced at 20° angular intervals ($18 \times 20^\circ \Rightarrow 1$ complete rotation), are sufficient to produce an acceptably accurate calculation of the dose distribution. The dose calculation formalism is similar to

that for the isocentric technique, except an average $\overline{\text{TPR}}$ is calculated from all the TPRs for individual beams:

$$\overline{\text{TPR}} = \sum_{i=1}^{n} \text{TPR}_i \tag{4.17}$$

where i represents a given beam angle.

A more conformal dose to the target may be achieved by continuously adjusting the shape of the field to match the beam's eye view (BEV) projection of a planning target volume (PTV) during an arc rotation. This can only be achieved by dynamically adjusting the MLC leaves during the rotation while radiation is on. Volumetric modulated arc therapy (VMAT) techniques evolved from this approach. Machine dose rate and gantry speed also change during rotation, for optimal dose delivery.

Example 4.11 A patient with prostate cancer is to be treated to a tumor dose of 4500 cGy in 25 daily fractions (fr), using 360° rotation therapy (18° × 20 fields) with a 17 × 12 cm^2 field at an SAD of 100 cm on a 15 MV photon beam, as shown in the diagram below (Fig. 4.30).

(a) Calculate the number of monitor units for daily dose delivery.
(b) Calculate the gantry speed in MU/degree for the daily treatment, given in *two* complete rotations.

Solution Since the contour is elliptical, the effective TPR calculation needs to be performed only for a quarter of the 360° rotation. The equivalent field size is 14 × 14 cm^2.

The TPRs for the various depths (Table 4.3) are averaged to obtain an effective TPR of 0.821

(a) Daily tumor dose = 4500 cGy/25 fr = 180 cGy/fr
Effective TPR = 0.821

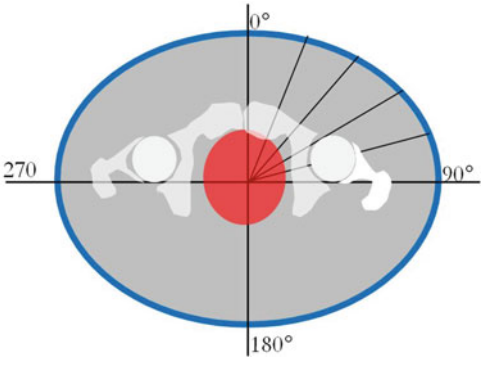

Fig. 4.30 Rotation therapy beam arrangements for a prostate treatment plan

Table 4.3 Effective TPR

Angle	Depth (cm)	TPR (Appendix-A3)
0°	10.5	0.860
18°	11.0	0.851
36°	12.0	0.830
53°	13.0	0.812
72°	14.0	0.790
90°	14.5	0.780
$\overline{TPR}$ **0.821**		

Dose rate for 14 × 14 cm^2 field size is 1.022 cGy/MU at d_m with isocentric setup:

$$\text{Daily } MU = \frac{180 \text{ cGy}}{0.821 \times 1.022 \text{ cGy}/MU} = 215$$

(b) Since 214 MUs are to be delivered in *two* complete rotations, the angular speed will be:

$$215MU/(2 \times 360^{\circ}) \approx 0.30MU/\text{degree})$$

4.1.19 IMRT

Based on the shape of the body contour and beam arrangements, wedge filters, compensators, or other modifying devices are employed in the field to modify the beam intensity. This is the simplest form of intensity modulation. The concept of the dynamic MLC may be extended to achieve more complicated and precise intensity modulation. This type of beam intensity modulation with the help of a computer-controlled dynamic MLC is known as intensity-modulated radiation therapy (IMRT) (IMRT Collaborative Working Group 2001). IMRT uses modern technology to manipulate radiation beams to conform the dose to the three-dimensional shape of the tumor. Multiple intensity-modulated radiation beams, irradiating the patient from different angles, are used. The dose distribution can be manipulated to avoid or minimize exposure to healthy tissue while delivering a therapeutic dose to the target volume. IMRT treatment planning is performed on three-dimensional CT or MRI images of the patient with the help of inverse dose calculation algorithms. Previously considered untreatable tumors may now be easily treated with the help of IMRT. Potentially, better quality of life and higher cure rates are observed in cancer patients treated with IMRT.

A number of inverse planning algorithms have been developed to calculate optimized fluences for IMRT (Webb 1989; Bortfeld et al. 1990b; Convery and Rosenbloom 1992; Holmes and Mackie 1994; Webb 1997). During the treatment

planning process, each beam is divided into multiple beamlets. The fluence associated with each beamlet is optimized based on predetermined dosimetric objectives and constraints. Inverse optimization methods include analytical methods (such as backprojection) and iterative methods (such as simulated annealing and constrained least squares) (IMRT Collaborative Working Group 2001).

During iterative optimization, fluences of the individual beamlets for all the fields are iteratively adjusted so that the value of a cost function $f_{T,N}$ is minimized. A cost function describes the deviations of the calculated dose distribution from the desired (prescribed) dose distribution. The process continues until no further improvement can be achieved. A cost function may be expressed as in Eq. (4.20):

$$f_{T,N} = \sum_i (D_i - D_o)_T^2 + \sum_i (D_j - D_o)_N^2 \tag{4.20}$$

where T stands for target volume and N for normal tissue, D_i and D_j are the expected (calculated) doses in respective volume elements, whereas D_o is the desired (prescribed) dose.

4.1.20 Plan Evaluation

3D-CRT and IMRT treatment plans are evaluated on the basis of the calculated dose distribution in the patient, using 2D isodose line displays over the region of interest on CT images (Figs. 4.26, 4.27, 4.28, and 4.29). This is a qualitative or visual analysis of the plan. For a summary, standardized evaluation of a plan, various tools have been developed (Halperin et al. 2008a) of which the dose-volume histogram (DVH) is widely considered to be the most useful (Drzymala et al. 1991). A DVH is a plot, showing the relationship between the volume of an organ or PTV and the dose the volume receives. It may be expressed in absolute or relative terms.

There are two ways to represent the dose-volume histogram: differential and cumulative. A differential DVH is a plot of the frequency of occurrence of different dose levels. The entire irradiated volume is divided into a finite number of small volume elements (voxels). Similarly, the 3D dose distribution is divided into dose bins. All the voxels receiving dose from a specific dose bin are counted. The process is repeated for all the voxels in the volume of interest. A graph showing the number of voxels in each bin and the bin dose range is a differential DVH. Figure 4.31a shows differential DVHs for a PTV and lungs in a mediastinum treatment plan.

A cumulative DVH describes how much of the volume receives a dose equal to or greater than the dose in question. In mathematical terms, a cumulative DVH can be calculated by integrating the differential DVH. Figure 4.31b shows the corresponding cumulative DVH for the PTV and the lungs. Radiation oncologists usually make their decisions for plan approval on the basis of a cumulative DVH as well as slice by slice evaluation of 2D dose distributions.

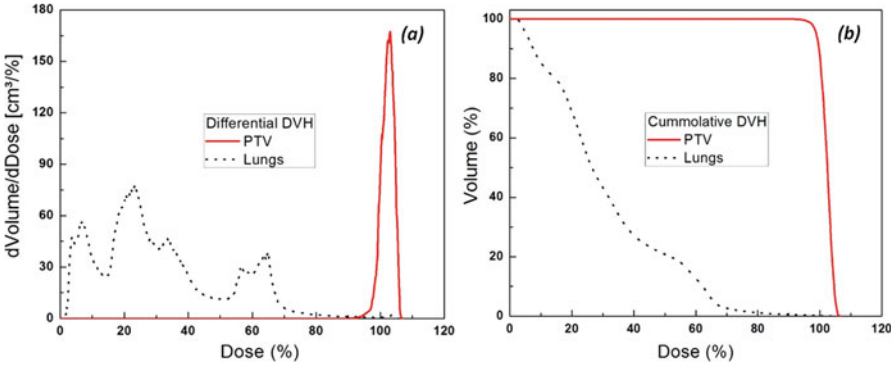

Fig. 4.31 Schematics of (**a**) differential DVHs and (**b**) cumulative DVHs for the PTV and lungs in a phase-2 mediastinum treatment plan

4.1.21 Treatment Verification

There are various methods used to verify whether or not the actual target area is irradiated and critical organs are shielded as prescribed. Some of these methods are summarized below.

4.1.21.1 Port Film (Radiograph)

This is a conventional radiographic method that can be performed in two different ways: (a) radiographic films with wet processing and developing technique or (b) a reusable digital imaging device. Each of these imaging devices has to be positioned manually every time, and the image is not available immediately for verification. The image quality is relatively poor at these high photon energies. For verification purposes, these images need to be compared visually against the simulation images or DRRs. If errors outside some stated level of acceptability are observed in the patient setup, adjustments are made accordingly and port films are repeated.

4.1.21.2 Electronic Portal Imaging Device (EPID)

An EPID is an online, standard imaging system, available with the majority of modern day linear accelerators. It consists of an imaging device opposite to the linac head in a C-arm type arrangement. The conventional imaging panels were made of a phosphor screen or a matrix of liquid filled ionization chambers. Amorphous silicon flat panels have replaced these systems in modern day EPIDs. An EPID provides "instantaneous" images, thus allowing in real time, both intra-

treatment and inter-treatment verification. Images can also be archived for later viewing. Image quality at megavoltage photon energies is reasonable, as image processing can be employed, but still a challenge.

4.1.21.3 kV Cone Beam Computed Tomography (kVCBCT)

A kV cone beam imaging system consists of a conventional kilovoltage x-ray source and a flat-panel x-ray detector, both mounted orthogonally to the beam central axis. Cone beam CT images are reconstructed by acquiring multiple planar, kV images, as the gantry rotates around the patient. Cone beam CT allows setup corrections in three dimensions, based on bony land marks, as well as soft tissues. kVCBCT can also produce simple planar images, with better quality than MV images, for treatment verification.

4.1.22 Photon Beam Treatment Planning Methods (Algorithms)

Treatment planning is one of the most important steps in the process of clinical radiotherapy. The goal is to prepare for the delivery of an accurate and uniform dose to the target and spare the organs at risk. Based on the available information of the patient, an optimized treatment plan is created, usually with multiple radiation beams. Target dose uniformity should be within +7% and −5% of the prescribed target dose for a better clinical outcome (International Commission on Radiation Units and Measurements (ICRU) 1993). Modern day EBRT is carried out with a variety of beam energies, beam geometries, and field sizes. Dose calculation algorithms in radiotherapy treatment planning systems can be broadly classified into *correction-based* and *model-based* algorithms. Both classes of algorithm require basic beam data, including depth dose profiles, off-axis profiles, dose rate tables, and transmission factors.

With the correction-based approach (Cunningham et al. 1972; Sontag and Cunningham 1978), dose distributions in a homogeneous water phantom is corrected to account for the internal inhomogeneities found in a real patient, beam modifiers, and body contour variations. With model-based algorithms, measured beam data is used to model physical descriptions of the primary photons, scattered photons, and electrons separately. Based on the physical parameters of the beam and anatomical information of the patient/phantom, dose calculation can be easily performed in any geometry, without any additional corrections. Accurate volumetric dose estimation in a patient is only possible with model-based algorithms.

4.1.22.1 Correction-Based Calculation Methods

Beam data is typically collected in a geometric setup, where a homogeneous, flat water phantom is irradiated with a perpendicular beam. In reality, however, a patient's body is nonhomogeneous, and there are large variations in body contours. To perform more accurate dose calculations in patients, a number of corrections need to be applied. Patient contour variation and tissue density information must be available to apply such corrections.

4.1.22.2 Correction for Contour Variation

The following methods have been widely used for dose calculations at points under an irregular body surface.

Effective SSD Method

This method is used for dose adjustment, based on variations in SSD due to an irregular surface and the inverse square reduction in fluence. As an example, suppose the dose at point A, away from the central axis, needs to be calculated (Fig. 4.32). The percent depth dose *(P)*, measured in a phantom with a flat surface, cannot be used for this situation. Due to a tissue deficit of thickness t cm, the dose at point A will be higher than at the same level at the central axis. Suppose, the beam is incident on a flat surface at level L_1. Another flat surface L_2 is assumed to be drawn at t cm below L_1. Depths of maximum dose relative to these levels are d_{m1} and d_{m2}. The isodose chart is shifted down by t cm at level L_2. Now the dose to point A can be approximated as:

$$D_A = P.D_{d_{m2}} \tag{4.21}$$

where P is the percent depth dose at A relative to dose at depth d_{m2} for surface L_2. The thickness t must be small to guarantee dos calculation accuracy.

Dose at point A with respect to $D_{d_{m1}}$ is:

$$D_A = P_c.D_{d_{m1}} \tag{4.22}$$

where P_c is the corrected percent depth dose.

From Eqs. (4.21) and (4.22):

$$P_c = P.\frac{D_{d_{m2}}}{D_{d_{m1}}} \tag{4.23}$$

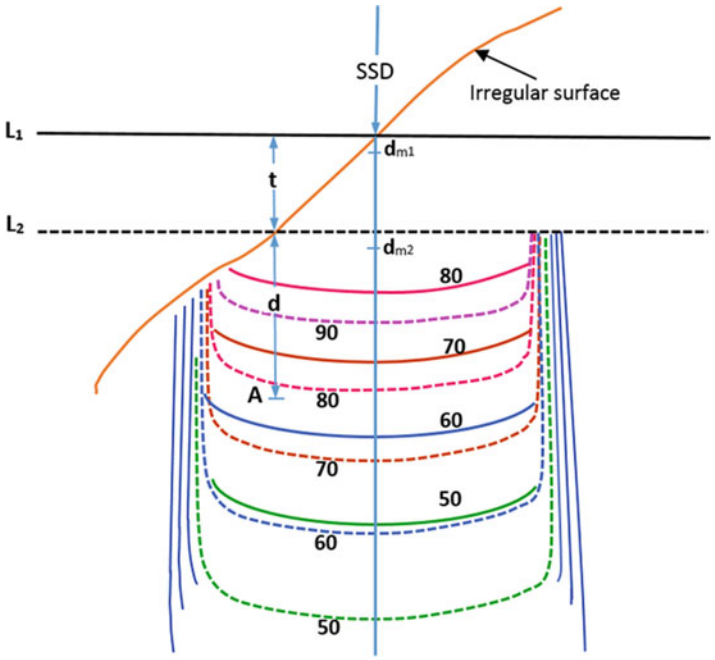

Fig. 4.32 An example of dose distribution determination under an irregular surface. The solid and dashed isodose curves are assumed for flat surfaces located at L_1 and L_2, respectively

Dose at d_{m2} and d_{m1} can be related each other by inverse square law (distance t cm):

$$\frac{D_{d_{m2}}}{D_{d_{m1}}} = \left(\frac{\text{SSD} + d_m}{\text{SSD} + d_m + t}\right)^2 \tag{4.24}$$

so:

$$P_c = P.\left(\frac{\text{SSD} + d_m}{\text{SSD} + d_m + t}\right)^2 \tag{4.25}$$

For excess tissues a similar approach can be used, while moving the isodose charts upward.

Tissue-Air Ratio Method

An alternative to the effective SSD method, TAR correction method can also be used. In this method the value of percent depth dose P_1 relative to surface L_1 is corrected for TAR ratio that differs by a depth of t cm. The correction factor CF is:

$$\mathrm{CF} = \frac{\mathrm{TAR}(d, r_\mathrm{A})}{\mathrm{TAR}(d+t, r_\mathrm{A})} \tag{4.26}$$

Therefore:

$$P_\mathrm{c} = P.\frac{\mathrm{TAR}(d, r_\mathrm{A})}{\mathrm{TAR}(d+t, r_\mathrm{A})} \tag{4.27}$$

Isodose Shift Method

The isodose shift method is a simplified manual correction method applied to irregular body contours. Figure 4.33 illustrates the method in detail. User-defined grid lines are drawn parallel to the beam central axis all across the field. The isodose chart is shifted partially along these rid lines by a factor $k \times t$, where k is a factor

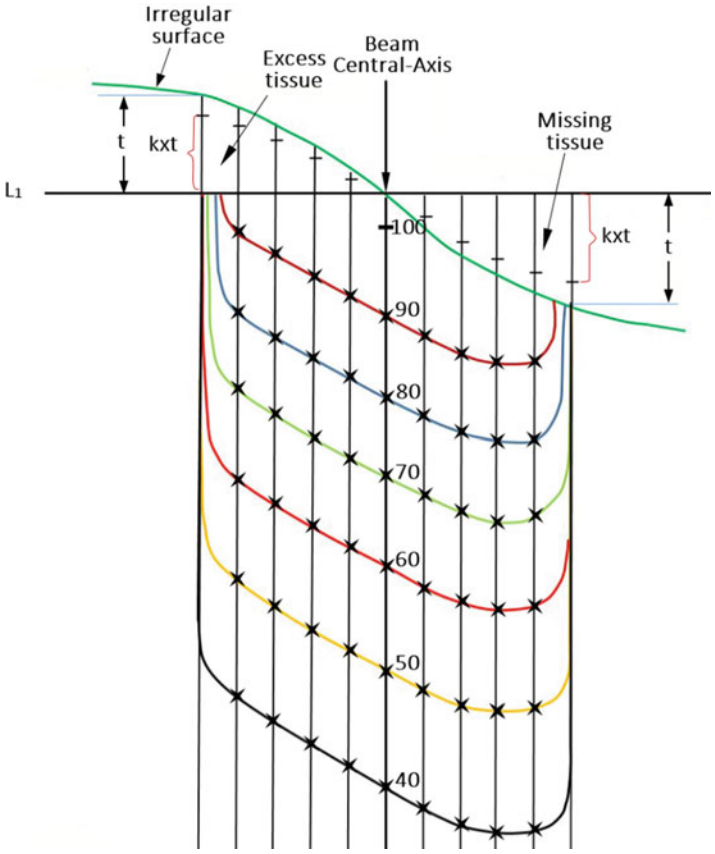

Fig. 4.33 An example of isodose shift method for dose determination under an irregular surface

Table 4.4 Values of k factor, defined for various beam energies

Photon energy (MV)	<1	Co^{60}-5	5–15	15–30	>30
k (approximate)	0.8	0.7	0.6	0.5	0.4

defined for various beam energies, given in Table 4.4 (Giessen 1973), and t is the thickness of missing or excess tissue along the grid line. k values are empirically generated by taking into account the primary and secondary radiations and inverse square effect.

With the help of isodose shift method, dose distribution in the entire plane is estimated.

4.1.22.3 Inhomogeneity Correction

The presence of an inhomogeneity, e.g., the air cavity, lung, tissue, or bone, alters the attenuation of primary as well as scattered radiation. The scatter correction is difficult to perform in the presence of inhomogeneities. We shall limit our discussion to primary radiation only. In the therapeutic range, the photon energy is high enough to assume that attenuation of radiation is predominantly due to the Compton interaction. Another assumption is that, the lateral dimensions of the inhomogeneity are infinite or much larger than the field size. Under these conditions, the absorption and scattering per unit mass, produced in the inhomogeneity will be proportional to the electron density. The following methods are used for inhomogeneity corrections.

TAR Method

Consider a simple geometry where a point A is located at depth d in a homogeneous medium $(\rho_w = 1.0)$, as in Fig. 4.34a. The absorbed dose at point A may be determined using standard depth dose data (e.g., TAR, TPR, or PDD). Now suppose an inhomogeneity of thickness t, with relative electron density $\rho_e = 1.5$ (with respect to water), is introduced above point A. The physical depth to point A' in Fig. 4.34b is the same as in Fig. 4.34a, whereas the effective depth d', to the same point as shown in Fig. 4.34c may be determined by Eq. (4.28).

$$d' = (d - t) + t.\rho_e \tag{4.28}$$

This makes the problem easy for dose estimation. The magnitude of the dose at point A′ depends on the type and thickness of the inhomogeneity. If ρ_e for the inhomogeneity is greater than 1, as in this case, the equivalent depth d' will be greater than the physical depth (Fig. 4.34c), and vice versa. The corresponding correction factor to the dose at point A', in the presence of an inhomogeneity, may be calculated by the following equation:

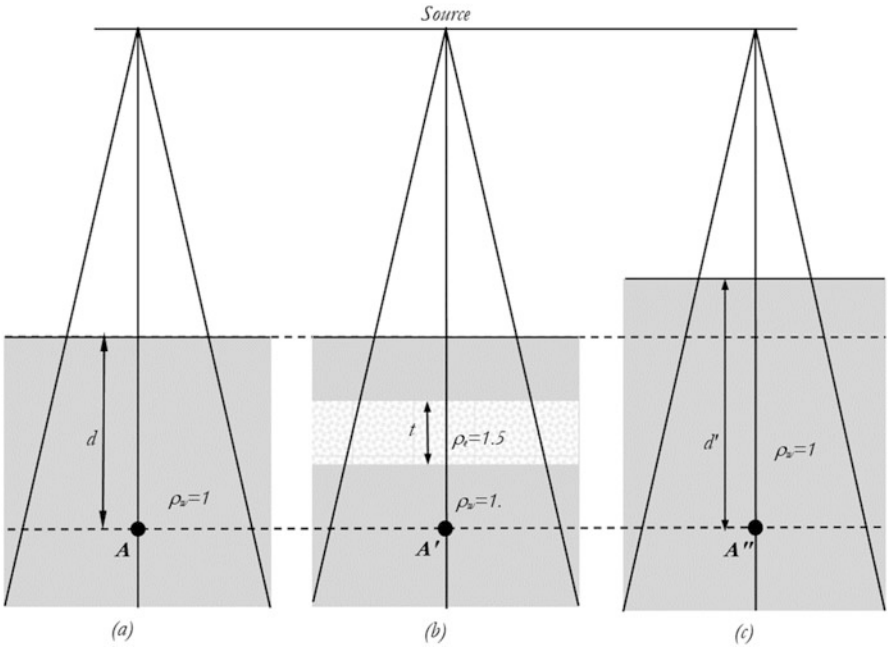

Fig. 4.34 Geometrical explanation of the effect of an inhomogeneity on dose. (**a**) Water-equivalent phantom, (**b**) inhomogeneity of thickness t is introduced, and (**c**) water-equivalent depth of point A′ in part (**b**)

Table 4.5 Approximate changes in dose per cm, beyond inhomogeneity as a function of beam energy

Beam quality	Air gap	Lung	Compact bone
Cobalt-60	+6%	+4%	−3%
6 mv	+3.5%	+3%	−2%
18 mv	+2%	+1.5%	−1%

$$\mathrm{CF} = \frac{\mathrm{TAR}(d', r_\mathrm{d})}{\mathrm{TAR}(d, r_\mathrm{d})} \tag{4.29}$$

where r_d is the field size at depth d.

A major limitation to this method is that the position of the inhomogeneity relative to the point of calculation is not taken into account. This method may be used to determine approximate correction factors for points beyond the inhomogeneity. Such corrections, in percent dose per centimeter of inhomogeneity are shown in Table 4.5 for different beam energies.

Batho's Method (Power Law TAR Method)

In the TAR method, described above, it was noted that the correction factor is independent of the position of the inhomogeneity relative to the point of dose calculation. However, in reality, the absorbed dose at P' in Fig. 4.34b does depend

on its distance from the lower border of the inhomogeneity. Batho's method takes this position dependence of the point of dose calculation into account. The correction factor is now given by:

$$\mathrm{CF} = \left[\frac{\mathrm{TAR}(d_2, r_\mathrm{d})}{\mathrm{TAR}(d_1, r_\mathrm{d})}\right]^{\rho_\mathrm{e}-1} \tag{4.30}$$

where d_1 and d_2 are the respective distances from the point of dose calculation to the lower and upper boundaries of the inhomogeneity.

Modified Batho Power Law Method (MBPL)

Batho's power law method does not apply to dose correction at points inside the inhomogeneity or in the dose buildup region in the vicinity of different tissue interfaces. MBPL uses the descending part of TMR curves, by adding depth of maximum dose to the depth, so that:

$$\mathrm{CF} = \left[\frac{\mathrm{TAR}(d_2 + d_\mathrm{m}, r_\mathrm{d})}{\mathrm{TAR}(d_1 + d_\mathrm{m}, r_\mathrm{d})}\right]^{\rho_\mathrm{e}-1} \tag{4.31}$$

Equivalent TAR Method

The amount of scatter, as discussed earlier is related to the amount of phantom/patient irradiated. In an inhomogeneity, the scatter is no longer equivalent to that produced in the same volume of water. To account for this scatter variation, the field size is scaled to the weighted density $(\widetilde{\rho})$ of the irradiated volume (Sontag and Cunningham 1978).

The correction factor is thus given by the following equation:

$$\mathrm{CF} = \frac{\mathrm{TAR}(d', r')}{\mathrm{TAR}(d, r)} \tag{4.32}$$

where d' is the effective depth and $r' = r.\widetilde{\rho}$ is the effective field size.

The weighted density $\widetilde{\rho}$ is determined using the following equation:

$$\widetilde{\rho} = \frac{\sum\limits_{i,j,k} \rho_{ijk} W_{ijk}}{\sum\limits_{i,j,k} W_{ijk}} \tag{4.33}$$

where W_{ijk} is the weighting of the scatter contribution from the relevant volume element (voxel) in the field.

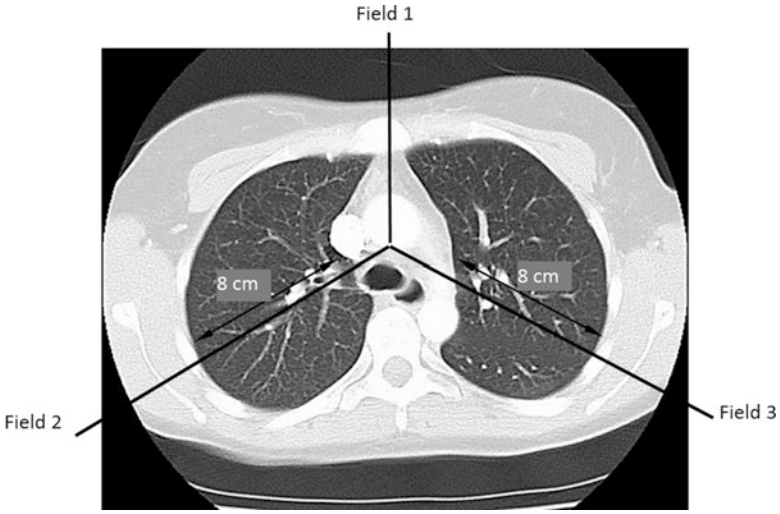

Fig. 4.35 Dose determination beyond inhomogeneity (lung tissue) with three-field technique

Example 4.12 A patient is treated with an SAD setup, using three fields on a 6 MV photon beam. Patient positioning and beam arrangements are shown in Fig. 4.35. The dose rate at isocenter at the calibration depth of d_m for the 10 cm × 10 cm field size is 1.0 cGy/MU. The average lung density (ρ) is 0.25 g/cm^3. Calculate the number of MU per field, for a tumor dose of 100 cGy from each field at the isocenter.

Solution *Field 1*; 10 × 8 cm^2, depth $d_1 = 7$ cm, ROF = 0.988, TMR = 0.866

MU for field 1 can be determined using Eq. (4.17):

$$\text{MU} = \frac{100}{0.988 \times 0.866} = 117$$

Field 2 ≡ *Field 3*; 10 × 12 cm^2, physical depth $d_2 = d_3 = 16$ cm, ROF = 1.009

Central axis of both Fields 2 and 3 passes through 8 cm lung tissue.

Use Eq. (4.28) to calculate water-equivalent depth *Fields* 2 and 3:

$$d_2' = d_3' = (16 - 8) + 8 \times 0.25 = 10 \text{ cm}$$

TMR for fields 2 and 3 is 0.779. Hence, the corresponding MUs can be calculated using Eq. (4.17):

$$\text{MU} = \frac{100}{1.009 \times 0.779} = 127$$

4.1.22.4 Model-Based Calculation Methods

More accurate and precise volumetric dose estimation in patient is only possible with the model-based dose calculation algorithms. The most difficult component of dose calculation in a heterogeneous media is estimating the scattered radiation. In the modern treatment planning systems (TPS), three-dimensional dose distributions are computed from first principles (Ahnesjö and Aspradakis 1999; Ahnesjö 1989; Mackie et al. 1985; Mohan et al. 1986). These algorithms generally model the primary photons, scattered photons, and electrons separately. Hence, any changes in the scattering, caused by variations in the radiation field size and shape, beam energy and intensity, patient geometry, and internal heterogeneities, can be modeled individually (Dyk 1999). However, in dose calculations, some approximations have also been introduced due to computer speed limitations and incomplete physics of the model.

4.1.22.5 Pencil Beam Convolution/Superposition Algorithm (PBCS)

Dose calculation with these models is based on the concept of dose deposition kernels (Knoos et al. 2006; Ulmer and Kaissl 2003; Ulmer et al. 2005; Ulmer and Harder 1996). The dose deposition kernel is a representation of the distribution of energy around the point of interaction of primary photon, as shown in Fig. 4.36a. This in reality models the transport of electrons and photons away from the interaction point. These kernels are usually calculated by Monte Carlo (MC) simulation for a given beam quality.

Dose deposition in a homogeneous medium can be calculated by a three-dimensional convolution of the energy released by the primary beam and the dose deposition kernel, as in the following equation:

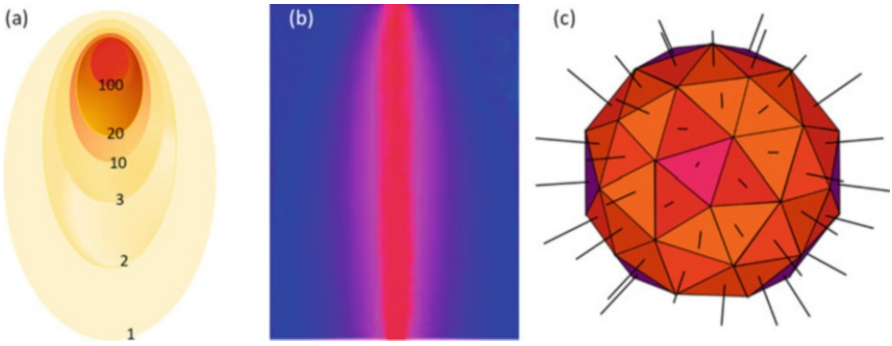

Fig. 4.36 Types of kernels. (**a**) Point scatter kernel, (**b**) line scatter kernel, and (**c**) collapsed cone approximation

$$D(\vec{r}) = \int_{v} \frac{\mu}{\rho}\psi(\vec{r}).k(\vec{r}-\vec{r}')d^3\vec{r}' \tag{4.34}$$

where $\frac{\mu}{\rho}\psi(\vec{r})$ is the total energy released per unit mass and $k(\vec{r}-\vec{r}')$ is a generalized scatter kernel.

To compensate for the scattering changes in a heterogeneous medium, the kernel is scaled to the density of inhomogeneities around the point of interaction. Total dose at a given point in the medium is obtained by the superposition of doses from primary and scattered photons and electrons.

A pencil beam kernel is obtained by convolution of the dose kernel along the depth in water (Fig. 4.36b). Hence, three-dimensional dose distribution can be generated by a two-dimensional integration of pencil beam kernel over the energy fluence across the field. This considerably reduces the calculation time as compared to convolution of the point dose kernel. Heterogeneities are corrected for via effective path length along the longitudinal axis only. With the PBCS model, the dose calculation accuracy in heterogeneous medium is less accurate unlike the modern calculation algorithms (Knoos et al. 2006).

Anisotropic analytical algorithm (AAA) is a modern version of the PBCS, introduced by Varian Medical Systems. AAA suggests separate modeling of the primary and scattered photons and electrons. The pencil beam in this case is acquired from Monte Carlo simulation and is further adjusted to conform to the measurements. The pencil beam along the longitudinal direction is scaled according to the equivalent (effective) path length (EPL), as in PBCS. The pencil beam is further scaled according to EPL in the lateral directions (i.e., normal to the pencil beam). This ensures more accurate and reliable dose calculation in heterogeneous media.

4.1.22.6 Collapsed Cone Convolution/Superposition Algorithm

The pencil beam convolution superposition formulation is the simplest and fast dose calculation formalism. However, there are several limitations to this method, e.g., kernel invariance due to heterogeneities and beam divergence (Ahnesjö and Aspradakis 1999). The collapsed cone convolution superposition (CCCS) model addresses these limitations by introducing a unique dose deposition kernel with a finer resolution than pencil kernel. The shape of the analytical kernel is in the form of multiple discretized conical sectors called collapsed cones (Fig. 4.36c) (Ahnesjö 1989). The CCCS algorithm has been reported to calculate more accurately dose distributions in the presence of inhomogeneities and at interfaces compared to the PBCS and AAA algorithms at the expense calculation speed (Knoos et al. 2006; Nakaguchi et al. 2010; Han et al. 2011).

Several other dose calculation engines are available in the market (Knoos et al. 2006; Fogliata et al. 2011).

4.1.22.7 Monte Carlo Method

Analytical dose calculation methods imply various approximations for increasing the calculation speed. This compromises the dose calculation accuracy, especially at the tissue interfaces. Monte Carlo, on the other hand, is the most accurate dose computation methodology, currently available. It is capable of accurately estimating doses near the interfaces as well as for small radiation fields (Sewchand et al. 1978). Slower calculation speed is however a major limitation to the Monte Carlo calculation. The Monte Carlo is a probabilistic method of dose calculation, based on known interaction cross sections for electrons and photons in different media. It calculates the trajectories and interaction probabilities for a large number (~ several millions) of photons and electrons, to accurately model the dose distribution. In the above mentioned algorithms, the Monte Carlo simulations are partially introduced for defining the physical characteristics of the photon beams and treatment head of linear accelerators (Sievinen et al. 2007).

4.2 Section B: Electron Beam Treatment Planning

4.2.1 Introduction

The purpose of this section is to discuss the treatment planning with electron beams. High-energy electron beams are considered crucial treatment modalities in radiotherapy. Electron therapy may be used for the treatment of superficial tumors (<5 cm deep), such as cancers of the skin and lips, chest wall boost in the breast treatment, and boost to various nodes in the body (Khan 2010; Podgorsak and IAEA 2005; Halperin et al. 2008b). It is preferred over orthovoltage therapy in cases where there are overlying cartilage or bone to the PTV that result in an increased photo absorption due to photoelectric effect. Megavoltage photon beams may also be used for the treatment of superficial tumors, provided a bolus of suitable thickness is applied to eliminate the skin-sparing effect. However, these photons have a higher penetration power and unnecessarily irradiate underlying normal tissue. On the other hand, there is a sharp dose fall off beyond the 90% isodose line for lower electron energies ($\leq$12 MeV). The rate of energy loss is ~2 MeV/cm in water and soft tissue for high-energy electrons (Podgorsak and IAEA 2005). The electron energy must be chosen so that the PTV is entirely encompassed by the 90% isodose line. Bolus may also be applied if necessary.

Modern megavoltage energy linear accelerators are typically equipped with a number of electron energies (4–22 MeV). Higher-energy electron beams (>12 MeV) may be used for the treatment of cervical lymph nodes and parotid tumors and in certain cases mixed with photon beams (Khan 2010; Halperin et al. 2008b).

4.2.2 Dosimetric Data for Clinical Electron Beams

4.2.2.1 Depth Dose Profiles

Percent depth doses for electron beams are measured in a water phantom similar to those for photon beams. There are, however, fewer standard square fields (cones or applicators), designed for electron beam delivery. Electron depth dose curves vary with varying field size, beam energy, and SSD.

Figure 4.37 shows a typical electron depth dose distribution in water. A number of important parameters associated with the electron PDD are presented and explained below:

D_{surf} – Surface dose
R_{90} – Depth of 90% dose beyond d_m
R_{50} – Depth of 50% dose
R_p – Practical range; the depth to the point where tangent to the descending linear portion of PDD intersects the extrapolated x-ray contamination, as shown in Fig. 4.37
$D_{x\text{-}ray}$ – Bremsstrahlung x-ray contamination beyond practical range

4.2.2.2 Variation with Beam Energy

As expected, the percent depth dose increases with increase in electron energy for a given field size (Fig. 4.38). A unique behavior shown by these percent depth doses is that the surface dose increases with increasing electrons energy. This phenomenon may be explained by understanding the electron scattering properties. Electrons at lower energies scatter through larger angles, and their scattering probability

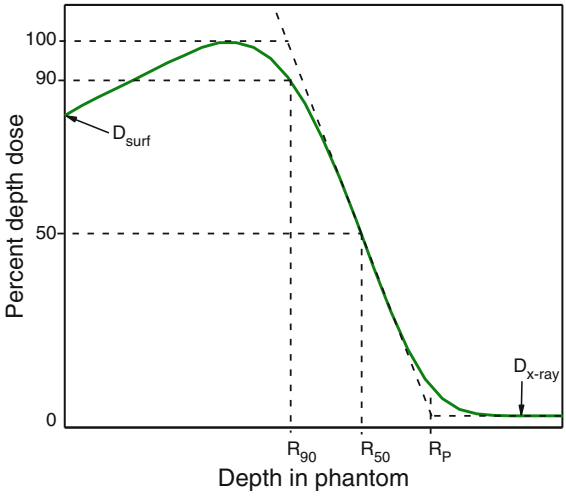

Fig. 4.37 Typical electron beam depth dose curve demonstrating the concepts of R_{90}, R_{50}, R_p, D_{surf}, and $D_{x\text{-}ray}$

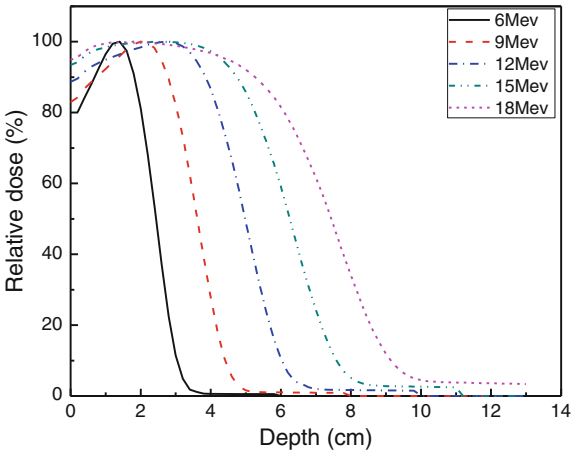

Fig. 4.38 Depth dose variation with increasing beam quality

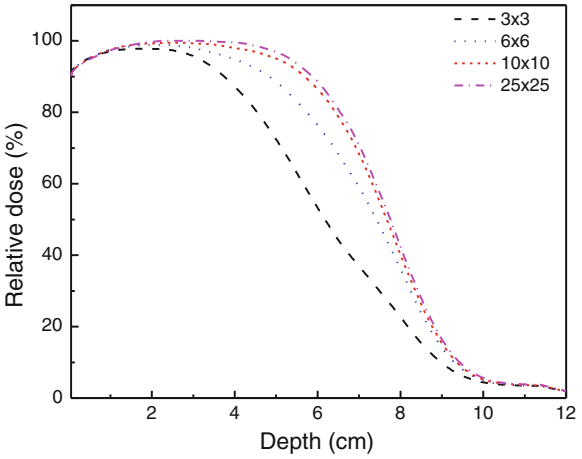

Fig. 4.39 Applicator/cone size dependence on % depth dose distribution for 18 MeV an electron beam

is also higher. This results in a higher electron fluence at a shorter distance relative to the fluence on the surface. Therefore, the ratio of these fluences is less for the low-energy electrons compared to the high-energy electrons (Khan 2010).

4.2.2.3 Variation with Field Size

Percent depth dose increases with field size, due to increased scatter from the collimator and the phantom (Fig. 4.39). Most of the electron beams are shaped by various applicator (cone) sizes and inserts (cutouts), provided a recommended fixed jaw opening. With the fixed jaw settings, variation in cone scatter is minimum and beam output is almost constant. The use of the applicators is essential for producing a uniform fluence at the patient surface.

The change in the shape of PDD is prominent for smaller fields than for larger field. Loss of the side-scatter equilibrium is the major reason for this behavior. It has been demonstrated that for the establishment of lateral scatter equilibrium, the minimum field diameter (D_{eq}) on the central beam axis may be approximated by the following relationship (Khan and Higgins 2001):

$$D_{eq} = 1.76\sqrt{E_{p,o}}\,\text{cm} \tag{4.35}$$

where $E_{p,o}$ (MeV) is the most probable energy, related to R_p by Eq. (4.36).

It is to be noted that the field-size dependence on PDD is more dominant for higher electron energies.

4.2.2.4 Off-Axis Dose Profile

Dose distributions in the direction normal to the central axis can be described by off-axis profiles. These dose profiles are measured in a water phantom and may also be used to describe the beam flatness and symmetry.

The specification for electron beam flatness and symmetry as per the IEC recommendations are as follows. The electron beam flatness is considered to be acceptable if the 90% isodose level is within 1.0 cm of the geometrical beam edge and 2 cm along the diagonals as shown in Fig. 4.40. The dark black line represents the geometrical beam edge. Furthermore, point dose in the plane bounded by the 90% isodose line should not exceed the central axis absorbed dose by more than 5%. For acceptable beam symmetry, any pair of the symmetric points of the beam profile on either side of the central axis should not differ by more than 3%. These definitions are valid at d_m only (Podgorsak and IAEA 2005).

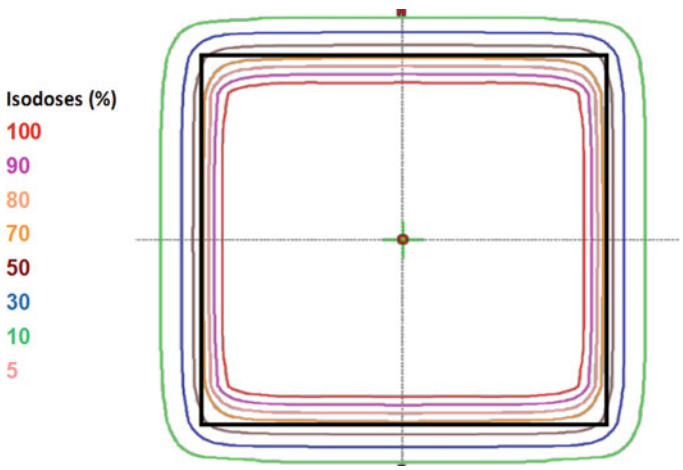

Fig. 4.40 Planar isodose distribution normal to the electron beam central axis, demonstrating beam penumbra, symmetry, and flatness

Table 4.6 Characteristics of the electron beams produced by Varian's accelerator (DHX), with a 15 × 15 cm^2 Applicator

Nominal electron energy (MeV)	R_{100} (mm)	R_{90} (mm)	R_{50} (mm)	R_p (mm)	E_{po} (MeV)	E_o (MeV)	$D_{x\text{-ray}}$ (%)
6	14	18.5	24.7	30.9	6.49	5.88	0.1
9	20	28.2	36.5	44.9	9.22	8.60	0.4
12	28	38.9	50.2	60.8	12.31	11.82	0.9
15	30	47.8	62.9	76.2	15.33	14.86	1.5
18	18	53.8	74.8	91.1	18.38	17.84	1.9

4.2.2.5 Electron Beam Energy Specification

A number of different parameters are used to describe the electron beam energy. The energy of electron beam on the phantom surface is expressed by the most probable energy $E_{p,o}$ and the mean energy $\bar{E}_0$. The most probable energy ($E_{p,o}$) is the energy carried by most of the electrons and may be estimated by the following relation:

$$E_{p,o}(\text{MeV}) = 0.022 + 0.198R_p + 0.00011R_p^2 \tag{4.36}$$

where R_p is in mm and $E_{p,o}$ in MeV.

The mean energy ($\bar{E}_0$) at the phantom surface may be calculated as follows (Podgorsak and IAEA 2005):

$$\bar{E}_0 = 2.33R_{50} \tag{4.37}$$

A detailed description of the electron beam characteristics is presented in Table 4.6.

4.2.2.6 Isodose Curves

The isodose curves measured for the electron beams are much different than those for the photons (Fig. 4.41). The dose distribution expands with depth in the medium due to side scattering of the electrons. The spread of the individual isodose curve varies as a function of the isodose level, beam quality, and field shape. To some extent, all the isodose curves bulge out for low-energy electrons, as a result of the increased side scattering. However, only low-level isodoses expand laterally in case of high-energy electron beams. The higher-value isodoses (>80%) narrow down for high-energy beams. The effective width of these curves is considerably smaller than the field size, and further decreases with depth. This is referred to as "tapering or constriction" of the high-value isodose curves. Keeping in view all these, it is extremely important to choose beam energy and field size such that the tumor is completely encompassed by the 90% isodose level. Depending on the situation, the clinician may accept tumor coverage at lower isodoses. Figure 4.41a, and b shows the isodose curves for 6 MeV and 18 MeV electron beams, respectively.

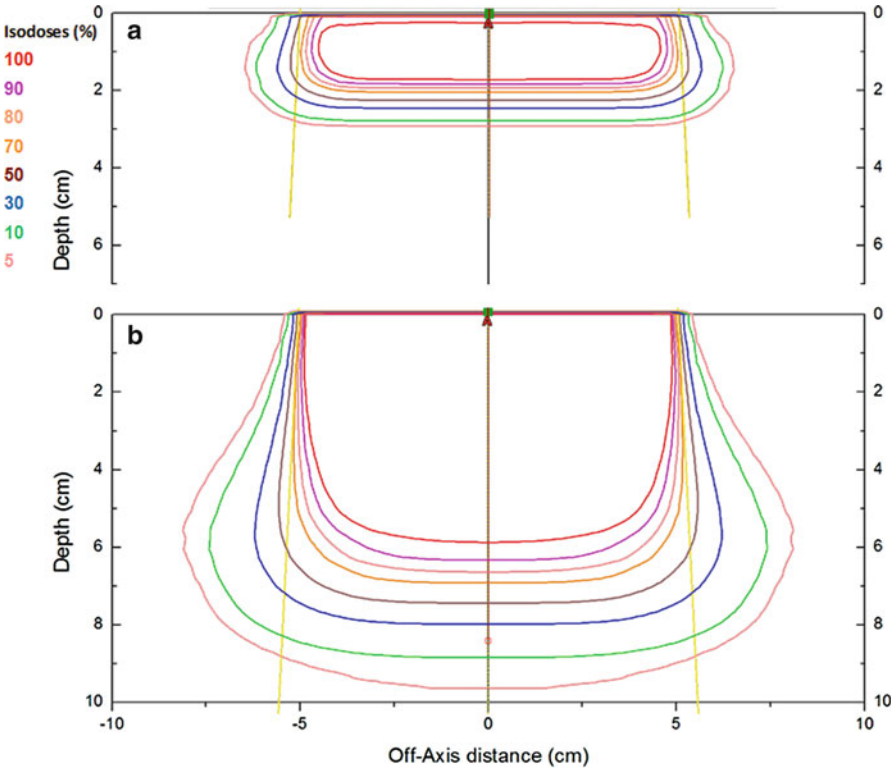

Fig. 4.41 Isodose distribution of electron beams with, (**a**) 6 MeV and (**b**) 18 MeV

4.2.3 Treatment Planning

Surface lesions extending to a depth of up to 5 cm may be easily treated with a single direct electron beam. The following practical considerations should be noted when preparing a treatment plan.

4.2.3.1 Treatment Setup

The majority of electron beam treatments are carried out with a single field and fixed SSD. A nominal treatment SSD of 100 cm is typically used. If required, however, extended SSDs may also be used. During lateral neck boost, an SSD of 115 cm is commonly used to avoid hitting of the patient shoulders by applicator.

4.2.3.2 Beam Energy and Field Size

Based on the above discussion on the electron isodose distribution, the beam energy and field size should be appropriately selected to provide adequate coverage of the lesion within the 80–90% isodose.

4.2.3.3 Field Shaping

Electron applicators (cones) as shown in Fig. 4.42a are typically used for field shaping and collimation. When required additional shielding cutouts may also be used.

The photon beam collimation system (movable jaws) alone cannot be used for electron beam shaping because of multiple scatterings in the space between the electron exit window and the patient. Electron dose uniformity in this case will be unacceptable for the treatment purposes. Electron beam applicators or cones are attached to the treatment unit head. The distal edge of the applicator is 95 cm away from the source, providing a 5 cm clearance from the patient surface.

Modern linear accelerators are equipped with various applicators, typically in square field sizes (5×5 cm^2 to 25×25 cm^2). For irregular field shapes, lead or Cerrobend cutouts (Fig. 4.42b) may be placed in the distal end of the applicator. Customized field shapes may be determined from conventional or virtual simulation, but are most often marked clinically by the physician. For electron beams in therapeutic range (6–20 MeV), a thickness of ~0.5 mm lead per MeV or 0.6 mm Cerrobend per MeV is sufficient for shielding purposes. A 1-cm-thick lead shield can attenuate $\geq$95% of the electrons in this energy range. Figure 4.42b shows an external shield to be used with a specific applicator.

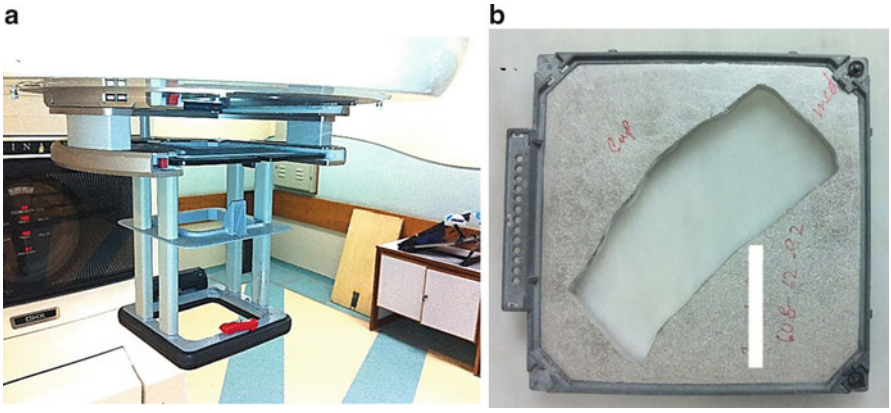

Fig. 4.42 (**a**) Electron applicator/cone (Courtesy: Varian Medical Systems, Palo Alto, CA), (**b**) Cerrobend cutout

Fig. 4.43 Internal eye shields made of silver (*left*) and Tungsten (*right*) (Courtesy: RPD©, Inc., Albertville, MN)

4.2.3.4 Internal Shielding

During treatment of the eyelid, lip, or buccal mucosa, where the underlying structures need to be spared from radiation, internal shields are used. Figure 4.43 shows two types of internal eye shields. Electron backscatter is a serious issue, associated with the internal shielding. An excess dose of about 30–70% magnitude may be received by the lead-tissue interface on the entrance side of the beam (Khan 2010). However, the dose drops exponentially with distance from the interface. To reduce this unnecessary dose from backscatter, internal shields are coated with a layer of wax (1 or 2 mm).

4.2.3.5 Use of Bolus

In electron therapy, bolus may be used to smooth out the sharp irregularities in the patient's surface, increase the surface dose, or decrease the effective depth of treatment. Bolus must be placed in close contact with the patient's skin to avoid air gapes.

4.2.3.6 Monitor Unit Calculation

Absolute electron dosimetry is performed using the available standard dosimetry protocols (e.g., TG-51 or TRS-398). Dose rate is usually adjusted to 1.0 cGy/MU at the depth d_m in water, for a standard field size (applicator) and given energy. Applicator factors are measured for other applicators relative to the standard one. The relative dose rates at d_m for other applicators are expressed in terms of applicator factors or cone factors. For example,

$$\text{Applicator Factor, AF}(C_a) = \frac{\text{Dose rate for } C_a}{\text{Dose rate for } C_o} \tag{4.38}$$

where C_a and C_o are the field sizes for a given applicator and reference applicator, respectively.

Additionally, if a cutout is used, the dose rate may further be changed. Cutout factors are defined relative to the applicator they are used with. The cutout factor for

a given cutout *(X)* used with a specific applicator (C_a) is given by the following relation:

$$\text{COF}(X) = \frac{\text{Dose rate with cut-out}(X)}{\text{Dose rate for } C_a} \tag{4.39}$$

For example, the cutout factor for a 3 × 5 cm^2 cutout used with a 6 × 6 cm^2 applicator may be calculated as below:

$$\text{COF}(X) = \frac{\text{Dose rate with cut-out}(3,5)}{\text{Dose rate for Applicator}(6,6)} \tag{4.40}$$

The output factor for a given applicator (C_a) and cutout *(X)* is:

$$O(C_a, X) = \text{AF}(C_a) \times \text{COF}(X) \tag{4.41}$$

For a prescribed dose PD, at nominal SSD, the number of MU can be calculated as:

$$\text{MU} = \frac{\text{PD} \times 100}{D'_o \times O(C_a, X) \times \text{PDD}} \tag{4.42}$$

where D'_o is the dose rate at the depth of maximum dose for the reference applicator.

The PDD is proved to be the insert size dependent, not the applicator size dependent (Tung et al. 1994).

Example 4.13 The chest wall of a mastectomy patient is to be treated with a single 6 MeV electron field, at 100 cm SSD, using a 4 × 5 cm^2 cutout with a 6 × 6 cm^2 applicator. A daily dose of 200 cGy per fractions is prescribed to d_m. Determine the number of MU per fraction.

Solution

Cone factor (6 × 6 cm^2) = 0.955
Cutout factor (4 × 5 cm^2) = 0.994
Dose prescription per fraction at d_m = 200 cGy

Using Eq. (4.42):

$$MU = \frac{200 \text{ cGy} \times 100}{1.000 \text{ cGy}/MU \times 0.955 \times 0.994 \times 100} = 211$$

4.2.4 Electron Beam Abutting

In certain situations electron beams may be abutted to other adjacent electron or photon fields. Examples are treating very large areas, a curved surface or conjunctions of electron, and photon beams in head and neck treatment.

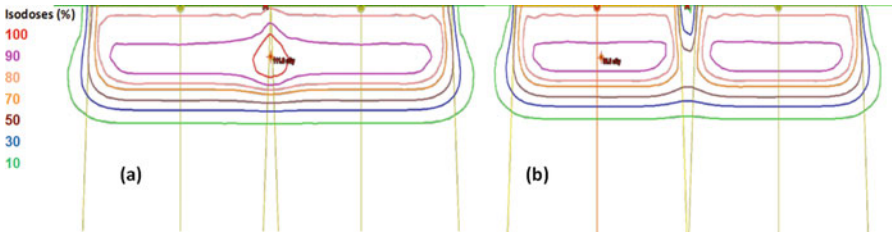

Fig. 4.44 Electron-electron (9 MeV) field junctions, (**a**) zero gap, (**b**) 1.0 cm gap

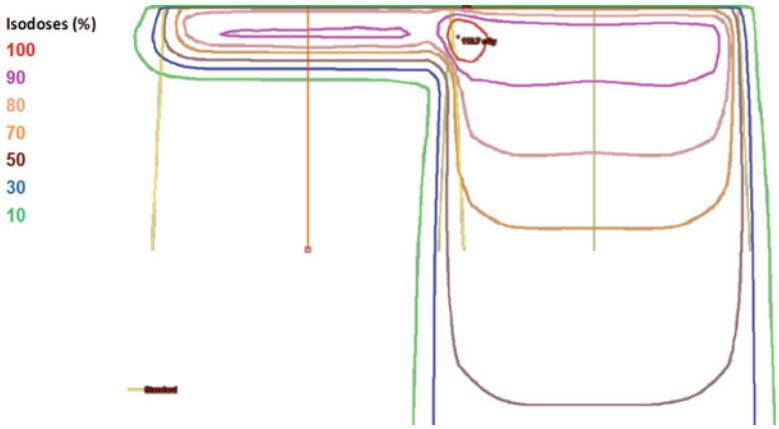

Fig. 4.45 Electron (9 MeV) and photon (6MV) beam junction with zero gap

Unlike photon fields, abutting of the electron-electron fields is very complicated and requires extreme caution. Bulging of the isodose lines result in under- or overdosage in the target volume. The dosimetric characteristics of the electron beams with depth need to be carefully assessed. Hot and cold spot sizes and their location depend on the gap between field edges (Fig. 4.44a, and b). Matching of the electron-photon fields is relatively simple because of the sharper penumbra of the photon beam. However, electron-photon field matching on the skin still produces a hot spot at a certain depth (Fig. 4.45).

4.2.5 Oblique Beam Incidence

Electron dose distribution in a medium is perturbed by surface irregularities. In cases when curved surfaces (e.g., chest wall, head and neck, and limbs) are irradiated with large electron fields, the dose distribution drastically changes due to oblique incidence. Figure 4.46a, and b demonstrates the changes in percent depth dose as a function of angle of incidence on a flat phantom. PDDs are taken along two different directions:

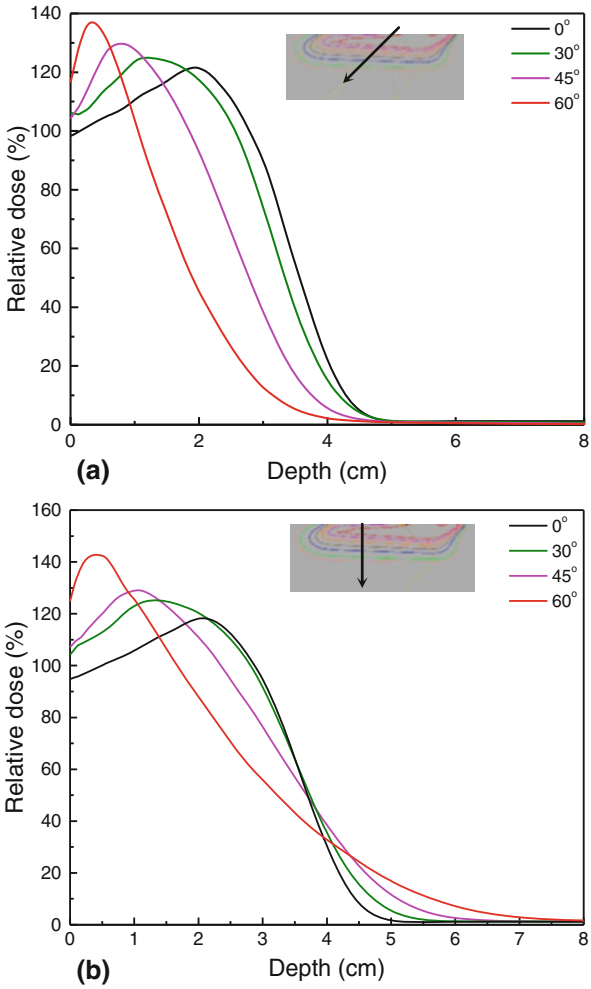

Fig. 4.46 Depth dose variation as a function of oblique incidence, (**a**) along the beam central axis, (**b**) normal to the phantom surface

- Along the beam central axis (Fig. 4.46a)
- Normal to the phantom surface (Fig. 4.46b)

It is clear that with the increasing angle of incidence (International Commission on Radiation Units and Measurements. Bethesda 2004):

- Depth of maximum dose (d_m) decreases.
- R_{90} decreases.
- Maximum dose increases.
- Surface dose increases.

In addition, there is an increase in the range of penetration along beam central axis. As a result of decrease in R_{90}, tumor coverage is compromised to a level that may be clinically significant. It is therefore recommended to avoid treatments with large angles of beam incidence.

4.2.6 Electron Treatment Planning Algorithms

Electron transport in a medium is dominated by multiple scattering and is difficult to model analytically with high accuracy, for treatment planning purposes. Such methods do not accurately predict doses for oblique incidences and tissue interfaces. Inhomogeneities are typically accounted for by scaling the depth dose curves.

Since 1981, the model-based pencil beam algorithm (PBA) is universally used for electron beam dose computation. The algorithm can account for tissue inhomogeneities, contour variation, and irregular cutouts. There are however limitations to PBA, when it comes to dose calculation at the interfaces. Currently, several, more accurate, analytical, and Monte Carlo-based dose calculation algorithms are commercially available.

Problems

1. 200 MU need to be delivered for a prescribed dose of 180 cGy to a point on the central axis. If the prescription point is changed to be 5 cm away laterally from the beam central axis where off-axis ratio (OAR) is 1.03, how many MU are required to deliver the same dose?
2. A tumor dose of 200 cGy is prescribed at a depth of 8 cm on a 15 MV linear accelerator for a field size of 15×20 cm^2. The machine is calibrated at d_m isocentrically, i.e., 100 cm SAD (1 cGy/MU). If the treatment SSD is 80 cm, calculate the number of MU.
3. The number of MU calculated for a given treatment field of 13×13 cm^2 is 204. The machine dose rate (beam output) was supposed to be 1.000 cGy/MU for a standard field size of 10×10 cm^2; however, on that morning, output was found to be 0.970 cGy/MU. If no adjustment was made to the dose rate, calculate the revised MU for the same tumor dose.
4. For a 6 MV photon beam of 12×12 cm^2 field (at isocenter), 200 cGy dose is prescribed at a depth of 7 cm in phantom, using as SAD setup.
   (a) What will be the dose at 12 cm for the same SAD and jaw settings?
   (b) If the SSD is now changed to 100 cm, what will be the dose at 12 cm for the same jaw settings?
5. An elliptical, water equivalent phantom is to be irradiated using an arc therapy technique with 20 beam angles such a point at the phanton centre receives 300 cGy dose. The long and short axis of the ellipse are 15 cm and 10 cm, respectively. Calculate the number of MU for each beam angle if the field size is 15×15 cm^2 and beam energy is 15 MV.
6. The relative out factors (ROF) for a given teletherapy machine are measured at d_m with an SAD setup. However, the chief physicist wants these factors to be determined at 5 cm depth. Devise a relation to calculate the ROF at 5 cm depth from those measured at d_m.

References

Ahnesjö A (1989) Collapsed cone convolution of radiant energy for photon dose calculation in heterogeneous media. Med Phys 16(4):577–592

Ahnesjö A, Aspradakis MM (1999) Dose calculations for external photon beams in radiotherapy. Phys Med Biol 44(1):R99–R155

Bortfeld T, Biirkelbach J, Boesecke R, Schlegel W (1990a) Methods of image reconstruction from projections applied to conformation radiotherapy. Phys Med Biol 35(10):1423–1434

Bortfeld TR, Burkelbach J, Boesecke R (1990b) Methods of image reconstruction from projections applied to conformation therapy. Phys Med Biol 35:1423–1434

Boyer AL, Ochran TG, Nyerick E, Waldron JT, Huntzinger JC (1992) Clinical dosimetry for implementation of a multileaf collimator. Med Phys 19:1255–1261

Clarkson JR (1941) A note on depth doses in fields of irregular shape. Br J Radiol 14:265

Convery DJ, Rosenbloom ME (1992) The generation of intensity-modulated fields for conformal radiotherapy by dynamic collimation. Phys Med Biol 37:1359–1374

Cunningham JR, Shrivastava PN, Wilkinson JM (1972) Program IRREG-calculation of dose from irregularly shaped radiation beams. Comput Programs Biomed 2(3):192–199

Curry TS, Dowdey JE, Murry RC (1990) Christensen's physics of diagnostic radiology. Lippincott Williams & Wilkins, Philadelphia

Drzymala RE, Mohan R, Brewster L (1991) Dose-volume histograms. Int J Radiat Oncol Biol Phys 15(21):71–78

Dyk JV (1999) Computerized radiation treatment planning systems. In: The modern technology of radiation oncology : a compendium for medical physicists and radiation oncologists. Medical Physics Publishing, Madison

Emami B, Lyman J, Brown A, Coia L, Goitein M, Munzenrider JE, Shank B, Solin LJ, Wesson M (1991) Tolerance of normal tissue to therapeutic irradiation. Int J Radiat Oncol Biol Phys 15 (21):109–122

Ferreri AJ, Dell'Oro S, Reni M, Ceresoli GL, Cozzarini C, Ponzoni M, Villa E (2000) Consolidation radiotherapy to bulky or semibulky lesions in the management of stage iii-iv diffuse large b cell lymphomas. Oncology:219–226

Fodo J, Polgar C, Nemeth G (2000) Evidence-based radiotherapy in the treatment of operable breast cancer: results. Orszagos Onkologiai Intezet 141(28):1551–1555

Fogliata A, Nicolini G, Clivio A, Vanetti E, Cozzi L (2011) Accuracy of Acuros XB and AAA dose calculation for small fields with reference to RapidArc® stereotactic treatments. MedPhys 38(11):6228–6237

Galvin JM, Smith AR, Lally B (1993) Characterization of a multileaf collimator system. Int J Radiat Oncol Biol Phys 25:181–192

Giessen PH (1973) A method of calculating the isodose shift in correcting for oblique incidence in radiotherapy. Br J Radiol 46:978

Hall EJ, Giaccia AJ (2006) Radiobiology for the radiologist, vol 6th. Lippincott Williams & Wilkins, Philadelphia

Halperin EC, Perez CA, Brady LW (2008a) Photon external-beam dosimetry and treatment planning. In: Perez and Brady's principles and practice of radiation oncology, 5th edn. Lippincott Williams & Wilkins, Philadelphia, pp 166–189

Halperin EC, Perez CA, Brady LW (2008b) Electron-beam therapy: dosimetry, planning, and techniques. In: Perez and Brady's principles and practice of radiation oncology, 5th edn. Lippincott Williams & Wilkins, Philadelphia, pp 190–217

Han T, Mikell JK, Salehpour M, Mourtada F (2011) Dosimetric comparison of Acuros XB deterministic radiation transport method with Monte Carlo and model-based convolution methods in heterogeneous media. Med Phys 38(5):2651–2664

Holmes T, Mackie TR (1994) A filtered back projection dose calculation method for inverse treatment planning. Med Phys 21:303–313

IMRT Collaborative Working Group (2001) Intensity-modulated radiotherapy: current status and issues of interest. Int J Radiat Oncol Biol Phys 51(4):880–914

International Commission on Radiation Units and Measurements (ICRU) (1993) Prescribing, recording, and reporting photon beam therapy. ICRU report 50. ICRU, Bethesda

International Commission on Radiation Units and Measurements (ICRU) (1999) Prescribing, recording, and reporting photon beam therapy (supplement to ICRU report 50). ICRU report 62. ICRU, Bethesda

International Commission on Radiation Units and Measurements. Bethesda (2004) ICRU report 71 "prescribing, recording, and reporting electron beam therapy". J ICRU 4(1):39–48

Keller-Reichenbecher MA, Bortfeld T, Levegrün S, Stein J, Preiser K, Schlegel W (1999) Intensity modulation with the "step and shoot" technique using a commercial MLC: a planning study. Int J Radiat Oncol Biol Phys 45(5):1315–1324. Multileaf collimator

Khan FM (2010) The physics of radiation therapy. Lippincott Williams & Wilkins, Philadelphia

Khan FM, Higgins PD (2001) Field equivalence for clinical electron beams. Phys Med Biol 46: N9–N14

Khan FM, Moore VC, Burns DJ (1970) The construction of compensators for cobalt teletherapy. Radiology 96:187

Knoos T, Wieslander E, Cozzi L, Brink C, Fogliata A, Albers D, Nystrm H, Lassen S (2006) Comparison of dose calculation algorithms for treatment planning in external photon beam therapy for clinical situations. Phys Med Biol 21(51):5785–5807

Kramme R, Hoffmann K, Pozos R (2011) Medical radiation therapy, Springer handbook of medical technology. Springer, New York, p 703

LoSasso T, Chui C, Ling CC (1998) Physical and dosimetric aspects of a multileaf collimation system used in the dynamic mode for implementing intensity modulated radiotherapy. Med Phys 25(10):1919–1927

Mackie TR, Scrimger JW, Battista JJ (1985) A convolution method of calculating dose for 15-MV x rays. Med Phys 12(2):188–196

Mohan R, Chui C, Lidofsky L (1986) Differential pencil beam dose computation model for photons. Med Phys 13(1):64–73

Nakaguchi Y, Araki F, Maruyama M, Fukuda S (2010) Comparison of RTPS and Monte Carlo dose distributions in heterogeneous phantoms for photon beams. Nihon Hoshasen Gijutsu Gakkai Zasshi 20(66):322–333

Podgorsak EB, IAEA (2005) Radiation oncology physics a handbook for teachers and students. International Atomic Energy Agency, Vienna

Porter A, Aref A, Chodounsky Z, Elzawawy A, Manatrakul N, Ngoma T, Orton C, Van't H, Sikora K (1999) A global strategy for radiotherapy: a WHO consultation. Clin Oncol (R Coll Radiol) 11(6):368–370

Sewchand W, Khan FM, Williamson J (1978) Variations in depth-dose data between open and wedge fields for 4-MV X-rays. Radiology 127(3):789–792

Sewchand W, Bautro N, Scott RM (1980) Basic data of tissue-equivalent compensators for 4 MV x-rays. Int J Radiat Oncol Biol Phys 6:327

Sievinen J, Ulmer W, Kaissl W (2007) Eclipse algorithms reference guide, vol P/N B500298R01C. Varian Medical Systems, Palo Alto, pp 1–18

Sofia JW (1979) Computer controlled, multileaf collimator for rotational radiation therapy. Am J Roentgeno 133(5):956–957

Sontag MR, Cunningham JR (1978) The equivalent tissue-air ratio method for making absorbed dose calculations in a heterogeneous medium. Radiology 129(3):787–794

Sterling TD, Perry H, Katz I (1964) Derivation of a mathematical expression for the percent depth dose surface of cobalt 60 beams and visualization of multiple field dose distributions. Br J Radiol 37:544–550

Tung A, Shiu SS, Nyerick CE, Ochran T, Otte VA, Boyer AL, Hogstrom KR (1994) Comprehensive analysis of electron beam central axis dose for a radiotherapy linear accelerator. Med Phys 21:559–566

Ulmer W, Harder D (1996) Applications of a triple gaussian pencil beam model for photon beam treatment planning. Z Med Phys 6:68–74

Ulmer W, Kaissl W (2003) The inverse problem of a gaussian convolution and its application to the finite size of the measurement chambers/detectors in photon and proton dosimetry. Phys Med Biol 48(6):707–727

Ulmer W, Pyyry J, Kaissl W (2005) A 3d photon superposition/convolution algorithm and its foundation on results of monte carlo calculations. Phys Med Biol 50(8):1767–1790

Vargas C, Kestin L, Weed D, Krauss D, Vicini F, Martinez A (2005) Improved biochemical outcome with adjuvant radiotherapy after radical prostatectomy for prostate cancer with poor pathologic features. Int J Radiat Oncol Biol Phys 61(3):714–724

Webb S (1989) Optimization of conformal dose distributions by simulated annealing. Phys Med Biol 34:1349–1370

Webb S (1997) The physics of conformal radiotherapy. IOP Publishing Ltd., Bristol

Chapter 5
Image-Guided Radiation Therapy

X. Sharon Qi

Contents

5.1 Introduction 131
5.2 Rationale for IGRT 132
5.3 Currently Available Image-Guided Techniques 134
5.4 Traditional IGRT Technologies 137
5.5 In-Room CT-Based IGRT Modalities 140
5.6 Real-Time Tracking Systems 148
5.7 Management of Imaging Dose 155
5.8 Image Registration and Correction Strategies 156
5.9 Clinical IGRT Workflow 159
5.10 Image Guided Adaptive Treatment (IG-ART) 160
5.11 Management of Respiratory Motion 163
5.12 Conclusion 166
References 167

5.1 Introduction

The goal of radiation therapy treatment is to deliver the therapeutic dose to target volumes while reduce the radiation exposure to the adjacent normal structures. In the past, a large three-dimensional planning margin was utilized to account for geometric and setup uncertainties, which resulted in unnecessary radiation doses to the surrounding normal tissues. Since the late 1990s, intensity-modulated radiation therapy (IMRT), which delivers highly conformal dose distributions to the target, has been widely adopted as standard treatment for treatment sites such as the head and neck, prostate, etc. (Butler et al. 1999; Manning et al. 2001; Zelefsky et al. 2000; De Meerleer et al. 2000). IMRT enables a more precise conformal radiation dose distribution to the target area without increasing radiation doses to the normal tissue. To translate the advantages of IMRT into better tumor control and reduction

X. Sharon Qi, PhD (✉)
Department of Radiation Oncology, University of California at Los Angeles, Los Angeles, CA, USA
e-mail: XQi@mednet.ucla.edu

M. Maqbool (ed.), *An Introduction to Medical Physics*, Biological and Medical Physics, Biomedical Engineering, DOI 10.1007/978-3-319-61540-0_5

of treatment-related toxicity, more accurate and reproducible patient setup is crucial (Qi et al. 2013a).

Recent developments in advanced treatment technology and medical imaging are essential for design of advanced treatment plans and to localize the target for precise administration of radiation. At planning stage, target definition is often based on CT, as well as other image modalities such as MRI and PET. At treatment stage, three-dimensional volumetric imaging can be used to localize the target and/or tumor motion. The changes in tumor position, size, and shape that take place during radiotherapy can be measured and accounted for to further improve geometric accuracy and precision of radiation delivery (Jaffray et al. 1999). By improving the accuracy of target delineation and treatment delivery through IGRT, radiation dose can be safely delivered to the target while reducing the doses to the surrounding healthy tissues resulting in better clinical outcome.

Image-guided radiation therapy (IGRT), broadly, involved any use of imaging to aid in decisions at various stages in the radiotherapy process: decision of whether and/or what to treat, delineation of range of interest in the planning process, aid in patient positioning, assessment of treatment outcome, etc. In the present context, the term IGRT signifies radiotherapy that used image-guidance procedures in two following aspects: (1) image-guided target delineation in radiation therapy and (2) image-guided treatment delivery. Target delineation refers to the use of advanced imaging modalities, including functional and/or biological images for target and normal structure delineation in RT planning. Imaged-guided treatment delivery refers to a process of frequent use of two-dimensional and/or three-dimensional imaging before, during, and/or after treatment using in-room technologies to guide radiation therapy. A wide variety of in-room IGRT modalities are available, such as matching planar kilovoltage (kV) radiographs or planar megavoltage (MV) images with digitally reconstructed radiographs (DRRs) from the planning CT and volumetric image technologies. An example of volumetric IGRT would include localization of a cone beam computed tomography (CBCT) dataset with the planning computed tomography (CT) dataset from planning. The IGRT procedures use imaging technology to identify and correct problems arising from inter- and intra-fractional variations in patient setup and anatomy, including shapes and volumes of treatment target, organ at risk, and surrounding normal tissues. IGRT is widely used for almost all treatment sites, i.e., prostate, head and neck, brain, lung, liver, etc.

5.2 Rationale for IGRT

Radiation therapy is considered as a local treatment that is designed to treat the defined targets in a specific area while sparing the surrounding normal tissue from receiving doses above specified dose tolerances. However, the doses delivered can be very different from the planned dose. There are many factors that may contribute to the dose deviations between the planned and the delivered dose distribution.

Among all, one important factor is patient setup error. Planning target volume (PTV) margins (Prescribing, Recording and Reporting Photon Beam Therapy 1999) are the most widely used method to account for geometric and/or setup uncertainties. In the past, larger PTV margins were used to compensate for setup errors. This resulted in healthy normal tissues receiving unnecessary radiation doses. With advent and increasing popularity of IMRT, highly conformal dose distribution is possible, and accurate target delineation and treatment dose delivery are of particular importance (Hong et al. 2005; Houghton et al. 2009). IGRT is expected to improve the patient-positioning precision and therefore the effectiveness of cancer treatment by targeting and/or tracking tumor more accurately.

Current IGRT routine is to image the patient prior to treatment delivery. Acquisition of pretreatment imaging on a regular basis allows us to assess more detailed treatment information, such as patient's immobilization, range of organ movement, changes in tumor size and shape, etc. The IGRT imaging process can be used as a regular quality assurance method to record the effect of changes in immobilization and other interventions (Dawson and Sharpe 2006). With daily IGRT imaging, interventions to reduce errors and/or generate a new adaptive plan might be implemented sooner, leading to an overall improvement in quality of treatment.

Secondly, current advanced radiotherapy planning, including three-dimensional conformal radiotherapy (3DCRT) and IMRT, produces plans in which high-dose radiation conforms tightly around the target, with reduced doses to healthy tissues, allowing possible dose escalation to the tumor. Such advanced planning has called for highly accurate dose delivery.

Thirdly, IMRT is associated with a steep dose falloff outside the target, calling for stringent requirements for control of geometric uncertainties (such as setup error and organ motion) and a need for enhanced target delineation at planning and target localization before treatment delivery. Geometric uncertainties and day-to-day variability in tumor position emphasize the need for image guidance in conjunction with IMRT.

In addition, the importance of IGRT has increased tremendously with growing interests of stereotactic body radiotherapy (SBRT). SBRT (Lo et al. 2010) is a novel technique and attracts growing interests for many treatment sites, such as the lung, liver, prostate, et al. (Lo et al. 2010; Fakiris et al. 2009; King et al. 2013). SBRT delivers high doses to (relatively) small targets in fewer numbers of fractions (five or fewer), which requires a high degree of confidence in tumor localization provided by high-quality imaging for accurate treatment delivery. Imaging at the time of treatment is needed to ensure that radiotherapy is delivered as intended as the number of fractions reduces.

Technological developments allow radiation delivery to be gated to a specific phase of respiration or to track targets that move because of breathing, thus reducing the volume of healthy tissues that are irradiated. With these strategies to decrease organ motion, frequent imaging of the tumor during radiation delivery is needed to ensure that the intended target volume is treated.

Volumetric and temporal imaging during radiotherapy also provides an opportunity to adapt the changes in the tumor or healthy tissues that arise during a course

of treatment, which otherwise were not apparent without IGRT. Such interventions can potentially lead to further clinical gains. Tumor sites at which such benefits are most likely include those that tend to recur locally rather than distantly, cancers in which increased dose has been associated with enhanced tumor control, lesions adjacent to dose-limiting healthy tissues, and cancers that change in position from day to day.

5.3 Currently Available Image-Guided Techniques

With the advent of fractionated radiation therapy, the patient-positioning reproducibility and uncertainty became a concern. The importance of accurate radiation delivery has been discussed theoretically and demonstrated clinically. The consequences of missing the target are a reduction in tumor control probability and an increase in normal tissue complication probability.

Many technologies have been developed and employed to help ensure the accurate placement of a treatment field (Verellen et al. 2008; Killoran et al. 1997; Marks et al. 1974; Hunt et al. 1995; Herman et al. 2000; Kutcher et al. 1994; Goitein et al. 1975), such as megavoltage (MV)- and/or kilovoltage (kV)-based radiographic 2D planar and volumetric IGRT approaches, non-radiographic approaches, etc. Many solutions have multiple features and continuously evolve into new applications.

5.3.1 2D Planar IGRT Approaches

Portal imaging using film was the standard for patient localization in the 1980s (Kutcher et al. 1994). X-rays or gamma rays were used to develop large-format radiographic films for inspection. The disadvantages of using film imaging are time-consuming, labor intensive, and reimbursed for only one port film verification per week (Herman et al. 2000). The electronic portal imaging device (EPID) gradually replaces the portal imaging using films in the 1990s and became the most widespread planar IGRT technology. The EPID provides a more efficient and effective method for determining radiation field placement accuracy. Various technologies used in EPID have been detailed in literatures (Goitein et al. 1975; Falco et al. 1998). Early array systems used diodes, scintillators, or liquid-based ion chambers. Early fluoroscopic systems were the precursors of the screen-mirror systems used today. Present commercial systems are replaced by flat-panel detector arrays (Falco et al. 1998; Munro 1995; Antonuk et al. 1998), which offer better resolution and faster response.

5.3.2 Volumetric IGRT Approaches

Various volumetric IGRT technologies became clinically available in the early 2000s (Verellen et al. 2008). The first way to visualize 3D anatomy soft tissue prior to treatment and to define the spatial relationship between target and organs at risk is diagnostic CT scanner inside the treatment room. Both the EPID and an orthogonally mounted X-ray imaging device can be used to acquire cone beam volumetric CT data (CBCT). Non-radiographic localization tools are also available, such as ultrasound (US). US devices have been introduced based on the advantage of not requiring a surrogate to visualize the target. On the other hand, these devices can only be used prior to treatment (not during beam on), and it has been argued that this solution is susceptible to interobserver variations and possible introduction of displacement due to pressure of the imaging probe on the patient's lower abdomen. The latest development of adopting introduces MRI in IGRT as it offers superior soft-tissue contrast compared to kV- or MV-based imaging, such as ViewRay system.

5.3.3 Image-Guided Target Delineation

Accurate target definition is vitally important in RT. To be able to "see" the extent of disease more clearly and better define the tumor target volume have been among the most important issues in radiation oncology. Computerized tomography is the most dominant imaging modality and cornerstone in treatment planning, such as (a) the delineation of target and normal structures and (b) quantitative data for tissue heterogeneity (Kijewski and Bjarngard 1978; Chernak et al. 1975). A CT simulation is normally acquired with proper patient immobilization device for patient in the treatment position, referred as the planning CT.

Nowadays, treatment planning relies heavily on the information obtained from CT scan, including high spatial integrity, high spatial resolution, excellent bony structure depiction, and the ability to provide relative electron density information used for radiation dose calculation. The recent development of ultra-fast multi-slice CT has opened a new dimension to CT technology and allows time-resolved (4D) CT imaging of patient's cardiac and breathing cycles. Using array detectors, multi-slice CT scanners can acquire multiple slices simultaneously and thereby greatly increase the speed of CT image acquisition. Currently, all manufactures are providing higher slice CT technology such as 16- and 64-slice CT scanner. The application of 4DCT will be discussed later in this chapter.

In addition to CT, other imaging modalities such as magnetic resonance imaging (MRI), position emission tomography (PET), and/or single-photon emission computed tomography (SPECT) can be acquired and registered with the CT scan to provide additional patient-specific anatomical/functional information that cannot be easily seen from CT image.

MRI is an imaging modality that uses non-ionizing radiation to generate diagnostic and/or treatment images. It uses a powerful magnetic field, radiofrequency

waves, and a computer to create detailed cross-sectional (two-dimensional) and three-dimensional images of the human body. MRI has a wide range of applications in medical diagnosis and treatment planning in many specialties (Magnetic Resonance, a critical peer-reviewed introduction 2013; Hollingworth et al. 2000). MRI and CT are complementary imaging technologies, and each has advantages and limitations for particular applications. The advantages of MRI include:

1. The ability to image without the use of ionizing radiation.
2. The superior soft-tissue contrast than CT scans, especially for the central nervous system (CNS), abdomen and pelvis, etc.
3. The advanced techniques such as diffusion and perfusion MRI, dynamic contrast MRI, MR angiography, MR spectroscopic imaging (MRSI), and functional MRI (fMRI) allow for specific tissue characterization.
4. Functional MRI allows visualization of both active parts of the brain during certain activities, understanding of the underlying networks, etc. It was reported that up to 80% of CNS tumors received improvement in terms of the target volume definition imaged with MRI into the planning process of CNS tumor (http://radiopaedia.org/articles/mri-introduction).

MRI has been widely used in the diagnosis and treatment for tumor delineation purpose. In a clinical setting at radiation oncology, MRI is typically employed together with CT images with the help of image fusion software to delineate the extent of the malignancy. The use of CT and MRI is becoming routine for treatment planning in CNS tumors, etc. Figure 5.1 shows the transverse view of (a) a CT image, (b) a T1-weighted MRI, and (c) a fluid-attenuated inversion recovery (FLAIR) image for a brain tumor.

One of the major issues with MR images in RT is image distortion. MRI technology is moving toward higher field strengths to further improve the MR image quality and the development of some specialized MRI scans (Mundt and Roeske 2006). Diffusion tensor imaging (DTI) (Merboldt et al. 1969; Taylor and

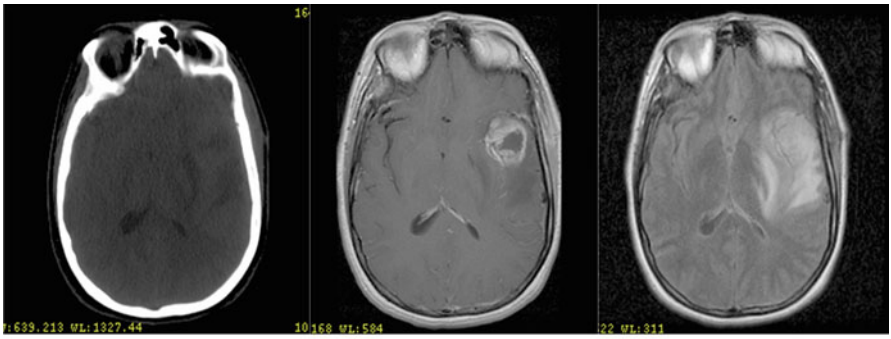

Fig. 5.1 Images of a representative case taken by (**a**) CT, (**b**) T1-weighted MRI, (**c**) FLAIR (Pictures from https://www.aapm.org/meetings/06ss/documents/2006summerschoolIGRTintro_000.pdf)

Bushell 1985), for instance, enables diffusion to be measured in multiple directions and the fractional anisotropy in each direction to be calculated for each voxel. Functional MRI (fMRI) measures signal changes in the brain that are due to changing neural activity. These techniques may allow better definition of brain tumors and better sparing of sensitive regions. Figure 5.1 compares different imaging techniques used in diagnostic and therapeutic applications.

Another imaging approach – positron emission tomography (PET) – has been introduced and now routinely used for RT planning for many disease sites, such as head-and-neck cancer, lung cancer, etc. PET (Bailey et al. 2005) is a functional imaging technique utilizing nuclear medicine to produce a three-dimensional image of functional processes in the body. The system detects pairs of gamma rays emitted indirectly by a positron-emitting radionuclide (tracer), which is introduced into the body on a biologically active molecule. Three-dimensional images of tracer concentration within the body are then constructed by computer analysis. Modern PET scanners are often integrated with CT scanners (so-called PET/CT), which allow PET and CT scans to be performed in immediate sequence during the same session with no need of patient repositioning. This is particularly important for the RT planning purposes (Schwartz et al. 2005; Spratt et al. 2010) so that the PET and CT images can be precisely registered to help delineation and the areas of abnormality on the PET imaging can be more perfectly correlated with anatomy on the CT images.

5.3.4 Image-Guided Treatment Delivery

As the planning target volumes (PTVs) are made increasingly conformal for IMRT, compared with the conventional three-dimensional conformal radiotherapy (3DCRT), the requirements of accurate target delineation and patient setup and its dosimetric coverage during each treatment become increasingly stringent. IGRT makes use of many different imaging techniques ranging from portal imaging, fluoroscopy, ultrasound, to in-room computed tomography systems, etc. In the current context, we classified the available IGRT technologies into three main categories: (A) traditional IGRT technologies, (B) in-room CT-based IGRT technologies, and (C) real-time tracking systems.

5.4 Traditional IGRT Technologies

5.4.1 Portal Imaging

Portal imaging is the acquisition of images with a radiotherapy beam. Traditionally, radiographic films (port films) were placed beyond the patient to produce an image. This method was time-consuming in terms of development and evaluation of the films and was limited to a setup accuracy of about 5 mm (Barry et al. 2012).

The modern era of electronic portal imaging began in the early 1980s (Herman et al., n.d.), and different EPID designs are available using the screen and/or camera imagers, liquid ionization chambers, and solid-state flat-panel detectors (Murphy et al., n.d.). Electronic portal imaging devices (EPIDs), mounted on a Linac using robotic arms, allow for online treatment verification and automatic analysis.

The flat-panel imager is emerging as the new standard detector for portal imaging in IGRT (Herman et al., n.d.). Modern accelerators, such as Varian TrueBeam and Trilogy and Elekta Synergy, are equipped with two kinds of portal imaging systems: (a) kilovoltage X-ray imager in which a conventional X-ray tube is mounted on the gantry with an opposing flat-panel image detector and (b) megavoltage (MV) electronic portal imaging device (EPID) with its own flat-panel image detector. The flat-panel image detector generally is a matrix of 256×256 solid-state detectors consisting of amorphous silicon (a-Si) photodiodes. The kilovoltage (kV) images generally have better contrast than the MV EPID images; both are of sufficiently good quality to visualize soft-tissue targets compared to the kV planning CT. However, the portal images are quite useful in determining the planning target volume in relation to the bony anatomy or implanted fiducials in the target area. Both the kV and MV imager can be used to check patient setup before each treatment as well as online monitoring of target positioning. For kV imager, it can also be used in both the radiographic and fluoroscopy modes to check patient setup before each treatment or to track the movement of fiducial markers due to respiratory motion.

In the past, the most conservative portal is weekly acquisition of images, which is appropriate for treatment plans that are not highly conformal (such as three-dimensional conformal radiotherapy). More precise targeting for the advanced treatment delivery techniques, such as intensity-modulated radiotherapy (IMRT), requests taking portal images daily to assess tumor position variability and systematic setup error, followed by weekly imaging after correction for systematic offsets.

The disadvantages of portal imaging techniques are that (1) the actual treatment target is not clearly defined and the verification is not performed in real time. Therefore, treatment margins are added to the target volumes to accommodate the uncertainty of patient setups and inter- and intra-fractional organ motion; (2) the doses needed for portal imaging is important and varies by application and EPID devices. Improper dose control could result in a useless image and/or extra dose required for obtaining subsequent images; and (3) 3D definition of anatomy information is not available through portal imaging (Fig. 5.2).

5.4.2 Fluoroscopic Imaging

Fluoroscopy is an imaging technique that uses X-rays to obtain real-time moving images of the interior of an object. Conventional fluoroscopic imaging is done at tube voltages between 60 kV and 120 kV. Typical tube currents limited to approximately 100 mA. The tube spectrum is typically filtered by 2–4 mm Al or its

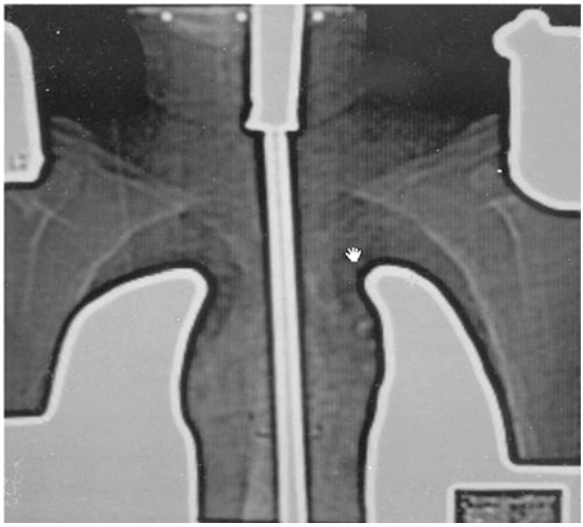

Fig. 5.2 Example of a portal image (Courtesy of Varian Associates, Palo Alto, CA)

equivalent (Leong 1986; Munro et al. 1990; Baily et al. 1980; Antonuk et al. 1996). Fluoroscopy is generally used in (1) pretreatment motion assessment, (2) setup of gating and tracking parameters, and (3) intra-fraction respiratory tracking and compensation. Traditional fluoroscopic system allows the observer to look directly at the phosphor screen to assess tumor motion. The phosphor screen is replaced by digital flat-panel in current design for fluoroscopy-based tracking system. Some of these systems are mounted on the accelerator gantry, while others are installed in the room such as Hokkaido university fluoroscopic system (Chaiken and Lisa 2005). One limitation of fluoroscopy-based tracking systems is the potential for excessive radiation exposure.

5.4.3 Ultrasound

Ultrasound is a noninvasive, non-radiographic real-time imaging technique for localizing soft-tissue structures and tumors, primary in the abdomen, pelvis, and breast. Ultrasound utilizes high-frequency (1 ~ 10 MHz) sound waves to generate anatomical images that have high spatial resolution and tissue characterization discrimination power through image texture analysis. Attached to the BAT system, there is an ultrasound probe mounted on a robotic arm to track the probe's position in space. Ultrasound is the imaging modality widely used in guiding the prostate seed implant procedure; it has been particularly useful to localize the prostate gland in external beam irradiation for prostate. A commonly used ultrasound system is NOMOS B-mode Acquisition and Targeting (BAT) system (NOMOS Corp., Sewickley, PA). Figure 5.3 (a) shows a BAT SXi Ultrasound unit from MONOS

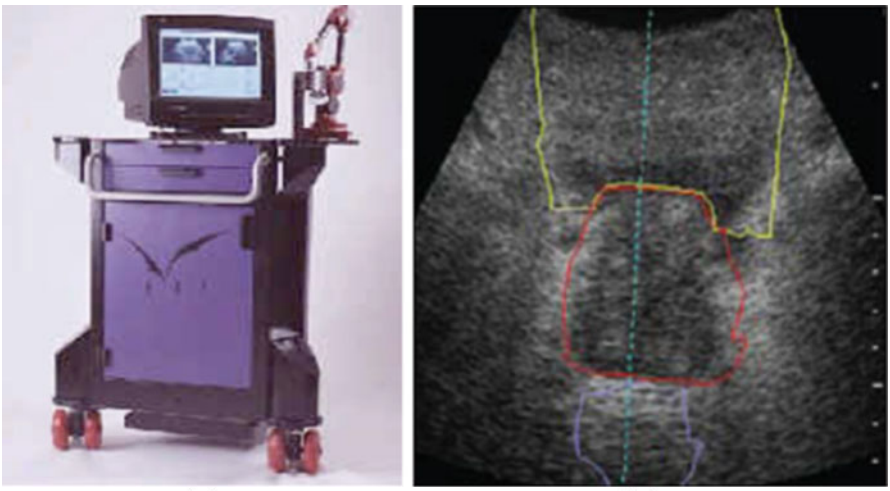

Fig. 5.3 (**a**) A BAT SXi Ultrasound unit from MONOS; (**b**) An Axial ultrasound image with contours overlaid (http://www.nomos.com/pdf/batcam_bro_03.pdf)

and (b) shows an axial ultrasound image with contours overlaid. BAT provides quick ways of localizing prostate before each treatment and making corrections for inter-fraction variations of prostate position (Chaiken and Lisa 2005; BATCAM, n.d.; B-mode Acquisition and Targeting (BAT), n.d.). The pretreatment ultrasound images are fused to the planning CT scans, so the current location of the target volume can be determined in reference to the treatment plan. The patient's position can then be adjusted accordingly so that the target volume is placed precisely and accurately.

The challenges of using ultrasound-guided procedures for localizing prostate are (1) the poor image quality; (2) an unfamiliar appearance of ultrasound images (for many observers), resulting in larger inter- and intra-observer variability (large planning margins have been recommended for ultrasound-guided radiotherapy); and (3) the potential anatomic distortions caused by the transducer pressure on the abdomen for ultrasound-guided prostate therapy. Too much of this pressure could induce a larger shift in the prostate in AP direction of as much as 10 mm (Langen et al. 2003; Peng et al. 2008; Artignan et al. 2004).

5.5 In-Room CT-Based IGRT Modalities

A wide variety of in-room IGRT technologies are available. These in-room CT-based systems provide volumetric anatomic information that is useful for accurate target localization, but also for dose computation that can be used to track the delivered dose distribution. Frequent comparisons of the delivered dose

to the planned dose distribution enable one to make setup corrections or adjust the treatment plan to minimize the variations between the planned and the actual delivered dose, which is the image-guided adaptive radiation therapy (IG-ART).

The advantages of the use of in-room CT-based IGRT technologies include**:**

- 3D definition of anatomy (volumetric imaging) in treatment room.
- Daily CT image can be used for dose calculation (planning or treatment evaluation).
- CT is a mature technology (with minor modifications for radiation therapy applications)
- CT images are widely accepted and familiar by radiation oncologists to determine target volumes and critical organs.
- No direct contact with patient.

5.5.1 CT-on-Rail

A CT-on-rail system integrates a diagnostic CT scanner with a treatment accelerator in RT treatment room. The CT scanner slides on rails in the floor so that the patient does not have to move between the pretreatment scan and treatment. Figure 5.4 shows a Siemens CT-on-rails system at the Department of Radiation Oncology, Medical College of Wisconsin, WI. The Linac and the CT scanner are positioned to the opposite end of the couch. The first integrated clinical system

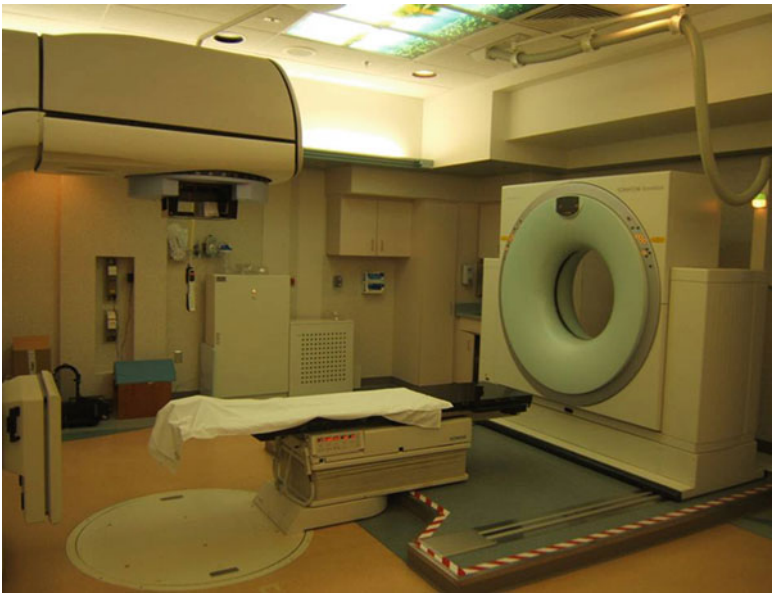

Fig. 5.4 (**a**) A Siemens CT-on-rails system at the Medical College of Wisconsin (Courtesy of Medical College of Wisconisn, Milwaukee, WI)

combining a Linac and an in-treatment-room CT unit was developed by Uematsu et al. in Japan (Uematsu et al. 1996; Kuriyama et al. 2003). The first Siemens CT-on-rails system (PRIMATOM™ Siemens Medical Solutions, Concord, CA) was installed in 2000 at the Morristown Memorial Hospital, Morristown, NJ. The system was equipped with a SOMATOM scanner, which is a single-slice scanner with minimum slice thickness of 1 mm and scan time of 1 s (or less) per rotation. The diameter of the CT gantry is 70 cm, and the FOV is 50 cm in diameter. The speed of the gantry along the rails can vary between 1 mm and 100 mm per second, and the gantry position accuracy is 0.5 mm (Peng et al. 2008). The initial clinical experience with this system was reported by (Ma and Paskalev 2006; Wong et al. 2001; Cheng et al. 2003; Thieke et al. 2006).

The CT-on-rails system allows the quantification and correction of inter-fractional variations between planning and each treatment delivery. To ensure accurate patient positioning, a CT scan is performed immediately before each treatment delivery. After proper patient setup on the couch using in-room lasers, the treatment couch is rotated 180° so that the Linac and the CT gantry are positioned. The pretreatment scan was then registered to the reference image set (the initial planning CT simulation) to verify patient positioning or to determine whether repositioning was required. Due to its diagnostic image quality, the CT-on-rails images were also used to study the anatomical variation during the course treatment.

5.5.2 Kilovoltage Cone Beam CT (kVCBCT)

The on-board kV imaging system provided a choice of imaging modalities of 2D radiographic, fluoroscopic, and 3D cone beam computed tomography (CBCT) imaging. kVCBCT (30–140 kV) imaging systems are commercially available: Varian On-Board Imaging (OBI) (Varian Medical Systems, Palo Alto, CA) and the Elekta XVI Synergy systems (Elekta, Stockholm, Sweden). Figure 5.5 shows pictures of Varian TrueBeam (a) and Elekta Synergy (b), both of which are equipped with kVCBCT systems. Compared to EPIDs, the use of kilovoltage CBCT shows a superior high-contrast resolution (due to the dominance of the photoelectric effect at kV energies) and lower imaging dose to the patients.

The kVCBCT involves acquiring planar projection images from multiple directions as the gantry is rotated through 180° or more. The kV X-ray tube (mounted on a retractable arm) and a kV detector are attached at 90° offset with respect to the central axis of the linear accelerator beam. Images are generated by the flat-panel detectors mounted opposite to the X-ray tube. Three-dimensional volumetric images are reconstructed from these multiple radiographs by the computer using a filtered back-projection algorithm (Feldkamp et al. 1984). The reconstructed CBCT images are fused to the planning CT using automatic or manual registration method to figure out the patient setup error in axial, sagittal, and coronal views; the setup errors will be then adjusted before treatment delivery.

Fig. 5.5 (**a**) Varian TrueBeam accelerator (Varian Oncology Systems, Palo Alto, CA). (**b**) Elekta Synergy (Elekta Inc.). Both accelerators are equipped with kilovoltage imaging systems capable of 2D planar radiography, fluoroscope, and cone beam CT modes

Compared to conventional kVCT images, kVCBCT images have increased artifacts and reduced contrast due to photon scatter (Srinivasan et al. 2014; Yang et al. 2007). However, kVCBCT imaging has shown great soft-tissue contrast and spatial resolution for soft-tissue-based setup, but the image quality can be affected by the acquisition parameters. Figure 5.6 shows a fusion of a planning CT and a kVCBCT of a prostate patient image on Elekta X-ray volume imaging (XVI) system.

5.5.3 Megavoltage Cone Beam CT (MVCBCT)

Another commercially available CBCT imaging system is the Siemens MVision system (Siemens Medical Solutions, Malvern, PA) (Pouliot et al. 2005; Morin et al. 2005). MVCBCT is made using the traditional EPID with the amorphous silicon (a-Si) flat-panel detectors (optimized for MV X-ray). The X-ray source is the megavoltage therapy beam of the accelerator (i.e., 6 MV). Planar projection images are acquired from multiple directions as the X-ray source and the detector rotate around the patient. Figure 5.7 shows a Siemens Primus accelerator equipped with megavoltage cone beam CT (MVCBCT) capability at the department of radiation oncology at UCLA.

To acquire MVCBCT images, the users need to create CBCT imaging protocols by specifying the following parameters: (1) the total dose for a CBCT acquisition (2–60 monitor units [MU]), (2) the reconstruction size (128, 256, or 512), (3) the reconstruction slice interval (1, 2, or 3 mm), (4) source to image distances (SID), etc. By default, the Linac gantry rotates in a continuous 200° arc (270°–110°, clockwise), acquiring one portal image for each angle. This acquisition procedure

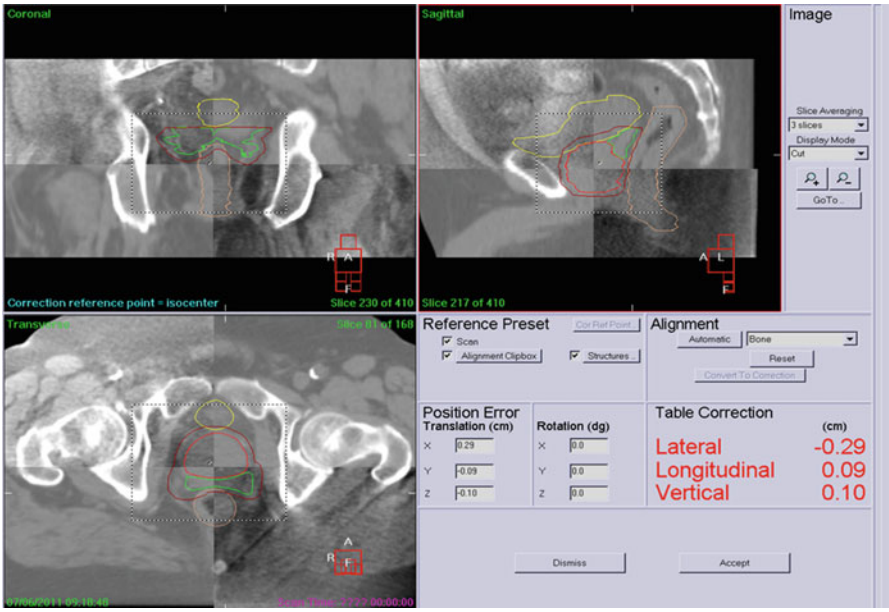

Fig. 5.6 A fusion of a planning CT and a kVCBCT of a prostate patient image on Elekta X-ray volume imaging (XVI) system. Registration can be done automatically or manually using axial, sagittal, and coronal views

Fig. 5.7 A Siemens Primus accelerator equipped with megavoltage cone beam CT (MVCBCT) capability at the department of radiation oncology at UCLA

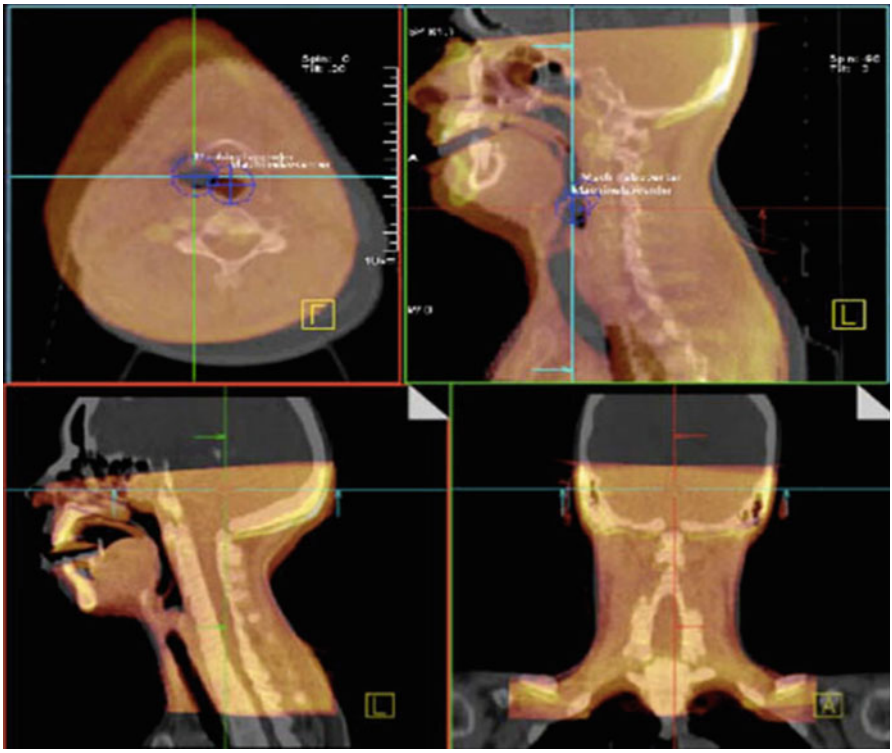

Fig. 5.8 Image registration of a reconstructed MVCBCT image to the planning CT (Courtesy of Jean Pouliot, PhD)

lasts ~45 s. An integrated computer workspace provides automated acquisition of projection images, image reconstruction, MVCBCT image to planning CT registration, and couch shift calculation. The image reconstruction starts immediately after the acquisition of the first portal image, and a typical 256 × 256 × 274 reconstruction volume (1.1 × 1.1 × 1.0 mm^3 voxel size) is completed in 110 s.

Figure 5.8 shows the image registration of a MVCBCT (brown) to the planning CT (gray). The system demonstrates submillimeter localization precision and sufficient soft-tissue resolution to visualize structures such as the prostate (Morin et al. 2005)

Compared to the kVCBCT image, the soft-tissue contrast in the MVCBCT is reduced due to the dominance of Compton scattering. The advantages of kVCBT over MVCBCT can be summarized below:

- Better contrast and spatial resolution
- Better soft-tissue visibility at much lower doses
- Compatibility of kVCBCT images with the reference treatment plan images for patient setup verification and correction

- Combination of radiography, fluoroscopy, and CBCT capabilities from the same source and detector, which provides great flexibility in implementing the goals of IGRT

The potential advantages of MVCBCT over kVCBCT are as summarized as follow:

- Less susceptibility to imaging artifacts due to mental objects such as hip implants, dental fillings, and surgical clips.
- No need for extrapolating attenuation coefficients from diagnostic (kV beams) to the therapeutic beam. CT numbers in MVCBCT correlate directly with electron density.
- The known dose distribution characteristics of the therapeutic beam allow more accurate calculation of imaging dose in the MVCBCT acquisition process.
- Implementation of MVCBCT does not require extensive modifications of a linear accelerator that is already equipped with an EPID.

5.5.4 Megavoltage Fan Beam CT (MVCT)

Helical TomoTherapy Hi-Art System (Accuray Inc., Sunnyvale, CA) is an integrated system that combines CT scanning technology with radiation therapy delivery. Figure 5.9 shows (a) a helical tomotherapy treatment unit and (b) schematic view of tomotherapy hardware components. The actual treatment beam from the linear accelerator is used as the X-ray source for image acquisition with detuned energy of 3.5 MV. The megavoltage fan beam is collimated to a length of 1 mm and

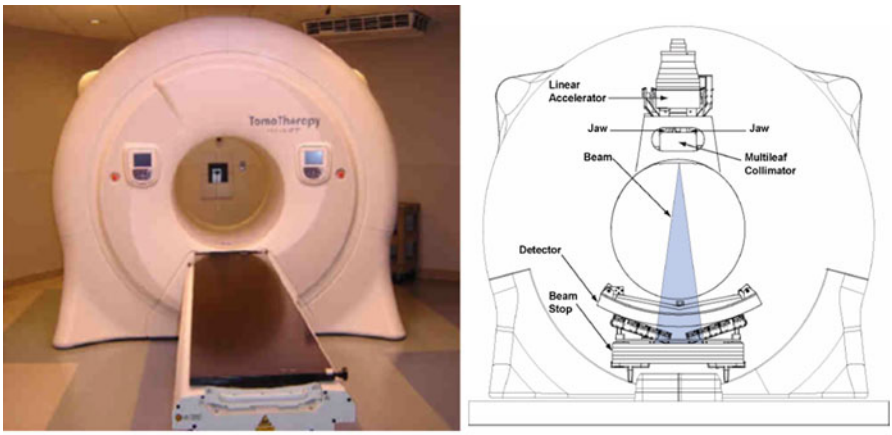

Fig. 5.9 (**a**) The helical tomotherapy treatment unit and (**b**) schematic view of tomotherapy hardware components (Courtesy of Tomotherapy Inc.)

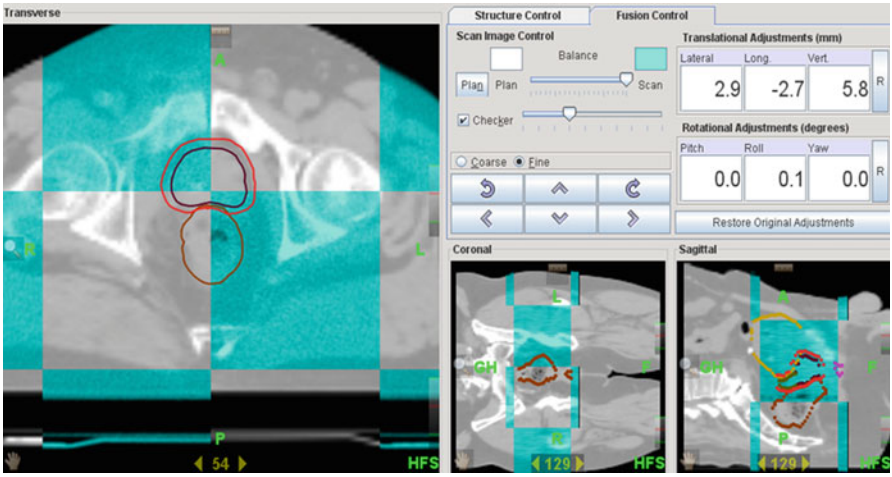

Fig. 5.10 Image registration on tomotherapy operating console

a width of 40 cm at isocenter for MVCT scan. The image reconstruction pixel matrix is defaulted at 512 × 512 with the FOV of 40 cm. Three clinical MVCT acquisition modes (fine, normal, and coarse) are available for (2, 4, and 6 mm) slice thickness, respectively. Tomotherapy is unique in its use of megavoltage computer tomography (MVCT) to guide the radiation treatment based on patient anatomy for that day via a fan beam.

Incorporating a CT scanner with a linear accelerator, the tomotherapy system features image-guidance capability in IG-IMRT using rotational fan beam. The on-board CT system can be used (a) to verify tumor's precise size, shape, and location and patient's setup immediately before or during the treatment to ensure accurate dose delivery, (b) to verify the leaf positions during treatment, (c) to evaluate the actual dose delivered to the patient (as compared to the planned dose), and (d) to adapt the original plan based on the daily image for subsequent fractions (if necessary). Generally, pretreatment MVCT scan takes 2–5 min depending on the scan length with additional imaging doses of 1.0–3.0 cGy. Fig. 5.10 shows Tomo MVCT image registration on tomotherapy operating console.

The MVCT in therapeutic range has less Z-dependence because of the increased Compton and pair-production interactions. Whereas, diagnostic imaging is generally performed at kilovoltage (kV) range which is dominant by the photoelectric interactions, resulting in good contrast resolution due to large atomic number (Z) dependence. Figure 5.11 shows the axial images for head-and-neck case with dental fillings for (a) kVCT scan and (b) MVCT image obtained on a tomotherapy unit. Tomotherapy's MVCT image allows visualization of soft tissues around metal (such as teeth filling and /or hip replacement) and more accurate dose calculation. Compared with the diagnostic kVCT scan, the uniformity and spatial resolutions of

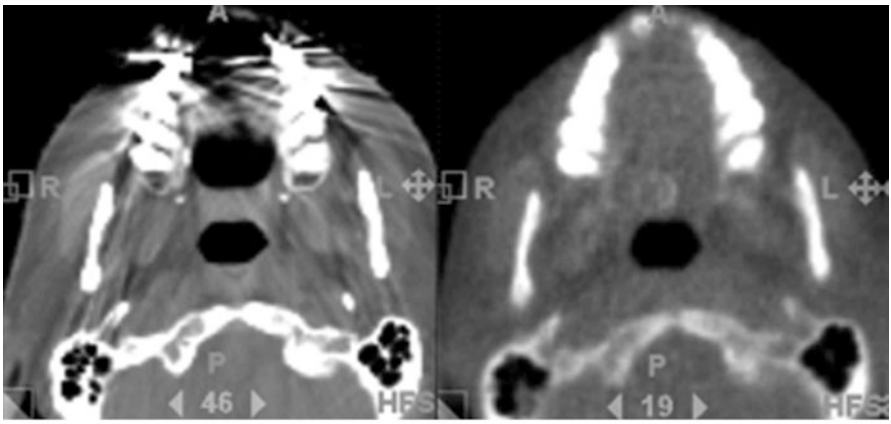

(a) (b)

Fig. 5.11 The axial images for a head-and-neck case with dental fillings. A kVCT planning image is shown on the left (**a**), and a MVCT image obtained on a tomotherapy unit is shown on the right (**b**). The severe streaking aberrations introduced by metal artifacts are clearly seen in kVCT image (Courtesy of Tomotherapy Inc.)

MVCT images generated by the tomotherapy are comparable to that of diagnosis CT images (Meeks et al. 2005; Hong et al. 1999; Forrest et al. 2004) but MVCT has inferior contrast resolution.

The pretreatment MVCT scan can also be used to perform dose verification (Kapatoes et al. 1999; Kapatoes et al. 2001a; Kapatoes et al. 2001b; Langen et al. 2005). The actual dose distribution delivered can be superimposed onto the daily images of the patient obtained at the time of treatment. The results can be compared with the planned isodose on the planning CT. This comparison may be used as an accurate basis for adaptive radiotherapy (ART) whereby the optimized delivery is modified before subsequent fractions.

5.6 Real-Time Tracking Systems

Detecting the tumor position is the most important and challenging task in real-time tracking. Currently, there are four possible means of locating the tumor during treatment: (1) real-time imaging of the tumor itself via, e.g., fluoroscopy; (2) real-time imaging of artificial fiducial markers implanted in the tumor; (3) inference of the tumor position from surrogate breathing motion signals; and (4) - non-radiographic tracking of an active or passive signaling device implanted in the tumor. All of these methods are currently under development or used clinically (Keall et al. 2006).

5.6.1 ExacTrac System

The Brainlab (Brainlab AG, Feldkirchen, Germany) provides versatile IGRT platform for all treatment sites for different imaging procedures. The Brainlab ExacTrac X-ray IGRT system uses a combination of optical positioning and kV radiographic imaging to accurately position patients and make online positioning corrections. The ExacTrac IGRT system is mainly an integration of two subsystems: (1) an infrared (IR)-based optical positioning system (ExacTrac) and (2) a radiographic kV X-ray imaging system (X-ray 6D). The infrared system consists of 2 IR cameras, which are used to monitor reflective body markers placed on the patient's skin to assist in patient initial setup, and an IR reflective reference star, which is attached to the treatment couch and assist in couch movement with spatial resolution to better than 0.3 mm (Jin et al. 2008). The radiographic kV devices consist of two oblique X-ray imagers to obtain high-quality radiographs for patient position verification and adjustment. In addition, the infrared markers provide a respiratory signal for tracking and gating of the treatment beam, with the X-ray system providing periodic confirmation of patient position relative to the gating window throughout treatment (Figs. 5.12 and 5.13).

ExacTrac 6.0 or later version (Jin et al. 2008; ExacTrac, Image-guided radiotherapy BrainLab, n.d.) also provides the possibility to perform 6D patient positioning based on kVCBCT images taken on a Varian OBI. The volumetric kVCBCT datasets will be automatically fused to the pretreatment CT images. The remote-controlled treatment couch and robotic module allow for any shifts to the detected and compensated from outside the treatment room. In July 2010, Brainlab announced the availability of ExacTrac® Infrared Monitoring, an add-on device to existing treatment machines for monitoring patient positioning during radiation therapy treatments. The Brainlab's new technology uses infrared tracking to continually monitor the patient's position and check the reference position for a wide range of treatment disease sites, including the cranial, head and neck, prostate, lung, liver, and spine. ExacTrac offers high-resolution stereoscopic X-ray imaging that targets tumors and corrects patient positioning with submillimeter precision in a quick and automated 2-min setup. The radiation delivered to the patient during imaging is negligible compared to cone beam CT or 2D MV portal images (ExacTrac, Image-guided radiotherapy BrainLab, n.d.).

5.6.2 CyberKnife

The CyberKnife Robotic Radiosurgery System (Accuray Inc., Sunnyvale, CA) is a frameless image-guided system that is specifically designed to deliver stereotactic body radiation therapy (SBRT) (also known as radiosurgery). The system includes a compact lightweight linear accelerator (6 MV) mounting on a true robotic manipulator, allowing for treatment beams deliver from thousands of

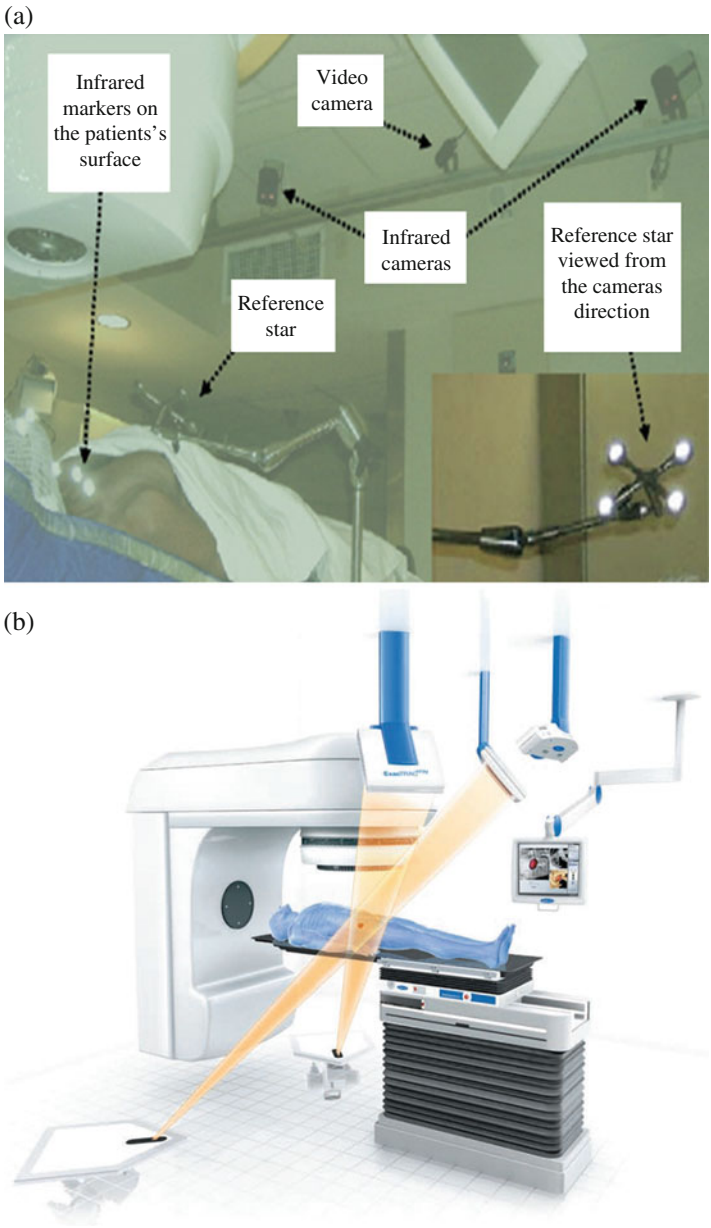

Fig. 5.12 (**a**) The infrared camera-based ExacTrac system; (**b**) the Novalis body image-guided system showing the X-ray imaging devices (Jin et al. 2008)

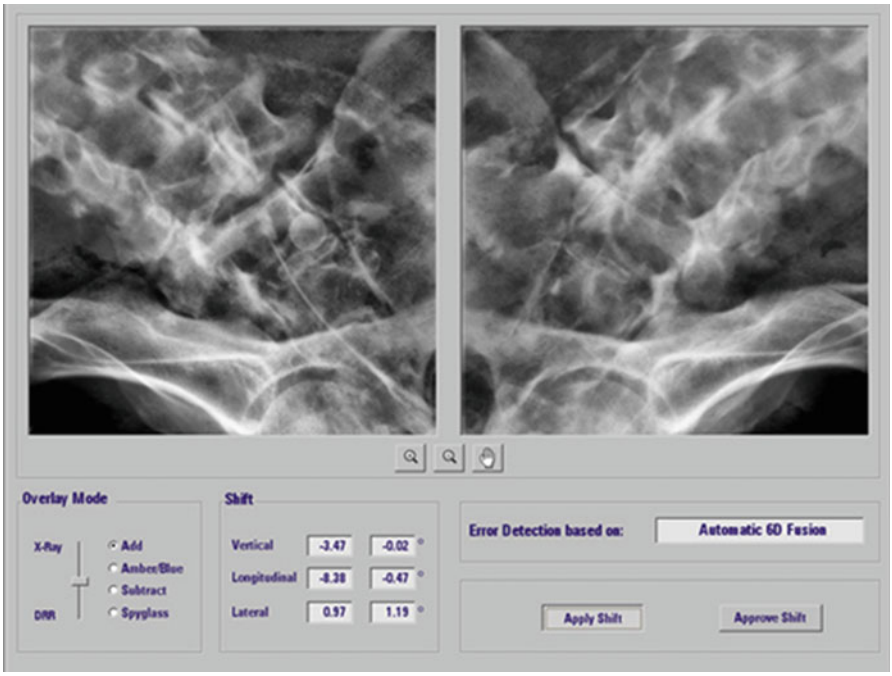

Fig. 5.13 ExacTrac images from a Novalis system (http://www.ofunachuohp.net/rt/machine.html)

non-coplanar, isocentric, or non-isocentric angles. The system provides a noninvasive alternative to surgery for the treatment of both cancerous and non-cancerous tumors anywhere in the body, including the prostate, lung, brain, spine, liver, pancreas, breast, etc. (Gibbs 2006; Nuyttens and van de Pol 2012; Coste-Manière et al., n.d.; Gerszten et al. 2003; Dieterich and Pawlicki 2008). Prior to and/or during treatment, the two diagnostic (kV) X-ray sources and digital amorphous silicon detectors provide a continuous update of the tumor motion and automatically correct the aims of the treatment beam when movement is detected. The CyberKnife system was invented by an American neurosurgeon at Stanford University named John R. Adler (Adler et al. 1997). The system was approved for clinical use by the US Food and Drug Administration in 2001.

Figure 5.14 illustrates the CyberKnife radiosurgery system in a treatment room. The imaging system consists of two orthogonal diagnostic X-ray sources mounted to the ceiling paired with amorphous silicon detectors to acquire live digital radiographic images of the tumor or tumor surrogates. This system allows the robotic manipulator to correct for changes in patient position during treatment beam delivery. In addition, the system equipped a real-time optical tracking subsystem for dynamic compensation of tumor movement due to respiration during

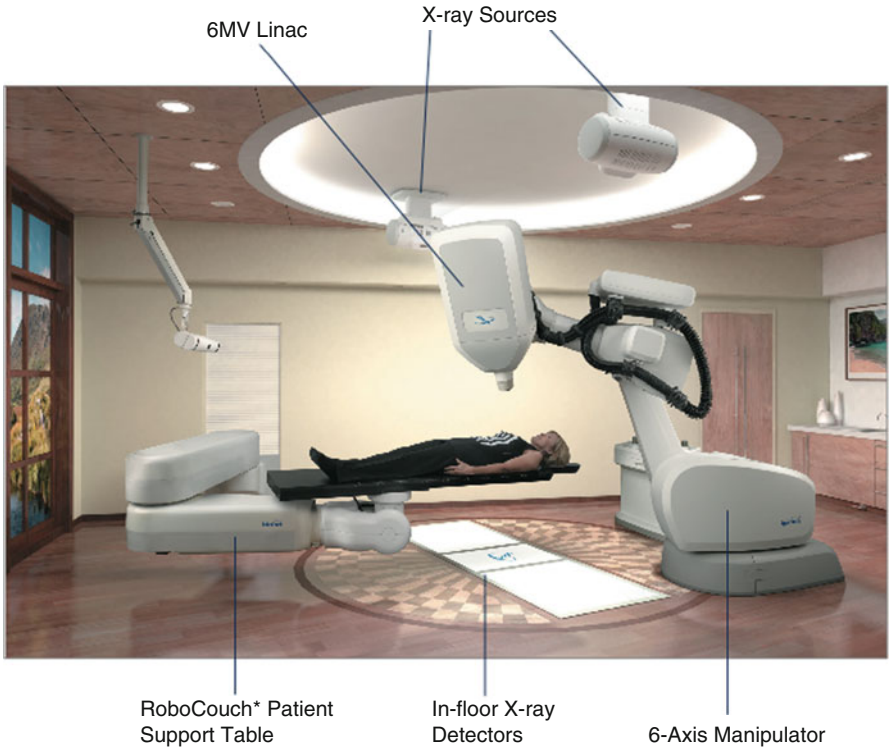

Fig. 5.14 The CyberKnife Robotic Radiosurgery System Stereotactic Radiosurgery system (Picture from http://www.cyberknifelatin.com/pdf/brochure-tecnico.pdf)

treatment delivery. The moving tumors can be treated with a high degree of accuracy while patients breathe normally.

Using its unique robotic mobility and continuous image guidance, the CyberKnife® System is capable of acquiring images for precision patient setup and tracking tumor motion in real time throughout the treatment. The system tracking capabilities eliminate the need for gating techniques and restrictive head frames, providing greater comfort for the patient.

Besides, the CyberKnife treatment delivery software provides an automatic, intuitive user interface to efficiently control all interactions between the robotic manipulator, treatment couch, and imaging system. Treatments have excellent tumor coverage, steep dose gradients, and tight dose conformality, regardless of target shape. The software quickly and automatically processes live images acquired throughout treatment at user-defined intervals, calculates offsets based on digitally reconstructed radiographs (DRRs), and sends offset data to the robotic manipulator for immediate and automatic motion compensation.

5.6.3 ViewRay System

The ViewRay™ system (ViewRay Inc., Oakwood Village, OH) is a unique medical device for radiation treatment that integrates a MRI system (MRIS) with a cobalt-60 (Co-60) radiation treatment machine. The system is specifically designed for MRI-guided radiation therapy with real-time tracking capability (ViewRay system Brochure, n.d.; Operator's manual for ViewRay system 3.5 2014).

Unlike the CT-based IGRT treatment units, the ViewRay system combines the superior imaging capabilities of MRI and RT machine to further optimize IMRT and IGRT and does not introduce additional ionizing radiation to patients. The ViewRay MRI system is a 0.35 T horizontal field MRI, which provides superior soft-tissue contrast and allows for continuously volumetric tracking of soft-tissue targets. If the tumor or critical structures move beyond a physician-defined boundary, the treatment beams automatically pause; when the structure moves back into the target zone, treatment automatically resumes *(ViewRay system Brochure,* n.d.*)*. Physicians can set both spatial and time thresholds for pausing treatment delivery, controlling for the motion of a patient's organs based on real-time 4D MRI data.

Other highlighted features of the ViewRay system include (ViewRay system Brochure, n.d.):

- Three Co-60 sources housed in shielding heads mounted on a ring gantry.
- Each Co-60 source equipped with computer-controlled multileaf collimator (MLC) for IMRT delivery.
- Dynamic images for real-time tracking when the treatment beams are on.
- An operator console for MRI acquisition, patient positioning, dose prediction and re-optimization, and real-time tumor tracking.
- Integrated treatment planning and delivery software for creating treatment plans and managing the treatment delivery process (Fig. 5.15).

Figure 5.16 displays the image registration on a ViewRay system. The primary image set is shown a rectangle. One can fuse MRI, CT, and PET images on the ViewRay system. There are three modes of registration available, including manual rigid registration, automatic rigid registration, and automatic deformable registration (Operator's manual for ViewRay system 3.5 2014)

5.6.4 Calypso 4D Localizing System

The Calypso system (Varian Medical Systems, CA) is a state-of-the-art imaging system designed for real-time tumor tracking for more precision radiation delivery. It combines real-time imaging and external beam radiation therapy to keep the radiation beam precisely focused on the moving target and minimizes damage to surrounding healthy tissue and lessens related side effects commonly associated with cancer radiation treatment. Figure 5.17 shows Calypso electromagnetic field real-time tracking system (Calypso, Varian Medical Systems, CA).

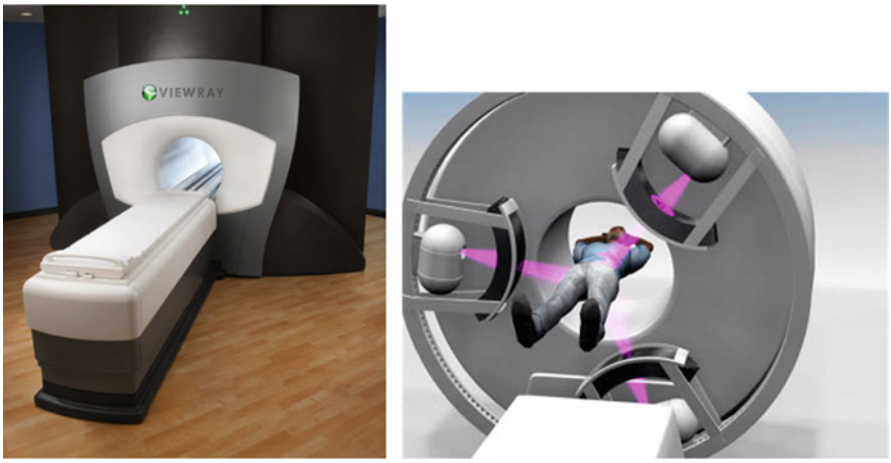

Fig. 5.15 (**a**) The ViewRay treatment unit and (**b**) a schematic of real-time MRI-guided soft-tissue imaging and volumetric tracking system (ViewRay Inc., Oakwood Village, OH) (Courtesy of ViewRay Inc.)

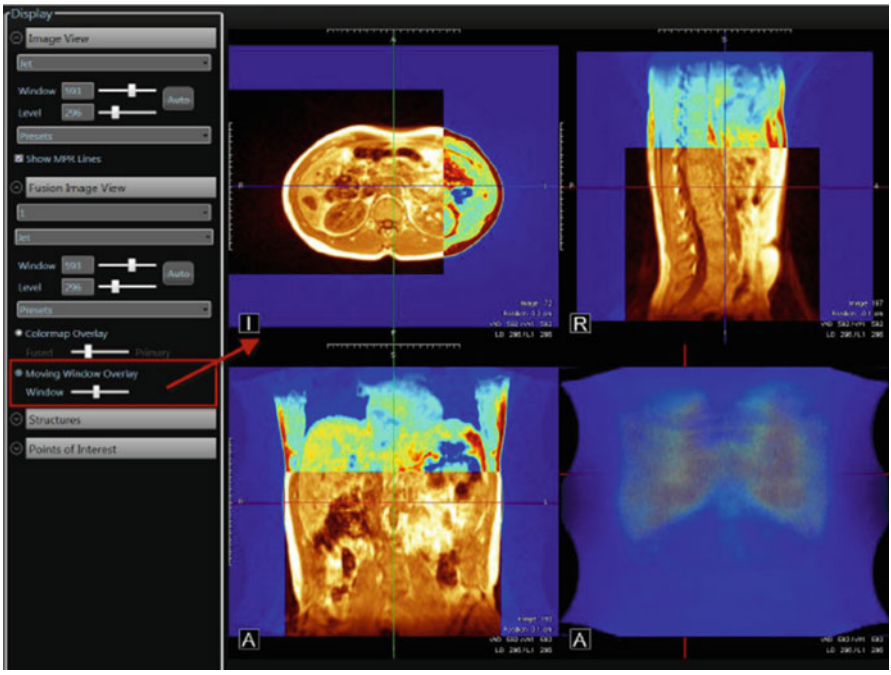

Fig. 5.16 The image registration on a ViewRay system. The primary image set is shown a rectangle (Operator's manual for ViewRay system 3.5 2014)

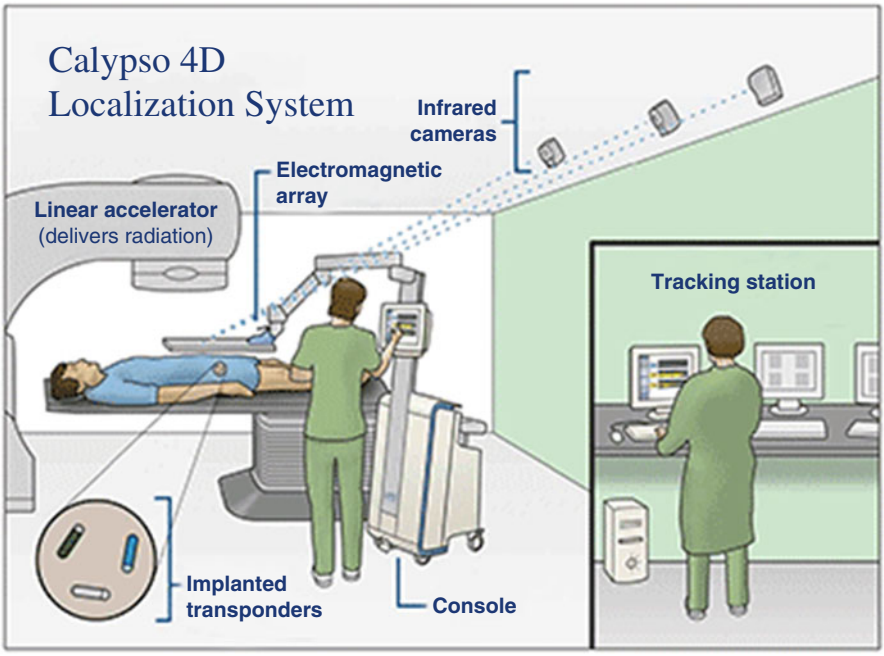

Fig. 5.17 The electromagnetic field real-time tracking system (Calypso, Varian Medical Systems, CA). Figure from https://www.massey.vcu.edu/patient-care/methods/radiation/therapies/calypso

Prior to radiation treatment, three electromagnetic transponders (in mms) called beacons are inserted in or near the tumor to monitor exact tumor motion using safe radiofrequency waves. During treatment, the transponders relay a constant signal, pinpointing the tumor's exact location. Outside the treatment room, a control computer displays the positional information and alerts therapists if and/or when the tumor or organ moves during treatment. No additional ionizing radiation will be needed for target tracking. The approach is feasible for monitoring of tumor position during radiation delivery (Balter et al. 2005) for numerous tumors such as prostate cancer.

5.7 Management of Imaging Dose

Volumetric CT-based IGRT technologies have emerged as the new paradigm for patient positioning, target localization, and external beam alignment in radiotherapy (Murphy et al. 2007). One problem with X-ray-based IGRT technologies is the potential for excessive imaging dose to the patients. Given the imaging procedure is performed on daily basis and repeated throughout the entire treatment fractions (up to 30 or 35 fractionations), imaging doses to patient may be excessive and result

Table 5.1 Comparison of various commercially available CT-based IGRT systems [AAPM TG 179]

CT-based IGRT system	Elekta XVI	Varian OBI	Siemens Artiste	Tomotherapy	Siemens Primatom
Imaging modalities	kV-CBCT	kV-CBCT	kV-CBCT	MV-FBCT	CT-on-rails
Field of view (cm)	50 × 50 × 25.6	45 × 45 × 17	40 × 40 × 27.4	40	50
Imaging dose (cGy)	0.1–3.5	0.3–2.0	3–10	0.7–3.0	0.05–1
Accuracy (mm)	<1	<1	<1	<1	<1
Image acquisition and reconstruction time (min)	2	1.5	1.5	5 s/slice	3 slice/s

in unnecessary toxicity for sensitivities structures. Furthermore, X-ray imaging irradiates a significantly larger region than the treatment volume, and therefore doses to critical structures may be even larger. The general rule for dose management is summarized by as low as reasonably achievable (ALARA) (Murphy et al. 2007).

Many literatures including the AAPM Task Group 75 have analyzed and reported the imaging dose for a number of IGRT protocols (Murphy et al. 2007; Bissonnette et al. 2012; Chan et al. 2011; Stutzel et al. 2008; Moseley et al. 2012). Table 5.1 shows the comparisons of various commercially available CT-based IGRT systems (Bissonnette et al. 2012). Improved image quality is achievable at higher doses for most commercial systems. However, image quality is to be judged based on the critical endpoint of the IGRT process – targeting. It is recommended that dose management techniques that decrease the ionizing radiation imaging dose without affecting targeting be implemented whenever possible (Murphy et al. 2007)

5.8 Image Registration and Correction Strategies

Image registration (Zitova and Flusser 2003) is the process of transforming multimodality images into a same coordinate system for a same target taken at different times. The registration geometrically aligns two images, including the reference (or source) and target images, to compare or integrate the information obtained from different image modalities. Image registration is important for treatment planning stage (i.e., target definition) and treatment delivery stage (i.e., patient alignment). Under the context of image-guided treatment delivery, the reference image generally refers to the planning CT, and the acquired daily images are the target images. Image registration may be challenging because of variability of patient's positioning for every modality and movement of internal organs. Often used image registration algorithm classification includes:

5.8.1 Single- vs Multimodality Methods

The CT images are the most widely used image modalities in radiation oncology; there is growing interests in adopting other image modalities, such as MRI, PET, etc. for better targeting. Single-modality methods tend to register images of the same modality acquired by the same scanner type, while multimodality registration methods tended to register images acquired by different scanner types. Multimodality registration methods are often used in medical imaging as images of a subject are frequently obtained from different scanners. Examples include registration of brain CT/MRI images, whole body PET/CT images for tumor localization, and registration of ultrasound and CT images for prostate localization in radiotherapy.

5.8.2 Rigid vs Deformable Image Registration

Rigid transformations are defined as geometrical transformations including translations and rotations. These transformations typically preserve the point-to-point distance, straightness of lines, and angles between straight lines. Registration problems that are limited to rigid transformations are called rigid registration (Fitzpatrick and West 2001). For example, the shape of a human brain changes very little with head movement, so rigid body registration can be used to fuse different head positions for different scans.

However, rigid alignment does not model anatomic changes from, e.g., organ deformation, patient weight loss, or tumor shrinkage. Nonrigid or deformable image registration (DIR) was developed to account for anatomic changes by finding the mapping between points in one image and the corresponding point in another image. DIR has the perspective of being widely integrated into many different steps of the radiotherapy process, such as treatment planning, treatment delivery (registration between the planning CT and treatment CT) for dose accumulation and contour propagation, etc. (Brock et al. 2006).

5.8.3 Automatic vs Manual Registration

Registration methods may also be classified according to the level of automation, such as automatic, interactive, and manual registration methods. Manual methods provide tools to align the images manually. Interactive methods reduce user bias by performing certain key operations automatically while still relying on the user to guide the registration. Automatic methods do not allow any user interaction and perform all registration steps automatically. The automatic registration algorithms based on mutual information algorithm (Ruchala et al. 2002; Pluim et al. 2003) were adopted for tomotherapy MVCT and Siemens MVCBCT and edge-matching algorithm (Borgefors 1988) adopted by Elekta kVCBCT.

5.8.4 Intensity-Based vs Feature-Based Registration

Image registration involves spatially registering the target image(s) to align with the reference image. The planning CT images are normally referred to as the reference, and the other pretreatment image modalities, such as cone beam CTs, etc., are, respectively, referred to as the target images. Intensity-based methods compare intensity patterns in images via correlation metrics, while feature-based methods find correspondence between image features such as points, lines, and contours (Goshtasby 2006). Intensity-based methods register entire images or sub-images. If sub-images are registered, centers of corresponding sub-images are treated as corresponding feature points. Feature-based methods establish a correspondence between a number of especially distinct points in images. Knowing the correspondence between a number of points in images, a geometrical transformation is then determined to map the target image to the reference images, thereby establishing point-by-point correspondence between the reference and target images.

5.8.5 Online and Offline Correction Strategies for Patient Positioning

There are two basic correction strategies used while determining the most beneficial patient position and beam structure (Jaffray et al. 1999): online and off-line correction. Both serve their purposes in the clinical setting and have their own merits. A combination of the both strategies is often employed. Often, a patient will receive corrections to their treatment via online strategies during their radiation session.

The online correction strategy acquires images prior to the treatment and makes treatment interventions during the current treatment session. The purpose of an online approach is to control and reduce both systematic and random errors. Online correction strategy usually requires a high level of integration of both software and hardware and fast speed.

The off-line correction strategy, however, acquires images before treatment and makes a match to a reference image off-line (i.e., without the patient on the couch). The purpose of the strategy is to reduce the magnitude of the individual patient systematic setup error and, when combined with other patient setup data treated under the same protocol, to calculate the population systematic error. The population-based systematic error is the standard deviation of the systematic errors of all patients within the treated population. Published off-line correction protocols that are widely used are the shrinking action level (SAL) and the no action level (NAL) protocols (National radiotherapy implementation group report 2012; Bel et al. 1993; de Boer et al. 2005; Qi et al. 2013b).

5.9 Clinical IGRT Workflow

The utility of IGRT allows for the verification of patient's anatomy and alignment through relatively low-dose CT imaging prior to each treatment delivery. In general, the IGRT workflow can be summarized as the following steps (Qi et al. 2013a; b):

5.9.1 Initial Patient Setup

Prior to each treatment fraction, appropriate patient alignement need to be ensured using patient-specific marks and/or tatoos to the in-room laser positions. To achieve proper reproducibility during radiotherapy treatment, external immobilization devices are often used and attach to the couch top in a unique position to avoid daily variation in patient repositioning. Figure 5.17 shows a customized head-and-neck and shoulder thermoplastic mask that was generally used to provide immobilization of the entire upper part of the body in the treatment position. Immobilization devices not only help the patient maintain the required consistent position but may also achieve an advantageous treatment position to reduce dose to normal tissue. However the benefit of these devices can be affected by the skill of the clinical staff making and/or positioning the devices and the cooperation of the patient. The most vital component of an accurate and reproducible treatment position is that the patient is comfortable, and the position can be easily reproduced by both therapeutic radiographer and patient (Fig. 5.18).

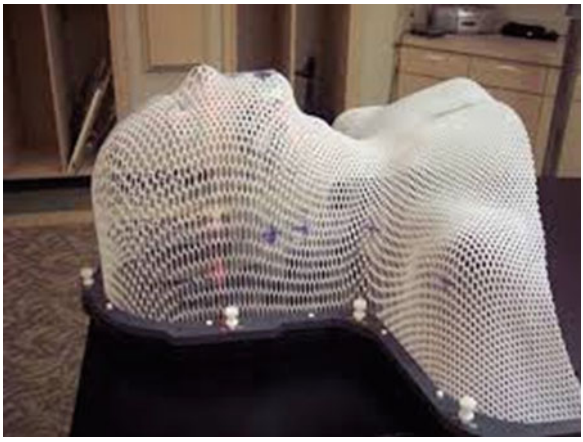

Fig. 5.18 Immobilization devices of head-and-neck and shoulder thermoplastic mask for H&N radiotherapy

5.9.2 Image Acquisition and Registration

The pretreatment IGRT image, such as CBCT or MVCT, is acquired in the treatment position immediately before each treatment delivery. The daily scans are then registered to the reference image set (the planning CT scan) on the treatment console to verify patient positioning or to determine discrepancies. The initial registration is normally done automatically and followed by manual adjustments if necessary. A rigid image alignment is generally performed initially in order to supply a suitable starting point for estimation of organ deformation for deformable registration.

5.9.3 Compensation for Patient Misalignment

Make appropriate shifts to compensate for patient misalignments. The adjustments are sent to the treatment unit and the couch shifts automatically to compensate for the differences.

Manual alignment is the most reliable and intuitive approach for volume alignment. However, manual alignment is subject to interobserver subjectivity/variations. When relatively large adjustments were required (i.e., >1 cm), the physician is called to verify the alignment on the treatment console.

5.10 Image Guided Adaptive Treatment (IG-ART)

Adaptive radiotherapy (ART) has been introduced as a feedback control strategy to include patient-specific treatment variation explicitly in the control of treatment planning and delivering during the treatment course (Yan 2008, 2010). Specifically, ART is referred to change the radiation treatment plan delivered to a patient during a course of radiation treatment to account for (1) temporal changes in anatomy (i.e., tumor volume changes, weight loss or gain, etc.) and (2) changes in tumor biology/function, etc. ART aims to adjust the treatment plan, with the aid of frequent (i.e., daily) image guidance, when the plan quality degrades. Various ART strategies were developed, such as off-line between fractions, online immediately prior to a fraction, and/or in real time during a fraction.

The integration of the image-guidance system into the radiation delivery system, such as OBI on Varian, XVI on Elekta, and MVCT image acquisition detector on tomotherapy, allows for image acquisition on a daily basis. These daily images ensure the accuracy of patient setup for every treatment, allowing the physician to check size, location, and the shape of the tumor before each treatment and compare that day's image with the treatment plan. This assures that the radiation treatment is directed at the tumor site and allows for modification of the treatment plan if

necessary, which, in turn, brings a higher level of precision and accuracy to cancer treatment. In addition, the actual dose delivered to the patient can be calculated based on daily volumetric CT scan. This delivered dose can be directly compared with the planned dose distribution to trigger a re-optimization process if necessary.

A representative application for using daily CT is to assess the tumor volume changes during the treatment course. The significant tumor volume changes as revealed from daily CT scans have been reported (Li et al. 2007) for a soft-tissue sarcoma case at the chest region. The CTVs for the sarcoma were contoured on a series of daily MVCT sets and were compared with the CTV and PTV obtained from the planning kVCT scan. Figure 5.19 (a) shows the inter-fractional variations

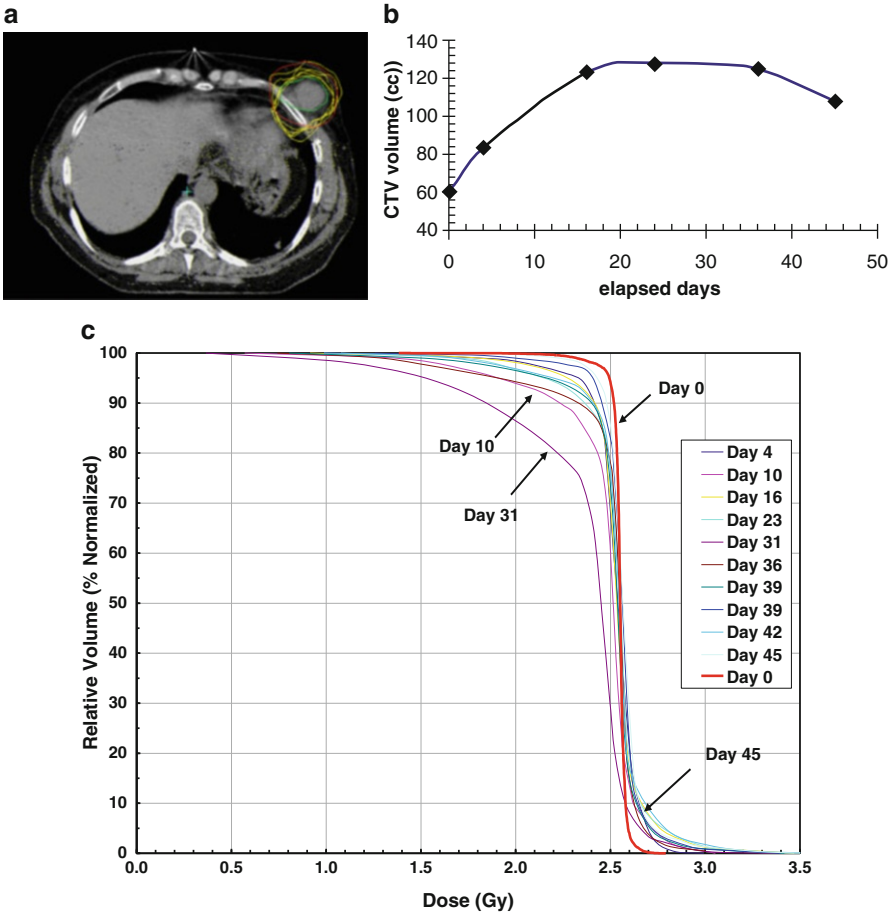

Fig. 5.19 The inter-fractional variations for a sarcoma case at chest region (Li et al. 2007). (**a**) The inter-fractional variations of daily CTV (*yellow*) contoured from daily MV CT, as compared with the planning CTV (*green*) and PTV (*red*) and overlaid on an axial kVCT image. (**b**) Variation of clinical target volume (CTV) during treatment course. Clinical target volume (in cubic centimeters) for each data point (e.g., at a given treatment-elapsed day) is indicated. (**c**) The verification DVHs based on given MVCT images and the planning DVH for PTV

of daily CTV (yellow) contoured from daily MVCT, as compared with the planning CTV (green) and PTV (red) and overlaid on an axial kVCT image. Figure 5.19 (b) displays quantitative variations of the daily CTVs during the treatment course. The CTV (in cubic centimeters) at a given elapsed day is indicated. It is clear that the CTV at the middle course of treatment was approximately doubled from the planning CTV (Day 0). The original PTV was not big enough to cover the enlarged daily CTVs. The verification DVHs based on given MVCT images were calculated and compared to the planning DVHs (Day 0) (Fig. 5.19 (c)). The significant tumor volume changes result in dramatic underdosing for PTV, e.g., the PTV coverage varies from 30% to 95% which depends on the given treatment factions.

The ART is an appealing concept that aims to adjust the treatment plan based on the anatomical changes assessed on a daily basis using pretreatment volumetric images (Schwartz et al. 2012; Castadot et al. 2010a; Castadot et al. 2010b; Nishi et al. 2013; Wu et al. 2009; Lee et al. 2008; Chen et al. 2014). Due to the flexibility of the head-and-neck region, radiation response often causes tumor and normal organ shrinkage and patient weight loss during their treatment course. Patient physiologic and anatomic variations cannot be fully accounted for and can cause the delivery doses of the tumor and normal organ to degrade from their initial planning dose distribution.

Despite marked advances in RT, radiation often causes significant functional deficits for the head-and-neck patients. Of particular importance for H&N cancer RT are the parotid glands. High-radiation doses to the parotid glands leads to xerostomia, where the patient's ability to swallow and eat is significantly degraded (De Meerleer et al. 2000). Wu et al. (Wu et al. 2009) reported that the dosimetric benefit of replanning with reduced margins could result in up to 30% parotid gland dose sparing. Lee et al. (Lee et al. 2008) reported an average of 15% parotid mean dose difference between the delivered vs the planned doses due to anatomic changes during a course of radiation treatment. Recently, Schwartz et al. (Schwartz et al. 2012) performed a prospective adaptive trial for a group of 24 H&N cancer patients with 1–2 replan(s) in the middle of the treatment course. The early outcomes indicated promising clinical outcome results including low initial toxicity and high disease control. Chen AM (Chen et al. 2014) also concluded that ART conveys a significant benefit in appropriately selected patients with H&N cancer. However, clinical implementation of ART remains challenging and labor intensive due to the complexity and lack of robustness in automated image registration/segmentation/dose summation.

Qi et al. (2015) presented a clinical application of a near real-time automated framework that could help decision-making process for adaptive planning to account for plan quality degradation for a group of H&N cases. A quantitative patient-specific biomechanical H&N anatomic model (Neylon et al. 2015) assembled using the conventional CT simulation (to account for subject specific sub-anatomy locations) is employed to register in real time with routine on-board CT (to monitor the effects of posture/physiologic variations in gross treatment volume). Such an automated framework will streamline the process of an accurate determination of the daily and integrated delivered dose for adaptive radiation therapy for H&N cases.

5.11 Management of Respiratory Motion

Respiratory motion can introduce significant errors in the external beam radiation therapy for patients with thoracic, abdominal, and pelvic tumors (Keall et al. 2006). The problems of unaccounted respiratory motion in radiotherapy can be summarized in the following aspects:

1. Image acquisition. Respiratory motion can generate artifacts for all image modalities, such as CT and PET, both of which are considered to be standard-of-care image modalities for lung cancers. Respiratory motion-induced artifacts can lead to difficulties in delineating target boundaries.
2. Treatment planning (Chen et al. 2004; Nehmeh et al. 2003; Caldwell et al. 2003; Balter et al. 1996; Ford et al. 2003). Target movement and patient setup uncertainty are generally accounted for using a planning margin. Larger treatment margins are generally needed to cover the limits of the moving targets, which is suboptimal. Since larger margin calls for larger radiation field size, resulting in larger volume of healthy tissues exposed to radiation doses. This increased treatment volume increases the likelihood of treatment-related complications. However, if the margins are not sufficiently large, part of the CTV will not receive adequate dose coverage resulting in potential tumor recurrence. The artifacts observed in CT images make it challenging to quantify the magnitude of margin (to allow for respiratory motion) particularly for individual patients in whom a wide range of tumor motion is observed.
3. Radiation delivery. Radiation delivery in the presence of intra-fraction organ motion causes an averaging or blurring of the static dose distribution over the path of the motion. This displacement results in a deviation between the intended and delivered dose distributions.

Precise geometric knowledge of the target volume is needed for treatment planning to better achieve therapeutic goal. Typically, a patient's radiotherapy plan is based on conventional CT scans. However, this conventional CT scan is only a "snapshot" of the patient and tumor position, i.e., it is acquired on 1 day and at one time. Patient and/or tumor changes can either occur daily (inter-fraction motion) or during the treatment delivery (intra-fraction motion). Besides, such conventional CT scan can include severe motion artifacts that result from interplay between the advancing scan plane and object motion. It has been recognized that severe artifacts can be introduced if organ motion is present during CT acquisition (Rietzel et al. 2005).

Although tumor displacement varies depending on the site and organ motion, it is most prevalent and prominent in lung cancers. To explicitly include organ/target motion in treatment planning and delivery, time-resolved 4D computed tomography (4DCT) is needed.

5.11.1 Four-Dimensional Computed Tomography (4DCT)

A common approach to obtain high-quality CT data in the presence of respiratory motion is time-resolved 3D CT imaging, often referred to as 4DCT. Generally, the 4DCT scan process includes two steps: (1) to acquire a set of CT images per slice through the volume and (2) to sort the images and assemble spatiotemporally coherent datasets from the data acquired (Xing et al. 2006). The 4DCT images essentially create a video sequence of how the tumor moves during the breathing cycle. The 4DCT provides clinicians with more data to determine the mean tumor position, tumor range of motion, tumor range of motion for treatment planning, etc.

4DCT data are normally acquired on a multi-slice CT scanner in axial or helical mode during normal breathing. Respiration signals during 4DCT scanning are acquired using surrogate signals such as the motion of the abdominal surface, internal anatomy, or volume of air measured by spirometer during inhalation and exhalation cycles. Varian Real-time Position Management (RPM) system (Varian Medical Systems, Palo Alto, CA) using an external respiration signal is widely adopted at clinical setting. The RPM system consists of an infrared source, a CCD camera, and a reflective plastic box (with two infrared-reflecting dots) (Fig. 5.20). The reflective box is usually placed on the anterior abdominal surface, typically midway between the xyphoid process and the umbilicus, and the exact position is chosen to maximize the anteroposterior (AP) motion. The motion is captured by the camera and analyzed in real time by RPM system on a computer connected to the RPM camera. A patient undergoing a 4DCT scan on a GE scanner is shown in Fig. 5.20a. The system captures the position of the abdominal surface as a function of time during respiration (Fig. 5.20a). The breathing pattern is recorded for the duration of the scan and is referred to as the "respiratory trace" (Fig. 5.20b). Once the 4DCT acquisition has finished, the software retrospectively computes the phase at each point of the respiratory trace by determining the location of the peaks at end-inspiration and assigning percentages to inter-peak points based on a linear interpolation of the peak-to-peak distance (so-called phase sorting). 4DCT Images are acquired at each couch position for many respiratory phases. Normally, each image is sorted into one of ten phase bins, and the phase bins are selected to be evenly spaced in time over the respiratory cycle. Under this scheme, end-inspiration occurs at 0%, while end-expiration typically appears near 50%. A 4DCT dataset may involve as many as 1000–2000 CT slices. The peak-to-peak distance, the position of end-expiration with respect to end-inspiration can vary between respiratory cycles.

The 4DCT dataset allows for the generation of individualized internal target volumes (ITVs) for treatment planning but also allows for the retrospective selection of phases for gated radiotherapy (Mageras et al. 2004; Underberg et al. 2005). The maximum intensity projection (MIP), defined as the highest data value encountered along the viewing ray for each pixel of volumetric data, giving rise to a full intensity display of the brightest object along each ray on the projection image. MinIP projections reflect the lowest data value encountered along the viewing ray for each pixel of volumetric data (Li et al. 2006). However, there are some unsolved issues in 4DCT (Xing et al. 2006; Pan et al. 2004; Pan 2005).

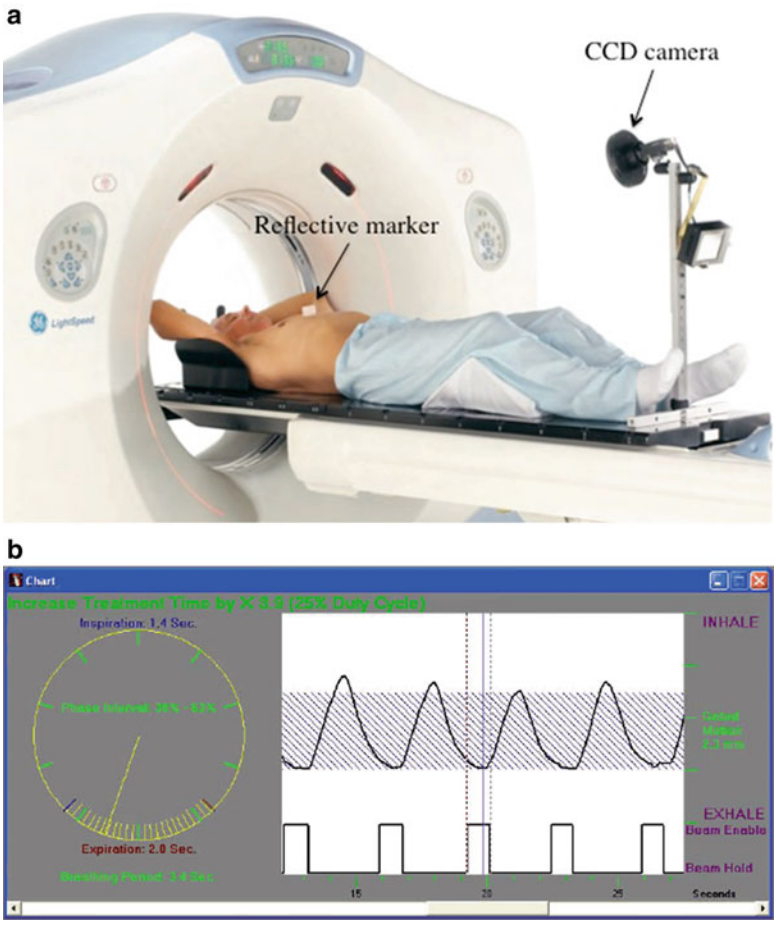

Fig. 5.20 (**a**) System setup for a 4DCT scan. (**b**) Respiratory waveform using an infrared-tracking camera and a reflective marker on Varian RPM system

5.11.2 Methods to Account for Respiratory Motion in Radiotherapy

A variety of treatment delivery techniques were developed to reduce the impact of respiratory motion in radiotherapy (Keall et al. 2006; Li et al. 2006). These techniques can be broadly stratified into the following four categories:

1. Respiratory gating methods. Respiratory gating involves the administration of radiation within a particular portion of the patient's breathing cycle (Keall et al.

2002; Kubo and Hill 1996), commonly referred to as the "gate." The position and width of the gate within a respiratory cycle are determined by monitoring the patient's respiratory motion, using either an external respiration signal or internal fiducial markers. Gated procedures are longer than non-gated procedures since the beam is turning on/off.

2. Breath-hold methods. The technique delivers radiation during a breath hold and predominantly applied to lung and breast radiotherapy. There have been several techniques developed, e.g., deep inspiration breath hold (Hanley et al. 1999; Wong et al. 1999) active breathing control (Wong et al. 1999) and self-held breath hold (Kim et al. 2001).
3. Forced shallow-breathing techniques. The technique employs a pressure plate against the abdomen in a reproducible fashion to minimize diaphragmatic excursions, thereby reducing breathing motion (Lax et al. 1994; Negoro et al. 2001).
4. Respiration synchronized techniques (such as real-time tumor tracking). Real-time tumor tracking dynamically shifts the radiation dose in space so as to follow the tumor's changing position during free breathing (Neicu et al. 2003; Shirato et al. 2000; Murphy 2004). In principle, real-time tracking can be achieved by using an MLC or a linear accelerator attached to a robotic arm or, alternatively, by aligning the tumor to the beam via couch motion. Under ideal conditions, continuous real-time tracking can eliminate the need for a tumor-motion margin in the dose distribution while maintaining a 100% duty cycle for efficient dose delivery (Keall et al. 2006).

Due to the concern regarding patient tolerance and compliance, as well as the availability of technology, the respiratory gating is, by far, the most clinically acceptable method to account for respiratory motion in radiation therapy. During a gating treatment, the computer synchronizes the beam with the respiratory cycles and switches the beam on only at the certain phases of respiration cycle. Typically, the gating interval is centered at end-expiration because of the increased reproducibility at this point and spans 20%–30% of the breathing period to provide a reasonable duty cycle. Treatment plans are optimized for this phase range by planning on an averaged composite of the scans within the interval. Gating treatment normally takes longer time to deliver the treatment due to treatment beam was turned on/off at some phases.

5.12 Conclusion

The importance of image-guided radiation treatment has increased tremendously for the IMRT and/or SBRT. Development of imaging technologies allows accurate pretreatment target definition but also patient localization prior to or during each treatment. The use of image guidance allows the tumor and adjacent healthy organs to be visualized to ensure radiation doses are delivered more precisely to the target tumors within the body without compromising health tissue.

IGRT has become a routine procedure of current clinical practice, despite of technical issues still need to be resolved or improved, such as a robust deformable registration method and auto-segmentation of the contours outlined on the planning CT to daily CTs (such as CBCT or MVCT, etc.). In addition, new IGRT technologies, such as MRI-guided radiotherapy, are continuously advancing to the field of radiation oncology. IGRT will continuously play important role in routine clinical practice and lead to better improve clinical outcome.

Questions

1. What is IGRT? Why IGRT is important and particularly important for IMRT?
2. What are the imaging modalities commonly used for target definition of brain tumor in treatment planning?
3. Name some of current available IGRT technologies. What are the advantages and disadvantages for the kilovoltage imagers compared to the megavoltage imagers in general?
4. List some treatment sites that IGRT is generally utlized. Why IGRT is especially helpful for prostate cancer radiotherapy?
5. List advantages of kilovoltage CBCT (kVCBCT) over Megavoltage CBCT (MVCBCT)?
6. What are the tumor site that ultrasound is generally applied to? List advantages and disadvantages of using ultrasound as an IGRT approach. with the use of Ultrasound for IGRT?
7. What are online and off-line correction strategies? The advantages and disadvantages for each strategy?
8. Definition of image registration. Why image registration is important in radiation therapy?
9. What is adaptive therapy? Describe the benefit and challenges of implementation of adaptive radiotherapy in clinical setting.
10. What is 4DCT? What is MIP? Descibe how a 4DCT is acquired and why it is important in radiation treatment.
11. What is potential concern of using CT-based IGRT technologies during radiation treatment?
12. What is real-time tracking? Name some the real-time tracking systems available in current clinical practice.

References

Adler JR Jr et al (1997) The Cyberknife: a frameless robotic system for radiosurgery. Stereotact Funct Neurosurg 69:124–128

Antonuk LE et al (1996) Megavoltage imaging with a large-area, flat-panel, amorphous silicon imager. Int J Radiat Oncol Biol Phys 36:661–672

Antonuk LE et al (1998) Initial performance evaluation of an indirect-detection, active matrix flat-panel imager (AMFPI) prototype for megavoltage imaging. Int J Radiat Oncol Biol Phys 42:437–454

Artignan X, Smitsmans M, Lebesque JV et al (2004) Online ultrasound image guidance for radiotherapy of prostate cancer: impact of image acquisition on prostate displacement. Int J of Radiat Oncol Biol Phys 59(2:595–601

Bailey DL, Townsend DW, Valk PE (2005) Positron emission tomography: basic sciences. Secaucus, Springer-Verlag. Isbn: 1–85233–798-2

Baily NA, Horn RA, Kampp TD (1980) Fluoroscopic visualization of megavoltage therapeutic x ray beams. Int J Radiat Oncol Biol Phys 6:935–939

Balter JM, Ten Haken RK, Lawrence TS, Lam KL, Robertson JM (1996) Uncertainties in CT-based radiation therapy treatment planning associated with patient breathing. Int J Radiat Oncol Biol Phys 36(1):167–174

Balter JM, Wright JN, Newell LJ et al (2005) Accuracy of a wireless localization system for radiotherapy. Int J Radiat Oncol Biol Phys 61:933–937

Barry A, Loredana M, Eva B (2012) Biomedical physics in radiotherapy for cancer. CSIRO Publishers, Collingwood

BATCAM (n.d.) Multi-probe image-guided radiation therapy. http://www.nomos.com/pdf/Batcam_bro_03.pdf

Bel A, van Herk M, Bartelink H, Lebesque JV (1993) A verification procedure to improve patient set-up accuracy using portal images. Radiother Oncol 29(2):253–260. PubMed PMID: 8310153

Bissonnette JP, Balter PA, Dong L, Langen KM, Lovelock DM, Miften M, Moseley DJ, Pouliot J, Sonke JJ, Yoo S (2012) Quality assurance for image-guided radiation therapy utilizing CT-based technologies: a report of the AAPM TG-179. Med Phys 39(4):1946–1963

B-mode Acquisition and Targeting (BAT) Ultrasound for image-guided radiotherapy. Ramer R, May 13, 2005. http://rii.uthscsa.edu/personalpages/lancaster/DI2_Projects_2005/BAT.pdf

de Boer HC, van Os MJ, Jansen PP, Heijmen BJ (2005) 17. Application of the no action level (NAL) protocol to correct for prostate motion based on electronic portal imaging of implanted markers. Int J Radiat Oncol Biol Phys 61(4):969–983

Borgefors G (1988) Hierarchical chamfer matching: a parameter edge matching algorithm. IEEE Trans Pattern Anal Mach Intell 10:849–865

Brock KK, Dawson LA, Sharpe MB et al (2006) Feasibility of a novel deformable image registration technique to facilitate classification, targeting, and monitoring of tumor and normal tissue. Int J Radiat Oncol Biol Phys 64(4):1245–1254

Butler EB, Teh BS, 3rd Grant WH et al (1999) SMART (simultaneous modulated accelerated radiation therapy) boost: a new accelerated fractionation schedule for the treatment of head and neck cancer with intensity modulated radiotherapy. Int J Radiat Oncol Biol Phys 45:21–32

Caldwell CB, Mah K, Skinner M, Danjoux CE (2003) Can PET provide the 3D extent of tumor motion for individualized internal target volumes? A phantom study of the limitations of CT and the promise of PET. Int J Radiat Oncol Biol Phys 55(5):1381–1393

Castadot P, Geets X, Lee JA, Christian N, Gregoire V (2010a) Assessment by a deformable registration method of the volumetric and positional changes of target volumes and organs at risk in pharyngo-laryngeal tumors treated with concomitant chemo-radiation. Radiat Oncol 95:209–217

Castadot P, Lee JA, Geets X, Gregoire V et al (2010b) Adaptive radiotherapy of head and neck cancer. Seminar Radiat Oncol 20:84–93

Chaiken, Lisa MD (2005) B-Mode acquisition and targeting stereotactic ultrasound: the ultimate in Tumor localization for prostate cancer. Cancer Care Center technologies. 13 May 2005. http://www.cancercareconsultants.com/technologies/articles/bmode-chaiken-article.htm

Chan M, Yang J, Song Y et al (2011) Evaluation of imaging performance of major image guidance systems. Biomed imaging Interv J 7:1–7

Chen GT, Kung JH, Beaudette KP (2004) Artifacts in computed tomography scanning of moving objects. Semin Radiat Oncol 14(1):19–26

Chen AM, Daly ME, Cui J et al (2014) Clinical outcomes among patients with head and neck cancer treated by intensity-modulated radiotherapy with and without adaptive preplanning. Head Neck 1:1–6

Cheng CW, Wong J, Grimm L, Chow M, Uematsu M, Fung M (2003) Commissioning and clinical implementation of a sliding gantry CT scanner installed in an existing treatment room and early clinical experience for precise tumor localization. Am J Clin Oncol 26:e28–e36

Chernak ES, Antunez RA, Jelden GL et al (1975) The use of computed tomography for radiation therapy treatment planning. Radiology 117:613

Coste-Manière E, Olender D, Kilby W, Schulz RA (n.d.) Robotic whole body stereotactic radiosurgery: clinical advantages of the cyberKnife® Integrated system. Reprinted by permission from The International Journal of Medical Robotics and Computer Assisted Surgery. http://www.robotics.org/content-detail.cfm/Industrial-Robotics-News/Robotic-Whole-Body-Stereotactic-Radiosurgery: Clinical-Advantages-of-the-CyberKnife®-Integrated-System/content_id/1085

Dawson LA, Sharpe MB (2006) Image-guided radiotherapy: rationale, benefits, and limitations. Lancet Oncol:848–858

De Meerleer GO, Vakaet LA, De Gersem WR, De Wagter C, De Naeyer B, De Neve W (2000) Radiotherapy of prostate cancer with or without intensity modulated beams: a planning comparison. Int J Radiat Oncol Biol Phys 47:639–648

Dieterich S, Pawlicki T (2008) Cyberknife image-guided delivery and quality assurance. Int J Radiat Oncol Biol Phys 71:S126–S130

ExacTrac, Image-guided radiotherapy BrainLab (n.d.) https://www.brainlab.com/wp-content/uploads/2014/01/Brochure-ExacTrac.pdf

Fakiris AJ, McGarry RC, Yiannoutsos CT, Papiez L et al (2009) Stereotactic body radiation therapy for early-stage non–small-cell lung carcinoma: four-year results of a prospective phase II study. Int J Radiat Oncol Biol Phys 75(3):677–682

Falco T, Wang H, Fallone BG (1998) Preliminary study of a metal/a-se-based portal detector. Med Phys 25:814–823

Feldkamp IA, Davis LC, Kress JW (1984) Practical cone-beam algorithm. J Opt Soc AmA 1:612–619

Fitzpatrick JM, West B (2001) The distribution of target registration error in rigid-body point-based registration. IEEE Trans Med Imaging 20:917–927

Ford EC, Mageras GS, Yorke E, Ling CC (2003) Respiration-correlated spiral CT: a method of measuring respiratory-induced anatomic motion for radiation treatment planning. Med Phys 30 (1):88–97

Forrest LJ, Mackie TR, Ruchala K, Turek M, Kapatoes J, Jaradat H, Hui S, Balog J, Vail DM, Mehta MP (2004) The utility of megavoltage computed tomotherapy images from a helical tomotherapy system for setup verification purposes. Int J Radiat Oncol Biol Phys 60 (5):1639–1644

Gerszten PC, Ozhasoglu C, Burton SA, Vogel WJ, Atkins BA, Kalnicki S, Welch WC (2003) Cyberknife frameless real-time image-guided stereotactic radiosurgery for the treatment of spinal lesions. Int J of Radiat Oncol Bio Phys 57(2):S370–S371

Gibbs IC (2006) Frameless image-guided intracranial and extracranial radiosurgery using the Cyberknife™ robotic system. Cancer Radiother 10:283–287

Goitein M, Busse J et al (1975) Immobilization error: some theoretical considerations. Radiology 117:407–12. Boyer AL et al (1992) A review of electronic portal imaging devices (EPIDs). Med Phys 19:1–16

Goshtasby A (2006) Ardeshir, 2-D and 3-D image registration for medical, remote sensing, and industrial applications, Wiley press, 2005. Int J Radiat Oncol Biol Phys 64:1245–1254

Hanley J, Debois MM, Mah D, Mageras GS, Raben A, Rosenzweig K et al (1999) Deep inspiration breath-hold technique for lung tumors the potential value of target immobilization and reduced lung density in dose escalation. Int J Radiat Oncol Biol Phys 45:603–611

Herman MG, Kruse JJ, Hagness CR (2000) Guide to clinical use of electronic portal imaging. JACMP 1(2):38–57

Herman MG, Balter JM, Jaffray DA, McGee KP, Munro P et al (n.d.) Clinical use of electronic portal imaging: report of AAPM radiation therapy committee task group 58. Med Phys 28 (5):712–737

Hollingworth W, Todd CJ, Bell MI, Arafat Q, Girling S, Karia KR, Dixon AK (2000) The diagnostic and therapeutic impact of MRI: an observational multi-centre study. Clin Radiol 55(11):825–831

Hong TS, Welsh JS, Ritter MA, Harari PM et al (1999) Megavoltage computed tomography- an emerging tool for image-guided radiotherapy. Am J of Clinical Oncol 30(6):617–623

Hong TS, Tome WA, Chappell RJ et al (2005) The impact of daily setup variations on head and neck intensity modulated radiation therapy. Int J Radiat Oncol Biol Phys 61:779–788

Houghton F, Benson RJ, Tudor GST et al (2009) An assessment of action levels in imaging strategies in head and neck cancer using TomoTherapy. Are our margins adequate in the absence of image guidance? Clin Oncol 21:720–727

Hunt MA, Schultheiss TE, Desobry GE, Hakki M, Hanks GE (1995) An evaluation of setup uncertainties for patients treated to pelvic sites. Int J Radiat Oncol Biol Phys 32:227–233

http://www.cyberknife.com/uploadedFiles/CyberKnife_Overview/500929.A_CyberKnife_Patient_Brochure_FINAL.pdf (n.d.)

Jaffray DA, Bissonnette JP, Craig T (1999) X-ray imaging for verification and localization in radiation therapy in modern technology of radiation oncology (suppl. 1). Modern technology of radiation oncology. Medical Physics Pub, Madison, WI. Isbn: 0–944838–38-3

Jin JY, Yin FF, Tenn S, Medin PM, Solberg TD (2008) Use of the brainlab exacTrac X-ray 6D system in image-guided radiotherapy. Med Dosim 33:124–134

Kapatoes JM, Olivera GH, Reckwerdt PJ, Fitchard EE, Schloesser EA, Mackie TR (1999) Delivery verification in sequential and helical tomotherapy. Phys Med Biol 4:1815–1841

Kapatoes JM, Olivera GH, Ruchala KJ, Smilowitz JB, Reckwerdt PJ, Mackie TR (2001a) A feasible method for clinical delivery verification and dose reconstruction in tomotherapy. Med Phys 28(4):528–542

Kapatoes JM, Olivera GH, Balog JP, Keller H, Reckwerdt PJ, Mackie TR (2001b) On the accuracy and effectiveness of dose reconstruction for tomotherapy. Phys Med Biol 46:943–966

Keall PJ, Kini VR, Vedam SS, Mohan R (2002) Potential radiotherapy improvements with respiratory gating. Australas Phys Eng Sci Med 25:1–6

Keall PJ, Mageras GS, Balter JM et al (2006) The management of respiratory motion in radiation oncology report of AAPM task group 76. Med Phys 33:3874–3900

Kijewski PK, Bjarngard BE (1978) The use of computed tomography data for radiotherapy dose calculations. Int J Radiat Oncolo Biol Phys 4:429

Killoran JH, Kooy HM, Gladstone DJ, Welte FJ, Beard CJ (1997) A numerical simulation of organ motion and daily setup uncertainties: implications for radiation therapy. Int J Radiat Oncol biol Phys 37:213–221

Kim DJ, Murray BR, Halperin R, Roa WH (2001) Held-breath self-gating technique for radiotherapy of non-small-cell lung cancer: a feasibility study. Int J Radiat Oncol Biol Phys 49:43–49

King CR, Freeman D, Kaplan I, Fuller D, Bolzicco G, Collins S, Meier R, Wang J, Kupelian P, Steinberg M, Katz A (2013) Stereotactic body radiotherapy for localized prostate cancer: pooled analysis from a multi-institutional consortium of prospective phase II trials. Radiother Oncol 109:217–221

Kubo HD, Hill BC (1996) Respiration gated radiotherapy treatment: a technical study. Phys Med Biol 41:83–91

Kuriyama K, Onishi H, Sano N et al (2003) A new irradiation unit constructed of self-moving gantry-CT and Linac. Int J Radiat Oncolo Biol Phys 55:428–435

Kutcher GJ et al (1994) Comprehensive QA for radiation oncology: report of AAPM radiation therapy committee task group 40. Med Phys 21:581–618

Langen KM, Pouliot J, Anezinos C, Aubin M, Gottschalk AR, Hsu IC, Lowther D, Liu YM, Shinohara K, Verhey LJ, Weinberg V, 3rd Roach M (2003) Evaluation of ultrasound-based prostate localization for image-guided radiotherapy. Int J Radiat Oncol Biol Phys 57:635–644

Langen KM, Meeks SL, Poole DO et al (2005) The use of megavoltage CT (MVCT) images for dose recomputations. Phys Med Biol 50:4259–4276

Lax H, Blomgren I, Naslund, Svanstrom R (1994) Stereotactic radiotherapy of malignancies in the abdomen: methodological aspects. Acta Oncol 33:677–683
Lee C, Langen KM, Lu W et al (2008) Assessment of parotid gland dose changes during head and neck cancer radiotherapy using daily megavoltage computed tomography and deformation image registration. Int J Radiat Oncol Biol Phys 71:1563–1571
Leong J (1986) Use of digital fluoroscopy as an on-line verification device in radiation therapy. Phys Med Biol 31:985–992
Li AX, Stepaniak C, Gore E (2006) Technical and dosimetric aspects of respiratory gating using a pressure-sensor motion monitoring system. Med Phys 33:145–154
Li XA, Qi XS, Pitterle M (2007) Interfractional variations in patient setup and anatomic change assessed by daily computed tomography. Int J Radiat Oncol Biol Phys 68:581–591
Lo SS, Fakiris AJ, El C et al (2010) Stereotactic body radiation therapy: a novel treatment modality. Nat Rev Clin Oncol 7(1):44–54
Ma CM, Paskalev K (2006) In-room CT techniques for image-guided radiation therapy. Med Dos 31:30–39
Mageras GS, Pevsner A, Yorke ED et al (2004) Measurement of lung tumor motion using respiration-correlated CT. Int J Radiat Oncol Biol Phys 60:933–941
Magnetic resonance, a critical peer-reviewed introduction. European Magnetic Resonance Forum. Retrieved 16 Nov 2013
Manning MA, Wu Q, Cardinale RM et al (2001) The effect of setup uncertainty on normal tissue sparing with IMRT for head-and-neck cancer. Int J Radiat Oncol Biol Phys 51:1400–1409
Marks JE, Haus AG, Sutton HG, Griem ML (1974) Localization error in the radiotherapy of Hodgkin's disease and malignant lymphoma with extended mantle fields. Cancer 34:83–90
Meeks SL, Harmon JF, Langen KM, Willoughby TR, Wagner TH, Kupelian PA (2005) Performance characterization of megavoltage computed tomography imaging on a helical tomotherapy unit. Med Phys 32(8):2673–2681
Merboldt K, Hanicke W, Frahm J (1969) Self-diffusion NMR imaging using stimulated echoes. J Magn Reson 64(3):479–486
Morin O, Gillis A, Chen J et al (2005) Megavoltage cone-beam CT: system description and clinical applications. Med Dosim 31:51–61
Moseley DJ, Pouliot J, Sonke JJ, Yoo S (2012) Quality assurance for image-guided radiation therapy utilizing CT-based technologies: a report of the AAPM TG-179. Med Phys 39 (4):1946–1963. doi:10.1118/1.3690466
Mundt AJ, Roeske JC (2006) In: Bortfeld T, Schmidt-Ullrich R (eds) Image-guided radiation therapy. Springer, Berlin Heidelberg
Munro P (1995) Portal imaging technology: past. Present and Future Semin Radiat Oncol 5:115–133
Munro P, Rawlinson JA, Fenster A (1990) A digital fluoroscopic imaging device for radiotherapy localization. Int J Radiat Oncol Biol Phys 18:641–649
Murphy MJ (2004) Tracking moving organs in real time. Semin Radiat Oncol 14:91–100
Murphy MJ, Balter J, Balter S et al (2007) The management of imaging dose during image-guided radiotherapy: report of the AAPM task group 75. Med Phys 34:4041–4063
Murphy MJ, Balter J, Balter S, BenComo JA, Das IJ et al (n.d.) The management of imaging dose during image-guided radiotherapy: report of the AAPM task group 75. Med Phys 34 (10):4041–4063
National radiotherapy implementation group report (2012) Image guided Radiotherapy (IGRT) guidance for implementation and use
Negoro Y, Nagata Y, Aoki T, Mizowaki T, Araki N et al (2001) The effectiveness of an immobilization device in conformal radiotherapy for lung tumor: reduction of respiratory tumor movement and evaluation of the daily setup accuracy. Int J Radiat Oncol Biol Phys 50:889–898
Nehmeh SA, Erdi YE, Rosenzweig KE, Schoder H, Larson SM, Squire OD, Humm JL (2003) Reduction of respiratory motion artifacts in PET imaging of lung cancer by respiratory

correlated dynamic PET: methodology and comparison with respiratory gated PET. J Nucl Med 44(10):1644–1648
Neicu T, Shirato H, Seppenwoolde Y, Jiang SB (2003) Synchronized moving aperture radiation therapy (SMART): average tumour trajectory for lung patients. Phys Med 48:587–598
Neylon J, Qi XS, Sheng K, Staton R, Pukala J, Manon R, Low DA, Kupelian P, Santhanam A (2015) A GPU based high-resolution multi-level biomechanical head and neck model for validating deformable image registration frameworks. Med Phys 42(1):232. doi:10.1118/1.4903504
Nishi T, Nishimura Y, Shibata T, Tamura M, Nishigaito N, Okumura M (2013) Volume and dosimetric changes and initial clinical experience of a two-step adaptive intensity modulated radiation therapy (IMRT) scheme for head and neck cancer. Radiother Oncol 106:85–89
Nuyttens JJ, van de Pol M (2012) The CyberKnife radiosurgery system for lung cancer. Expert Rev Med Devices 9(5):465–475
Operator's manual for ViewRay system 3.5 (2014), Document No. L-0009
Pan T (2005) Comparison of helical and cine acquisitions for 4DCT imaging with multi-slice CT. Med Phys 32:627–634
Pan T, Lee T, Rietzel E et al (2004) 4DCT imaging of a volume influenced by respiratory motion on multiple-slice CT. Med Phys 31:333–340
Peng C, Kainz K, Lawton C, Li XA (2008) A comparison of daily megavoltage CT and ultrasound image guided radiation therapy for prostate cancer. Med Phys 35(12):5619–5628
Pluim JP, Maintz JBA, Viergever MA (2003) Mutual-information-based registration of medical images: a survey. IEEE Trans Med Imaging 22:986–1004
Pouliot J, Bani-Hashemi A, Chen J et al (2005) Low-dose megavolt- age cone-beam CT for radiation therapy. Int J Radiat Oncol Biol Phys 61:552–560
Prescribing, recording and reporting photon beam therapy (1999) (Supplement to ICRU Report 50):62
Qi XS, Hu A, Lee SP, Lee P, DeMarco J, Li XA, Steinberg ML, Kupelian P, Low D (2013a) Assessment of interfraction patient setup for head-and-neck cancer intensity modulated radiation therapy using multiple computed tomography-based image guidance. Int J Radiat Oncol Biol Phys 86(3):432–439
Qi XS, Wu ST, Newman F, Li AX, Hu AY (2013b) Evaluation of interfraction patient setup errors for image-guided prostate and head-and-neck radiotherapy using kilovoltage cone beam and megavoltage fan beam computed tomography. J Radiotherapy in Practice 12:334–343
Qi XS, Santhanam A, Neylon J et al (2015) Near real-time assessment of anatomic and dosimetric variations for head-and-neck radiotherapy via a GPU-based dose deformation framework. Int J Radiat Oncol Biol Phys 92(2):415–422
Rietzel E, Pan T, Chen GT (2005) Four-dimensional computed tomography: image formation and clinical protocol. Med Phys 32(4):874–889
Ruchala K, Olivera GH, Kapatoes J (2002) Limited-data image registration for radiotherapy positioning and verification. Int J Radiat Oncol Biol Phys 54:592–605
Schwartz DL, Ford EC, Rajendran J et al (2005) FDG-PET/CT-guided intensity modulated head and neck radiotherapy: a pilot investigation. Head Neck 27(6):478–487
Schwartz DL, Garden AS, Thomas J, Chen YP, Zhang YB et al (2012) Adaptive radiotherapy for head-and-neck cancer: initial clinical outcomes from a prospective trial. Int J Radiat Oncol Biol Phys 83:986–993
Shirato H, Shimizu S, Kitamura K, Nishioka T et al (2000) Four-dimensional treatment planning and fluoroscopic real-time tumor tracking radiotherapy for moving tumor. Int J Radiat Oncol Biol Phys 48:435–442
Spratt DE, Diaz R, McElmurray J et al (2010) Impact of FDG PET/CT on delineation of the gross tumor volume for radiation planning in non-small cell lung cancer. Clin Nucl Med 35(4):237–243
Srinivasan K, Mohammadi M, Shepherd J (2014) Applications of Linac-mounted kilovoltage cone-beam computed tomography in modern radiation therapy: a review. Pol J Radiol 79:181–193

Stutzel J, Oelfke U, Nill S (2008) A quantitative image quality comparison of four differernt image guided radiotherapy devices. Radiother Oncol 86:20–24

Taylor DG, Bushell MC (1985) The spatial mapping of translational diffusion coefficients by the NMR imaging technique. Phys Med Biol 30(4):345–349

Thieke C, Malsch U, Schlegel W, Debus J, Huber P, Bendl R, Thilmann C (2006) Kilovoltage CT using a Linac-CT scanner combination. Br J Radiol 79:S79–S86

Uematsu M, Fukui T, Shioda A et al (1996) A dual computed tomography and linear accelerator unit for stereotactic radiation therapy: a new approach without cranially fixated stereotactic frame. Int J Radiat Oncol Biol Phys 35:587–592

Underberg RWM, Lagerwaard FJ, Slotman BJ et al (2005) Benefits of respiration-gated stereotactic radiotherapy for stage I lung cancer—an analysis of 4DCT data sets. Int J Radiat Oncol Biol Phys 62:554–560

Verellen D, Ridder MD, Storme G (2008) A (short) history of imaged-guided radiotherapy. Radiother Oncol 86:4013

ViewRay system Brochure (n.d.) http://www.viewray.com/product/L0013_RevCMRIdian+Overiew+Brochure-2.pdf

Wong W, Sharpe MB, Jaffray DA, Kini VR, et al The use of active breathing control (ABC) to reduce margin for breathing motion., Int J Radiat Oncol Biol Phys 1999;44:911–919

Wong JR, Grimm L, Uematsu M, et al (2001) Treatment of lung tumor with stereotactic radiation therapy using the world's first PRIMATOM system: a case report. Electromedia 69:127–130

Wu Q, Chi Y, Chen P, Krauss J, Yan D, Martinez A et al (2009) Adaptive replanning strategies accounting for shrinkage in head and neck IMRT. Int J Radiat Oncol Biol Phys 75:924–932

Xing L, Thorndyke B, Schreibmann E et al (2006) Overview of image-guided radiation therapy. Med Dosim 31:91–112

Yan D (2008) Developing quality assurance processes for image-guided adaptive radiation therapy. Int J Radiat Oncol Biol Phys 71:S28–S32

Yan D (2010) Adaptive radiotherapy: merging principle into clinical practice. Semin Radiat Oncol 20:79–83

Yang Y, Schreibmann E, Li T, Wang C, Xing L (2007) Evaluation of on-board kV cone -beam CT (CBCT)-based dose calculation. Phys Med Biol 52(3):685–705

Zelefsky MJ, Fuks Z, Happersett L, Lee HJ et al (2000 Jun) Clinical experience with intensity modulated radiation therapy (IMRT) in prostate cancer. Radiother Oncol 55:241–249

Zitova B, Flusser J (2003) Image registration methods: a survey. Image Vis Comput 21:977–1000

Chapter 6
Introduction to Radiological Images

Sikander M. Mirza

Contents

6.1 Introduction 175
6.2 X-ray Generator 176
6.3 Attenuation 178
6.4 Collimators 180
6.5 Anti-scatter Grids 180
6.6 Screens 182
6.7 Photo-stimulable Phosphor (PSP) 184
6.8 Image Quality Measures 186
6.9 Tomographic Projections 190
References 198

6.1 Introduction

Most of imaging modalities in medical science map some spectroscopic property of object onto sensor. The electromagnetic radiations have widely been used for this purpose, and the corresponding imaging modalities use emission, absorption, scattering, or reflection of these radiations. The X-ray radiography, positron emission tomography, fluorescence imaging, and magnetic resonance imaging (MRI) are few examples of the electromagnetic imaging. The electromagnetic spectrum covers a wide range of wavelengths and frequencies as shown in Fig. 6.1.

S.M. Mirza, PhD (✉)
Department of Physics & Applied Mathematics, Pakistan Institute of Engineering & Applied Sciences, Nilore, Islamabad, Pakistan
e-mail: sikander.m.mirza@gmail.com

M. Maqbool (ed.), *An Introduction to Medical Physics*, Biological and Medical Physics, Biomedical Engineering, DOI 10.1007/978-3-319-61540-0_6

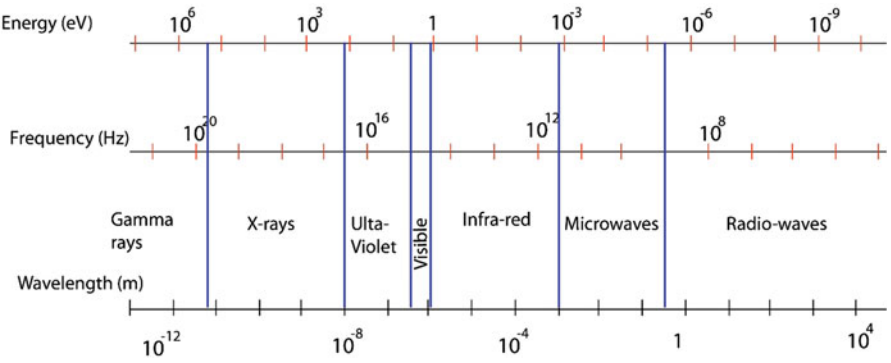

Fig. 6.1 The electromagnetic spectrum in energy, frequency, and wavelength ranges

6.2 X-ray Generator

In clinical environment, X-ray radiographs are obtained using X-ray generator which has X-ray tube at the heart of generation process. It is essentially a vacuum diode valve with an evacuated glass tube containing two electrodes called anode and cathode. The cathode is a filament heated by passage of current, and electrons are released by thermionic emission. These tend to collect around the cathode, forming space charge and inhibiting further emission of electrons. The anode, placed at some distance from cathode, is held at positive potential relative to cathode and attracts these electrons. At low voltage, some of electrons stream out of space charge and reach the anode, while cathode keeps on releasing electrons. Consequently, current is established from cathode to anode. The space charge near the cathode tends to limit the value of this current. As anode voltage is increased, more and more electrons escape the space charge region and tube current increases, while the space charge tends to be depleted. At certain high anode voltage, the space charge disappears altogether, and the tube current reaches maximum value called the "saturation current." The ultimate value of this saturation tube current proportionately depends on the filament heating and in turn on the filament heating current.

The electrons are accelerated as they move from cathode to anode gaining kinetic energy. Just before hitting anode, they have maximum value of kinetic energy (K.E.):

$$\text{K.E.} = \frac{1}{2}mv^2 = eV, \tag{6.1}$$

where m is the mass of electron, v is the speed of electron just before hitting the anode, e is the value of electronic charge, and V is the anode voltage which is typically in tens of keV range. For example, in case of mammography, the value of V is around 30 keV; for chest X-ray, it is around 70 keV; and for skull X-ray,

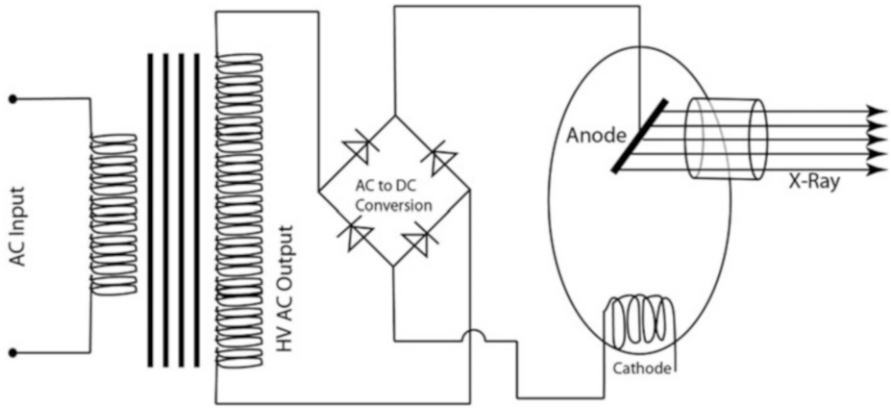

Fig. 6.2 A circuit diagram of a typical X-ray generator highlighting the step-up transformer, the rectifier, and the X-ray tube

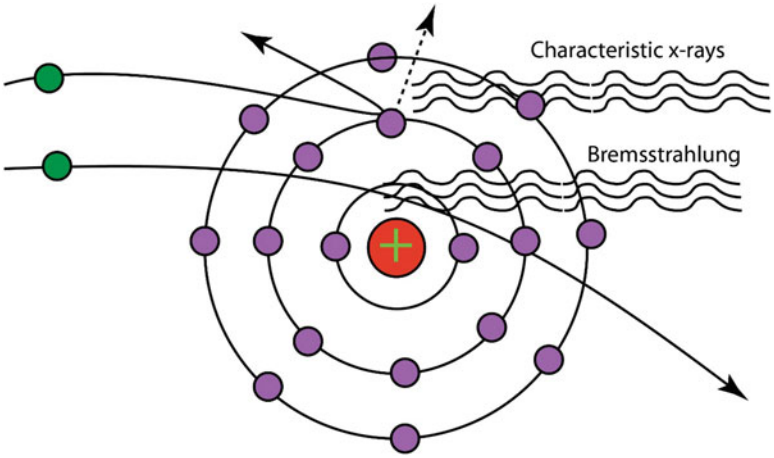

Fig. 6.3 Electrons hitting the anode region can possibly emit Bremsstrahlung or lead to emission of characteristic X-rays by ionizing the anode atoms

120 *keV* is needed. A simplified circuit diagram for a typical X-ray generator is shown in Fig. 6.2.

The electron undergoes abrupt deceleration as it hits the anode material and emits *Bremsstrahlung* (German word for "breaking radiations"). These form a continuous spectrum with maximum energy equal to the kinetic energy of electron hitting the anode. Some of these electrons hit the anode atoms and ionize them which subsequently deionize and emit characteristic X-rays with discrete lines in spectrum. Both of these processes are shown schematically in Fig. 6.3.

For typical X-ray machine, the Bremsstrahlung emission dominates the emitted X-ray intensity, while the fraction emitted as characteristic X-rays is relatively

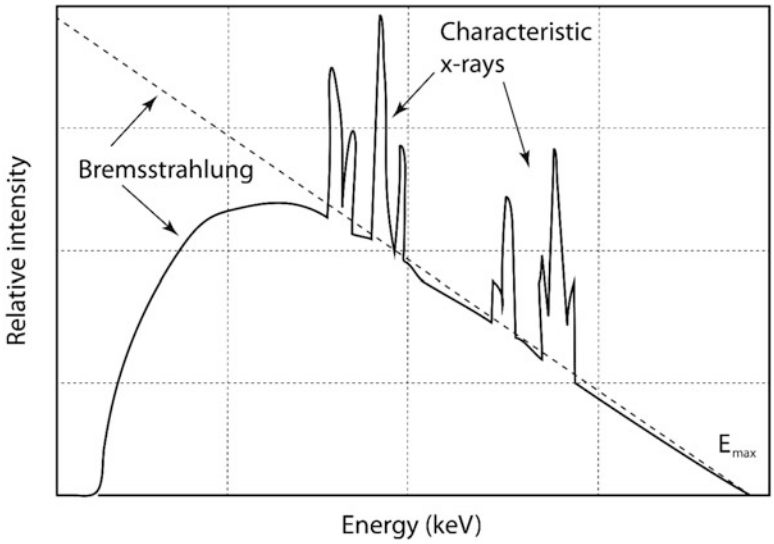

Fig. 6.4 Sketch of a typical emitted X-ray spectrum indicating the relative strengths of Bremsstrahlung and characteristic X-rays

small. For normal diagnostic radiology and for therapy, Bremsstrahlung kind of X-rays is well suited. However, for special applications, in relatively small number of cases, the characteristic X-rays find their use. The emitted X-ray spectrum from a typical X-ray machine is sketched in Fig. 6.4.

6.3 Attenuation

6.3.1 Major Types of Interactions

Incident beam of X-rays interacts with the matter placed in its path via photoelectric effect and Compton scattering. For low-energy X-rays, photoelectric effect dominates, while Compton scattering prevails in the remaining cases. When the energy of X-rays or gamma-rays is higher than threshold value of 1.022 *MeV*, pair production also becomes feasible (Fig. 6.5).

As the result of these interactions, the intensity ($I(x) \equiv$# of photons passing per unit area per unit time) of incident beam decreases, and after penetration Δx distance, it decreases by amount ΔI such that

$$\Delta I \propto -I \times \Delta x, \tag{6.2}$$

and by using μ (attenuation coefficient) as constant of proportionality, we get

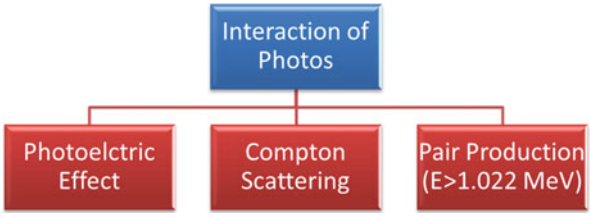

Fig. 6.5 Dominant interaction of X-ray and gamma-ray photons with matter

$$\Delta I = -\mu\, I\, \Delta x, \tag{6.3}$$

which, after integration, yields

$$I(x) = I_0 \exp(-\mu x). \tag{6.4}$$

Starting with incident intensity I_0, the intensity decreases exponentially. Denser materials as well as large thicknesses of materials tend to yield larger decrease in the intensity. While passing through the body, photons get predominantly absorbed in bones while they get transmitted up to some extent while passing through the normal tissue. Consequently, a map of anatomy is projected onto radiographic film or sensitive detector, and a radiographic image is formed.

6.3.2 *Half-Value Layer and Tenth-Value Layer*

Thickness of material attenuating the incident intensity to half of its original value is called half-value layer (HVL), while thickness needed to reduce it to one-tenth of the original value is called tenth-value layer (TVL). Mathematically,

$$\begin{aligned} I = \frac{I_0}{2} &= I_0 \times \exp(-\mu \times \mathrm{HVL}), \\ \Rightarrow \mathrm{HVL} &= \ln(2)/\mu \end{aligned} \tag{6.5}$$

and similarly,

$$\mathrm{TVL} = \frac{\ln(10)}{\mu}. \tag{6.6}$$

We note that a small value of attenuation coefficient implies larger corresponding values of the HVL and TVL.

Solved Example
Statement: Find the HVL and TVL for Al and Cu used as filters in X-ray machines for 80 keV X-rays.

Solution:
Using the Nowotny's "XMuDat" program available freely from the Internet, we find the value of attenuation coefficients:

Material	$\mu/\rho\left(\frac{\text{cm}^2}{\text{gm}}\right)$	$\rho\left(\frac{\text{gm}}{\text{cm}^3}\right)$	Attenuation coefficient (μ, cm^{-1}) at 80 keV
Al	0.2018	2.7	0.54486
Cu	0.7631	8.96	6.83737

Using these data, we get:

Material	HVL (cm)	TVL (cm)
Al	1.272	4.226
Cu	0.1013	0.3367

Due to a larger value of the attenuation coefficient, copper exhibits smaller values of HVL and TVL as compared with the corresponding data for aluminum.

6.4 Collimators

For medical imaging, divergent beams of X-rays must be restricted in order to limit over a desired field of view (FOV). This is achieved with the help of collimators. Additionally, the use of collimator results in a smaller value of patient dose, and also, it tends to reduce the effect of multiple Compton scattered X-ray photons, and consequently, image quality is also improved.

Physically, collimator is generally made of lead or similar high "Z" substance having considerably large value of attenuation coefficient. In simplest configuration, it is composed of two "L-shaped" segments which can slide while placed as a camera aperture. The opening is at some distance from the X-ray "focus," and thereby, a rectangular cone of X-rays is formed defining the FOV at the patient plane. The size of this cone and of the resulting FOV can be adjusted by sliding the "L-shaped" segments of collimator relative to each other.

Such simple arrangements suffer from gradual decrease of X-ray intensity to complete blackness called the penumbra region which is considered unwanted. More complex collimators are designed to overcome such issues.

6.5 Anti-scatter Grids

Due to substantial thickness of the patient body, normally, the X-rays undergo multiple scatterings before getting registered at the radiographic plate. The scattered light results in a decreased value of image contrast and loss of image sharpening which is highly desirable for some situations including heart vein blockage where precise, well-defined boundaries are needed. The anti-scatter

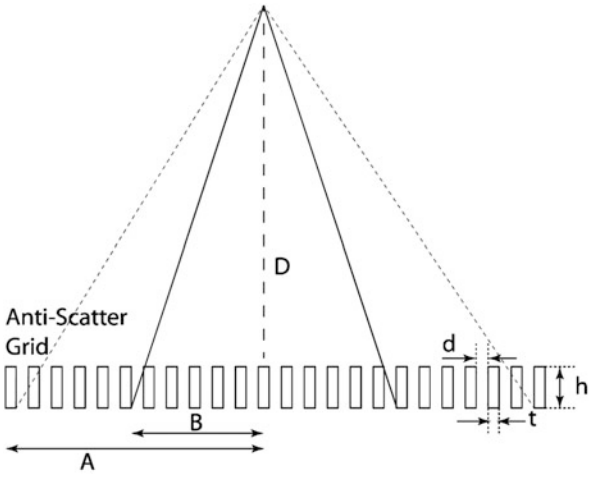

Fig. 6.6 One-dimensional view of the anti-scatter grid indicating the dimensions of lead foils and their mutual separation

grids are used in such cases. These grids are made of lead foils suspended in place by aluminum. The spacing between grid foils is adjusted in order to minimize the passage of scattered X-rays. Let us assume that lead foils of thickness "*t*" each having height "*h*" are separated from each other by distance "*d*" as shown in Fig. 6.6. Then, one can define two following properties of grid:

Grid ratio (GR)

$$\mathrm{GR} = \frac{h}{d}. \tag{6.7}$$

Strip line density (SLD)

$$\mathrm{SLD} = \frac{1}{d+t}. \tag{6.8}$$

The grid ratio is representative of the angle restriction for multiple scattered light control, while the strip line density is indicative of the transparency of the grid itself toward X-rays. As the value of "*d*" (and/or "*t*") is increased, the value of SLD decreases, and at the same time, the value of transparency also decreases.

It is also clear from this figure that for source-to-detector distance (SDD) equal to "*D*," the X-rays can reach up to a critical horizontal distance "*B*" beyond which the shadow of lead foil covers the entire distance "*t*." Using trigonometry, we have

$$\frac{t}{h} = \frac{B}{D}. \tag{6.9}$$

In order to increase the value of distance "*B*" for a broader FOV, the value of SDD must also be increased which entails longer exposure time and the corresponding loss of image quality due to image blur. Another possibility is to

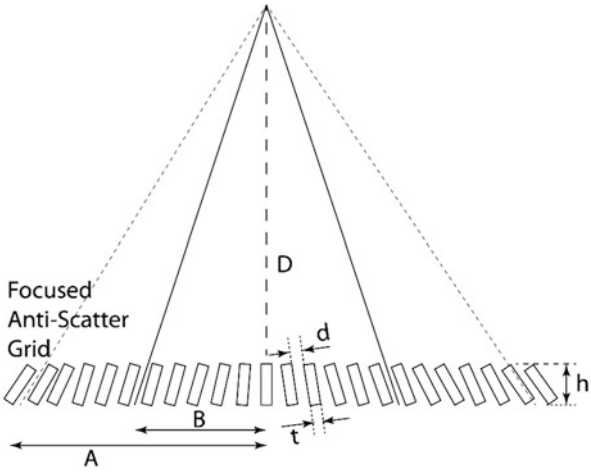

Fig. 6.7 One-dimensional view of the focused anti-scatter grid indicating the dimensions of lead foils and their mutual separation

increase the ratio "t/h" which can be achieved either by increasing the value of "t" or by decreasing the value of "h". Both of them lead to attaining a grid with higher transparency and, at the same time, a grid which allows a higher number of multiply scattered photons thereby killing the original objective for the anti-scatter grids.

The solution to this problem is the use of "focused" grids which have all lead foils aligned to the "focus" as shown in Fig. 6.7.

6.6 Screens

Radiographic film normally used in diagnostic imaging is usually quite thin and consequently does not absorb much of X-rays transmitted by the object. In order to increase their sensitivity, screens are used. These contain scintillation material which converts invisible X-ray photons to multiple numbers of visible range photons. The screens multiply the number of photons while converting them to visible range where the radiographic film sensitivity is high. This double action of screens increases the sensitivity of system by 50-fold typically (Fig. 6.8).

It may also be noted that at low photon count, even the small statistical noise becomes important, while at high photon counts, it becomes insignificant. The screens improve "signal-to-noise ratio" (SNR). One defines the *quantum detection efficiency (QDE)* as the fraction of incident X-ray photons that are absorbed by the screen:

$$\text{QDE} = \frac{\text{No. of photons absorbed in screen}}{\text{Total number of photons incident on screen}}. \tag{6.10}$$

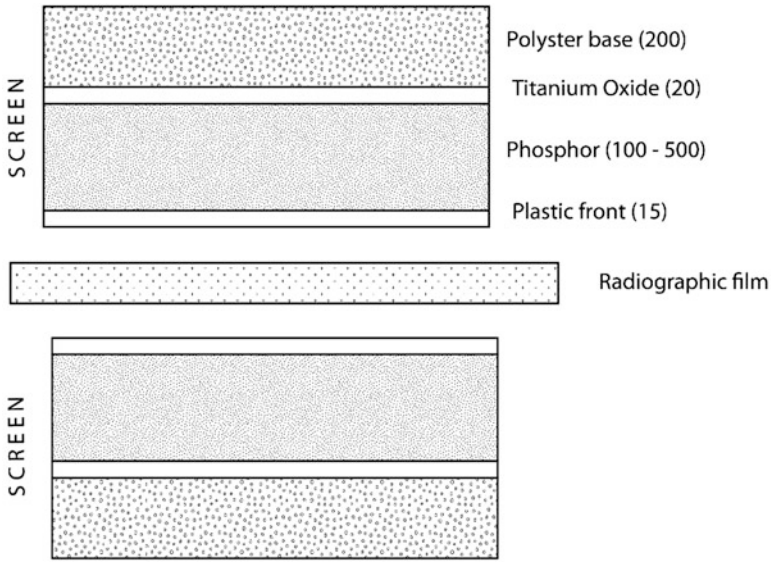

Fig. 6.8 Structural details of typical screen used in radiography (all indicated dimensions are in μm)

The ratio of the number of visible photons absorbed in the film to the number of visible photons emitted by the screen is called the *conversion efficiency (CE)*:

$$\mathrm{CE} = \frac{\text{Number of visible photon absorbed in the film}}{\text{Total number of visible photon emitted by screen}}. \tag{6.11}$$

The overall value of screen efficiency (SE) is the product of the two (Fig. 6.9):

$$\mathrm{SE} = \mathrm{QDE} \times \mathrm{CE}. \tag{6.12}$$

The above figure clearly shows a decreasing trend with increasing X-ray energy for all screen scintillators. The degree of darkness of image on film is quantified by *optical density (OD)* which relates to the corresponding value of *transmittance (T)* such that

$$\mathrm{OD} = \log(1/T). \tag{6.13}$$

A film with 0 value of optical density has 100% transmittance through it, while OD values 1, 2, and 3 have "good exposure," "lung-field," and "very dark" categories correspondingly. A film with OD = 3.5 has maximum possible radiographic darkness.

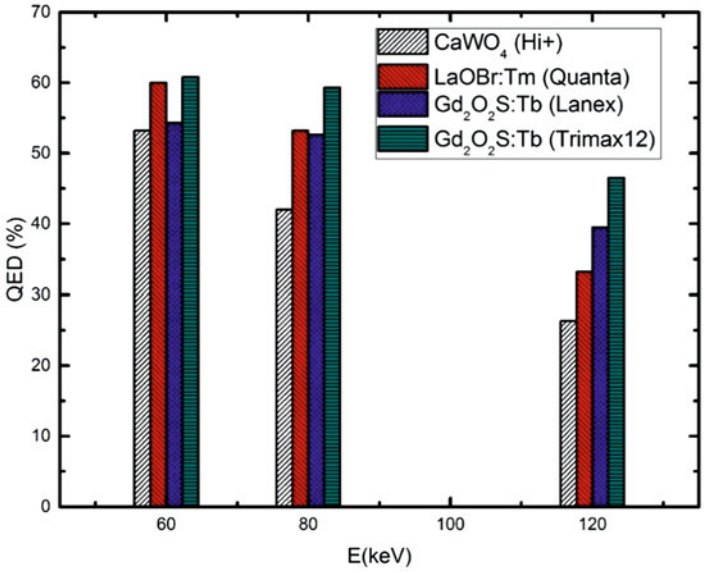

Fig. 6.9 Variation of QED with X-ray energy and type of screen scintillator

6.7 Photo-stimulable Phosphor (PSP)

A class of X-ray scintillators has delayed emission of visible light. It absorbs in incident X-rays in metastable states such that energy becomes stored for a suitable long period of time after the exposure. These metastable states are "read" by stimulus such as laser photons. Many photoluminescence materials exist in nature including ZnS natural diamond, various oxides of silica, and alkali-halides. After exposure to X-rays, sheets of these materials (called image plates, IP for short) store the X-ray energy in the form of latent image which is "read" using laser beam later.

The PSP remains applicable for a wide range of exposure conditions. Consequently, the "retake" frequency of radiographs becomes hugely low.

The image plate is typically barium-fluoro-halide which works as storage medium. The exposure to X-rays leads to the formation of a latent image in the form of electrons trapped in higher energy levels just below conduction band. These electrons can remain trapped in these sites for considerably long times in normal conditions. At reading stage, 633 nm exciting laser beam is used which excites the trapped electrons back to conduction band which subsequently fall to the lower energy levels emitting 390 nm light. The intensity of this visible light is proportional to the incident X-ray intensity for each "pixel." After reading the image plate with laser, the IP is illuminated with light to erase it completely. In this manner, the IP can be reused a large number of times typically exceeding 50,000 cycles.

In the case of PSPs, the workflow does not require any "dark room" or "film processing" delays. Instead, the PSPs are "read" quickly, and instead of a person

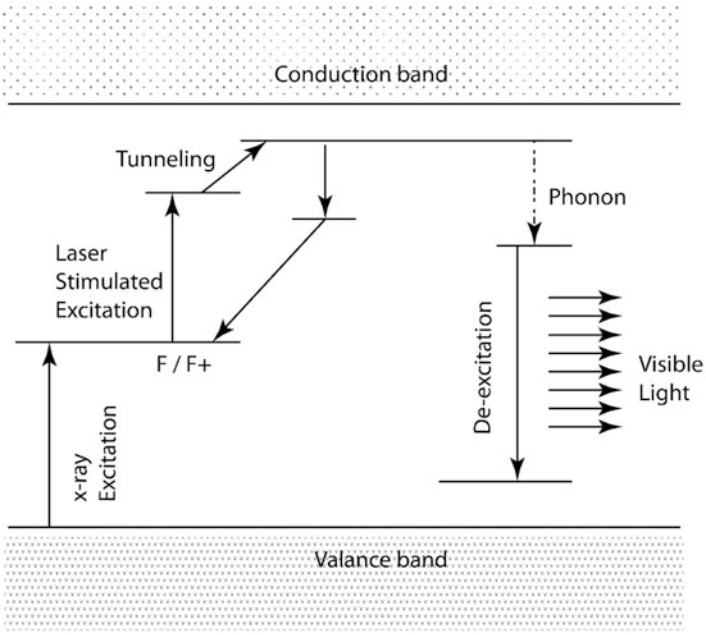

Fig. 6.10 Energy level diagram for excitation through X-ray absorption and subsequent "reading" using laser stimulation (Source: AAPM Report No. 93, 2006)

delivering the processed radiograph to the radiologist, the digital image data is sent instantaneously and, also, saved to permanent storage devices. Note that in conventional radiography, the film is the first thing, while in PSPs, the film storage is the last step (Fig. 6.10).

The detective quantum efficiency (DQE) of PSP is given by the following relation:

$$\mathrm{DQE_{PSP}} = F_{\mathrm{abs}} / \left[(1 + \sigma_{\mathrm{E}})(1 + \sigma_{\mathrm{el}})(1 + \sigma_{\mathrm{S}}) + < N_{\mathrm{PMT}} >^{-1} \right], \tag{6.14}$$

where

F_{abs}= fraction of incident number of photons absorbed in PSP
σ_{E} = coefficient of variation of energy absorbed per X-ray photon in PSP
σ_{el} = coefficient of variation of number of trapped electrons for a given X-ray photon energy in PSP
σ_{S} = coefficient of variation of visible light output for a given number of electrons trapped in PSP
$<N_{\mathrm{PMT}}>$ = average number of photoelectrons detected by PMT per incident X-ray photon

Numerical Example

Statement: Determine the value of detective quantum efficiency (DQE) for PSP using the following data: $\sigma_E = 0.15$, $\sigma_{el} = 0.05$, $\sigma_S = 0.8$, $g = 10$, and $F_{abs} = 0.5$ for normal phosphor, while $F_{abs} = 0.26$ for high-resolution phosphor.

Solution:

As $\mathrm{DQE}_{PSP} = F_{abs}/[(1+\sigma_E)(1+\sigma_{el})(1+\sigma_S) + <N_{PMT}>^{-1}]$,

using the given data,

for normal phosphor, $\mathrm{DQE}_{PSP} = 0.5/[(1+0.15)(1+0.05)(1+0.8)+1/10]$,

we have $\boxed{\mathrm{DQE}_{PSP} = 0.2199 \cong 22\%}$ For high-resolution phosphor,

$$\mathrm{DQE}_{PSP} = 0.26/[(1+0.15)(1+0.05)(1+0.8)+1/10],$$

$$\boxed{\Rightarrow \mathrm{DQE} = \frac{0.26}{2.2735} = 0.114 \cong 11.4\%}$$

6.8 Image Quality Measures

The X-ray image quality indicators typically include various quantitative measures including signal-to-noise ratio (SNR), spatial resolution (SR), line spread function (LSF), modulation transfer function (MTF), and contrast-to-noise ratio (CNR). Each of these measures encompasses some particular attribute of image quality and collectively represents diverse nature of information content of X-ray image.

6.8.1 Signal-to-Noise Ratio (SNR)

The ratio of useful information (signal) to the background (noise) called signal-to-noise ratio represents the degree by which the signal is prominent over the noise. The SNR is affected by statistical distribution (quantum mottle) of X-rays recorded and the spatially nonuniform response of the radiographic film. The value of SNR is dominated by quantum mottle. For a radiograph recorded with tube current value "*I*" with exposure time value "*T*", the value of SNR is given by

$$\mathrm{SNR} \propto \sqrt{IT}. \tag{6.15}$$

Furthermore, the value of SNR shows increasing trend with increase in the kV_p value and thickness of phosphor used in the intensifying screen, while a decreasing trend of SNR is observed with increase in patient body thickness, in the degree of X-ray filtration, and in the degree of absorption in anti-scatter grid.

6.8.2 Spatial Resolution

The ability of radiographic film to show two closely spaced objects separately is called spatial resolution (SR). The value of spatial resolution depends on the following factors:

- *Film grain size:* Slow radiographic films having very small grain size show higher value of SR, while fast films are coarse-grained and exhibit lower value of SR.
- *Thickness of intensifying screens:* The value of SR is affected adversely by thickness of intensifying screen as thicker screens have larger value of light spread function which reduces the value of SR.
- *Focal spot size:* Finite size of focal spot also affects SR adversely since it generates penumbra "P" such that

$$P = f \times (D - H)/H, \tag{6.16}$$

where D is the focal spot distance from detector and H is the distance of the patient body from focal spot. Clearly, it is highly desirable to keep focal spot size as low as possible.

- *Image magnification factor:* A higher value of magnification factor $m = D/H$ also leads to decrease in SR value.

If the ith of above factors leads to contribution R_i toward SR, then, the total resolution is given by

$$R = \sqrt{\sum_{i=1}^{4} R_i^2}. \tag{6.17}$$

6.8.3 Point Spread Function (PSF)

A very small object described by function $O(x, y, z)$ casts image $I(x, y, z)$ in some imaging modality. These are related via expression:

$$I(x, y, z) = O(x, y, z) \otimes h(x, y, z), \tag{6.18}$$

where $h(x, y, z)$ is called point spread function (PSF) and the $\otimes$ operator represents convolution. For ideal imaging system, $I(x, y, z) = O(x, y, z)$ and PSF is represented by delta function. However, all practical imaging systems have intrinsic "noise" which tends to introduce blur in the image through various levels including detector (h_{det}), sampling (h_{samp}), reconstruction (h_{rec}), filter (h_{flt}), etc. The total PSF is

$$h_{\text{tot}} = h_{\text{det}} \otimes h_{\text{samp}} \otimes h_{\text{rec}} \otimes h_{\text{flt}}. \tag{6.19}$$

While the individual components of overall PSF may have different mathematical expressions, the overall PSF may well be approximated by a Gaussian profile in one dimension:

$$h(x) = \frac{1}{\sqrt{2\pi}\,\sigma} \exp\left(-(x - x_o)^2/\sigma^2\right), \tag{6.20}$$

where x_o is the mean or average value of x and σ represents the standard deviation given by

$$\sigma \cong \text{FWHM}/2.36, \tag{6.21}$$

with *FWHM* representing the value of full width at half maximum (spread of Gaussian).

6.8.4 Line Spread Function

For a two-dimensional point spread function PSF(x, y), the line spread function LSF (x) is obtained simply by integrating out the other dimension:

$$\text{LSF}(x) = \int \text{PSF}(x, y)dy. \tag{6.22}$$

The determination of the LSF can be carried out by using line phantom which is typically a wire composed of any high Z-number material such as lead, tungsten, etc. Practically, one can measure the edge spread function (ESF) with the help of a plate placed in the path of X-ray beam. Mathematically, it is convolution of the LSF with a step function (Fig. 6.11).

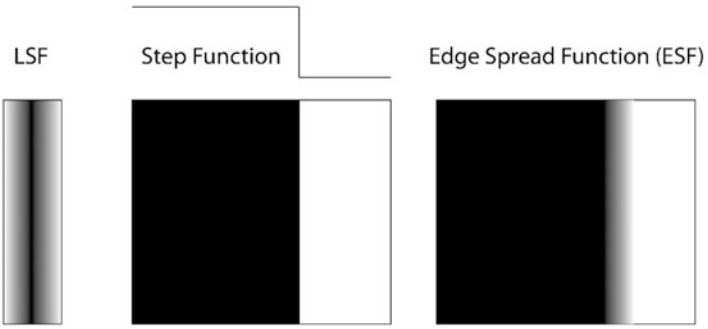

Fig. 6.11 Convolution of LSF with a step function forming the edge spread function

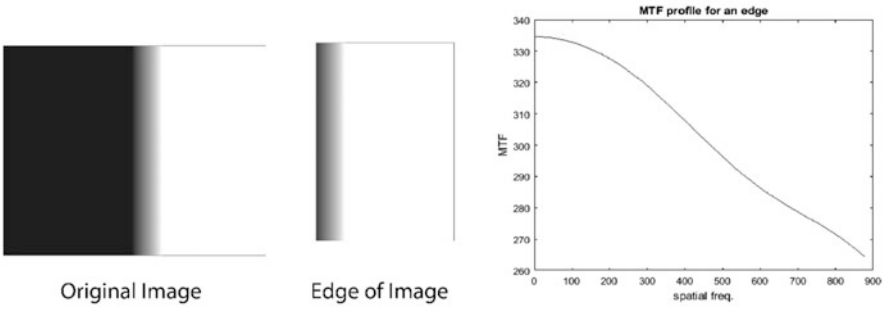

Fig. 6.12 Computed profile of MTF using one-dimensional LSF

6.8.5 Modulation Transfer Function

While the PSF of each component in an imaging system can be quite complicated, taking it from spatial domain to frequency domain makes it easier to combine them. For this purpose, Fourier transform is used:

$$\mathrm{MTF}(k_x, k_y, k_z) = \iiint \mathrm{PSF}(x, y, z)\exp(-j2\pi k_x x)\exp(-j2\pi k_y y)\exp(-j2\pi k_z z) \times dx\, dy\, dz, \tag{6.23}$$

where k_x, k_y, and k_z are spatial frequencies along x, y, and z directions with units cycles/mm or lines/mm (Fig. 6.12). The Matlab code for performing MTF calculations is given below:

```
function getMTF
e=rgb2gray(imread('edge.bmp'));
e=(e); imshow(e(:,2482:end)); figure; %pause;
e=double(e);
esf=e(:,2482);
lsf=gradient(esf);
f=fft(lsf);
mtf=abs(f);
mtf=mtf(1:end/4);
plot(mtf); xlabel('spatial freq.');
ylabel('MTF'); title('MTF profile for an edge');
end
```

6.8.6 *Contrast-to-Noise Ratio*

While the SNR is well established for MRI, the fMRI data does not yield a clear way to use SNR in the same manner. For such type of situations, the use of contrast-to-noise ratio has been proposed. It uses the difference signal in place of signal itself. The image contrast between two regions "A" and "B" is defined as

$$C = (S_A - S_B)/(S_A + S_B), \tag{6.24}$$

where S_A and S_B are image signal intensities in regions "A" and "B," respectively, with "A" as region of interest and "B" as background. The above expression can yield negative values; a better definition could be

$$C = |S_A - S_B|/S_{ref}, \tag{6.25}$$

where S_{ref} represents the value of background signal. For image with a large constant high-intensity offset throughout, the SNR may be high, but a low CNR value will reveal poor image quality.

6.9 Tomographic Projections

The main drawbacks of conventional radiography include its inability to distinguish between objects extended in the direction of X-rays and a high-density material. Both of these may lead to same result on radiographic film. Another drawback is the size of image on the radiographic film which is dependent on the location of the object. If it is closer to focal spot, the image will be larger in size, and if it is closer to the radiographic film, the size becomes closer to its actual size. Both of these limitations are overcome in the tomographic imaging technique. The name "tomo" is derived from Greek where it means a section or a cut. In tomography, projections of X-ray intensity in a perpendicular direction to the viewing direction are used to reconstruct the "density" map of the object as shown in Fig. 6.13.

The collection of projections for various angles $0^o - 180^o$ is called sinogram which is same as the Radon transform of "density" or "μ" profile of the section ("tomo") being studied. The corresponding inverse Radon transform yields the required "density" or "μ" profile. The coordinates (r, s) in the rotated frame are related to the standard coordinates (x, y) as

$$r = x\cos\theta + y\sin\theta, \tag{6.26}$$

$$s = -x\sin\theta + y\cos\theta. \tag{6.27}$$

The Radon transform of the "μ" profile $f(x, y)$ of an object is the collection of ray sums for all angles $\theta \in [0, 180^o]$. If the "abnormality" is in asymmetric position, then the corresponding Radon transform shows a higher value for same set of "r"

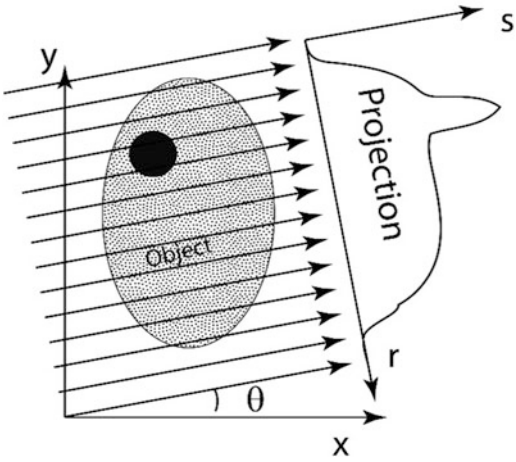

Fig. 6.13 Schematic view of a projection for angle θ of a brain-shaped object containing tumor

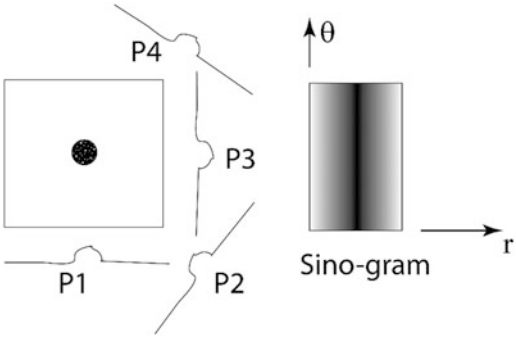

Fig. 6.14 An object with "abnormality" at the center of symmetry along with the corresponding sinogram (Radon transform) of the object

values for all angles. The corresponding data shows symmetric profile in $F(r, s)$ map for all angles as shown in Fig. 6.14.

6.9.1 Image Reconstruction Using Back Projection

Using the sinogram $F(r, s)$, the image reconstruction $f(x, y)$ can be carried out using the simple technique of back projection. In this method, each projection is smeared back onto the pixels by adding the ray-sum values on the previous pixel data. Finally, the data is normalized. This is illustrated in the following example.

Numerical Example
Let us start with a known profile of μ values:

8	3
5	7

The corresponding ray-sum data is shown below:

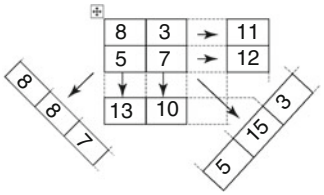

Now, let us start with a blank slate and start back projection by using horizontal direction first:

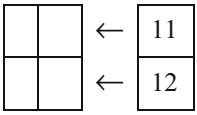

After back projection, the data becomes:

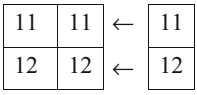

Now, let us project in vertical direction:

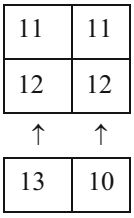

which, after projection, becomes:

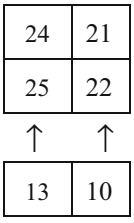

Now, we back project right diagonal data (5,15,3) and it becomes:

39	24
30	37

Finally, we back project the left diagonal data (8,8,7) and it becomes:

47	32
38	44

which, after normalization, becomes:

6.7	4.5
5.4	6.3

which resembles the original (starting data). The results will show improvement if more number of projections are used. The only drawback of this technique is the streaking artifact which arises simply due to smearing of the data back to the region which did not contribute originally. The back projection results in smeared data along the projection direction.

The Shepp-Logan phantom is commonly used for the assessment of the performance of various image reconstruction algorithms (Fig. 6.15). It is a

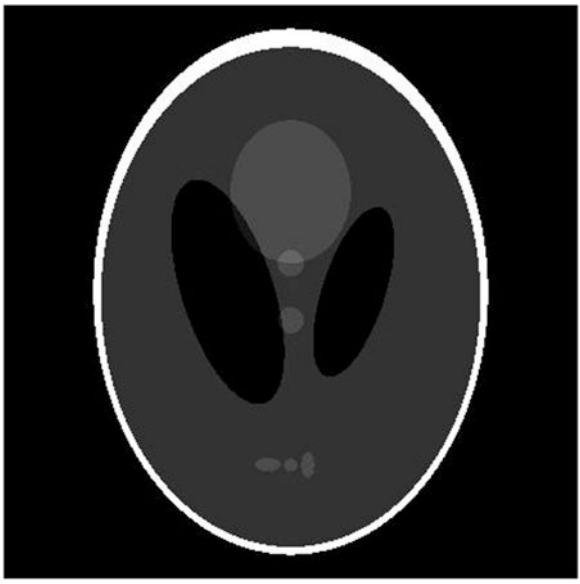

Fig. 6.15 Image view of Shepp-Logan phantom using Matlab®

mathematically constructed phantom, and as such, it does not have any intrinsic data errors. It represents a section of the skull viewed from the top, and the resulting oval-shaped domain has few "abnormalities" representing tumors. The idea is to check if the reconstructed image is also crisp and clear when compared with the original data. The Matlab code for viewing Shepp-Logan phantom is:

```
P = phantom('Modified Shepp-Logan',200);
imshow(P).
```

For taking the Radon transform (sinogram) of the Shepp-Logan phantom, the following code can be used:

```
function test1
P = phantom('Modified Shepp-Logan',400);
%imshow(P)
theta=[0:180];
[R,xp] = radon(P,theta);
iptsetpref('ImshowAxesVisible','on')
imshow(R,[],'Xdata',theta,'Ydata',xp,...
            'InitialMagnification','fit')
xlabel('\theta (degrees)')
ylabel('x''')
colormap(hot), colorbar
iptsetpref('ImshowAxesVisible','off')
end
```

The resulting image is (Fig. 6.16):

Note the sinusoidal wiggles in the sonogram which are due to nonsymmetric data in the phantom. Now, the projection data (sonogram or Radon-transformed data) needs to be inverted into the original phantom profile. For this purpose, one can use the "iRadon" function in Matlab. If crude steps in angles are used, then the reconstructed image shows streaking artifacts. In the following code, a 10^o step size has been used and the results are shown (Fig. 6.17):

```
function test1
P = phantom('Modified Shepp-Logan',400);
%imshow(P)
theta=[0:10:180];
[R,xp] = radon(P,theta);
subplot(121);imagesc(theta,xp,R); colormap(hot); colorbar
xlabel('\theta'); ylabel('x\prime');

I = iradon(R,10); subplot(122); imshow(I);
end
```

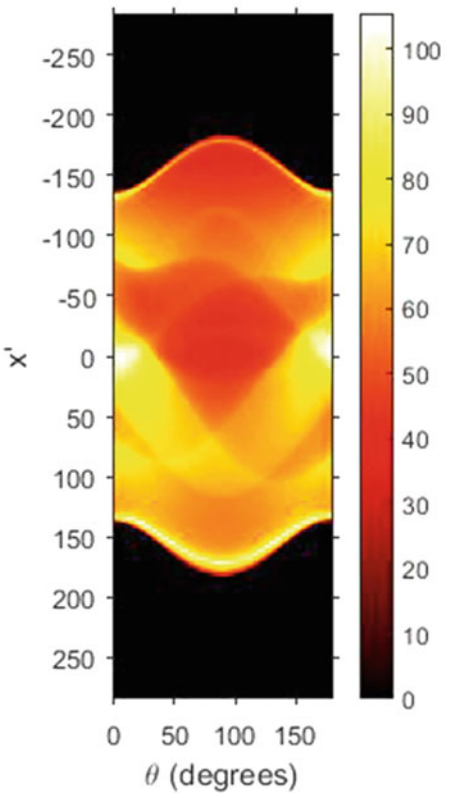

Fig. 6.16 Radon transform of the Shepp-Logan phantom for $\theta \in [0, 180^o]$ range

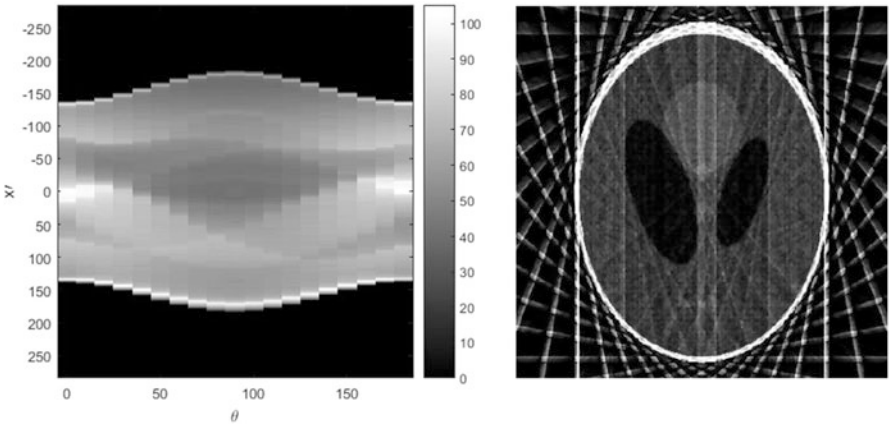

Fig. 6.17 The inverse Radon transform of the Shepp-Logan phantom using crude angular steps ($\Delta\theta = 10^o$)

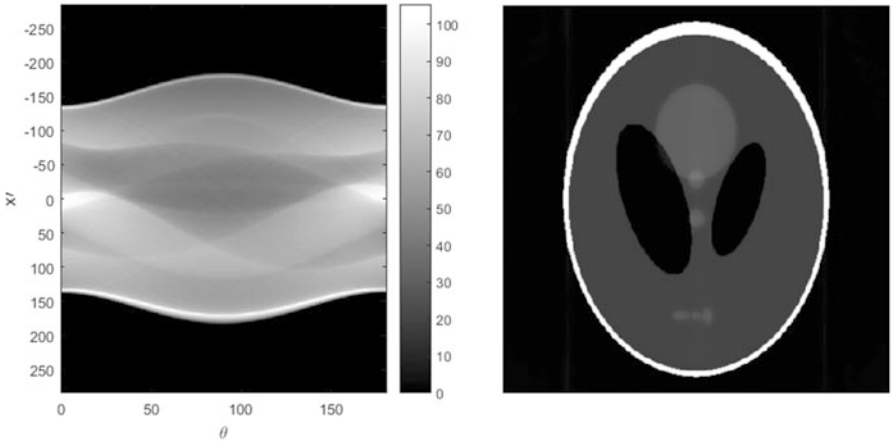

Fig. 6.18 As the angular step size is reduced, the streaking artifacts in the reconstructed image tend to disappear ($\Delta\theta = 1^o$)

For smaller angular steps, the streaking artifacts tend to disappear (Fig. 6.18):

```
function test1
P = phantom('Modified Shepp-Logan',400);
%imshow(P)
theta=[0:1:180];
[R,xp] = radon(P,theta);
subplot(121);imagesc(theta,xp,R); colormap(hot); colorbar
xlabel('\theta'); ylabel('x\prime');

I = iradon(R,1); subplot(122); imshow(I);
end
```

6.9.2 *Filtered Back Projection*

The streaking artifact always affects the reconstructed image. For correction, Ramachandran-Lakshminarayanan (Ram-Lak) proposed a filter which has negative lobes just around the central peak:

$$h(r) = \frac{1}{2dr^2}\left[\sin c\left(\frac{r}{\mathrm{dr}}\right) - \frac{1}{2}\sin c^2\left(\frac{r}{2\mathrm{dr}}\right)\right], \tag{6.28}$$

where dr is sampling interval along r axis. Graphically, we have (Fig. 6.19):

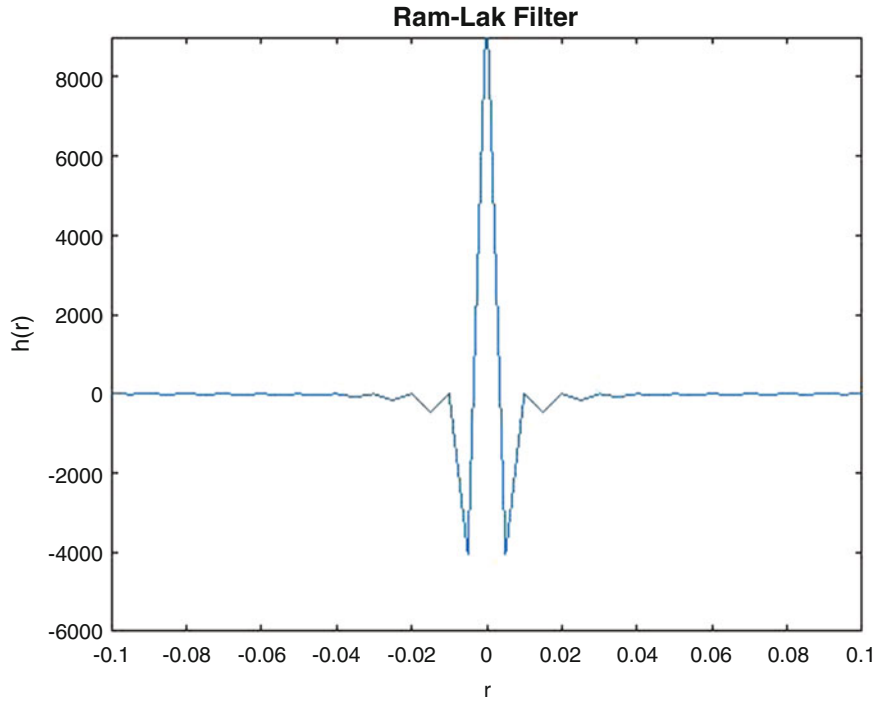

Fig. 6.19 Ram-Lak filter commonly used for removing streaking artifact in the back projection-based image reconstruction

Fig. 6.20 Comparison of reconstructed image without and with Ram-Lak filter

Matlab code for comparing the effect of Ram-Lak filter on reconstructed image and the corresponding output is given below (Fig. 6.20):

```
function test1
P = phantom('Modified Shepp-Logan',400);
%imshow(P)
theta=[0:1:180];
[R,xp] = radon(P,theta);

subplot(131); imshow(P,[]); title('Original');
I = iradon(R,1,'nearest','none'); subplot(132); imshow(I,[]); title('Un-Filtered');
I2 = iradon(R,1,'nearest','Ram-Lak'); subplot(133); imshow(I2,[]); title('Ram-Lak Filtered');
end
```

References

Buhr E, Gnther-Kohfahl S, Neitzel U (2003) Simple method for modulation transfer function determination of digital imaging detectors from edge images. Proc Of SPIE 5030:877–884

Cunningham IA, Reid B (1992) Signal and noise in modulation transfer function determinations using the slit, wire and edge techniques. Med Phys 19:1037–1044

Doyle P, Martin CJ, Gentle D (2006) Application of contrast-to-noise ratio in optimizing beam quality of digital chest radiography: comparison of experimental measurements and theoretical simulations. Phys Med Biol 51:2953–2970

Fujita H, Tsai DY, Itoh T, Doi K, Morishita J, Ueda K, Ohtsuka A (1992) A simple method for determining the modulation transfer function in digital radiography. IEEE Trans Med Imaging 11:34–39

Prabhat P, Arumugam S, Madan VK (2012) Filtering in filtered backprojection computerized tomography. Proc. Natl., Conf. NCNTE-2012 at C.R.I.T., Vashi, Navi Mumbai, 24–25 Feb 2012

Samei E, Flynn MJ (1997) Physical measures of image quality in photostimulable phosphor radiographic systems. SPIE 3032:328–338

Sandborg M, Dance DR, Carlsson GA, Persliden J (1993) The choice of anti-scatter grids in diagnostic radiology: the optimization of image quality and absorbed dose, Dept. of Radiation Physics, Linköping University, US, ISSN 1102–1799

Suetens P (2009) Fundamentals of medical imaging, 2nd edn. Cambridge University Press, Cambridge

Chapter 7
Mammography

Bing Ma

Contents

7.1 Introduction 199
7.2 Interactions Between X-Rays and Breast Tissues 202
7.3 Imaging System 205
7.4 Digital Mammography 217
References 218

7.1 Introduction

Statistics show that about one in eight women will develop invasive breast cancer in her lifetime in the United States. While there has been a decline in the mortality rate from breast cancer in recent years, it is still the second leading cause of cancer death in women according to the American Cancer Society (Siegel et al. 2014). The bright side is that breast cancer is one of the most treatable malignancies when detected early. If a patient's breast cancer is discovered and diagnosed in its early stages when tumors are small and local, the chance for successful treatment is close to 100%. Therefore, early detection of abnormal breast lesions is crucial for patient's long-term survival and thus reducing mortality (Swedish Organized Service Screening Evaluation, G 2006; Tabar et al. 2003; Tabar et al. 2011). Most cancer experts agree that among a variety of breast screening technologies, mammography is currently the most effective image modality for the early detection of breast cancer for its high sensitivity, excellent benefit to risk ratio, low cost, and low radiation exposure (Nyström et al. 2002; Tabar et al. 2003). Regular mammograms are recommended as a preventive measure for at-risk women and any woman aged over 40 in the states.

Mammography is a specialized radiographic examination of breast tissue using low-energy X-rays. It allows to identify anomalies (typically characteristic masses

B. Ma, PhD (✉)
Department of Health Physics and Diagnostic Sciences, University of Nevada, Los Vegas, NV, USA
e-mail: bing.ma@unlv.edu

M. Maqbool (ed.), *An Introduction to Medical Physics*, Biological and Medical Physics, Biomedical Engineering, DOI 10.1007/978-3-319-61540-0_7

or microcalcifications) in the breast tissue that may be a sign of breast cancer. Mammography is primarily used as a screening and diagnostic tool for the early detection of breast cancer but also as a localization tool of suspicious area to guide needle biopsy and therapy. It can also be used to detect and evaluate breast changes and thus plays a role in treatment monitoring.

Albert Salomon, a German surgeon, used X-rays to examine mastectomy specimens in 1913. His study demonstrated the spread of breast carcinoma to the axillary lymph nodes and was considered the beginning of mammography. Stafford L. Warren, a radiologist at Rochester Memorial Hospital, New York published the first article on mammographic technique in 1930 (Warren 1930). Modern mammography started to advance in full swing in the late 1960s, when special X-ray machines were designed and used just for breast imaging. In 1965, radiologist Robert Egan at MD Anderson Hospital developed mammographic standards that became widely adopted in the field. The first mammogram machine was introduced in 1966, and dedicated mammographic equipment was used in France in 1974. By 1976 the mammogram had become the standard test for breast cancer detection. New technologies have been continually developed to reduce the amount of radiation required for a mammogram as well as to enable the detection of smaller lesions at an earlier stage. Since the Food and Drug Administration (FDA) approved the first digital mammography system in 2000, digital mammography has witnessed fast-pace advance in its technology. Digital mammography, unlike conventional mammography using film to capture and display the images, acquires the images using solid-state detectors and employs computer-aided viewing of the mammogram images, often resulting in a more detailed and accurate diagnosis.

In the early stage of X-ray mammography, direct exposure film was used without intensifying screen. Even though high-radiation doses were applied, the produced mammograms featured low contrast and thus poor diagnostic quality. As a matter of fact, they most likely did not provide much useful information for the early detection of breast cancer. In the late 1950s, Egan made significant improvement in mammographic imaging technology. He used a combination of a high milliamperage–low voltage technique, a fine-grain intensifying screen, and industrial film to produce mammographic images that were clearer and therefore easier to interpret. In 1971, motivated by dry processing technique developed by Xerox, mammography using the xeroradiographic process became very popular. While such mammograms showed good spatial resolution and sharpened edges at the cost of higher radiation doses, their contrast sensitivity remained poor. During the same period of time, technology in screen-film mammographic imaging systems was dramatically refined and improved. Screen-film mammography has been the mainstream in screening breast cancer since the early 1980s. Since its first public release in 2000, full-field digital mammography systems have shown great advantages in fast image acquisition and display with better image quality. Furthermore, anatomy-specific image processing and computer-aided detection tools have demonstrated to be capable of assisting the radiologist in identifying suspicious features in the images.

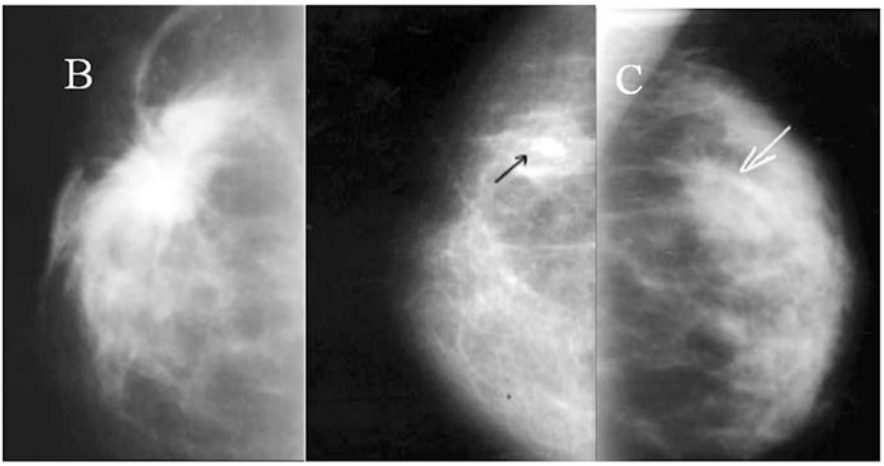

Fig. 7.1 Mammographic features of breast cancer. (**a**) mass with speculated margins, (**b**) clustered microcalcifications, (**c**) architectural distortion (Images are from Popli (2001))

Mammography can be classified into two main categories based on its functionality: screening and diagnostic mammography. Screening mammography attempts to look for signs of cancer in the asymptomatic women and thus is used as a preventative measure.

The primary mammographic signs of breast abnormalities include masses, clusters of calcifications, and architectural distortion (Fig.7.1). Masses with irregular or speculated margins raise high suspicion and need to be carefully evaluated. Calcifications are specks of calcium hydroxyapatite or phosphate. Their location, size, shape, and density are assessed to make the clinical decision. There is a large range of size for calcifications – from extremely small to several millimeters. It is important for screening to detect minute calcifications in breast tissues because of the high correlation between calcification patterns with disease. It has shown that mammography is an effective tool of early detection of breast cancer as it is able to detect calcifications as small as 100 microns. Architectural distortion is seen as straight lines radiating from a central area and retraction or bulging of a contour. Architectural distortion is often subtle and difficult to perceive without high-quality images.

The objective of screening mammography is to identify early-stage breast cancer when it is too small to be felt by palpation. Finding breast cancers early (before they have grown and spread) greatly improves the patient's chance for successful treatment. Mammography is the only validated imaging method in screening that contributes to reduction of mortality due to breast cancer (Swedish Organized Service Screening Evaluation, G 2006). In routine screening mammography, two X-ray images of each breast are acquired. The two images are usually in the mediolateral oblique (angled side view) and craniocaudal (head-to-foot) views.

More images may be necessary for large breasts in order to provide information on as much breast tissue as possible.

Another category is diagnostic mammography, which is performed to assist in the diagnosis of women with symptoms such as the presence of a lump. It can also be a follow-up examination when a suspicious area is identified during screening. Diagnostic mammography includes additional X-ray projections taken at different angles tailored to the specific area of concern. Furthermore, magnification views or spot compressions can be used to further assist the evaluation of the area. Magnification views amplify the mammographic image to show a specific area in greater detail. They are especially useful in evaluating microcalcifications. Spot compression applies compression to a local and smaller area of the breast, rather than the entire breast, achieving better separation of the breast tissue in the area of question. This technique facilitates easier visualization and assessment of suspicious areas. While diagnostic mammography alone is not capable of providing a definitive diagnosis of breast cancer, it can be used to evaluate whether breast abnormalities have a high likelihood of being malignant and whether a biopsy should be performed to confirm the existence of cancer.

There are both benefits and risks associated with any medical imaging procedures where ionizing radiation is utilized, and mammography is no exception. In general, the higher the radiation dose is applied to the organ (or area) in question, the better image quality (including resolution and contrast) can be obtained. However, unnecessary high radiation is hazardous to the patient as ionizing radiation may induce cancer. Since the breast is one of the most sensitive tissues to some adverse effects of ionizing radiation, a delicate balance between the mammogram quality and the radiation dose is demanded. The goal of mammography is to provide adequate information for appropriate medical decision-making, while keeping the radiation to the patient as low as possible. In the following sections, we will explain how current mammographic technologies achieve the trade-off between image quality and radiation dose.

7.2 Interactions Between X-Rays and Breast Tissues

Unlike general radiography, mammographic equipment operates at low X-ray tube voltages, typically 20–40 kV. The photon interactions in this energy range include the photoelectric effect and scattering processes. The photoelectric effect is the dominant interaction when the tube voltage is less than 22 keV. It causes most of the energy absorption from the incident X-rays and hence is the main source of the breast dose. There are two scattering processes in mammography: Rayleigh (also called coherent) scattering and Compton (also called incoherent) scattering. In Rayleigh scattering no energy is transferred between particles involved in the interaction, while there is transfer of energy between interacting particles in Compton scattering.

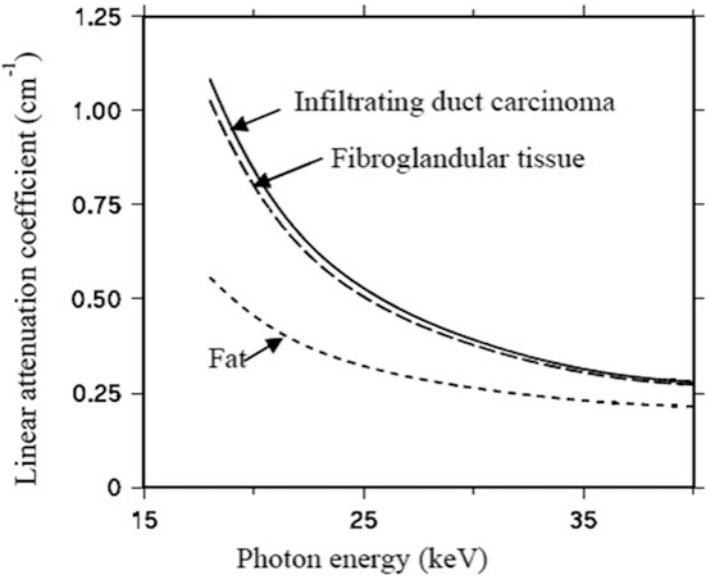

Fig. 7.2 Linear attenuation coefficient of different breast tissues as a function of X-ray energy. Small attenuation difference between the fibroglandular and cancerous tissues decreases with increasing X-ray energy (Data taken from Johns and Yaffe (1987))

Photon interactions between the incident X-rays and the breast tissues lead to the attenuation of the X-rays. The difference in composition of the normal and cancerous tissues in the breast results in different X-ray attenuation, which is used by mammography to accomplish screening and diagnosis. However, the attenuation differences (represented by the difference in linear attenuation coefficients) are very small. Figure 7.2 demonstrates the attenuating characteristics of three breast tissues: infiltrating duct carcinoma, fibroglandular tissue, and fatty tissue. Fibroglandular tissue has a much higher attenuation coefficient than fatty tissue. However, the difference in attenuation between fibroglandular tissue and carcinoma can be small. The attenuation differences between these tissues are decreased as the X-ray energy increases in the low-energy spectrum ($<$100 keV). The highest differences are observed at very low X-ray energies.

Another important factor of image quality for breast imaging is subject contrast. Adequate subject contrast is required for the detection of the minute difference between the normal and cancerous breast tissues. Figure 7.3 shows that the contrast of the ductal carcinoma declines with energy. Both the differential attenuation and subject contrast characteristics between the normal and malignant tissues require that mammography operates at a low energy level for the best screening and diagnostic capabilities.

As mentioned earlier, photoelectric effect occurs with high probability in the low X-ray energy range. Heavy photoelectric effect at very low energy range significantly increases the absorption dose and exposure time for the patient. Thus there must be a compromise between image quality and patient dose for mammography.

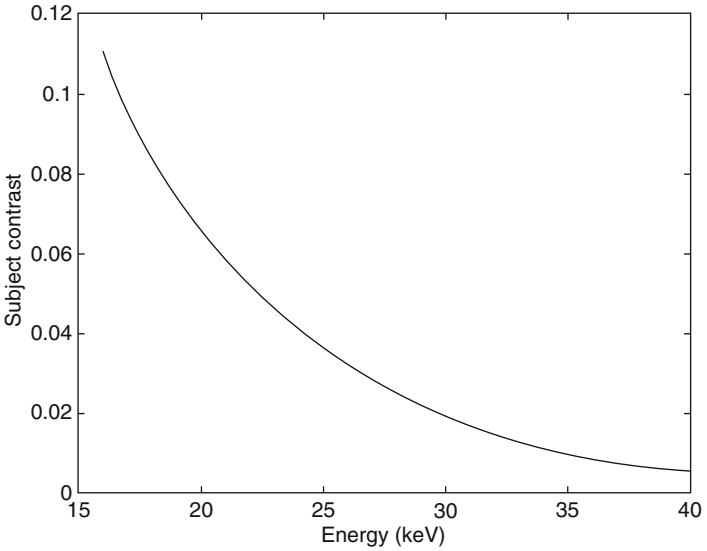

Fig. 7.3 Rapid declining of contrast of the ductal carcinoma indicates that it is necessary to use a low-energy X-ray tube for mammogram to successfully detect breast cancer (Adapted from Yaffe (1995) and Haus and Yaffe (1994))

Fig. 7.4 Components of a typical mammography system

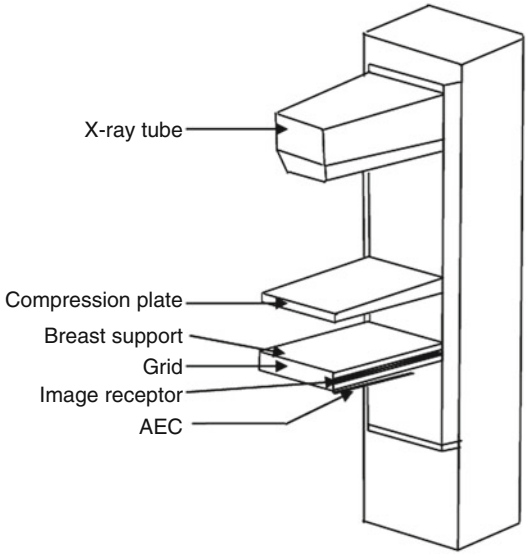

In order to minimize patient dose while acquiring high-quality mammograms for optimal detection of breast cancer, mammography employs a complex system of technology including dedicated X-ray equipment, specialized X-ray tubes, compression devices, anti-scatter grids, and sensitive image receptors (refer to Fig. 7.4 for an illustration). Modern mammography also utilizes sophisticated image

processing and viewing components to maximize the likelihood of detecting small breast tumors. Computer-aided detection and diagnosis tools can further improve the performance of mammography.

7.3 Imaging System

The mammogram is produced when X-rays irradiate the breast, and the transmitted X-rays are recorded by an image receptor. The mammogram exhibits the differential attenuation of X-rays along paths through the structures of the breast.

Currently, there are two distinct mammographic techniques primarily based on image formation: analog and digital mammography. Analog mammography refers to screen-film mammography. X-rays are captured using a screen-film cassette, and the image is recorded and stored on the film. The film is subsequently hung on a viewing board for the reading radiologist.

Digital mammography is a rapidly progressing newer technique. In digital mammography, X-ray beams are captured on a specially designed digital detector. This detector then converts the X-ray photons into electronic signals, which are then transferred to a computer. Digital mammography can reduce 30–40% radiation dose. The computerized image is then available for the radiologist to review on a high-resolution monitor. Images may be manipulated by the radiologist using the tools such as magnifying, masking of light, windowing, leveling, and comparison to prior mammograms on the computer.

In spite of the different image acquisition and display principles used in analog and digital systems, they share some components in the procedure of mammographic imaging, especially before the X-ray beams strike on the image receptors. We will discuss the common components without specifying analog or digital systems while devoting some sections to their individual components.

The goal of mammography is to achieve the image quality required for a given detection task while keeping the radiation dose absorbed by the patient as low as reasonably achievable (ALARA principle) (Huda et al. 2003). To achieve the optimal balance between high-image quality and low radiation exposure, the mammographic unit is specifically designed for examination of the breast tissues. The main components of a typical mammography system are illustrated in Fig. 7.4. The patient may be examined standing or sitting, with her breast resting on a support plate. The X-ray tube and breast support plate are mounted on a mechanical assembly. The assembly may be rotated to achieve different projection angles. Its height can be adjusted to accommodate patients of different size. An anti-scatter grid is placed between the breast support and image receptor. An image receptor is a device used to absorb X-rays transmitted by the breast and acquire the image. The receptor is a screen-film cassette for traditional screen-film mammography and digital detectors for digital mammography. Firm compression is applied to the breast using a plastic compression plate. An automatic exposure control (AEC) device is used to adaptively adjust the exposure amount to the individual patient. It

terminates the radiation when the required clinical quality is achieved in the image or the permissible amount of radiation dose is exceeded. All these components have been optimized to deliver the best trade-off between the mammogram quality and radiation exposure.

7.3.1 X-Ray Tube

Low-energy X-rays for mammographic imaging are produced in a specially designed tube housed in a metal envelope. The window of the X-ray tube is made of beryllium (not glass) with a maximum thickness of 1 mm. Electrons are emitted from a heated negatively charged cathode. They are accelerated in an imposed electric field and focused to strike a positively charged anode. The area on the anode upon which the X-rays impinge is referred to as the *target* or *focal spot*. The X-ray tube is specially designed and constructed for imaging the soft tissue of the breast. The range of X-ray tube operating potentials is from 20 kV to 40 kV for clinical imaging. The exact value of the tube potential is chosen based on the thickness and composition of the breast for a specific patient.

7.3.1.1 Anode

Mammographic X-ray tubes use rotating anodes. The most commonly used material for anode is molybdenum (Mo, $Z = 42$). Rhodium (Rh, $Z = 45$) and tungsten (W, $Z = 74$) are also used. Molybdenum and rhodium are chosen for the target material primarily because of their desired X-ray spectra. The spectra consist of both bremsstrahlung radiation and characteristic X-rays specific to the target material. Characteristic X-rays are of particular interest in mammographic imaging. Characteristic radiation occurs at 17.5 and 19.6 keV for molybdenum and 20.2 and 22.7 keV for rhodium. These characteristic X-ray energies satisfy the requirement of mammography's low-energy spectrum (~20 keV) to provide adequate discrimination between cancerous and normal breast tissues (referred to Fig. 7.2).

The X-ray spectrum from a molybdenum target at 25 kV is shown in Fig. 7.5a. The low-energy bremsstrahlung X-rays deliver significant breast dose with little contribution to the clinical capability of the image. The higher-energy bremsstrahlung X-rays significantly reduce subject contrast. To mitigate undesired low- and high-energy bremsstrahlung X-rays, additional filters are needed for the target. These filters are often made of the same material as the target so that they can reduce the low- and high-energy bremsstrahlung X-rays but allow efficient transmission of the characteristic X-rays. Usually a filter of molybdenum is used with a molybdenum target (Mo/Mo target/filter), and a filter of rhodium is used with a rhodium target (Rh/Rh target/filter). An exception is that a molybdenum target can be combined with a rhodium filter (Mo/Rh target/filter), which performs exceptionally well for imaging thicker and denser breast. This combination produces a

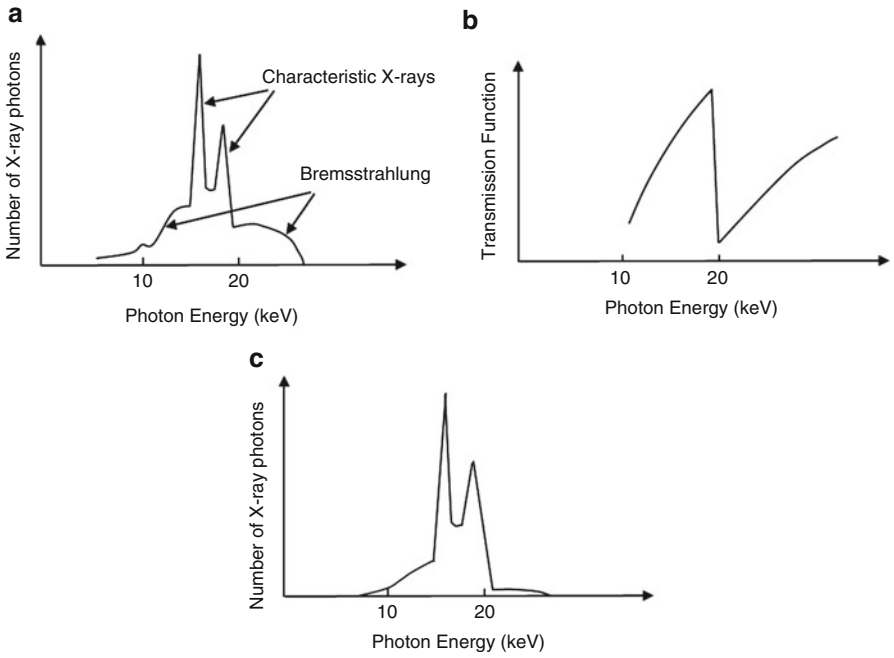

Fig. 7.5 (**a**) X-ray energy spectra for a molybdenum anode, including both bremsstrahlung and characteristic X-rays; (**b**) transmission function of a molybdenum filter of 30 μm thick. The molybdenum K-edge is at ~20 keV, resulting in reduced X-ray transmission above the K-edge; (**c**) X-ray energy spectra for a molybdenum anode with a molybdenum filter of 30 μm thick

slightly higher effective energy than the Mo/Mo target/filter, allowing transmission of X-ray photons between 20 and 23 keV.

The transmission property of a 30 μm thick molybdenum filter is shown in Fig. 7.5b. This filter attenuates both X-rays in the low energy range and those above its own K-absorption edge, while the characteristic X-rays from the molybdenum target pass through the filter with high efficiency. This type of filter is called K-edge filter.

The X-ray spectrum from a molybdenum target at 25 kV with this filter is shown in Fig. 7.5c. Comparison of targets without (Fig. 7.5a) and with filters (Fig. 7.5c) shows the significant removal of undesired X-rays and relative enrichment of X-rays in the range of 17–20 keV, ensuring the Mo/Mo target/filter combination suitable for mammographic imaging.

Since the atomic number of rhodium is higher than that of molybdenum, the X-ray spectrum using a rhodium target is harder than that for a molybdenum target. Thus rhodium anodes offer advantages for imaging the thicker, denser breast at a lower absorbed dose than with the molybdenum anodes. Multiple targets or filters are commonly included in a modern X-ray tube design. The technologist selects the appropriate target/filter combination based on the size and density of the breast to be examined.

7.3.1.2 Focal Spot Size

High resolution and high contrast are essential for mammographic images in order to visualize small calcifications and fine structures in the breast. The size of the focal spot of the X-ray tube is one of the main factors that determine the image resolution. Most X-ray tubes used for mammography have small focal spots, typically 0.3–0.4 mm. These are less than half the size used in general radiography. Such small focal spots are needed to image fine detail such as microcalcifications, whose size may be less than 100 μm. For general mammography purposes, a dual-focus X-ray tube is usually required. An even finer focus spot (0.1–0.15 mm) is used for magnification techniques exclusively. The tube current is 75–125 mA for the large focal spot (0.3 mm) and 15–35 mA for the small focal spot (0.1 mm).

7.3.2 Breast Compression

Since mammography is projection imaging, the highly irregular and easily varying structures in the breast overlap one another in the mammogram. The superimposition of different structures often causes difficulty in distinguishing tissue features. Compressing the breast spreads apart the structures and hence allows better visualization of the breast tissues. When the breast is compressed thinner, less X-rays are needed to penetrate the tissue, and thus the radiation dose will be lower to achieve images of similar quality. Furthermore, compressing the breast reduces the thickness of the back of the breast (close to the chest wall) and makes the breast under examination more uniform in thickness. Hence, tissues near the chest wall are less likely to be underexposed, and tissues near the nipple are less likely to be overexposed. An immediate benefit of minimizing over- and underexposure in regional areas of the breast to X-ray radiation is that the mammographic image is easier to interpret.

Making the breast thinner with more uniform thickness, breast compression reduces scattered radiation and beam hardening amount that occur as the X-ray beam passes through the tissues and thus improves the image contrast. Motion of the breast can greatly blur the image and thus make it impossible to observe small details. Breast compression will hold the breast still so motion is restricted. In summary, breast compression is essential in mammography for immobilizing the breast, separating superimposed tissue components, reducing scattered radiation, reducing radiation dose, and facilitating image interpretation (Saunders and Samei 2008). All dedicated mammographic systems have a built-in stiff compression device that is parallel to the image receptor.

7.3.3 Anti-scatter Grids

X-rays transmitted through the breast consist of primary and scattered radiation. Primary radiation is the radiation that passes through the breast without absorbed or scattered by the breast tissue. It contains the information regarding the attenuation characteristics of the breast. On the other hand, scattered radiation recorded by the image receptor does not reflect the characteristics of the breast tissue. Instead, it is an additive radiation that generates a noisy background to the image. Therefore scattered radiation can significantly degrade contrast of the breast tissue of interest in the mammographic image. The degradation of contrast depends on photon energy, breast size, and image receptor characteristics. It can be quantified using the contrast degradation factor (CDF) as defined by

$$\text{CDF} = \frac{\text{Image contrast with scattered radiaiton}}{\text{Image contrast without scattered radiaiton}}$$

The CDF decreases with thicker breast. For example, the CDF for a 50 mm thick breast is 0.65, resulting in a very low quality of the mammographic image. Low-quality mammographic images are inadequate for the detection of subtle features indicating malignant tissue. This urges adoption of anti-scatter techniques to improving contrast. In mammography, reduction of scattered radiation is commonly achieved by utilizing anti-scatter grids.

X-ray photons transmitted through the breast and the breast support platform are incident on an anti-scatter grid. An illustration of an anti-scatter grid can be found in Fig. 7.6. The primary beams pass through the grid, while scattered radiation is maximally attenuated by the grid. There are two types of anti-scatter grids: stationary and moving grids. The stationary grid makes use of high line density, for instance, 80 lines/cm grid to prevent scattered X-rays from reaching the image receptors. The interspace material is usually aluminum. The moving grid employs

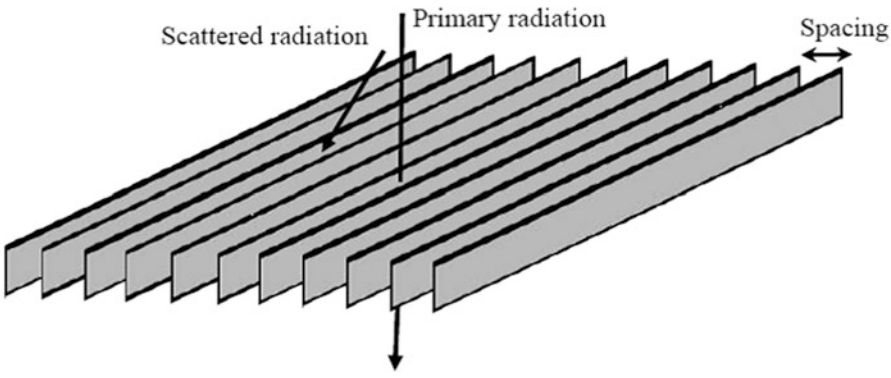

Fig. 7.6 Illustration of an anti-scatter grid

Table 7.1 CIF and BF values for the Philips moving anti-scatter grid

Breast thickness (cm)	CIF	BF
2	1.25	1.68
4	1.38	1.85
6	1.54	2.06
8	1.68	2.24

lower line density, e.g., 30 lines/cm, and paper or cotton fiber is used as interspace material.

Anti-scatter grids do not only reduce the amount of scattered radiation, but they also attenuate primary radiation. A higher radiation dose is needed in order to compensate for such unintended attenuation of primary radiation.

The performance of the anti-scatter grid can be assessed in terms of the contrast improvement (CIF) and Bucky factors (BF). The CIF is the ratio of the contrast with the grid to that without the grid. The BF represents the increase in radiation dose associated with the use of grid. The values for CIF and BF for the moving Philips anti-scatter grid are shown in Table 7.1. Significant improvement in contrast is achieved in thick breast (e.g., 8 cm thick breast) at the cost of increased breast dose.

After most scattered photons are removed by the anti-scatter grid, a large portion of the remaining X-rays are primary radiation and reflect the breast tissue characteristics. The remaining X-rays will impinge on the image receptors to form the image.

7.3.4 Mammography Image Receptors

Image receptors are devices that are used to absorb X-rays transmitted by the breast (after anti-scatter grids) and to acquire the mammographic images. When the X-rays strike on the image receptor, they interact and deposit most of their energy locally. Two types of image receptors will be discussed here: screen-film combination for conventional mammographic systems and digital detectors for digital mammographic systems.

7.3.4.1 Screen-Film Mammographic Image Receptor

When first introduced, mammographic systems used direct exposure radiographic film to obtain the high spatial resolution required at the cost of high radiation dose. Since the mid-1970s, intensifying screens were used in conjunction with radiographic film and greatly reduced the radiation exposure while maintaining the high image resolution. At present, the most common image receptor used in conventional mammography is the screen-film combination (shown in Fig. 7.7). The receptor comprises a film mounted onto an intensifying screen. The screen-film combination is housed in a light-tight cassette. Intensifying screens are used to

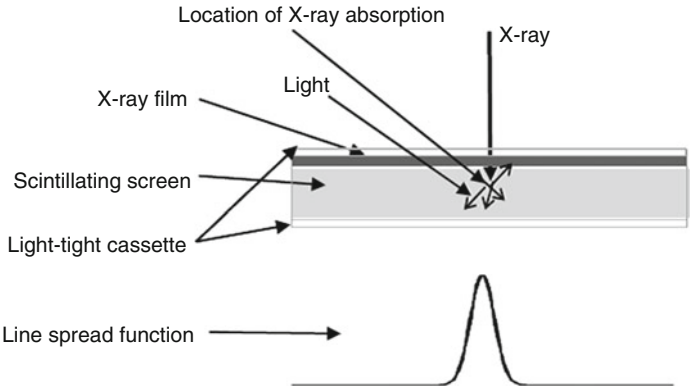

Fig. 7.7 Illustration of the components and blurring effect of screen-film mammographic image receptors

capture X-rays and then emit visible light. When an X-ray is absorbed by the intensifying screen, the light scintillation produces several light photons. The film next to the screen captures these light photons and produces the mammographic image.

Intensifying screens are highly effective in this type of image receptor because film is much more sensitive to light than to X-radiation. Without intensifying screens, approximately 100 times as much X-radiation would be required to expose a film of similar quality. The major drawback of using intensifying screens is that they introduce blurring into the imaging process, which is quantified by a line spread function (illustrated in Fig. 7.7). The blurring effect lowers the image resolution and needs to be carefully considered when selecting screens for specific clinical applications.

The thickness of the intensifying screen shapes the spreading of the line spread function and thus determines the quality of the mammographic image. Thicker screens are more dose efficient as they capture more X-rays. In the meantime, thicker screens also cause more light scatter, and their line spread functions become wider. This causes blurring and thus lowers resolution of the image. Appropriate screen thickness must be selected to compromise radiation dose and image quality based on the specific clinical application.

Since the intensity of transmitted (and thus attenuated) X-rays is inversely proportional to an exponential function of the transmitting distance, the film should be placed as close as possible to the X-ray source to maximize the intensity of the X-rays incident onto the film. By doing this, the resultant mammographic image shows the best quality given the same amount of exposure to the breast. In a screen-film mammography system, the film is placed next to the surface where the X-rays enter the scintillating screen.

After decades of steady research and technical advancement, current screen-film systems produce mammographic images with high spatial resolution, which is

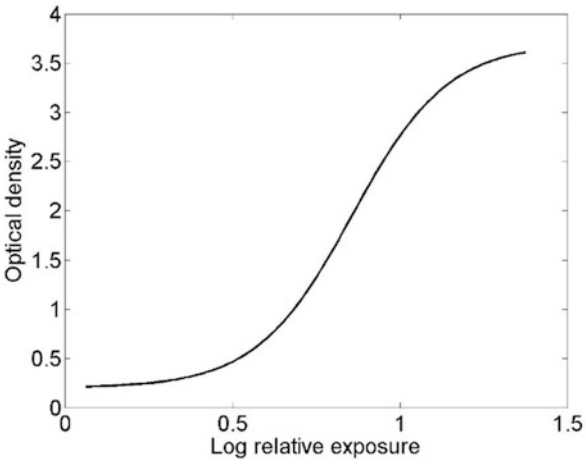

Fig. 7.8 Film characteristic curve for a screen-film mammographic system

suited for detection of fine structure such as microcalcifications of a considerably small size. However, there are inherent limitations to further technical improvement for such systems.

The performance of the screen-film receptor is strongly limited by the characteristics of the film. Although the conversion of X-ray to light photons by the intensifying screen is almost a linear transformation, the response of the film to light photons is nonlinear as shown in Fig. 7.8. The achievable contrast of the film is proportional to the gradient of this curve. The gradient of the central section of the response curve is steep, and over this exposure range, small differences in contrast can be detected on the developed film. Unfortunately the response curve is very flat at both high and low exposures, which results in very little change of optical density seen on the processed film over largely varying X-ray exposure. Under such circumstances it is very difficult to distinguish different tissues over these exposure ranges. The range of X-ray exposure over which the film response gradient is adequately large for clinical imaging is called *dynamic range*. Figure 7.8 shows the narrow dynamic range for the film response. Such narrow dynamic range of the film requires strict exposure conditions. Otherwise the resultant image can be of poor image quality, and breast imaging needs to be repeated, especially when imaging low-contrast lesions in dense breasts (Pisano et al. 2000).

Another major problem is film granularity, which introduces structural noise into the image and thus reduces visibility of microcalcifications and other fine details within the breast. Furthermore, a large amount of storage space is needed for mammographic films. As mammogram became the standard screening test for breast cancer, most women have their mammogram performed every 1 or 2 years. The demand for film storage grows dramatically. Film also must be physically transported to the physician for viewing, causing extra labor and time delay.

7.3.4.2 Digital Mammographic Detectors

Digital detectors are the image receptors for digital mammographic systems. They were developed to overcome the limitations of screen-film systems mentioned above. In digital mammographic systems, images are generated and stored as a digital signal. Transfer and storage of such images are achieved using electronic devices (including computers and networks), and thus no hard copy storage and distribution are needed as by film, saving both time and space.

Unlike stringent requirements for proper exposure demanded by film receptor, digital detectors provide a much larger dynamic range of operation, improving visualization of all areas of the breast. One of the most pronounced advantages of the digital system is the involvement of advanced computer processing of the acquired mammographic images. Stored in digital format, the image content can be manipulated to optimize contrast for each individual clinical task, accomplished by sophisticated and powerful image processing techniques. Computer-aided diagnosis further assists physicians in the interpretation of mammographic images to derive earlier and more accurate diagnostic outcome.

Two methods of image capture have been used in digital mammography, representing different generations of technology: indirect conversion and direct conversion.

Indirect Conversion Digital Detectors

Indirect conversion detectors were used in early digital mammography systems in the states. The GE 2000D or Fischer SenoScan uses indirect flat panel detectors made with cesium iodide (CsI). Such detectors use a two-step process for X-ray detection and image formation, as shown in Fig. 7.9. Similar to the screen-film system, a scintillating layer is first employed to capture the X-ray photons and convert them to light. The difference and advancement of digital detectors over the film-screen combination is shown in the next step. Instead of the film used in the screen-film system, an array of thin-film diodes (photodiodes) converts light

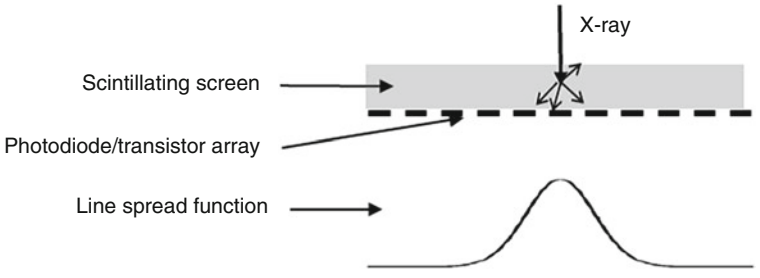

Fig. 7.9 Indirect conversion detectors utilize a scintillating layer to absorb the X-ray and to generate light photons. A photodiode array detects the light photons, and a transistor array converts the light photons to electronic signals

photons to electronic signals. Electronic signals are subsequently captured using thin-film transistors, and the digital mammographic image is produced, i.e., film imaging is replaced by digital imaging using thin-film diodes/transistors. We can say that digital mammography using indirect conversion detectors is a digital extension of screen-film imaging to some extent. Similarly to screen film, a performance compromise between the image resolution and radiation dose has to be made for indirect conversion digital mammography.

Despite the great performance similarity between the indirect conversion digital mammography and screen-film mammography, the digital evolution of the film receptor to the indirect conversion digital detector gives rise to complications for the placement of the scintillator. In screen-film systems, film is placed next to the surface where the X-rays enter the scintillator in order to achieve the highest intensity for the mammographic image. In the indirect conversion digital system, because X-rays cannot pass through the photodiode/transistor array, the array must be placed next to the scintillator surface that is farthest from the X-ray source. With this setup additional scattering of photons through the scintillator results in a wider line spread function, lowering the spatial resolution compared to the screen-film system.

Direct Conversion Digital Detectors

Direct conversion digital detectors are also called photoconductors. Systems like the Hologic Selenia or Siemens Novation use direct flat panel detectors made with amorphous selenium (α-Se). The layer of α-Se in the detector absorbs the X-ray photons transmitted by the breast and directly converts them to an electronic signal that is linearly proportional to the intensity of the photons (illustrated in Fig. 7.10).

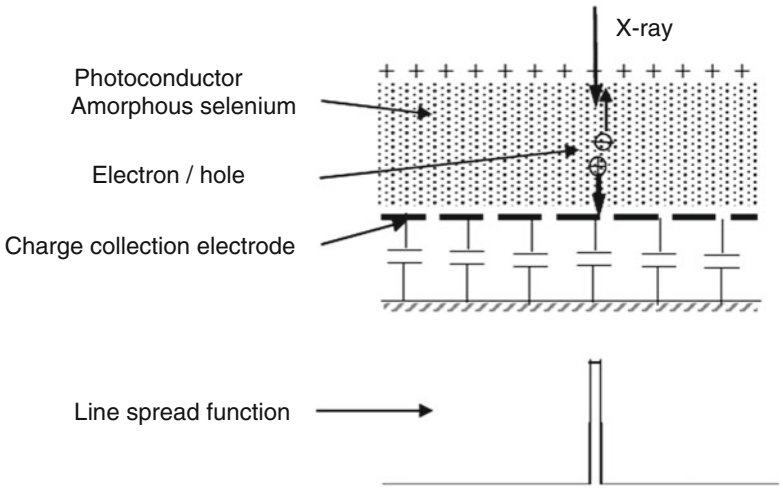

Fig. 7.10 A direct conversion detector uses a photoconductor to absorb the X-ray and directly generate the signal

These direct conversion digital detectors completely replace the screen-film combination, and there is no need for the intermediate step of light emission resulted from the scintillator. An external electric field is imposed across the detector system. As the photoconductor absorbs the incident X-rays, it produces electron hole pairs (see Fig. 7.10). The imposed electric field drives the electron (hole) to the photoconductor's surface with the positive (negative or ground) potential. As illustrated in Fig. 7.10, the holes drift toward a charge collection electrode and are then collected on a capacitor. Because the electrons and holes travel along the direction of the external electric field, there is no laterally spreading charge. This results in an exceptionally narrow point spread response, of about 1 micron (illustrated in Fig. 7.10). The immediate consequence of such narrow line spread functions is superior spatial resolution in digital mammographic images.

In direct conversion detectors, the sharpness of the response function is independent of the thickness of the photoconductor. Thicker photoconductors do not compromise image resolution; however, they attenuate much more X-rays. In practice, sufficiently thick photoconductors are commonly used in order to stop the majority of the incident X-rays without adversely affecting the spatial resolution. Therefore, a significant advantage of direct conversion digital detectors is that they can simultaneously achieve both high resolution and low radiation exposure. Based on the efficiency of direct conversion and its elimination of light scatter, direct conversion digital detectors are able to offer higher image resolution compared to the indirect conversion detectors. The major drawback of direct conversion systems is that they are more costly.

7.3.5 Automatic Exposure Control System

Breasts vary in composition and thickness, so the imaging parameters (X-ray tube voltage, tube current, scan time, etc.) for mammography should be adaptively selected for individual patients to optimize image quality and reduce radiation dose. For example, the time duration of radiation exposure needed to achieve desirable diagnostic quality mammograms vary with different sizes and densities of the breasts. It is difficult for the technologist to estimate the attenuation caused by the breast by visual inspection, and therefore all mammography units are equipped with automatic exposure control (AEC). AEC enables consistently optimal image exposure despite variations in tissue density, thickness, and the user skill level.

In screen-film mammographic systems, the AEC sensor is placed behind the film cassette in the imaging flow (see Fig. 7.4). If the AEC sensor were placed in front of the imaging cassette as in conventional radiography, it would attenuate the X-rays too severely and cast its own X-ray shadow on the mammographic image. The shadow is very severe especially at the low X-ray energies used in mammography. The sensor is connected electrically to an exposure control circuit. When the AEC

system has detected the predetermined amount of radiation transmitted through both the breast and the cassette, the circuit automatically terminates the exposure. The location of the sensor must be adjustable so that it can be placed beneath the appropriate region of the breast in order to obtain adequate image signal in that region.

Due to the complexity of soft tissue in the breast, the attenuation of X-rays is highly heterogeneous over the whole region of the breast. The signal from the AEC sensor is heavily affected by such regional inhomogeneity in attenuation of the breast tissue. Therefore, the size of the sensor and its location under the breast can greatly affect the exposure used to acquire the mammogram. In modern mammographic equipment, AEC is computer controlled so that sophisticated automatic corrections can be made during the exposure (Haus and Jaskulski 1997). For screen-film mammography, AEC devices play a critical role to maintain a desired optical density on the processed film, independent of variations in breast attenuation caused by spatial variations in tissue composition and thickness, X-ray tube voltage setting, or imaging field size.

Full-field digital mammography systems cannot employ conventional AEC methods because digital receptors have absorbed almost all the X-ray beam. As a matter of fact, the design of AEC in the digital system is simpler. The digital detector itself is used as the AEC sensor. Since the image brightness and contrast can be easily adjusted using the computer display, the goal of including AEC device in the digital system is different from that for the screen-film system. Here, the exposure level is set to achieve a desired image signal-to-noise ratio. With the assistance from AEC, direct conversion digital detectors optimize the conversion from the X-ray radiation to electronic signals and thus keep image quality approximately constant while maintaining patient dose as low as reasonably achievable (Huda et al. 2003).

Because of film's narrow exposure dynamic range, appropriate AEC operation in screen-film systems is critical. On the other hand, digital detectors have a much larger dynamic range and consequently are more tolerant of exposure variations. Therefore, in digital mammography, image retaking occurs less frequently, and thus patient dose can be potentially reduced compared to film-screen mammography. Digital mammographic systems also employ more advanced AEC methods with the assistance of computer technologies. The function of an AEC can be expanded to automatically choose tube voltage and current. The digital system can be designed to obtain a fast low-dose pre-image. AEC will analyze the pre-image in real time and determine whether the selected tube voltage would achieve the desired image quality in a short scan time. If not, an optimum tube voltage–current combination will be selected to ensure that the exposure time limit is not exceeded. Information on breast density can also be measured and used to further improve the functionality of the AEC system.

7.4 Digital Mammography

With the technical perfection of mammographic components including the X-tube, focal spot size, breast compression, anti-scatter grid, and screen-film cassette, screen-film mammography is capable of producing images with high spatial resolution and contrast at a low-dose radiation. It has been the gold standard in screening breast cancer. However, there exist limitations in its ability to acquire and display the finest or most subtle details and to produce images at the most efficient radiation dose to the patient.

With the extraordinary advance of computer technology in everyday life, the transfer of imaging from film to the digital format started three decades ago with the introduction of digital radiography. However, the transition from conventional mammography to its digital counterpart was not intermediate because it was challenging to design and develop a full-field digital detector (Van Ongeval et al. 2006). The first full-field digital mammography unit was approved for sale by the Food and Drug Administration in January 2000 (Pisano et al. 2004). Since then a large number of hospitals and medical centers worldwide have installed and screened patients with digital mammographic systems.

The most outstanding difference between digital mammography and conventional screen-film mammography lies in the fact that image acquisition is decoupled from image display, archiving, and retrieval in digital mammography (Feig and Yaffe 1995; Pisano et al. 2000). In conventional mammography, the image is obtained and displayed on the same film, and thus the functionalities of image acquisition and display are highly correlated through the same media–film. In digital mammography, the image is acquired as an electronic signal by the digital detectors which subsequently stored in a computer. The digital image can later be displayed either in the format of "soft copy" or "hard copy." In soft copy display method, the image is viewed on a high-resolution video monitor. In hard copy display method, the image is printed onto a light-sensitive material such as film. The film is then viewed on a light box as in the conventional screen-film system.

The independent operation of image acquisition, display, and storage in digital mammography allows for optimization of each process separately. For example, acquisition is performed using highly efficient, low-noise X-ray digital detectors. Stored digitally, the image can be displayed on the monitor with adjusted contrast based on the radiologist's diagnostic criteria. Image display is completely independent of the detector's properties and solely relies on the monitor's performance characteristics and the computer's capability of manipulating image gray scales. Digital mammograms can be stored on a variety of storage devices, including hard disk drives, optical disks, etc., which is much less bulky compared to the screen-film system. Again, the storage has nothing to do with either the digital detectors or display monitors.

The complete decoupling and full optimization of the digital detector, the viewing system, and the storage device in the digital system leads to impressive advantages over the screen-film systems. The digital mammography offers a larger

dynamic range, remarkably improved contrast and considerably increased signal-to-noise ratio. As a result, digital mammography exhibits increased sensitivity and specificity in breast cancer detection.

One of the most valuable benefits of digital mammography is that because the image data are presented in digital form, advanced data processing techniques can be developed to fully utilize the data quantitatively in specialized applications. Data (image) processing has been widely used to enhance the acquired digital mammographic images. Any beneficial processing techniques, for instance, contrast enhancement, edge sharpening, and noise reduction filtering, can be conveniently applied to improve the image appearance. Another class of image processing techniques can be used to analyze the mammogram with feature identification tools to search for signs of cancer. This approach is called computer-aided diagnosis (CAD) and provides invaluable information and assistance to the physician for better and faster diagnosis. Other advanced applications made possible through digital imaging, such as dual energy and 3D tomosynthesis, are expected to further improve diagnostic sensitivity and specificity.

References

Feig SA, Yaffe MJ (1995) Digital mammography, computer-aided diagnosis, and telemammography. Radiol Clin N Am 33(6):1205–1230

Haus AG, Jaskulski SM (1997) The basics of film processing in medical imaging. Medical Physics Pub Corp, Madison

Haus AG, Yaffe MJ (eds) (1994) Syllabus: a categorical course in physics: technical aspects of breast imaging. RSNA, Oak Brook, IL

Huda W, Sajewicz AM, Ogden KM, Dance DR (2003) Experimental investigation of the dose and image quality characteristics of a digital mammography imaging system. Med Phys 30 (3):442–448

Johns PC, Yaffe MJ (1987) X-ray characterisation of normal and neoplastic breast tissues. Phys Med Biol 32(6):675–695

Nyström L, Andersson I, Bjurstam N, Frisell J, Nordenskjöld B, Rutqvist LE (2002) Long-term effects of mammography screening: updated overview of the Swedish randomised trials. Lancet 359(9310):909–919

Pisano ED, Yaffe MJ, Hemminger BM, Hendrick RE, Niklason LT, Maidment AD, Kimme-Smith CM, Feig SA, Sickles EA, Braeuning MP (2000) Current status of full-field digital mammography. Acad Radiol 7(4):266–280

Pisano ED, Yaffe MJ, Kuzmiak CM (eds) (2004) Digital mammography. Lippincott Williams & Wilkins, Philadephia

Popli MB (2001) Pictorial essay : mammographic features of breast cancer. Indian J Radiol Imaging 11:175–179

Saunders RS, Samei E (2008) The effect of breast compression on mass conspicuity in digital mammography. Med Phys 35(10):4464–4473

Siegel R, Ma J, Zou Z, Jemal A (2014) Cancer statistics, 2014. CA Cancer J Clin 64(1):9–29

Swedish Organised Service Screening Evaluation, G (2006) Reduction in breast cancer mortality from organized service screening with mammography: 1. Further confirmation with extended data. Cancer Epidemiol Biomark Prev 15(1):45–51

Tabar L, Yen MF, Vitak B, Chen HH, Smith RA, Duffy SW (2003) Mammography service screening and mortality in breast cancer patients: 20-year follow-up before and after introduction of screening. Lancet 361(9367):1405–1410

Tabar L, Vitak B, Chen TH, Yen AM, Cohen A, Tot T, Chiu SY, Chen SL, Fann JC, Rosell J, Fohlin H, Smith RA, Duffy SW (2011) Swedish two-county trial: impact of mammographic screening on breast cancer mortality during 3 decades. Australas Radiol 260(3):658–663

Van Ongeval C, Bosmans H, Van Steen A (2006) Current status of digital mammography for screening and diagnosis of breast cancer. Curr Opin Oncol 18(6):547–554

Warren SL (1930) A Roentgenologic study of the breast. Am JRoentgenol Radium Ther 24:113–124

Chapter 8
Computed Tomography

Muhammad Maqbool

Contents

8.1 Introduction 221
8.2 Basic Principles 222
8.3 History and Generations of Computed Tomography 224
8.4 CT Numbers, Hounsfield Unit, and Gray Scale 235
8.5 Image Formation and Back Projection 240
8.6 Image Quality 250
8.7 Image Artifacts 252
References 262

8.1 Introduction

The ability of each tissue of the human body to X-rays is different than other tissues. Quantitatively, the absorption of X-rays varies from tissue to tissue. These characteristic properties of tissues can be exploited for some useful applications. Computed tomography or CT is one of those important applications that work on the principle of X-ray absorption by body tissues. CT (CAT) scanning is a noninvasive medical test that helps physicians to diagnose and treat medical conditions. This technique uses special X-ray equipment and high-quality computers to produce multiple images of the inside of a desired part of the body. The images taken are 3-D usually. Those images are then examined on a computer, and appropriate treatments are prescribed by the physicians accordingly.

A CT image is usually called a *slice*, as it corresponds to what the object being scanned would look like if it were sliced open along a plane. An even better analogy is a slice from a loaf of bread, because just as a slice of bread has a thickness, a CT slice corresponds to a certain thickness of the object being scanned. So, while a typical digital image is composed of pixels (picture elements), a CT slice image is

M. Maqbool, PhD (✉)
Department of Clinical and Diagnostic Sciences, Health Physics Program,
The University of Alabama at Birmingham, Birmingham, AL 35294, USA
e-mail: mmaqbool@uab.edu

M. Maqbool (ed.), *An Introduction to Medical Physics*, Biological and Medical Physics, Biomedical Engineering, DOI 10.1007/978-3-319-61540-0_8

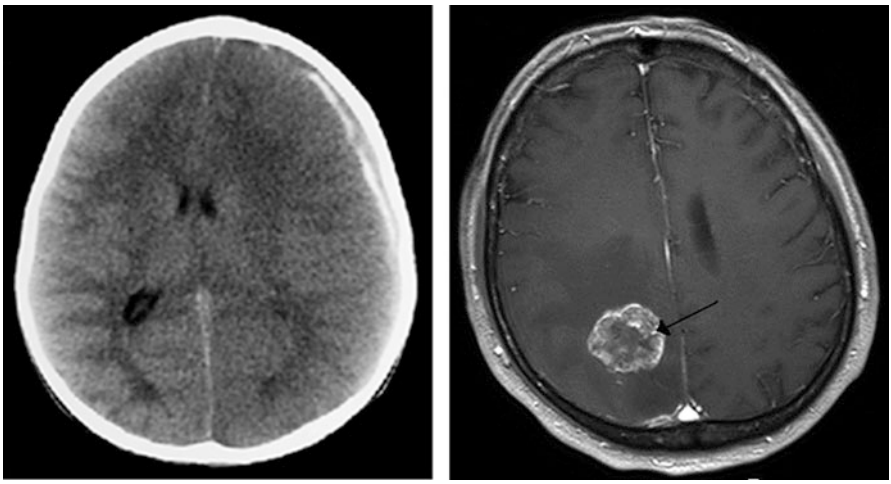

Fig. 8.1 CT image of normal human brain (*left*) and human brain containing a tumor (*right*)

composed of *voxels* (volume elements). Taking the analogy one step further, just as a loaf of bread can be reconstituted by stacking all of its slices, a complete volumetric representation of an object is obtained by acquiring a contiguous set of CT slices. A typical CT image of the brain is given in Fig. 8.1.

8.2 Basic Principles

In CT scan, multiple pencil or fan beams of kilovoltage (kV) X-rays (photons) pass through a desired volume of body from multiple angles (usually over 180 degrees). A dosimeter is placed on the opposite side of the volume which measures the amount of X-rays reaching it. This allows determination of the attenuation of individual beams as they pass through the volume. It must be noted that when high-energy X-rays pass through a tissue or a material, attenuation (absorption + scattering) of the beam occurs. However, at low energies (kV) scattering is negligible; therefore, only absorption of X-rays is considered in CT where kV beam is used. Each part of the volume may be considered a "voxel" (a three-dimensional pixel) with width, height, and depth. Each beam will pass through a number of voxels as it traverses the volume. The absorption of the beam as it passes through the volume may be considered to be the sum of absorptions in each voxel it has passed through. This may be up to 512 voxels for modern scanners. The passage of X-ray beams from different directions, passing and absorbed by a slice of the body and detected by detectors, is given in Fig. 8.2.

A computer is then used to solve a simultaneous equation with up to 512 variables, using the absorption information from each beam in the form of absorption coefficients "μ." This is a process which computers are able to perform quickly and

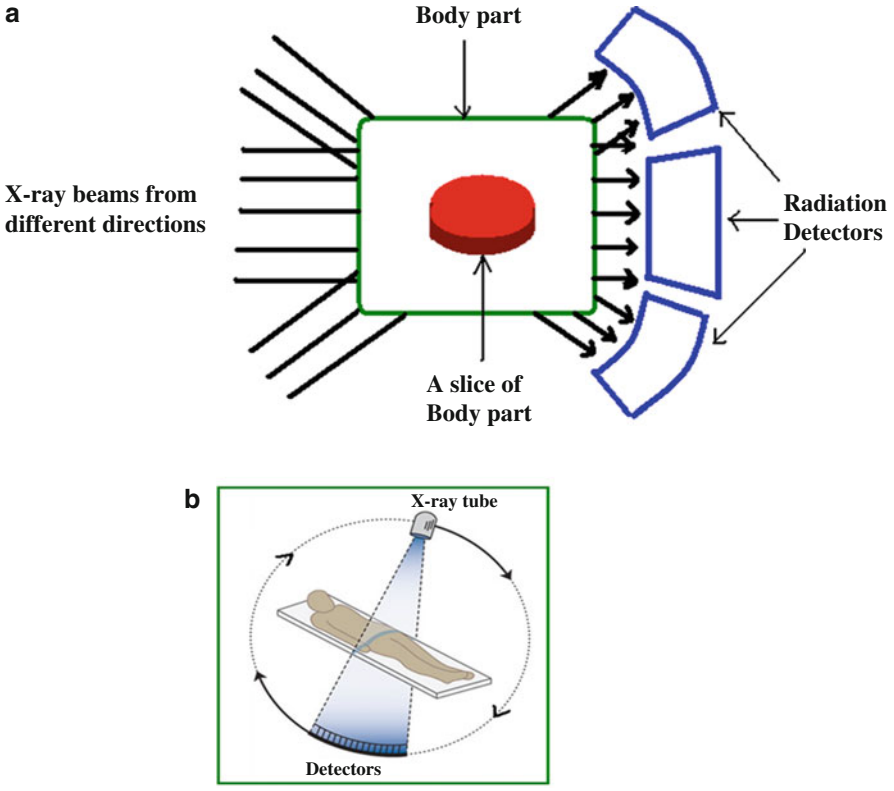

Fig. 8.2 (**a**) Absorption of multidirectional X-ray beams by a body slice; (**b**) detectors record the X-rays passed through the body section

Table 8.1 Absorption coefficients of various body tissues

Tissue	Absorption coefficient μ (cm^{-1})
Air	0.0004
Fat	0.185
Water	0.206
Blood	0.208
Gray matter	0.212
White matter	0.213
Bone	0.528

precisely, so long as they have been given good information from the photon absorption. Once the absorption for each voxel is determined, the computer system assigns a Hounsfield unit to each part of the volume. Hounsfield units (special units in CT) range from −1000 (air) to 0 (water) and to +1000 (cortical bone). Table 8.1 shows the absorption coefficients (μ) of various parts of the body as compared to the absorption coefficients of air and water (Anne et al. 2010).

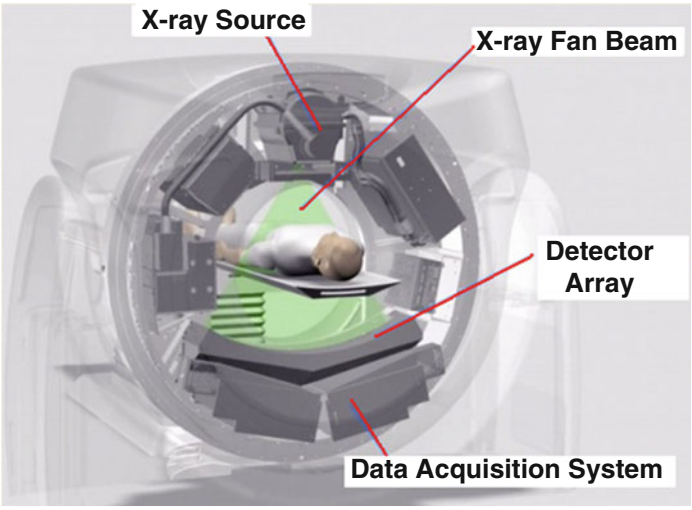

Fig. 8.3 A typical CT machine showing various parts around a patient

The use of kilovoltage photons allows a good discrimination between tissues of different atomic numbers. Because so many beams are used, CT is able to discriminate between different soft tissues (such as adipose and muscular tissue) even though they have similar atomic numbers.

Another important feature is the kilovoltage photons are only affected by the intervening tissue, and spatial resolution (the accuracy of determining the physical position of each voxel) is very high and allows accurate planning.

8.3 History and Generations of Computed Tomography

A CT scan machine consists of an X-ray source providing X-ray fan beam, detector array, and data acquisition system. A typical CT scan machine is given in Fig. 8.3. A rotating X-ray source, collimated as a fan beam, is subtended by a group of detectors, usually up to 800. In modern tomographic machines, the fan is rotated in a series of projections or angles covering the entire 360° around the patient. Usually up to 1000 projections are recorded in the process. Beam attenuation is measured at each projection. The figure shows that the X-ray fan beam and the detector array are rotated around the patient, and projections are taken. Collimators are used to control the thickness of slice under irradiation.

CT was invented in 1972 by British engineer Godfrey Hounsfield and by South Africa-born physicist Allan Cormack of Tufts University, Massachusetts. Hounsfield and Cormack were later awarded the Nobel Peace Prize for their contributions to medicine and science. The journey of CT scan started from its first-generation machine. With the passage of time, new generations of CT machines were made

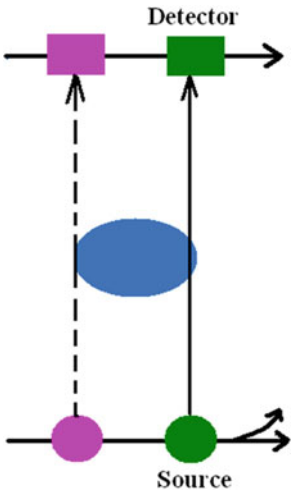

Fig. 8.4 First-generation CT

based on the needs and requirements. Based upon the arrangement of components and mechanical motion required to collect data, these machines are divided into seven generations. It should be noted that the higher generation number does not project a higher performance system. Each generation has its own uses and can work better under certain specific circumstances.

8.3.1 First Generation

The first generation was built by EMI in 1971. In this generation, a single X-ray source and a single X-ray detector are used to collect all the data for a single slice of the body part under treatment procedure. Figure 8.4 shows an image of the first-generation CT system (Brink and Helical 1994).

In the first generation, X-ray source (X-ray tube) and detector are rigidly coupled and work as a single system attached together. Pencil beam of X-rays is obtained to produce image. The source and detector system is translated across the patient to obtain a set of parallel projection measurements at one angle as shown in Fig. 8.5. Source and detector rotate slightly, and a subsequent set of measurements is obtained during a translation past patient. The system is reset for each angle, and the process is repeated for each projection angle until 180 projections are obtained. The scanning process is slow, and in some early versions, it takes over 4 min for a single scan. In later versions the procedure time is reduced by using two detectors to obtain two parallel sections in a single scan. Spatial resolution is very poor, and contrast resolution of internal structures is unprecedented.

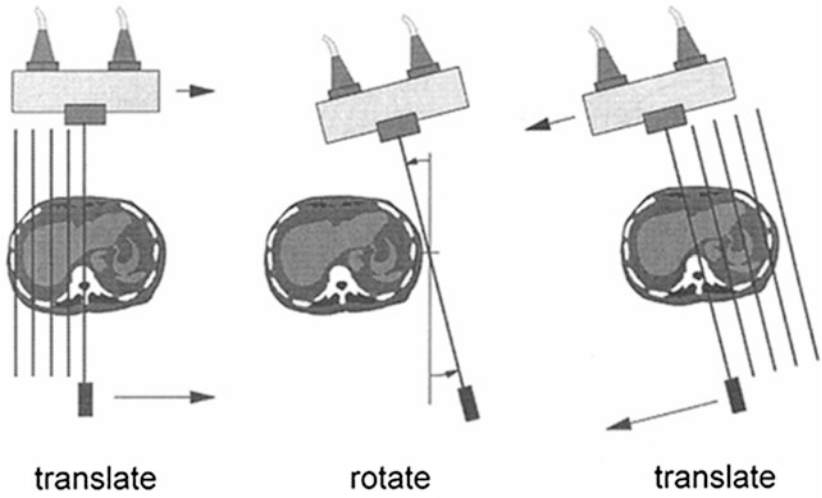

Fig. 8.5 Translation and slight rotation of source and detector system

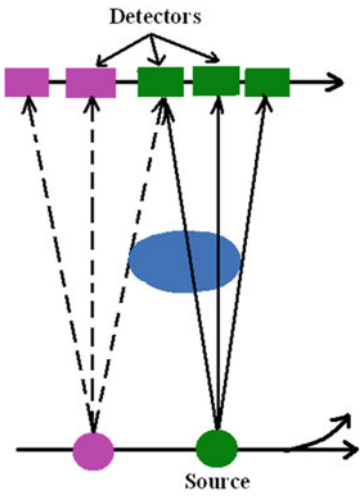

Fig. 8.6 Second-generation CT

8.3.2 Second Generation

The second generation came into use in 1975. This generation consists of a single X-ray source and multiple detectors as shown in Fig. 8.6. The major difference between first generation and second generation is the use of multiple detectors in second generation as compared to a single detector in the first generation. In the second generation, a single X-ray source and multiple detectors are used in this generation. Since X-ray source emits radiation over a large angle, therefore, the

efficiency of measuring projection is much better than the first generation. Source and array of detectors are translated as in a first-generation system, but, since beam measured by each detector is at a slightly different angle with respect to object, therefore, each translation step generates multiple parallel ray projections. The source and detector system is translated across the patient and rotated at the same time to obtain a set of parallel projections. Due to multiple detectors, several projections could be obtained in a single translation. As a result the scanning time of the procedure is much shorter than the first generation. In the latest version, up to 53 detectors are used, and the acquisition time is as low as tens of seconds.

8.3.3 Third Generation

The third-generation CT was also invented in 1975. This generation of CT machine contains larger array of detectors as shown in Fig. 8.7, and the image processing is significantly faster than first and second generations. Thick section of body part can be scanned in this generation with a reduced time (2 s) of scan. Scan time is usually a few seconds or less. Recent versions are capable of sub-second scan time. X-ray source is collimated to a wide fan-shaped beam where translational motion is replaced by smooth rotational motion. The fan-shaped X-ray beam is directed toward an arc-shaped row of detectors. X-ray tube and detector array rotate around the patient, and projections are obtained during this rotation. The rotating fan beam spatially constructs a matrix of data cells over the patient slice during its 360° rotation; these are stored in computer memory as a data matrix or attenuation values. The detector and data acquisition technology improved in this generation with high spatial resolution to allow measurement of a fan-beam projection of the entire patient cross section. One of the most significant advantages of this

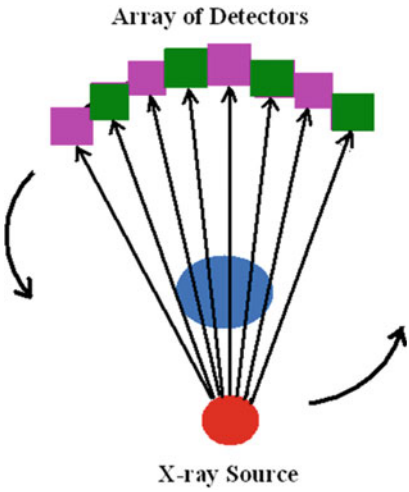

Fig. 8.7 Third-generation CT

generation is its wide fan-shaped beam and rotation. The number of detectors has increased up to 800 or even more in some cases, and the angle of fan beam increased to cover the entire patient, eliminating the need of translator motion. One of the disadvantages of this generation is that it requires very high performance detectors to avoid ring artifacts.

8.3.4 Fourth Generation

Fourth generation of CT is different from the previous three generations because in this generation only the source rotates within a stationary ring of detectors. The detectors are arranged in a 360° around the patient (or body part of the patient), hence no need of rotating those detectors. Only the source is rotated, and no matter where the source is, one or more detectors will receive and record X-rays after passing through the patient's body part. Figure 8.8 shows a rotating X-ray source and array of detectors in 360° around the patient's body slice. This generation has even larger fan beam with full FOV (field of view) that tremendously reduces the scan time. Early versions had about 600 detectors, but the latest machines use up to 4800 detectors. This generation has the limitation of less efficient use of detectors. Less than one quarter of the total detectors are used at any point during scanning. Only the X-ray generator and tube rotate at 360°, thus shortening the scanning time even more. Scattered radiation and the use of a large number of detectors are the main drawbacks of this generation. A comparison of third and fourth generations is given in Fig. 8.9 (Brink and Helical 1994).

A full comparison of all four generations is given in Fig. 8.10. The figure shows an additional or improved aspect in the next generation as compared to the previous generations.

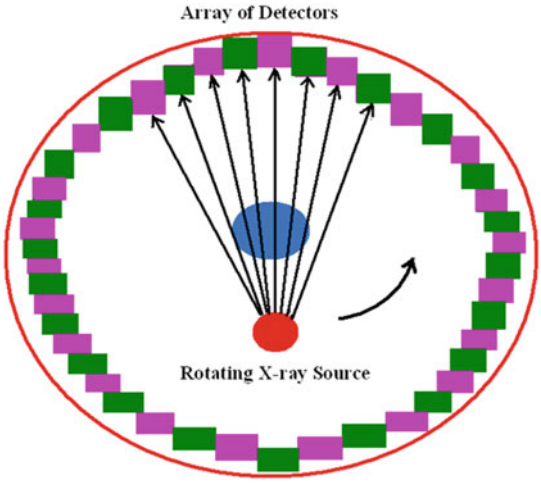

Fig. 8.8 Fourth-generation CT

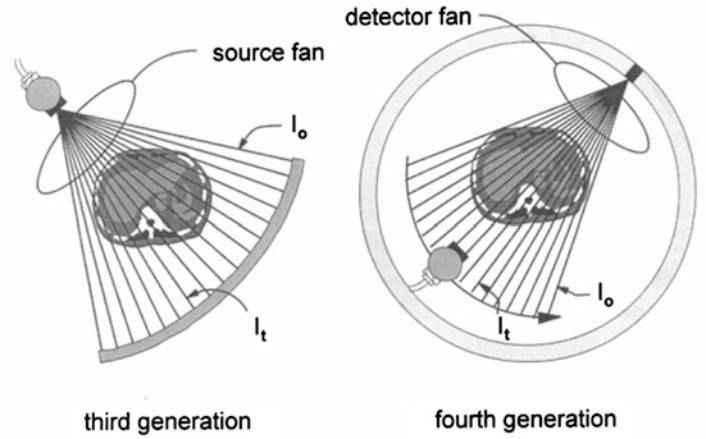

Fig. 8.9 Comparison of third and fourth generations of CT

8.3.5 Fifth Generation

In this generation X-ray tube is a large ring that circles the patient, opposed to detector ring. This generation CT is mainly used for cardiac tomographic imaging called *cine* or cinematograph. No parts of the gantry (rotating parts of the scanner) move. The scanning machine is capable to reduce the scanning time to 50 ms. As a result 17 CT slices can be scanned per second. Figure 8.11 provides a description for the fifth-generation CT. In this generation X-ray detector and tube anode are stationary, and hence no mechanical scanning motion occurs to acquire data. Anode (where X-rays are generated) is a very large semicircular ring that forms an arc around the patient scan circle. X-rays are emitted from the point where electrons strike target anode. X-rays are transmitted through the body slice and are measured through stationary array of detectors.

8.3.6 Sixth-Generation or Spiral/Helical CT

Sixth-generation CT, which is also called spiral or helical CT, was introduced in 1990. This generation allowed 3-D image acquisition within a single breath hold. In helical CT, X-ray tube rotates, and the patient is moved along with his table slowly and smoothly into X-ray scan field. Typically, a full 360° is covered to collect a complete set of data. The image is then reconstructed and the patient table moved a small distance through the gantry for the next transverse section or slice. This procedure is repeated slice by slice. Since power and data are transmitted by cable, the tube/detectors are rotated 360° in one direction, stopped, and then rotated 360° in the opposite direction. This is necessary to allow the connecting power and data

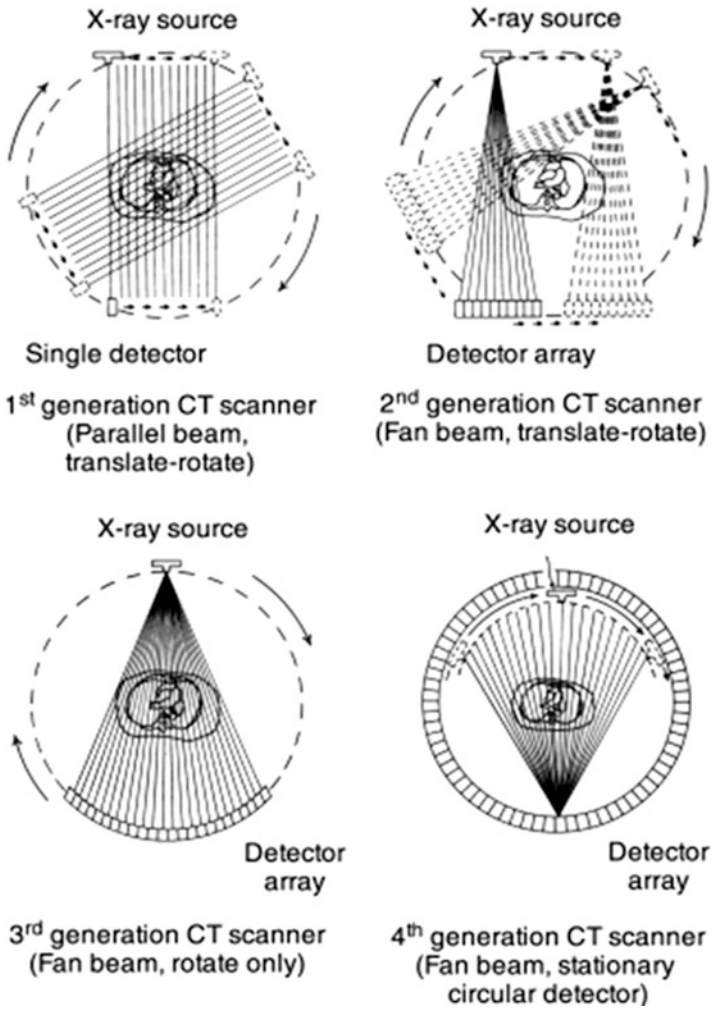

Fig. 8.10 A comparison of the first four generations of CT

cable to unwind. Data acquisition is also performed at the same time, and one continuous set of data for the entire region volume is taken. Data acquisition rate is 1 s per slice. The entire chest or abdomen can be scanned and imaged in 30 s. Figure 8.12 shows how the Spiral or Helical CT works (Dowsett et al. 2006; Jastaniah et al. 2015).

Spiral CT has advantages and disadvantages listed below. High speed, improved detection, and better contrast all are the advantages of this generation. Another advantage of spiral CT is the imaging in space and time simultaneously. This gives the opportunity to examine each part of the body in 3-D. Transverse data can be reconstructed in any plane; stripe away skin, muscles, and other tissues to improve

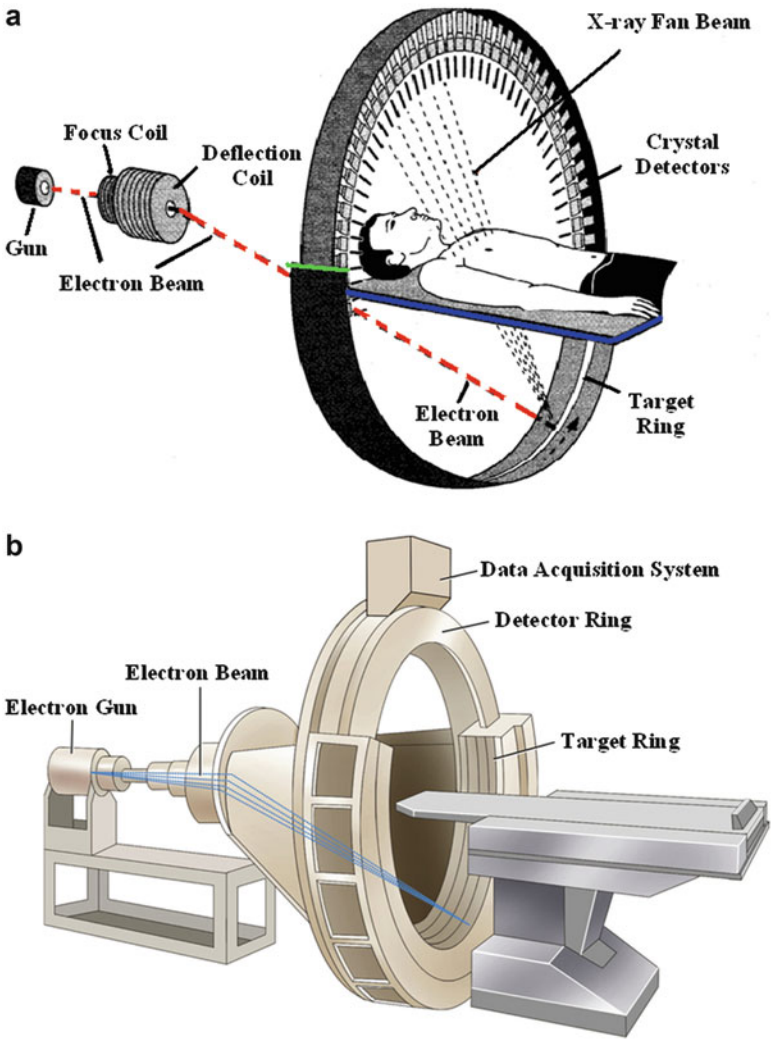

Fig. 8.11 Fifth-generation CT: (**a**) how it works and (**b**) how it looks

reconstruction and manipulation. The disadvantages include certain limitations to collecting data as sequential axial slices particularly when small lesions are being imaged since these can be missed if they are located between adjacent slices. Delays between slices can occur in the sequential slice protocol due to a number of reasons including time taken by fan beam assembly to accelerate the scan speed, X-ray tube pulse and data collection, fan beam assembly halts and return to its original position, and table indexing to the next longitudinal position while X-ray tube cools. This series of events constitutes the interscan delay time (ISD) and adds a significant time to the clinical study causing problems if the patients have to hold their breath or patient movement is present.

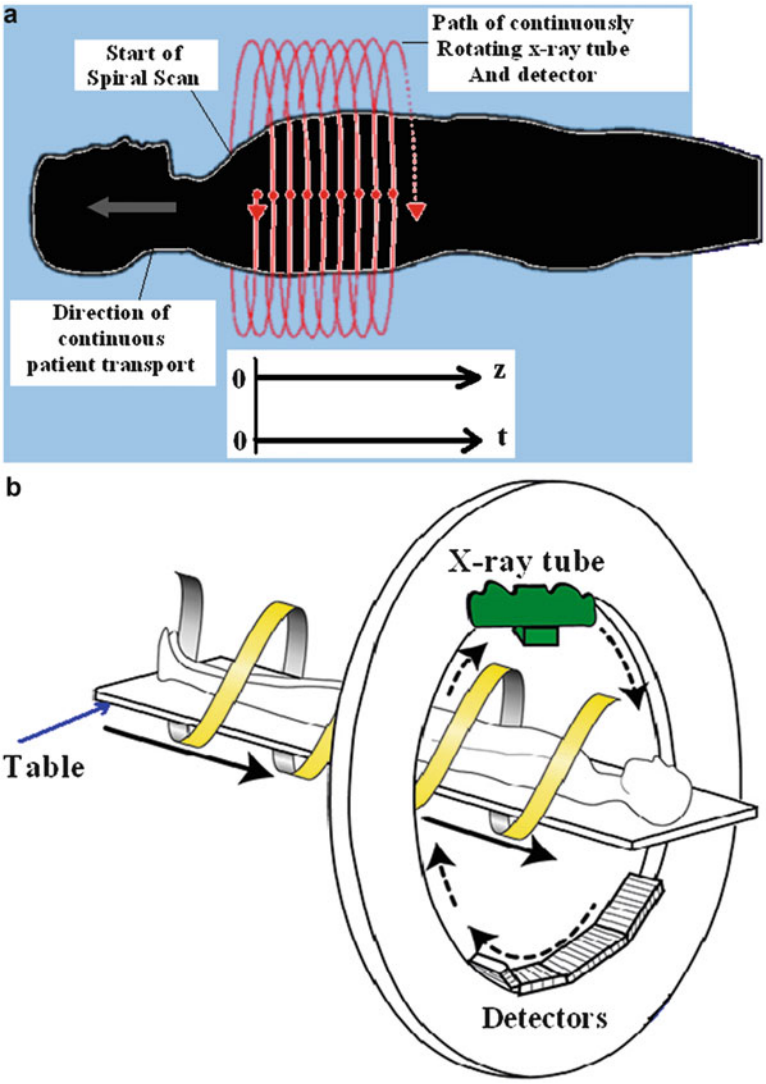

Fig. 8.12 Sixth-generation or spiral/helical CT (**a**) Spiral path of patient's scan in space and time (**b**) Motion of table in z-direction, passing through tube and detectors

Eliminating interscan delays required continuous (nonstop) rotation, a capability made possible by the low-voltage slip ring. A slip ring passes electrical power to the rotating components (e.g., X-ray tube and detectors) without fixed connections. The idea is similar to that used by bumper cars; power is passed to the cars through a metal brush that slides along a conductive ceiling. Similarly, a slip ring is a drum or annulus with grooves along which electrical contactor brushes slide. Data are transmitted from detectors via various high-capacity wireless technologies, thus allowing continuous rotation to occur. A slip ring allows the complete elimination

of interscan delays, except for the time required to move the table to the next slice position. However, the scan–move–scan sequence (known as axial step-and-shoot CT) is still somewhat inefficient. For example, if scanning and moving the table each take 1 s, only 50% of the time is spent acquiring data. Furthermore, rapid table movements may introduce "tissue jiggle" motion artifacts into the images.

An alternate strategy is to continuously rotate and continuously acquire data as the table (patient) is smoothly moved though the gantry; the resulting trajectory of the tube and detectors relative to the patient traces out a helical or spiral path as shown in Fig. 8.12. This powerful concept allows for rapid scans of the entire z-axis regions of interest, in some cases within a single breath hold.

Certain concepts associated with helical CT are fundamentally different from those of axial scanning. One such concept is how fast the table slides through the gantry relative to the rotation time and slice thicknesses being acquired. This aspect is referred to as the helical pitch and is defined as the table movement per rotation (usually in millimeters) divided by the slice thickness.

Mathematically, the pitch "P" is given by

$$P = \text{Tabletravel per rotation}/\text{slice width} \tag{8.1}$$

Some examples are as follows: if the slice width or thickness is 5 mm and the table moves 10 mm during one tube rotation, then the pitch = 10/5 or 2.0; if the slice thickness is 6 mm and the table moves 9 mm during one tube rotation, then the pitch = 9/6 or 1.5; and if the slice thickness is 10 mm and the table moves 7 mm during one tube rotation, then the pitch is 7/10 or 0.70. Usually a low pitch causes better image quality. However, the choice of pitch is examination dependent, involving a trade-off between coverage and accuracy.

Since the spiral pitch or simply pitch plays an important role in image construction and quality and it depends upon the speed of the table per rotation, therefore, the speed per rotation controls the pitch for a fixed slice width. The desired table speed T_s is given by

$$T_s = (P \times M \times S)/\text{rotation time} \tag{8.2}$$

where S is the slice width and M is the number of slices per rotation. T_s is usually measured in millimeters per second.

8.3.7 Seventh Generation

Seventh-generation CT is an advanced or latest version of the spiral CT. In this generation several rows of detector arrays are arranged in the direction of the scan/the direction of the motion of the patient and table as shown in Fig. 8.13. As a result the collimator is made wider, and hence more X-rays, making cone shape, are used in producing image data, causing an increase in the slice thickness. The widened

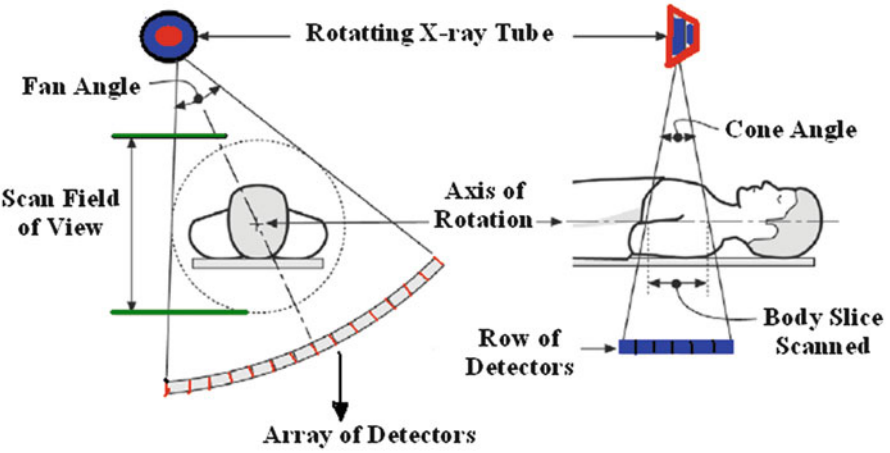

Fig. 8.13 Seventh-generation CT

Fig. 8.14 Single- and multi-slice scans

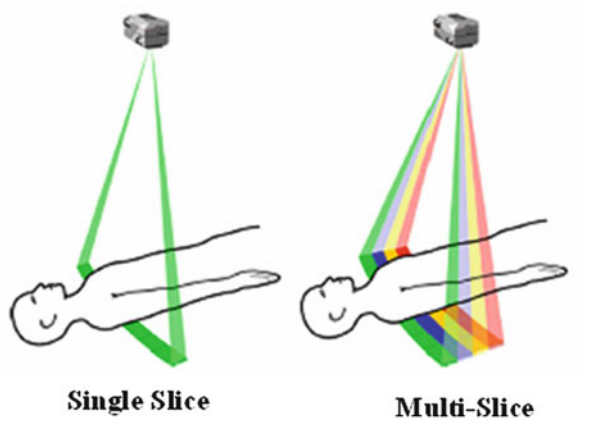

X-ray beam and detector array (in z-direction) acquire multiple slices (4–64) simultaneously (Jastaniah et al. 2015). Figure 8.14 compares a single-slice and multi-slice scanning.

Multi-slice spiral CT and simultaneous acquisition of four slices were introduced by all major manufacturers. Later on, 8-slice CT was introduced in 2000 followed by 16 slices in 2001.

Most modern generation of multi-slice CT is 64 slices per rotation, enabling a whole-body CT acquisition with 1500 mm scan range in 22–25 s. Development in software and computer capacity leads to processing and reconstruction in a short time.

All generations of CT are compared in Table 8.2. The comparison provides basic difference between all seven generations of CT.

Table 8.2 CT generations

Generation	Source	Source collimation	Detector
First	Single X-ray tube	Pencil beam	Single
Second	Single X-ray tube	Fan beam (not enough to cover FOV)	Multiple
Third	Single X-ray tube	Fan beam (not enough to cover FOV)	Many
Fourth	Single X-ray tube	Fan beam (covers FOV)	Stationary ring of detectors
Fifth	Many tungsten anodes in a single large tube	Fan beam	Stationary ring of detectors
Sixth	Single X-ray tube	Fan beam	Single array of detectors
Seventh	Single X-ray tube	Cone beam	Multiple array of detectors

8.4 CT Numbers, Hounsfield Unit, and Gray Scale

CT number is a special number which is a normalized value of the calculated X-ray absorption coefficient of a pixel (picture element), in a computed tomogram. The absorption coefficient of a tissue varies with the nature of the tissue and the energy (kV) of X-ray beam. However, if the tissue absorption coefficient is related to that of water absorption coefficient at the same kV, a reference number independent of kV change can be obtained. This number is called CT number. CT number is represented by a specific unit or number called Hounsfield unit (HU). CT number or Hounsfield unit can be calculated as follows (Anne et al. 2010):

$$\mathrm{HU} = [(\mu_{\mathrm{tissue}} - \mu_{\mathrm{water}})/(\mu_{\mathrm{water}} - \mu_{\mathrm{air}})] \times 1000 \tag{8.3}$$

Since the absorption coefficient of air is negligibly small, therefore, Eq. (8.3) modifies to

$$\mathrm{HU} = [(\mu_{\mathrm{tissue}} - \mu_{\mathrm{water}})/\mu_{\mathrm{water}}] \times 1000 \tag{8.4}$$

The following example will help calculating CT number or HUs for muscle and bone.

Example 8.1 Calculate the CT number for the muscle with the following available data:

μ	80 keV	100 keV	150 keV
μ_{water}	0.1835	0.1707	0.1504
μ_{muscle}	0.1892	0.1760	0.1550

Table 8.3 Tissues' CT numbers and gray scale

Tissue	Range of CT Numbers (HU)
Bone	500 to 3000
Liver	40 to 60
Grey Matter (Brain)	35 to 45
WhiteMatter(Brain)	20 to 30
Blood	30 to 45
Muscle	10 to 40
Water	0
Fat	- 60 to - 150
Lung	- 500
Air	- 1000

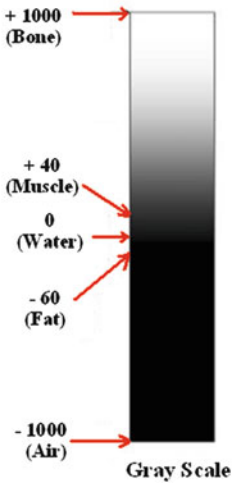

Solution $(CT)_{muscle}$.
At 80 keV = [(0.1892–0.1835)/(0.1835)] × 1000 = 31
At 100 keV = [(0.1760–0.1707)/(0.1707)] × 1000 = 31
At 150 keV = [(0.1550–0.1504)/(0.1504)] × 1000 = 31

Gray scale is a measure or scale on which HU is represented. In regular or fan-beamed-based computed tomography (CT), HU is proportional to the degree of X-ray attenuation, and it is allocated to each pixel to show the image that represents the density of the tissue. In cone beam computed tomography (CBCT), the degree of X-ray attenuation is shown by gray scale (voxel value). In general, CBCT manufacturers and software providers present gray scales as the HUs. Gray scale is used in cases like determining the kind of bone in placing dental implants, pathologic lesions, evaluation of the airways, and determining the stability of the implant. On the other hand, HU is used in CT mainly. Table 8.3 gives CT numbers of various tissues in HUs.

8.4.1 Variation in CT Numbers with X-ray Energy

When an X-ray beam of varying energy over a range of energies is passed through the body of a patient, low-energy X-ray photons are absorbed and removed from the beam within a short length. As a result the average energy of the remaining beam gets higher. This process is called hardening of the beam. The hardening of the beam continues as the beam further penetrates in the body. Since the average energy of the hardened beam is higher than the original beam allowed to fall on

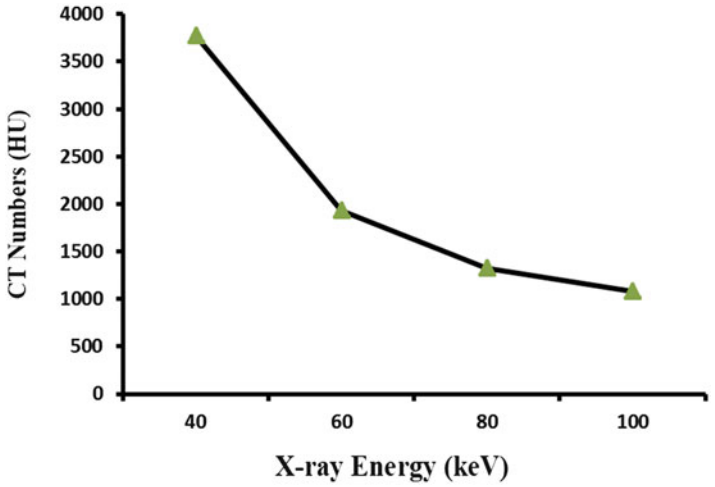

Fig. 8.15 Variation in CT number with X-ray beam energy

the body, therefore, its penetration ability also increases. Since the CT numbers depend upon the absorption ability of X-rays, therefore, variation in X-ray energy causes a change in CT numbers of the same tissue as illustrated in Fig. 8.15.

Example 8.2 Calculate the CT number for fat and cartilage bone with the following data:

μ	40 kV	60 kV	80 kV	00 kV
μ_{water}	0.268	0.206	0.184	0.171
μ_{fat}	0.228	0.188	0.171	0.160
$\mu_{cart.bone}$	1.28	0.604	0.428	0.356

Solution: $(CT)_{fat}$.

At 40 keV = [(0.228–0.268) / (0.268)] × 1000 = − 149
At 60 keV = [(0.188–0.206) / (0.206)] × 1000 = − 87
At 80 keV = [(0.171–0.184) / (0.184)] × 1000 = − 71
At 100 keV = [(0.160–0.171) / (0.171)] × 1000 = − 64

$(CT)_{cart.bone}$.

At 40 keV = [(1.28–0.268) / (0.268)] × 1000 = 3776
At 60 keV = [(0.604–0.206) / (0.206)] × 1000 = 1932
At 80 keV = [(0.428–0.184) / (0.184)] × 1000 = 1326
At 100 keV = [(0.356–0.171) / (0.171)] × 1000 = 1081

Figure 8.15 shows variation in the CT numbers of cartilage bone with the energy of X-ray beam. The figure shows that the CT number of a tissue decreases with increasing beam energy. This variation in CT number also brings changes on the

gray scale, causing complications in the imaging process. Therefore, a better option is to use a monochromatic beam of X-ray photons. The energy of X-ray beam is controlled by and proportional to the X-ray tube voltage. The higher the tube voltage, the more energetic X-ray beams are obtained. Thus, controlling the tube voltage can solve the problem of variation in energy and can produce a monochromatic beam to avoid variation in CT numbers. Proper X-ray generator calibration is important for accurate and reproducible CT numbers.

8.4.2 Dynamic Range

In the digital image formation, analogue-to-digital converter (ADC) needs to be capable of responding to a wide variation of attenuation in the part of patient's body under irradiation. The dynamic range shows the ratio of the largest signal (in the absence of any absorption) to the smallest signal (with maximum absorption) that can be detected. This allows obese and slim patients to be imaged with the same standard and definition including bone (high density) and soft tissues (low density). Dynamic range depends on the accuracy and precision of the ADC of the voltage signal.

8.4.3 CT Numbers and Windowing

CT numbers are just numbers expressed in Hounsfield units. On the other hand, gray scale is a way CT numbers are expressed. In general CT numbers in an image are mapped onto an 8-bit gray scale. When the dynamic range of the CT number scale exceeds the gray scale, all numbers cannot be accommodated on the gray scale. In that condition the way in which CT numbers are mapped needs to be adjusted by windowing. The display window represents the CT number interval of interest and is defined by two parameters: window level and window width.

Window level is the CT number on which the window is centered. On the other hand, window width is the magnitude of the range of CT numbers covered by the window. The window width determines the contrast in the displayed image. CT window describes the difference between the upper and lower limits of the window. Voxels with CT numbers above the limit appear white, while those below the lower limit appear black. A narrow window spreads a large range of gray scale values over a small range of CT numbers, allowing detection of very small differences in tissues densities. For example, in order to evaluate and find subtle masses in the liver, one might use liver windows. Choosing 60 HU as an average HU value for liver, the shades of gray scale can be distributed over a narrow window range. One could use 160 HU as the narrow window, with 80 HU above the 60 HU average value and 80 HU below it. Therefore the liver window would extend from -20 HU to $+140$ HU. All the shades of gray for the image would be distributed in this range

Table 8.4 Window settings in computed tomography

Tissue	Window level (HU)	Window width (HU)
Lungs	−500	1500
Brain	40	80
Chest	50	350
Abdomen	60	400
Bone	300	1500

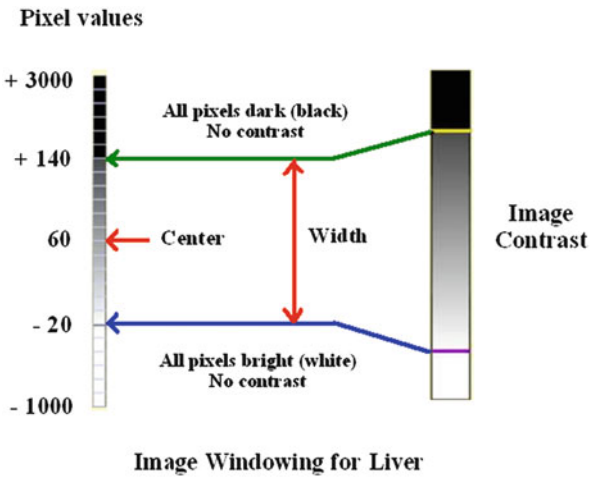

Fig. 8.16 Image window level and window width for liver

of Hounsfield values. Any HU value below −20 would be pure black, and any HU value above +140 HU would be pure white in this example. Using the same logic, bone windows would use a "wide window" to evaluate everything from fat-containing medullary bone that contains the marrow to the dense cortical bone, and the center or level would be a value in the hundreds of Hounsfield units. Typical window settings for various body parts in CT imaging are given in Table 8.4. Figure 8.16 shows image windowing for the liver.

8.4.4 Data Matrices

After calculating the CT numbers, they are stored in computer memory and represent a volume slice element called voxel. A voxel along with tissue slice is given in Fig. 8.17. These voxels form a matrix. The matrix for the CT numbers must be able to hold a range of voxel values over 4000 to handle CT number values from −1000 to 3000. A 512 × 512 voxel memory with 16 bits deep represents a total storage of 500 kB. A collection of transverse images represents a three-dimensional volume of voxel values.

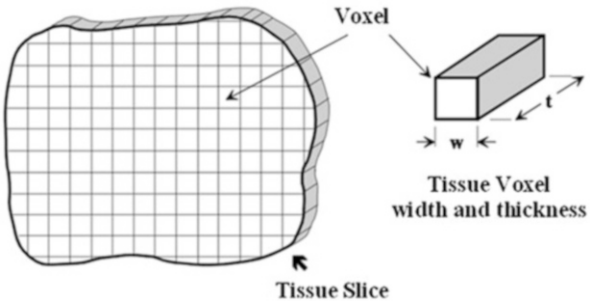

Fig. 8.17 A single voxel and tissue slice

8.5 Image Formation and Back Projection

CT images are formed using the data for attenuation coefficients of the body slice X-rays passing through (Dowsett et al. 2006). Several approaches are adapted to construct image. One very effective approach is the back projection and reconstruction to obtain a clear image of the scanned part of the body. This is a standard method of reconstructing images in computed tomography.

In this method, any attenuation of the X-ray beam is assumed to have occurred uniformly along the entire ray path.

8.5.1 Back Projection

The process of back projection works on smearing back the projection across the image at the angle it was acquired. By smearing back all of the projections, an image is reconstructed. This image looks similar to the real picture but is blurry due to smearing bright pixels across the entire image instead of putting them exactly where they belonged. Figure 8.18 gives a smeared back projection. To reconstruct an image, 180° of data is needed in addition to the fan beam angle. The remaining 180° is simply a mirror image of the first. Choosing the direction of 180° does not matter because no matter which way a photon travels through tissue, it will be attenuated the same amount. Because of the fan-beam geometry, measuring an extra amount, equal to the fan angle, is needed to get all of the data. In a fan-beam geometry, the angle of the fan determines how much of the object is included in the reconstructible field of view. A point must be included in all 180 degrees of projections in order to be reconstructed correctly.

To understand the process of back projection, let us take an example of a 2×2 matrix where the elements of the matrix represent the attenuation (or the absorption) coefficients.

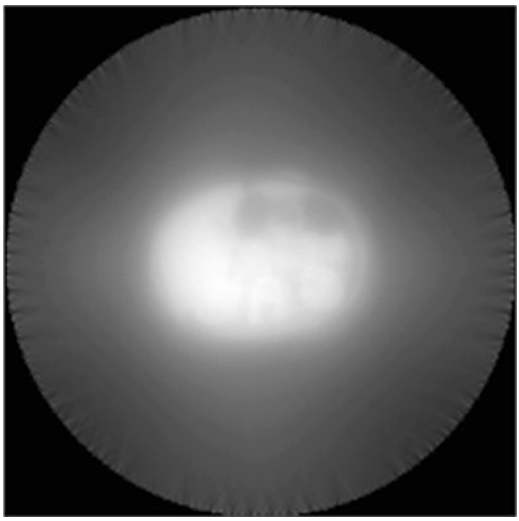

Fig. 8.18 Back projection of a slice

Example 8.3 Consider the following 2×2 matrix with elements μ_1, μ_2, μ_3, and μ_4. Let us start from $\mu_1 = 3$, $\mu_2 = 2$, $\mu_3 = 5$, and $\mu_4 = 7$:

μ_1	μ_2
μ_3	μ_4

(a)

3	2
5	7

(b)

A process of back projects is performed, and the original matrix is then derived back by (1) subtracting a background (bg) or offset value from each element and (2) dividing by a number "n" called the normalization or renormalization or rationalization factor.

To work on the given matrix, perform the following steps:

(a) Take the original matrix given in (b).
(b) Sum in the horizontal direction placed in the corresponding pixels to get matrix.

5	**5**
12	**12**

(c)

In this process if we add the elements horizontally, we get $3 + 2 = 5$, and $5 + 7 = 12$.

(c) Sum the elements of original matrix (b) at 45° (diagonal) to obtain matrix (d) below.

10	**2**
5	**10**

(d)

(d) Sum the elements of original matrix (b) at 90° (downward) to obtain matrix (e).

8	**9**
8	**9**

(e)

(e) Sum the elements of original matrix (b) at 135° (back diagonal) to obtain matrix (f).

3	**7**
7	**7**

(f)

(f) Sum all the ray elements for each pixel to obtain new element. For the element at first row first column, $5 + 10 + 8 + 3 = 26$. For the element at first row

second column, $5 + 2 + 9 + 7 = 23$. For the element at second row first column, $12 + 5 + 8 + 7 = 32$. For the element at second row second column, $12 + 10 + 9 + 7 = 38$. Thus, we get the following matrix.

26	**23**
32	**38**

(g)

(g) Subtract a background (bg) of 17 from pixel to obtain matrix (h).

9	**6**
15	**21**

(h)

(h) Divide each element by $n = 3$ to normalize or rationalize it. This will give us the original matrix (b) back.

3	**2**
5	**7**

(i)

The question is how to calculate the background (bg) and the normalization factor (n)? In order to calculate bg and n, we know that since (g) is the sum of all the CT scans, it is equivalent to the original matrix (b). Take each pixel of the top row of (g). We know that if we subtract the background from each pixel and divide by the normalization factor n, it will give us the magnitudes of the original pixels. Therefore, we can develop the following equations:

$$(26 - bg)/n + (23 - bg)/n = 5 \tag{8.5}$$

$$(32 - bg)/n + (38 - bg)/n = 12 \tag{8.6}$$

Solving (3) and (4) simultaneously, we get $bg = 17$ and $n = 3$.

Example 8.4 Consider the following 3×3 matrix with elements μ_1, μ_2, μ_3, μ_4, μ_5, μ_6, μ_7, μ_8, and μ_9 with their values given in the matrix (a):

1	**1**	**1**
1	**2**	**1**
1	**1**	**1**

(a)

Sum in the horizontal direction gives

3	**3**	**3**
4	**4**	**4**
3	**3**	**3**

(b)

Sum along the diagonal (45°) provides

4	**2**	**1**
2	**4**	**2**
1	**2**	**4**

(c)

Sum in the (vertical) downward direction gives

3	**4**	**3**
3	**4**	**3**
3	**4**	**3**

(d)

Sum along the back diagonal (135°) gives

1	**2**	**4**
2	**4**	**2**
4	**2**	**1**

(e)

Sum of all the ray elements for each pixel gives

11	**11**	**11**
11	**16**	**11**
11	**11**	**11**

(f)

To calculate the background and the normalization factor, we develop a pair of linear equations like those in Example 8.3. Looking at the (f) and original matrix, we get

$$(11 - bg)/n + (11 - bg)/n + (11 - bg)/n = 3 \tag{8.7}$$

$$(11 - bg)/n + (16 - bg)/n + (11 - bg)/n = 4 \tag{8.8}$$

Solving the two equations, we get $bg = 6$ and $n = 5$, thus subtracting 6 from (f) and dividing by 3 to get the original matrix:

1	**1**	**1**
1	**2**	**1**
1	**1**	**1**

8.5.2 Filtered Back Projection and Convolution

Filtered back projection is used to fix the blurring problem created by the back projection. In this process, the projection data obtained from back projection is altered to remove the blurring effect in the reconstruction of the image.

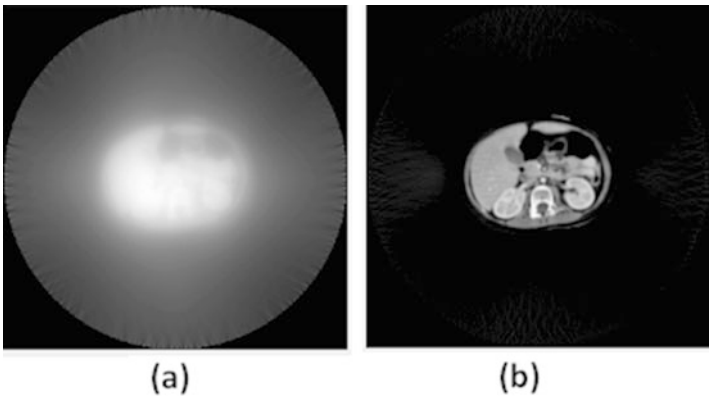

Fig. 8.19 (**a**) Back projection. (**b**) Filtered back projection

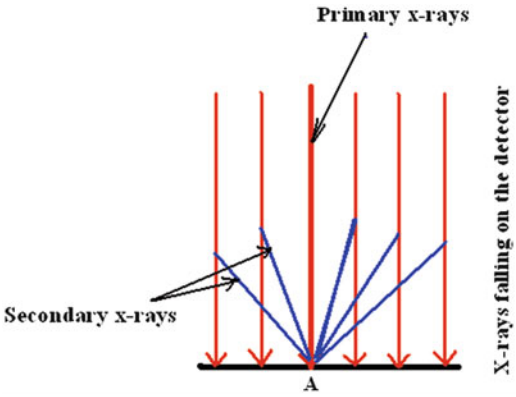

Fig. 8.20 Primary and scattered X-rays received at point A and considered in convolution

This alteration to the data obtained by back projection is called filtering. The filter used in this process is called a high-pass filter or a sharpening filter or a mask. The filter picks up sharp edges within the projection (and hence in the underlying slice) and tends to ignore flat areas. The high-pass filter creates kind of negative pixels at the edges and hence subtracts out the extra smearing caused by back projection. As a result, the correct reconstruction is obtained that removes blurring from the image as shown in Fig. 8.19.

Convolution is a process that takes care of the overlapping effect in the filtered back projection. Figure 8.20 explains the process of convolution. X-ray beam of certain field size is falling on the detector or screen after passing through a body slice. Let us concentrate on the X-rays being received at point A on the detector. In this process, majority of the X-ray photons arriving at A are the primary X-rays, falling directly on A. However, X-rays going in different directions are also falling at point A due to scattering from body tissues in the slice. The amount of the scattered radiation falling on A depends upon where from and at what angle those

radiation are being scattered. The process of convolution counts for all those radiation falling at point A but not going in the direction of A primarily.

The filtered back projection and convolution by applying a filter are described in Example 8.5 (Heverhagen 2016).

Example 8.5 Consider the following matrix (a) and filter to obtain filtered image:

-1	-1	-1
-1	8	-1
-1	-1	-1

Filter

1	1	1	1	1
1	1	1	1	1
1	1	8	1	1
1	1	1	1	1
1	1	1	1	1

(a)

First, we perform back projection in the following steps:

(i) Add the pixel elements of the matrix (a) in horizontal direction to obtain matrix (b).

5	5	5	5	5
5	5	5	5	5
12	12	12	12	12
5	5	5	5	5
5	5	5	5	5

(b)

(Ii) Add the elements of matrix (a) diagonally (at 45° below horizontal) to get matrix (a_1) and add to matrix (b). This will give matrix (c).

12	4	3	2	1
4	12	4	3	2
3	4	12	4	3
2	3	4	12	4
5	5	5	5	5

(a_1)

17	9	8	7	6
9	17	9	8	7
14	15	24	15	14
7	8	9	17	9
6	7	8	9	17

(c)

(iii) Add the elements of matrix (a) vertically to get matrix (a_2) and add to matrix (c). This will give matrix (d).

5	5	12	5	5
5	5	12	5	5
5	5	12	5	5
5	5	12	5	5
5	5	12	5	5

(a_2)

22	14	20	12	11
14	22	21	13	12
19	20	36	20	19
12	13	21	22	14
11	12	20	14	22

(d)

(iv) Add the elements of matrix (a) diagonally (at 45° above horizontal) to get matrix (a_3) and add to matrix (d). This will give matrix (e).

1	2	3	4	12
2	3	4	12	4
3	4	12	4	3
4	12	4	3	2
12	4	3	2	1

(a_3)

23	16	23	16	23
16	25	25	25	16
22	24	48	24	22
16	25	25	25	16
23	16	23	16	23

(e)

(v) Apply the filter to each 3x3 sub-matrix in (e) by multiplying the elements of the filter and then adding. This will give us a filtered value for the central element or pixel of that sub-matrix. In this process, we start from the sub-matrix "1" of matrix (e) as follows:

23	16	23
16	25	25
22	24	48

(1)

Multiply each element of the filter to the respective element of "1." This will give

-23	-16	-23
-16	200	-25
-22	-24	-48

The sum of all these elements will give 3. The number 3 will take the central spot of 3x3 sub-matrix within (e). This is shown below.

	3			

(vi) Repeat the same process using the next 3 × 3 sub-matrix "2" given below.

16	**23**	**16**
25	**25**	**25**
24	**48**	**24**

(2)

The sum of all elements gives −1. This number takes the central spot of sub-matrix "2." The filtered elements of (e) now look like

	3	**-1**		

Repeating this process to all 3x3 sub-matrices in (e) gives us filtered matrix (e). This matrix represents filtered back projection given in (f).

	3	**-1**	**3**	
	-10	**186**	**-10**	
	3	**-1**	**3**	

(f)

8.6 Image Quality

The quality of an image in CT helps a radiologist to get as much important information out of the image as possible (Goldman 2007). Therefore, the choice of a CT machine depends on the type of patient, tissues or part of the body involved (e.g. heart, brain, liver), and the nature of tumor or abnormal tissues. Different factors are responsible to affect the quality of an image. For example, fast scan times (< 1 s) will reduce motion artifact which is useful in pediatrics. Some of the image characteristics that affect the quality of an image are as follows (Dowsett et al. 2006).

8.6.1 Calibration

System calibration is very important in computed tomography. All detectors, X-ray tube, and electronics used in the system must be calibrated prior to the imaging. Problems can occur if system is not calibrated. For example, if a detector remains uncalibrated, the image gets ring artifacts which reduce the quality of image.

8.6.2 Uniformity

Another important factor that affects the image quality in CT is the uniformity or homogeneity of the phantom used. The degree of uniformity determines the accuracy of CT number measurement. The difference in the mean CT number between a peripheral (edges) and a central region of a homogeneous test object should be ≤ 8 HU. Such differences are largely due to the phenomenon of beam hardening and results in image artifacts. Computer corrections can help to achieve uniformity.

8.6.3 Contrast

In general, an image has good contrast if the darker parts are more dark and lighter parts are more light. In CT, the image contrast is measured as differences between the object density (in CT numbers) and its background. High-quality images have the ability to make the smallest object size visible at a given percentage contrast level called low contrast detectability. Mathematically, contrast is expressed in terms of percent difference in CT numbers "ΔCT(%)" as given in Eq. (5). Big difference in CT numbers corresponds to good contrast:

$$\Delta CT(\%) = [|CT_2 - CT_1|/1000] \times 100 \tag{8.9}$$

Since CT numbers depend upon the attenuation of the tissues, therefore, object contrast depends upon the attenuation property of the tissues.

Example 8.6 Find the contrast between the muscle and liver and between the muscle and fat. The CT numbers for these body parts in the unit of HU are liver = 60, muscle = 40, and fat = − 150.

Solution Contrast between the muscle and liver = $\Delta CT(\%) = [|CT_2 - CT_1|/1000] \times 100$

$$= [\,|\,60–40\,|\,/1000] \times 100$$
$$= 2.0$$

Contrast between the muscle and fat = $\Delta CT(\%) = [\,|\,40-(-150)\,|\,/1000] \times 100$
$$= [(40 + 150)/1000] \times 100$$
$$= 19$$

Results show that the contrast between the muscle and fat is high as compared to the contrast between the muscle and liver. Thus it will be easy to differentiate between the muscle and fat in an image as compared to differentiation between the muscle and liver.

8.6.4 Resolution

Resolution is characterized by the ability to distinguish high contrast small objects (with high CT number) as well as to differentiate between small objects very close to each other. Spatial resolution at high and low contrast is interdependent and critical to image quality and good imaging of diagnostically important structures.

The spatial resolution at high contrast determines the minimum size of detail visualized in the plane of the slice with a contrast $\geq$10%. It is affected by the following factors:

- Slice thickness
- Detector width
- Display matrix and pixel size (reconstruction algorithm)
- Field of view
- Object-to-detector distance
- X-ray tube focal spot size

The spatial resolution at low contrast or low contrast resolution determines the size of detail that can be visibly reproduced when there is only a small difference in density relative to the surrounding area. Low contrast resolution is affected by dose and image noise. The perception threshold in relation to contrast and detail size can be determined, for example, by means of a contrast-detail curve.

8.6.5 Noise

In general, every measurement is associated with a certain margin of error, and all measured values fluctuate around the true value (ICRU 1995). In CT the value that is measured is the attenuation caused by body parts or tissues, represented by its Hounsfield (HU) value. Each volume element (voxel) of a CT image is a measurement of the respective attenuation caused by the scanned object. Therefore, if a CT scan of the same object is repeated, the scan will always yield a slightly different CT value for this voxel. If a homogeneous object such as a water phantom is scanned, each voxel in the image can be interpreted as an independent measurement of the same material. Thus, a CT scan of a homogeneous object can be interpreted as many independent measurements of the same material carried out at the same time. All voxel values will fluctuate around the true value of the object, for example, water or a tissue. The measurement error is directly visible in the image and is usually called image noise.

If a sufficiently large amount of measurements are carried out, the average of the measured values is close to the true value. In a CT image, the image noise and the true HU value can be estimated by evaluating a sufficiently large homogeneous region of interest (ROI) in the image and calculating the standard deviation of the CT numbers.

8.6.6 Slice Thickness

Slice thickness affects the quality of image because of variation in noise due to slice thickness. Thin slices are more noisy and hence soft tissue contrast is lost if slice is too thin. Bone contrast is not affected by slice thickness due to the existence of greater image contrast.

8.7 Image Artifacts

Any discrepancy between the CT numbers represented in the image and the expected CT number based on the linear attenuation or absorption coefficient is called an artifact (ICRU 1995). Artifacts appear in the CT image as lines, rings, dark spots, and ghost image (blurry image) (Ketcham and Carlson 2001). Artifacts are divided into four categories: steaks (or lines), shading, bands, and rings.

Artifacts mainly appear because of two sources: the patient and the equipment and image processing (Razi et al. 2014).

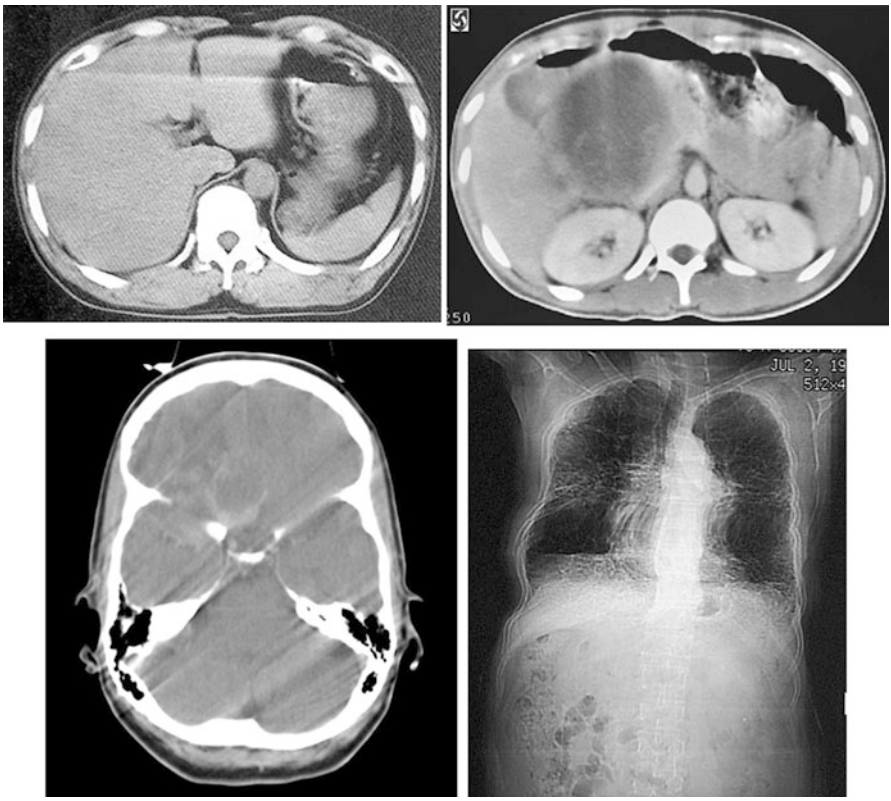

Fig. 8.21 Motion artifacts in the CT images of various body parts

8.7.1 Patient-Induced Artifacts

Patient-induced artifacts appear because of the presence of the patient's body directly or indirectly. They are further classified into four types.

8.7.1.1 Motion Artifacts

Such kind of artifacts appears due to the motion of a patient during the CT scan process. For example, if the motion of patient in the CT scanner is too fast, the image obtained could be blurred. It produces a "ghost effect," and the CT image appears as if composed of superimposed images. Figure 8.21 shows motion artifacts in various CT images. Motion artifacts are minimized by good communication with the patient and explaining the procedure well. Shorter scan time also helps reducing motion artifacts.

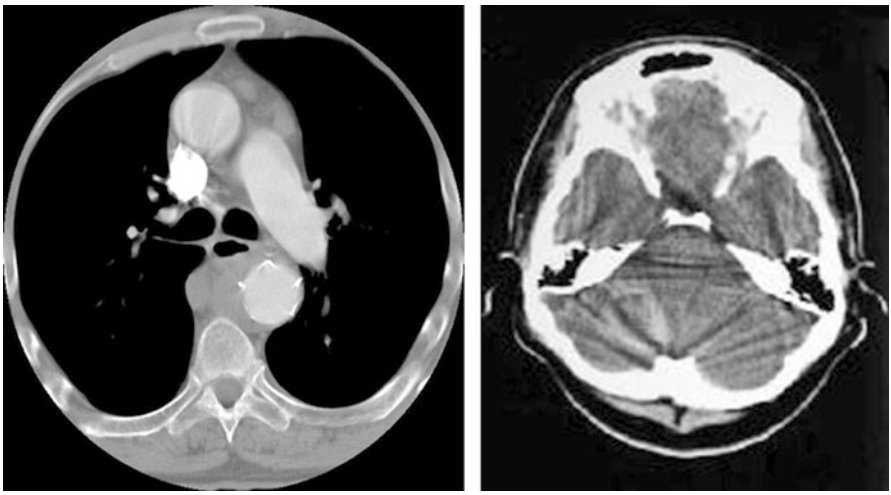

Fig. 8.22 Cupping artifacts in the CT images due to beam hardening

8.7.1.2 Cupping Artifacts

This kind of artifact comes due to beam hardening. It occurs when the average energy of X-ray beam passing through the patient increases. High-energy photons are attenuated less by the tissue and beam is hardened. The artifact is called "cupping" artifact because the hardening is more pronounced in the center and less at the periphery, resembling a cup. It mostly occurs in the skull, upper chest and shoulders, and hips. These artifacts are minimized by increasing tube voltage (kV_p), decreasing slice thickness, and increasing filtration. Increasing X-ray tube voltage minimizes the energy difference between the X-rays in the center of the beam and at the periphery. As a result a decrease in the beam hardening occurs that reduces the cupping artifacts. Decreased slice thickness also reduces the beam hardening, hence decreasing the cupping artifacts. Filtration removes too high or too low energetic X-rays from the beam, resulting in the reduction of cupping artifacts (Fig. 8.22).

8.7.1.3 Metal Artifacts

This kind of artifact is caused by the presence of metallic objects inside or outside the patient. Metal artifact manifests itself as "streaking" artifact. Metallic object absorbs the photons, causing an incomplete profile. Figure 8.23 gives streaking effect in images due to metal artifacts.

Metal artifacts can be removed by removal of external metallic objects before patient is passed through scanner. Gantry angulation can also help reduce this artifact.

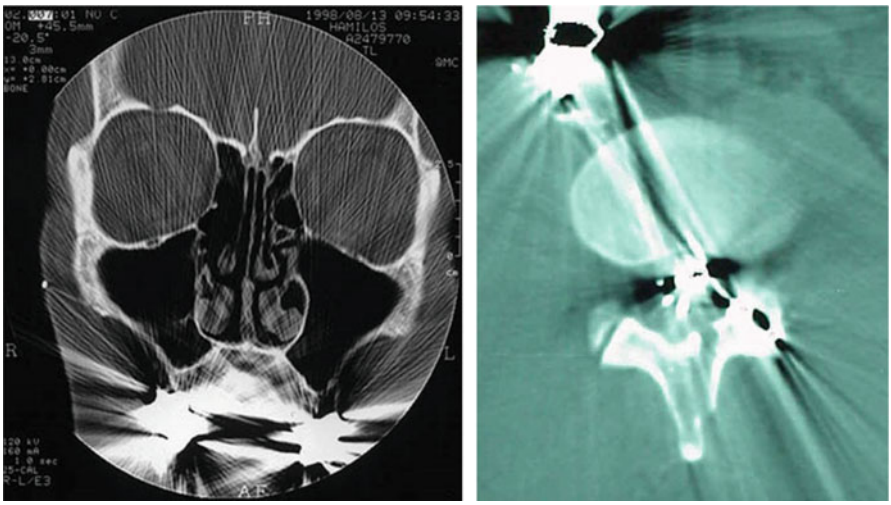

Fig. 8.23 Streaking effect due to metal artifacts

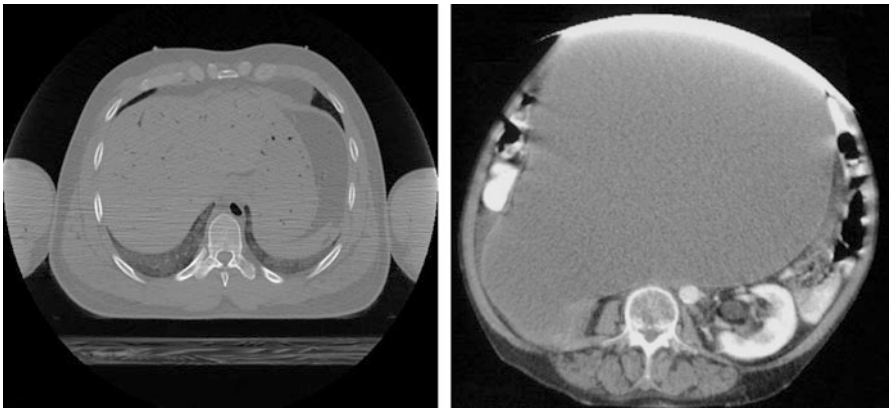

Fig. 8.24 Shading effect due to out-of-field artifacts

8.7.1.4 Out-of-Field Artifacts

This artifact appears when the patient is not entirely enclosed in the scanning field of view (SFOV). Parts of the patient's body can obstruct the detectors, and patient's tissues outside the SFOV will further harden the beam by making the overall body part side thicker for the X-rays. Out-of-field artifacts appear as shading and streaks. Figure 8.24 shows shading due to out-of-field artifacts.

These artifacts can be avoided by selecting larger SFOV, taping patient's tissue, and raising patient's arms above his head on the chest and abdomen scan.

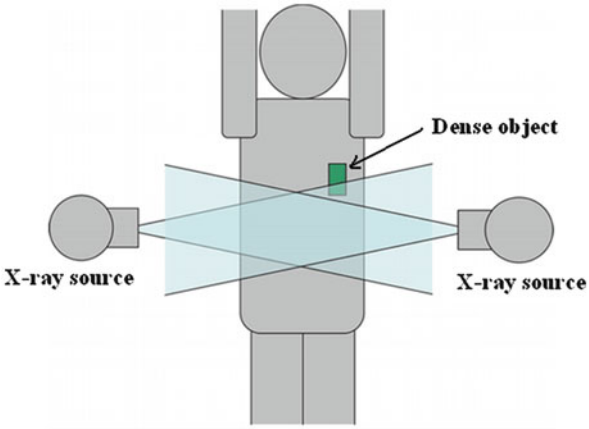

Fig. 8.25 Off-centered dense object causing partial volume artifacts

8.7.2 Equipment Imaging Process Artifacts

Equipment imaging process artifacts appear because of the presence of limitations in the use of or errors in the equipment used during the CT imaging process or patient's body directly or indirectly. They are classified into several types.

8.7.2.1 Partial Volume Artifacts

These artifacts occur when a dense object lying off-center protrudes part of the way into the X-ray beam. Figure 8.25 gives the mechanism of partial volume artifacts. It is clear from the figure that one X-ray beam is partially obstructed by a dense hard object, while the other beam is not affected by the dense object. Such kind of artifacts can be minimized by selecting thin slices for scan.

8.7.2.2 Aliasing Artifacts

The appearance of fine lines on the CT image due to the edge or periphery effect is called aliasing artifacts. Fig. 8.26 shows fine line on the image due to aliasing artifacts.

The artifacts can be removed by increasing scan time and by using complete arc scan.

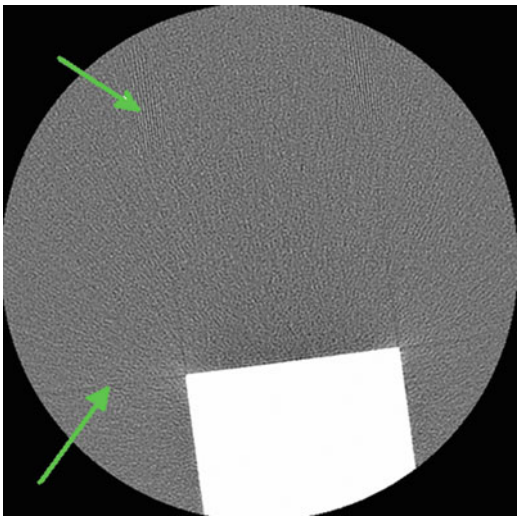

Fig. 8.26 Fine lines due to aliasing artifact

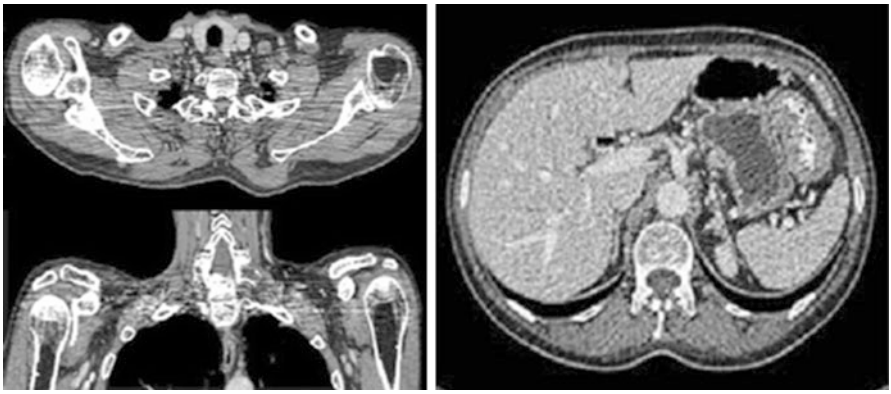

Fig. 8.27 Photon starvation artifacts

8.7.2.3 Photon Starvation Artifacts or Noise

The attenuation or absorption of photons by a material or body tissue is statistical in nature, and hence slight fluctuation is always expected even if the same beam passes through the same material or tissue again. This natural fluctuation causes minor changes in the CT number between points in the image for a scan of uniform material or tissue like liver or water. As a result artifact appears in the image. Figure 8.27 gives photon starvation artifacts in images.

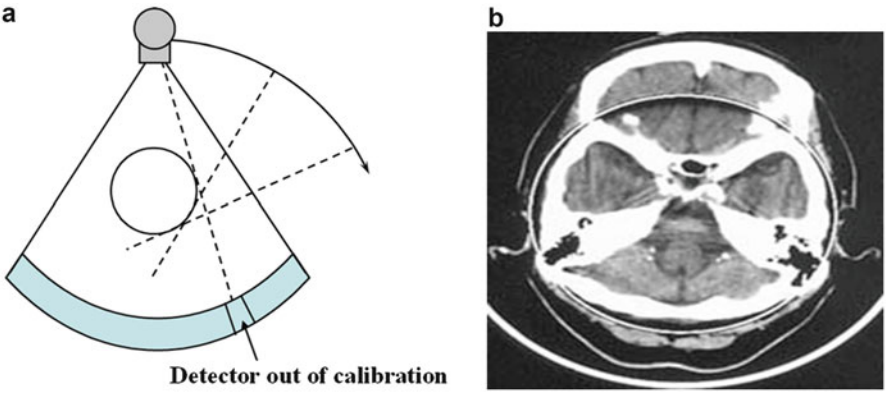

Fig. 8.28 (**a**) Mechanism of ring artifact and (**b**) ring artifact in an image

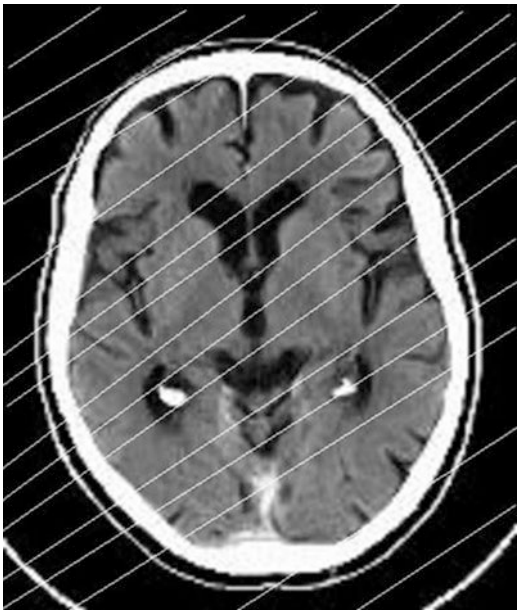

Fig. 8.29 Lines in the image due to tube arcing

This artifact can be removed by increasing the tube voltage (kV_p) and the slice thickness.

8.7.2.4 Ring Artifacts

Ring artifacts appear when one or more detectors are out of calibration. This problem appears mainly in the third generation. Figure 8.28a and b shows the path leading to ring artifacts and the artifact appearance in the image. This artifact

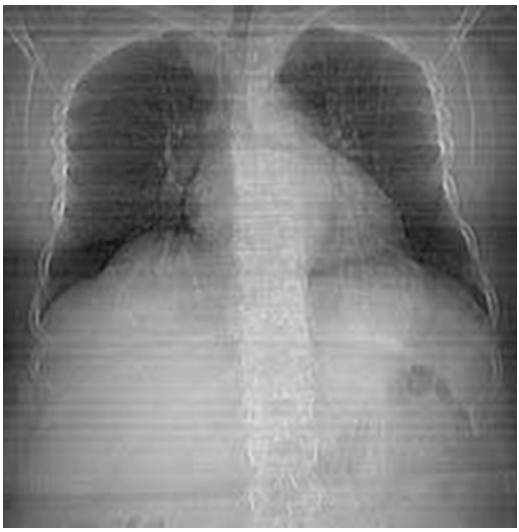

Fig. 8.30 Lines on topogram

can be removed either by proper calibration of the specific detector causing the problem or replacing that detector at all.

8.7.2.5 Tube Arcing

In this artifact is caused by an old X-ray tube. Tungsten vapor from anode and cathode intercepts the projectile electrons intended for collisions with target. As a result cracking sound and lines appear in the image. This problem can be removed by replacing the old tube. Figure 8.29 shows lines in the image due to tube arcing.

8.7.2.6 Line in Topogram

A bad detector causes many problems. One of the drawbacks of bad detector is that it causes continuous lines on the topogram as shown in Fig. 8.30. The detector needs to be replaced.

8.7.2.7 Staircase

The appearance of stair-like shapes in the image occurs in this artifact. Improper selection of slice thickness and slice incrementation causes this problem. The artifact is minimized by using thin slice and proper overlap in slice incrementation. Figure 8.31 provides staircase effect in CT images.

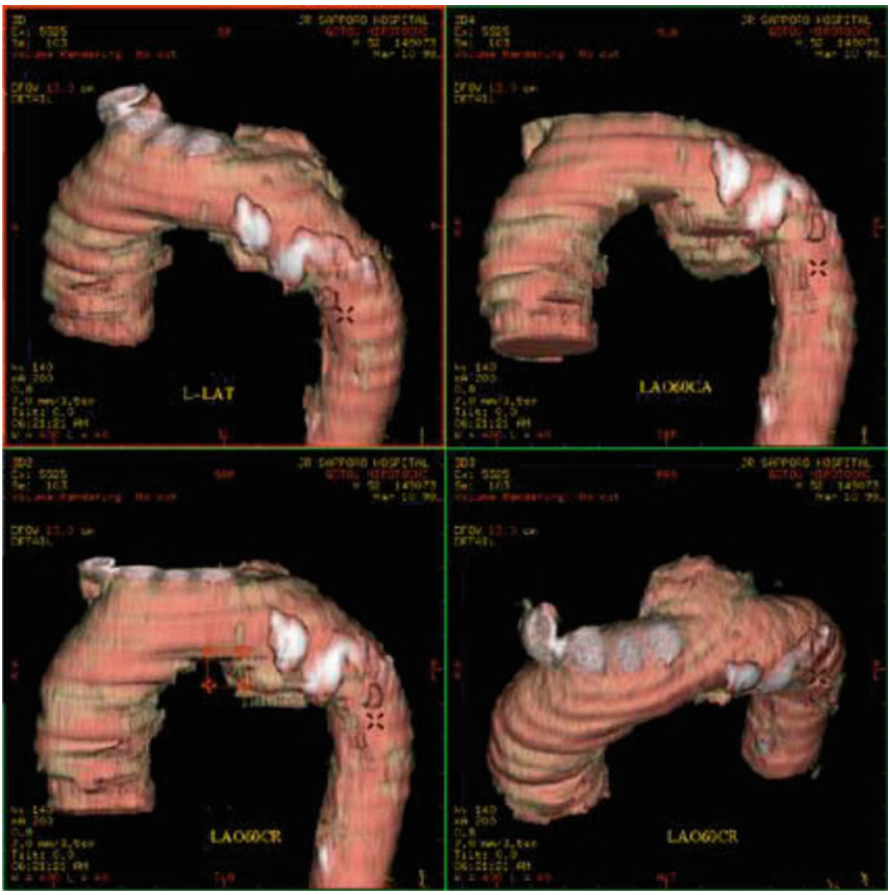

Fig. 8.31 Staircase artifacts in CT image

Problems

1. Calculate the CT number of blood with the following given data:

μ	80 keV	100 keV	150 keV
μ_{water}	0.1835	0.1707	0.1504
μ_{blood}	0.1906	0.1772	0.1560

   (b) CT number of liver is 60. Find the CT number of another tissue whose contrast with liver is 2.

2. Absorption coefficients of a body slice are given in the form of the following matrices.

   Perform the back project and calculate the background (bg) and the normalization number (n) in each case.

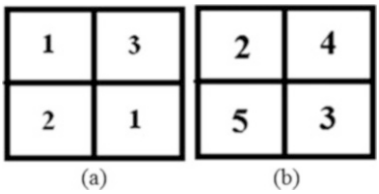

3. Perform the back projection on the following 3 × 3 matrices.

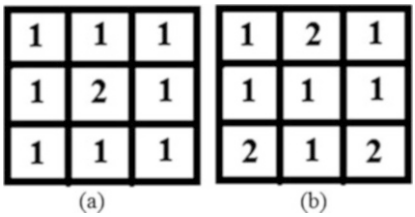

4. A matrix representing a wide body slice is given by the matrix below.

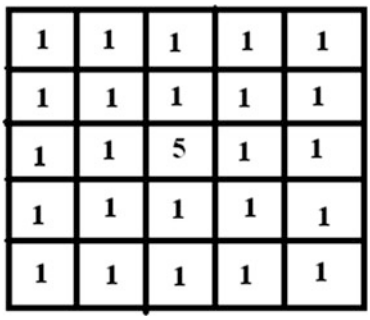

Find the matrix corresponding to the filtered back projection using the following filter or mask.

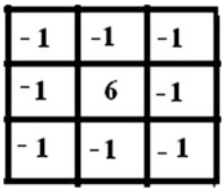

5. In a certain CT imaging process, the table moves by 12 mm in a single rotation for an 8 mm thick slice. If the total time of rotation is 16 s in which four slices were scanned, then find the pitch and table speed of the CT machine.

Acknowledgement In preparing this chapter I have taken help from many books, research papers and published articles. I am very thankful to their authors, writers and contributors for letting me taking help from their intellectual properties.

References

Anne TK et al (2010) Evaluation of subjective assessment of the low-contrast visibility in constancy control of computed tomography. Radiat Prot Dosim 139(1–3):449–454

Brink JA, Helical CT (1994) Principles and technical considerations. Radiographics 14(4):887

Dowsett DJ, Kenny PA, Johnston RE (2006) The physics of diagnostic imaging, second edn. CRC Press, Taylor & Francis Group, London/New York

Goldman LW (2007) Principles of CT and CT technology. J Nucl Med Technol 35(3):115–128

Heverhagen JT (2016) Physics of computed tomography scanning, handbook of neuro-oncology neuroimaging chapter 16, science direct. Elsevier, San Diego

ICRU (1995) Report 54: medical imaging – the assessment of image quality, (7910 Woodmont Ave., Bethesda, Maryland USA 20814)

Jastaniah SD et al (2015) CT optimization for diagnosis of some acute abdomen cases. Advances in Comput Tomogr 4:19–26

Ketcham RA, Carlson WD (2001) Acquisition, optimization and interpretation of X-ray computed tomographic imagery: applications to the geosciences. Comput Geosci 27:381–400

Razi T, Niknami M, Ghazani F (2014) Relationship between Hounsfield unit in CT scan and gray scale in CBCT. J Dent Res, Dent Clin, Dent Prospects 8(2):107–110

Chapter 9
Magnetic Resonance Imaging (MRI)

Steffen Sammet

Contents

9.1 MRI 263
9.2 Contrasts in MRI 267
9.3 Physiological and Functional MR Imaging 271
9.4 MRI Safety 275
9.5 Future MRI Applications 277
References 278

9.1 MRI

MRI is a noninvasive cross-sectional imaging modality that does not require any ionizing radiation (Sammet et al. 2010). For acquiring images, MRI uses the physical principle of magnetic resonance that was first described by Felix Bloch and Edward Purcell in 1946 who then received the Nobel Prize in Physics in 1952 for their discovery (Nature 1952). Paul Lauterbur and Peter Mansfield received a Nobel Prize in Medicine in 2003 for their description on how to acquire MR images from the human body (Lauterbur 1973; Lauterbur 2004). Since then the field of MRI has grown tremendously and is now an established and advanced imaging modality in radiology that allows to acquire high-resolution anatomical images as well as time-resolved physiological and functional datasets (Roldan-Valadez and Lopez-Mejia 2014).

S. Sammet, MD, PhD, DABR, DABMRS, FAMP (✉)
University of Chicago Medical Center, Department of Radiology, Chicago, IL, USA
e-mail: ssammet@radiology.bsd.uchicago.edu

M. Maqbool (ed.), *An Introduction to Medical Physics*, Biological and Medical Physics, Biomedical Engineering, DOI 10.1007/978-3-319-61540-0_9

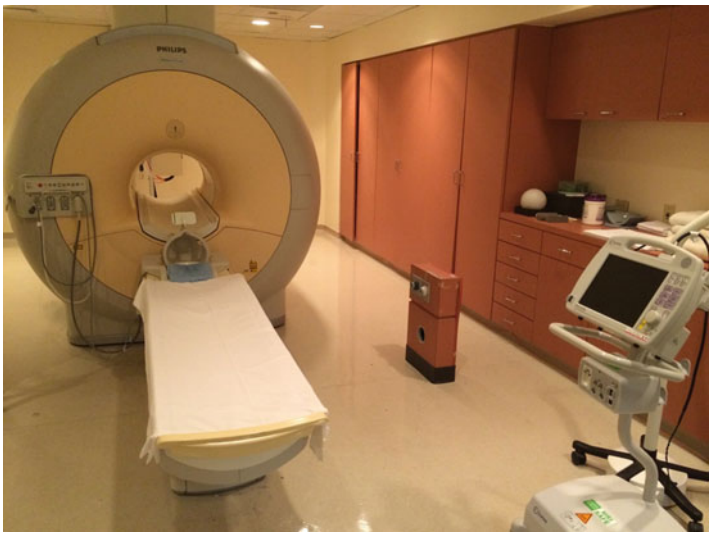

Fig. 9.1 Clinical MRI system with the patient table in the front that can be moved inside the bore of the magnet

9.1.1 MR Imaging Principle

A patient will be moved inside the bore of a magnet with a strong static magnetic field B_0 that is in the range of 0.2 T–3 T for clinical MRI scanners (Fig. 9.1). For the typical clinical magnetic field strengths of 1.5 T and 3 T, strong superconducting magnets are required (Sammet et al. 2010).

The human body is composed of water molecules, which contain two hydrogen nuclei, or protons. The magnetic moments of these protons align with the direction of the static magnetic field inside the scanner. Oscillating electromagnetic radiofrequency fields and gradient fields are then used to acquire images from the body of the patient. The radiofrequency field B_1 is produced by an RF coil, and the fast-switching gradient fields are produced by three different coil systems (G_x, G_y, and G_z) that are embedded in the bore of the MRI scanner (Kanal et al. 1990).

9.1.1.1 Static Magnetic Field B_0

The strong static magnetic field B_0 is used to prepare chemical compounds (mainly hydrogen protons in water and fat) for imaging. The strength of the static magnetic field B_0 of an MR scanner, the magnetic flux density, is measured in the SI unit Tesla (T). Stronger static magnetic fields lead to a higher signal-to-noise ratio (SNR) and subsequently to a better image quality in the MR images or to a faster scan time. The static magnetic field of a 3 T MRI scanner is approximately 60,000 times stronger than the magnetic field of the Earth (~50 μT) (Sammet et al. 2010).

Fig. 9.2 Superconducting magnet of a clinical MRI system after the removal of the covers and the patient table

These high magnetic fields cannot be achieved with permanent magnets and require superconducting magnets. A superconducting magnet is an electromagnet that is made from superconducting wires that are cooled with liquid helium (Fig. 9.2). For clinical MRI systems, these superconducting wires are most commonly made of an alloy of niobium and titanium (NbTi). The wires will be cooled below their critical temperature, the temperature at which the winding material changes from the normal resistive state to a superconducting state. The wires can conduct large electric currents in the superconducting state and have zero electrical resistance to produce strong magnet fields.

9.1.1.2 Radiofrequency Field B_1

Radiofrequency (RF) coils are designed as antennas that can transmit radiofrequency waves inside the human body and also receive the radiofrequency waves from the human body. The radiofrequency coils are built for different body parts of the patient (e.g., head coils, abdominal coils, knee coils, extremity coils) and are positioned as close as possible to the anatomical structures of interest to achieve a good image quality. A dedicated head coil is shown in Fig. 9.1 at the head end of the patient table.

The radiofrequency field B_1 causes the protons to alter their alignment relative to the static magnetic field B_0 at a higher energy state. This process is called excitation. The protons that were excited by the B_1 field will then return to their lower-energy state in a process called relaxation and will reemit RF radiation at the Larmor frequency:

$$\omega_0 = \gamma B_0 \tag{9.1}$$

Returning RF waves from the patient are picked up by the RF coils, stored in an intermediate image space (k-space), and then used to calculate an MR image with the mathematical fast Fourier transform (FFT).

9.1.1.3 Gradient Magnetic Fields G_x, G_y, and G_z

Gradient fields are used to localize the MR signal from a specific location in the human body. The three different gradient coils G_x, G_y, and G_z are embedded inside the bore of the MRI scanner and are used for slice selection (z), phase encoding (x), and frequency encoding (y) to acquire cross-sectional 2D images from any angulation or 3D datasets of the human body (Fig. 9.3). The gradient coils are responsible for the acoustic noise in an MRI scanner caused by magnetic Lorentz forces from the static magnetic field B_0 on the electric currents flowing in the gradient coils (Kanal et al. 1990).

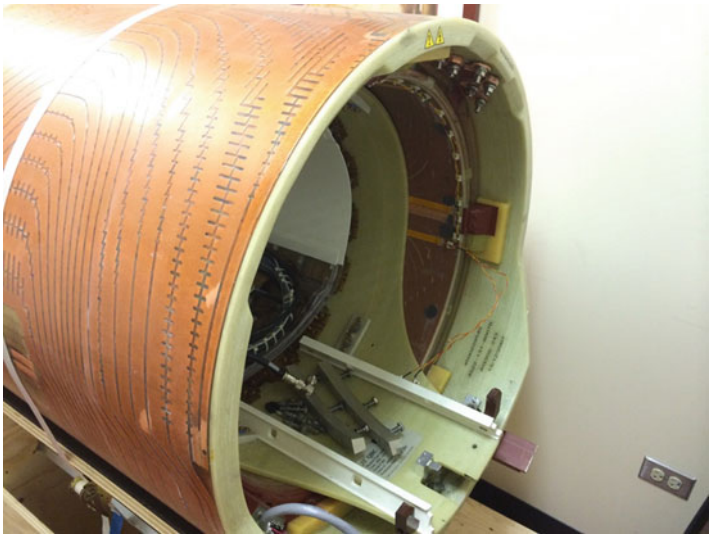

Fig. 9.3 Gradient system of an MRI system with x-, y-, and z-gradient coils embedded in epoxy. The gradient coils are used to localize the MR signal from a specific location in the human body

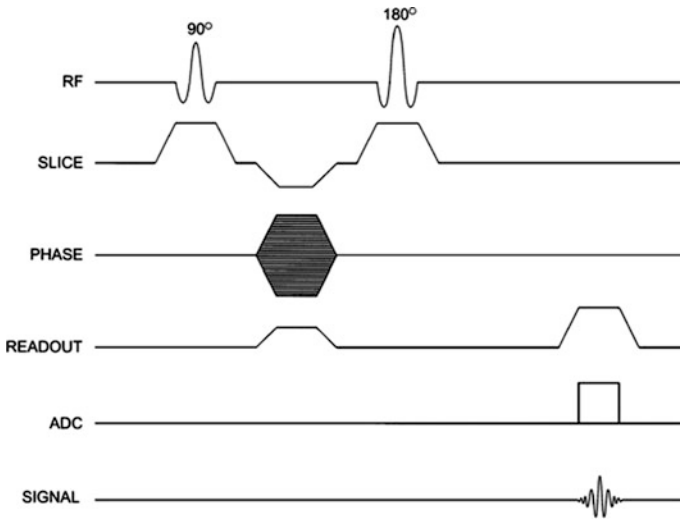

Fig. 9.4 Spin echo (SE) pulse sequence diagram with a slice selective 90° excitation pulse followed by a 180° refocusing pulses and the gradients in slice, phase, and frequency/readout direction. ADC is the time of signal acquisition and analog-to-digital signal conversion (http://bitc.bme.emory.edu/images/se_pt_1.jpg)

9.1.2 MRI Pulse Sequences

MRI pulse sequences are programs that contain the timing and duration of radiofrequency pulses and magnetic gradients to produce an image. In MRI there are two major pulse sequence groups: spin echo (SE) sequences and gradient echo (GRE) sequences. Spin echo sequences include a slice selective 90° excitation pulse followed by one or more 180° refocusing pulses (Fig. 9.4) (Mitchell et al. 1986).

Gradient echo sequences are characterized by the use of excitation pulses with flip angles of usually less than 90°, the absence of 180° RF refocusing pulses, and the use of dephasing and rephrasing gradient pulses (Fig. 9.5).

Gradient echo sequences are in general faster than spin echo sequences and allow real-time imaging of moving organs in the human body such as the heart (Li and Mirowitz 2004).

9.2 Contrasts in MRI

MRI pulse sequences are used to produce the contrast in an MRI image. In a spin echo sequence, there are generally two parameters that influence the contrast of a tissue with the spin density ρ: the repetition time (TR) and the echo time (TE):

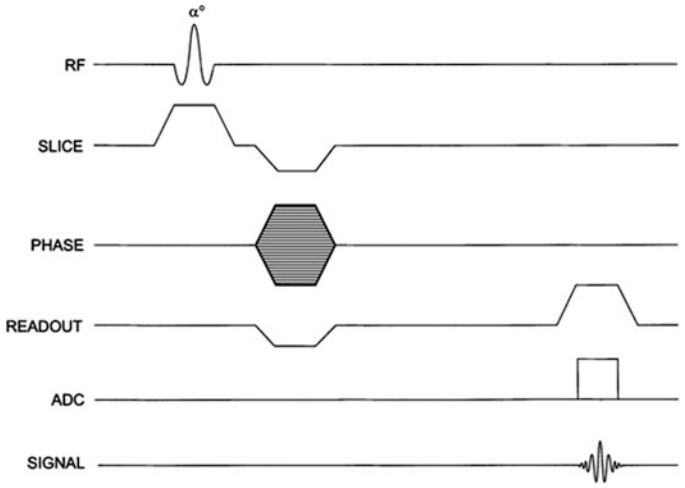

Fig. 9.5 Gradient echo (GRE) pulse sequence diagram with a slice selective excitation pulse α, which is typically smaller than 90°. The gradients in readout direction are used to produce a gradient echo when the ADC is turned on during signal acquisition (http://bitc.bme.emory.edu/images/ge_pt_1.jpg)

$$S = \rho \cdot \left(1 - e^{-\frac{TR}{T_1}}\right) \cdot e^{-\frac{TE}{T_2}}. \tag{9.2}$$

The repetition time TR is the time between two excitation pulses. The echo time (TE) is the time between an excitation pulse and MR signal sampling when the echo maximum occurs (Fig. 9.4). In a gradient echo sequence, there are in general three parameters that influence the contrast: the flip angle of the excitation pulse α, TE, and TR (Fig. 9.5) (Sammet et al. 2002).

9.2.1 T_1 Contrast

T_1 is the longitudinal or spin-lattice relaxation time. Not all energy that was put into the system with an RF pulse during the excitation returns to the RF coil. Some of the energy is lost and heats up the surrounding tissue, referred to as the lattice. The time course that describes the system's return to thermal equilibrium is mathematically described by an exponential curve. This recovery rate is characterized by the time constant T_1 (Sammet et al. 2002).

T_1-weighted pulse sequences use short TR and short TE. Different body tissues have different T_1 relaxation times. After an excitation pulse, the longitudinal magnetization vector of fat realigns relatively quickly with the static magnetic field B_0 again, and it therefore appears bright on a T_1-weighted image. Water

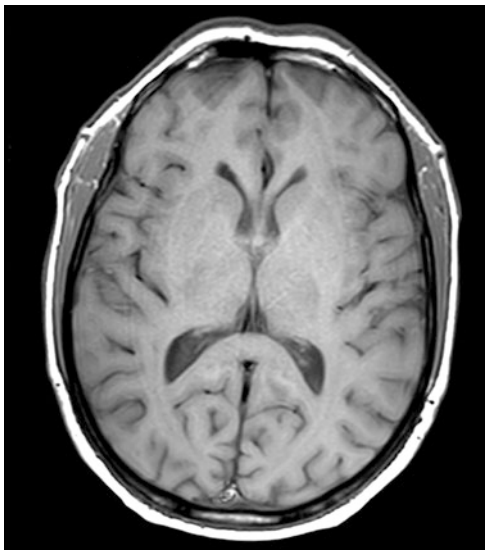

Fig. 9.6 Axial T_1-weighted MR image of the human brain

shows much slower longitudinal magnetization realignment after a radiofrequency pulse and appears relatively dark on T_1-weighted images (Fig. 9.6) (Sammet et al. 2002).

9.2.2 T_2 Contrast

T_2 is the transverse or spin-lattice relaxation time. Random fluctuations of the local magnetic field lead to random variations in the precession frequency of the nuclear spins in the human body. After an excitation pulse, the initial phase coherence of the nuclear spins will be lost when they get out of phase which is described by an exponential decay with the time constant T_2. T_2 relaxation occurs more rapidly than T_1 relaxation (Sammet et al. 2002).

T_2-weighted pulse sequences use long TR and long TE. Fluid (e.g., in the cerebrospinal fluid (CSF) spaces of the brain) appears bright on T_2-weighted images (Fig. 9.7).

9.2.3 Proton Density Contrast

Proton density-weighted images are produced by controlling the selection of scan parameters to minimize the effects of T_1 and T_2 resulting in an image dependent primarily on the density of protons in the imaging volume. Proton density-weighted sequences use a long TR and a short TE (Fig. 9.8) (Sammet et al. 2002).

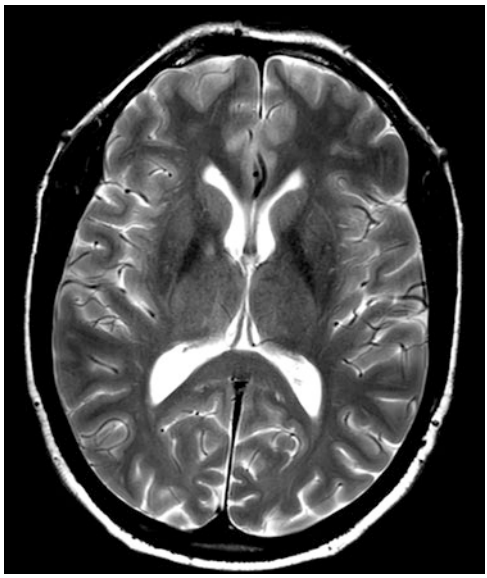

Fig. 9.7 Axial T_2-weighted MR image of the human brain

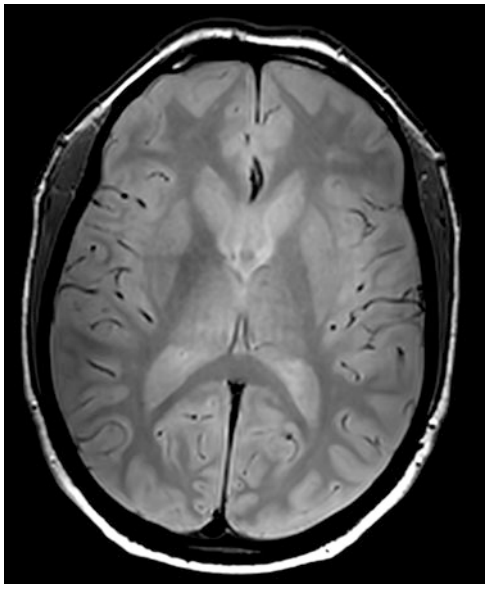

Fig. 9.8 Axial proton density-weighted MR image of the human brain

9.2.4 T_2^* Contrast

T_2^* relaxation is caused by a combination of spin-spin relaxation and magnetic field inhomogeneities. T_2^* relaxation occurs with gradient echo imaging sequences. T_2^* relaxation is faster than T_2 relaxation. In spin echo sequences, the transverse

relaxation caused by magnetic field inhomogeneities is eliminated by the 180° refocusing pulse; in gradient echo sequences, the relaxation due to magnetic field inhomogeneities cannot be eliminated. A T_2^* weighting can be achieved with a low flip angle, long echo time, and long repetition time (Yang et al. 2010).

9.3 Physiological and Functional MR Imaging

The strength of MRI is not only its great soft tissue contrast in high-resolution images but also its sensitivity to measure physiological and functional parameters in the human body. There are numerous MRI techniques and pulse sequences with different excitation pulse schemes and gradient schemes that were specifically developed to acquire anatomical physiological images from different parts of the human body (Minati et al. 2007).

9.3.1 Cardiac MRI

Cardiac MRI assesses noninvasively the function and structure of the cardiovascular system (Mousseaux et al. 1995). Gradient echo pulse sequences are important for cardiac imaging because of their speed and versatility. These gradient echo sequences are used to assess ventricular function, blood velocities, flow, valvular function, and myocardial perfusion (Wang and Amini 2012).

9.3.1.1 Cardiac Gating

There are two different gating techniques that are used in cardiac MRI: prospective gating and retrospective gating.

In prospective gating the MR data acquisition begins only after a desired physiologic signal (e.g., the R wave of the electrocardiogram (ECG)). A trigger is used to obtain MR images only at a particular time in the cardiac cycle.

In retrospective gating, the MRI data are acquired continuously, and an ECG is recorded simultaneously. The MR data can then be reordered, grouped, or correlated with phase of the cardiac cycle. Retrospective gating is typically used for cine MRI cardiac motion studies (Brinegar et al. 2008).

9.3.1.2 Cine MRI

Cine MRI produces short movies to display heart motion throughout the cardiac cycle. Cine MR images are obtained with electrocardiography (ECG) triggered segmented imaging. The segmented acquisition divides the cardiac cycle into

multiple segments (frames) to produce a series of images that can be displayed as a movie (cine) (Larson et al. 2004).

9.3.1.3 Delayed Enhancement

Delayed enhancement is performed after administration of MR contrast agents (e.g., gadolinium-based chelates). Delayed myocardial enhancement MR imaging is important to evaluate myocardial scar due to infarction. The washout of the MR contrast agent is slow in infarcted areas of the myocardium resulting in delayed enhancement after approximately 10–15 min compared to the normal myocardium (Goetti et al. 2011).

9.3.2 Magnetic Resonance Angiography (MRA)

Magnetic resonance angiography (MRA) techniques are used to display the vasculature and the blood flow in the human body. These sequences have clinical significance in displaying vessel occlusion and in surgical planning. MRA can be performed with an endogenous tracer (spin labeling of the flowing blood) or by injecting an exogenous contrast agent (e.g., gadolinium-based chelate) in the vasculature (Stafford Johnson et al. 1998).

There are two different MR angiography contrasts: dark blood and bright blood. Dark-blood MRA suppresses the flowing blood and displays it dark in contrary to bright-blood MRA techniques. In dark-blood MRA, the intraluminal signal is suppressed and does not generate pulsation artifacts as in the bright-blood techniques. The lack of intraluminal signal allows a better delineation of the walls of vessels or the cardiac chambers. Dark-blood techniques are used in cardiac imaging and for evaluation of atherosclerotic plaques and dissections of vessel walls (Stafford Johnson et al. 1998; Tello et al. 2003).

9.3.2.1 Time-of-Flight MRA

Time-of-flight (TOF) is a bright-blood MRA technique that uses the blood as an endogenous tracer: Fresh spins from flowing blood that enter the imaging plane produce a bright signal on time-of-flight MRA images (Heverhagen et al. 2008). Three-dimensional datasets of the vasculature can then be calculated from stacks of individual time-of-flight MRA images (maximum intensity projection) (Fig. 9.9).

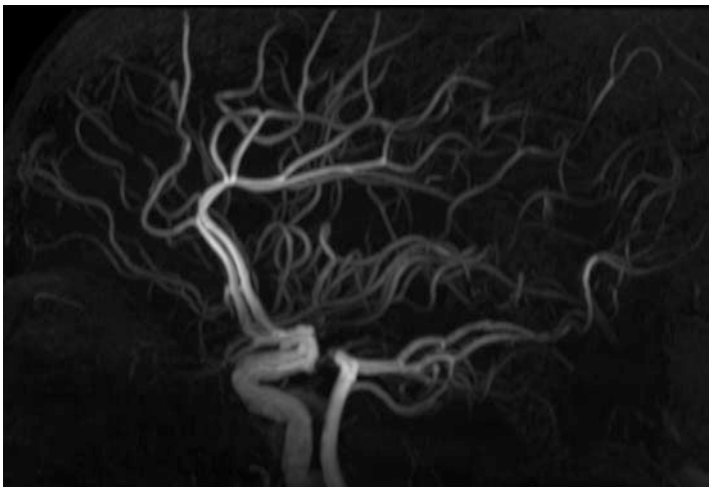

Fig. 9.9 Time-of-flight (TOF) MR angiography datasets allow displaying the vessels three-dimensionally as a maximum intensity projection (MIP) by using the flowing blood as an endogenous tracer. This MIP of the human brain vasculature was generated using a magnetic field strength of 7 T

9.3.2.2 Phase-Contrast MRA

Phase-contrast angiography (PCA) is another MRI sequence that uses blood as an endogenous tracer to quantitatively assess blood flow velocities in vessels. The blood velocity is assessed by measuring the phase shift of flowing spins in the direction of magnetic field gradients. The measured phase shift is proportional to the velocity of the spins (Yamada et al. 2015).

9.3.2.3 Contrast-Enhanced MRA

In contrast-enhanced MR angiography, an exogenous contrast agent (e.g., gadolinium-based chelate) is injected into the bloodstream, while MR images are acquired. Contrast-enhanced MR angiography allows the displays of vascular structures in great detail (Ouzounian and Liu 2007).

9.3.3 Perfusion MRI

Perfusion MRI can measure parameters of tissue microvascularization, e.g., regional blood volume, mean transit time, and regional blood flow. It can be performed with an endogenous tracer (spin labeling) or an exogenous contrast agent (e.g., gadolinium-based chelate). Perfusion MRI is an important diagnostic

tool in pathological processes where perfusion changes play an important role (e.g., tumors) (Huang et al. 2014).

9.3.4 fMRI

Functional MRI (fMRI) uses the blood oxygenation level-dependent contrast and measures brain activity by detecting changes in blood oxygenation in brain tissue. fMRI is based on the fact that neuronal activation and cerebral blood flow changes are coupled (Detre and Floyd 2001). Deoxyhemoglobin is paramagnetic in contrary to diamagnetic oxygenated hemoglobin. Oxygenation changes of the hemoglobin molecule change the magnetic qualities of blood and subsequently the MRI signal (Janoos et al. 2010).

9.3.5 Diffusion-Weighted MRI

Diffusion-weighted MRI (DWI) is able to measure the random Brownian motion of water molecules within a voxel of tissue. The diffusion of water molecules parallel to geometrically aligned anatomical structures (e.g., nerve fibers) is higher than across anatomical borders of these structures (e.g., the myelin sheets of nerve fibers) (Irfanoglu et al. 2008). A DWI sequence has clinical applications in the evaluation of strokes, especially in the early phase of infarcts (Kremer et al. 2007). Conventional T_1- and T_2-weighted MR images often show an infarct only after hours in contrast to early stroke signs on DWI (Roldan-Valadez and Lopez-Mejia 2014). Diffusion-weighted MR images with two different b-values and the corresponding calculated apparent diffusion coefficient (ADC) map are shown in Fig. 9.10a, b, c.

9.3.6 MR Spectroscopy

Magnetic resonance spectroscopy (MRS) is an analytical technique that allows the measurement of metabolic changes in tissues. MRS gives information about biochemical processes and can complement the anatomical information of MRI. Standard MRS techniques measure the signal from hydrogen protons ^{1}H of different chemical compounds and display them in a frequency spectrum or even as parametric maps overlaid on anatomical images (Fig. 9.11). Multinuclear MRS techniques can also measure signals from nuclei other than ^{1}H, which have odd numbers of nucleons (^{13}C, ^{23}Na, ^{19}F, ^{31}P). Current multinuclear MRS research might lead to novel clinical applications to determine metabolic changes and alterations in different diseases (Baltzer et al. 2012).

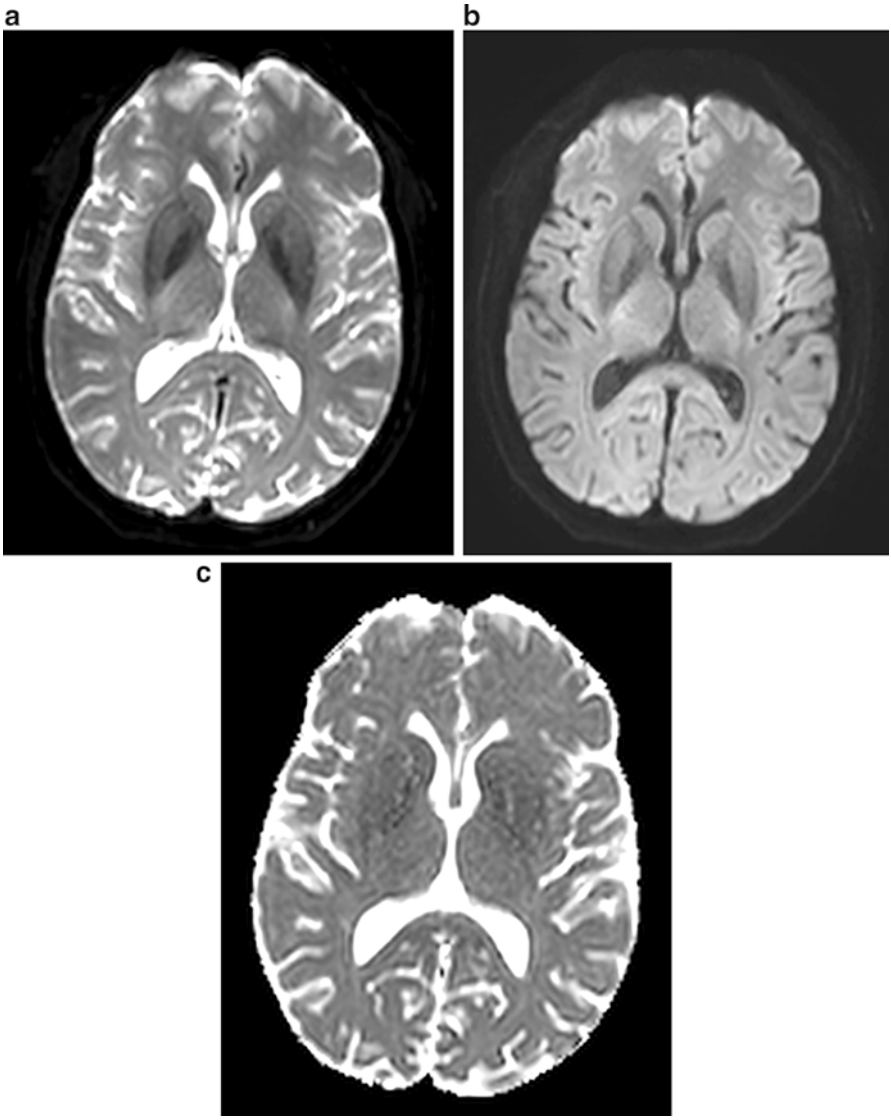

Fig. 9.10 (**a**) Diffusion-weighted MRI: axial DWI image of the human brain with $b = 0$ s/mm^2, (**b**) with $b = 500$ s/mm^2, and (**c**) corresponding calculated ADC map

9.4 MRI Safety

MRI is a very safe noninvasive imaging technique that does not require any ionizing radiation, but it is important to be aware of potential MRI safety risks for patients and personnel (Shellock and Crues 2004).

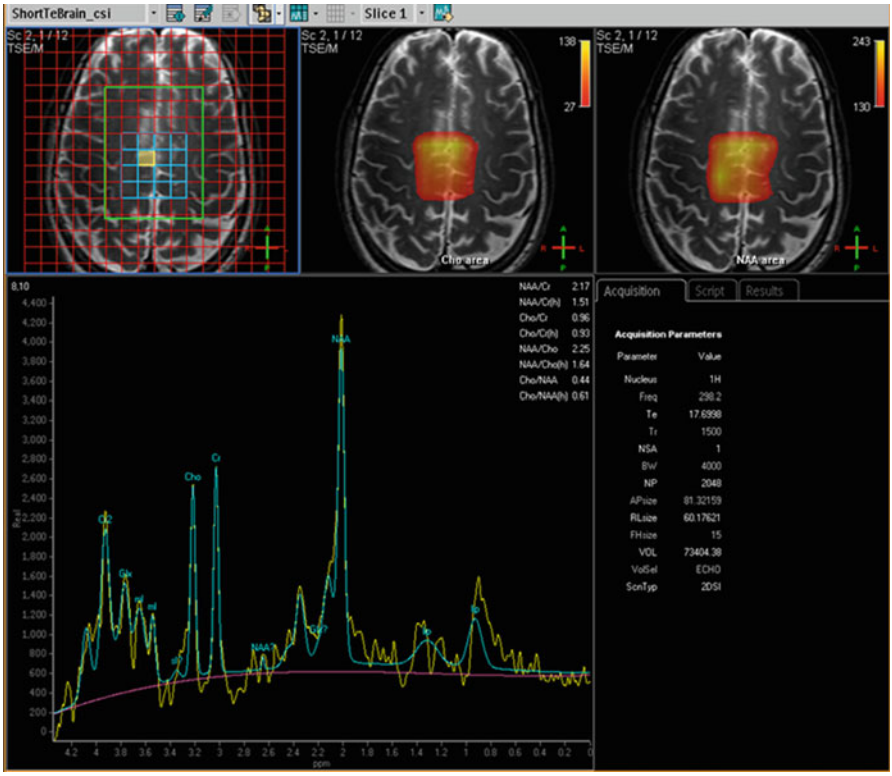

Fig. 9.11 Measurement of brain metabolites with MR spectroscopy. Chemical shift imaging at 7 T can display spectral maps and metabolic maps on top of anatomical base images

The strong static magnetic field B_0 can attract ferromagnetic objects and accelerate them in direction of the center of the bore of the MRI scanner. The static magnetic field can also influence implants and medical devices. It is therefore necessary to screen anybody before entering an MRI suite. Dedicated questionnaires are used to make sure that nobody can be injured during an MRI exam (Kanal et al. 2015).

The gradient fields G_x, G_y, and G_z are responsible for the loud noise during MRI exams and require ear protection to avoid hearing damage. Fast-switching gradient fields can also produce peripheral nerve stimulations if they exceed certain thresholds (Kanal et al. 1990).

The radiofrequency field can produce heat in body tissue. The radiofrequency exposure is limited to a maximum specific absorption rate (SAR) to avoid this heating (Kanal et al. 1990).

9.5 Future MRI Applications

9.5.1 Ultrahigh-Field MRI

In recent years more ultrahigh-field MRI scanners ($B_0 \geq 7$ T) became commercially available. The major benefits of ultrahigh-field MRI are an increased signal-to-noise ratio (SNR), an improved T_2^* contrast for susceptibility-weighted MRI sequences, and a greater chemical shift dispersion, which is greatly beneficial for MR spectroscopy (van der Kolk et al. 2013). The higher SNR at higher static magnetic field strengths can be used for higher spatial resolution of the MR images or a faster scan time (Speck and Tempelmann 2010).

9.5.2 Ultrafast Sequences

Ultrafast MR sequences allow the acquisition of an MR image in less than a second per slice. Ultrafast MR protocols use gradient echo sequences with small flip angles, very short TR, and optimized k-space filling to reduce acquisition time (Yamashita et al. 1998). The k-space trajectory determines the image contrast. Especially the fastest MRI sequence, echo planar imaging (EPI), which was first described by Mansfield in 1977 and allows the acquisition of an MR image in less than 100 ms by filling the entire k-space after one excitation, has important clinical applications in real-time cardiac imaging and in abdominal imaging to monitor contrast agent bolus arrival (Mansfield 1984).

9.5.3 MRI-Guided Interventions

Interventions using MRI for therapy guidance have become increasingly popular because there are many advantages of interventional MRI, including no exposure to ionizing radiation and the ability to obtain soft tissue images and to measure temperature and blood flow. MRI guidance is used, for example, for biopsies, laser therapy, high-intensity focused ultrasound (HIFU), and radiotherapy (von Schulthess and Hilfiker 1998; Da Rosa et al. 2011).

9.5.4 Hybrid MR Imaging (MR/PET)

Hybrid imaging is the combination of two imaging modalities into one (Pichler et al. 2008). Particularly, the combination of positron emission tomography (PET) and MRI to a whole-body MR-PET system shows the potential for various new

clinical applications to gain new insights in metabolic and functional processes in oncology as well as cardiovascular and neurologic diseases (Tudisca et al. 2015; Shah and Huang 2015).

References

Baltzer PA, Dietzel M, Kaiser WA (2012) MR-spectroscopy at 1.5 tesla and 3 tesla. Useful? A systematic review and meta-analysis. Eur J Radiol 81(Suppl 1):S6–S9

Brinegar C, Wu YJ, Foley LM, Hitchens TK, Ye Q, Ho C et al (2008) Real-time cardiac MRI without triggering, gating, or breath holding. Conf Proc IEEE Eng Med Biol Soc 2008:3381–3384

Da Rosa MR, Trachtenberg J, Chopra R, Haider MA (2011) Early experience in MRI-guided therapies of prostate cancer: HIFU, laser and photodynamic treatment. Cancer Imaging 11 (Spec No A):S3–S8

Detre JA, Floyd TF (2001) Functional MRI and its applications to the clinical neurosciences. Neuroscientist 7(1):64–79

Goetti R, Feuchtner G, Stolzmann P, Donati OF, Wieser M, Plass A et al (2011) Delayed enhancement imaging of myocardial viability: low-dose high-pitch CT versus MRI. Eur Radiol 21(10):2091–2099

Heverhagen JT, Bourekas E, Sammet S, Knopp MV, Schmalbrock P (2008) Time-of-flight magnetic resonance angiography at 7 Tesla. Investig Radiol 43(8):568–573

Huang Z, Yuh KA, Lo SS, Grecula JC, Sammet S, Sammet CL et al (2014) Validation of optimal DCE-MRI perfusion threshold to classify at-risk tumor imaging voxels in heterogeneous cervical cancer for outcome prediction. Magn Reson Imaging 32(10):1198–1205

Irfanoglu MO, Machiraju R, Sammet S, Pierpaoli C, Knopp MV (2008) Automatic deformable diffusion tensor registration for fiber population analysis. Med Image Comput Comput Assist Interv 11(Pt 2):1014–1022

Janoos F, Machiraju R, Sammet S, Knopp MV, Morocz IA (2010) Unsupervised learning of brain states from fMRI data. Med Image Comput Comput Assist Interv 13(Pt 2):201–208

Kanal E, Shellock FG, Talagala L (1990) Safety considerations in MR imaging. Radiology 176 (3):593–606

Kanal E, Froelich J, Barkovich AJ, Borgstede J, Bradley W Jr, Gimbel JR et al (2015) Standardized MR terminology and reporting of implants and devices as recommended by the American College of Radiology Subcommittee on MR Safety. Radiology 274(3):866–870

Kremer S, Oppenheim C, Schmitt E, Dietemann JL (2007) Diffusion MRI: technique and clinical applications. J Radiol 88(3 Pt 2):428–443

Larson AC, White RD, Laub G, McVeigh ER, Li D, Simonetti OP (2004) Self-gated cardiac cine MRI. Magn Reson Med 51(1):93–102

Lauterbur PC (1973) Image formation by induced local interactions. Examples employing nuclear magnetic resonance. Clin Orthop Relat Res 1989(244):3–6

Lauterbur PC (2004) Nobel lecture. All science is interdisciplinary–from magnetic moments to molecules to men. Biosci Rep 24(3):165–178

Li T, Mirowitz SA (2004) Fast multi-planar gradient echo MR imaging: impact of variation in pulse sequence parameters on image quality and artifacts. Magn Reson Imaging 22(6):807–814

Mansfield P (1984) Real-time echo-planar imaging by NMR. Br Med Bull 40(2):187–190

Minati L, Grisoli M, Bruzzone MG (2007) MR spectroscopy, functional MRI, and diffusion-tensor imaging in the aging brain: a conceptual review. J Geriatr Psychiatry Neurol 20(1):3–21

Mitchell MR, Tarr RW, Conturo TE, Partain CL, James AE Jr (1986) Spin echo technique selection: basic principles for choosing MRI pulse sequence timing intervals. Radiographics 6(2):245–260

Mousseaux E, Sapoval M, Gaux JC (1995) MRI in cardiology: clinical applications and perspectives. Ann Radiol (Paris) 38(1–2):55–68

Nature (1952) Nobel prize for physics, 1952. Nature 170(4335):911–912

Ouzounian M, Liu PP (2007) Review: contrast-enhanced MRA is more sensitive and specific than CT angiography or ultrasonography for detection of lower-limb PAD. ACP J Club 147(3):77

Pichler BJ, Judenhofer MS, Wehrl HF (2008) PET/MRI hybrid imaging: devices and initial results. Eur Radiol 18(6):1077–1086

Roldan-Valadez E, Lopez-Mejia M (2014) Current concepts on magnetic resonance imaging (MRI) perfusion-diffusion assessment in acute ischaemic stroke: a review & an update for the clinicians. Indian J Med Res 140(6):717–728

Sammet S, Bock M, Streckenbach M, Bachert P (2002) Proton spinlocking and T1 rho-weighted MR imaging at 1.5 T. Z Med Phys 12(1):16–23

Sammet S, Koch RM, Aguila F, Knopp MV (2010) Residual magnetism in an MRI suite after field-rampdown: what are the issues and experiences? J Magn Reson Imaging 31 (5):1272–1276

Shah SN, Huang SS (2015) Hybrid PET/MR imaging: physics and technical considerations. Abdom Imaging *40*(6):1358–1365

Shellock FG, Crues JV (2004) MR procedures: biologic effects, safety, and patient care. Radiology 232(3):635–652

Speck O, Tempelmann C (2010) Human 7T MRI: first clinical and neuroscientific applications. Neuroradiol J 23(5):535–546

Stafford Johnson DB, Prince MR, Chenevert TL (1998) Magnetic resonance angiography: a review. Acad Radiol 5(4):289–305

Tello R, Mitchell PJ, Witte DJ, Thomson KR (2003) T2 dark blood MRA for renal artery stenosis detection: preliminary observations. Comput Med Imaging Graph 27(1):11–16

Tudisca C, Nasoodi A, Fraioli F (2015) PET-MRI: clinical application of the new hybrid technology. Nucl Med Commun 36(7):666–678

van der Kolk AG, Hendrikse J, Zwanenburg JJ, Visser F, Luijten PR (2013) Clinical applications of 7 T MRI in the brain. Eur J Radiol 82(5):708–718

von Schulthess GK, Hilfiker P (1998) Interventional MRI: the way to the future. J Invasive Cardiol 10(9):571–577

Wang H, Amini AA (2012) Cardiac motion and deformation recovery from MRI: a review. IEEE Trans Med Imaging 31(2):487–503

Yamada S, Tsuchiya K, Bradley WG, Law M, Winkler ML, Borzage MT et al (2015) Current and emerging MR imaging techniques for the diagnosis and management of CSF flow disorders: a review of phase-contrast and time-spatial labeling inversion pulse. AJNR Am J Neuroradiol 36 (4):623–630

Yamashita Y, Tang Y, Takahashi M (1998) Ultrafast MR imaging of the abdomen: echo planar imaging and diffusion-weighted imaging. J Magn Reson Imaging 8(2):367–374

Yang X, Sammet S, Schmalbrock P, Knopp MV (2010) Postprocessing correction for distortions in T2* decay caused by quadratic cross-slice B0 inhomogeneity. Magn Reson Med 63 (5):1258–1268

Chapter 10
CT and MRI in Radiotherapy

Minsong Cao

Contents

10.1 Introduction 281
10.2 CT based Treatment Simulation and Planning 283
10.3 Magnetic Resonance Imaging (MRI) in Radiotherapy 292
Reference 299

10.1 Introduction

Cancer is the second most common cause of death in the USA, exceeded only by heart disease, accounting for nearly one of every four deaths (American Cancer Society 2015). Radiation therapy which uses high dose of radiation to kill or slow the growth of cancer cells is one of the common treatments for cancer. Over 50% of cancer patients in the USA receive radiation therapy alone or combined with other treatment methods. Computer tomography (CT) and magnetic resonance imaging (MRI) are two major medical imaging modalities widely used to assist in accurate treatment planning and delivery of radiation treatment. The basic mathematical concepts, principles, and physics of these imaging technologies are elaborated in Chaps. 8 and 9. In this chapter, their clinical roles and methods by which these modalities can be used to improve the treatment accuracy will be discussed. This chapter will also provide an overview of the guidance and issues related to effective implementation of CT and MRI in routine clinical procedures in radiation therapy.

Before an in-depth discussion of the roles of CT and MRI in radiotherapy, it is necessary to understand the basic workflow in modern radiation therapy which is illustrated in Fig. 10.1 and explained as follows. After informed consent by radiation oncologist physician and a decision to receive radiation therapy is made, the patient will undergo treatment simulation procedure during which the patient's body is carefully positioned so that the potential benefits of radiotherapy

M. Cao, PhD (✉)
Department of Radiation Oncology, University of California at Los Angeles, Los Angeles, CA, USA
e-mail: MinsongCao@mednet.ucla.edu

M. Maqbool (ed.), *An Introduction to Medical Physics*, Biological and Medical Physics, Biomedical Engineering, DOI 10.1007/978-3-319-61540-0_10

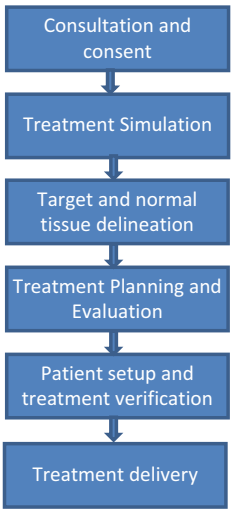

Fig. 10.1 A brief overview of the clinical workflow in radiation therapy

can be realized. The positioning is extremely important because treatment planning and treatment delivery which usually spans multiple days and weeks are all based on this position. Therefore the position needs to be designed so that it can be easily reproduced during multiple treatment fractions, and potential patient movement during the treatment is minimized. This is usually facilitated with the assistance of proper fixation and immobilization devices. Under this carefully designed position, patient's anatomy and physiology information is acquired through volumetric imaging during the simulation procedure. Following treatment simulation, radiation oncologist delineates the treatment target on the acquired simulation images. Radiation not only kills or slows the growth of tumor cells; it can also damage the nearby healthy tissues. Therefore normal tissues and organs that might be potentially irradiated during the treatment should also be contoured on these images. A treatment plan is designed with the purpose to deliver adequate radiation dose to the target while minimizing the radiation dose to the surrounding organs at risk (OAR) based on treatment prescription made by physician. After plan evaluation and acceptance process, the treatment planning is ready for delivery once it passed appropriate quality assurance procedures. Right before treatment delivery, the patient body is carefully positioned to reproduce the same position as planned in simulation and planning phase. This is usually verified by online imaging of the patient position which is compared with initial simulation images. Position deviation detected from the image guidance will be corrected before the start of treatment delivery. Patient position may also be monitored during the treatment delivery to minimize patient motion during treatment. The treatment verification and delivery process will be repeated for multiple fractions until the entire prescribed dose is delivered. An in-depth description of the clinical workflow of radiation therapy can be found elsewhere (Khan 2007, 2010). To summarize, the key to a favorable outcome of radiation therapy includes careful positioning which can be easily and

accurately reproduced during daily treatment, meticulous treatment planning, and careful implementation and delivery of the treatment plan during each treatment fraction to maximize the benefits of radiotherapy.

Medical imaging is inevitably involved in modern radiotherapy procedures. Its roles can be categorized in two main aspects: (1) acquisition of patient anatomic and physiological information for treatment planning and (2) image-guided patient setup, verification, and motion management before and during treatment delivery. The latter is usually referred as image-guided radiation therapy (IGRT) which is addressed in Chap. 5. In this chapter, the roles of CT and MRI for acquisition of patient data for treatment planning will be elaborated in detail with a brief discussion of image-guided patient setup and treatment verification.

10.2 CT based Treatment Simulation and Planning

The goal of radiation therapy is to deliver adequate dose of radiation to a predefined target area to eradicate or control the growth of tumor. This is usually realized by delivery of radiation through a medical linear accelerator (Linac). An excellent review of the mechanisms and functions of medical linear accelerator can be found elsewhere (Karzmark et al. 1993). The treatment beam generated by the medical linear accelerator consists of high-energy photons or electrons which can penetrate tissues and deposit a desired radiation dose to the tumor inside patient body. However, ionizing radiation can also damage normal tissues when it passes through patient body and cause acute or long-term side effects. The therapeutic efficacy of radiation treatment highly depends on the dose delivered to the tumor. Inadequate dose to the tumor volume may lead to treatment failure. On the other hand, excessive radiation dose will increase the probability of normal tissue complications. Modern radiation therapy techniques such as three-dimensional (3D) conformal and intensity-modulated radiation therapy (IMRT) are capable to deliver high conformal dose distribution to target while sparing the normal tissues by optimized beam angles, conformal beam aperture, and dose intensity modulation inside the treatment field (Khan 2007). Successful implementation of these advanced treatment techniques requires accurate knowledge of the location, shape, and extent of the treatment volume and normal tissues, as well as the relative geometric relationship between treatment volume and adjacent normal organs. It also requires sophisticated dose calculation algorithm for which tissue properties such as electron density and anatomic composition of tissues are essential. In summary, geometric and dosimetric accuracy are two important key factors in treatment simulation and planning for advanced radiation therapy. Medical imaging, with its ability to visualize and quantify patient anatomy, plays a critical role to ensure geometric and dosimetric accuracy for radiation therapy. Among all the image modalities, CT and MRI are the most commonly used ones for patient data acquisition for treatment simulation and planning.

10.2.1 CT Simulator

CT has a few unique features that make it a powerful tool for patient data acquisition. Most commercial CT scanners have submillimeter spatial resolution with high geometrical and spatial integrity which is ideal for accurate localization and delineation of anatomy. Volumetric imaging of patient anatomy can be obtained in a fairly short period of time using multi-slice detectors with helical scanning mode. In addition, relative linear attenuation coefficient, a function of tissue electron density and anatomic composition, can be accurately quantified by CT which is essential for accurate dose calculation.

In modern radiotherapy treatment, simulation is usually performed with a special system called CT simulator. CT simulator is very similar to conventional CT scanner used for diagnostic purpose with a few unique components (Mutic et al. 2003).

1. Patient support table

   In diagnostic CT scanner, the patient support couch usually has curved surface for patient's comfort. A couch with flat top surface similar to the one used in treatment machine is implemented in CT simulator, with the desire to reduce potential position variation between simulation and treatment. This also enables patient immobilization devices to be easily fixed to the couch top through registration notches in a manner that can be reproduced on treatment machine couch.
2. Large gantry bore

   In treatment simulation patients are commonly set up in special positions, for example, elbows widely extended. In order to accommodate all possible treatment positions with a variety of immobilization devices, gantry opening of CT simulator is usually larger than those of diagnostic scanners. The bore size of commercial CT simulator ranges from 70 cm to 85 cm. This not only creates adequate spatial clearance for patient positioning with immobilization devices but also provides increased image field of view (FOV) allowing fully acquisition of patient external dimensions which is necessary for accurate dose calculation.
3. Simulation software

   In additional to image acquisition and reconstruction software, special software for treatment simulation is also incorporated in CT simulator. There are several key functions that most simulation software provides. Target definition and normal tissue contouring can be performed by using simulation software. Treatment isocenter or setup reference point can be defined by either manual placement on the acquired images or automatically position at the centroid of selected contour. The purpose of defining a reference point during simulation is to establish the origin of the treatment coordinate system in which the geometric relationship between beam isocenter, treatment target, OAR, etc. can be defined and precisely reproduced during treatment setup. Some simulation software enables placement and design of treatment beams, and secondary images such as digital reconstructed radiograph (DRR) can also be generated. In other words,

advanced simulation software has the capability to perform like a treatment planning system except for the dose calculation-related functions.

4. Laser positioning system

   The defined treatment isocenter or reference point usually resides inside patient body and needs to be mapped and marked on the external surface of the patient so that it can be accurately visualized and localized to guide patient setup during treatment session. Most CT simulators are equipped with laser positioning system which can be used to facilitate this process. The laser system usually consists of horizontal, vertical, and sagittal lasers that interact at a virtual isocenter whose position in relative to the image isocenter is known. Once the isocenter or reference point is selected on the acquired images, the coordinates of this point will be transferred to laser system; skin markers can be placed with the assistance of lasers while patient is still on the couch.

10.2.2 CT Imaging for Treatment Planning

As noted earlier, the patient data acquired during CT simulation procedure are used in two major processes in radiation treatment planning:

1. Target and normal tissue delineation

   Recommendations for target delineation and definition, dose prescription, and reporting are discussed in depth in International Commission on Radiation Units and Measurement (ICRU) Report No. 62 (International Commission on Radiation Units and Measurements 1999). In general, the high spatial resolution and geometric integrity of CT are ideal for delineating treatment target and organs at risk. Figure 10.2a shows a lung tumor delineated on CT images in which the tumor and most organs are clearly visible. However, sometimes, it is difficult to fully visualize the tumor and surrounding organs due to insufficient soft tissue contrast of CT. A liver cancer tumor is shown in Fig. 10.2b which can be barely differentiated from the surrounding normal liver tissues. To help delineate the target, additional anatomic and/or functional information from other imaging modalities such as magnetic resonance imaging (MRI) and positron emission tomography (PET) are usually incorporated. For instance, functional information obtained from PET imaging is very useful to assist target delineation for the liver case as shown in Fig. 10.2b.

2. Dose optimization and calculation

   Most modern treatment planning software requires tissue electron density information for accurate dose calculation. A unique feature of CT is that it directly measures the linear attenuation property of tissues which is a function of tissue electron density and anatomic composition. The measured linear attenuation coefficient is usually presented as CT Hounsfield (HU) number which is a linear transformation of the linear attenuation coefficient by the following equation:

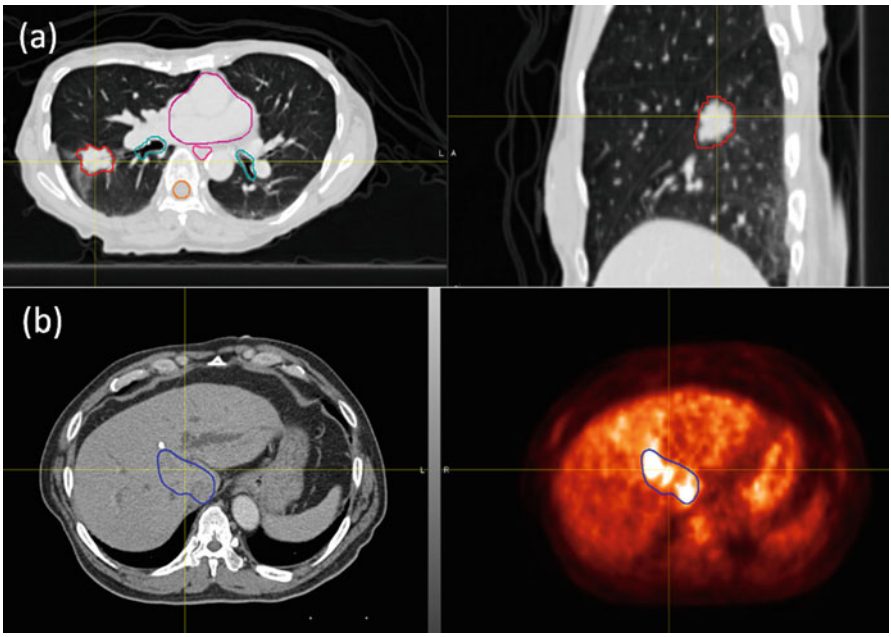

Fig. 10.2 (**a**) Axial and sagittal CT images showing a lung tumor delineated by red contour and major organs at risk outlined. (**b**) *Left*: a liver lesion outlined by the blue contour which can be barely differentiated from the surrounding normal liver tissues due to the low soft tissue contrast of CT image. *Right*: the liver lesion can be better delineated on PET image

$$\text{CT Number (HU)} = \frac{\mu_{\text{tissue}} - \mu_{\text{water}}}{\mu_{\text{water}}} \times 1000 \tag{10.1}$$

where μ_{tissue} and μ_{water} are the linear attenuation coefficients of the tissue of interest and water, respectively.

The conversion from linear attenuation to electron density can be simply established by calibration using a special phantom which includes multiple inserts made of various tissue materials with known electron and physical densities. The HU number of each insert can be directly measured from the acquired CT images of the phantom. A calibration curve can be established based on the measured CT numbers and known electron densities as demonstrated in Fig. 10.3. This calibration curve which is typically scanner dependent can be incorporated in the treatment planning software and used to convert volumetric CT images into electron density information for dose calculation.

3. Generation of reference image dataset for patient treatment setup

An important product of CT simulation and treatment planning process is the generation of reference images for patient treatment setup. Prior to radiation treatment, multiple radiograph images are usually acquired by the image detector and X-ray tube mounted on the treatment machine or by the megavoltage beam directly irradiated from the treatment head. These online images can be

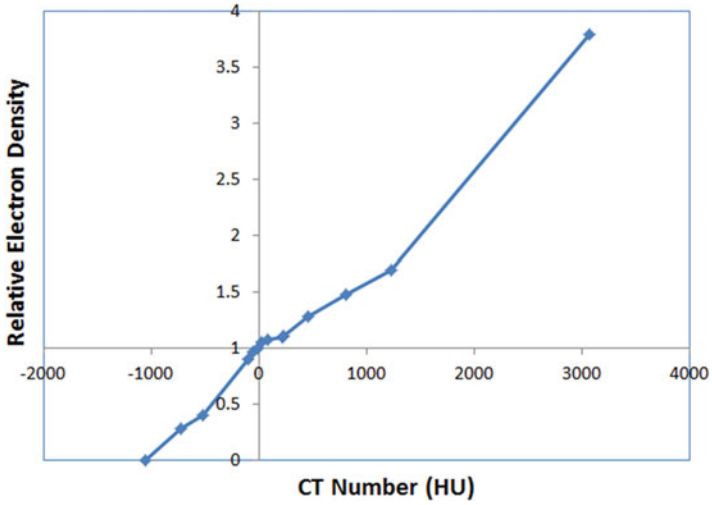

Fig. 10.3 A calibration curve between CT number (HU) and relative electron density for dose calculation in radiation therapy treatment planning

used to ensure that the relative positioning of the patient and the treatment machine agrees with the simulation position used for treatment planning. Digitally reconstructed radiograph (DRR) can be calculated from the simulation CT dataset based on treatment geometry and used as reference images for online image-guided verification and correction of patient position. The quality of DRR can affect the physician's ability to verify and adjust patient position. As the direct input of the DRR generation, the quality of the CT images has a strong impact on the quality of DRR. For instance, the spatial resolution of DRR is affected by the slice thickness and spacing of the CT dataset. Two DRRs generated from CT images of different slice thickness are compared in Fig. 10.4 where the DRR calculated from CT with thinner slice thickness allows better visualization of anatomical details. Image artifacts in the CT dataset can translate into DRR and degrade the quality and integrity of DRR. In addition to secondary images as DRR, the simulation CT dataset itself can be directly used as reference for cone-beam CT (CBCT)-based patient setup. Similarly, the geometric accuracy and image contrast of the simulation CT can directly impact the patient position verification through online volumetric imaging. Details of the onboard image-guided patient setup will be discussed in depth in Chap. 9.

To achieve acceptable geometric and dosimetry accuracy for treatment planning, the technical factors for CT acquisition need to be carefully considered and selected. First, the image field of view (FOV) should be large enough to outline the patient body with CT couch top in the axial plane. Most CT simulators have large bore size, thus extended image FOV allowing patient scanned with immobilization devices in treatment position. The scan range in the longitudinal direction should include target, organs at risk, and enough tissues allowing accurate

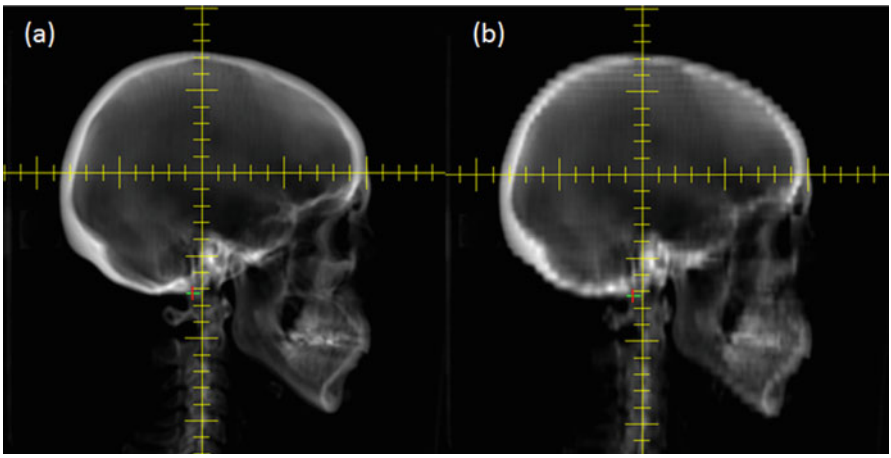

Fig. 10.4 Digital reconstructed radiograph (DRR) generated from (**a**) CT with 1.5 mm slice thickness showing better visualization of anatomical details than (**b**) the DRR generated from CT with 5 mm slice thickness

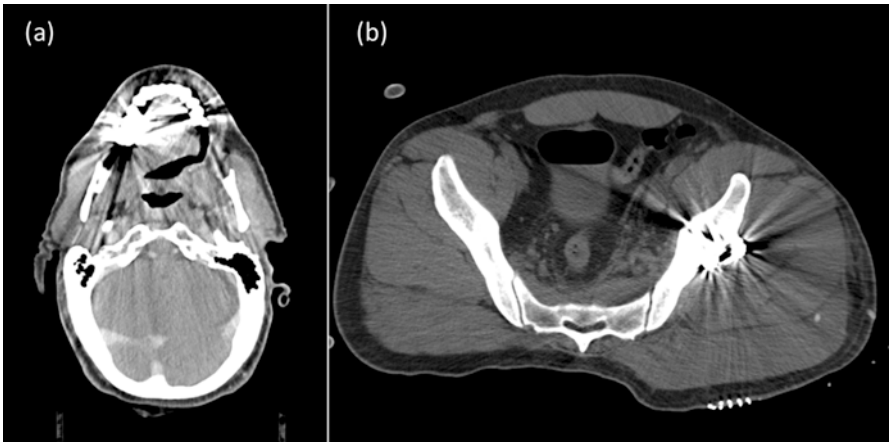

Fig. 10.5 Streaks and dark bands artifacts caused by (**a**) dental and (**b**) metal implants

calculation of dose scattering. Secondly, technical factors such as tube voltage, tube current, collimation, and filtration are important parameters affecting image quality and patient dose. Details of optimization of imaging acquisition parameters for best image quality are discussed in Chap. 8. Finally image artifacts can significantly impair tissue delineation and dose calculation. For example, artifacts caused by metal objects such as dental implant, surgical clips, and prosthesis are commonly seen on CT image as shown in Fig. 10.5. The streaks and dark bands across the image not only hinder visualization and delineation of anatomical structures but

also corrupt the integrity of CT numbers and electron density, resulting in errors in dose calculation. Advanced correction algorithms have been developed to overcome the issues associated with metal artifacts and shown promising results (Axente et al. 2015).

10.2.3 Four-Dimensional CT (4DCT)

Thoracic and upper abdominal cancer remains a primary challenge in radiation therapy because of respiratory-induced motion of tumor and organs. Regular CT scan suffers from geometrical distortion and artifacts caused by the respiratory-induced motion which can hinder the ability to visualize anatomical details and reduce the accuracy in delineation of target and organs at risk. Four-dimensional CT (4DCT) has become an important tool in evaluation and assessment of respiratory motion to reduce the uncertainties associated with motion in radiation therapy. 4DCT, as its name suggests, provides temporal information of patient anatomy in addition to the 3D volumetric data acquired by regular CT. The basic principle of 4DCT is that image data are over-sampled over multiple respiration cycles at every position of interest along the patient's longitudinal axis. Each image or projection is tagged with respiratory signal obtained from an external measuring device. The image or projection data are then retrospectively sorted based on the corresponding respiratory signal resulting in multiple 3D CT datasets. Each of these 3D CT datasets represents the patient anatomy at a particular respiratory phase. Overall these 3D CT data constitute a 4DCT dataset over the entire respiration cycle. The respiratory signal can be obtained by optical tracking of surrogate placed on patient thorax or monitoring of abdominal expansion and contraction by an elastic belt. The retrospective sorting can be done for images or projections based on either amplitude or phase of the tagged respiratory signals.

A basic assumption of 4DCT is that patient's respiration is regular and reproducible over time. Therefore image data acquired from different respiration cycles can be combined into one dataset associated with a particular phase or amplitude. However, it is very common that patient has irregular respiration, and the datasets acquired from multiple breath cycles are inconsistent, which can lead to significant image artifact or distortion on the 4DCT images. Secondly, the respiratory signal is usually measured from external surrogate that may not correlate well with the internal tumor motion. This out-of-sync issue can cause substantial deviation and errors in treatment planning and delivery. Finally, large radiation ionizing dose is usually associated with 4DCT acquisition because of its over-sampling nature. The imaging protocol needs to be carefully reviewed and optimized to prevent excessive radiation dose to patient. In summary, 4DCT provides very useful information for tumor motion management for treatment planning and delivery. However, careful review of the image and comprehensive quality assurance of the process are critical in clinical implementation of 4DCT for radiation therapy.

10.2.4 Quality Assurance (QA) of CT Simulator

To ensure geometric and dosimetric accuracy, rigorous quality assurance (QA) program needs to be developed and implemented for CT simulator, simulation software, and the simulation process. Recommendations and guidance for development of a comprehensive QA program can be found in the task group report No. 66 of the American Association of Physicists in Medicine (AAPM) (Mutic et al. 2003). In general there are three major aspects to be considered for the CT simulator:

1. Safety and radiation dosimetry

   Radiation exposure from the CT scanner poses health hazard to both patients and hospital staffs. Generally speaking, the radiation doses received by patients from the CT simulation process are much lower than the treatment doses that they will receive from radiation therapy; thus the radiation exposure of the CT simulator is not a major concern for patients. However, one should note that the treatment doses are usually well collimated to be conformal to a relatively small treatment area, while the radiation exposures imposed by CT scanner are much widely spread to the normal tissues within the scanning range. It is important to evaluate and monitor the dosimetry of the scanner during initial acceptance followed by periodic QA to prevent unnecessary radiation exposure to patients. Radiation exposure to hospital staff and public must be carefully controlled to be below the regulatory limits and based on the principle of ALARA (as low as reasonably achievable) (NCPR 1993). This is usually achieved by proper radiation shielding of the CT room. The details of radiation shielding design for CT-scanner rooms can be found in in the National Council on Radiation Protection and Measurement (NCPR) report No. 147 (NCPR 2004). Emergency safety equipment such as emergency-off switches are usually installed inside the CT room and at the control consoles to allow interruption of scanner operation under emergency situation. The functionality of these switches needs to be checked during acceptance testing and at regular basis.
2. Performance of electromechanical components

   CT scanner itself is a very sophisticated system integrated from multiple electromechanical components such as X-ray generator, collimation, detectors, gantry, patient support couch, and laser marking and positioning device. Specific quality assurance tests need to be performed periodically to evaluate the performance of these components. For example, incorrect calibration of the X-ray generator can lead to significant degradation of the image quality and/or unnecessary imaging dose to patient. Thus the beam properties such as the energy and intensity of photons generated from the X-ray generator need to be checked with the programmed settings on the control console during acceptance testing followed by annual test. For mechanical systems such as patient support couch and laser positioning device, the geometric and motion accuracy is critical and needs to be evaluated at regular basis. The QA equipment and test methods for

each electromechanical component are elaborated in detail in AAPM task group No. 66 (Mutic et al. 2003).

3. Image quality performance

Image quality is the ultimate evaluation of the entire system performance of CT simulator. Suboptimal image quality may impair the ability to identify and delineate tumor target and organs at risk for treatment planning, which can lead to significant errors such as inadequate radiation dose to tumors or overdose to normal tissues. Inferior image quality can also cause degradation of the secondary image such as DRR, resulting in uncertainties and errors in patient positioning during treatment. The image quality metrics to be evaluated are similar to those for diagnostic CT scanner, including spatial resolution and integrity, imaging noise and contrast resolution, image uniformity and accuracy of CT HU numbers, etc. The evaluation of these quality metrics is usually performed by using specific QA phantom as shown in Fig. 10.6. The phantom consists of multiple sections with each section designed for a specific QA test. For instance,

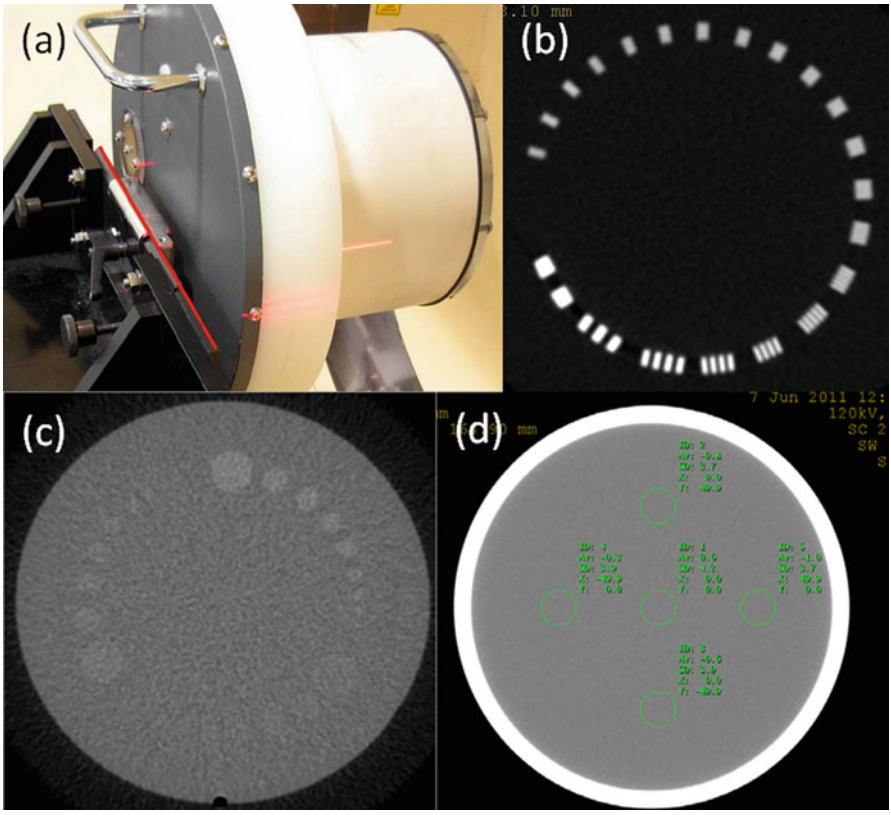

Fig. 10.6 (**a**) A quality assurance (QA) phantom for evaluation of image performance quality metrics with multiple sections for assessment of (**b**) spatial resolution, (**c**) low contrast resolution, and (**d**) uniformity

images of the sections designed for spatial resolution, contrast resolution, and image uniformity tests are shown, respectively, in Fig. 10.6. In general, the test methods for image quality are very similar to those of diagnostic scanner which were outlined in detail in AAPM task group reports No. 39 and 66 (Mutic et al. 2003; Lin et al. 1993).

In summary, comprehensive QA program needs to be developed and implemented for the hardware, software, and process associated with CT simulation for radiation therapy. Based on the impact to patient treatment and the likelihood of quality degradation of the tested parameter over time, the QA testing is usually distributed among daily, monthly, and annual tests. For example, the misalignment of lasers to the imaging isocenter can cause catastrophic mistake in patient treatment. As a result it is recommended to be checked during daily QA. The test methods and tolerance levels vary between different scanners and need to be carefully designed based on recommendations and guidelines established by premier scientific and professional organizations such as AAPM.

10.3 Magnetic Resonance Imaging (MRI) in Radiotherapy

Magnetic resonance imaging (MRI) is an imaging technique that measures magnetic resonance signals from tissues under strong magnetic field. The basic physics of MRI can be briefly described below (Khan 2010; Hendee and Ritenour 2002). Each hydrogen nucleus behaves as a tiny magnet with a magnetic moment. Under a strong external magnetic field, the nuclei align with the direction of the magnetic field and also precess about the field at a certain frequency called resonance frequency. When a second alternating magnetic field is applied by a pulse of electromagnetic radio-frequency (RF) signal, the nuclei absorb energy from the RF pulse and then precess around the new field in the transverse direction, a process usually referred as tissue excitation. When the RF is turned off, the nuclei start to release energy by two independent relaxation processes which happen simultaneously along different directions. The nuclei return back to their original status along the longitudinal direction of the external magnetic field by releasing the absorbed energy to the surrounding tissue which is known as T_1 relaxation. On the other hand, the process of relaxation of nuclei in the traverse direction is often referred as T_2 relaxation. The relaxation properties and the resonance frequency for nucleus heavily depend on the characteristics of tissues and its surrounding environment, such as the presence of chemical bonds, paramagnetic ions, and even the rate of flow of fluids (Hendee and Ritenour 2002). As a result the signal induced by the relaxation processes can be different from various tissues which constitute the image contrast. The physics and image formation, as well as pulse sequences of MRI, are discussed in detail in Chap. 9. This chapter focuses on the review of clinical applications of MRI in radiation therapy field.

10.3.1 MRI for Radiation Therapy Treatment Planning

There are a few unique features of MRI which make it an ideal image tool for treatment planning and delivery verification of radiation therapy. As discussed early, MRI signals are not only sensitive to the proton density but also the environment that the protons reside in. The highly versatile MR pulse sequences can be programmed to further exploit the difference in chemical compositions of different types of tissues to provide superior soft tissue contrast and tumor conspicuity. Consequently MRI has been widely used to assist target delineation in radiation therapy. CT and MRI images of a patient with a brain tumor are compared in Fig. 10.7. The tumor outlined by the red contour is indiscernible to the normal brain tissue on the CT image due to similar X-ray attenuation properties of tumors and normal brain tissue. On the other hand, the lesion is clearly highlighted on the T_1-weighted MRI image. In addition, notable edema surrounding the tumor which is usually included as treatment target can be easily identified on the T_2-weighted image.

While it has become a mainstay for target delineation, anatomic image typically does not provide physiological information, which can be important biomarker suggestive of early change in tumor, or provide information characterizing microenvironment surround tumor and identifying microscopic diseases which are not easy to be detected on anatomic image. Not only does MRI provide superior soft tissue contrast for anatomic imaging, but it also can be programmed to measure physiological and functional information of tissues. Functional MRI provides a powerful tool for the detection and characterization of tumors as well as for monitoring their response to therapy. For instance, dynamic contrast-enhanced MRI (DCE-MRI) (Matsuo et al. 2014) can be used to estimate blood flow, permeability, and blood volume which are important biomarkers for tumor angiogenesis, a physiological process through which new blood vessels develop to support tumor growth (Birbrair et al. 2014). The ability of a tumor to initiate angiogenesis and divert blood flow to the tumor plays important role in tumor progression and metastasis. Quantitative imaging of tumor vascular physiology both spatially and

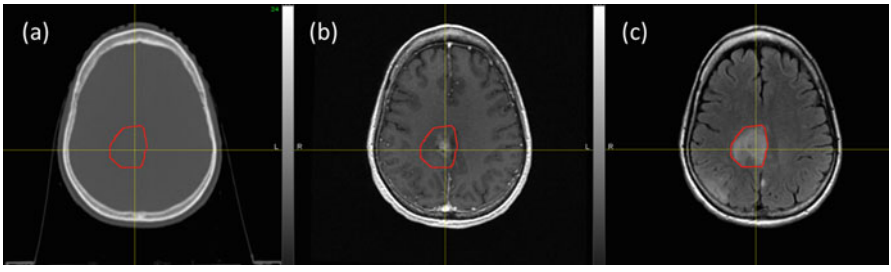

Fig. 10.7 (**a**) A brain tumor outlined by the red contour on CT image is indiscernible to the surrounding normal tissue, while (**b**) the lesion is clearly visible on T_1-weighted MRI image, and (**c**) edema surrounding the tumor is highlighted on the T_2-weighted MRI image

temporally not only allows accurate detection of tumor at early stage but also provides valuable assessment of treatment response.

Another advantage of the MRI is that it does not impose ionizing radiation to patient which is ideal for continuous imaging, for example, tumor and organ motion tracking. Using a similar method as 4DCT, 4DMRI can be generated by continuous acquisition throughout breathing cycles and retrospectively sorting of the images by its associated respiration phase. Without concern of excessive radiation dose to patient, the acquisition of 4DMRI can be optimized to minimize image artifacts and distortion. In addition, the excellent soft tissue contrast of MRI makes it highly desirable for motion management for abdominal cancers which are hardly to be detected on 4DCT. Another area that MRI has significant potential is real-time dynamic tracking of tumor or organs during radiation treatment delivery.

Despite the tempting benefits discussed above, MRI still remains as auxiliary image modality for radiotherapy due to a few deficiencies described below. As a result, MRI images are usually co-registered with CT images and used as complement to CT in target delineation. However, additional uncertainties can be induced by image registration which can result in geometric errors up to a few millimeters as demonstrated in a multi-institutional benchmark study for cranial CT-MRI registration (Ulin et al. 2010). Extra cost and time associated with multimodality imaging also impose obstacle to obtain high-quality MRI suitable for treatment planning. For example, most MRI images used for radiation treatment planning are from diagnostic scans in which the patient is scanned in a position very different from the CT simulation. These diagnostic scans often have limited image FOV and large slice thickness and spacing, increasing the uncertainties and difficulties in image registration. Recently there has been a growing interest of developing cost-effective MRI-based treatment simulation and planning process. The following obstacles need to be overcome in order to fully exploit the advantages of MRI for radiation treatment planning:

1. Image distortion

   MRI image is prone to geometric distortion which impairs the accuracy in target delineation and dose calculation for radiation treatment planning. The image distortion is caused by both system-related and patient-specific factors such as field inhomogeneity, nonlinearity of gradient field, and chemical shifts induced by magnetic susceptibility variations (Walker et al. 2014). The image distortion can be significant even for simple geometry, such as the sphere phantom shown in Fig. 10.8a. The magnitude of distortion varies across the image field of view and usually increases toward the periphery of the FOV. A number of post-processing correction methods have been developed to mitigate the distortions (Karger et al. 2006; Doran et al. 2005; Reinsberg et al. 2005). However, residual distortions can still impose uncertainties for target delineation and dose calculation, and rigorous quality assurance needs to be implemented to ensure the accuracy of using MRI for radiation therapy. The spatial integrity of MRI images can be quantified by scanning of a geometric phantom as shown in Fig. 10.8b. The phantom is made from a grid of cylindrical landmarks whose

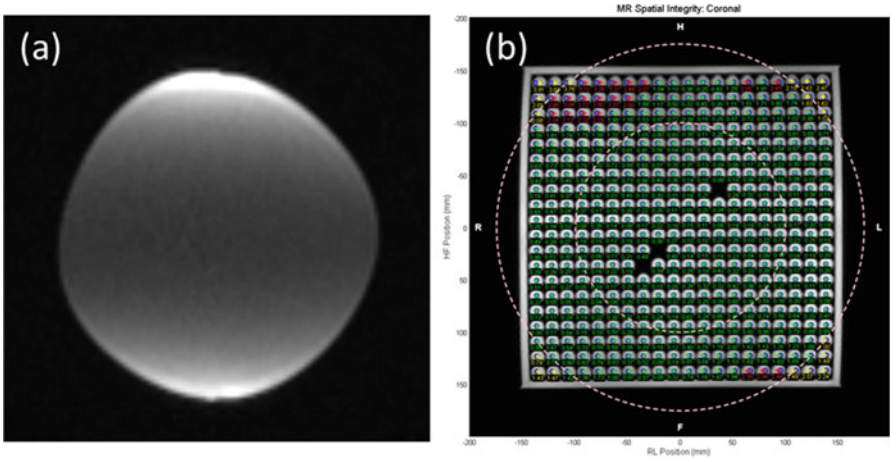

Fig. 10.8 (**a**) MRI image of a sphere phantom showing significant geometric distortion. (**b**) Image of a spatial integrity phantom consisting of a grid of cylindrical landmarks. The location of each grid point is detected from the image and compared with its known position. Deviations greater than 2 mm are identified by the red crosses

geometric locations are preciously known. From the acquired image, the locations of these grids can be detected, and the deviation from its known locations can be used to quantify the spatial distortion as shown in Fig. 10.8b. With the improvement of MRI system hardware design and rigorous quality assurance of image performance, it is possible to maintain the spatial integrity within 1–2 mm across the imaging field of view (Walker et al. 2014).

2. Lack of information for dose calculation

   As noted early, most modern treatment planning software requires tissue electron density information to account for inhomogeneity in dose calculation which can be directly converted from HU numbers of CT images via a calibration curve or look-up table. The signals measured from MRI do not directly correlate with tissue electron density and thus cannot be used solely for dose calculation. One simple approach is to ignore the heterogeneous anatomy and consider the entire body as water in dose calculation. This simplification has minimal impact to dose calculation in the regions where tissue density is relatively homogenous such as the brain. The dose calculations based on MRI have been reported to be less than 2% for brain tumors compared with CT-based planning (Kristensen et al. 2008). However large dose calculation errors can occur in the region with a large amount of bone, lung tissues, and air cavity if everything is simplified as water in calculation. A second approach is to segment various tissues from MRI images and assign bulky density to these segmented structures. This method improves the accuracy of dose calculation in regions such as the lung but can be labor intensive and time consuming. Efforts have been made to develop atlas- or voxel-based automatic segmentation methods, and the optimal bulky density values of different tissues were also investigated

in many studies. It has been shown that the dose calculation based on the bulk density assignment approach achieves reasonable accuracy for treatment planning for various disease sites (Jonsson et al. 2010).

3. Lack of information for patient setup

Daily patient treatment setup heavily relies on the reference images such as DRR generated from treatment planning. Bony anatomy on the DRR is commonly used to guide patient position adjustment during treatment setup. However the low signal intensity of bones on MRI makes it difficult to generate reference images with bony anatomic features. This has become a limiting factor to implement MRI-based treatment simulation and planning. To overcome this issue, imaging sequences to depict bones on MRI have been investigated, and one of the promising methods is based on the ultrashort echo time (UTE) technique. The low signal intensity of the bone is resulted from the extremely short T_2 relaxation time of cortical bones. To capture the short T_2 signals from the bone, the UTE method acquires images at two different echo times, resulting in different T_2 weighting. As the cortical bone has shorter transverse relaxation time (T_2) compared with other tissues, subtraction of the two acquired images results in enhancement of bony anatomy. Excellent depiction of bony anatomy details can be observed on the UTE-MRI volumetric images which allow to generate high-quality DRRs solely based on MRI as demonstrated in Fig. 10.9 (Yang 2016).

To facilitate MRI-based treatment simulation, dedicated MRI system – MR simulator – has been developed which incorporates similar components as CT simulator. In addition to the laser position system, flat tabletop, and enlarged bore size, the MR simulator is also equipped with software for distortion

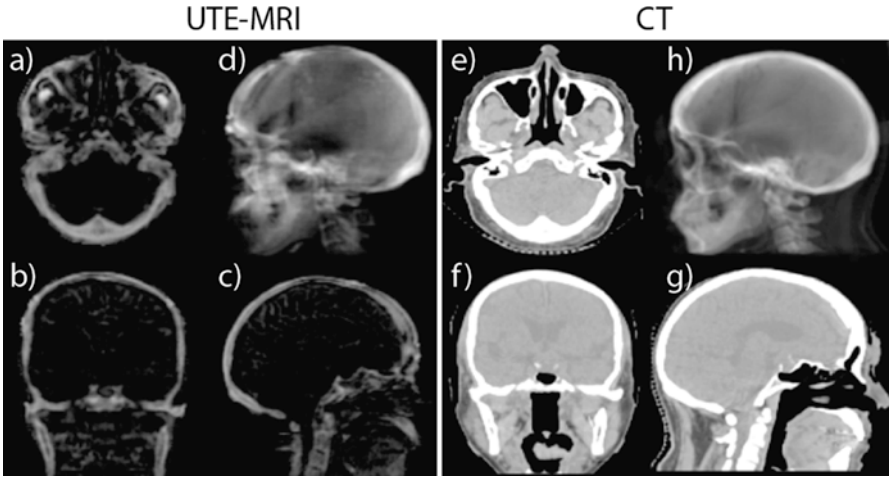

Fig. 10.9 *Left*: three orthogonal planes (**a**–**c**) of UTE-MRI image showing clear bony anatomy features and a digital reconstructed radiograph (DRR) (**d**) generated from UTE-MRI. *Right*: three planes of corresponding CT image (**e**–**g**) and a DRR (**h**) generated from CT of the same patient

correction and special imaging sequences for bony anatomy and functional imaging as discussed earlier. Special considerations also need to be paid for the patient immobilization devices for MR simulation. The powerful magnetic field of MRI system may pose a safety risk to patient and staff because it can attract ferromagnetic objects and cause a sudden movement of these objects. In addition, the metal objects can also cause signal loss and distortion and generate artifacts on MRI images. Therefore the patient immobilization devices need to be carefully designed to minimize the metal components. In general, great care has to be taken to ensure the safety of patient, staff, and equipment during the entire MRI simulation process.

Similar to CT simulator, comprehensive quality assurance program needs to be established to ensure the performance of MR simulator and the entire clinical simulation workflow. The QA program should include acceptance tests prior to MR system clinical operation followed by periodic QA procedures to evaluate the system and image performance as well as MR safety. Details of the QA procedures for MRI systems can be found in the practical guidelines published by American Association of Physicists in Medicine (AAPM) (Jackson et al. 2010).

10.3.2 MRI-Guided Radiation Therapy (MRIgRT)

The advent of the integrated imaging system with radiotherapy machine provides online image guidance to minimize setup errors and refine target localization following the initial patient positioning. The ability to visualize patient anatomy by either 2D projection or 3D volumetric image allows comprehensive assessment of patient positioning uncertainties prior to every treatment delivery. Currently most clinical imaging guidance systems are based on X-ray technology, such as radiograph and onboard cone-beam CT (CBCT), which can clearly depict bony anatomy details, but suffer with limited ability to differentiate soft tissues. Patient positioning based on bony anatomy only is certainly not ideal if tumor targets cannot be directly visualized. In addition, the position of tumor and organs relative to the treatment beam may change during treatment due to physiological motions such as breathing, cardiac, and intestine movement as well as swallowing. Real-time tracking of tumor motion can be made by online X-ray fluoroscopic imaging; however, it also suffers poor soft tissue contrast and often requires implanted fiducial marker as surrogate. Radiation dose from continuous fluoroscopic imaging also poses a major concern and makes it less practical to be implemented in daily clinical practice.

With the superior soft tissue contrast and nonionizing properties of MRI, it is natural to strive for MRI-based patient setup and treatment delivery. In addition to the issues described in the last section, there are a few more challenges to overcome when integrating a MRI system with radiotherapy machine. First, electromagnetic interference between the two systems needs to be minimized. The radio-frequency

(RF) signals generated from tissues for MR imaging are very weak, and any external RF noise can easily destroy the fidelity of the signal and corrupt the image. Modem medical linear accelerator (Linac) is a very complicated system consisting of sophisticated mechanical and electromagnetic components which constitute significant sources of RF noises. Even the motor driving the multileaf collimator can generate enough RF noise to totally corrupt the MRI image. On the other hand, the strong magnetic field of MRI can affect the performance of the medial linear accelerator significantly through Lorentz force. Under external magnetic field, the trajectory of a moving charged particle will deviate from its original direction and result in change in dose distribution. As a result, the dose point spread kernel becomes asymmetrical in homogenous medium, leading to reduced buildup and asymmetrical beam penumbra. The dose perturbation due to magnetic field is more severe at the tissue-air interface where significant dose increase occurs due to secondary electrons being forced back into the tissue by the Lorentz force (Raaijmakers et al. 2008). The dosimetric disturbance due to the magnetic field needs to be carefully considered when designing MRI-guided radiotherapy machine and accurately modeled in the treatment planning system.

In addition to the challenges related to basic physics, there are a few practical issues to be considered for clinical implementation of MRI-guided radiotherapy. Diagnostic MRI imaging usually takes about 10–20 min or longer, making it impractical to be incorporated into daily radiation treatment session which is usually less than 20 min. It is imperative to develop fast MRI image acquisition protocols for patient setup and positioning. Site planning is another area that needs special attenuation when integrating MRI with radiotherapy system. The RF shielding for MRI is necessary to prevent RF noise from corrupting the image signal. Retrofitting of existing treatment vault to accommodate RF shielding in additional to the radiation shielding can be challenging. One should also consider the potential interference of magnetic field on treatment machines, patient, and staff next to the MRI room which may require additional magnetic shielding. Most quality assurance equipment and devices are either incompatible or not safe to be used under strong magnetic field. Development of new QA equipment for MRI-guided radiotherapy is an important area which warrants additional resources and investment. Finally, physicians, physicists, and technicians in radiation oncology field may have relatively limited experiences with MRI. Staff training is a major component in clinical implementation of MRI-guided radiotherapy.

MRI-guided radiotherapy systems are in the very early stage with most systems still under development. Recently a Cobalt radiotherapy-based system – ViewRay – has become clinically available (Mutic and Dempsey 2014). Instead of integrating a linear accelerator with MRI, radioisotope Cobalt-60 is used as radiation source which effectively mitigates the interference issues between magnetic field and radiotherapy machine. Three Cobalt-60 sources are mounted on a rotating gantry 120 degrees apart, providing a dose rate around 600 cGy/min. Each source head is equipped with an individual multileaf collimator consisting of 30 pair of leafs for intensity-modulated radiation therapy (IMRT). The gantry is sandwiched by a split superconductor magnet with a bore size of 70 cm. A low-strength magnetic field of

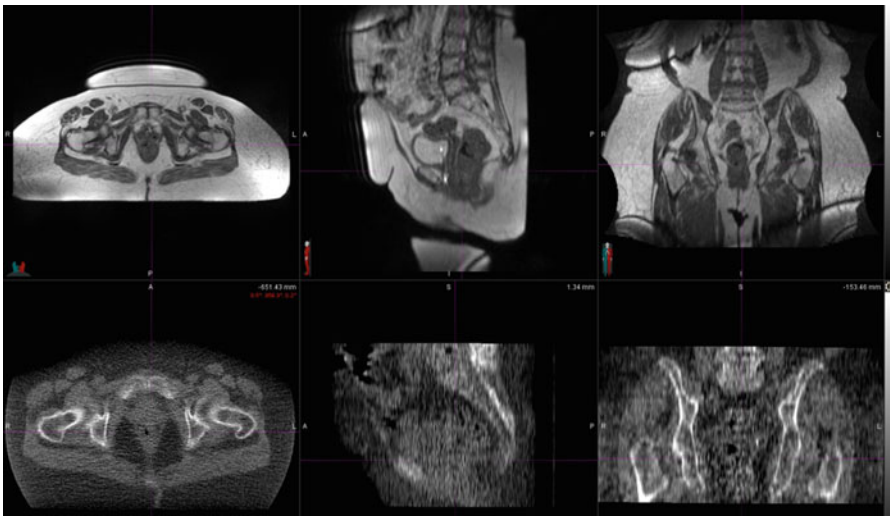

Fig. 10.10 Superior soft tissue contrast was achieved on the online MRI setup images (*top row*) where tumor and normal organs such as the rectum and bladder can be easily delineated for accurate patient setup and adaptive planning. In contrast, the image quality was significantly inferior on the cone-beam CT (*bottom row*)

0.35 Tesla is chosen aimed to reduce the image geometric distortion and minimize the Lorentz force effect. A 3D volumetric image with 1.5 mm isotropic resolution can be acquired within 3 min. As shown in Fig. 10.10, the soft tissue contrast on the MRI is much superior to the CBCT, which not only helps improve the accuracy of patient treatment setup, but it also facilitates better assessment of treatment response for timely adaptive therapy. In addition to static imaging, it also allows 2D real-time imaging on the sagittal plane with a rate of four frames per second. The dynamic imaging capability enables real-time tumor motion tracking for gated radiotherapy.

Reference

American Cancer Society (2015) Cancer Facts & Figures 2015. American Cancer Society, Atlanta

Axente M et al (2015) Clinical evaluation of the iterative metal artifact reduction algorithm for CT simulation in radiotherapy. Med Phys 42(3):1170–1183

Birbrair A et al (2014) Type-2 pericytes participate in normal and tumoral angiogenesis. Am J Physiol Cell Physiol 307(1):C25–C38

Doran SJ et al (2005) A complete distortion correction for MR images: I. Gradient warp correction. Phys Med Biol 50(7):1343–1361

Hendee WR, Ritenour ER (2002) Medical imaging physics, 4th edn. Wiley-Liss. xix, New York, p 512

International Commission on Radiation Units and Measurements (1999) Prescribing, recording, and reporting photon beam therapy. ICRU report, Bethesda, Md.: International Commission on Radiation Units and Measurements. 52 p

Jackson EF et al (2010) Acceptance testing and quality assurance procedures for magnetic resonance imaging facilities: report of the AAPM MR subcommittee task group No. 100

Jonsson JH et al (2010) Treatment planning using MRI data: an analysis of the dose calculation accuracy for different treatment regions. Radiat Oncol 5:62

Karger CP et al (2006) Accuracy of device-specific 2D and 3D image distortion correction algorithms for magnetic resonance imaging of the head provided by a manufacturer. Phys Med Biol 51(12):N253–N261

Karzmark CJ, Nunan CS, Tanabe E (1993) Medical electron accelerators. McGraw-Hill, Inc., Health Professions Division. xiv, New York, p 316

Khan FM (2007) Treatment planning in radiation oncology, 2nd edn. Lippincott Williams & Wilkins, Philadelphia. xv, 527 p., 16 p. of plates

Khan FM (2010) The physics of radiation therapy, 4th edn. Lippincott Williams & Wilkins, Philadelphia. x, 531, 30

Kristensen BH et al (2008) Dosimetric and geometric evaluation of an open low-field magnetic resonance simulator for radiotherapy treatment planning of brain tumours. Radiother Oncol 87 (1):100–109

Lin P-JP et al (1993) Specification and acceptance testing of computed tomography scanners: report of the AAPM diagnostic X-ray imaing committee task group No. 2

Matsuo M et al (2014) Magnetic resonance imaging of the tumor microenvironment in radiotherapy: perfusion, hypoxia, and metabolism. Semin Radiat Oncol 24(3):210–217

Mutic S, Dempsey JF (2014) The view ray system: magnetic resonance-guided and controlled radiotherapy. Semin Radiat Oncol 24(3):196–199

Mutic S et al (2003) Quality assurance for computed-tomography simulators and the computed-tomography-simulation process: report of the AAPM radiation therapy committee task group no. 66. Med Phys 30(10):2762–2792

NCRP, (1993) Recommendations on limits for exposure to ionizing radiation: recommendations of the National Council on Radiation Protection and Measurements. NCRP report., Bethesda

NCPR, (2004) Structural shielding design for medical X-Ray imaging facilities. National Council on Radiation Protection and Measurement. NCRP Report 147., Bethesda

Raaijmakers AJ, Raaymakers BW, Lagendijk JJ (2008) Magnetic-field-induced dose effects in MR-guided radiotherapy systems: dependence on the magnetic field strength. Phys Med Biol 53(4):909–923

Reinsberg SA et al (2005) A complete distortion correction for MR images: II. Rectification of static-field inhomogeneities by similarity-based profile mapping. Phys Med Biol 50 (11):2651–2661

Ulin K, Urie MM, Cherlow JM (2010) Results of a multi-institutional benchmark test for cranial CT/MR image registration. Int J Radiat Oncol Biol Phys 77(5):1584–1589

Walker A et al (2014) MRI distortion: considerations for MRI based radiotherapy treatment planning. Australas Phys Eng Sci Med 37(1):103–113

Yang Y et al (2016) Accuracy of UTE-MRI-based patient setup for brain cancer radiation therapy. Med Phys 43(1):262–267

Chapter 11
Nuclear Medicine Physics

Jianqiao Luo and Muhammad Maqbool

Contents

11.1 Introduction 301
11.2 Radiation in Nuclear Medicine 302
11.3 Radioactive Decay Law and Activity 306
11.4 Examples 307
11.5 Physical Half-Life, Biological Half-Life, and Effective Half-Life 310
11.6 Radiation Detectors in Nuclear Medicine 311
11.7 Gamma Cameras in Nuclear Medicine 312
11.8 SPECT 315
11.9 PET 320
11.10 Multimodality Imaging 323
11.11 PET-CT QC 323
References 328

11.1 Introduction

Nuclear medicine physics is a subspecialty of medical physics. Nuclear medicine practice includes diagnostic procedures of imaging and non-imaging and radionuclide therapy protocols primarily for cancer treatment. Nuclear medicine physics is to apply physics principles and technology to support clinical nuclear medicine. Nuclear medicine is a branch of physics that utilizes nuclear technology for the diagnosis and treatment of diseases. It covers radionuclide production, interaction, detection, and imaging. It also involves radiation dosimetry and radionuclide therapy procedures.

J. Luo, PhD (✉)
Department of Radiology, Virginia Commonwealth University, Richmond, VA, USA
e-mail: Jianqiao.Luo@vcuhealth.org

M. Maqbool, PhD
Department of Clinical & Diagnostic Sciences, Health Physics Program, The University of Alabama at Birmingham, Birmingham, AL 35294, USA

M. Maqbool (ed.), *An Introduction to Medical Physics*, Biological and Medical Physics, Biomedical Engineering, DOI 10.1007/978-3-319-61540-0_11

Nuclear medicine is very unique, because it helps doctors view how your body is functioning. This type of imaging takes very small amounts of radioactive pharmaceuticals and follows their path and progress through your body.

In nuclear medicine procedures, chemical compounds are labeled with radio isotope to form radiopharmaceuticals. The radiopharmaceutical is administered through intravenous injection for majority of nuclear medicine studies. Some are taken in the form of gas or pill. Following the administration, these radioactive drugs can localize to specific organs or cellular receptors. Isotope attached to the molecule emits gamma ray, i.e., photons. Some of those photons interact with tissue through photoelectric absorption or Compton scattering or pair production depending on their initial energy and interaction probability. Others travel through the tissue and hit the detectors on a gamma camera. The gamma camera detects those photons and forms a distribution of the radioactivity in the patient body to generate an image. The images represent the distribution of the radiopharmaceutical, which may not necessarily be the anatomical structure of organs. This is a key difference between nuclear medicine image and X-ray CT scan. Similar to X-ray CT and other tomographic imaging modalities, nuclear medicine imaging can provide three-dimensional distribution of radiopharmaceuticals using image reconstruction to generate single photon emission computed tomography (SPECT) or positron emission tomography (PET) (Cherry et al. 2012). In recent years, multimodality imaging with combination of two or more imaging modalities has been widely used in clinical radiology, nuclear medicine, and radiation oncology such as SPECT-CT, PET-CT, and PET-MRI.

An essential function of medical physicists is providing technical support on quality assurance for imaging equipment. American College of Radiology (ACR) issues accreditation to major imaging modalities including nuclear medicine cameras: SPECT and PET-CT. Medical physicists play a key role in the ACR accreditation.

A medical physicist is also responsible for safe use of radionuclides in clinical nuclear medicine. The physicist participates in the hospital radiation safety program as divisional radiation safety officer or provides technical support to radiation safety officer and radiation safety committee to maintain regulatory compliance with radiation safety codes. It has been an ongoing effort by medical physicists to work with radiologists to reduce radiation exposure to patients during radiology procedures using X-ray or radiopharmaceuticals.

11.2 Radiation in Nuclear Medicine

Various radiations are used in nuclear medicine. Those radiations are usually obtained from radiation-emitting materials called radioisotopes or radiopharmaceuticals. Radioisotopes could be a naturally existing radioactive material like $_{92}U^{238}$ or a stable atom of a material can be converted to a radioisotope by destabilizing it (Cherry et al. 2012; Chandra et al. 2011). The following radiations are usually used in nuclear medicine.

11.2.1 Alpha Radiation

Alpha radiation or α-rays (also called α-particles) are considered to be the helium nuclei. A helium atom consists of two protons and two neutrons inside its nucleus. Two electrons orbit around the nucleus. When these two electrons are knocked out of a helium atom, the remaining part is called an α-ray. The mass of an α-ray is $M_\alpha = 6.6447 \times 10^{-27}$ kg or 4.00153 u. In terms of energy, the rest mass energy of an α-particle is 3727.4012 MeV. An α-ray carries two units of charge number Z and four units of mass number A. Therefore, when an α-ray is emitted from a radioisotope isotope (usually called parent element), the charge number of the radioisotope decreases by 2 and its mass number goes down by 4 units. Charge number of an atom represents the nature of the atom; therefore, after the emission of an α-ray, then new atom or element (usually called daughter element) is a different element based on the elements' periodic table classification. The following reaction shows the emission of an α-ray from a radioisotope:

$$_{\mathbf{Z}}\mathbf{X}^{\mathbf{A}} \rightarrow {}_{(\mathbf{Z}-\mathbf{2})}\mathbf{Y}^{\mathbf{A}-\mathbf{4}} + {}_{\mathbf{2}}\mathbf{He}^{\mathbf{4}}(\boldsymbol{\alpha} - \mathbf{ray}) \tag{11.1}$$

where X and Y represent the parent and daughter elements, respectively.

11.2.2 Beta Radiation

Beta radiation or β-rays originate from the nucleus of an unstable atom as a result of nuclear transitions. β-rays are of two types: β − rays and β + rays.

11.2.2.1 β − Rays

Negative beta radiations or β − rays are considered to be like an electron. The charge, mass, and other properties of a β − ray are exactly the same as an electron. The only difference is in their origin. A β − ray comes out of a nucleus as a result of nuclear transitions, but an electron is obtained from an atom as a result of transitions in atomic orbits. The rest mass of a β − ray is $M_{\beta^-} = 9.109 \times 10^{-31}$ kg or 5.4858×10^{-4} u. In terms of energy, the rest mass energy of a β − ray is 0.511 MeV. The charge number of a β − ray is $Z = -1$ and its mass number is $A = 0$. Therefore, when a β − ray is emitted from a radioisotope isotope, the charge number of the radioisotope increases by 1 and its mass number does not change at all. Due to the change in charge number, a daughter element obtained in a β − emission is different than its parent element. The following reaction shows the emission of a β − ray from a radioisotope:

$$_{\mathbf{Z}}\mathbf{X}^{\mathbf{A}} \rightarrow {}_{(\mathbf{Z}+\mathbf{1})}\mathbf{Y}^{\mathbf{A}} + \boldsymbol{\beta}- \tag{11.2}$$

11.2.2.2 β + Rays

Positive beta radiations or β + rays are considered to be like a positron. Like the case of a β − ray and an electron, the charge, mass, and other properties of a β + ray are exactly the same as a positron. The only difference is in their origin. A β + ray comes out of a nucleus as a result of nuclear transitions, but a positron is obtained as a result of pair production, where a photon converts into an electron-positron pair in the presence of heavy nucleus. The rest mass of a β + ray is $M_{\beta+} = 9.109 \times 10^{-31}$ kg or 5.4858×10^{-4} u. In terms of energy, the rest mass energy of a β + ray is 0.511 MeV. The charge number of a β + ray is $Z = +1$ and its mass number is $A = 0$. Therefore, when a β + ray is emitted from a radioisotope isotope, the charge number of the radioisotope decreases by 1 and its mass number does not change at all. Due to the change in charge number, a daughter element obtained in a β + emission is different than its parent element. The following reaction shows the emission of a β + ray from a radioisotope:

$$_{\mathbf{Z}}\mathbf{X}^{\mathbf{A}} \rightarrow {}_{(\mathbf{Z-1})}\mathbf{Y}^{\mathbf{A}} + \boldsymbol{\beta}+ \tag{11.3}$$

11.2.3 Gamma Radiation

Gamma radiations or γ-rays are radiation with zero charge number and zero mass number. These radiations also originate inside the nucleus of an unstable element. These are electromagnetic radiations or photons of high energy. They travel with the speed of light and carry no rest mass. The entire mass of a γ-ray is in the form of energy. Since a γ-ray has $Z = 0$ and $A = 0$, therefore, when a γ-ray is emitted from a radioisotope isotope, both Z and A do not change at all. As a result, the parent and daughter elements are the same, but the daughter element has less energy and in many cases more stable than the parent element. The following reaction shows the emission of a γ-ray from a radioisotope:

$$_{\mathbf{Z}}\mathbf{X}^{\mathbf{A}} \rightarrow {}_{\mathbf{Z}}\mathbf{Y}^{\mathbf{A}} + \gamma \tag{11.4}$$

11.2.4 Common Radioisotopes

Radioisotopes are produced by two methods. One method is called accelerator-based production method and the other method is known as nuclear reactor-based radioisotope production method (Chandra et al. 2011). Common accelerators to produce radioactive isotopes are cyclotron and linear accelerator. A cyclotron is pictured in Fig. 11.1.

A list of commonly used radioisotopes along with their uses is given Table 11.1.

Fig. 11.1 Cyclotron used for radioisotopes production

Table 11.1 Commonly used radioisotopes

Radioisotope	Emitting radiation	Energy of emission (keV)	Half-life	Uses
$^{m}Tc^{99}$	γ	140	6.02 h	Used in more than 70% of all medical applications
Ra^{226}	γ α	186 4871	1600 year	Bone cancer treatment
Ga^{67}	γ	93 184 300	78.3 h	Tumor localizing agent
I^{131}	β− γ	606 364	8.02 day	Thyroid cancer detection
I^{123}	γ	159	13 h	Imaging thyroid
$^{m}Kr^{81}$	γ	190	13 s	Lung ventilation
Sr^{89}	β−	1492	50.52 day	Treating bone pain
Sm^{153}	γ β−	103 807 703 634	1.93 day	Treating bone pain
Re^{189}	β−	1007.74	24.3 h	Treating bone pain

11.3 Radioactive Decay Law and Activity

All radio isotopes emitting radiation follow radioactive decay law. Consider N_0 number of nuclei or atoms of parent element are present at certain instant. The material is disintegrating and losing number of nuclei. Assume that dN is the number of nuclei decayed in this time dt and N is the number left behind then mathematically:

$$\mathrm{dN} = -\lambda N\ \mathrm{dt}$$

or $\mathrm{dN}/N = -\lambda\ \mathrm{dt}$
Integrating $\ln \mathrm{N} = -\lambda t + C$
Using the initial condition, at $t = 0$, $N = N_0$, we get

$$\ln(N_0) = C$$

The last equation becomes

$$\ln \mathrm{N} = -\lambda t + \ln \mathrm{N}_0$$

Simplifying, we get

$$N = N_0 \mathrm{e}^{-\lambda t} \tag{11.5}$$

Equation (11.5) is called radioactive decay law. Radioactive isotopes obey radioactive decay law when emitting radiation. Moreover, λ is called radioactive decay constant. Each radioactive element has its own unique λ.

11.3.1 Activity

Activity of a radioactive element is defined as

$$A = \mathbf{dN}/\mathbf{dt} = \lambda N \tag{11.6}$$

It is a measure of how many nuclei or atoms disintegrate in a unit time. The unit of activity is curie (Ci). One Ci is defined as (Cherry et al. 2012; Christian et al. 2011)

$$1\ \text{Curie} = 3.7 \times 10^{10}\ \text{disintegrations per second}$$

A smaller unit of activity is becquerel (Bq):

$$1\ \text{Bq} = 1\ \text{disint./s}$$

11.3.2 Half-Life

The time taken by a radioisotope to reduce to half of its initial number of atoms is called its half-life $T_{1/2}$. A mathematical expression for half-life is obtained by replacing $N = N_0/2$ and $t = T_{1/2}$. Making these substitutions, we get

$$T_{1/2} = 0.693/\lambda \tag{11.7}$$

This natural half-life of a radioisotope is also called its physical half-life.

11.3.3 Mean Life

When a radioactive element decays, the first atom takes almost no time to decay. On the other hand, some atoms may take hours, days, and years to decay. Therefore, the idea of mean life describes the average time for which an atom survives before it decays. Mathematically, the mean life T is defined as

$$T = 1/\lambda \tag{11.8}$$

11.4 Examples

Knowing the activity, mass, number of atoms, volume, and other parameters of a radioisotope is very important before it can be used in nuclear medicine. The following examples give an idea how to work on finding various parameters before a radioisotope is used clinically.

Example 11.1: ***Calculating Mass*** A patient needs iodine (I^{131}) for treatment. What is the mass of iodine in 550 MBq of I^{131} used as therapy dose? Half-life of I^{131} is 8.04 days.

Solution

Half-life of $I^{131} = T_{1/2} = 8.04$ days $= 694{,}000$ s

$\lambda = 0.693/T_{1/2} = 0.693/694{,}000$

$\lambda = 9.985 \times 10^{-7}$ s

Activity $= A = 550$ MBq $= 550 \times 10^6$ disint./s

Activity $= A = \lambda N => N = A/\lambda$

$N = 550 \times 10^6 / 9.985 \times 10^{-7}$

$N = 5.508 \times 10^{14}$

To calculate the mass, we take help of Avogadro's number $N_A = 6.02 \times 10^{23}$ atoms/mole

1 mole of $I^{131} = 131$ g

6.02×10^{23} atoms of I^{131} has mass = 131 g

Therefore,
The mass of 5.508×10^{14} atoms of $I^{131} = 131 \times 5.508 \times 10^{14} / 6.02 \times 10^{23}$
Thus, the mass of 550 MBq $I^{131} = 1.2 \times 10^{-7}$ g

Example 11.2: ***Calculating Mass*** What is the mass of 1×10^{-3} Ci of mTc^{99}? mTc^{99} has a decay constant of
$\lambda = 3.2 \times 10^{-5}\ s^{-1}$.

Solution
$\lambda = 3.2 \times 10^{-5}\ s^{-1}$, mass =?
$A = \lambda N = 1 \times 10^{-3}$ Ci
Since 1 Ci $= 3.7 \times 10^{10}$ disint./s, therefore
$A = 1 \times 10^{-3} \times 3.7 \times 10^{10}$
$A = 3.7 \times 10^{7}$ disint./s
Using $A = \lambda N => N = A/\lambda$
$N = 3.7 \times 10^{7} / 3.2 \times 10^{-5}$
$N = 1.156 \times 10^{12}$
1 mole of $mTc^{99} = 99$ g
6.02×10^{23} atoms of mTc^{99} has mass = 99 g
Therefore,
The mass of 1.156×10^{12} atoms of $mTc^{99} = 99 \times 1.156 \times 10^{12} / 6.02 \times 10^{23}$
Thus, the mass of 1×10^{-3} Ci $mTc^{99} = 1.9 \times 10^{-11}$ g

Example 11.3: ***Calculating Activity*** Find the activity of 160 g of Ga^{67} with half-life of 78.3 h. This source is used to inject in a patient after 2 days. What is its activity at that time?

Solution
Activity $= A = \lambda N$
To find λ, we have $T_{1/2} = 78.3$ h = 281,880 s.
$\lambda = 0.693/T_{1/2} = 0.693 / 281{,}880 = 2.46 \times 10^{-6}$/s
To find N, we take help of $N_A = 6.02 \times 10^{23}$ atoms per mole
67 g of Ga has number of atoms $= N_A = 6.02 \times 10^{23}$
160 g of Ga has number of atoms $= N = 160 \times 6.02 \times 10^{23}/67$
which gives $N = 1.4376 \times 10^{24}$
Activity $= A = \lambda N = 2.46 \times 10^{-6} \times 1.4376 \times 10^{24}$
$A = 3.536 \times 10^{24}$ disint./s
Since 1 Ci $= 3.7 \times 10^{10}$ disint./s
Therefore, $A = 3.536 \times 10^{24} / 3.7 \times 10^{10}$
or $A = 9.55 \times 10^{13}$ Ci
To calculate its activity after $t = 2$ days, we have to find N after 2 days. Using radioactive decay law,
$N = N_0.e^{-\lambda t}$
Using $N_0 = 1.4376 \times 10^{24}$,
$t = 2$ days = 48 h,
and $\lambda = 0.693/T_{1/2} = 0.693/78.3 = 0.00885\ h^{-1}$, we get
$N = 1.4376 \times 10^{24} \times e^{(-\ 0.00885\ \times\ 48)}$

which gives $N = 9.4 \times 10^{23}$ atoms
Therefore, the activity after 2 days is
$A = \lambda N = 0.00885 \times 9.4 \times 10^{23} = 8.319 \times 10^{21}$ disintegrations/h
which gives $A = 2.31 \times 10^{18}$ disintegrations/s
or $A = 6.243 \times 10^{7}$ Ci

Example 11.4: Volume of Radioisotope A radioactive sample of mTc^{99} with half-life of 6 h was calibrated at 7:00 AM and contained 15 mCi/ml (555 MBq/ml) of radioactivity at that time. If this is the desired amount of radioactivity to be administered to the patient, determine the volume of the preparation which will have to be injected at 10:00 AM?

Solution Using the radioactive decay law and replacing number of atoms by the volume of the radioactive solution,
$N_0 = V_0 = 15$ mCi/ml, $T_{1/2} = 6$ h
$N = V = ?$ $\lambda = 0.693 / T_{1/2} = 0.693 / 6 \times 3600$
$\lambda = 3.21 \times 10^{-5}$/s
$t =$ 10:00 AM–7:00 AM = 3 h = 10,800 s.
using $N = N_0.e^{-\lambda t}$
$N_0 = (15$ mCi/ml).exp.$(-3.21 \times 10^{-5} \times 10{,}800)$
$N = 10.5$ mCi/ml or 388.5 MBq/ml
Amount desired = 15 mCi
Volume needed = 15 mCi / 10.5 mCi/ml
Volume needed = 1.43 ml

Example 11.5: Disposal Time A sealed bag of contaminated waste measures 185 MBq. This bag is contaminated by radioactive I^{125} with half-life of 60 days. The permitted activity of I^{125} for waste discharge is 45,000 Bq. How long this contaminated bag should be stored before safe discharge?

Solution
$T_{1/2} = 60$ days $\Rightarrow \lambda = 0.693/60 = 0.01155$ /day, $t = ?$
$N_0 = 185 \times 10^6$ Bq, $N = 4.5 \times 10^4$ Bq
Using $N = N_0.e^{-\lambda t}$
Simplifying $N / N_0 = e^{-\lambda t}$
$N_0 / N = e^{\lambda t}$
$\ln (N_0 / N) = \lambda t$
$t = \ln (N_0 / N) / \lambda$
$t = [\ln (185 \times 10^6 / 4.5 \times 10^4)] / 0.01155$
$t = [\ln (4111.11)] / 0.01155$
$t = 8.32 / 0.01155$
$t = 720.5$ days or about 2 years

11.5 Physical Half-Life, Biological Half-Life, and Effective Half-Life

Physical half-life $T^{p}_{1/2}$. The natural half-life of a radioactive isotope (discussed already).

Biological half-life $T^{b}_{1/2}$. The time in which half of the radioisotope is excreted by the body through metabolic activities. Bodies' metabolic activities affect different foods and materials in a different way. Some materials can be excreted by the body with a slower rate and others can be excreted faster.

Effective half-life $T^{e}_{1/2}$: The time in which a radioisotope reduces to half when both methods of decay (natural decay and biological excretion) act at the same time. Mathematically,

$$1/T^{e}{}_{1/2} = 1/T^{p}{}_{1/2} + 1/T^{b}{}_{1/2} \tag{11.9}$$

Example 11.6 A radioisotope is taken inside the body of a patient to treat a tumor. The physical half-life of this radioisotope is 6 h. The body excretes the isotope with a half-life of 8 h. Find the effective half-life of this radioisotope.

Solution

$T^{p}{}_{1/2} = 6$ h, $T^{b}{}_{1/2} = 8$ h, $T^{e}{}_{1/2} =?$
$1/T^{e}{}_{1/2} = (1/T^{p}{}_{1/2} + 1/T^{b}{}_{1/2})$
$1/T^{e}{}_{1/2} = 1/6 + 1/8 = 14/24$
$T^{e}{}_{1/2} = 1.7$ h

Example 11.7 The physical half-life of a radioactive material is 40 min. With what rate (biological half-life) should the body excrete the materials so that its effective half-life is one fifth of its biological half-life?

Solution

$T^{p}{}_{1/2} = 40$ m, $T^{b}{}_{1/2} =?$, $T^{e}{}_{1/2} = (T^{b}{}_{1/2}) / 6$
Using $1/T^{e}{}_{1/2} = (1/T^{p}{}_{1/2} + 1/T^{b}{}_{1/2})$
Replacing $T^{e}{}_{1/2}$ by $(T^{b}{}_{1/2}) / 6$
$6/T^{b}{}_{1/2} = (1/T^{p}{}_{1/2} + 1/T^{b}{}_{1/2})$
Which gives $6/T^{b}{}_{1/2} - 1/T^{b}{}_{1/2} = 1/T^{p}{}_{1/2}$
$5/T^{b}{}_{1/2} = 1 / 40$ or $T^{b}{}_{1/2} = 200$ m or 3 h and 20 m

11.6 Radiation Detectors in Nuclear Medicine

There are many radiation detectors which can be divided into four categories: gas-filled detectors, scintillation detectors, semiconductors, and others. These detectors are designed for detection of different particles at various energy levels (Christian et al. 2011; Buschberg et al. 2011).

Gas-filled detector has an air chamber where with incoming gamma phones deposit energy to generate electrons. Those electrons are collected through electrical field produced by applied voltage. When the voltage increases, the interaction mechanism changes from ionization, proportional, and Geiger-Müller, respectively. Thus ionization chamber and GM counter are manufactured based on their working voltages and are widely used in medical facilities. A dose calibrator is an ionization chamber. It is built as a well counter to increase geometric efficiency. It is common to have the air in the chamber be pressurized to increase detection efficiency. The dose calibrator measures every dose to be administered to patient. Thus it is essential to ensure the quality and reliability of the dose calibrator by performing routine quality assurance (Q/A) procedures which includes daily constancy, quarterly linearity, annual accuracy, and geometry upon installation and major repair. The GM counter is primarily used as a survey meter for low-level contamination of radioactivity and patient measurement. It is required to have the GM detector checked before its use and calibrated annually.

Thyroid uptake probe is a NaI (Tl) crystal in a cylindrical collimation that focuses the radiation detection to thyroid or other organ of interest. The NaI (Tl) detector is able to record low activity admitted to a patient and then distributed in the thyroid. Using the thyroid uptake measurement, the patient thyroid function could be evaluated. Quality assurance of the thyroid uptake probe includes daily constancy, quarterly energy calibration, Chi-square test, minimum detectable activity, and annual evaluation. In modern thyroid uptake system, there is a well counter attached to the same computer as the uptake probe. This well counter is built with a NaI (Tl) crystal which is manufactured as a well in geometry to increase detection efficiency. The well counter is widely used to measure a sample of blood or other body fluid containing radioactive material. It is also used in package receiving, contamination survey, etc. where low-level radioactivity is normally involved. The thyroid uptake system is not intended for high-activity measurement due to the saturation of the NaI (Tl) crystal with a large amount of photons. Quality assurance for the well counter is similar to the uptake probe.

The daily constancy test is to ensure the detectors are functioning consistently every day in clinical service. It measures a radioactive sample, like Cs-137. This sample is used every day in the same condition so that similar reading is expected after decay correction. The numbers from multiple measurements may not be identical because of statistical nature of the radiation.

Scintillation detectors have a scintillation crystal, for example, NaI (Tl), to stop the gamma ray and then convert the gamma ray energy to visible light photons. This is called scintillation process. The visible light photon then interacts with photocathode on surface of a photoelectrical multiplier (PMT) to generate electrons.

Those electrons travel through multiple collisions within the PMT to be "multiplied" to form electrical signals. The scintillation crystals are used to build scintillation detectors with high detection efficiency and good energy resolution. It is also used to generate energy spectrum in multichannel analyzer. However, the most important application of the scintillation detection in nuclear medicine is for gamma photon imaging. Another form of the scintillation detection is to use liquid scintillation counter (LSC). The LSC is primarily used in beta detection since the sample has directly contacted with scintillation material to avoid absorption of beta rays by the protection coating of the scintillation crystals.

Semiconductors have the advantage of high efficiency and excellent energy resolution compared with gas-filled and scintillation detectors. However, Ge and Si are to be kept at very low temperature which makes it difficult for general purpose applications. In recent years, some semiconductor materials are introduced in nuclear medicine for detection (gamma probe) and imaging (cardiac scanner).

Film badge is used for monitoring radiation exposure. It is named film badge for its original design of a film as detection medium to record the exposure level. New generation of radiation exposure monitoring device uses optically stimulated luminescence dosimeters (OSL badges) to assess total body, eye (lens), and shallow (skin) exposures, and thermoluminescent dosimeters (TLD or ring badges) are used to monitor hand exposures. The OSL/TLD is assigned to radiation worker for a period of time (monthly or quarterly). Radiation exposure recorded on to the OSL badge is measured by stimulating the detector material and causing it to luminesce in proportion to the exposure (Table 11.2).

The TLD is collected and read by a device that measures ionizing radiation exposure by recording the intensity of visible light emitted from a crystal in the TLD detector when the crystal is heated. The intensity of light emitted is dependent upon the radiation exposure. The TLD is based on a thermoluminescent process which is different from any of the gas-filled, scintillation, or semiconductor detectors.

In nuclear medicine, survey meters, dose calibrator, and uptake probe and well counter are the most important detectors. GM counter is widely used as survey meter in nuclear medicine and other departments in a medical facility. Dose calibrator is a key element of nuclear medicine instrumentation. It is used to measure every dose before administration to patient.

11.7 Gamma Cameras in Nuclear Medicine

In gamma photon (gamma ray and X-ray) detection, scintillation crystals are used for their high detection efficiency and good energy resolution. Among the crystals, NaI(Tl) is by far the most widely used in detectors to record counts of photons similar to GM counter, in spectrometer to record the counts and energy information to generate energy spectrum, and in scanner to register events of photon emission to produce distribution (image) of the photon emission including the counts and the

Table 11.2 Summary of radiation detectors in nuclear medicine

Detectors	Type	Applications	QC
Dose calibrator	Gas-filled ionization chamber	Assay patient doses	Constancy, linearity, geometry, and accuracy
GM survey meter	Gas-filled GM counter	Contamination survey Patient survey Package survey	Daily check and annual calibration
Uptake probe	NaI (Tl)	Thyroid uptake measurement	Constancy, autocalibration, X-square testing, accuracy, and MDA(minimum detectable activity)
Well counter	NaI (Tl)	Wipe testing Blood sample measurement	Constancy, autocalibration, X-square testing, accuracy, and MDA(minimum detectable activity)
Personal dosimeter	OSL / TLD	Staff monitoring	Returned to manufacturer
Ionization chamber	Gas-filled ion chamber	Contamination survey Patient survey Package survey	Daily check and annual calibration
Scintillation spectrometer	NaI (Tl)	Spectrum analysis	Energy peaking and calibration

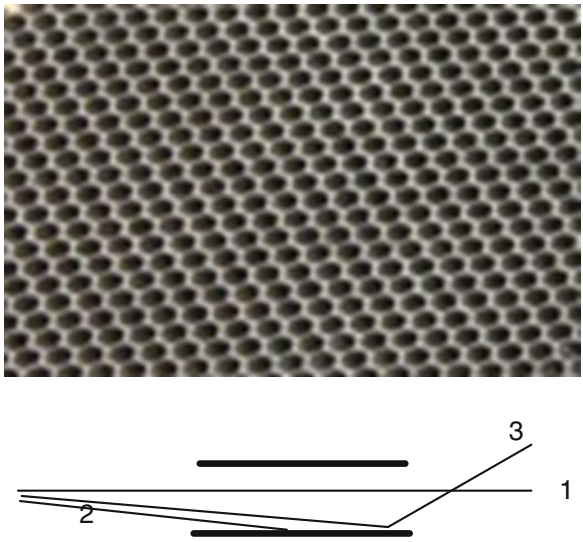

Fig. 11.2 A parallel hole collimator. Gamma ray 1 passes through, gamma ray 2 hits the septa and being absorbed, gamma ray 3 hits the septa then being Compton scattered to a different direction at lower energy

energy spectra. Furthermore, gamma camera can generate images without rectilinear scan but utilizing array of PMTs to record spatial information of gamma emission. The key component in a gamma camera to locate a gamma emission is the collimator (Fig. 11.2) (Bushberg et al. 2011; Chandra et al. 1992).

An Anger camera consists of collimator, scintillation crystal, array of PMTs, electronics, and display device. Gamma photons emitted from radioactive decay of

the radioisotope attached to the pharmaceutical compound administered to patient are statistically independent. They are emitted randomly toward to all directions. In order to localize those photons (to define the positions of the emission from the patient body), a collimator is needed to register a photon from an emission site to a picture element of imaging metrics. This is called a pixel. The imaging metrics normally has 64 by 64, 128 by 128, 256 by 256, or 1024 by 1024 pixels in a two-dimensional image (or planar image). The position of the pixel in the metrics corresponds to the emission site of the patient body. The intensity of the pixel reflects the number of photons registered on to that pixel. A photon can only pass through a collimator hole when it is in the right direction; otherwise, it will hit the collimator hole septum and then be absorbed. Therefore the primary function of the collimator is to define the location of emission site. Since the emission site is where the radioisotope decays, and the radioisotope is attached to (labeled) the pharmaceutical, then the image is the distribution of the compound. This way, the gamma camera image provides the biological and physiological distribution of the compound to describe the physiological function. Thus the gamma camera imaging is called function imaging.

There are parallel hole, diverging hole, converging hole, and pine hole collimators in clinical nuclear medicine imaging. The parallel hole collimator is the most widely used in gamma cameras. It is made of lead. The parallel hole collimators are composed of thousands of aligned holes parallel to each other, which are formed by casting hot lead in most of collimators. The collimator conveys only those photons traveling directly along the long axis of each hole. Photons emitted in other directions are absorbed by the septum wall between the holes through photoelectric interaction. Compton scattering and septum penetration can reduce image quality of the gamma camera (Table 11.3).

In summary, gamma camera imaging involves of following:

1. Injection of radio isotope-labeled radiopharmaceutical to patient.
2. After certain period of time for uptake of the radiopharmaceutical, the patient is positioned on the imaging table for scan (planar or SPECT).
3. Gamma rays emitted may have photoelectric interaction which leads to tissue absorption of the gamma photons or may be Compton scattered which lose some of the initial energy and change the direction of traveling. If the gamma ray energy is higher than 1.02 MeV, there may be chance to have pair production.

Table 11.3 Scintillation crystals used for gamma cameras and PET

Scintillation crystals	Gamma ray energy	Clinical applications	Scintillation efficiency	Stopping power	Scintillation recover time (speed)
NaI (Tl)	Around 140 keV	Gamma cameras Planar and SPECT	High	Low	Low
BGO	511 keV	PET	Moderate	High	Low
LSO, LYSO, GSO	511 keV	PET	High	High	High

Therefore, photons traveling through patient body may end up with photon beams with an energy distribution and emissions from scattered photons.

4. When the photon arrives at the surface of the collimator, only the gamma rays passing through the holes may deposit their energy to crystal to generate scintillation lights. Many photons are absorbed; some may make their way to the crystal at lower energy since a fraction of the initial energy is carried away during the Compton scattering.
5. When incoming gamma rays interact with scintillation crystal, they may go through photoelectric interaction which lead to full absorption of the gamma photon or may be scattered to different direction at lower energy in Compton scattering. Some scattered photon may be absorbed by photoelectric interaction after being scattered once or more times.
6. Scintillation lights are converted to electrons on the surface of those PMTs, and then the electrons are collected and processed to generate pulse signals. Three components are included in the pulse signals: location, intensity of the event, and energy of the gamma rays.
7. Those signals are further processed (smoothing, enhancing contrast, etc.) in planar imaging.
8. Images are archived, transferred, and displayed for analysis and clinical diagnosis.

11.8 SPECT

A planar image is a 2-D picture of 3-D distribution of radioactivity. Tomographic imaging is to generate a 3-D picture of the 3-D distribution. In order to collect 3-D data, a SPECT (single photon emission computed tomography) camera scans patient from multiple angles (e.g., 180 or 360°) to generate a set of 2-D images (projections). Those 2-D projection images form the basis for reconstruction (Buschberg et al. 2011). Similar to X-ray CT, SPECT utilizes image reconstruction from multiple projection images to provide a set of images (e.g., transverse slices) to represent 3-D distribution. A key difference between the SPECT and the X-ray CT is that the SPECT is emission tomography and the X-ray CT is transmission tomography. This is due to the fact that gamma camera and SPECT scanner detect gamma rays emitted from patient and the X-ray pass through patient body before being detected.

Filtered back projection is an image reconstruction method to mathematically construct a 3-D image based on the multiple projection date from tomographic scan. Iterative reconstruction is developed to improve image quality by including physics characters in the imaging process. It has been used as a major reconstruction method in emission tomography.

Mathematical filters are used in the image reconstruction and processing to remove noise and select useful components in image data by filtering some spatial frequency out. It is an important part of imaging processing to select a filter and set up filter parameters in clinical nuclear medicine imaging.

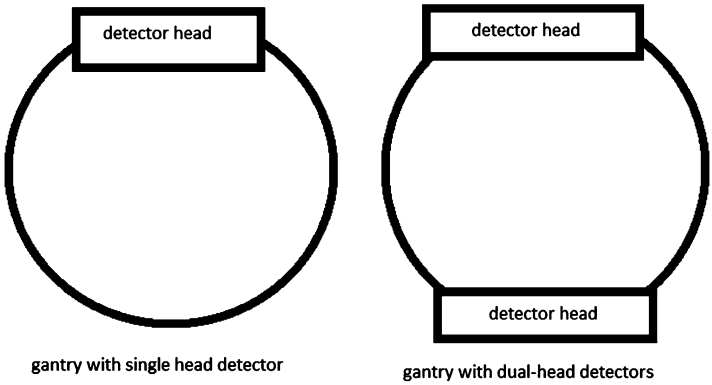

Fig. 11.3 Modern SPECT camera design. There are single-head, dual-head, and triple-head configurations. The dual-head SPECT cameras are the most widely used for clinical services

SPECT imaging can provide quantitative information for data analysis. Those quantitative data can be used for dosimetry and diagnostic evaluation of disease. Therefore a SPECT image provides pictures and quantitative data to describe 3-D distribution of radionuclides in patient body. It is essential to maintain quality of the SPECT and gamma camera images to the level that that current technology can provide. This involves quality product by manufacturer, equipment quality assurance, and right clinical protocol by nuclear medicine service (Fig. 11.3).

The dual-head detectors can be arranged 180° or 90° (for cardiac scan) or other angles for certain imaging protocols. Those configurations are to position the detector heads close to the patient for better special resolution.

There are many factors that may impact performance of a gamma camera: photon attenuation, Compton scattering, and source to detector distance. In addition to those factors, tomographic acquisition, reconstruction, and image processing will change the SPECT images.

Nuclear medicine services have quality control/assurance program for all gamma cameras. These include daily testing, periodic testing, and calibration of the gamma cameras. The following table lists the tests and calibrations as routine QC procedures.

A common QC test is uniformity imaging of a flood source or a point source to simulate a uniform flood emission where uniformity analysis provides four parameters: integral and differential uniformity in central field of view and in useful field of view (Table 11.4) (Figs. 11.4, 11.5, 11.6, and 11.7).

American College of Radiology (ACR) implemented an accreditation program for advanced imaging. Since 1987, the ACR has accredited more than 35,000 medical facilities in 10 imaging modalities, which includes CT, MRI, ultrasound, mammography, nuclear medicine, and PET. Medical physicists work together with physicians and technologists to obtain and maintain the accreditation Figs. 11.8 and 11.9.

Table 11.4 Gamma camera QC. Extrinsic imaging acquires data with collimator loaded, and intrinsic scan runs with the collimator removed

QC tests	Frequency	Description
Uniformity	Daily	Extrinsic or intrinsic
Energy window and peaking	Daily	For example, 140 keV, 20% window for Tc-99 m
Spatial resolution and linearity	Weekly	Extrinsic or intrinsic
Detector sensitivity	Quarterly, annual	Extrinsic or intrinsic
High count rate uniformity	Quarterly, annual	Extrinsic or intrinsic
Qualitative collimator Uniformity check	Annual	Visual inspection to check for collimator damage
Energy resolution	Annual	Extrinsic or intrinsic

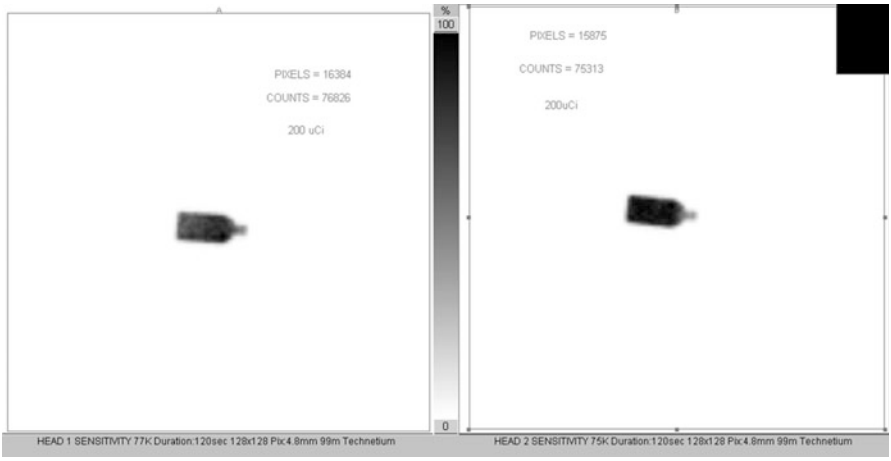

Fig. 11.4 Planar image of Tc-99 m source to measured camera sensitivity. Source activity was 200 uCi in a plastic container. Imaging time: 120 s. Detector 1: 77,000 counts per 200 uCi, Detector 2: 75,000 counts per 200 uCi (Images were from Nuclear Medicine Service, Virginia Commonwealth University Hospital System, Richmond, Virginia)

In summary, SPECT imaging involves of following:

(1) to (6) are similar to the planar imager.

(7) Multi-angle acquisitions are needed to provide set of projections.

(8) Image reconstructed of the projection data is to provide tomographic images in SPECT.

(9) Image processing before and/or after reconstruction may be used to improve images for reading.

(10) Images are archived, transferred, and displayed for analysis and clinical diagnosis.

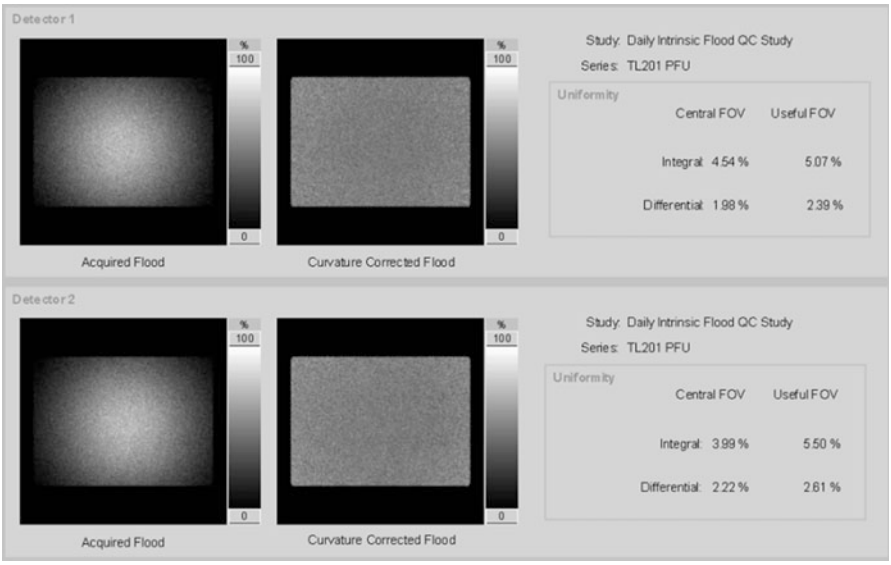

Fig. 11.5 Intrinsic uniformity image of Tl-201 point source on a Siemens eCam Gamma Camera. A point source of Tl-201 was positioned in the center of two detector heads. Since the source to detector distance was too short, the gamma emission to the two heads was not uniform as shown on the left. Images on the right were curvature corrected (Images were from Nuclear Medicine Service, Virginia Commonwealth University Hospital System, Richmond, Virginia)

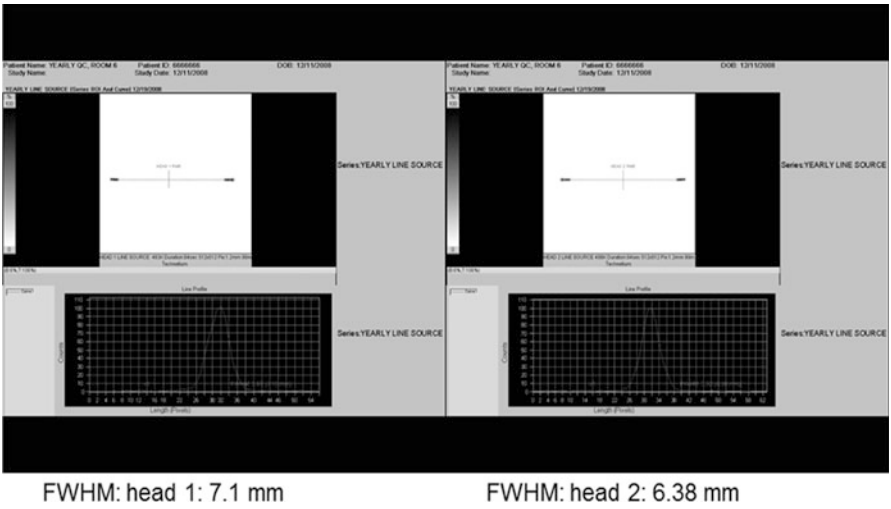

Fig. 11.6 Planar image of a Tc-99 m line source and count profile showing spatial resolution measured by FWHM. The line source was a glass tube filled with radioactivity and then positioned at the center of the two detector heads. Upper part of the display below are images from the two heads, and lower portion show the profile of the activity distribution on images (Images were from Nuclear Medicine Service, Virginia Commonwealth University Hospital System, Richmond, Virginia)

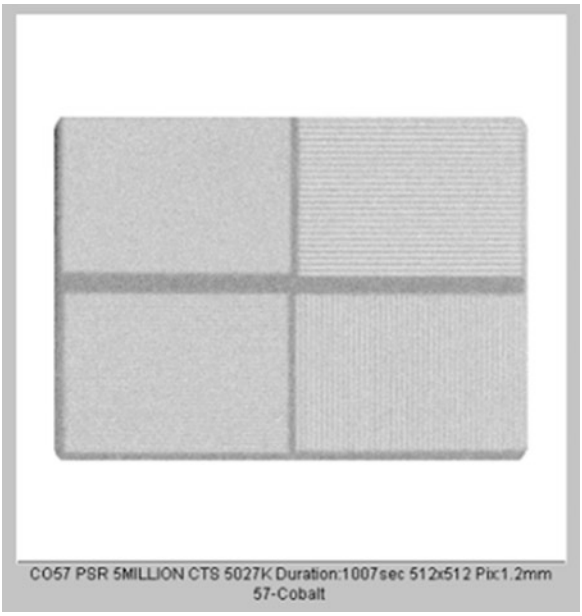

Fig. 11.7 Extrinsic resolution image of Co-57 flood source on parallel hole collimator. A Co-57 sheet source was on top of a four-quadrant resolution phantom positioned on top of the parallel hole collimator loaded onto the detector head (images were from Nuclear Medicine Service, Virginia Commonwealth University Hospital System, Richmond, Virginia)

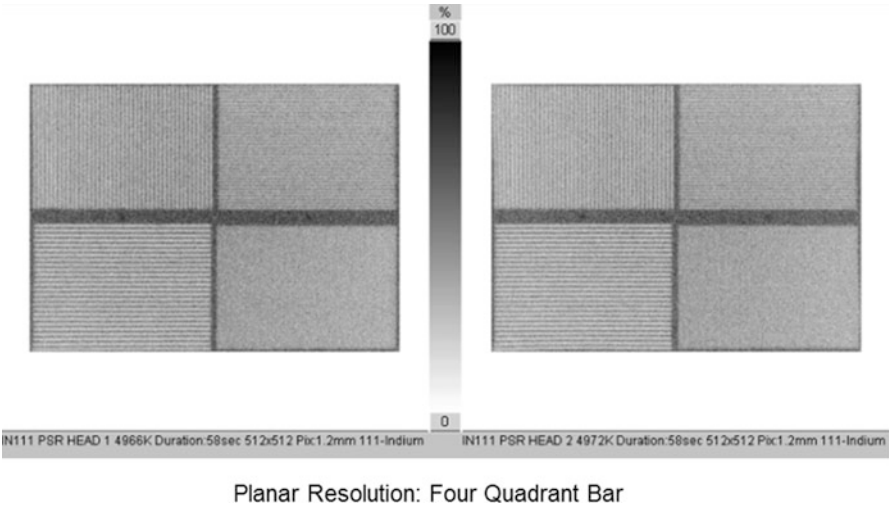

Fig. 11.8 Intrinsic resolution image of In-111 point source on dual-head camera. A point source of I-111 was at certain distance from the four-quadrant resolution phantom. The collimator was removed from detector head (images were from Nuclear Medicine Service, Virginia Commonwealth University Hospital System, Richmond, Virginia)

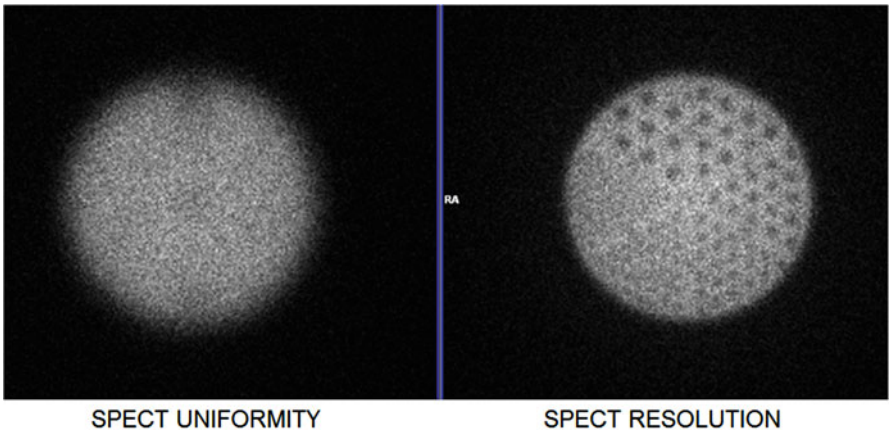

Fig. 11.9 SPECT uniformity and resolution images of Tc-99 m filled ACR phantom on a dual-head camera. 15 to 20 mCi of Tc-99 m was normally put in to the phantom. Transverse images below were from image reconstruction following tomographic acquisition. Image on the left was a slice in the upper section where there was no inserts but only water. Image on the right was a transverse display of the rods in the phantom (images were from Nuclear Medicine Service, Virginia Commonwealth University Hospital System, Richmond, Virginia)

11.9 PET

In gamma camera imaging (planar and SPECT), photons are emitted and then detected as single photons. Therefore, a collimator is needed to define the locations of the events. However, the collimator can only pass a small fraction of photons hit the surface of the camera. It significantly reduces gamma camera detection efficiency. PET (positron emission tomography) detects pairs of gamma rays of 511 keV which are emitted through radioactive decay of positron emitter (positron-emitting radionuclide). The positron then interacts with electron to have a positron-electron annihilation. This annihilation generates a pair of gamma rays of 511 keV, at 180° and emitted the same time (Buschberg et al. 2011; Sorenson et al. 1987). Because of these three features of the gamma rays, they can be imaged without collimation but through coincidence detection (Fig. 11.10).

In the coincidence detection, two 511 keV gamma rays are detected with a pair of detectors at opposite direction (180°). The PET registers an event of positron-electron annihilation only when the two photons are within 511 keV energy window (e.g., 30% peaked at 511 keV) at 180° and hit the detector at the same time. Here, the same time actually means within a timing window of about 10 ns. Comparing this detection with single photon imaging, an event of gamma emission is recorded only when the photons are within energy window (e.g., 20% centered at 140 keV for Tc-99 m) and pass through collimator holes; here the coincidence detection is similar to electronics collimation (Fig. 11.11).

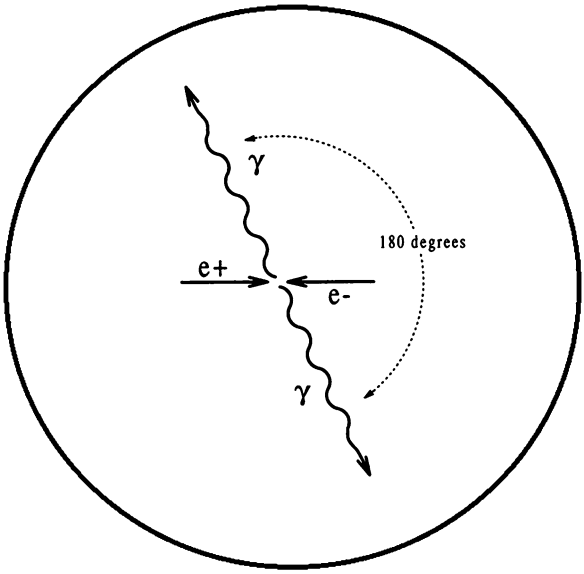

Fig. 11.10 Positron-electron annihilation and coincidence detection. Two gamma rays are 511 keV, emitted at the same time and in opposite direction. The event is recorded when the two gamma rays are detected by a pair of detectors at 180°; they are within energy window (30%) centered at 511 keV and arrived (being detected) detectors within a timing window (<10 ns)

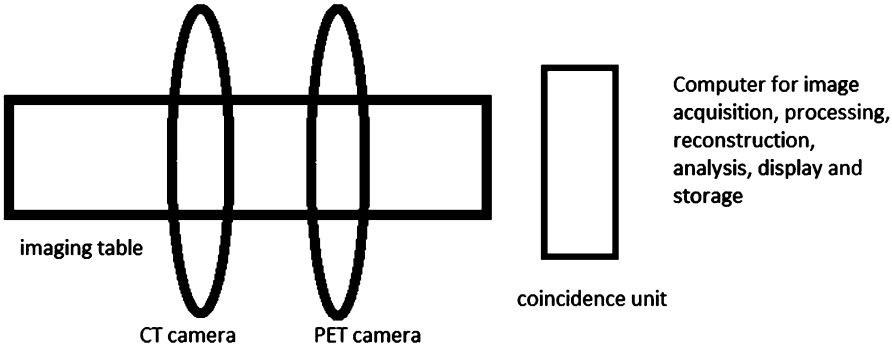

Fig. 11.11 Modern PET camera design

A modern PET camera utilizes multiple rings of thousands of scintillation detectors. The ring structure provides many paired detectors for coincidence detection. The multiple rings cover a "section" rather than a "slice" of the imaging subject to improve efficiency of the PET imaging. A typical whole-body scan can be done with five to seven sections.

Scintillation crystals in PET scanner must be able to stop 511 keV photons. NaI (Tl) crystal is the primary detector in nuclear medicine imaging because of its high

Table 11.5 SPECT and PET

Features	SPECT	PET
Detection mode	Single photon	511 keV photon pairs
Scintillation crystal	NaI(Tl)	BGO, LSO, etc.
Gantry	Rotating detector heads	Fixed rings

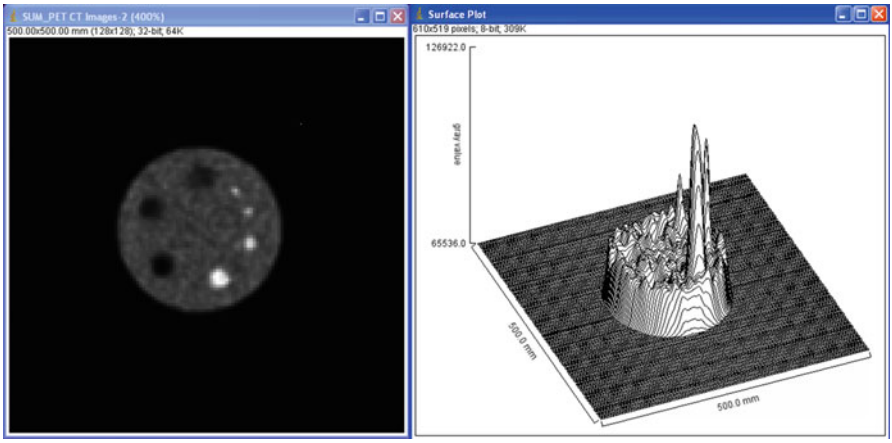

Fig. 11.12 PET image of F-18 in an ACR phantom. *Black holes* are cold spheres, *white holes* are hot spheres, and *gray region* shows background activity in the cylindrical container. Picture on the right describes distribution of the activity in each sphere (Images were from Nuclear Medicine Service, Virginia Commonwealth University Hospital System, Richmond, Virginia)

scintillation efficiency for gamma ray energy of 140 keV (Tc-99 m). However, the NaI (Tl) is not the choice for PET scanner since its stopping power for high-energy photons is low compared with BGO or LSO.

BGO (bismuth germanate) is the standard crystal for PET before LSO was introduced to improve scintillation speed or to reduce decay time of the crystal. With its elevated stopping power, high scintillation efficiency, good energy resolution, and non-hygroscopes, BGO is an excellent scintillation material and is ideal for PET imaging. LSO crystal is a new-generation scintillator crystal. LSO (lutetium orthosilicate) crystal has the advantages of high light output and density, quick decay time, excellent energy resolution, and low cost. These properties make LSO an ideal candidate for a range of gamma ray detection applications in PET imaging. Similar to the LSO crystal, GSO (gadolinium oxyorthosilicate) and LYSO (cerium-doped lutetium yttrium orthosilicate) are used by different manufacturers of PET scanners (Table 11.5) (Fig. 11.12).

11.10 Multimodality Imaging

The highly sensitive PET scan images the biological and physiological process to find disorders at the molecular level (functional imaging), while the CT scan provides a detailed picture of the body's internal anatomy (anatomical imaging). The PET-CT scan combines the strengths of these two well-established imaging modalities into a single scan. The CT portion of a PET-CT scanner provides anatomical definition of an internal organ and body attenuation map for attenuation correction. In recent years, MRI has been used to build a PET-MRI imaging unit to take advantage of both well-established imaging modalities.

Similar to PET-CT scanner, there is SPECT-CT imaging system for single photon imaging where the CT portion is to generate attenuation map and to provide anatomical definition of the organ of interest.

Since the imaging modalities (PET and CT or PET and MRI) are available before they are merged into one imaging unit, most multimodality imaging systems use image registration techniques to "combine" images from different modalities to generate a "fussed" image. For example, in PET-CT, the fussed image maintains the functional distribution of radioactive isotope with anatomically defined organ structure by CT scan.

Since the two modalities are calibrated at the factory by manufacturer, then there is no need for users to create calibration factors to register two sets of images. However, if the two sets of images come from different modalities that are independent imaging units, software fusion is needed and the calibration factors may be generated by using face markers.

11.11 PET-CT QC

Similar to SPECT, a routine QC (quality control) program is a key component in a clinical PET-CT facility. ACR established an accreditation program for PET and then PET-CT. Manufacturers of the PET-CT provide users with a guideline for routine QC protocols. Because of variety in PET-CT design, those QC guidelines are specific for each unit. ACR listed general steps in performing the QC procedures, which normally involves imaging a line source of a positron emitter and scanning a phantom of F-18 similar to the SPECT phantom (Figs. 11.3 and 11.14).

An important part of nuclear medicine practice is radionuclide therapy. The therapy procedures apply radionuclides to treat various diseases including cancer. The radionuclide (e.g., I-131) is administered orally or through intravenous injection (e.g., Sm-153 Quadramet) or by catheter (e.g., Y-90 microspheres) inserted by interventional radiologists. Medical physicists support physicians to handle the radioactive materials and provide dosimetry calculations (Ollinger et al. 1997; Muehllehner et al. 2006).

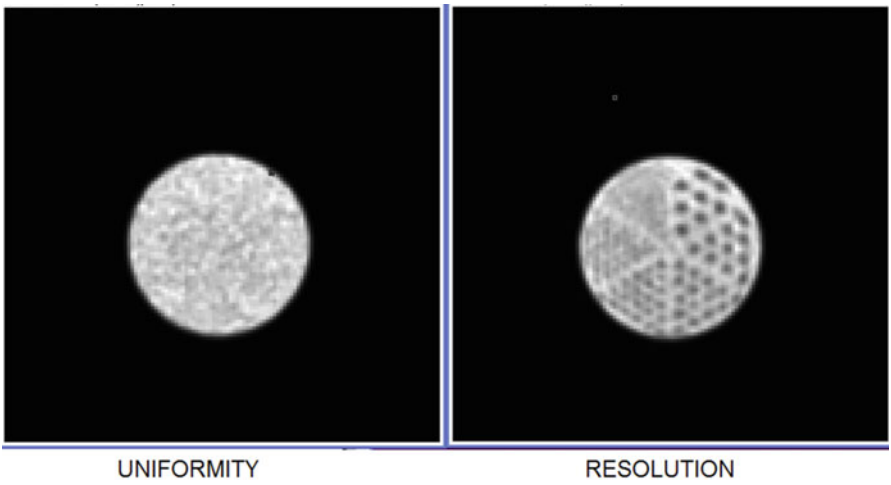

Fig. 11.13 PET image of F-18 ACR phantom showing a slice of uniform region and a slice of rod section. The images have been corrected for attenuation using CT imaging data (Images were from Nuclear Medicine Service, Virginia Commonwealth University Hospital System, Richmond, Virginia)

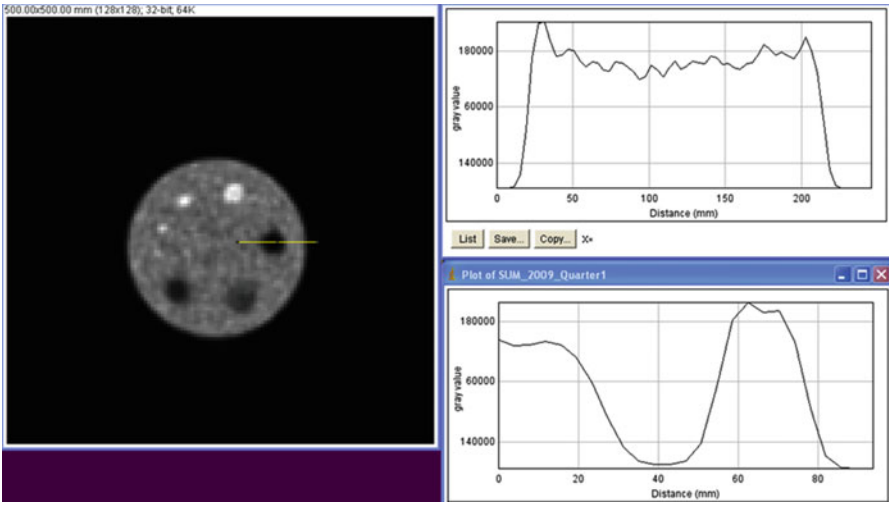

Fig. 11.14 PET image of F-18 ACR phantom showing hot (*white*) cold (*black*) lesions. Upper curve shows count profile across the phantom and lower count profile measures the size of the lesion and counts (activity) distribution (Images were from Nuclear Medicine Service, Virginia Commonwealth University Hospital System, Richmond, Virginia)

Questions

1. Why is Tc-99 m chosen as the radioisotope to label majority of the pharmaceuticals in clinical nuclear medicine?
2. What is the primary function of a collimator in a gamma camera? There are three parameters in a parallel hole collimator design: hole length, hole diameter, and septa thickness. Fill in the table for effect of adjusting those parameters (change one of the two parameters while keep the other two) to camera detection efficiency and special resolution.

Parallel hole collimator	Detection efficiency	Spatial resolution
Increase length of the hole		
Increase diameter of the hole		
Increase septa thickness		
Decrease length of the hole		
Decrease diameter of the hole		
Reduce septa thickness		

3. NaI (Tl) crystal is installed on most of gamma cameras. However, it is not the choice of detector for PET. An important feature of BGO or LSO crystal is their high stopping power for 511 keV gamma rays. Why is the BGO or LSO not a good candidate for SPECT cameras?
4. Gamma rays may have photoelectric absorption and/or Compton scattering when traveling through tissue and interacting with scintillation crystal. What is going to happen when a group of photons is attenuated in tissue or when those photons are absorbed by scintillation crystal?
5. In gamma camera imaging, one challenge is limited counts of gamma rays being detected. List possible ways to increase the counts in clinical imaging.
6. Select detectors for the following applications, and justify your selection based on physics and instrumentation:

   (a) Contamination survey
   (b) Wipe test
   (c) Measure doses to be injected to patients
   (d) Thyroid uptake
   (e) Lymph node localization during breast surgery
   (f) Area monitoring
   (g) Real time monitoring of personnel exposure
   (h) Personal dosimeter (film badge in the past)

7. Select parallel hole collimators (LEGP, MEGP, HEGP, LEHR) or pinhole collimators for the following clinical applications, and justify your selection based on physics of the radionuclides and characteristics of the collimators:

   (a) Tc-99 m brain
   (b) Tc-99 m whole body
   (c) In-111 whole body

(d) I-131 whole body
(e) I-131 thyroid

where LEGP stands for low-energy general purpose collimator,
MEGP stands for medium-energy general purpose collimator,
HEGP stands for high-energy general purpose collimator, and
LEHR stands for low-energy high-resolution collimator.

8. The following diagram shows the camera system spatial resolution (top) and system efficiency (bottom) vs. distance between patient and camera head:

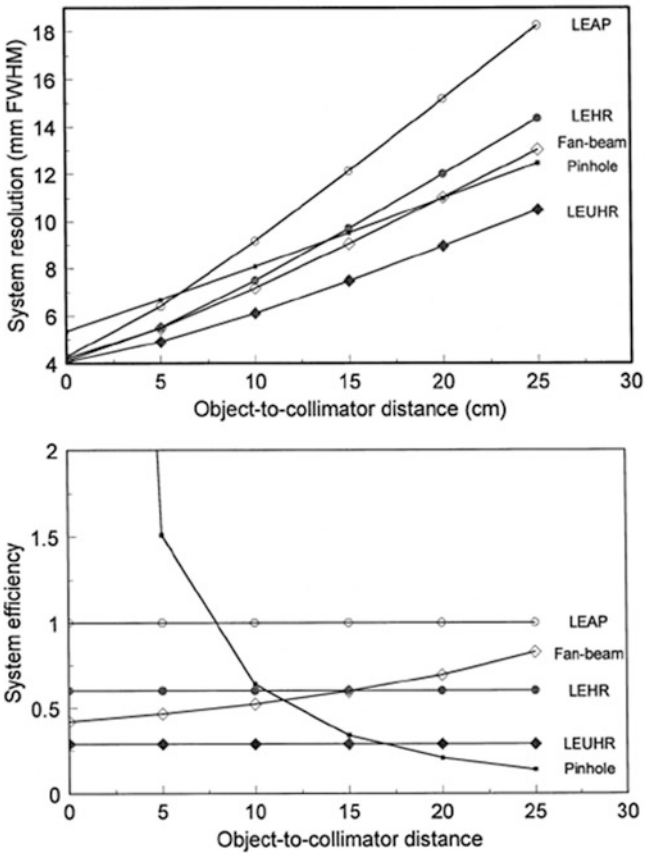

(a) Would you position a patient at 5 cm, 10 cm, or 20 cm from the collimator?
(b) Do you expect the same spatial resolution for organs near body surface as organs deep inside the body?
(c) Does the system spatial resolution change with the distance if parallel hole collimator is loaded?
(d) Does the system detection efficiency change with the distance if the parallel hole collimator is loaded?

9. Major problems in PET imaging include the following:
   (a) Attenuation, random coincidence, center of rotation, dead time, and collimator penetration
   (b) Uniformity, random coincidence, Compton scattering, and dead time
   (c) Spatial resolution, random coincidence, and Compton scattering
   (d) Attenuation, random coincidence, Compton scattering, and dead time
   (e) None of the above
10. Key features of the 511 keV gamma rays from positron-electron interaction are that:
   (a) Each photon has energy of 511 keV, two photons travel in opposite direction (about 180°), and both are emitted at the same time.
   (b) Two photons have total energy of 511 keV, two photons travel in opposite direction (about 180°), and both are emitted at the same time.
   (c) Each photon has energy of 511 keV, two photons travel in same direction, and both are emitted at the same time.
   (d) Each photon has energy of 511 keV, two photons travel in opposite direction (about 180°), and two photons are emitted within 12 ns.

Key

Gas-filled detectors	Detector medium is a chamber filled with air or a specific gas. When radiation hits the chamber, ionization of the molecules in the air occurs. The positive ions will be attracted to the negative side of the detector (the cathode), and the free electrons will travel to the positive side (the anode). These charges are collected by the anode and cathode which then form a current.
Scintillation crystals	The crystal will generate visible light photons when excited by ionizing radiation. Then the visible light photons are collected and converted to electrons on surface of the photomultiplier tube (PMT). The electrons get multiplied in the PMT and form a pulse as signal.
Uptake probe	A NaI (Tl) well counter to measure the tissue/organ uptake of radioisotope-labeled compound.
Survey meters	Radiation detectors used to check out possible contaminations of radioactive materials and exposure from majority of radioactive sources and from X-rays.
Anger cameras	Gamma camera developed by Hal Anger in 1957. An array of PMTs is behind a scintillation crystal. The crystal is covered with a collimator to locate sites of gamma emissions.
SPECT	Based on the Anger camera, applied multi-angle acquisition and tomographic image reconstruction to form three-dimensional distribution of the radiopharmaceutical in tissue The gamma rays are detected as independent events.

PET	Similar to the SPECT but with a key difference in detection method. The gamma rays are detected in a coincidence mode
Image registration	It is to register multiple image sets into one to take advantage of unique features from each imaging modality.
Multimodality imaging	More than one imaging modality is utilized to image one subject.
Radiation dosimetry	Measurement of ionizing radiation to determine energy deposit to the tissue or organ.

References

Bushberg JT, Anthony Seibert J, Leidholdt EM. Jr, Boone JM (2011) Essential physics of medical imaging, 3rd edn. ISBN-13: 978–0781780575

Chandra R (1992) Introductory physics of nuclear medicine, 4th edn. Lea & Febiger, Philadelphia

Chandra R (2011) Nuclear medicine physics: the basics, 7th edn. Wolters Kluwer Health/ Lippincott Williams & Wilkins, Philadelphia. ISBN-13: 978–1451109412

Cherry SR, Sorenson JA, Phelps ME (2012) Physics in nuclear medicine, 4th edn. Saunders, Philadelphia. ISBN: 978–1–4160-5198-5

Christian PE, Waterstream-Richand KM, Langan JK (2011) Nuclear medicine and PET/CT - technology and techniques, 7th edn. Mosby-Year Book, Inc. ISBN-13: 978–0323071925

Muehllehner G, Karp JS (2006) Positron emission tomography. Physics in Medicine and Biology 51(13):R117

Ollinger JM, Fessler JA (1997) Positron emission tomography. IEEE Signal Process Mag 14(1):43–55

Sorenson JA, Phelp ME (1987) Physics in nuclear medicine, 2nd edn. Grune and Stratton, New York

Chapter 12
Ultrasound

James R. Costello, Hina Arif, Bobby Kalb, and Diego R. Martin

Contents

12.1 Introduction 329
12.2 Contrast Versus Resolution 331
12.3 Acoustic Theory 331
12.4 Ultrasound Transducer 340
12.5 Ultrasound Beam Properties 343
12.6 Ultrasound Image Acquisition 348
12.7 Doppler Ultrasound 352
12.8 Bioeffects of Ultrasound Imaging 363
12.9 Advancements in Ultrasound 364
12.10 Compound Imaging 367
12.11 Three-Dimensional Imaging 367
12.12 Extended Field of View 368
12.13 Conclusions 368
References 370

12.1 Introduction

Over the past few decades, there has been a driving push in medical imaging to develop techniques that are noninvasive and without exposure to potentially harmful ionizing radiation. The two imaging modalities that are leading this initiative are ultrasound and magnetic resonance imaging (MRI).

J.R. Costello, MD, PhD (✉)
Department of Medical Imaging, University of Arizona, 1501 North Campbell Ave, P.O. Box 245067, Tucson, AZ 85725, USA

Radiology Associates of Macon, PC, 770 Pine Street, Macon, GA 31201, USA
e-mail: jcostello@radiology.arizona.edu

H. Arif, MD • B. Kalb, MD • D.R. Martin, MD, PhD, FRCPC
Department of Medical Imaging, University of Arizona, 1501 North Campbell Ave, P.O. Box 245067, Tucson, AZ 85725, USA
e-mail: hinaarif@radiology.arizona.edu; bkalb@radiology.arizona.edu; dmartin@radiology.arizona.edu

M. Maqbool (ed.), *An Introduction to Medical Physics*, Biological and Medical Physics, Biomedical Engineering, DOI 10.1007/978-3-319-61540-0_12

Ultrasound generates images through the interaction of the body with sound waves. Through differences in the interaction of tissue with incident, high-frequency sound waves, two-dimensional (2D) grayscale images of the body can be generated. Additionally, ultrasound can measure blood flow and velocity, provide multiplanar and three-dimensional (3D) imaging, visualize dynamic moving structures such as a fetus and the heart, and evaluate superficial structures such as the thyroid and joints with high-resolution imaging. All of these imaging features are provided by hardware which is portable and easy to transport, unlike the bulky stationary scanners of computed tomography and MRI. Additionally, ultrasound represents a cost-effective examination that can be repeated on regular intervals but without the significant cost burden of other imaging exams.

The origins of ultrasound imaging began well over 200 years ago. In the late 1700s Lazzaro Spallanzani identified that bats used a sensory tracking system other than sight to navigate. Spallanzani detailed this process as echolocation or spatial navigation through the emission and detection of inaudible sound. In 1826 Jean-Daniel Colladon introduced the underwater church bell as the first ultrasound transducer. With this first instrument, Colladon proved that the speed of sound traveled faster in water than in air. In 1880 Pierre and Jacques Curie described the piezoelectric effect and how electricity can be generated within a quartz crystal when mechanically vibrated. Acoustic energy potentially serves as a source for such mechanical vibration. This idea serves as the operating principle for the modern-day medical ultrasound transducer.

During World War I and II, military sonar research helped advance the field of ultrasound. In 1915 Paul Langevin constructed the hydrophone to help ships detect icebergs and to locate underwater submarines. In 1937 Sergei Sokolov described the "Sokolov tube" for underwater imaging. This device advanced the field of underwater sonography and introduced the first real-time sonar display. From these developments in military sonar research, applications in medical imaging would soon arise. In 1942 Dr. Karl Dussik described the application of ultrasound to visualize the mass effect of brain tumors and the resulting effect upon the cerebral ventricles. Later in 1948 George Ludwig and Francis Struthers detailed the application of ultrasound for imaging of gallstones which was later followed by Dr. Ian Donald's use of ultrasound in obstetric imaging to measure the parietal diameter of the fetal head. All of this work materialized in 1963 with the introduction of the first commercial ultrasound scanner (Kremkau 1998; Goldstein 1993; Hendrick et al. 1995; Zagzebski 1996; Bushberg et al. 2002).

Within this chapter, we will discuss the physics of sound, transducer design and optimization, the generation of an ultrasound image, artifacts of ultrasound imaging, and Doppler imaging. Through this discussion, we hope the reader acquires an understanding of the current applications of ultrasound and the promise for this technique's continued maturation within medical imaging.

12.2 Contrast Versus Resolution

Fundamental to a discussion of medical imaging is differentiating between the properties of image contrast versus image resolution. Image contrast distinguishes an object of interest from the surrounding background tissue that contains it. For example, contrast refers to the ability of ultrasound to distinguish a hepatic mass such as a hepatocellular carcinoma, a type of liver cancer, from the background liver parenchyma which surrounds the mass. Image resolution reflects the ability of an imaging system to resolve two adjacent structures of interest from each other. For example, an ultrasound image with sufficient spatial resolution can distinguish two adjacent hepatic masses as opposed to a lower-resolution image which displays a single lobulated mass with no demarcation where one mass ends and the other begins as shown in Fig. 12.1.

12.3 Acoustic Theory

Ultrasound generates medical images through the interaction of sound with different tissue types. Sound represents mechanical energy that travels through an elastic medium (air, water, tissue) as a longitudinal wave with an alternating sequence of compression and rarefaction of its constituent particles. Rarefaction is defined as a decrease in the density of the medium or the opposite effect of compression (Bigelow et al. 2011). Compression of the elastic medium is represented by positive displacement of the wave's pressure amplitude, while rarefaction closely follows the compressive event with a mirrored response of negative displacement of the

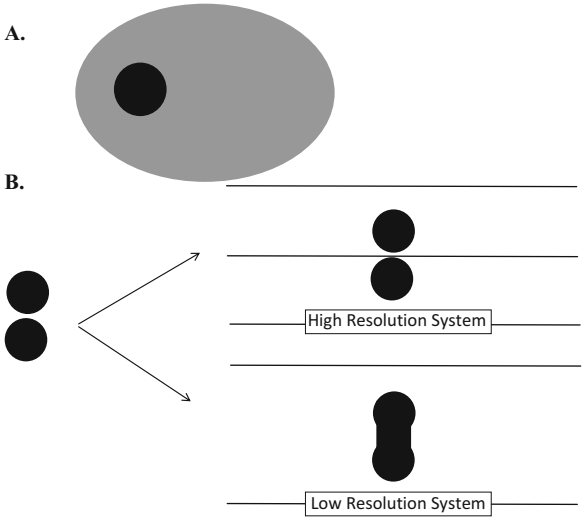

Fig. 12.1 *Image contrast versus image resolution*. (**a**) Contrast: a high-contrast imaging system can resolve the *black* ball from the background *gray* area. (**b**) A high-resolution system can distinguish the two *black* balls from each other, whereas the low-resolution system volume averages the two *black* balls into one imaged *black* object

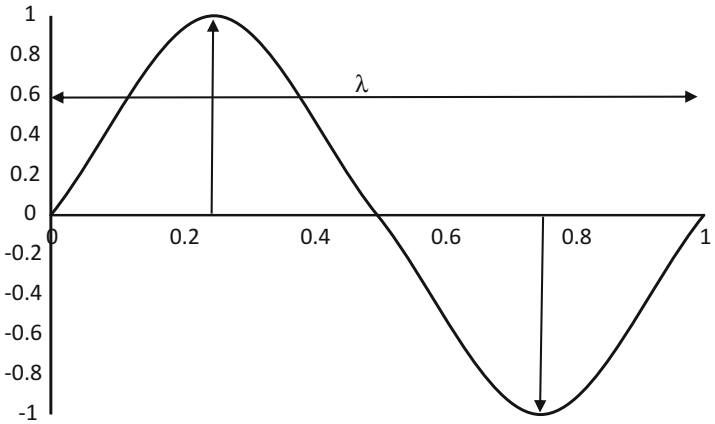

Fig. 12.2 *Pressure wave*. Ultrasound represents a traveling wave of mechanical energy with alternating compression and rarefaction of the elastic medium

wave's pressure amplitude. Through this repetitive cycle, mechanical energy or sound is transported through the elastic medium as shown in Fig. 12.2.

12.3.1 Properties of Sound

The wavelength of sound, λ (meters), is defined as the distance between successive compressive peaks, while the frequency of sound, f, reflects the number of times that the wave cycle repeats per second. Frequency is measured in cycles per second or Hertz. Human hearing falls within a frequency range of 20 Hertz (Hz)–20 kilohertz (kHz). Ultrasound transmission occurs at a frequency range above the upper limit of human hearing. For medical imaging, this range is defined between 1 and 20 megahertz (MHz). The period of the wave, T (seconds), represents the time between successive compressive peaks or the reciprocal of the frequency. The speed of sound, c (meters/second), reflects the distance traveled by the wave over the length of time needed to complete 1 cycle which can also be expressed as:

$c = \lambda/T$

or

$$c = \lambda^* f \tag{12.1}$$

If sound is traveling within muscle with a speed of 1585 m/sec and a frequency of 3 MHz, then the wavelength will be equal to 0.528 mm.

The speed of sound varies depending on the properties of the elastic medium.

$$c = \sqrt{\beta/\rho} \tag{12.2}$$

β (kilogram/meter) represents the bulk modulus which reflects the stiffness of the elastic medium, while ρ (kilogram/meter^3) represents the density of the elastic medium. For a compressible medium such as gas, the speed of sound will be slower in comparison to a less compressible medium such as metal or calcified bone. Additionally, a less dense medium such as dry air will demonstrate a faster speed of sound than a denser medium such as humid air. For reference, the speed of sound in air is 330 m/sec, in soft tissue is 1540 m/sec, and in fatty tissue is 1450 m/sec. As the mechanical sound energy travels between elastic mediums with different speeds of sound, the frequency remains constant, while the wavelength either contracts or expands.

Why is the frequency and wavelength of the transmitted acoustic energy important for ultrasound? As the frequency increases, the wavelength decreases. With a smaller wavelength, the ultrasound possesses greater axial spatial resolution to distinguish between two adjacent structures along the line of transmission or the ultrasound pulse beam. Frequently in medical imaging, an improvement in one imaging parameter comes at a sacrifice to another imaging parameter. With an increase in frequency, the sound energy is attenuated faster, and the depth of penetration for the ultrasound to provide imaging is reduced. With these parameters in mind, high-frequency probes (7.5 MHz–10 MHz) are used to image superficial structures such as the thyroid and musculoskeletal tissue where increased resolution is needed for improved diagnosis. Lower-frequency probes (3.0 MHz–5.0 MHz) are used to image the abdomen where structures are deeper and greater acoustic penetration is needed.

12.3.1.1 The Decibel Scale

When sound travels through an elastic medium, particles vibrate with variations in pressure amplitude reflected by the wave displacement of compression and rarefaction. The intensity of sound reflects the transmitted power per unit area and is roughly equivalent to the square of the pressure amplitude.

$$\text{Intensity} \sim (\text{Pressure})^2 \tag{12.3}$$

As the pressure amplitude doubles, the absolute intensity value increases by four times. The units of absolute intensity level are watts/m^2. Relative sound intensity is measured on the logarithmic scale with decibels (dB) where

$$\text{Relative Intensity (dB)} = 10 \log_{10} \frac{I}{I_o} \tag{12.4}$$

I is the newly measured intensity, while I_o is the original signal intensity which functions as a reference. A change of 10 dB is reflected by a tenfold increase in intensity, while a change of 3 dB is signified by a two-time increase in intensity. A decrease in intensity is shown by a negative decibel value. For example, a reduction

in intensity by 50% equals a change of −3 dB, while a reduction in intensity by 90% relates to a change of −10 dB.

12.3.2 The Dynamics of Sound Interaction

Ultrasound generates images through the interaction of sound with tissue of differing acoustic properties. This interaction is largely governed by the acoustic impedance, *Z*, of the tissue. Acoustic impedance is defined as the product of the density, ρ (kg/m^3), and the speed of sound, c, in the elastic medium.

$$Z = \rho^* c \tag{12.5}$$

The units of acoustic impedance are the Rayl (kg/m^2/sec). The acoustic impedance of air is 0.0004 Rayl, muscle is 1.70 Rayl, and bone is 7.8 Rayl.

When sound travels through the body and encounters an interface with an acoustic impedance mismatch, four different interactions can occur: reflection, refraction, absorption, or scatter.

12.3.2.1 Reflection

Reflected ultrasound energy is critical to the generation of an ultrasound image. The reflected ultrasound energy is called an echo (Fig. 12.3). Reflection occurs at tissue interfaces where there is a difference in the acoustic impedance.

A larger acoustic impedance mismatch results in a larger percentage of the incident energy being reflected. Assuming an angle of incidence from elastic

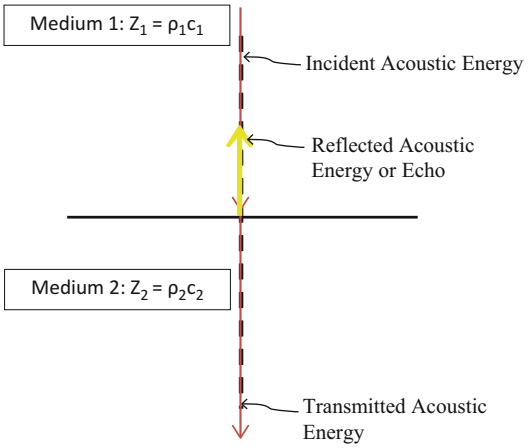

Fig. 12.3 *Reflection of sound with perpendicular incidence to a boundary layer*. At a boundary layer with a difference in acoustic impedance between two mediums and perpendicular incidence (90°) of the incident acoustic energy, a portion of the beam is reflected back to the source, and a portion is transmitted into medium 2

medium 1 perpendicular (90°) to the interface with elastic medium 2, the percentage of incident ultrasound intensity reflected is equal to R_I.

$$R_I = \frac{(Z_2 - Z_1)^2}{(Z_2 + Z_1)} \tag{12.6}$$

Since the percentage of energy reflected plus the energy transmitted must equal 1, the percentage of incident ultrasound intensity transmitted is equal to R_T.

$$R_T = 1 - R_I$$

or

$$R_T = \frac{4Z_1Z_2}{(Z_1 + Z_2)^2} \tag{12.7}$$

For a liver to fat interface, Z_{fat} equals 1.38 Rayl, and Z_{liver} equals 1.65 Rayl. The R_I equals 0.0086 and the R_T equals 0.9914. Given an incident intensity of 50 mW/cm^2, the incident intensity reflected equals 0.43 mW/cm^2, while the incident intensity transmitted equals 49.57 mW/cm^2. Between an air and soft tissue interface, the incident ultrasound energy is near completely reflected. This interaction leads to the generation of a mirror image artifact which will be discussed later. The dynamics of this scenario becomes clear when inputting the low acoustic impedance of air (0.004 Rayl) into the R_T or Eq. (12.7). With the numerator approaching zero, very little acoustic energy is transmitted but rather near completely reflected. To help minimize this effect, acoustic coupling gel or ultrasound jelly is applied between the transducer and the underlying skin.

Other factors that impact reflection include the interface surface characteristics, the size of the interface, and the angle of incidence. The angle of reflection for the echo is equal to the angle of incidence. With an increase in the angle of incidence, the likelihood of the echo being detected by the receiving transducer decreases. Specifically, if the angle of incidence exceeds 3° from the perpendicular interface, a reflected echo is not detected by the ultrasound transducer (Ziskin 1993).

12.3.2.2 Refraction

Refraction describes the change in direction of a transmitted ultrasound beam when the incident ultrasound beam is not orthogonal to the tissue interface, and there is a difference in the speed of sound between the two elastic mediums. In optics this is observed by the redirection of the transmitted light following its passage through a lens. With the difference in the velocity of sound between the two mediums, the frequency of the transmitted pulse will remain constant, but the wavelength will vary in size. The angle of refraction is determined by Snell's law where Θ_t is the

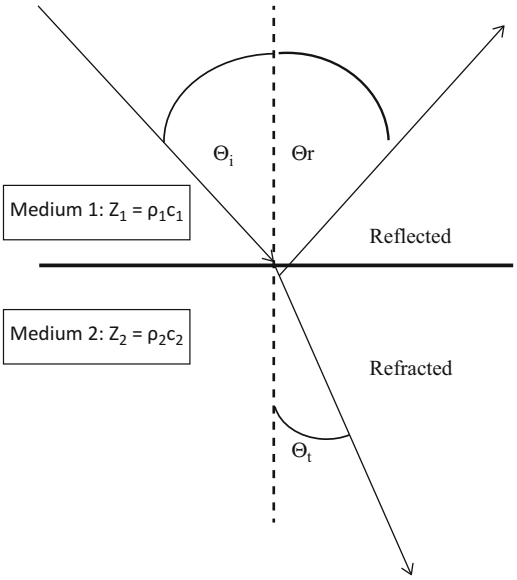

Fig. 12.4 *Reflection and refraction.* Reflection and refraction of acoustic energy occurs at a tissue boundary interface where there is a difference in acoustic impedance (Z) between medium 1 and medium 2. When the incident ultrasound beam is directed toward the boundary interface with nonperpendicular incidence, the reflected echo demonstrates a Θ_r which is equal to Θ_i. The transmitted beam is refracted, and Θ_t or the angel of refraction is defined by Snell's law

angle of refraction, Θ_i is the angle of incidence, and c_1 and c_2 are the respective speed of sounds in mediums 1 and 2 (Fig. 12.4).

$$\frac{\text{Sin}\,(\Theta_t)}{\text{Sin}\,(\Theta_i)} = \frac{c_2}{c_1} \tag{12.8}$$

Diagnostically, refraction is important for it can result in spurious localization of an object of interest through duplication of deeper imaged structures (this is the refraction artifact which will be discussed later). This dynamic is observed frequently at fat/soft tissue interfaces. The speed of sound in fat is 1450 m/sec, while the speed of sound in soft tissue is about 1540 m/sec. This refraction artifact is frequently observed in imaging of the kidneys which are surrounded by prominent retroperitoneal fat.

There is no refraction of sound when $\Theta_i = 90^\circ$ (Fig. 12.3) or c_1 is equal to c_2. Total reflection occurs when c_2 exceeds c_1, and Θ_i is greater than the critical angle (Θ_c). When total reflection occurs, Θ_t equals 90°, and the refracted beam does not travel into medium 2, but rather it runs parallel along the boundary. The critical angle is defined by:

$$\sin\,(\Theta_c) = \frac{c_1}{c_2} \tag{12.9}$$

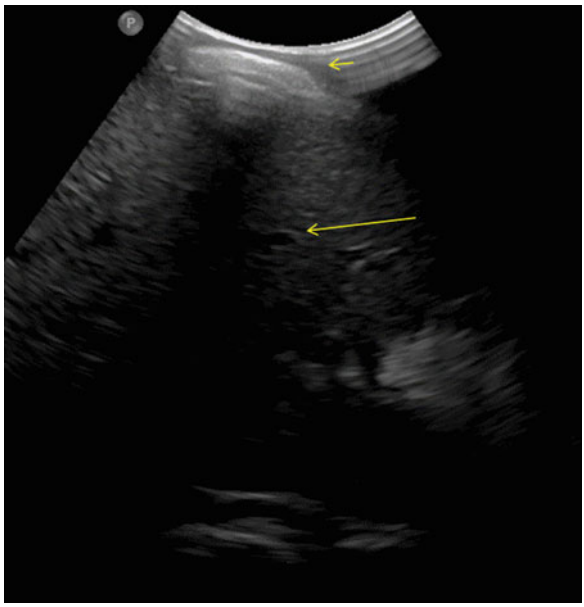

Fig. 12.5 *Absorption*. The ultrasound beam is absorbed by the overlying rib or bone (*small arrow*) and converted into thermal energy. No acoustic energy is transmitted posteriorly, resulting in the clean shadow (*long arrow*)

If sound is traveling from subcutaneous fat ($c_1 = 1.38$ Rayl) into muscle ($c_2 = 1.70$ Rayl), total reflection will occur if the angle of incidence (Θ_i) exceeds the critical angle (Θ_c) of 54.3°.

12.3.2.3 Absorption

Absorption arises when sound energy is lost and converted by a boundary interface from resonating mechanical energy into thermal energy or heat. Absorption occurs more frequently in soft tissue than in fluid, and it happens far more often with bone than with soft tissue. With the loss of sound energy, there is failure to transmit sound beyond the interface of absorption, leading to a posteriorly projecting area devoid of echoes or shadowing. An example of sound energy absorption occurs when an ultrasound beam interacts with an extremely dense tissue such as bone. Posterior to the bone only a clean projecting shadow is visualized (Fig. 12.5).

12.3.2.4 Scatter

Scatter occurs when sound energy interacts with a boundary interface where there is nonspecular reflection. Nonspecular reflection occurs when sound energy interacts with a "rough" surface where the encountered objects are about the same size or smaller than the wavelength of the incident sound. An example would be sound energy interacting with the hepatic parenchyma or tissue of the liver. The liver

contains multiple soft tissue interfaces which are smaller than the wavelength of the incident sound which results in scatter. In contrast, a specular reflector has a smooth surface where the encountered objects at the interface have dimensions much larger than the wavelength of the incident ultrasound energy. Specular reflectors result in reflection and refraction as earlier discussed (Figs. 12.3 and 12.4). If the specular reflector is oriented at 90° to the incident sound, a stronger reflected echo will be generated than if the specular reflector is oriented off-axis from 90°.

When scatter occurs, sound energy is redirected in multiple directions, resulting in weaker echoes with smaller pressure amplitudes returning to the ultrasound probe. While this interaction may seem undesired, scatter actually provides important information about the imaged tissue. Since most tissue types have different cell composition and anatomical structure, a unique scatter "pattern" is generated by how these various organs and tissue interact with ultrasound. This unique "pattern" helps to provide much of the useful diagnostic information within an ultrasound image. Differences in scatter amplitude between regions of an imaged tissue will show as different levels of brightness or echogenicity on the displayed image. Echoes with higher scatter amplitude will be hyperechoic or bright, while echoes with lower scatter amplitude will be hypoechoic or darker. The amplitude of the scattered echo will vary based upon the scatter density (or the extent of scatter per unit volume of tissue), the difference in acoustic impedance at the tissue interface, and the frequency of the ultrasound pulse.

With increases in the frequency of transmitted sound, the wavelength will decrease which will increase the acoustic scatter. With a smaller wavelength, the sound is now able to distinguish some of the small surface irregularities which were indistinguishable with the larger wavelength or smaller frequency transmission. With the tissue interface now appearing "rougher," more acoustic scatter will occur.

Large differences in acoustic impedance are reflected by changes in the speed of sound. With a change in the speed of sound, the transmitted frequency will remain constant, but the wavelength will vary in size. As just described, this change in wavelength will affect the extent of scatter. Unlike specular reflectors which lead to reflection, scatter from nonspecular reflectors are not as significantly impacted by beam direction or angle of incidence (Θ_i) of the ultrasound transducer. When scatter occurs, diffuse echoes are generated unlike the focused and directed echo of reflection.

Through the interactions of reflection, refraction, absorption, and scatter, diagnostic medical images can be generated by an ultrasound machine. A discussion of a representative image of the abdomen best describes these interactions (Fig. 12.6). In the first image, a calcified stone is observed within the gallbladder. The gallbladder is an organ along the undersurface of the gallbladder which stores bile. The calcified stone absorbs the majority of the incident ultrasound energy, resulting in posterior shadowing. The posterior wall of the gallbladder is a specular reflector, and since it is perpendicular to the ultrasound beam, reflection occurs with a bright or hyperechoic wall. The gallbladder lumen is black or anechoic, illustrating through transmission of sound with little or no reflection. The parenchyma of the surrounding liver is intermediate and mixed in echogenicity, indicative of multiple boundary interfaces resulting in scatter.

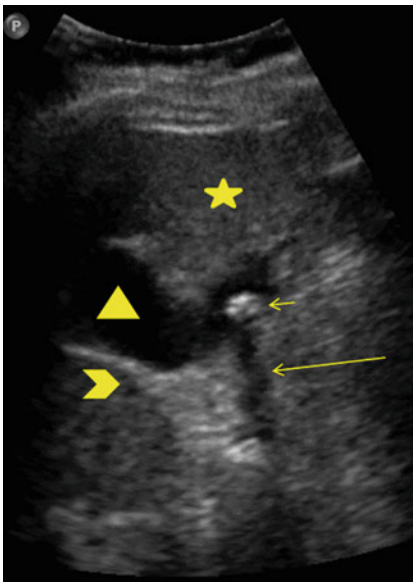

Fig. 12.6 *Acoustic interaction resulting in generation of an ultrasound image*. This is an ultrasound image of the liver and gallbladder. The *star* is in the center of the liver. Scatter of ultrasound energy occurs within the liver, leading to the generation of its unique imaging pattern. The *triangle* is in the center of the gallbladder. The gallbladder contains bile or fluid which neither leads to reflection, absorption, scatter, or reflection. As a result, the sound energy passes through the gallbladder, and its lumen appears dark or anechoic. The *short arrow* is the calcified gallstone. The calcified gallstone absorbs the incident ultrasound energy. Since it absorbs the energy, no ultrasound pulse travels behind the gallstone, resulting in the posterior acoustic shadow, the *long arrow*. The *chevron* illustrates the echogenic posterior wall of the gallbladder where reflection of ultrasound energy occurs

12.3.2.5 Attenuation

As ultrasound energy travels through tissue, the strength of the acoustic energy attenuates or weakens through scatter and absorption. The rate of attenuation of the ultrasound energy will vary depending on the tissue type. For soft tissue, the attenuation coefficient can be generally estimated as:

$$\mu(\text{soft tissue})(\text{dB}) \sim 0.5 * x * f \tag{12.10}$$

The attenuation of sound increases with both distance traveled from the ultrasound probe and increasing frequency. For soft tissue, the attenuation is near linearly proportional to frequency, while for water and bone, the attenuation changes by the frequency squared. Given this relation and when imaging a deep structure such as the pancreas within the abdomen (Fig. 12.7a), a transducer with lower frequency (3–5 MHZ) provides optimal images. When imaging a more superficial structure such as the thyroid gland within the neck (Fig. 12.7b), a higher-frequency transducer (7.5–10 MHz) is used.

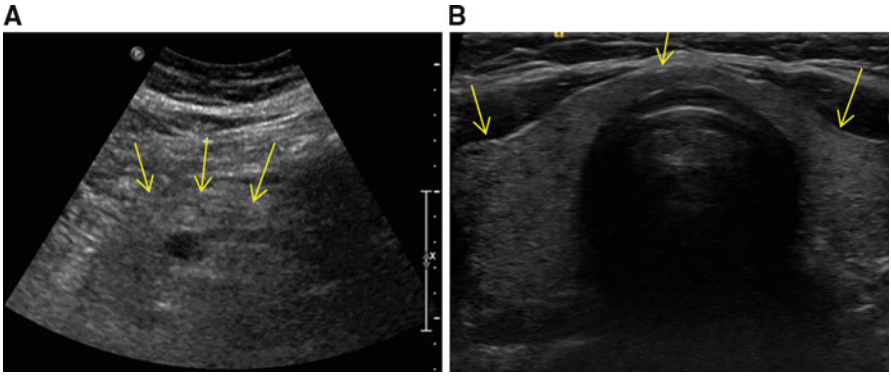

Fig. 12.7 *Ultrasound images using a low-frequency transducer and a high-frequency transducer*. (**a**) Ultrasound image of the pancreas using a 5.5 MHz curvilinear transducer. Pancreas outlined by *arrows*. (**b**) Ultrasound of the thyroid using an 11 MHz linear transducer. Thyroid outlined by *arrows*

12.4 Ultrasound Transducer

12.4.1 Transducer

Ultrasound is generated by a transducer which contains one or more crystals composed of ceramic or naturally occuring piezoelectric materials. Such an example is quartz which following exposure to an applied voltage will provide a consistent mechanical vibration of 32.768 kHz. A quartz crystal commonly provides the fundamental timing element for watches. Examples of synthetic piezoelectric materials include ceramics such as lead-zirconate-titanate (PZT) or plastic composites such as polyvinylidene difluoride (PVDF).

The piezoelectric material converts an electrical pulse from the ultrasound machine's pulse generator into acoustic energy which can be transmitted for imaging. The electrical pulse induces a change in shape of the piezoelectric material. The expansion and contraction of the piezoelectric material propagates an acoustic wave with compression and rarefaction of a pressure amplitude front. Following interaction of the transmitted pulse with tissue, the transducer will function as a receiver and will detect the returning echoes. The returning acoustic energy deforms the piezoelectric material and generates a sequence of electric signals which are transferred to the ultrasound unit to help create a medical image. An ultrasound transducer can be used in both pulsed and continuous wave mode. In medical imaging, ultrasound is primarily used in pulse wave mode.

The natural resonance frequency of the crystal (f_o) is determined by the crystal's thickness. The wavelength of the emitted sound pulse is twice the thickness of the crystal. Using Eq. (12.1):

$$f_o = c*(2*t) \tag{12.11}$$

where c is the speed of sound in PZT (4000 m/sec) and t is the crystal thickness.

12.4.1.1 The Q Factor

When a crystal is excited, ultrasound energy is generated which is directed both in front of and behind the transducer. To improve the purity of the sound pulse, a damping block is positioned along the back of the piezoelectric element. The damping block will absorb the sound energy directed backward from the piezoelectric element and dampen the transducer vibration. This process of dampening the transducer vibration is called "ring down" and results in shortening of the spatial pulse length (SPL) of the emitted sound pulse. For medical imaging, ultrasound is predominantly used in pulse echo mode. With this approach, a burst of emitted ultrasound cycles are emitted for a finite period of time. The SPL is the summated distance of the transmitted ultrasound pulse. For an ultrasound pulse with three emitted wave cycles, the SPL is equal to 3 times the wavelength (λ). The frequency of how often this string of three successive wave cycle is emitted is referred to as the pulse repetition frequency. By shortening the SPL, the axial resolution of the transmitted pulse is improved (see section on spatial resolution).

Through the process of dampening the transducer's vibration, the bandwidth of the ultrasound pulse or range of transmitted frequencies is increased. Dampening introduces frequencies both above and below the center resonance frequency. The Q factor reflects the extent of the bandwidth or frequency range originating from the transducer.

$$\mathrm{Q} = \frac{fo}{\text{bandwidth}} \tag{12.12}$$

A high Q factor reflects a narrow bandwidth with little associated damping, while a low Q factor reflects a wider bandwidth with a greater degree of associated damping. Since many imaging applications demand increased axial resolution (the ability to distinguish adjacent objects along the axis of ultrasound beam transmission), low Q transducers are frequently used with their smaller SPL. For color Doppler imaging, transducers with a high Q are needed. The smaller bandwidth helps to preserve the frequency shift information which is critical to color Doppler imaging (Fig. 12.8).

12.4.1.2 Matching Layer

In order to minimize the acoustic impedance mismatch between the transducer surface and the patient, a layer of material is positioned in front of the transducer between the soft tissue and the piezoelectric material. This material or matching layer has an acoustic impedance or Z intermediate to that of the soft tissue and the piezoelectric crystal. The thickness of the matching layer is chosen so that it is ¼ of the wavelength of the transmitted pulse as determined by the f_o.

In addition to using a matching layer, the acoustic mismatch between the transducer surface and the patient is also reduced by using ultrasound gel or jelly.

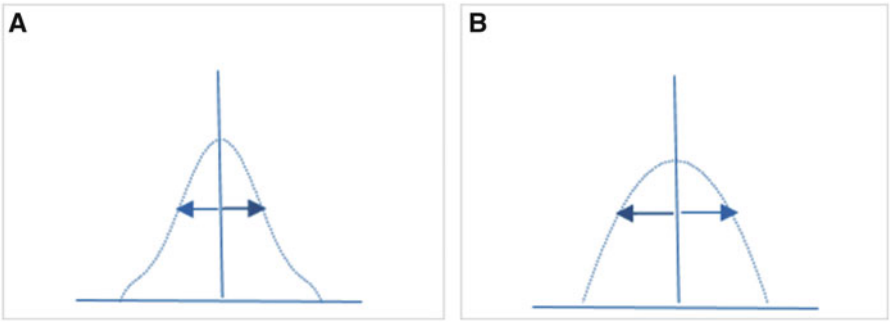

Fig. 12.8 *Q factor*. The figures below demonstrate frequency spectrum for transducers with a narrow (**a**) and a wide bandwidth (**b**). The Q factor is equal to the center frequency (f_o) divided by the bandwidth. A high Q transducer (**a**) has very little damping, while a low Q transducer (**b**) has heavier damping

The ultrasound gel also has the added benefit of helping remove air pockets between the transducer surface and the patient's skin.

12.4.2 Types of Transducers

Modern-day medical transducers consist of either linear or curvilinear arrays composed of many rectangular piezoelectric elements. Within the transducer, there may be anywhere from 128 to 512 piezoelectric elements. Based upon the activation mode of how the ultrasound pulse is generated, transducers can be divided into two different types: (1) linear array and (2) phased array.

12.4.2.1 Linear Array

Within a linear array transducer, there is simultaneous activation of a small group of piezoelectric elements. For example, if the linear array transducer consists of 512 elements, the first activated group may consist of 32 activated piezoelectric elements. While the 32 element group is transmitting, the remaining transducer elements are then utilized for echo reception. Following the transmission of the first ultrasound pulse, a second small group of piezoelectric elements, usually removed from the first group by one or two piezoelectric elements, are activated and generate a second pulse. This sequential pattern of activation then continues across the remaining transducer surface. Through the sequential transmission and reception of pulse echoes, information for generating an ultrasound image is collected.

12.4.2.2 Phased Array

In contrast to a linear array, a phased array transducer produces a single ultrasound pulse from all of the transducer piezoelectric elements. With a phased array, a time delay is introduced in the process of activating the piezoelectric elements across the face of the transducer. Through the introduction of this time delay, the ultrasound pulse can be steered without moving the transducer at all. When the phased array listens for the returning echoes, all of the transducer elements are recruited, and the aggregate information from all of these elements is used to generate an image.

12.5 Ultrasound Beam Properties

For a single piezoelectric element, the transmitted ultrasound beam focuses upon a single point or focal point. The focal point occurs at a focal distance from the transducer surface and signifies where the sound energy converges. The distance preceding this point is referred to as the near field or Fresnel zone. The distance beyond this point is referred to as the far field or Fraunhofer zone. The majority of medical ultrasound imaging occurs within the near field. Within the far field, the ultrasound beam diverges and the intensity of the sound quickly attenuates.

12.5.1 The Near Field

The ultrasound energy within the near field converges toward the focal point. This property of beam convergence is the result of the constructive and destructive interactions between adjacent sound waves that occur just after the sound has been emitted from the transducer surface. The aggregate ultrasound beam converges at the focal distance which signifies the end of the near field (Fig. 12.9). At this point, the beam diameter is approximately half of the diameter of the transducer. The near-field length or focal distance depends upon the transducer diameter (d) and the wavelength of sound (λ) within the transmission medium:

$$\text{Focal Distance} = \frac{d^2}{4^*\lambda} \tag{12.13}$$

With an increase in the transducer diameter and/or an increase in the transmission frequency, the near-field distance will increase. As an example, with a 7.5 mm piezoelectric element, the near field at a transmission of 5 MHz is 4.6 cm, while the near field at a transmission of 7.5 MHz is 6.8 cm.

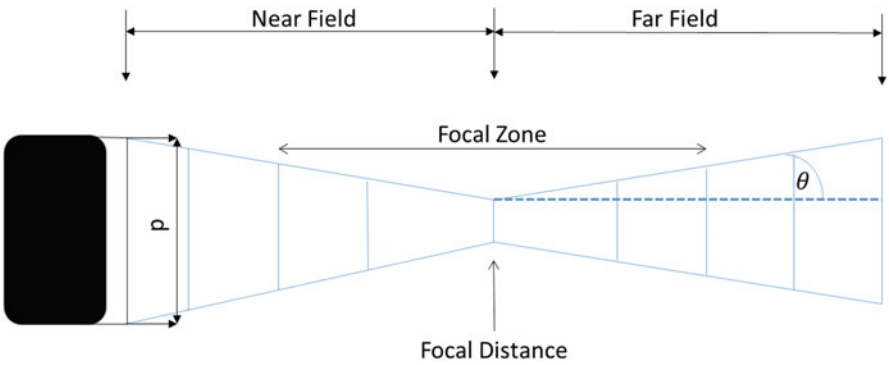

Fig. 12.9 *Near field and far field*. For a single element transducer, the ultrasound beam demonstrates a unique pattern with both a region of convergence, the near field, and a region of divergence, the far field. The length of the far field and the angle of divergence of the far field (Θ) vary with changes in the width of the piezoelectric element (d) and the λ of the transmitted pulse

12.5.2 The Far Field

The far field or Fraunhofer zone occurs beyond the outer limits of the near field and outlines where the ultrasound beam begins to diverge or widen (Fig. 12.9). The far field highlights where the ultrasound beam begins to rapidly attenuate or weaken in strength or signal intensity. The rate at which the beam diverges is determined by the angle of ultrasound beam divergence (Θ_{div}) where:

$$\text{Sin}\,(\Theta_{div}) = 1.22^{*}\frac{\lambda}{d} \tag{12.14}$$

The rate of beam divergence increases with a decrease in frequency and/or a decrease in the diameter of the emitting transducer. For example, with a 7.5 mm piezoelectric element and a transmission frequency of 5 MHz (or λ equal to 0.308 mm), the angle of ultrasound beam divergence equals 2.87°, while with a frequency of transmission of 7.5 MHz, the angle of ultrasound beam divergence equals 1.91°.

12.5.3 Ultrasound Beam Formation and Focusing

Optimal medical imaging occurs within the focal zone (Fig. 12.9). The focal zone comprises the distal end of the near field and the proximal end of the far field. The focal zone is defined as the distance over which the width of the transmitted ultrasound beam is no greater than two times the width of the ultrasound beam at the focal distance. Since the best medical images will occur within the focal zone, this fact impacts the type of transducer that the technologist will choose.

Clinically, the most frequently used transducers are linear array or phased array transducers rather than single element transducers. The above discussion of ultrasound beam properties focused upon a single element transducer. How do these properties change with multi-array transducers?

For a linear array transducer, groups of piezoelectric elements are sequentially activated across the face of the transducer. When determining the near field, the transducer diameter is equivalent to the width of the simultaneously activated group of piezoelectric elements.

For a phased array transducer, the piezoelectric elements are near simultaneously activated across the face of the transducer but with the introduction of a small time delay from one piezoelectric element to the next. By varying this small time delay and the location of the initial piezoelectric element activation, the ultrasound beam can be modified to converge at selectable focal distances. In abdominal imaging, you may be interested in focusing the transducer upon a more shallow structure. For example, the patient may have a mass in the liver along the outer surface. In such a situation, you are interested in a smaller focal distance (Fig. 12.10). In the same patient after you have finished imaging the liver, the technologist will then want to evaluate structures deeper within the abdomen such as the inferior vena cava or pancreas, and a larger focal distance will be needed (Fig. 12.10). When first imaging the outer surface of the liver, a shorter focal distance will be chosen by first activating the piezoelectric elements at the periphery of the transducer followed by sequential activation of the remaining piezoelectric elements as we progress toward the center of the probe. When imaging the pancreas, the focal distance can be increased by decreasing the delay time between sequential activation of individual piezoelectric elements. By reducing the delay time, this change causes the aggregate ultrasound beam to converge at a greater depth.

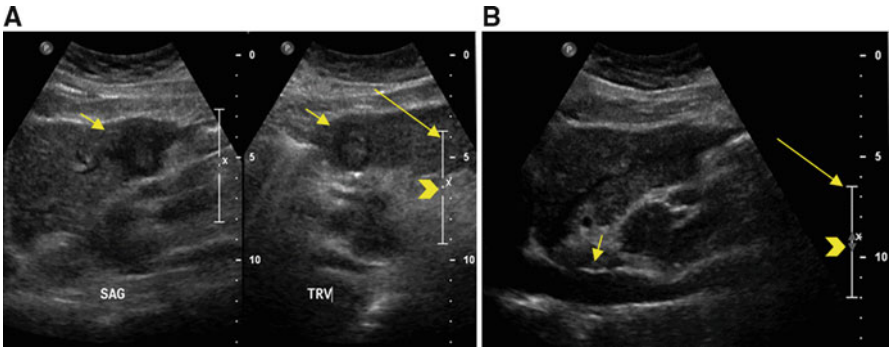

Fig. 12.10 *Different focal distances using a phased array transducer to image the abdomen.* For a phased array transducer, these two images demonstrate the ability to vary the depth of the focal zone and focal distance. (**a**) This is an image of a mass (*small arrow*) within the periphery of the left lateral segment of the liver. The *large arrow* highlights the focal zone, while the chevron illustrates the focal distance. (**b**) This is an image of the inferior vena cava (*small arrow*), the large vein located deep within the abdomen, just above the spine. Notice the positioning of the focal zone (*large arrow*) and focal distance (*chevron*) at a greater depth of penetration

When creating the displayed medical image, all of the piezoelectric elements within the array transducer will receive information from returning echoes. This information will be summed together to generate the image displayed on the monitor. The echo signal received by the piezoelectric elements along the periphery of the transducer will have traveled a greater distance than the elements in the center of the transducer. Just as the ultrasound beam converges toward the focal distance, the returning echoes must diverge out to the periphery of the transducer (Fig. 12.9). Since the received echoes from the outer piezoelectric elements will have traveled a greater distance, their signal will be delayed in time with respect to the reception of the received signals from the elements toward the center of the transducer. To align the timing of the signals, electronic delays are introduced to the earlier received signal before their information is added to the signals from the later received echoes. This process is called dynamic receive focusing.

12.5.4 Ultrasound Spatial Resolution

The spatial resolution of ultrasound imaging is described in three different dimensions: axial, lateral, and elevational. Each of these dimensions helps to detail the volume of the acoustic pulse. The smaller the volume of the emitted acoustic pulse augments the ability of the ultrasound pulse to distinguish between two adjacent objects (Fig. 12.1b and discussion of imaging resolution).

12.5.4.1 Axial Resolution

Axial resolution reflects how well ultrasound imaging can distinguish between two objects which are next to each other and are in line with the direction of the emitted ultrasound beam. In order to achieve good axial resolution, the returning echoes cannot overlap and must maintain distinction from the trailing echo. In order to avoid overlap, two imaged objects must be separated from each other by a distance greater than or equal to one-half of the spatial pulse length (SPL). As discussed earlier, the SPL is the summated distance of the transmitted ultrasound pulse. If objects are closer than ½ SPL, the returning echoes will overlap, and the adjacent objects cannot be resolved.

For example, if a 3.5 MHz transducer is being used, the wavelength of the pulse is equal to 0.51 mm. For an ultrasound pulse with 3 cycles, the SPL is equal to 1.53 mm. In order to distinguish two adjacent objects along the direction of the ultrasound beam, they have to be separated by greater than ½ SPL or 0.765 mm. For this example, the axial resolution is equal to 0.765 mm (Fig. 12.11). If the distance separating the two objects is less than 0.765 mm, overlap or volume averaging of the two objects will occur. This concept of volume averaging is further discussed in the slice thickness artifact section (Fig. 12.23).

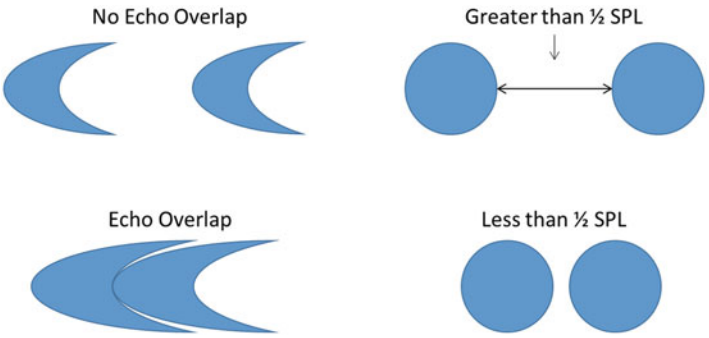

Fig. 12.11 *Axial resolution*. In order to distinguish two adjacent objects along the axial plane of the ultrasound pulse, the distance separating the two objects must exceed ½ of the spatial pulse length (SPL). If the distance does not exceed ½ of the SPL, the returning echoes will overlap, and the two objects will be volume averaged into one structure on the displayed image

12.5.4.2 Lateral Resolution

Lateral resolution reflects the ability of ultrasound to distinguish between two adjacent objects which are at a 90° angle to the direction of the ultrasound beam. The lateral resolution is reflected by the diameter of the ultrasound beam. As the diameter of the ultrasound beam decreases, the lateral resolution improves. As discussed earlier, the beam diameter will vary with distance from the transducer. The best lateral resolution is achieved within the focal zone. The ideal point of imaging occurs at the focal distance where the ultrasound beam is the narrowest. Beyond the outer limit of the focal zone, the beam will continue to diverge, and the lateral resolution will quickly deteriorate (Fig. 12.12). The typical lateral resolution is between 2 and 5 mm.

Phased array transducers help to optimize lateral resolution. Phased array transducers can vary the focal distance of the transmitted ultrasound pulse by altering the timing delay of piezoelectric element activation. By being able to change the focal distance and emit several different ultrasound pulses, the lateral resolution can be preserved even with increasing distance from the transducer. This objective is accomplished by transmitting successive pulse echoes with an overlap of focal zones with increasing depth into the tissue. This approach effectively increases the length of the focal zone and avoids the rapid decay of the lateral resolution. Since this method requires multiple pulse echo sequences to be transmitted along a single beam line, the frame rate or amount of time needed to create an image increases.

12.5.4.3 Elevational Resolution

Elevational resolution reflects the ability of the ultrasound beam to distinguish two adjacent objects which are perpendicular to the imaging plane (Fig. 12.12). Elevational resolution varies based upon the height of the transducer element. As the height of the transducer element decreases, the elevational resolution improves.

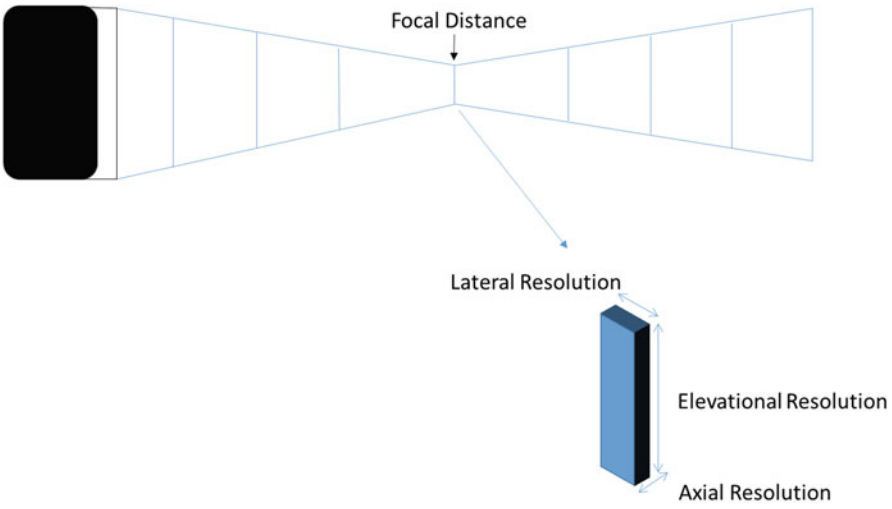

Fig. 12.12 *Lateral resolution and imaging volume*. The lateral resolution reflects the ability to distinguish two adjacent objects which are within the imaging plane but at a 90° angle to the direction of the propagating ultrasound pulse. Lateral resolution improves as the width of the ultrasound beam decreases. The optimal lateral resolution occurs at the focal distance where the beam width is the narrowest. At the focal distance, an imaging volume is detailed. The three dimensions of spatial resolution (*axial*, *lateral*, *and elevational*) are illustrated

Elevational resolution is also referred to as the slice thickness. As the slice thickness increases, objects that are contained within that imaging volume are averaged across the imaging plane. Since the object's echo is averaged over a larger volume, the object's outline will lose some of its distinction or resolvability. This concept of volume averaging is further discussed in the slice thickness artifact section (Fig. 12.23).

12.6 Ultrasound Image Acquisition

Ultrasound images are acquired by emitting a train of short pulses with a duration of less than 1 μs. In between pulses, the transducer listens for the echoes. This method is called pulse echo. The longer the amount of time that it takes an echo to return to the transducer, then the more attenuated the signal amplitude becomes. The extent of attenuation provides information regarding the depth of the imaged object. To improve image quality and uniformity, the signal of the returning echo can be amplified using time gain compensation (TGC). TGC is a dynamic adjustment that will vary the signal gain for echoes that take longer to return to the transducer. This process will compensate for the attenuation that occurs with greater depth.

For example, a greater degree of TGC will be applied to echoes returning from the inferior vena cava than echoes returning from the capsular surface of the liver (Kremkau 1993).

12.6.1 Types of Echo Display

The returning echo to the transducer can be displayed in one of three different ways: A-mode, B-mode, and M-mode.

12.6.1.1 A-Mode

A-mode represented the first type of ultrasound display and stands for amplitude mode. Echo amplitude was displayed on the vertical axis, while echo return time was displayed on the horizontal axis. As described earlier, echo return time is an indication of depth or distance of a tissue interface from the transducer. One A-line of data was generated for each pulse repetition period. Initially, A-mode was used to evaluate midline displacement of the brain in patients suffering from a brain tumor. Today, A-mode can be used by ophthalmologists (eye doctors) for precise measurements of the eye.

12.6.1.2 B-Mode

B-mode displays a grayscale image of a tissue section and stands for brightness mode. The greater the intensity of the returning echo, then the greater the displayed signal brightness or level of echogenicity. The returned echoes are displayed as a function of depth from the transducer and position across the sector scan of the emitted ultrasound beam. Essentially, one 2D B-mode image is generated by a number of A-lines spanning across the transducer's field of view. Using a multielement phased array transducer, real-time imaging can be performed with 15–40 frames (grayscale static images) being displayed per second. The frame rate or number of static images displayed per second inversely relates to the number of A-lines used to compose the frame (N) and the depth of tissue (D) from where the echoes are returning. When the amount of data (N) used to compose the static image increases or the depth of ultrasound penetration (D) lengthens, the frame rate will decrease. For example, if the density of scan lines (scan lines per centimeter) is increased in order to provide enhanced axial resolution, the frame rate will decrease. Also, if a deeper anatomical structure such as the inferior vena cava (the large vein that lies next to the spine) is imaged, the frame rate will also drop.

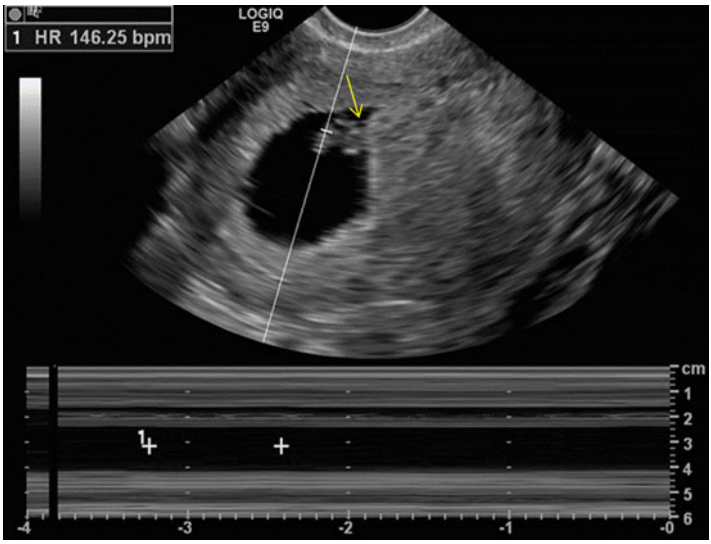

Fig. 12.13 *M-mode image*: This is an M-mode image focused on a single tissue interface of the beating heart of a fetus with an estimated gestational age of 6 weeks. Note the M-mode display on the bottom of the grayscale image. Also note how the point of interrogation is fixed on one point (*arrow*)

12.6.1.3 M-Mode

This technique stands for motion mode. This imaging approach uses the signal from B-mode imaging to describe the echoes of a moving structure such as the heart with the transducer oriented on a fixed position or tissue interface within the patient. M-mode displays depth on the vertical axis and time on the horizontal axis. By displaying successive ultrasound pulses next to each other, the change in the position of a single tissue interface can be monitored, and M-mode can be used to illustrate time-dependent motion. This display technique can be used to focus on the tissue interface of a beating heart and to help estimate the heart rate of a 6-week live fetus (Fig. 12.13). M-mode can only focus on the motion of a single tissue interface or line through the patient. Given this limitation and advancements in two-dimensional echocardiography, this technique has been largely replaced by color Doppler imaging.

12.6.2 Components of an Ultrasound Machine

For the pulse echo method of ultrasound image acquisition, several hardware components are needed within the ultrasound machine including: a beam former, a pulser, a receiver, a scan converter, and a video display.

12.6.2.1 Beam Former

The beam former performs the previously discussed process of dynamic receive focusing (see section on *ultrasound beam formation and focusing*). The beam former applies electronic delays to help align the phases of the echoes returning to the many individual elements of an array transducer. The realigned signals from all the transducer elements are then summated, creating an output signal which represents the acoustic information from a pulsed ultrasound beam.

12.6.2.2 Pulser

The pulser generates the electric voltage which is applied to the piezoelectric elements within the transducer and produces the acoustic signal.

12.6.2.3 Receiver

The receiver accepts signal information from the beam former and performs post-processing such as TGC and filtering of noise and clutter.

12.6.2.4 Scan Converter

Scan converter is a device within the ultrasound machine that takes the signal information from the returning echo and translates it into a data format which can be displayed as a 2D image. The data format from scan acquisition and scan display are very different, and the scan converter is a critical hardware piece for a functional ultrasound machine to display a medical image that can be read by a clinician. Initially, scan converters were analog devices that used storage cathode ray tubes to consolidate image data. Modern-day scan converters use digital methods for data processing and storage.

Image data is stored into a 512×512 matrix of pixel elements where each pixel corresponds to a rectangular coordinate on the image display. During image acquisition, the returning echo is processed by the scan converter, generating a digital signal. This digital information is assigned to a pixel within the image data matrix based upon the orientation of the transducer beam and the time needed for the echo to return to the transducer (echo delay time). For a grayscale ultrasound image, one displayed image frame requires 0.25 MB of memory storage. The amount of memory storage is equivalent to the image data matrix size (512×512) times the number of bytes per grayscale pixel which is equal to one. One byte is equivalent to 8 bits where each pixel can display up to 256 or 2^8 different grayscale levels. For color Doppler images, 3 bytes of storage are needed per color scale pixel.

12.6.2.5 Video Display

Once the digital information is acquired and assigned to a memory location, the digital to analog converter converts the matrix of digital data into an analog signal which can be displayed on a video monitor. In addition to the grayscale information from a 2D B-mode image, the video display can show information acquired from M-mode and Doppler ultrasound.

12.7 Doppler Ultrasound

Up to this point, discussion has focused upon the generation of grayscale ultrasound imaging. These grayscale images are composed from pressure amplitude information regarding returning echoes which have either been reflected or scattered. Additional imaging information can also be found in the frequency variation of the returning echoes. This detection of a change in echo frequency serves as the basis for Doppler ultrasound imaging.

Frequency shift occurs when incident sound energy reflects off a moving object. If the object is moving away from the source of sound, the returning echo travels at a lower frequency than the initial incident sound, while if the object is moving toward the source of sound, the returning echoes travel at a higher frequency than the initial incident sound. The Doppler frequency shift (F_d) is defined as the difference in frequency between the initial incident sound (F_t) and the returning echo (F_r).

$$F_d = F_t - F_r \tag{12.15}$$

A practical application of this effect is noticed when an ambulance travels by you. As the ambulance approaches a stationary listener, the emitted siren noise demonstrates an even higher frequency (or higher audible pitch) as the emitted sound undergoes a Doppler frequency shift from the forward motion of the ambulance. Similarly, as the ambulance moves away from the stationary listener, the audible sound heard by the listener exhibits a lower frequency (or attenuated audible pitch) from the sound emitted by the siren. The frequency shift (F_d) is defined by the following equation:

$$F_d = 2 * F_t * \left(\frac{V}{c}\right) * \cos(\theta) \tag{12.16}$$

c is the speed of the transmitted sound, and V is the speed of the moving object. θ is the angle between the transmitted sound and the direction of blood flow or moving red blood cells (Fig. 12.14). On an ultrasound image, θ is measured by adding the angle indicator line (Fig. 12.15). If the transducer is perpendicular to blood flow, no frequency shift can be detected since the cos (90°) is equal to zero. Optimal imaging

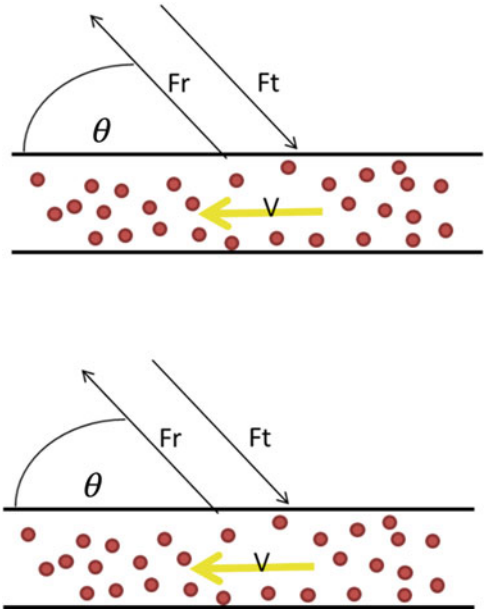

Fig. 12.14 *Doppler ultrasound: Doppler frequency shift.* Incident sound energy is transmitted as F_t. This energy is then reflected and scattered off of moving red blood cells with echoes (F_r) returning to the ultrasound transducer. Θ is the angle between the incident sound energy and the direction of the flowing red blood cells. V is the velocity of a red blood cell

is performed with the transducer as close as parallel to the vessel of interest so that the cos (θ) is maximized. As demonstrated by Eq. (12.16), velocity (V) is directly proportional to frequency shift. For Doppler ultrasound imaging, the moving object is usually a red blood cell in either a vein or artery. When the sound hits the moving red blood cell, the incident energy is both reflected and scattered. When the transducer detects the returning echo, the change in frequency can be used to measure the velocity of the blood. In addition, detailed color maps can be generated which outline the anatomy of the vasculature tree and potentially highlight such disease processes as atherosclerotic disease or plaque formation along the vessel wall.

We have introduced two different concepts in this discussion, blood flow and blood velocity. Blood velocity measures the rate that a particle of interest, i.e., a red blood cell, travels per unit time. Blood velocity is measured in cm/sec. Blood flow measures the volume of blood that travels per unit time and is measured in cm^3/sec.

Under conditions of fully developed, steady-state flow, the blood flow is related to the mean velocity by the following equation:

$$\text{Flow} = V * A \tag{12.17}$$

where V is the mean velocity and A is the cross-sectional area of the vessel.

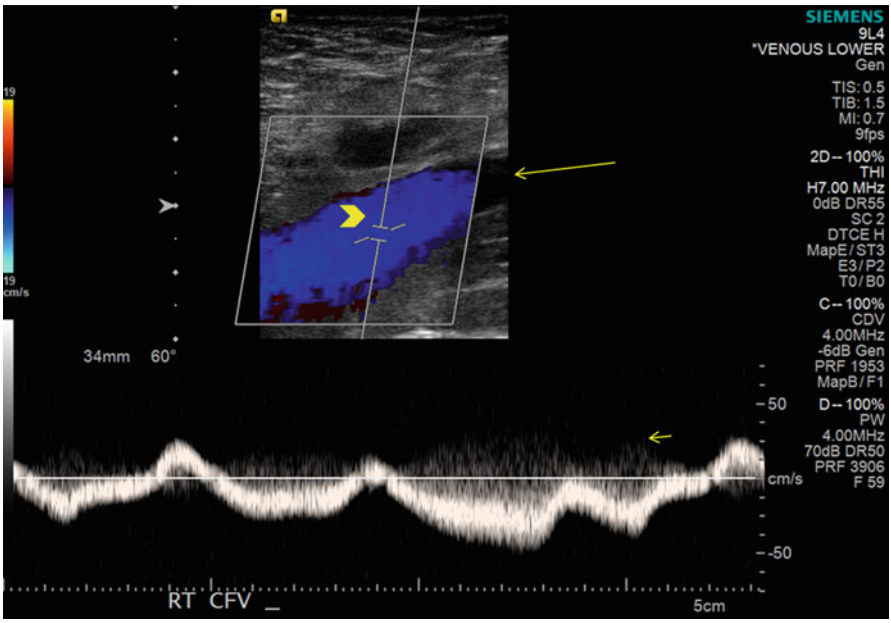

Fig. 12.15 *Duplex Doppler ultrasound:* The center box (*large arrow*) displays the grayscale image. The trapezoid represents the Doppler sample volume. The angle indicator line (*chevron*) provides a quantitative measurement of Θ or the Doppler angle. The velocity of the blood as a function of time is displayed by the graph on the bottom of the image (*small arrow*). The *blue color* within the vessel and the velocity below the zero line highlights flow away from the transducer

Pulsed Doppler imaging can evaluate both velocity and range (or the distance from where the moving object originates). The transducer obtains information from a specific location of interest or the Doppler sample volume. The size of the Doppler sample volume can be changed by adjusting the amount of time that the transducer receives or listens for returning echoes. By first imaging with grayscale ultrasound imaging, the vessels of interest can be visualized, and the Doppler sample volume can be positioned within the lumen of the vessel which will be evaluated. Duplex scanning is defined as this combined use of both grayscale and pulsed Doppler imaging (Fig. 12.15). The velocity is represented on the vertical scale, while time is indicated on the horizontal scale. When flow is toward the transducer, this results in a positive frequency shift and a positive magnitude velocity value, while the opposite relation holds true for flow away from the transducer. Generally, flow toward the ultrasound transducer is color-coded as red, while flow away from the transducer is color-coded as blue (Fig. 12.15).

Aliasing represents the most significant artifact associated with Doppler ultrasound imaging. According to the Nyquist criteria, the sampling rate must exceed twice the highest frequency component of the sampled signal. Practically, this means that the rate at which the ultrasound transducer evaluates the Doppler frequency shift must exceed twice the magnitude of the frequency shift. If the

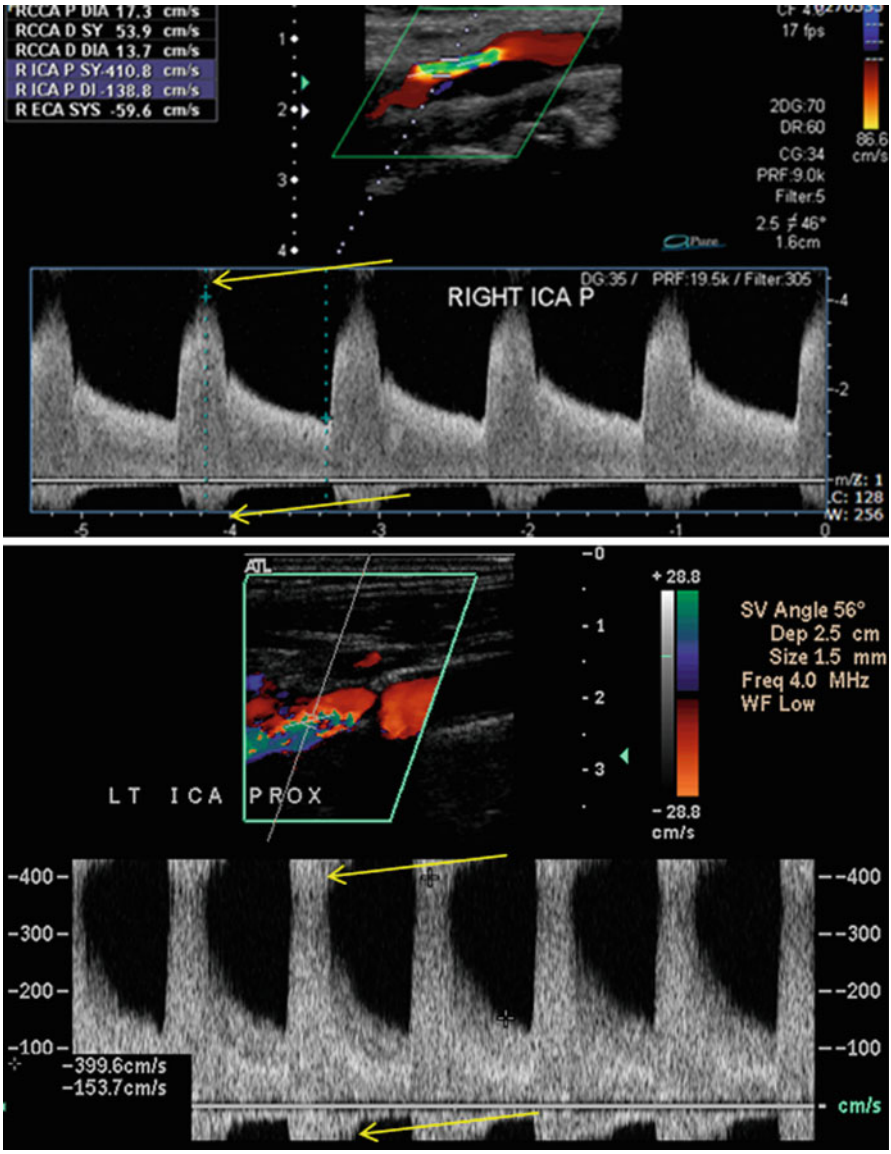

Fig. 12.16 *Aliasing*. When the Nyquist criteria are not satisfied, undersampling occurs which results in aliasing. With aliasing, the high-frequency components are wrapped around from the negative end of the scale to the positive end of the scale (*long arrows*)

Nyquist criteria are not satisfied, undersampling occurs which results in the artifact of aliasing. When aliasing occurs, the high-frequency components are wrapped around from the positive end of the scale to the negative end of the scale (Fig. 12.16). Aliasing can be addressed in several ways. The most easily executed method is to increase the sampling rate or the pulse repetition frequency (PRF).

The PRF reflects how many packets of successive sound cycles are emitted per second (also discussed in the Q factor section). For example, in pulse echo mode, three successive cycles of sound (or a packet) are sent out at 3000 times per second for a PRF of 3KHz. The PRF is not to be confused with the inherent frequency of 1 cycle of generated sound which composes one of the 3 cycles of the packet or sonic pulse. For example, in abdominal imaging, the inherent frequency of 1 cycle is generated by a 3.5 MHz phased array transducer. Generally speaking, the PRF will be measured in kHz, while the frequency of the sound wave is measured in MHz.

Returning to the subject of aliasing, increasing the PRF can eliminate this artifact. If the frequency shift (F_d) is 1.5 kHz, then the PRF must satisfy the Nyquist criteria and be greater than 3 kHz or greater than two times the frequency shift. Practically, an increase in the PRF increases the scale of the Doppler display and allows for a display of higher velocity values. Other methods of decreasing aliasing involve decreasing the extent of the frequency shift such as by making the value of cos (θ) smaller by increasing the Doppler angle. Lastly, aliasing can be reduced by using a lower-frequency probe or decreasing the frequency of the sound waves which compose the sound packet or sonic pulse (Bude and Rubin 1996; Rubin 1994).

12.7.1 Color Doppler

Color Doppler provides an excellent means to evaluate vessel anatomy, vessel patency, flow direction within the vessels, and magnitude of velocity. Color Doppler displays real-time color Doppler data which is superimposed upon a grayscale ultrasound image. The grayscale image provides information regarding the vessel morphology. Velocity is represented by color data where a higher velocity (greater frequency shift) is indicated by a lighter color, while a lower velocity (smaller frequency shift) is displayed with a darker color. The direction of the flow is reflected by red hues which signify flow toward the transducer and blue hues which indicate flow away from the transducer. Color Doppler provides useful information regarding small structures that may be difficult to evaluate with pulsed Doppler. For example, small vessels such as the pampiniform plexus in the scrotum can be evaluated for vessel patency. Additionally, color Doppler is very useful for demonstrating the vascularity of a mass such as a thyroid nodule (Fig. 12.17).

12.7.2 Power Doppler

Power Doppler displays patency or flow within a vessel but without quantitative information related to velocity or flow direction. Power Doppler detects the frequency shift but does not preserve the information that allows for a measurement of

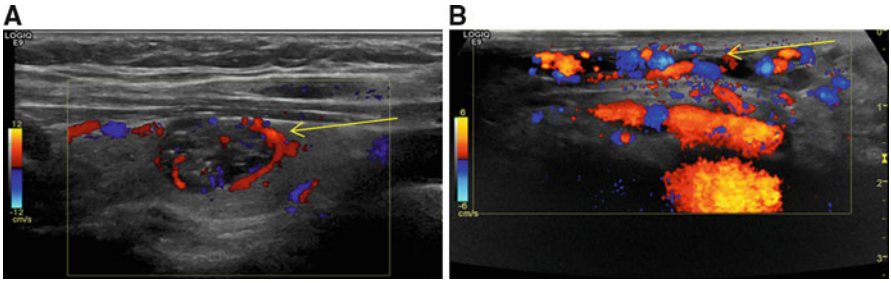

Fig. 12.17 *Doppler imaging*. (**a**) Color Doppler imaging demonstrates flow (*arrow*) within a solid thyroid nodule. (**b**) Color Doppler imaging demonstrates flow (*arrow*) within the pampiniform plexus of the male spermatic cord

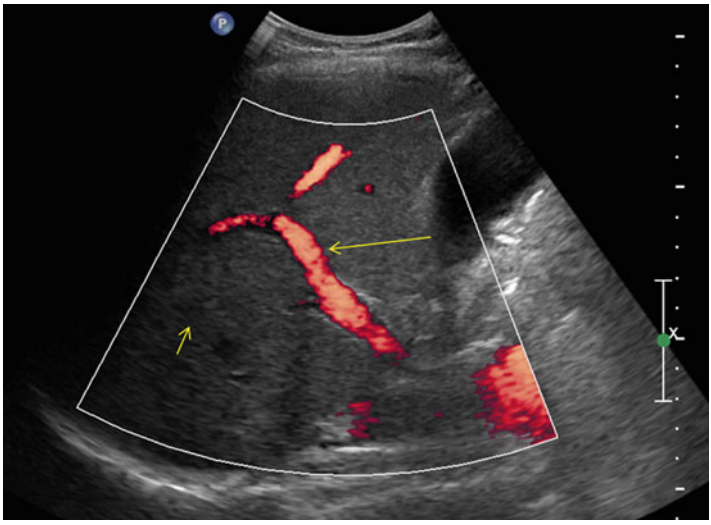

Fig. 12.18 *Power Doppler*. The power Doppler image displays patent flow within the portal vein (*long arrow*) of the liver (*short arrow*). No quantitative information is provided in regard to the direction of flow or the magnitude of the velocity

velocity magnitude or phase. Instead, power Doppler imaging measures only the strength of the returned Doppler signal. Since power Doppler does not preserve the frequency information, the Doppler angle is not as critical a component as with pulsed Doppler, and flow traveling near perpendicular to the transmitted sound can be detected. Power Doppler has the advantage of being slightly more sensitive to blood flow detection. This feature allows for its application in detecting slow blood flow within small vessels. Since power Doppler discards the frequency shift information, aliasing artifacts do not occur. Practically, power Doppler is only utilized when color Doppler fails to demonstrate flow patency. Since velocity and phase information is lost, power Doppler can only highlight whether flow is present or absent (Fig. 12.18).

12.7.3 Ultrasound Artifacts

With all of medical imaging, misrepresentations of imaged structures or artifacts provide an inaccurate description of the imaged area. While artifacts can impair the image quality, sometimes they are used to help characterize the tissue of interest and provide additional information about its internal composition. Some of these artifacts have been described previously, and this section will help complete the discussion.

12.7.3.1 Mirror Images

Mirror images occur where there is near-complete reflection of the incident ultrasound signal. This occurs frequently at an air-soft tissue interface such as the base of the lungs. In the right upper quadrant, the air-soft tissue interface with the right hemidiaphragm can produce mirror images of the liver and/or masses within the liver (Fig. 12.19).

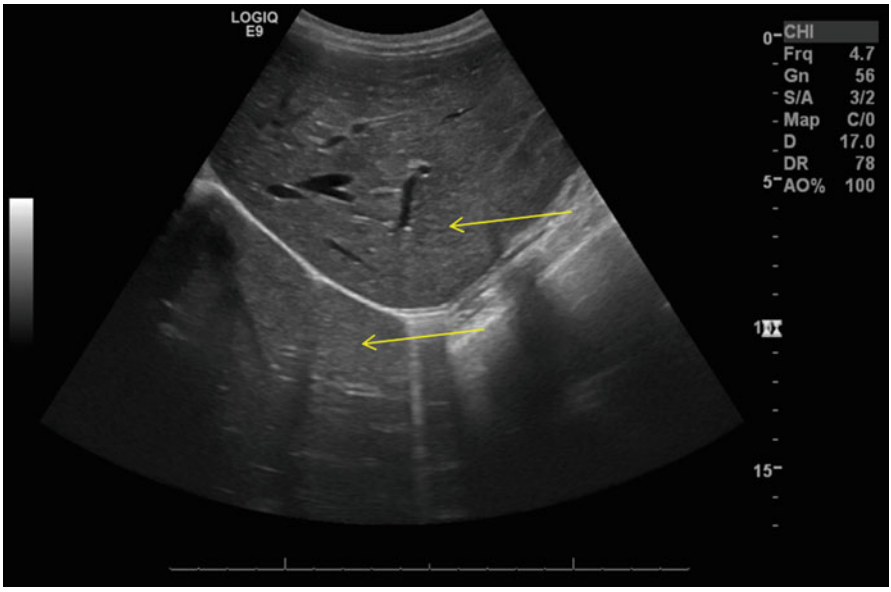

Fig. 12.19 *Mirror image artifact*. This artifact occurs at a tissue interface where complete reflection occurs. An example would be an air-soft tissue interface such as the hemidiaphragm which separates the lungs (air containing) from the abdomen (soft tissue containing). At this interface, a mirror image of the liver (two *long arrows*) is created

12.7.3.2 Reverberation

Reverberation occurs from multiple reflections of the same ultrasound pulse at an acoustic interface. This interaction occurs when the ultrasound beam is reflected at an acoustic interface which is positioned within the near field of the ultrasound beam. The returning echo is then reflected off the transducer, resulting in a second interaction and potentially additional cascading interactions with the same interface. This process can generate multiple reflections or reverberations. How does the reverberation artifact affect the displayed image? The reverberation can give the appearance that the acoustic interface is more deeply positioned within the tissue. This artifact is best seen when imaging a fluid contained structure such as the bladder. The reverberation can lead to low-level internal echoes within the bladder that should otherwise appear black or anechoic (Fig. 12.20). The low-level echoes within the bladder result from the reverberations generated by the overlying soft tissue superficial to the bladder being displaced into the anechoic center of the bladder. Generally, the reverberation artifacts are not visible for they are superimposed onto a background signal of soft tissue; and therefore, they cannot be seen.

Ring down or comet tail artifacts are also a type of reverberation artifact. These artifacts occur when the incident ultrasound pulse interacts either with gas, cholesterol crystals, or metal. The incident ultrasound energy bounces off the highly reflective interface of the metal, crystal, or gas only to be immediately reflected again by another highly reflective interface caused by an adjacent focus of gas,

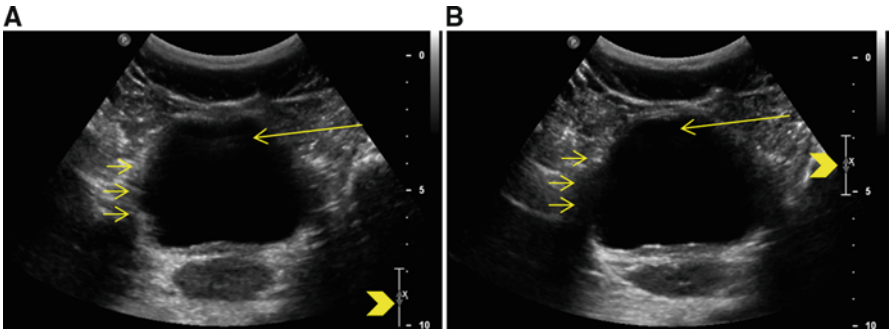

Fig. 12.20 *Reverberation artifact*. In image (**a**), there are low-level echoes (*long arrow*) within the superior aspect of the bladder (outlined by *short arrows*). These echoes are evident when the bladder is imaged well within the near field. Note the position of the focal zone in the lower left corner of the image (*chevron*). How do these reverberation artifacts arise? The incident sound initially reflects off the soft tissue/bladder interface. This echo can then reflect off the transducer probe only to be reflected again by the same soft tissue/bladder interface, creating a cascade of echoes (reverberation artifacts) which appear to originate deep to the original bladder/soft tissue interface. Normally, these echoes are lost within the background of the soft tissue, but they become more conspicuous when imaging an anechoic structure such as the bladder within the near field. In image (**b**), the focal zone is repositioned so that the bladder is positioned within the center of the focal zone, and the reverberation artifacts disappear

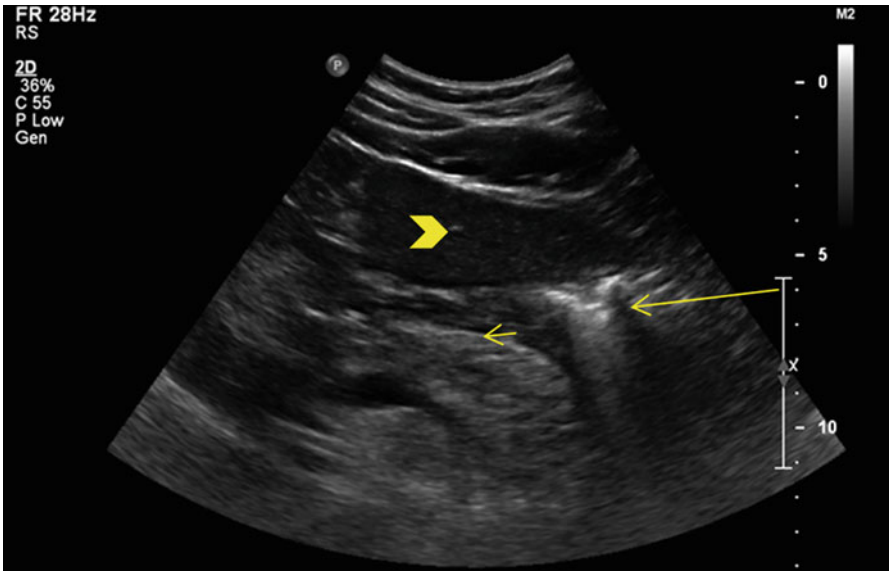

Fig. 12.21 *Ring down artifact*. Ring down artifact (*long arrow*) originating from a gas filled loop of small bowel is demonstrated along the undersurface of the liver (*chevron*). The pancreas is also visible within this image (*small arrow*)

crystal, or metal. Since these reflective interactions occur within such a small area, the returning echo is perceived by the transducer as representing a singular echo. With each reflective interaction, the echo amplitude decreases, and the echo will resemble a "comet tail" with weakening signal strength as distance from the ultrasound transducer increases. Overall, these interactions will give the appearance of multiple bright echoes originating deep to the original site of reflection with the gas, metal, or crystal (Fig. 12.21).

12.7.3.3 Side Lobes and Grating Lobes

When the piezoelectric element is exposed to a voltage, a sound beam is generated in the general direction of crystal distortion. A small amount of crystal distortion occurs orthogonal or radial to this central axis and generates weak side lobes of ultrasound energy which radiate off-axis from the central sound beam. If these weak side lobes interact with a reflector, they can produce an echo artifact. When imaging soft tissue, these side lobes are frequently concealed by the background scatter signal, but when imaging an anechoic fluid-filled structure such as a cyst or the gallbladder, they can become more conspicuous (Fig. 12.22). This side lobe artifact can simulate the appearance of sludge (or pseudosludge) within a homogeneously echo-free organ.

Grating lobe artifacts arise from multielement array transducers and are emitted at large angles to the transducer surface. This artifact is created by the composition

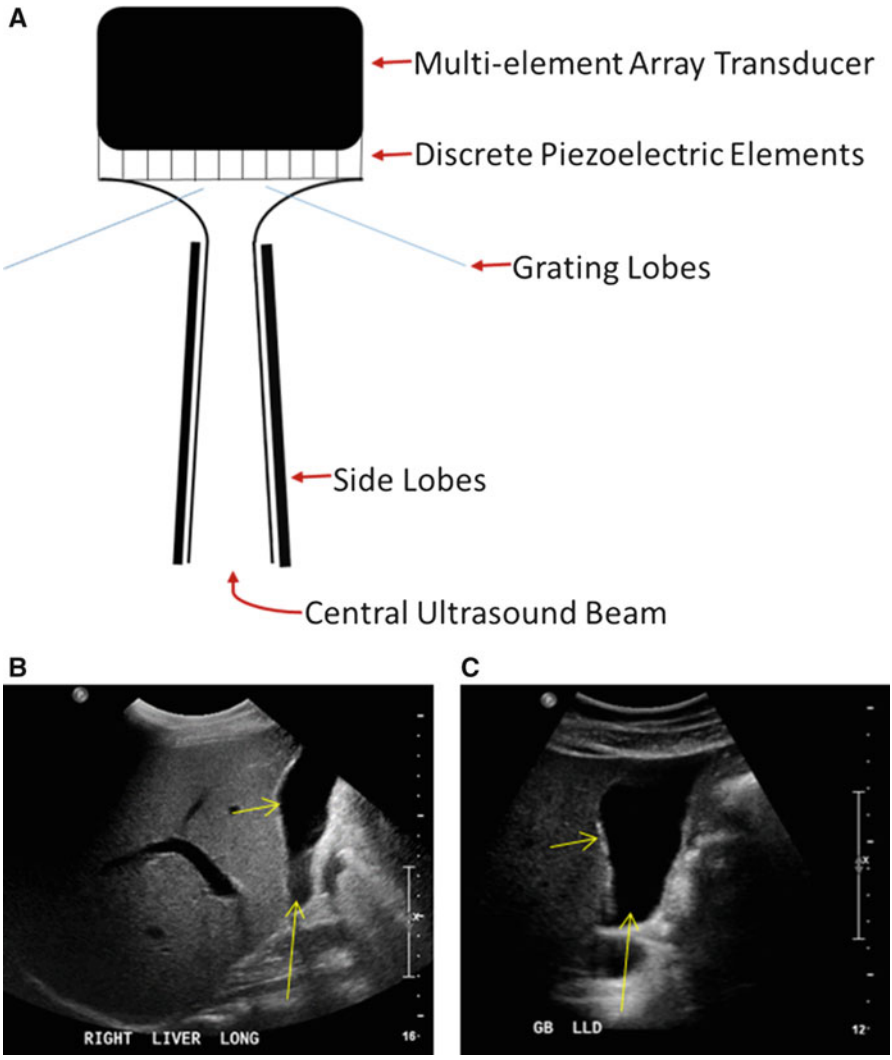

Fig. 12.22 *Side lobe and grating lobe artifacts.* (**a**) This schematic demonstrates where the side lobe echoes and grating lobe echoes are generated with respect to the ultrasound beam and the multielement transducer. The side lobe echoes radiate off-axis from the ultrasound beam, while the grating lobe echoes are generated at large angles to the transducer surface. (**b**) This grayscale image details the gallbladder (*small arrow*) within the periphery of the ultrasound image volume. The image suggests that there is layered echogenicity (*large arrow*) within the gallbladder, otherwise called sludge. (**c**) This dedicated image displays the gallbladder (*small arrow*) within the center of the ultrasound imaging volume. This dedicated image of the gallbladder illustrates that there is in fact no sludge (*arrow*) within its lumen, and the appearance of sludge within image B was attributable to a side lobe artifact or so-called pseudosludge

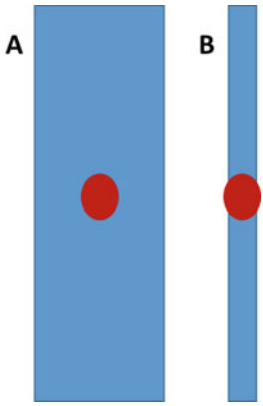

Fig. 12.23 *Partial volume averaging*. (**a**) Slice thickness greater than the imaged object results in averaging of the object's signal within the volume slice. This causes loss of signal and partial volume averaging. (**b**) Slice thickness smaller than the imaged object provides for improved axial spatial resolution

of the perceptibly smooth surface of the multi-array transducer surface by a collection of many closely assembled and discrete piezoelectric elements. This misdirected low-energy signal can produce ghost images of off-axis objects which are highly reflective within the image's central field of view (Fig. 12.22).

Grating lobe artifacts can be reduced by creating multielement array transducers that have the individual piezoelectric elements more tightly packed together with less intervening space.

12.7.3.4 Slice Thickness

An ultrasound beam possesses a finite thickness. The width of this slice thickness varies with distance from the transducer surface where it is greatest close to the transducer surface, most narrow at the focal distance, and progressively increasing with distance from the focal distance. A narrow image slice thickness provides for improved axial resolution. If an object is much smaller than the slice thickness, the signal from the object will be averaged within the slice volume, resulting in signal loss and partial volume averaging (Fig. 12.23).

12.7.3.5 Tissue Vibration

Tissue vibration is an artifact that arises when flow within a vessel is markedly disturbed from its normal developed flow pattern. This artifact emerges in vessels which are markedly narrowed at a focal stenosis with the creation of a vortical or swirling flow pattern downstream of the stenosis (Fig. 12.24). This disturbed flow with its separated or vortical pattern will create pressure fluctuations within the vessel lumen that will subsequently cause the vessel wall to resonate. Like all resonating structures discussed in this chapter, this resonance will generate a sound wave. Since the entire circumference of the vessel will vibrate, sound waves will emanate radially from the vessel. This radial emanation of low-amplitude sound

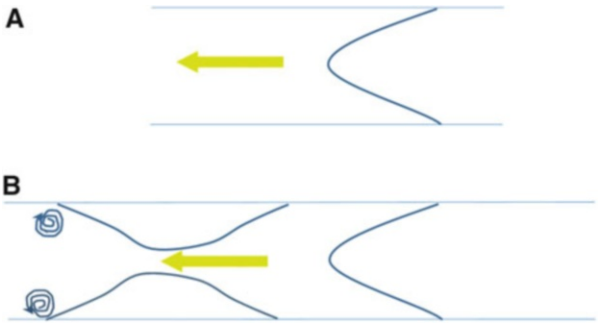

Fig. 12.24 *Vibration artifact*. As the blood travels through a stenotic area, the flow profile is disrupted from a developed parabolic description (**a**) to a separated waveform with areas of vortical flow (**b**)

waves will generate Doppler noise or a mixture of Doppler signal centered around the vessel. While the tissue vibration does create an artifact, the recognition of this artifact represents an important diagnostic clue for high-grade stensoses such as in the carotid arteries.

12.7.3.6 Speed Displacement

The speed of displacement artifact introduces a small element of error in ultrasound estimates of range and distance. This artifact results from the variation of the speed of sound in soft tissue (c_{fat} is equal to 1450 m/sec, $c_{\text{soft tissue}}$ is equal to 1540 m/sec) as opposed to the assumption that the speed of sound remains constant. This artifact can cause edges to be slightly mapped outward and introduce up to 6% error (Kremkau and Taylor 1986; Keogh and Cooperberg 2001).

12.8 Bioeffects of Ultrasound Imaging

Ultrasound imaging has been widely considered safe with negligible safety concerns. Unlike plain films and CT imaging, there is no associated radiation. For years, ultrasound has been utilized for obstetric imaging of pregnant patients and their babies with no reported adverse effects (Fig. 12.25). Within the published literature, there is no report of significant detrimental effects of ultrasound either on the patient or the sonographer.

Ultrasound generates images by observing the interaction of the body with sound energy. Anytime that energy is transmitted into the body, there exists the possibility of adverse effects such as tissue heating. Thermal deposition or tissue heating happens when transmitted sound energy is absorbed by tissue and converted to heat.

The amount of energy transmitted by ultrasound is reflected by the intensity value. Intensity is defined by the amount of energy per unit time that is transmitted through a unit area. Alternatively, intensity can be described as the power per unit area and is measured in terms of Watts/cm^2.

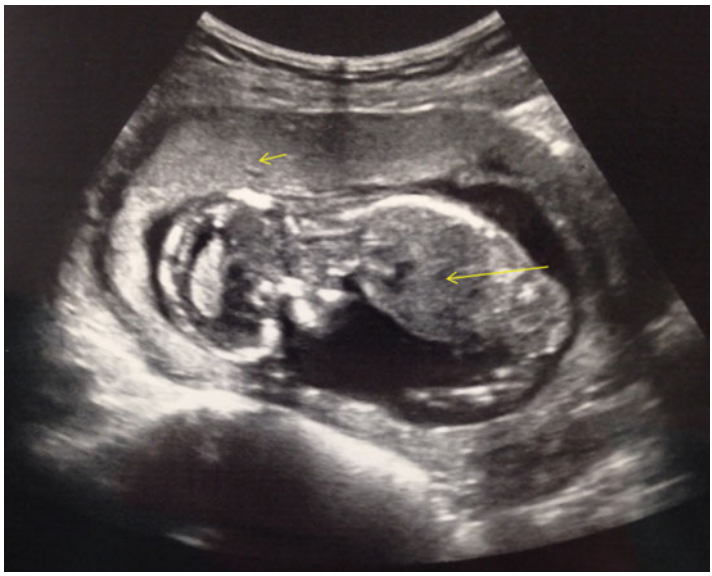

Fig. 12.25 *Obstetric ultrasound image*. Grayscale B-mode ultrasound image of a 12.5-week fetus (*long arrow*). The placenta (*short arrow*) is along the anterior surface of the uterus

All ultrasound equipment is evaluated and certified by the US Food and Drug Administration (FDA). The FDA has determined that there are no significant biological effects for diagnostic grayscale imaging obtained with ultrasound intensity transmitted below 100 mW/cm^2 or for Doppler imaging acquired with ultrasound intensity emitted below 1 W/cm^2. When imaging patients for diagnostic purposes, the intensity values are kept well below these threshold levels. Conventional intensity values in medical imaging range from 1 to 10 mW/cm^2.

Although ultrasound has long been considered safe with minimal side effects, this imaging tool, and for that matter all of imaging, should still be reserved for patients that will directly benefit from the acquired imaging information. When generating images, information should be obtained with the smallest amount of energy being transmitted into the patient. This approach reflects the ALARA principle or imaging with energy *as low as reasonably achievable* to obtain useful diagnostic information.

12.9 Advancements in Ultrasound

12.9.1 Harmonic Imaging

As with all of medical imaging, there is continuous advancement within the field. Most modern-day ultrasound machines acquire information using harmonic imaging. Up to this point, we have described a process where the images are generated

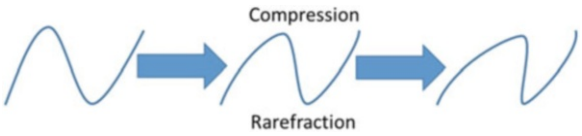

Fig. 12.26 *Harmonic frequency generation.* Harmonic frequencies are generated by the distortion of the transmitted ultrasound beam. The positive pressure amplitude portions of the wave (*compression*) travel faster than the negative pressure amplitude portions of the wave (*rarefaction*)

from sound frequencies that are identical to the initial transmitted ultrasound pulse. When ultrasound energy is transmitted into the body, its interaction with adjacent tissue produces sound waves with frequencies that are integer multiples of the initial transmitted or fundamental frequency (f_0). The harmonic frequencies originate when the ultrasound energy interacts with tissue and the positive pressure amplitude portions of the wave (compressions) travel faster than the negative pressure amplitude portions of the wave (rarefactions). This interaction results in distortion of the wave (Fig. 12.26). As the sound wave travels farther into the tissue, this nonlinear distortion of the wave increases in extent. The higher-order harmonics will be weakened in strength from the fundamental harmonic, but since they will only travel the return distance to the transducer, their signal strength remains relatively strong. Additionally, since the harmonic signal avoided the fundamental frequency's initial interaction with the overlying skin, subcutaneous tissue, and body wall, its signal is less contaminated by noise or the clutter commonly encountered near the ultrasound transducer. This helps to augment the signal to noise ratio (SNR) of the returned signal.

When the harmonics return to the ultrasound transducer, a filter is employed to isolate the higher-order harmonic information. Generally, the first harmonic (f_1) or twice the fundamental frequency is isolated for imaging. Harmonic imaging is best suited for applications such as abdominal imaging where a lower-frequency transducer probe is employed (3.5–5 MHz), and the harmonic imaging allows for evaluation with the higher-frequency harmonics which are less contaminated by the noise originating close to the probe (Fig. 12.27).

12.9.2 Ultrasound Contrast Agents

Ultrasound contrast agents have gained growing attention in recent years. While use within the United States is limited to echocardiography (functional ultrasound imaging of the heart), ultrasound contrast agents are used with far greater application in Canada and Europe for vascular imaging and perfusion imaging of abdominal masses, particularly within the liver. The ultrasound contrast agents are microbubbles, measuring between 3 and 6 μm in diameter, which contain either air, nitrogen, or perfluorocarbons. The encapsulation material, typically albumin, is

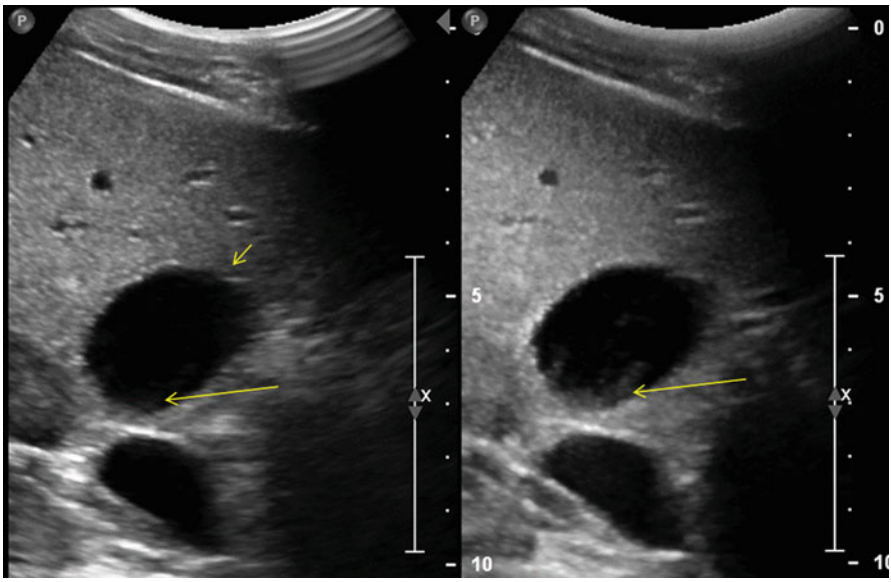

Fig. 12.27 *Harmonic imaging*. The image on the left demonstrates conventional fundamental frequency imaging of the gallbladder (*short arrow*). Within this image, there is some suggestion of echogenic material which is dependently layered (*long arrow*). The image on the right illustrates harmonic imaging of the gallbladder. The dependently layered echogenic material is more conspicuous (*long arrow*) and is consistent for a small amount of sludge

designed to contain the gas within the microbubble until the agent has reached the target tissue to be imaged. An image is generated due to the large difference in acoustic impedance between the ultrasound contrast agent and the surrounding tissue. For vascular imaging, the microbubbles increase the scatter signal from the blood, providing for far greater conspicuity of Doppler signal from flowing blood. Since the microbubbles contain compressible gas, their interaction with the incident ultrasound energy produces oscillations. These oscillations generate higher-order harmonics with higher signal amplitude than the harmonics generated by soft tissue. These higher amplitude harmonics are then detected by a technique called pulse inversion harmonic imaging. With pulse inversion harmonic imaging, the information from the surrounding soft tissue is removed which isolates the signal from the contrast agent. This technique improves the ability to observe tissue perfusion. This is critically important when evaluating masses within the liver and attempting to observe their dynamic perfusion characteristics (Bushberg et al. 2002; Weng et al. 1997; Balen et al. 1994).

12.10 Compound Imaging

This is a relatively new technique which can be performed in two different approaches: (1) frequency compounding and (2) spatial compounding. With compound imaging, multiple imaging frames are acquired either at different frequencies (frequency compounding) or at different angles (spatial compounding). This information is combined into a single multifrequency or multi-angle image which demonstrates enhanced image contrast. This imaging technique has the ability to improve image conspicuity so that pathology that was otherwise inapparent can now be visualized and evaluated.

12.11 Three-Dimensional Imaging

Three-dimensional (3D) images are generated from a series of contiguous two-dimensional images acquired from a volume of tissue. Using a stack of 2D images, data reordering can be used to create a 3D image. The 3D image is displayed using either maximum intensity projection (MIP), multiplanar reformatting (MPR) (Fig. 12.28), or surface rendering (most frequently used for displaying facial structures in obstetric imaging).

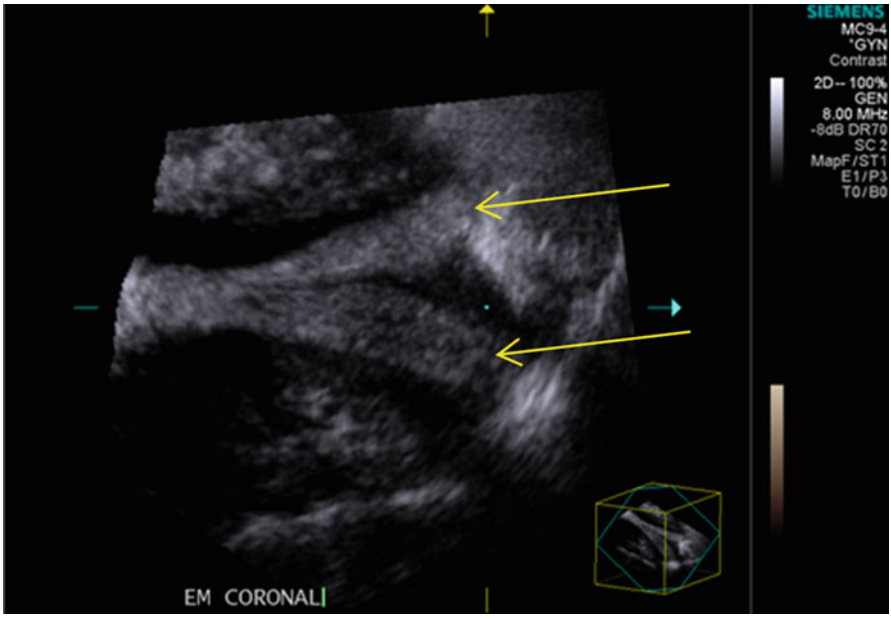

Fig. 12.28 *Three-dimensional ultrasound imaging*. Multi-planar reformatting of the uterus demonstrating the two uterine horns (*arrows*) in a didelphys uterine malformation

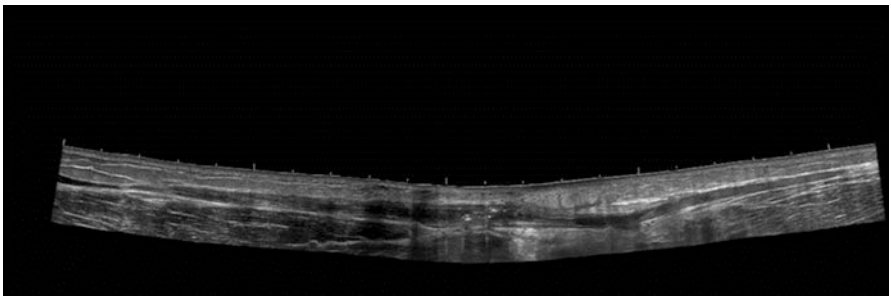

Fig. 12.29 *Extended-field-of-view imaging*. This image represents an extended field of view of the cephalic vein (a small superficial vein) within the left forearm

12.12 Extended Field of View

One recognized constraint of ultrasound imaging is how its field of view is limited to what the transducer can visualize within its plane of interrogation. For visualizing objects that extend over more than one field of view, this constraint can make image interpretation by the radiologist more difficult. New ultrasound machines have the ability to generate a panoramic view in real time which extends beyond the limits of one single field of view. New image processing software provides image registration of probe position which can lead to the synthesis of the extended-field-of-view image (Fig. 12.29) (Weng et al. 1997).

12.13 Conclusions

Ultrasound represents a noninvasive, radiation-free technique that provides imaging in real time. With continued advancements in hardware design and image post-processing techniques, the scope of ultrasound application continues to expand. Ultrasound has always been able to provide functional information through color Doppler imaging and real-time imaging of moving structures such as the heart. With further development of microbubble contrast agents, ultrasound imaging has only just started to investigate the growing field of dynamic perfusion imaging. With the mounting emphasis to develop techniques that are accurate and less expensive, ultrasound is assured to maintain an eminent role in medical imaging.

Questions

1. If a forearm muscle is evaluated with a 10 MHz linear array transducer, what is the wavelength (λ) of the transmitted ultrasound pulse? The velocity of sound in muscle is 1585 m/sec.
2. An ultrasound beam passes through the liver, and its intensity is attenuated by 70%. By how many dB has the intensity decreased?

3. Describe the four different interactions that can occur when sound encounters an acoustic interface.
4. For an incident sound intensity of 100 mW/cm^2, calculate the transmitted sound intensity as the pulse travels from fat to muscle. Z_{fat} equals 1.38 Rayl, and Z_{muscle} equals 1.70 Rayl.
5. Sound passes from retroperitoneal fat into the kidney. The initial angle of incidence, Θ_i, is equal to 45°. What is the angle of refraction, Θ_t? The speed of sound in fat is 1450 m/sec, while the speed of sound in soft tissue is 1540 m/sec.
6. For a transducer with an element length of 7 mm, calculate the focal distance for transmission in soft tissue at a frequency of 5 MHz and 10 MHz. The speed of sound in soft tissue is 1540 m/sec.
7. For a transducer with an element length of 8 mm, calculate the angle of ultrasound beam divergence (Θ_{div}) within the far field for transmission in soft tissue with a frequency of 5 MHz. The speed of sound in soft tissue is 1540 m/sec.
8. Ultrasound spatial resolution is described in three different dimensions. List them.
9. A 5 MHz phased array transducer is used to transmit a pulse echo with 5 cycles. For transmission in soft tissue with a speed of sound of 1540 m/sec, calculate the spatial pulse length. What is the axial resolution or the minimum distance that can separate two adjacent objects along the axial direction of the ultrasound pulse?
10. A. What is the type of echo display mode that is used to generate a grayscale image of the liver? B. What is the type of echo display mode that is used to estimate the heart rate of a fetus?
11. Using a 5 MHz transducer, calculate the frequency shift for blood moving at 100 cm/sec with the speed of sound measuring 1540 m/sec and θ, the angle between the transmitted sound and the direction of blood flow, equal to 45°.

Answers

1. 0.159 mm.
2. The intensity has decreased by −5.23 dB.
3. Reflection, refraction, scatter, and absorption.
4. 98.92 mW/cm^2.
5. 48.7°.
6. At 5 MHz the focal distance equals 39.8 mm, while at 10 MHz the focal distance equals 79.6 mm.
7. 2.69°.
8. Axial resolution, lateral resolution, and azimuthal resolution.
9. The spatial pulse length equals 1.54 mm. The axial resolution equals 0.77 mm.
10. A. B-mode. B. M-mode.
11. 4.591 kHz.

References

Balen FG, Allen CM, Lees WR (1994) Ultrasound contrast agents. Clin Radiol 49(2):77–82
Bigelow TA, Church CC, Sandstrom K et al (2011) The thermal index: its strengths, weaknesses, and proposed improvements. J Ultrasound Med Off J Am Inst Ultrasound Med 30(5):714–734
Bude RO, Rubin JM (1996) Power Doppler sonography. Radiology 200(1):21–23
Bushberg J, Seibert J, Leidholdt E et al (2002) The Essential Physics of Medical Imaging, 2nd edn. LWW, Philadelphia
Goldstein A (1993) Overview of the physics of US. Radiogr Rev Publ Radiol Soc North Am Inc 13 (3):701–704
Hendrick WR, Hykes DL, Starchman DE (1995) Ultrasound physics and instrumentation, 3rd edn. Mosby, St Louis
Keogh CF, Cooperberg PL (2001) Is it real or is it an artifact. Ultrasound Q 17(4):201–210
Kremkau FW (1993) Multiple-element transducers. Radiogr Rev Publ Radiol Soc North Am Inc 13(5):1163–1176
Kremkau FW (1998) Diagnostic ultrasound: principles and instruments, 5th edn. WB Saunders, Philadelphia
Kremkau FW, Taylor KJ (1986) Artifacts in ultrasound imaging. J Ultrasound Med Off J Am Inst Ultrasound Med 5(4):227–237
Rubin JM (1994) Spectral Doppler US. Radiogr Rev Publ Radiol Soc North Am Inc 14 (1):139–150
Weng L, Tirumalai AP, Lowery CM et al (1997) US extended-field-of-view imaging technology. Radiology 203(3):877–880
Zagzebski J (1996) Essentials of ultrasound physics. Mosby, St. Louis
Ziskin MC (1993) Fundamental physics of ultrasound and its propagation in tissue. Radiogr Rev Publ Radiol Soc North Am Inc 13(3):705–709

Chapter 13
Radiation Shielding and Protection, Part I: Measurement, Dosimetry, Shielding, and Protection

Christopher J. Watchman

Contents

13.1 Fundamental Radiation Protection Principles 371
13.2 Medical Radiation Sources 372
13.3 Dose 373
13.4 Radiation Dosimetry 374
13.5 Radiation Detection 384
13.6 Radiation Shielding 393
Additional Reading 402

Shielding and protection are essential to the safe practice of radiation oncology, radiology, and other medical specialties that use radiation. Medical health physics is essentially the study and practice of radiation safety as it relates to the use of radiation in medicine. This encompasses two distinct areas: (1) physical methods of measuring and calculating radiation dose and (2) the regulatory environment. In this chapter the physics methods will be discussed. Areas discussed will include (1) radiation measurement and its associated devices; (2) radiation dosimetry, both external and internal; and (3) radiation shielding design.

13.1 Fundamental Radiation Protection Principles

13.1.1 Time

Exposure to radiation as a function of time increases the number of interaction that occurs. Consequently, there is an increased amount of damage that may result. Reduction of time of exposure is the simplest method to reduce radiation dose to an individual or area. This can be accomplished by different methods including simply

C.J. Watchman, PhD, DABR (✉)
Department of Radiation Oncology, University of Arizona, Tucson, AZ, USA
e-mail: watchman@email.arizona.edu

M. Maqbool (ed.), *An Introduction to Medical Physics*, Biological and Medical Physics, Biomedical Engineering, DOI 10.1007/978-3-319-61540-0_13

limiting time in a radiation field to physical controls that limit access to the radiation field. Minimizing exposure time is also the most cost-effective method of radiation safety.

13.1.2 Distance

Maximizing distance between the radiation source and the individual or object is the next basic radiation safety principle. Radiation fields decrease from a sources as a function of $1/r^2$. Therefore increasing distance by a factor of two decreases the radiation exposure by a factor of one fourth. Maximizing distance may be done by process controls, physical barriers, or other methods.

13.1.3 Shielding

Shielding involves placing a physical barrier between the radiation source and the area/personnel/public that needs to be protected. The goal is to reduce the overall exposure of radiation to the subject. Shielding can be quite expensive depending on the source of radiation. For photon applications high-Z materials are needed to reduce the intensity of the photon. Beta particles on the other hand may only require thin sheets of plastic. Energy of the particles also plays an important role. For example 100 KeV photons may only require a thin sheet of lead to reduce their intensity to acceptable levels. High-energy photons from a linear accelerator used in radiation therapy may require meters of concrete to do the same job. Radiation shielding is a major undertaking and will be discussed in greater depth at the end of this chapter.

13.2 Medical Radiation Sources

In medicine sources of radiation are varied in their origin, physical type, application, and dangers. Different areas of medicine where radiation is normally used include radiology, radiation oncology, nuclear medicine, cardiology, and interventional radiology. These examples are by no means the only disciplines that may use radiation but are the most common specialties that do. In radiology the sources of radiation are primarily artificially produced by machines. These sources tend to be of an energy range on the order of 20–200 kVp. Interventional radiology is also included in this but may also involve the use of radioactive isotopes as well. Nuclear medicine primarily uses unsealed sources of radioactivity. Unsealed describes the state of the radioactive isotope being “uncontained” but is freely combined with a pharmaceutical compound. Energies seen in this discipline are on

Table 13.1 Common medical isotopes

Isotope	Energy	Particle	T1/2	Application
^{131}I	364 keV (82%) / 192 keV(89%)	γ/β	*8.02 day*	Hyperthyroidism, Grave's disease
^{125}I	35 keV/150.61 keV	γ/β	*59.4 day*	Radioimmunoassay, brachytherapy
^{99m}Tc	140 keV	γ	*6.01 h*	Multiple medical imaging applications
^{192}Ir	380 keV (avg)	γ	*73.83 day*	High-dose rate brachytherapy
^{32}P	1.709 MeV	β	*14.29 day*	Nuclear medicine, biochemistry
^{18}F	633.5 keV/511 keV	$\beta+/\gamma$	*1.83 h*	Positron emission tomography imaging

the order of ~500 keV. Cardiology applications are actually nuclear medicine applications used for heart problem diagnosis. Radiation oncology, the practice of treating cancer with radiation, is somewhat different than the other specialties discussed in that it uses both sealed and unsealed isotopes and it uses a much broader range of energies than in the others (~50 keV to 20 MeV). In Table 13.1 is a list of common radiation isotopes used in medicine.

Depending on the form/type of radiation, a different hazard is present. The basic hazard types may be broken down into internal hazard or external hazard types. Internal hazard radiation is of little risk when it is present outside of the body, but when it is internalized, it can deliver a significant dose of radiation. An example of this would be an alpha particle emitting radionuclide. Despite having high energy, alpha particles travel only small distances due to their large charge. Consequently, a sheet of paper is capable of blocking them. Lighter charged particles are also internal hazards but do travel farther than alpha particles. Photons on the other hand are usually considered external hazards to do their exponential absorption rate through matter. Neutrons are also external hazards and behave similarly to photons. In medicine each of these hazard types may be present. As a result it is imperative that proper methods be used to measure, calculate dose, and create protective measures for each.

13.3 Dose

Radiation dose in its fundamental form can be described by the following equation:

$$D = \lim_{m \to 0} \frac{dE}{dm} \tag{13.1}$$

Where E is energy deposited (units J or MeV or eV), m is mass (units g, kg), and D is dose (units J/kg or Gy or MeV/g). Note that in Eq. A, the value of dose is a point value in space. Consequently, it is more of a theoretical definition that should

more accurately be described by the value average dose since the energy deposition over the volume may not be uniformly distributed. Equation 13.1 could more usefully be written as

$$\langle D \rangle = \frac{dE}{dm} \text{ or } \bar{D} \frac{\int_{E_0}^{E} dE}{\int_{0}^{m} dm} \tag{13.2}$$

Or more simply as

$$\langle D \rangle = \frac{E}{m} \tag{13.3}$$

Thus, average absorbed dose will simply be referred to as dose from this point on.

Calculation of dose is dependent on the particle type being evaluated. Dose calculations for photons, electrons, neutrons, and heavy charged particles each rely on different physical phenomena and therefore are calculated differently. Each will be discussed below, but before this we must define the basic descriptors for radiation fields.

13.4 Radiation Dosimetry

Radiation dosimetry is the process whereby radiation energy deposited in matter is either measured or calculated. In this section computational methods for determining radiation dose will be presented. In medical health physics applications, how radiation dose is calculated can be separated into two categories: (1) external methods where the radiation source is outside the body and (2) internal methods where the radiation source is inside the body.

13.4.1 External Radiation Dosimetry

13.4.1.1 Radiation Field Descriptors

A radiation field may be described in terms of particles or energy radiance. Particle or N is simply the number of particles in the field. Radiance or R is the number of particles multiplied by their energy. For example, 10^6 particles of 1 MeV per particle would result in a radiance of 10^6 MeV.

$$\Phi = \frac{dN}{da} \quad \left(\frac{\#}{\text{cm}^2}\right) \tag{13.4}$$

Another way to describe a radiation field is by how many particles pass a unit area. This is called fluence. Fluence and its units are given in Eq. 13.4.

Time can also be used to describe the field in terms of the number of particles passing by the unit area. This is called flux and it has units of particles per second.

$$\dot{N} = \frac{dN}{dt} \quad \left(\frac{\#}{s}\right) \tag{13.5}$$

Each of these also has their correlate in terms of radiance termed the energy flux and energy fluence as shown in the two equations below:

$$\dot{R} = \frac{dR}{dt} \quad (\text{watts}) \tag{13.6}$$

and

$$\Psi = \frac{dR}{da} \quad \left(\frac{\text{MeV}}{\text{cm}^2}\right) \tag{13.7}$$

Lastly, and generally most usefully, we can describe the field in terms of time and area. This is called the flux density or fluence rate as shown in the following equation:

$$\phi = \frac{d}{dt}\left(\frac{dN}{da}\right) \quad \left(\frac{\#}{\text{cm}^2 - \text{s}}\right) \tag{13.8}$$

The radiance equivalent is called the energy fluence rate as shown below:

$$\Psi = \frac{d}{dt}\left(\frac{dR}{da}\right) \quad \left(\frac{\text{MeV}}{\text{cm}^2 - \text{s}}\right) \tag{13.9}$$

The use of these radiation field descriptors allows us to calculate dose from each of the radiation particles we will discuss starting with photons.

13.4.1.2 Photons

Photons interact with matter by way of exponential attenuation which is the reduction in number of photons passing through a material. The attenuation rate is dependent on the attenuation coefficient μ $(1/x)$ where x is the depth in a material. Equation 13.10 describes the process, and Fig. 13.1 presents an example of the decrease in number of photons with depth for three different μ.

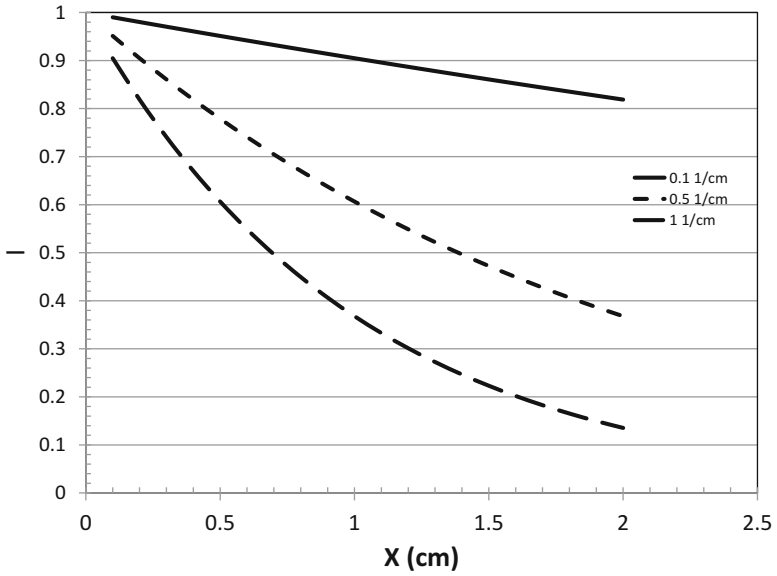

Fig. 13.1 Exponential attenuation for $\mu = 0.1\ \text{cm}^{-1}$, $0.5\ \text{cm}^{-1}$, and $1\ \text{cm}^{-1}$

$$I = I_0 e^{-\mu x} \tag{13.10}$$

The attenuation coefficient is the sum of the interaction probabilities of each of the types of photon interactions that can occur and represents the rate at which photons leave the primary field. Therefore,

$$\mu = \sigma + \tau + \kappa + \sigma_R$$

or the combination of Compton scatter, photoelectric effect, pair production, and Rayleigh scattering. Each of these interaction processes may or may not transfer energy to the material that it interacts with. Consequently we need to track the energy that is transferred to the system, and this is called the attenuation transfer coefficient as shown in Eq. 13.11.

$$\mu_{\text{tr}} = \tau_{\text{tr}} + \kappa_{\text{tr}} + \sigma_{\text{tr}} \tag{13.11}$$

Note that the Rayleigh scattering component is no longer part of the equation since this interaction does not transfer energy.

Although energy is transferred to the system or material the photon field is encountering, that energy may not remain in the system but escape. Only energy that remains in the system will result in energy deposition or in other words dose to the material. Photon energy may escape by simply continuing to pass through the material. Scattered photons may also escape the system, or bremsstrahlung may occur. Bremsstrahlung occurs when electrons encounter a coulombic field and

change direction, and in order to conserve momentum and energy, a photon is released. These photons may then escape the system. Due to this escape fraction on the energy transferred to the material system, another attenuation factor has been described to show the energy that remains in the system, and it is called the energy absorption coefficient as shown it the equation below:

$$\mu_{\text{en}} = \mu_{\text{tr}}(1 - g) \tag{13.12}$$

Here the value g represents the average secondary electron energy lost to bremsstrahlung and other radiative processes, one last item to note in regard to the attenuation coefficients. Most often they are written in terms of per mass or in other words the mass attenuation (μ/ρ), mass transfer (μ_{tr}/ρ), and mass energy absorption coefficients (μ_{en}/ρ). This is done to eliminate the mass dependence of these coefficients for both ease of use in dose calculations and so that coefficients for different materials may be more easily compared. From this point on, these will all be referred to by their mass coefficient name.Using these different parameters we can begin to calculate radiation dose from photons for different radiation fields. Equation 13.13 shows the basic calculation for photon dose based upon the mass energy absorption coefficient, energy, and fluence:

$$D = \frac{d\varepsilon}{dm} = \Psi\frac{\mu_{\text{en}}}{\rho} = \Phi E\frac{\mu_{\text{en}}}{\rho} \tag{13.13}$$

Note that e is the energy imparted to the system and that the energy fluence can be broken down into the fluence and particle energy. If the field contained multiple energies, you would need to integrate over the energy regime. This would require a new μ_{en} for each of the energies used. We can use unit analysis to determine the final units of dose based on the above equation where:

$$\frac{\gamma}{\text{cm}^2} \bullet \frac{\text{J}}{\gamma} \bullet \frac{\text{cm}^2}{\text{kg}} = \frac{\text{J}}{\text{kg}} = \text{Gy}$$

The gray is the standard unit of dose for radiation measurement and is consistent with the SI unit system.

We can also look at dose in terms of the rate at which the field is interacting with a material. The equation is the same as Eq. 13.13 except that we use fluence rate/flux density in the place of fluence. Equation 13.14 shows this:

$$\dot{D} = \frac{d\varepsilon}{dmdt} = \psi\frac{\mu_{\text{en}}}{\rho} = \phi E\frac{\mu_{\text{en}}}{\rho} \tag{13.14}$$

And we can similarly analyze the units.

$$\frac{\text{J}}{\text{cm}^2\text{s}} \bullet \frac{\text{cm}^2}{\text{kg} \bullet \text{s}} = \frac{\text{J}}{\text{kg} \bullet \text{s}} = \frac{\text{Gy}}{\text{s}}$$

Alternate methods for photon dose calculation are all dependent on these basic principles and can be derived based on the above methods.

Reference values for mass attenuation coefficients are available from the National Institute of Standards and Technology (NIST) in their XCOM database located online at http://www.nist.gov/pml/data/xcom/index.cfm.

13.4.1.3 Electrons

When discussing electron dose we must realize that we are talking about particles that may either collide inelastically or elastically. Inelastic collision results when some of the particles kinetic energy is lost in the interaction. This may be by way of ionization, excitation, or conversion to photons (bremsstrahlung). Elastic collisions on the other hand do not lose energy but are capable of redistributing energy among the particles in the collision. This is classically looked at as the billiard ball example.

Unlike photons, which are neutral, electrons have a negative charge associated with them. Consequently, their primary mode of interaction is with the Coulomb field of the atom or nucleus or other electrons depending on how far the electron passes with respect to the atomic nucleus. In cases where the electron passes very far from the nucleus, we get what are termed "soft collisions." These interactions occur with respect to the outermost electrons of the atom, and the energy transferred to them is locally absorbed. Each one of these collisions is small resulting in a very small amount of energy transferred per collision. Despite the small energy transfer, these collisions are high probability and result in high numbers of collisions. If the electron passes closer to the atom in the area of the inner orbital electron shells, we begin to get harder collisions known as "Hard Collisions or knock on collisions." These types of collisions result in substantial energy loss but are lower probability and fewer in number as compared to soft collisions. Notwithstanding, these collisions can result in some of the energy being lost by way of delta rays, characteristic x-rays, and auger electrons.

If the electron passes even closer, on the order of the atomic radius, we begin to see direct interaction with the coulombic field of the nucleus. In this collision scenario, the majority of collisions are elastic (~97%) proportionally to Z^2. Here both energy and momentum are conserved with slight energy loss. In the other 3% of cases, we have bremsstrahlung occur. Note that these percentages are approximate and are dependent on the material.

Unlike photon dose, electron dose requires the use of a different parameter than attenuation. This is due to the small deflection paths caused by soft collisions. In order to calculate electron dose, we must define stopping power or mass stopping power. Equation 13.15 shows mass stopping power which is the spatial rate of energy loss:

$$\frac{S}{\rho} = \frac{dT}{\rho dx} \tag{13.15}$$

Where S/ρ is mass stopping power, T is the electron kinetic energy, ρ is the density of the material, and x is the distance in the material. In this equation we must note that dT and dx are finite energies and distances, respectively. The mass stopping power consists of two components: collisional and radiative. Collisional losses are the interactions discussed earlier excluding the radiative losses described by bremsstrahlung and the other radiative process. It is important to note that mass collisional stopping power for electrons is greater for low-Z materials than for high-Z materials. Radiative mass stopping power is the opposite and is proportional to EZ^2.

The simplest use of stopping power to calculate electron dose is found in Eq. 13.16:

$$D = \frac{\Phi\left(\frac{dT}{\rho dx}\right)_c}{\rho t}\rho t = \Phi\left(\frac{dT}{\rho dx}\right)_c \tag{13.16}$$

where t is a small thickness of the medium the electrons are entering and c signifies the collisional components of mass stopping power and the other parameters that have previously been described. Here the units of the solution are in MeV/g, but a conversion factor or 1.602×10^{-10} can be applied to change the units to Gy. For mathematical simplicity, this conversion factor will not be used in the following descriptions. Equation 13.16 gives us the dose for a thin layer of medium, but as we add layers, the solution becomes more of an average dose as individual electrons travel very different paths in their particle tracks leaving different amounts of energy at depth. So if these small layers are put together into thicker layers, we get the following average dose relationship:

$$\bar{D} = \Phi_c \frac{\Delta T_c}{\rho t} = \Phi \frac{T_0(1 - Y(T_0))}{\rho t} \tag{13.17}$$

where T_0 is the initial energy and $Y(T_0)$ is the radiative yield. As the thickness of the material becomes ever greater, we then can integrate over these other thicknesses to achieve the dose at some depth x as shown in Eq. 13.18.

$$D_x = \Phi\left(\frac{dT}{\rho dx}\right)_{c,m} \tag{13.18}$$

Here x is the depth and m is the medium.

Reference values for electron mass stopping powers and other electron dosimetry values are available from NIST in their ESTAR database located online at http://physics.nist.gov/PhysRefData/Star/Text/ESTAR.html.

13.4.1.4 Heavy Charged Particles

Dose calculations for charged particles that are heavier than the electron (HCP) also rely on stopping power. Unlike electrons an approximation is used to calculate dose in a medium. This is called the continuous slowing down approximation (CSDA), and it shown in Eq. 13.19.

$$R_{\mathrm{CSDA}} = \int_0^{T_0} \left(\frac{dT}{\rho dx}\right)^{-1} dT \tag{13.19}$$

The CSDA assumes that uniform energy deposition and linear particle tracks occur. For HCPs this is a reasonable assumption due both to their heavy mass and charge. Using this approximation we can then calculate and average dose through a thin medium as

$$\bar{D} = \Phi \frac{\Delta T \cos\theta}{\rho t} \tag{13.20}$$

where ΔT is the difference between the range through the medium and the remaining energy of the particle as it passes through the thin medium. If the particle does not enter perpendicularly, then the addition of the $\cos\theta$ is needed.

This description of dose is acceptable for thin mediums, and as the medium increases we see a change in the behavior of the energy deposition. At the end of the particles energy, it begins to deposit large amount of its energy and peaks near the end of its path. This is called the Bragg peak, and a full discussion of the dose calculation for this is beyond the scope of this chapter and will not be discussed further.

Reference values for protons and alpha particle mass stopping powers and other dosimetry values are available from NIST in their PSTAR and ASTART database located online at http://physics.nist.gov/PhysRefData/Star/Text/PSTAR.html and http://physics.nist.gov/PhysRefData/Star/Text/ASTAR.html, respectively.

13.4.1.5 Neutrons

Neutrons are neutral nucleons that can be produced by different interaction in medical health physics, specifically by high-energy photons and protons. These interactions result in varying energy regimes that make simple dose calculations very difficult and beyond the scope of this chapter. Generally these calculations require Monte Carlo or discrete linear Boltzmann methods. Therefore in medical health physics, measurement of these fields and doses is the methodology of choice and will be discussed in the radiation detection and measurement section.

13.4.2 Internal Radiation Dosimetry

Internal radiation dose is more complicated than external dose due to the inclusion of not only the physics but also the biology of the subject. Consequently, we can break down internal radiation dose into two components. First, a component that includes the biology of the subject and the total number of nuclear transitions. The second is a physical dose conversion factor that gives the total energy deposited per unit mass for a specific source and target combination. Two systems were developed to do these dose calculations, but both are simply the same physics with different descriptions. These two methods are the International Commission on Radiological Protection (ICRP) method and the Medical Internal Radiation Dose (MIRD) method. Equations 13.21 and 13.22 show both of these methods.

$$H_T = U_s \text{SEE} \tag{13.21}$$

$$D = \tilde{\text{A}}\text{S}(r_t \leftarrow r_s) \tag{13.22}$$

Each of these equations breaks down into two components, one that relates the total number of nuclear transformations and the other that relates the energy deposition within the material. In Eqs. 13.21 and 13.22, the first portion is represented by U_s and $\tilde{A}$ that are called the number of decays and the accumulated activity, respectively. The energy deposition portions are SEE – specific effective energy – and S ($r_t \leftarrow r_s$) the S-value. Each of these values further breaks down into an absorbed fraction and the mass of the target tissue/organ. This is shown below:

$$S = EY\frac{\phi(r_t \leftarrow r_s)}{m_t} = \Delta_i \frac{\phi(r_t \leftarrow r_s)}{m_t} \tag{13.23}$$

Where E is the energy of the radiation particle, Y is the yield of the particle, m_t is the mass of the target, and $\phi(r_t \leftarrow r_s)$ is the fraction of the initial energy E that is absorbed in the target. Δ_i is the product of EY. If multiple energies are part of the radiation isotope or isotopes being calculated, the above equation would need to be integrated over each energy and yield along with their corresponding absorbed fraction. In Fig. 13.2 is a simple illustration of the interplay between a source and target.

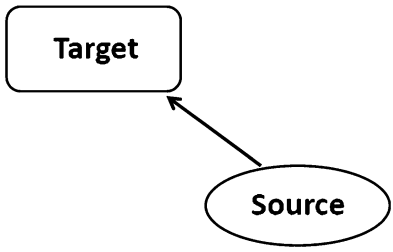

Fig. 13.2 Simple interplay between source and target

Note that in the above figure, the radiation particles may pass between the source to the target and deposit energy. Loss of energy between the source/target combination results in an absorbed fraction that is less than 1. The absorbed fraction may be 1 if and only if there is self-absorption of the radiation in the target. This methodology may be used for photon, beta emitters, and alpha emitters.

When comparing these two methodologies, the physics remains the same, but the objective in the dose calculation is different. In the MIRD system the end point of the calculation is to evaluate some biological end point of the dose. For example, dose from an isotope may result in suppression of the bone marrow. On the other hand, the ICRP methodology is looking at estimates of radiation risk to a person or population. Consequently, the ICRP method has greater uncertainty in what the dose means since the time and amount of radiation received can be variable or unknown, unlike the MIRD objective where the radiation quantity is known. Despite these differences for the purposes of this chapter, we will use the MIRD mathematics to describe internal dose.

Internal dosimetry innately means that the radiation dose has been incorporated into the body. How the radiation entered the body can vary from ingestion, injection, inhalation, absorption, and through wounds. Each of these pathways allows for the radioactive material to enter the body and then enter the blood stream. Translocation of the radiation through the blood allows for dispersion of the radiation throughout the entire body. Preferential deposition of the radiation in different areas and organs of the body is dependent on the nature of the radioactive material, chemical composition, and physical properties. Chemical composition alters how the body and the radioactive material interact and can allow for quicker or slower deposition, retention, and loss of the material in an organ or body region. The physical properties, such as Z, can also directly change where the isotope deposits. For example, materials that are in the column of the periodic table such as Ca would also preferentially deposit in regions of high Ca content such as the bones. ^{90}Sr and ^{226}Ra would be examples of such isotopes. The physical decay of the isotope along with the biological half-life also plays a role in the dose. The physical half-life is an innate property of the isotope, while the biological half-life describes how the isotope leaves the body or organ, and it is reliant on the previously discussed parameters.

How the radiation enters the body and then is translocated is the biological part of the internal dose calculation. To obtain this information, we have different biological modeling methods. First we can directly measure radiation from the body and apply modeling (curve fits) to obtain the accumulated activities in each organ and in the whole body. The second methodology is to use biokinetic or pharmacokinetic models with known model and transfer parameters. Fortunately there are several published compartmental models describing the major pathways for intake of radioactive materials into the body. The International Commission on Radiological Protection (ICRP) has models for the following intake pathways: respiration, wounds, and ingestion. They also provide biokinetic models for many different elements and some organ specific models. One can obtain these reports on their website at http://www.icrp.org/publications.asp.

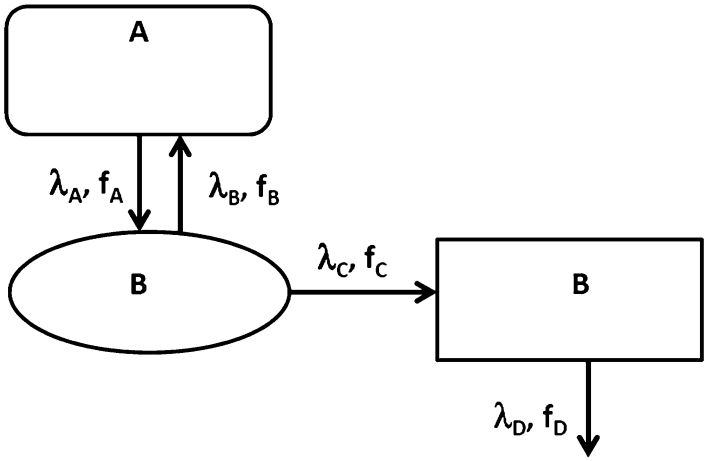

Fig. 13.3 Simple three-compartment internal dosimetry kinetics model

Models of this nature may be complex or fairly simplistic. We will discuss a simple three-compartment model as an example. Figure 13.3 illustrates the model.

In this figure three different compartments are present. Each compartment can contain radioactive material. The arrows indicate paths of translocation between the compartments and out of the system. Each of these paths has a transfer constant (λ) (similar to a decay constant) and a retention function (f) which describes the fraction of the material that remains in the compartment. Each of these functions is time dependent, so this needs to be accounted for. Note that there is also a possibility of material going back and forth between two different compartments, and this must be included in any solution. Material may also exit the system completely as shown in the arrow exiting compartment three. This is often an excretion pathway.

A series of kinetic equations may be developed to describe the behavior of this system as shown below in this series of equations:

$$\frac{dA}{dt} = -f_A A\lambda_A \tag{13.24}$$

$$\frac{dB_A}{dt} = f_B B\lambda_B \tag{13.25}$$

$$\frac{dB}{dt} = f_A A\lambda_A - f_B B\lambda_B - f_C C\lambda_C \tag{13.26}$$

$$\frac{dC}{dt} = f_B B\lambda_B - f_C C\lambda_C - f_D C\lambda_D \tag{13.27}$$

In these equations λ is a combined decay constant that includes both physical decay and physiological half-life, ABC are the compartment activity content, and f is the fraction of the activity uptake in the compartment of the total activity that entered the body.

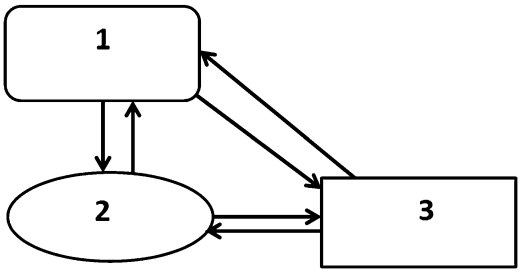

Fig. 13.4 Multiple target irradiation from different source compartments

Once the kinetics component of the calculation is determined, then the physics of the energy deposition may be addressed. Figure 13.4 shows that each compartment may irradiate the other resulting in multiple components to the dose of the target.

Here we see that compartment 1 may irradiate compartments 2 and 3 as well as itself. The same holds true for each of the other compartments. As a result, each of the absorbed fractions from the source compartment must be individually calculated and then summed together to calculate the total dose from Eqs. 13.22 and 13.23.

13.5 Radiation Detection

As discussed in a previous chapter, ionizing radiation interacts with matter by way of several mechanisms depending on the particle type. Detection of radiation relies upon these interaction types, and each measurement tool is specifically designed to take advantage of these interactions. In this section we will focus on the basic detectors used in medical health physics.

13.5.1 Gas-Filled Chambers

One of the most commonly used methods for detecting radiation is to use a gas-filled chamber and a voltage potential difference across the chamber to measure current changes in the presence of radiation. Separation of positive and negative ions which are then moved through the electric field potential allows for the measurement of current. The amount of current and the relationship to the potential allow for different types of gas-filled detectors. Two different detectors are most commonly used, an ionization chamber and a Geiger-Muller tube. Other detectors can be used but will not be discussed here as they are infrequently used in medical health physics.

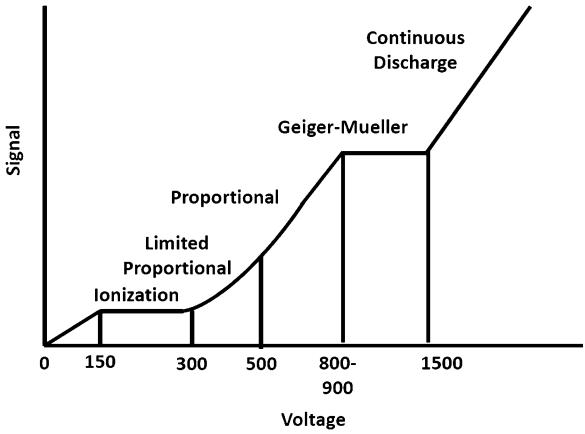

Fig. 13.5 Ionization curve for detection

Gas-filled chambers rely upon the breaking down of the gas by the incoming radiation particle into ion pairs. Then an applied electric field separates the ions as they move toward the anode and cathode of the system. A resulting current is then obtained and can be measured to evaluate the radiation field. Depending on the operating voltage, as will be discussed next, the gas-filled chamber may be calibrated to several different parameters such as exposure (measure of ionization in air for photon energies <3 MeV), dose, or simply radiation counts.

In Fig. 13.5 seen below shows the relationship of operating voltage and measured signal for the full range of gas-filled chambers. Note that the ionization chamber runs at a much lower potential than the Geiger-Muller tube. In each region of the curve, the amount of ionization of the gas varies and results in significantly different behaviors. Consequently, each region has its specific useful application, and we will only discuss the most pertinent application to medical health physics.

13.5.2 Ionization Chambers

Ionization chambers are one of the most common devices used in medical health physics. They are gas-filled chambers that are sensitive and allow for absolute calibration of the ionization charge collected to dose. They operate in the low-voltage region of the curve shown in Fig. 13.5. Figure 13.6a illustrates the basic electrical diagram of an ion chamber. The basic design is simple, an enclosed chamber that may be sealed or open to the atmosphere, an anode, cathode, voltage potential, and some device to measure the current or charge developed. When radiation particles pass into the chamber region, they may ionize the gas. The amount of energy needed at a minimum to ionize the gas is called the W value or average energy lost per ion pair formed. It is sometimes listed W/e. The exact value of this is dependent on the gas used in the chamber. Most often air is the gas, and the

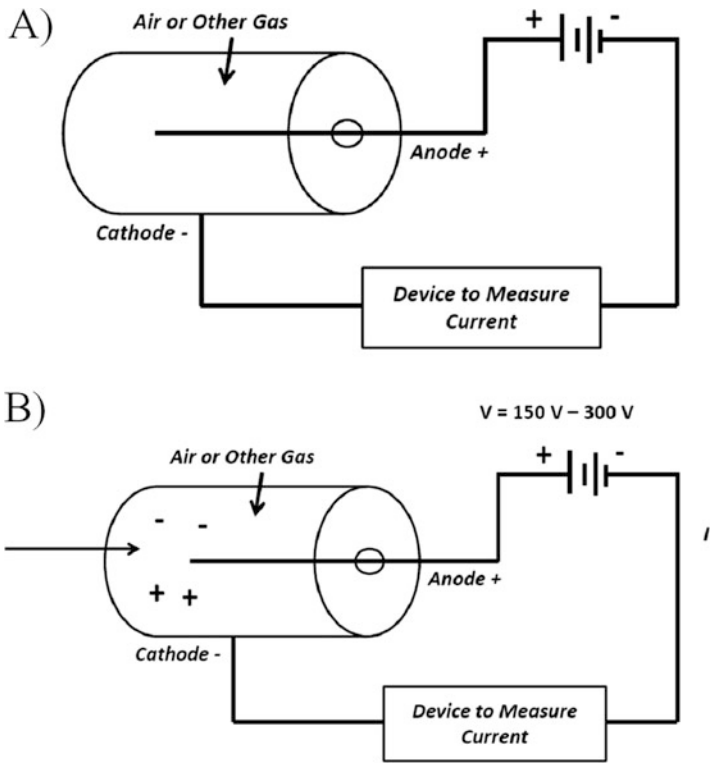

Fig. 13.6 (**a**) Schematic for basic ion chamber, (**b**) ionization and current in an ion chamber

required energy is 33.8 eV/ion pair. These ion pairs may recombine and not contribute the measured current. If the voltage is sufficient, then they are measured as part of the current. The operating voltage of 150–300 V is used for ion chambers and results in an accurate indication of the rate of ionization pairs created in the gas volume of the chamber. Figure 13.6b shows this relationship.

Ion chambers are most often used to for calibration of radiation-producing machines, to evaluate dose, and for evaluating radiation field exposures. Figure 13.7 shows two different types of ion chambers commonly used in medical health physics.

13.5.3 Geiger-Muller Detector

The Geiger-Muller (GM) detector, commonly referred to as the Geiger counter, is widely used as a radiation detection device. Unlike the ionization chamber, the GM detector does not allow for absolute calibration to dose. It is valued as a radiation detection device as it is highly sensitive to radiation and allows for easy detection of

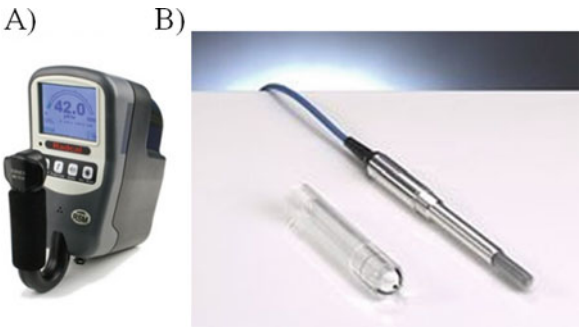

Fig. 13.7 (**a**) A survey ion chamber, (**b**) a farmer ionization chamber

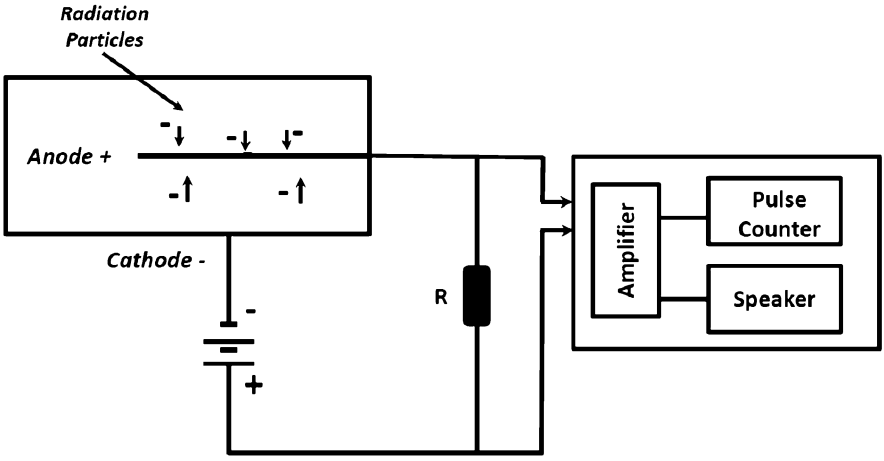

Fig. 13.8 GM detector schematic and discharge

the presence of radiation. Using a GM detector to locate small radiation fields has the analogy of using a flashlight in in a very dark room where the flashlight provides substantial contrast to the dark room. The GM detector does the same with respect to radiation; in other words, it readily identifies the region of radiation. Consequently, GM detectors are radiation locators or identifiers but do not give quantitative information about the amount of radiation or dose of radiation. These detectors have two methods of display for describing the intensity of the radiation field, a pulse counter or an audible speaker. The pulse counters usually have a range from 1 to100,000 counts. The audible alert is also useful as it increases in volume intensity with the increase in the counts of radiation and serves as a very efficient warning system.

As shown in Fig. 13.8, GM detectors also depend on the production of ion pairs in the gas-filled chamber, but due to the high-voltage potential used (Fig. 13.5: 800–1500 V), a single ion pair creates a large number of additional ion pairs. This process is called the Townsend avalanche, where a single ion pair causes a cascade

reaction of additional ion pairs that are then collected. These avalanches mean that GM detectors are highly sensitive to radiation as discussed earlier. One issue with this is that the gas can become fully ionized and any new radiation particles will not cause additional events to count. Consequently, two methods for quenching the gas and allowing for better detection are used. The first is to use an external RC circuit to decrease the potential across the resistor and allow for recombination of the gas. The alternate method is to include a quench gas into the chamber. This gas may be a polyatomic gas, organic gas, or halogen. These quench gases reduce the amount of photoelectrons produced in the avalanche thus reducing the total ionization of the chamber gas.

13.5.4 Semiconductor Detectors

Also widely used in medical health physics are semiconductor detectors which are solid-state devices. These detectors rely upon similar principles to gas-filled chambers except that they instead use "defects" in the crystal structure of the gas as the charge carrier. These "defects" are called holes, and electrons act as the other carrier. Figure 13.9 illustrates these devices. In Fig. 13.9a the basic design of the semiconductor detector is shown where there are two regions, the valence band and conduction band, separated by a small energy gap of ~1 eV. The valence band is the highest energy region where electrons can exist in the semiconductor, and the conduction band is the region where electrons do not exist in their normal energy state. The addition of energy into the semiconductor (Fig. 13.9b) greater than the energy gap will allow for electrons to move into the conduction band. A hole is then left in the valence band, and the resulting difference in the charge movement will result in an electrical signal that may be measured and calibrated to the amount of radiation encountered by the semiconductor detector.

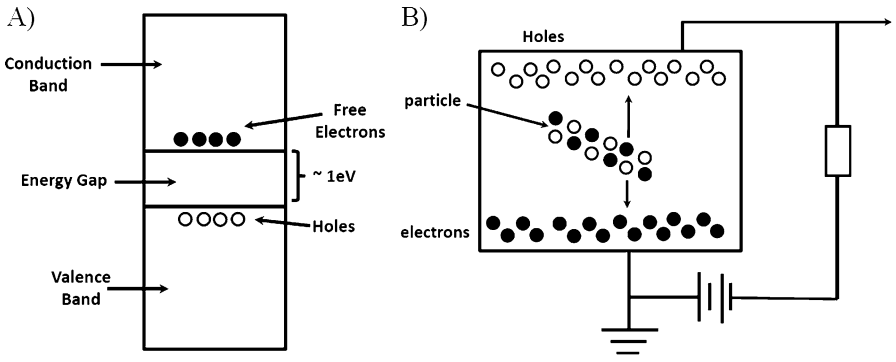

Fig. 13.9 (**a**) Simple illustration of the basic design of a semiconductor detector. (**b**) Illustration of the movement of holes and electrons in a semiconductor detector

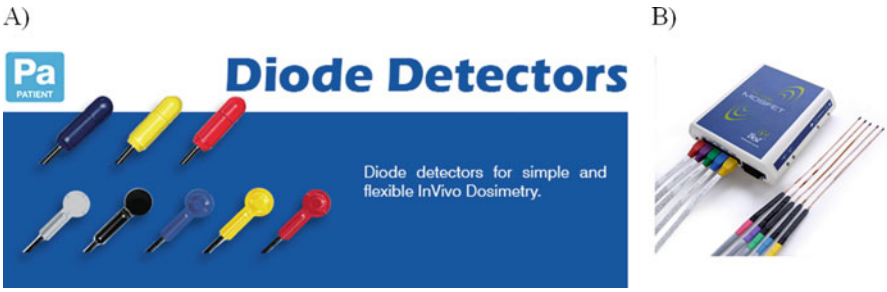

Fig. 13.10 (**a**) Diode detector from Sun Nuclear Corporation, (**b**) MOSFET detector from Best Medical LLC

Semiconductor detectors come in two different types, P-type and N-type. P-type semiconductors have a structure where there is an empty space in the structure (hole) that wants an electron to fill it in order to stabilize the structure. N-type semiconductor detectors, on the other hand, have an extra electron in the structure and want to lose that electron to the valence shell. In order for the semiconductor to work as a radiation detector, an electric field is applied which allows for the semiconductor to transport the electrons to the holes. This essentially makes the system a P-type semiconductor on one side of the device and an N-type on the other as seen in Fig. 13.9b. This is called the p-n junction.

Semiconductor detectors are widely used as they have small variations in signal response and good energy resolution. They also have the ability to resolve interactions quickly making their measurement time dependence very good. Common examples of these types of detectors are diode detectors or metal oxide field effect transistor (MOSFET) detectors as shown in Fig. 13.10 below.

13.5.5 Thermoluminescent Dosimeters

Another crystal structure radiation dose detector widely used in medical health physics is the thermoluminescent crystal dosimeter or TLD. TLDs are crystals that similar to semiconductor detectors have a valence and conduction band. Unlike semiconductor, TLDs have a series of intermediated energy traps within their crystal structure that allow for trapping of electrons in an excited state in the crystal. Figure 13.11a shows the basic arrangement of these crystals. These traps are impurities in the crystal structure that may hold onto electrons freed by incoming ionizing radiation or an electron/hole pair may be created as shown in Fig. 13.11b. Trapped electrons in this system allow for information about the amount of energy deposited into the crystal to be stored. This information may be released by heating the crystal which then emits light proportional to the dose received. To release the light a TLD reader, as shown in Fig. 13.12, is required.

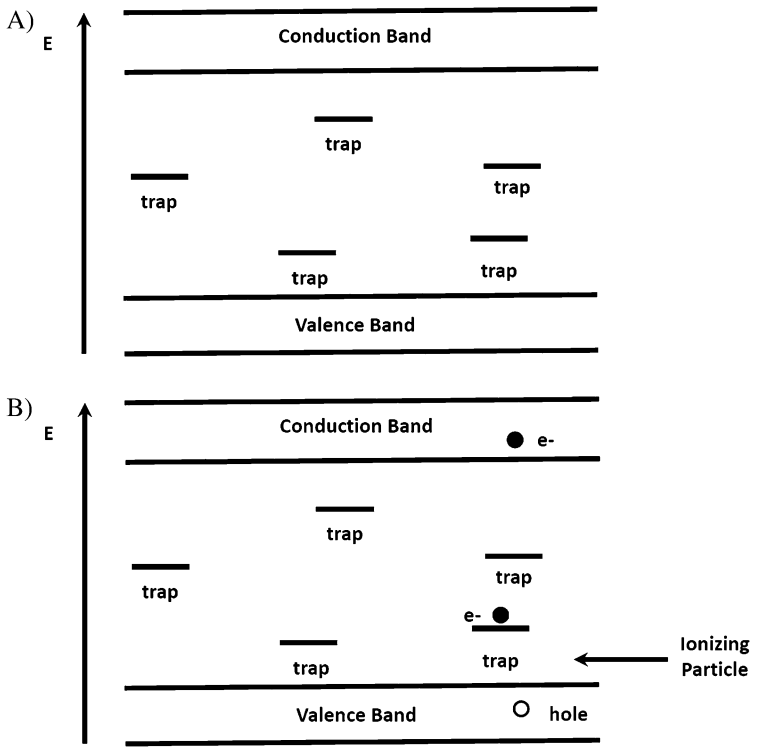

Fig. 13.11 (**a**) TLD crystal structure, (**b**) electron/hole traps with incoming radiation

The TLD reader consists of an oven for heating the crystals to release the trapped electrons. A thermocouple is used to measure the rate of heating of the crystals. Filters bring the emitted light into the effective measurement range of the photomultiplier tube (PMT). A high-voltage power supply to the PMT and a readout device are the remaining major components.

Readout of the emitted light is done by slowly heating the crystals to release the traps at a known rate. A glow curve is then generated that is a direct measure of the radiation dose to the crystals. Figure 13.13 shows a typical glow curve. Note that in the glow curve, there are different peaks which relate to different energy levels of the different traps in the crystal. The example in Fig. 13.13 is a fairly simple example with only two peaks, but more complicated glow curves are possible.

Optimal TLD crystals for dosimetry applications have a large linear range over a large dose range. They retain the trapped carriers during the temperatures of the irradiation. Additionally, they should produce large amounts of light and be able to be completely annealed following the reading of the crystal. Annealing is the final process where the crystal is returned to its baseline state by heating it to the point that all traps are released. This allows for the crystals to be reused regularly.

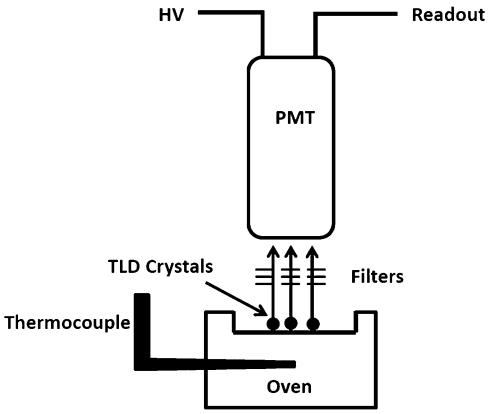

Fig. 13.12 TLD reader

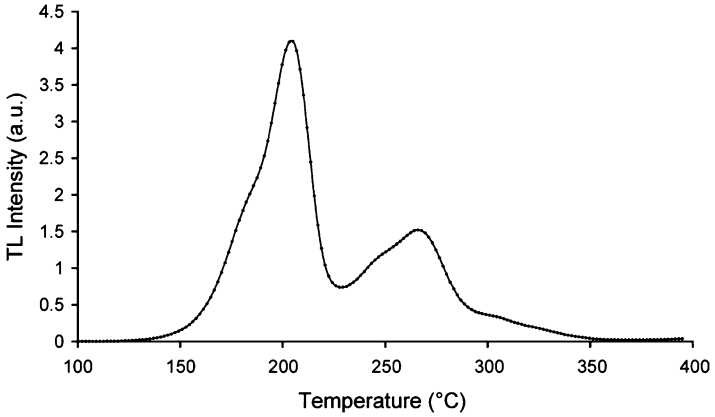

Fig. 13.13 TLD glow curve

Different types of crystals can be configured to specifically measure different types of radiation. Depending on the doping of the crystal, they could measure photon, beta particles, alpha particles, or neutrons. Typical TLD crystals include LiF, $Li_2B_4O_7$:Mn, Al_2O_3:C, CaF_2:Mn, CaF_2, $CaSO_4$:Mn, and $CaSO_4$:Dy. TLDs are most commonly used for area monitoring or personnel dosimetry.

13.5.6 Neutron Detectors

Neutrons, being neutral particles, can be very difficult to detect. Their interactions are based on ballistic interaction or absorption interactions. Two types of methods are commonly used to detect neutrons; these include proportional counters with gases sensitive to neutrons and activation foils. Activation foils, such as gold, rely

on the absorption of a neutron to activate the foil into an excited state where it will then become radioactive. Measurement of the radiation produced by the activated foil allows for measurement of the neutron field strength. This method is not commonly used in medical health physics and will not be discussed further. It should also be noted that semiconductor detectors can also be manufactured for neutron detection as well but are less common in medical health physics applications.

The more common tool used to measure neutrons is a proportional counter. In Fig. 13.5 the proportional range was after the ionization voltage range and was between 500 and 800 V. Over this range the potential is sufficient that additional ion pairs are created in a process called gas multiplication. Unlike the GM detector discussed earlier, the multiplication does not result in a Townsend avalanche but a proportional multiplication to the neutron field. This proportionality allows for calibration of the measured output to the neutron field strength.

The design of these proportional counters is similar to the ionization chamber in Fig. 13.6. Different gases than air are used due to their affinity for neutron absorption interactions. These most commonly include ^{3}He and ^{10}B. Equation 13.28 shows each of these interactions.

$$\begin{aligned} &^{3}\mathrm{He} + n = {}^{3}H + {}^{1}H + 0.764\mathrm{MeV} \\ &^{10}B + n = {}^{7}Li + \alpha \end{aligned} \tag{13.28}$$

Figure 13.14 shows that the boron also has an alternative excited state

One of the other common tools used to measure neutrons is the REM ball, which is so called as it is used to measure dose equivalent. It is also a proportional counter but is designed such that the readings relate units of rem instead of absorbed dose. REM is a unit of dose equivalent which estimates the biological effects of ionizing radiation. Figure 13.15 shows a cartoon of one.

In medical health physics, neutrons are generally only encountered when using high-energy linear accelerators in radiation oncology. Consequently, neutron

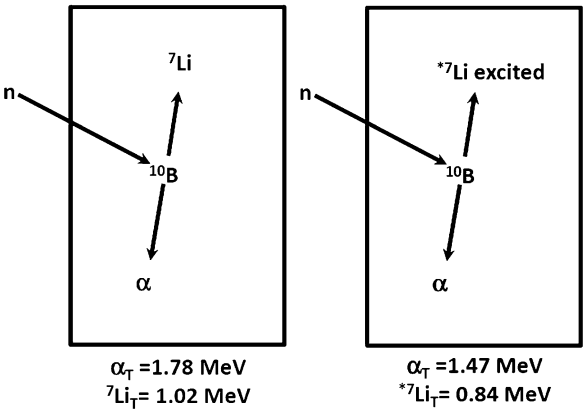

Fig. 13.14 Excited and baseline boron capture interaction used in neutron detection

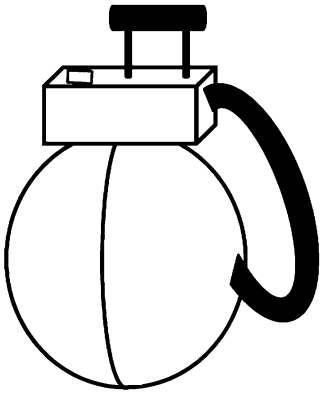

Fig. 13.15 REM ball

detectors are not common tools used by the medical health physicist except during machine commissioning or facility construction. Often these types of tools will need to be borrowed or rented.

13.6 Radiation Shielding

Radiation shielding is the process by which the intensity of radiation is reduced by the use of different materials. This consists of two parts: (1) shielding calculations and (2) shielding construction. Each will be discussed starting with shielding calculation methods.

13.6.1 Shielding Calculation Methods

Radiation shielding is specific to the type of radiation and energy of the particles. It can be further complicated by the presence of a mixed field of radiation types. Additionally, the type of facility also plays a large role in how these facilities are shielded. In medical health physics, we can define these facility types into the following categories: (1) diagnostic, (2) nuclear medicine, (3) radiation oncology, and (4) others. Guidance on how to do radiation shielding has been provided by the National Council on Radiation Protection (NCRP) in two documents. For diagnostic shielding NCRP Report 147 Structural Shielding Design for Medical X-ray Imaging Facilities is the core document used. When therapeutic of higher-energy photons are to be shielded NCRP Report 151 Structural Shielding Design and Evaluation for Megavoltage X- and Gamma-Ray Radiotherapy Facilities is the gold standard. Neither of these reports addresses positron emission tomography (PET), but in 2006 the American Association of Physicists in Medicine (AAPM) produced a Task Group Report entitled, "AAPM Task Group 108: PET and

PET/CT Shielding Requirements." This report is now the current standard reference for this type of shielding. This report is freely available at http://www.aapm.org/pubs/reports/RPT_108.pdf and will not be discussed in this chapter. The reader is strongly encouraged to review it. While these three reports tend to cover most situations that the medical health physicist will encounter, there are situations that fall outside of these reports. The specific principles and techniques discussed in the reports mentioned may be applied but interpreted to the situation. Prior to discussing each of these report methods, we will first discuss the common areas between these reports.

When planning any shielding project, the scope of the project must be clearly laid out. Shielding a diagnostic x-ray radiograph room is grossly different than that of a linear accelerator room. Even shielding a CT scanner room has differences, compared to a radiograph room, that need to be addressed to properly achieve ones goal. In the planning process, every attempt should be made to include the fundamental principles of time and distance in the design of the facility. Doing so will help to reduce the costs of the shielding component of the project. Assessment of budget, materials, location of rooms, types of radiation-producing devices, architecture design, and building construction issues will be needed. Key to this process is the understanding of the regulator limits, as discussed in an other chapter of this book, so that your design meets but does not exceed requirements. Exceeding requirements may result in a substantial increase in costs of the project.

For the purpose of shielding design, we break down areas that need to be protected into controlled and uncontrolled areas. A controlled area is a space where access is restricted to occupational exposures by radiation worker personnel. Uncontrolled areas are any other areas where the public may be, for example, hallways, exam rooms, and reception areas. Due to the open access, these areas require a stronger dose limit than controlled areas. In controlled areas for diagnostic imaging applications, the design goal (P) is 0.1 mGy air kerma strength per week. In therapeutic applications in controlled areas, P is 0.1 mSv per week or an annual 5 mSv per year. Note that the diagnostic application uses units of mGy and not the effective dose (mSv). This is due to the lower-energy regime of diagnostic beams as compared to therapy beams. Regardless, the 5 mSv per year recommendation is the same for both applications. Uncontrolled areas P are 0.02 mGy per week and 0.02 mSv per week for diagnostic and therapy, respectively. This design goal ensures that an annual limit of 1 mSv is not exceeded.

Upon completion of the project, a radiation survey is needed to ensure that the design goal was achieved. Failure of this survey may result in not obtaining a license or additional reconstruction costs to fix the problem. Consequently, these types of calculations should be done by a professional health, medical health, or medical physicist with experience in shielding calculations and design. It is recommended that all calculations be double-checked by additional parties in order to assist the shielding designer. Once the final survey is done and a license is issued, passive area monitoring of the room is warranted. This may be done with TLDs or other devices.

Certain commonalities are seen in both reports with respect to defined factors used in the calculations. One of these is the idea of occupancy factor (T) which is the fraction of beam on time that an area is occupied by an individual. It is used to better estimate the exposure to individuals. For fully occupied areas, such as offices, labs, x-ray control rooms, etc., a factor of 1 is given. This factor decreases with different areas. Patient exam rooms and treatment rooms have a T of 0.5, while corridors, patient rooms, employee lounges, and staff restrooms have a value of 0.2. Corridors are assigned a value of 0.125. Public restrooms, vending areas, storage rooms, outdoor seating, unattended waiting rooms, and patient holding rooms are given a T of 0.05. Other outdoor areas, unattended parking lots, janitor's closets, attics, unattended elevators, and stairways are assigned a value of 0.025.

We will now discuss each of these reports mentioned. Due to the extensive nature of each report, these discussions will only cover a basic introduction to the report. The reader is encouraged to probe deeper by obtaining these reports which will be listed at the end of this chapter.

13.6.1.1 NCRP 147 Methods

In NCRP 147 methodology, they identify specific position of interest outside of the shielded area where calculations should be made. This position is based upon the assumptions that the closest a person will nominally have their sensitive organs relative to the beam is <0.3 m from a wall, ≤ 1.7 m from the floor, and 0.5 m above the floor. It is considered unlikely or rare for any other combination of distances.

Shown in Fig. 13.16 is a typical configuration of a radiographic room with an x-ray source tube pointed toward the patient. Note that the patient is on top of a rectangular box in the picture. This represents the image receptor. Several

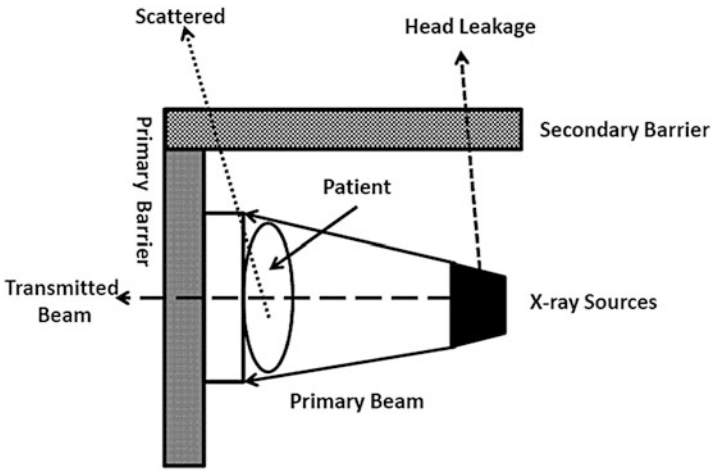

Fig. 13.16 Example radiographic room

important concepts to NCRP 147 are illustrated here. First is the transmittance through the patient from the primary beam. As is shown part of the primary beam passes through the patient, image receptor, and the barrier behind the image receptor. Transmitted primary beam passing through the wall is the reason for the addition of shielding materials to the wall. We define here the primary barrier as any wall or subregion of a wall where the primary beam is directed. A secondary barrier is any wall or region where scattered radiation may hit. Two types of scatter radiation exist, leakage and patient/object scatter. Leakage radiation comes from the x-ray tube itself due to scatter within it. Patient/object scatter comes from the primary beam hitting the patient/object, and partial scattering radiation interactions cause out scatter toward other barriers. It is important to account for all of this in the design goal shielding calculation.

Another important concept is the idea of workload (W) which is a factor that relates the x-ray tube's usage. Mathematically it is the time integral of the tube current with units of mA-min/week. To obtain W a survey of the department may be done, or standard values from NRCP 147 may be used. These standard values are radiographic rooms 277 mA-min/week, chest rooms 45 mA-min/week, and cardiac angiographic rooms 3050 mA-min/week. Equation NCRP 1 shows how to calculate this where W_{tot} is the total workload, N is the number of patients per week, and W_{norm} is the nominal workload for the system.

$$W_{\text{tot}} = NW_{\text{norm}} \tag{13.29}$$

NCRP 147 contains more detailed reference information for this concept.

The next factor that must be accounted for is the use factor (U) which relates the fraction of time the primary beam workload is directed to the primary barriers. Due to the primary beam hitting this region, it will require greater shielding to reduce the beam to the design goal. The report lists some typical U for the following barriers: chest image receptor 1.00, floor 0.89, and cross-table wall 0.09.

Figure 13.17 presents a typical radiographic room configuration and distances needed for the dose calculation.

In the figure we see multiple secondary barriers and an occupied control room. The control room is where the x-ray technician operates the system. Although not noted on in the diagram, the entire wall surrounding the control room is also secondary barriers. Several distances are shown in the diagram that relate to how the calculation is done. They are:

- d_{f} – distance from x-ray source to image receptor.
- d_{p} – distance from x-ray source to shielded area.
- d_{s} – patient scatter distance: this may be to any secondary barrier.
- d_{L} – leakage distance from x-ray source: this may be to any secondary barrier.
- F – the primary x-ray beam area.

These parameters will be used to get barrier thickness, but first we will go through how the thickness is calculated from basic physics. For the purposes of the transmitted beam through a barrier of some thickness, we know that the ratio of

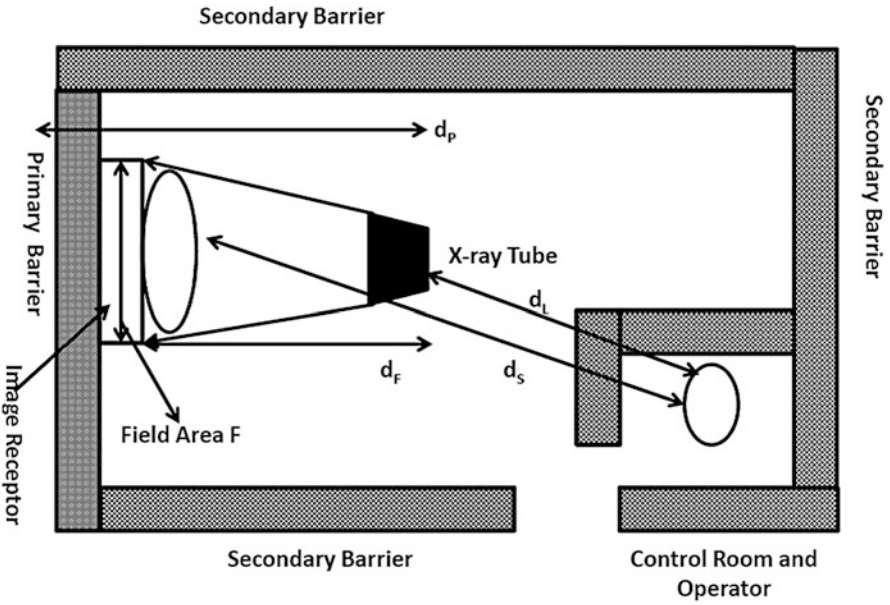

Fig. 13.17 Typical radiographic room

the measured KERMA at a detector and some known distance will be less than that with a barrier between the detector and the source. This is mathematically described in Eq. 13.30.

$$B(x) = \frac{K(x)}{K(0)} \tag{13.30}$$

These can be measured and fit to a solution called the Archer equation that uses three fit parameters. Solving this equation for thickness x, we get:

$$x = \frac{1}{\alpha\gamma} \ln\left[\frac{B^{-\gamma} + \frac{\beta}{\alpha}}{1 + \frac{\beta}{\alpha}}\right] \tag{13.31}$$

The specific fit values of a, b, and g are specific to the material being used as the barrier and cannot be listed here. Instead the report uses the transmission factor as parameter for evaluation, and tables in NCRP 147 give the thickness of the material needed to achieve the design goal. Equation 13.32 shows the calculation for the primary barrier:

$$B_{\text{primary}}\left(x_{\text{barrier}} + x_{\text{preshielding}}\right) = \frac{P}{T}\frac{d_P^2}{K_P^1 UN} \tag{13.32}$$

where

- B_{primary} – primary barrier transmission
- x_{barrier} – primary barrier thickness
- $x_{\text{preshielding}}$ – any attenuating thickness prior to the primary barrier
- P – shielding design goal
- T – occupancy factor
- D_{p} – distance to primary barrier
- $K^{1}{}_{\text{p}}$ – primary unshielded air kerma at 1 m per patient
- U – use factor
- N – number of patients

Secondary barriers are calculated using Eq. 13.33:

$$B_{\text{secondary}}(x_{\text{barrier}}) = \frac{P}{T}\frac{d^2_{\text{secondary}}}{K^1_{\text{sec}} N} \tag{13.33}$$

where

- B_{primary} – primary barrier transmission
- x_{barrier} – primary barrier thickness
- P – shielding design goal
- T – occupancy factor
- $K^{1}{}_{\text{sec}}$ – secondary unshielded air kerma at 1 m per patient
- N – number of patients
- $d_{\text{secondary}}$ – distance to secondary barrier

Values for several of these parameters require use of tables in NCRP 147. Common materials used for these barriers are lead, concrete, gypsum wall board, glass plated, steel, and wood. Of these lead is most commonly associated with diagnostic x-ray imaging.

13.6.1.2 NCRP 151 Methods

NCRP report 151 is focused on high-energy radiation beams although it shares many similarities to NCRP 147 in aspects discussed earlier. Once again the goal is to achieve sufficient shielding to reduce the exposure outside the room to the design goals which are the same as NCRP 147. Due to the nature of the higher energies (MeV vs. keV), several additional assumptions are made. These include, 30% attenuation of the primary beam by the patient, assumption of perpendicular distances to the primary barrier, leakage radiation assumed to be at maximum value, and conservative occupancy factors.

Calculation of the primary and secondary barriers is well defined based on the geometry of the radiation vault. In Fig. 13.18, the basic geometry is shown. Here the source to primary barrier is perpendicular to one another. The patient is in the beam path with secondary barriers being any wall that is not directly in the beam path. This means that any wall where the machine gantry rotates may be a primary

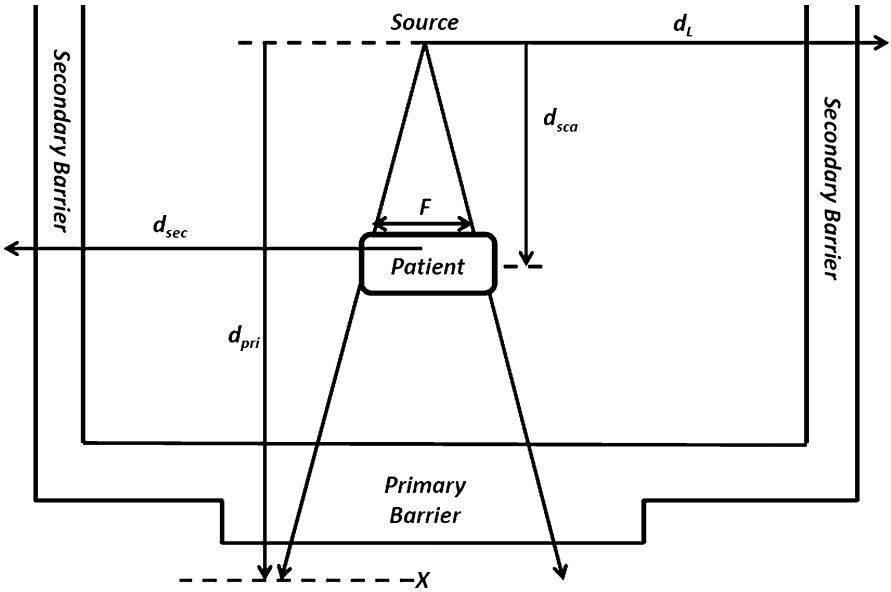

Fig. 13.18 NCRP 151 barrier thickness geometry

barrier. This includes the ceiling. Similar to diagnostic beams the patient is a source of scatter as is the leakage from the machine source housing. Unlike in NCRP 147 the leakage can be a large component of the secondary barrier transmission. This is a result of the fact that linear accelerators are high energy (4 MV–18 MV nominally). Note that in Fig. 13.18, the position x is the same as the reference position in NCRP 147 being 0.3 m from the wall as well as the same height, etc. It should be noted that linear accelerators may be run in photon and electron mode. Generally only the photon component is used in shielding calculations but as energy increases beyond 10 MV photon, neutrons may be produced. Consequently, addition of neutron shielding materials will need to be included. This usually involves the addition of borated polyethylene to the shield if concrete is not used (Fig. 13.18).

In Eq. 13.34 the calculation for the primary barrier is shown:

$$B_{\text{pri}} = \frac{P d_{\text{pri}}^2}{WUT} \tag{13.34}$$

where

- B_{pri} – transmission factor for primary barrier
- P – shielding design goal
- T – occupancy factor
- d_{pri} – distance to primary barrier
- U – use factor is the fraction of the workload directed to the primary barrier

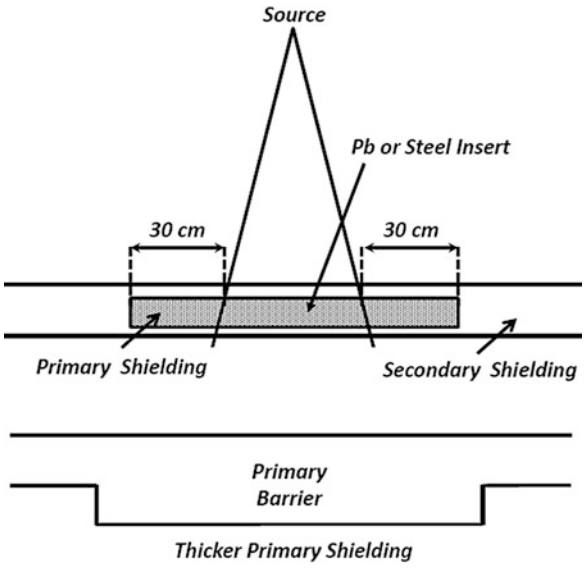

Fig. 13.19 Primary barrier design types

- W – workload or photon absorbed dose at 1 m from the target per week (Gy/wk)

To obtain the thickness from the transmission, one must use the data in the appendices of the NRCP 151 to obtain tenth value layers (TVL). A TVL is the thickness required to reduce the dose to one tenth its unshielded value. Then using this transmission factor the correct number of TVL is obtained by $n=-\log(B_{pri})$. Using n the total thickness fo the barrier is $t_{barrier}=TVL_1+(n-1)TVL_2$.

The primary barrier can be designed in several different ways. First the primary barrier may simply be a thickened wall that is 30 cm wider on each side of the maximum width of the treatment beam at the barrier wall. This is shown in Fig. 13.19 at the bottom of the figure. An alternate method may be to include a high-Z material inside of the primary barrier wall to further reduce the intensity of the beam as seen in the top of the same figure.

For secondary barriers two components are needed: the scatter from the patient and the leakage. Calculation of the secondary barrier is done using Eq. 13.35 and 13.36:

$$B_{sca} = \frac{P}{dWT} d_{sca}^2 d_{sec}^2 \frac{400}{F} \tag{13.35}$$

and

$$B_L = \frac{P d_L^2}{10^{-3} WT} \tag{13.36}$$

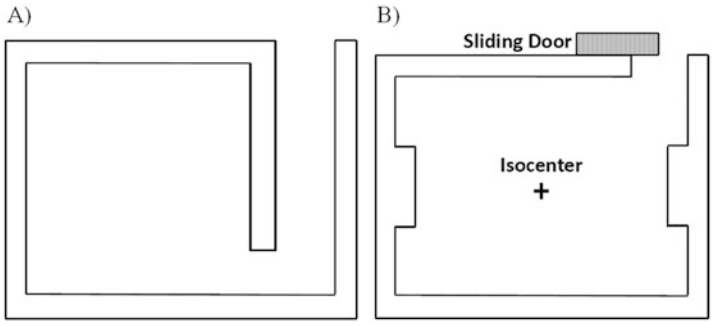

Fig. 13.20 (**a**) A maze design, (**b**) a maze less vault design

where

- d_{sca} – is the distance from the x-ray target to the patient
- d_{sec} – distance to the secondary barrier point
- a – scatter fraction: fraction of the beam that scatters to the secondary barrier
- F – size of field at midpoint of patient at isocenter (1 m)
- d_L – distance from source to secondary barrier

Determination of the thickness from the transmission values also requires review of the appendices in the report.

Additional computation is needed in the design of the vault. Two primary vault designs exist: maze and maze less. Each has their positive and negative aspects. Figure 13.20 shows these two designs. The maze design relies upon increasing the path through the vault that radiation may travel. It has the benefit of minimizing the amount of radiation shielding at the door. To do this does require more area for the vault to be built which can limit its application in some facilities. The mazeless design can be more compact and is appropriate in space limited situations. The major drawback is the size of the door needed to shield the room. These doors are very heavy requiring strong motors to move the system. Failure of these doors may increase risk to patients in the room. A hand crank mechanical device to open the door is always included in the design but does take time to open.

Construction of the vault should account for several factors including facility needs, future needs, location, and size of treatment room needed for the machine size. Thought should also go into workflow and storage needs. Plans for interlocks and the control console should also be well thought out prior to the project.

Common construction materials used in the linear accelerator shield projects include concrete (of varying densities), steel, rebar, and lead for photon components. Wood and earth are also often used although wood provides very little shielding. Earth is used for economic reasons, and it can be a logistic boon. For example, if the facility were built into the side of a hill and the vault location were adjacent to the hill, one of the barriers could use the thickness of the hill as shielding, thus saving costs of other shielding materials. Shielding materials for

neutron components include polyethylene and paraffin. Other consideration for construction of the vaults is unfortunately beyond the scope of this chapter. Review of the report in full is encouraged for complete details.

Additional Reading

Attix FH (2004) Introduction to radiological physics and radiation dosimetry. Wiley-VCH Verlag GmbH & Co. KGaA, Weinheim, Germany

Cember H (2008) Introduction to health physics, 4th edn. Thomas Johnson Publisher: McGraw-Hill Medical. ISBN-13: 978–0071423083

Martin JE (2013) Physics for radiation protection, 3rd edn. Wiley-VCH. ISBN-13: 978–3527411764

Nahum A (2007) Principles and basic concepts in radiation dosimetry. In: Mayles P, Nahum A, Rosenwald JC (eds) Handbook of radiotherapy physics: theory and practice. CRC Press, pp. 89–114

Orabi M (2017) Radon release and its simulated effect on radiation doses. Health Phys 112 (3):294–299

Podgorsak EB (2005) External photon beams: physical aspects. In: Podgorsak EB (ed) Radiation oncology physics: a handbook for teachers and students. International Atomic Energy Agency (IAEA), Vienna, pp 161–217

Stabin MG (2007) Radiation protection and dosimetry: an introduction to health physics. Springer Science & Business Media, pp. 67–74

United States Nuclear Regulatory Commission: NUREG-1556 Vol-9 Rev 2: Consolidated Guidance About Materials Licenses Program-Specific Guidance About Medical Use Licenses, Final Report, Published: January 2008; Prepared by D.B. Howe, M. Beardsley, S. Bakhsh, Office of Federal and State Materials and Environmental Management Programs

Chapter 14
Radiation Shielding and Protection, Part II

Jianqiao Luo

Contents

14.1 Medical Radiation Safety 403
14.2 Radiation Safety Committee and Radiation Safety Officer 405
14.3 Authorized Users of Radioactive Materials 407
14.4 Occupational Dose Limits and Monitoring 408
14.5 Pregnant Policy and Procedures to Protect Pregnant Workers 409
14.6 Area Contamination Survey and Spill of Radioactive Materials 410
14.7 Receipt, Transfer, and Disposal of Radioactive Materials 412
14.8 Radiotherapy Procedures 412
References 416

14.1 Medical Radiation Safety

The medical radiation safety program is a subset of the overall radiation protection. Major source of radiation in the medical facilities are from radioactive decay of various radionuclides, from X-ray-generating machines, and from particle accelerators for radiation therapy. And patients have been administered radioactive material for diagnostic or therapeutic purposes. Those sources of radiation could be sealed source (e.g., Co-57 flood for gamma camera QC), unsealed sources (e.g., radiopharmaceuticals in nuclear medicine), X-rays produced from CT or fluoroscopy units, and particle beams for therapy in radiation oncology. Another source of radiation is from patients who have taken radiopharmaceuticals by injection or other methods of administration in nuclear medicine or implanted with sealed sources in radiation oncology (radioactive I-125, Pd-103 implants). The goal of the radiation safety program in medical facility is to manage staff exposure as low as reasonably achievable (ALARA), to minimize patient exposure, to protect general public, and to prevent radioactive waste from contaminating environment.

J. Luo, PhD (✉)
Department of Radiology, Virginia Commonwealth University, Richmond, VA, USA
e-mail: Jianqiao.Luo@vcuhealth.org

M. Maqbool (ed.), *An Introduction to Medical Physics*, Biological and Medical Physics, Biomedical Engineering, DOI 10.1007/978-3-319-61540-0_14

Several scientific organizations conducted research and data analysis of radiation effects on the human body. The National Academy of Sciences Committee on the Biological Effects of Ionizing Radiation (BEIR) published report on Health Effects of Exposure to Low Levels of Ionizing Radiation. United Nations Scientific Committee on the Effects of Atomic Radiation (UNSCEAR) also produced many reports on effects and risks of ionizing radiation. International Commission on Radiological Protection (ICRP) and National Council on Radiation Protection and Measurements (NCRP) are the organizations to provide recommendations based on the scientific research.

Nuclear Regulatory Commission (NRC) is a federal agency to enforce regulations for radiation protection. It delegates the authority to states that agreed to take the responsibility at state level (agreement states) to provide oversight of radiation safety programs. Majority of the 50 states within the USA have been the agreement states.

The NRC maintains regulatory guidelines in the form of Code of Federal Regulations. Among those regulatory documents, 10 CFR 20, Standards for Protection Against Radiation, and 10 CFR 35, Medical Use of By-product Material, are the basis for medical facilities. All agreement states adopted the NRC regulations and may install additional components to meet with the need of each individual state.

NRC/agreement state issues a radioactive material license to a medical facility. The license could be in one of the following: limited scope or broad scope. Furthermore, the broad scope license can be in type A, B, or C per 10 CFR 33.11. In general, the limited scope license is issued to physicians and clinics to perform some specific clinical procedures specified in the license. The broad scope license is normally for large hospitals and clinics to perform many kinds of clinical procedures, to develop new protocols, and to support research projects. It is required that a broad license holder must have a radiation safety committee and appoint a radiation safety officer to enforce radiation safety regulations.

In a medical facility, the Radiation Safety Program is administered by the Radiation Safety Committee (RSC), with technical support of the Radiation Safety Officer (RSO) and the Radiation Safety Office/Physics staff. Many RSOs are medical physicists and/or health physicists. Some RSOs are physicians or technologists. The RSOs are appointed by senior management of the medical facility and must be approved by the NRC or the agreement state.

In every medical facility where hazardous materials are utilized, it is necessary to maintain a radiation safety policy document which establishes specific methods and procedures to develop and maintain safety and compliance. Safety is the practice of a set of rules, guidelines, and procedures which protect workers, facilities, the general public, and the environment. Compliance is the maintenance of procedures, practices, documents, and records which demonstrate that federal, state, and local laws and regulations are not compromised. It is a necessary challenge for all users of radioactive materials and X-ray-generating machines to maintain safety and compliance. In clinical departments, laboratory, and research

facilities, the challenge is accentuated with the myriad of procedures and materials utilized and the continuous change and evolution of these conditions.

Example 14.1 Can a license holder develop local policy and procedures that deviate from NRC/agreement state regulations for their routine practice?

Answer No. The licensee must maintain full compliance with the regulations. However, the license holder can develop some local policy and procedures to implement the regulations and recommendations from the regulatory agency.

14.2 Radiation Safety Committee and Radiation Safety Officer

The general responsibilities of the RSC are to ensure that all individuals who work with or in the vicinity of radioactive materials (RAM) have sufficient training and experience to enable them to perform their duties safely and in accordance with NRC/agreement state regulations and the conditions of the radioactive materials license.

The RSC provides administrative and technical oversight over the use of radioactive materials at the medical institution. Those radioactive materials are by-products of nuclear reactors and the products of particle accelerator (e.g., cyclotron) as well. The oversight extends to the use of machine-generated radiation for diagnostic imaging, therapeutic procedures, and research purposes. This includes the use of X-ray, fluoroscopy, CT, and accelerators. Practically, a hospital RSC may be charged to oversight laser safety, MRI safety, etc., although those are not ionizing radiation equipment.

The RSC membership normally includes a RSC chairperson who is a physician in the field of radiation; the RSO, a management representative; nursing representative; and experts (physician, medical physicist) from radiation oncology, radiology, nuclear medicine, and divisions using radioactive materials or X-ray machines. Patient safety and dose reduction in X-ray imaging procedures have attracted great attention from lawmakers, regulatory agencies, and industry and clinical users of the X-ray equipment nationwide. It is also an important area where RSC and RSO are deeply involved to establish programs for radiation protection.

Specific duties of the RSC include:

Implementing all pertinent NRC regulations, the terms of the materials license, and documents submitted in support of the request for the materials license and its amendments. All RSC actions and decisions made by the committee must agree with the license condition.

Reviewing the training and experience of all individuals who use RAM (including physicians, other practitioners, technologists, physicists, and pharmacists) to determine that their qualifications are sufficient to enable them to perform

their duties safely and in accordance with NRC regulations and the conditions of the materials license.

Establishing a program to ensure that all individuals whose duties may require them to work in the vicinity of RAM and X-ray machines (e.g., nursing, police and security, and environmental management service).

Reviewing and approving all requests for the use of RAM within the institution.

Prescribing special conditions that will be required during a proposed use of RAM such as requirements for bioassays, physical examinations of users, and special monitoring procedures.

Reviewing the radiation safety program at least annually to determine that all activities are being conducted safely and in accordance with NRC regulations and the conditions of the material license. The review includes an examination of all records, reports from the RSO, results of NRC inspections, written safety procedures, and the adequacy of the medical facility's radiation protection program.

Recommending remedial action to correct any deficiencies identified in the radiation safety program.

Maintaining written records of all RSC meetings, actions, recommendations, and decisions.

Ensuring that the materials license is amended, when necessary, prior to any changes in facilities, equipment, policies, procedures, and personnel as specified in the materials license.

The RSC conducts quarterly meeting under normal conditions or as often as necessary to handle all issues in radiation safety.

The RSO is appointed by the president of the medical center and approved by a regulatory agency who issues radioactive material license to the institution. NRC sets up qualification requirements for an individual to be qualified as RSO in 10 CFR 35.50 Training for a Radiation Safety Officer. AAPM published guidelines (Report of AAPM Task Group 160, November 2010) for the RSO qualification. The requirements for a radiation safety officer also depend on the type of license and types of materials used. The RSO oversees the medical center's radiation safety program.

Example 14.2 How frequent a radiation safety committee must meet to manage the issues related to hospital radiation safety? Who must attend such meeting?

Answer The radiation safety committee must meet at least four times a calendar year. Key members of the committee including RSC chairperson, RSO, management representative, and nursing representative must attend the meetings.

14.3 Authorized Users of Radioactive Materials

In order to have only the qualified individuals to handle the radioactive materials in clinical procedures and research projects, the RSC or a regulatory agency approves the users per NRC guidelines to be authorized in a specific field, for example, physicians in radiation oncology, nuclear medicine, and radiology and medical physicists in radiation oncology and other divisions conducting radiation therapy procedures. For research groups, principle investigators are normally approved as the authorized users to use radioactive materials in human and nonhuman subjects as well. Responsibilities of the authorized users are:

Comply with medical center's radiation safety policy.
Ensure that personnel under their supervision comply with the rules and regulations governing the use of RAM.
Ensure that employees are instructed in the use of safety devices, personal protective equipment, and procedures.
Conduct and record appropriate radiation surveys as necessary to ensure a safe working environment.
Maintain current authorization, RAM inventory, and disposal records.
Notify the RSO of any changes in operational procedures or facilities which might lead to increased personnel exposure or contamination levels in the laboratory or the surrounding areas.
Upon termination of employment or RAM use at the medical center, account for and dispose of all RAMs and arrange for a final survey by the RSO. The RSO should be notified no less than 30 days before vacating the premises. If the premises have been contaminated with RAM, the user shall be responsible for decontaminating the area to a level which would permit its use as an unrestricted area.
Notify the RSO prior to any disposal of any equipment containing radioactive sources.

Example 14.3 In a medical center with limited scope license, the RSC and RSO can approve a board-certified radiation oncologist to an authorized user without approval from regulatory agency who issued the license.

Answer No. The RSC/RSO will review the credential of the candidate for the authorized user, then submit request to the regulatory agency for approval. While a broad license holder can authorize qualified individual to be the authorized user following the guidelines from the regulatory agency.

14.4 Occupational Dose Limits and Monitoring

NRC sets up maximum absorbed dose from annual radiation exposure for radiation workers based on research data provided by professional organizations. Those limits do not apply to patients. Medical exposures received as a patient and/or family members are not occupational exposures and are, therefore, excluded from the NRC limits. The patients' radiation dose is evaluated for both treatment and protection. The use of any radiation (radioactive materials or external beams) in diagnostic procedures and radiation therapy is based on a factor of risk and benefit.

Exposure from occupational sources of radiation should be kept below the following annual limits specified in 10 CFR 20.1201:

(a) The more limiting of a total effective dose equivalent equal to 5 rem or the sum of the deep-dose equivalent and the committed dose equivalent to any individual organ or tissue (except the lens of the eye) equal to 50 rem
(b) A lens dose equivalent of 15 rem
(c) A shallow-dose equivalent of 50 rem to the skin of the whole body or to the skin of any extremity

The medical center, in accordance with its program for maintaining occupational radiation exposures as low as reasonably achievable (ALARA), has established exposure action levels which when exceeded will trigger investigation by RSO and RSC. The specific action levels established by many institutions are as ALARA Level I and Level II.

Table 14.1 provides data about dose equivalent per quarter corresponding to exposed volume.

Radiation dosimeters are utilized to monitor personnel exposures. The Radiation Safety Office staff is responsible for issuing dosimeters to radiation workers who may be exposed to radiation levels that will result in a total body exposure dose exceeding 10% of the maximum allowable annual limit of 5000 mrem. Dosimeters are also issued for other conditions as determined by the Radiation Safety Office.

Optically stimulated luminescence dosimeters (OSL badges) are used to assess total body, eye (lens), and shallow (skin) exposures. Thermoluminescent dosimeters (TLD or ring badges) are used to monitor hand exposures. The dosimeters are collected each month (or quarter) by RSO and returned to the dosimetry company for processing. The dosimetry company provides monthly exposure reports for each separate group of workers in the hospital. The reports are reviewed by the RSO and kept on file in the Radiation Safety Office. Individual radiation workers who exceed

Table 14.1 Exposed volume and corresponding dose equivalent per quarter

Exposed volume	Dose equivalent (mrem) per quarter	
	Level I	Level II
Whole body (Level I is 10% of NRC limit)	125	375
Lens of eyes	375	1125
Skin and extremities	1875	5625

specific exposure trigger levels are identified and notified depending on the level of exposure. The dosimeter badges have a minimum reporting dose of 1 mrem for X- and gamma rays and 10 mrem for beta particles. Ring dosimeters have a minimum reporting dose of 30 mrem for X- and gamma rays and 40 mrem for beta particles. Whole body dosimeters and ring badges are also distributed to individuals in the research groups who work with gamma and high-energy beta emitters.

In vivo bioassays (thyroid counts using an uptake probe) are required at quarterly intervals or after a high-dose radionuclide therapy if I-125 or I-131 are used in levels which exceed the amounts listed in NRC regulation. This is to monitor internal contamination from handling those radioactive materials.

Permanent records of personnel exposures are maintained by the RSO. Any employee can review and discuss his/her radiation exposure records with the RSO. The RSO will review employee records annually to determine the need for the continued use of monitoring devices. Each radiation worker is responsible to wear badges at all times when working with sources of ionizing radiation at the medical center.

Example 14.4 If a radiation worker received 100 mrem in August, 50 mrem in September, and 200 mrem deep dose in October, respectively, RSO must report to NRC or agreement state.

Answer No. Sum of the exposures from the quarter is 350 mrem which is less than ALARA II. There is no need to report. Only when quarterly exposure excessed ALARA II (375 mrem). The RSO should investigate the cause of the exposure and report to the RSC. The RSC/RSO may recommend certain steps to reduce the personnel exposure.

14.5 Pregnant Policy and Procedures to Protect Pregnant Workers

Pregnant workers should meet with the RSO as early as possible in the pregnancy to determine if modifications of duties are necessary to insure that fetal exposure will not exceed 500 mrem over the course of the pregnancy. An employee declaration of pregnancy may be signed at that time. If one plans to become pregnant or is pregnant, the individual has several choices regarding declaration of pregnancy. One may (a) decide to keep her pregnancy confidential or (b) inform her supervisor and RSO and formally declare her pregnancy in writing. Before the declaration of pregnancy is made in writing, the individual will be treated as nonpregnant worker regardless the fact if she is actually pregnant or not. The choice whether to declare her pregnancy is completely voluntary. One has the option of formally declaring her pregnancy. If she does so, actions will be taken to limit the dose to the embryo/fetus to 500 mrem during the entire pregnancy. The declaration remains in effect until the declared pregnant woman withdraws the declaration in writing or is no longer

pregnant. After a written declaration is filed, instruction will be provided and may include limitation of normal job functions if they could cause the individual to receive more than 500 mrem.

Example 14.5 RSO and supervisor must take action (e.g., relocate the radiation worker to an office far away from radiation area) to protect a female employee if she is pregnant, she appears pregnant, and her co-worker reports that she is pregnant.

Answer No. Only when the radiation worker declares her pregnancy in writing to the supervisor and the RSO will she be treated as a pregnant worker. Then depending on the nature of her work, she may or may not change job assignment. However, the management and RSO should make every effort to provide necessary information regarding to radiation safety policy and procedure for pregnant workers.

14.6 Area Contamination Survey and Spill of Radioactive Materials

In a hospital, nuclear medicine and radiation oncology are major users of the radioactive materials, while radiology along with cardiology cath lab, surgery, and other divisions, where fluoroscopy systems are used, are primary users of radiation-generating machines. There are X-ray machines introduced into nuclear medicine (SPECT/CT, PET/CT) and radiation oncology. Also many other divisions within the hospital may use radioactive materials and/or radiation-generating machines.

Any laboratory or room containing radioactive material shall be designated as a restricted area. All individuals working in or spending significant amount of time in any restricted area should receive training in radiation safety precautions associated with exposure to machine-generated radiation or radioactive materials. As a general practice, work with radioactive materials should be confined to the restricted area necessary to carry out the procedure. This simplifies the problem of confinement and shielding and aids in limiting the affected area in case of a spill. All radioactive materials shall be secured against unauthorized removal: any laboratory in which the radioactive materials are stored will be locked when not attended by laboratory personnel. If the room cannot be locked or radioactive materials are stored outside the laboratory, the radioactive materials must be stored in a lockable device which cannot be readily moved.

An area in which the general public has free access and for which there is no control over public traffic, e.g., a corridor, shall be designated as an unrestricted area. Radiation levels in unrestricted areas must be kept below both: (a) 2 mR in any 1-h period (not 2 mR per hour) and (b) a total effective dose equivalent to an individual member of the general public of 100 mrem per year. Each user of the radioactive materials is responsible for performing surveys of the restricted areas to

assure that radiation sources are adequately shielded and to check for any possible radioactive contamination. It is also necessary to perform such survey for some unrestricted areas for possible radioactive contamination. Those routine surveys consist of a measurement of radiation exposure levels with a survey meter sufficiently sensitive to detect 0.1 mR/h (a GM counter is normally used) and a series of wipe tests to measure removable contamination levels. The device for performing the wipe tests will be sufficiently sensitive to detect 200 dpm per 100 square centimeter for the contaminant involved. NaI (Tl) well counter is commonly used for the wipe tests. The area survey with a GM counter is normally used to detect gamma photons. However, the GM detector is not able to locate contamination with low-energy bate or other particles. Thus, the wipe test can be applied to detect such radiation.

It is the responsibility of the user to post appropriate caution signs in all areas and on all containers where significant amounts of radiation or radioactive materials may be found. The signs and labels used must describe the actual situation. For example, do not use a Caution Radiation Area sign unless it really is a radiation area. All radiation signs or labels must be removed when the reason for posting no longer exists. Prior to disposal of any empty uncontaminated container into the regular trash, the labels of radioactive material must be removed or defaced.

Radioactive spills range from minor spills of radioactivity involving essentially no significant hazard to major radiation incidents involving extreme hazards. Because of the wide range and variety of hazards and the numerous possible complicating factors, specific rules of emergency procedures cannot be made to cover all situations. In any emergency, however, the primary concern must always be the protection of personnel from radiation contamination. If radioactive contamination is involved, all persons who were in the area at the time of the incident must be surveyed and checked for possible contamination. Next concern is confinement of contamination to the local area of the accident to avoid spreading out the radioactivity to a wider area. Cleanup of the radioactive contamination has to follow spill procedure specified in radiation safety policy and procedure manual of the institution. A medical physicist may supervise the procedure, and the RSO is normally notified. The radioactive spills in a medical facility are most likely minor. However, personnel injury, wide area contamination, and loss of radioactive material need to be reported to RSO immediately.

Example 14.6 A technologist holed a survey meter in a hallway next to PET/CT scanner room and found the meter reading fluctuated around 18 mR/h for about 10 min and then the reading dropped to 0.3 mR/h. Should the hallway be treated as a restricted area?

Answer Not necessarily true. Since the limit for unrestricted area is 2 mR in any 1 hour not per hour, the reading may not be any overexposure. It could be from a patient injected with radiopharmaceutical for imaging. However, it is a good practice to do a follow-up survey.

14.7 Receipt, Transfer, and Disposal of Radioactive Materials

Any radioactive drug or radiopharmaceutical is ordered by a licensed user from licensed radiopharmaceutical providers. The user of radioactive material must ensure that possession limits specified in the license are not exceeded. Authorized personnel (normally radiation safety office staff or nuclear medicine technologists) receive packages, perform contamination survey, open the package, and maintain records. The package is kept in a nuclear medicine hot lab. Hospital security personnel are notified and escort the delivery of shipments during off-duty hours according to the instructions of radiation safety policy for receipt of radioactive shipments.

DOT (Department of Transportation) and NRC established guidelines and specific requirements for shipping and receiving radioactive materials. Disposal of radioactive waste is governed by strict federal and state regulations. The method of waste disposal must be specified for each use of radioactive materials. Each authorized user is responsible for ensuring that employees under his/her supervision understand and follow the procedures for disposal of radioactive waste.

14.8 Radiotherapy Procedures

An important part of radiation safety is the protection of staff, patients, and general public in radiotherapy procedures. The therapy procedures include therapeutic use of radiopharmaceuticals (radionuclide treatment) and therapeutic use of sealed sources (radioactive seeds implant).

The radiotherapy procedures normally involve beta emitter or a combination of the beta and gamma emitter. In some cases, alpha particles or protons, even neutrons, may be used to deliver significant amount of radiation dose to the target. While in imaging procedures, low-energy X-ray or gamma emitters are used to produce images for diagnostic purposes. Patient exposure is much lower in diagnostic imaging than in therapeutic procedures. In radionuclide therapy, patients are radioactive for a certain period of time even the procedure is completed. For example, I-131 has been used to treat thyroid cancer. When the I-131 is taken by a patient, the radiation exposure from the patient may stay for days or even months since the effective half-life is normally in order of days. Here the effective half-life is determined by the physical half-life (8.2 days) and biological half-life depending on the patient body excretion or clearance. Therefore, it is necessary to protect the patient by increasing the biological clearance and to reduce exposure to staff, family members, and general public applying the principle of time, distance, and shielding. Regulatory agency (NRC, agreement state) sets up specific guidelines for those therapy procedures.

Example 14.8 A patient received 150 mCi of I-131 pill for cancer treatment. If the patient would have to stay in hospital, what are the major steps of radiation safety procedures?

Answer The following are the major steps of radiation safety procedures:

1. The patient will be placed in a private room that has a toilet. The patient's room will be properly posted or attended in accordance with 10 CFR Part 20 Subpart J. Some surfaces in the room and toilet areas that are more likely to be contaminated will be covered with absorbent pads or protective sheet.
2. Radiation safety staff or medical physicist will survey the room and surrounding areas, and surveys of the patient's room and surrounding areas will be conducted as soon as practical after administration of the treatment dose. Measure exposure at the patient's bedside, 3 feet from the patient after administration, and at the entrance to the room. The RSO will then determine how long a person may remain at these positions and will post these times in the patient's chart and on his/her door. The results of daily surveys will be used to recalculate the permitted times, and the postings will be updated accordingly. Radiation exposure in unrestricted areas will be maintained below the limits specified in 10 CFR 20.1301 (2 mrem in any 1 h and 0.1 rem a year).
3. RSO or medical physicist will provide a nursing instruction to patient care team.
4. All linens will be surveyed for contamination before being removed from the patient's room and, if necessary, will be held for decay. Disposable items will be placed in a specially designated container, then be checked by the RSO or medical physicist for possible contamination, and disposed of appropriately.
5. Before the therapy patient's room is released to the nursing staff, the room will be surveyed for contamination and decontaminated by the RSO if necessary. All radioactive waste and waste containers will be removed by the RSO.
6. The patient cannot be discharged until his/her exposure is below 5 mrem/h at 1 m. The RSO or medical physicist will discharge the patient based on the survey. In many cases of I-131 radionuclide therapy today, the patient is released from treatment facility right after the therapy procedure. In that situation, the medical facility is responsible to provide instruction to the patient family to follow necessary safety precautions to protect the family members and the general public. The instruction is based on an estimate of radiation exposure from the patient.

While for therapeutic use of sealed sources, for example, I-125 seed implant to prostate, similar radiation safety procedures are installed. However, the seeds are low-energy beta emitters. When the seeds are in the patient's body, the exposure is low compared with I-131 which emits over 360 keV gamma rays. The patient is normally released after an exposure survey.

Questions

1. What is the major difference between a professional organization like ICRP and a regulatory agency like NRC in radiation protection?
2. Can a RSO be assigned RSC chairperson in a hospital?
3. What is the purpose of authorizing someone to be the user of radioactive materials?

   When an authorized user physician performs a clinical procedure involving radioactive materials with a supporting team including nurses and technologists, does he/she need to provide necessary training and supervision to the team members to ensure the compliance with regulatory codes?
4. A patient is a nuclear physicist. After going through a nuclear cardiac scan, he found the radiopharmaceutical injected to his body would make his absorbed dose higher than the ALARA II level. Is this a violation of NRC's rule? Is it needed for RSC/RSO to investigate since it is over ALARA II?
5. A nuclear medicine technologist declared her pregnancy in writing to her supervisor and RSO. Her exposure record showed that her average monthly deep dose was 25 mrem. Should the RSO recommend to the supervisor to change the pregnant worker's duty to avoid any radiation?
6. A medical physicist surveyed a patient with I-125 (X-ray energy is about 25 keV) prostate seed implant using a GM survey meter. The GM counter was calibrated with Cs-137, and energy response curve demonstrated a 75% decrease in terms of detection efficiency compared with energy higher than 70 keV. Can the physicist take the survey meter reading and put it in the record?
7. A research lab received a shipping box. They noticed that there was some leakage of certain liquid to the inner surface of the box. A GM survey meter did not detect any radiation exposure. What are the necessary steps they have to follow to identify the possible contamination and to ensure being in compliance of radiation safety policy?
8. NRC established a guideline about medical event in the federal code (10 CFR 35.3045 – Report and Notification of a Medical Event).

   A licensee shall report any event, except for an event that results from patient intervention, in which the administration of by-product material or radiation from by-product material results in:

   (a) A dose that differs from the prescribed dose or dose that would have resulted from the prescribed dosage by more than 0.05 Sv (5 rem) effective dose equivalent, 0.5 Sv (50 rem) to an organ or tissue, or 0.5 Sv (50 rem) shallow-dose equivalent to the skin.
   (b) The total dose delivered differs from the prescribed dose by 20% or more.
   (c) The total dosage delivered differs from the prescribed dosage by 20% or more or falls outside the prescribed dosage range.
   (d) The fractionated dose delivered differs from the prescribed dose, for a single fraction, by 50% or more.

9. A nuclear medicine technologist injected 20 mCi Tc-99 m MDP instead of 30 mCi Tc-99 m MIBI prescribed by doctor. The patient received 150 mrem whole body dose equivalent. Should this incident be reported to regulatory agency as a medical event?

Key

Diagnostic procedures	Imaging procedure for diagnosis of certain disease. It normally involves small amount of radiation.
Therapy procedures	Using radioactive material and/or machine-generated radiation to treat cancer or other disease. It normally involves large amount of radiation.
RSC	A committee appointed by senior management to manage all aspects of radiation safety in a medical institution.
RSO	An individual who meets NRC qualification requirements and is appointed by the president of the medical institution to provide oversight of the radiation program and overall operation related to radiation.
Authorized user	Qualified users of radioactive material or machine-generated radiation to perform clinical or research procedures in a medical institution.
Occupational dose	Radiation dose received by radiation workers from performing their duties at work.
ALARA	As low as reasonably achievable is a principle for radiation protection based on the fact that there is no threshold to cause damage from radiation exposure, and any effort to control radiation depends on technology and economical resource.
Dosimeter	Radiation detectors to measure amount of radioactivity.
Declaration of pregnancy	Notification of pregnancy from an individual to supervisor and RSO.
Area survey	Contamination survey in an area to identify possible radiation exposure from contamination of radioactive materials.
Wipe test	Contamination survey in an area to identify possible removable contamination of radioactive materials.
Spill	Radiation incident due to unexpected drop of radioactive fluid to floor or other area.
Beta emitter	Decay of radio isotopes to produce emission of beta rays.
Radionuclide therapy	Using radionuclides for therapy purposes.
Medical event	Radiation incident defined in 10 CFR 35.3045.

References

Cember H (2008) Introduction to health physics, 4th edn. Thomas Johnson Publisher: McGraw-Hill Medical. Chicago ISBN-13: 978-0071423083

Martin JE (2013) Physics for radiation protection, 3rd edn. Wiley-VCH. Chicago ISBN-13: 978-3527411764

United States Nuclear Regulatory Commission (2008) NUREG-1556 Vol-9 Rev 2: consolidated guidance about materials licenses program-specific guidance about medical use licenses. Final Report, Published: January 2008; Prepared by D.B. Howe, M. Beardsley, S. Bakhsh, Office of Federal and State Materials and Environmental Management Programs

United States Nuclear Regulatory Commission (2014) 10 CFR part 20—standards for protection against radiation

United States Nuclear Regulatory Commission (2014) 10 CFR part 35—medical use of byproduct material

Erratum to: An Introduction to Medical Physics

Muhammad Maqbool

Erratum to:
M. Maqbool (ed.), *An Introduction to Medical Physics*, Biological and Medical Physics, Biomedical Engineering, https://doi.org/10.1007/978-3-319-61540-0

The name of the editor was printed incorrectly (Muhammed Maqbool) in the previous version. The correct name of the Author is Muhammad Maqbool.

The updated online version of this book can be found at
https://doi.org/10.1007/978-3-319-61540-0

M. Maqbool (ed.), *An Introduction to Medical Physics*, Biological and Medical Physics, Biomedical Engineering, https://doi.org/10.1007/978-3-319-61540-0_15